Author:
Mahoney, Ed J D

Title:
Alternative Excitation Mechanisms Occurring within Microwave-activated Plasmas under Conditions Relevant to the Chemical Vapour Deposition of Diamond

Alternative Excitation Mechanisms Occurring within Microwave-activated Plasmas under Conditions Relevant to the Chemical Vapour Deposition of Diamond

By

Edward J. D. Mahoney

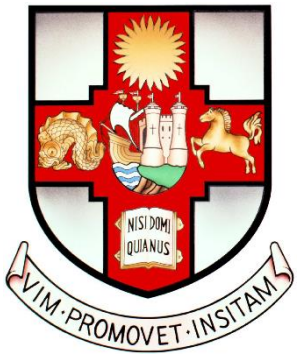

School of Chemistry

University of BRISTOL

A thesis submitted to the University of Bristol in accordance with the requirements for the award of the degree of **DOCTOR OF PHILOSOPHY** in the Faculty of Science.

May 2019

Word count: 71,937

Abstract

Optical diagnostic techniques are employed to investigate a range of microwave-activated (MW-activated) plasmas under conditions that are relevant to the synthesis of diamond via the chemical vapour deposition (CVD) process. In particular, spatially-resolved optical emission spectroscopy has been implemented to monitor a number of emitting species present within MW-activated H, H/Ar, C/H, C/H/Ar, Si/H, Si/H/Ar, and Si/C/H plasmas. Cavity ring down spectroscopy is implemented to measure the column densities of various spin-orbit states belonging to the Si atom triplet ground state within MW-activated Si/H and Si/C/H plasmas. The understanding behind many of the results presented in this thesis has been developed by self-consistent 2-D plasma modelling carried out by collaborator Yuri Mankelevich.

The first two introductory chapters develop a motivation for the interest in diamond grown via CVD, whilst providing a summary understanding of the prominent chemical and physical gas phase processes that occur within MW-activated C/H plasmas. These chapters develop a feel for some of the open questions within the field and provide an overview of the experimental techniques that (i) have previously been implemented and (ii) are implemented within this thesis.

Chapter 3 investigates MW-activated H and H/Ar plasmas under conditions relevant to hydrogen-termination and etching of diamond. The investigations focus on spatially-resolved emissions originating from the high energy states of H_2, H and Ar as a function of plasma operating conditions (pressure, forward MW power, gas content, and two relatively unexplored parameter spaces, substrate diameter and temperature). The findings develop a new probe that is sensitive to the hyper-thermal component of the electron energy distribution function (EEDF) and have also been used to develop the first self-consistent 2-D physical chemical kinetic model of moderate pressure MW-activated H plasmas. A deeper understanding underpinning the interdependencies of plasma parameters and gas phase processes is demonstrated, highlighting an intimate coupling between excited states of H (and H_2) with ground state H_2 (and H) respectively.

The second results chapter, Chapter 4, demonstrates the first direct evidence for the existence of charged species within MW-activated C/H (and C/H/Ar) plasmas by monitoring optical emissions from the C_2^- anion through the $C_2^-(B\rightarrow X)(0\text{-}0)$ transition, which is embedded within the high J tail of the $C_2(d\rightarrow a)$, $\Delta v = -1$ emission. The variation of these emissions with process conditions are compared to predictions made by an appropriately developed 2-D physical chemical kinetic plasma modelling, establishing the prominent formation mechanisms of various C_2 and C_2^- states. There is also an attempt to monitor emissions originating from the $CH^+(A\rightarrow X)$ transition, however this is unfruitful.

Chapter 5 focusses on spatially-resolved emissions originating from the three lowest lying excited doublet states of the CH radical (i.e. $CH(A\rightarrow X)$, $CH(B\rightarrow X)$ and $CH(C\rightarrow X)$) generated within MW-

activated C/H plasmas. These emissions are investigated as a function of process conditions in an attempt to probe the thermal component of the EEDF. The assumption that these emitting states are only produced through electron impact excitation is drawn into question by 2-D plasma modelling. In order to describe the full set of experimental observations, there is a requirement for a significant chemiluminescent contribution towards the production of lower-lying excited states belonging to the CH radical.

Chapter 6, the fourth and final results chapter, combines optical emission studies carried out on Si-related species (singlet and triplet states of atomic Si, and the (A→X) transition of SiH radical) in MW-activated Si/H, Si/H/Ar, and Si/C/H plasmas. Si has been introduced into the gas phase through dilute silane and by etching a Si substrate. Cavity ring down spectroscopy was also implemented for column density measurements on Si atoms. This work speculates on the prominent gas phase processes occurring within such plasma systems.

Chapter 7 provides a summary of the key questions addressed within this thesis, as well as a brief description of the more important findings. Chapter 7 also discusses relevant further work that could help reinforce and further the understanding developed in this work.

Acknowledgements

I have worked on numerous projects in my three and a half years at The University of Bristol. Many of which feature to some extent within this thesis. Consequently, I have worked with a number of people who I'd like to thank from the Bristol Laser and Molecular Dynamics Group and the Bristol Diamond Group.

First and foremost, I would like to take this opportunity to thank Professor Mike Ashfold. Thank you Mike, for your continuous positive energy, patience, support, guidance, encouragement, enthusiasm, wisdom, optimism, friendship and sense of humour – while I'm sure I have driven you mad at times and contributed to your more recent white hairs, you have always managed to maintain a calm, collected and thoughtful attitude, which I very much admire. It has been an honour to work with you, and I cannot thank you enough. You are an inspiration and an excellent role model.

Secondly, I would like to thank Dr. Yuri Mankelevich for all his enthusiasm and modelling contributions. Without your invaluable contributions, many of the experimental results presented in this thesis would have been uninterpretable. Thank you.

I would like to extend major gratitude and thanks to Dr. Ben Truscott for his daily morals, continued support and friendship, for the encouragement of me to acknowledge my strengths and my weaknesses, for teaching me how to set up and carry out spatially-resolved Optical Emission Spectroscopy and encouraging me to take pride in experimental results by achieving the highest possible standard. That same gratitude and thanks extends to Dr. James Smith for his friendship, joyful presence, support, and for teaching me how to align lasers in setting up the Cavity Ring Down Spectroscopy experiment.

I would also like to thank: Dr. Colin Western for his wisdom on the spectroscopy of the hydrogen molecule, his development of the spectral simulation package, PGOPHER, and for his advice and interest, whilst keeping an eye on my progress; Dr. Alex (E.) Croot for his expert guidance on leak rate testing, for bouncing ideas with, for acknowledging my strengths, as well as my weaknesses, for his kindness, support, diplomacy, and unmatched friendship within the Diamond Group; Drs. Tom Oliver, Hugo Andrade, Mitch Quinn, Christopher Hanson and Prof. Andrew Orr-Ewing for their wisdom and humour during some of the more trialling times of a PhD; Prof. Paul May for organising the lighthearted diamond group meals; Dr. Sohail Mushtaq for challenging me to question my experimental approach; Element Six Ltd for sponsoring half of my PhD, the loan of the microwave reactor and for the opportunity to practice my presentation skills; thanks and congratulations go to all the undergraduate (and postgraduate) research students that I have had the pleasure of working alongside over the duration of my PhD, particularly; Talia Solel, Bruno Rodriguez, Alim Lalji, and John Allden. You each achieved the highest grades for your respective research projects, I wish you all the best for the future; the people

who have made (and continue to make) the Bristol Diamond Group, the Bristol Laser and Molecular Dynamics Group, and the School of Chemistry generally a more enjoyable environment to work in. This includes but is not limited to: Marta Duchi, Victoria Taylor, Edward Aldred, Xian (Cathy) Zhang, (Muhammad) Zamir Orthman, Hugo Andrade, Sarah Halliwell, Emily Pole, Gary Wan, Michael James, Max Williams, Edmund Smith, Dominic Palubiski, Robbie Mackenzie, Ramiz Zlkharnay, Fabian Fogarty, Limin Yang, Jenny Cook, Lara Lalemi, and Jess Eastwood; the Diamond Science and Technology Centre of Doctoral Training, in particular the members of Cohort 1, Profs. Mark Newton and Julie MacPherson for encouraging me to apply to the Diamond Science and Technology Centre for Doctoral Training; Drs. Hugo Andrade and Alex Croot for involving me in an interesting side project, making use of my developed skillsets; Dr. Neil Fox and Prof. Mike Ashfold for the opportunity to continue working within the department as a post-doctoral researcher on an additional spin-out project after the submission of my PhD Thesis; Bristol University Hot Air Ballooning Society, the pilots, the drivers, and the executive members (including, but not limited to; Jenny Chakravarty, Fred Wiffen, Patrick Metcalfe, Oliver James and his wife Kristy James, John Harris, and Phil Anthony) that I have had the pleasure of working with, for providing unique experiences and insights into the world of ballooning, aeronautical and road navigation alike, the rich history that hot air ballooning has within the City of Bristol, a behind the scenes involvement in the Bristol International Balloon Fiestas, the associated night glow, and, of course, for exposure to the stunning views of Bristol, Bath, and Somerset.

Finally, I would like to thank the friends that I have made outside of the University of Bristol, whilst I cannot list you all, I'd like to say thank you. A special thanks goes to: Shereen Tucker, for your hilarious and brutally honest friendship; my supportive boyfriend, Danial Dadgostar; those I have met in Bristol, particularly; Chelsie Maroño and the Shambala crew; Cate Jackson, Hannah Sweetnam, Mary Jenkinson-Finch, Alex Croot, Ali Anthony, Joanna Sparks, Jonny Furze, Kathy Cox, Sam Briggs, Ronan Nobel, thanks for the friendships and the support; undergraduate, postgraduate, and home friends, particularly those who have taken the time to visit me in Bristol and/or kept me sane over the phone; Sarah Shuster, Matthew Taylor, Rianna Kelly, Branislav Džepina, Daniela Džepina, and their family, Chris Evered, Jimmy Edgell, Carl Oliver, Hannah Victoria, Ben Truscott, Dominic Madar, my aunt Elizabeth Johnston, and my brother William Mahoney; Kevin Haymes-O'neill, Melissa Haymes-O'neill and their family (and Bob Haymes, Shan O'neill, Connor Fox, and Keifer Jones) for hosting me after the Diamond Conference each year; thanks (and apologies) also go to my flatmates, past and present; including, but not limited to; Doris Marajo, Alex Millest, Karenza Fafoo, Milda Brazauskeite, Chris Moloney, Jenny Stapleton, Stefano Pietrocola, Koral Matos, Simran Kothari, Naohiro Sato, Nuntali Kamara, and Shereen Tucker; Chris and Jade Beasley; Mari Mason; Yasmin Kosar; Lucy Parsons and her family; my extended family; my grandparents, aunts, uncles and cousins, and last but not least, thanks (and congratulations) go to my more immediate family; my overachieving siblings; Emma, Jamie, William, Lucy, and our amazing parents; Mum and Dad, thank you both.

Author's Declaration

I declare that the work in this thesis was carried out in accordance with the requirements of the University's Regulation and Code of Practice for Research Degree Programmes, and that it has not been submitted for any other academic award. Except where indicated by specific reference within the text, the work is the candidate's own work. Work done in collaboration with, or with assistance of, others, is indicated as such. Any views expressed in this thesis are the views of the author.

SIGNED: ……. DATE: …….....……

Table of Contents

Contents

Chapter 6: Diagnostic Studies carried out on MW-activated Si/H and Si/C/H plasmas

List of Figures

Chapter 1: Introduction

Chapter 2: Experimental Theory and Practice

Chapter 3: Investigating Hydrogen Emissions Originating from MW-activated H and H/Ar Plasmas

Chapter 5: Is it Possible to Probe the Thermal Component of the Electron Energy Distribution Function (EEDF) in MW-activated C/H plasmas?

Chapter 6: Diagnostic Studies carried out on MW-activated Si/H and Si/C/H Plasmas

List of Tables

Chapter 3: Investigating Hydrogen Emissions Originating from MW-activated H and H/Ar Plasmas

Chapter 6: Diagnostic Studies carried out on MW-activated Si/H and Si/C/H Plasmas

Chapter 1: Introduction

This chapter provides the background for contextualising this thesis. It describes structure, properties and applications of diamond material, as well as two methods of synthesis – high pressure, high temperature synthesis and the chemical vapour deposition process. The interest in microwave-activated C/H plasmas is justified and a brief overview of the prominent physical and chemical processes is provided. This understanding has been developed through experimental diagnostic methods and 2-D physical chemical kinetic modelling, which are also discussed. The chapter concludes by describing the structure of this thesis. This chapter has been adapted from a short review article [a] featuring in The Atlas of Science co-written by the PhD Candidate, Edward Mahoney and supervisor Prof. Mike Ashfold.

1.1: Diamond Structure, Properties and Applications

Diamond is a metastable allotrope of carbon renowned for its many outstanding properties. Diamond defines the top (10) of the Mohs scale for measuring hardness.[1] It has the highest bulk thermal conductivity (up to 2 $kWm^{-1}K^{-1}$ at room temperature)[2,3,4,5], and a low coefficient of thermal expansion (0.8×10^{-6} K^{-1}).[2,3,4] The large indirect band gap (5.47 eV) of diamond results in optical transparency across a wide wavelength range (infra-red through to ultraviolet), as well as electrically insulating properties for the undoped material.[2,3,4]

The tetrahedral sp^3-hybridised bonding structure of diamond contrasts to the most thermodynamically stable allotrope of carbon, graphite under standard conditions of temperature and pressure (STP), i.e. 1 atmosphere and 20 °C. Graphite consists of 2-Dimensional inter-planar sp^2 carbon bonded layers, which are hexagonal in shape.[6] Whilst the bond strengths within a graphitic layer are stronger than in diamond, reflected by the shorter C-C bond length (1.41 Å versus 1.54 Å for diamond), the planes in graphite are held together by delocalised electrons through weak Van der Waal's forces.[6] This allows layers to slide over one another with a relatively low force. The delocalised electrons occupy the conduction band of graphite, which leads to significantly different electronic behaviour to that of diamond. In spite of a small difference in standard enthalpy of formation (2.9 $kJmol^{-1}$), the significant structural difference between the two allotropes, visible in Figure 1.1, results in a large energy barrier between the two structures (730 $kJmol^{-1}$ or 4.56 eV).[4,6] This prevents a thermodynamic conversion between graphite (or any other carbon allotrope) and diamond without the application of molten metals under high pressure

[a] Mahoney, E.J.D. and Ashfold, M.N.R., "Diamond growth using microwave-activated methane/hydrogen plasmas," Atlas of Science. [online] Atlasofscience.org, 2018, Available at: http://atlasofscience.org/diamond-growth-using-microwave-activated-methane-hydrogen-plasmas/ [Accessed 31 Aug. 2018].

and high-temperature conditions (HPHT growth), activated gases, or lasers – hence the popular phrase 'diamonds are forever'.[7]

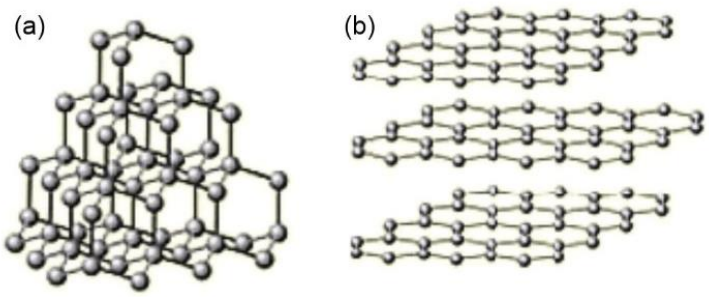

Figure 1.1: Structure of 2 carbon allotropes: (a) diamond and (b) graphite. Figures adapted from Reference 7.

It is the rigidity and kinetic stability of the diamond structure that gives rise to some of the more desirable thermal and mechanical properties of bulk diamond. Such properties make diamond an active area of research and applicable to a range of technologies.[4] Diamond can be grown through multiple methods to various shapes and sizes. The two most prominent methods of diamond synthesis are discussed in Section 1.2, with each method lending itself to specific applications.

For instance, nanodiamonds can be grown through both methods described in Section 1.2, but in order to generate a large quantity of nanodiamonds, detonation of graphitic material is most commonly used. Detonation creates high pressure high temperature (HPHT) conditions on the timescale of a few microseconds facilitating brief diamond formation. The HPHT method itself is described further in Section 1.2.1. Nanodiamonds are bio-inert and can be manipulated as large organic molecules.[2,4,8] As such, there is on-going research into possible biomedical applications.[8,9] Functionalising the surface of a nanodiamond enables pH-sensitive drug delivery,[8] whilst optical centre defects within a nanodiamond can be manipulated with magnetic fields and detected through fluorescence and Coherent Anti-Stokes Raman Scattering can be used to detect a carbon-carbon bond in a higher purity nanodiamond for in vivo cellular bio-imaging.[9]

The magnetic properties (electron spin, $S = 1/2$) of the neutral nitrogen-vacancy (NV^0) centre within a nanodiamond lends itself to such applications, as well as to more fundamental science research; a collaboration of scientists are attempting to make use of the NV^0 centre within an optically levitating microcrystalline diamond to demonstrate 'macroscopic' quantisation. The ambition of the work is to create a sensitive tool for testing theories of quantum gravity.[10]

Nanocrystalline diamond films can be produced via the Chemical Vapour Deposition (CVD), outlined in Section 1.2.2. Manipulation of operating conditions allows a control over crystallite size and morphology. Such a material has a range of applications. Extending on those aforementioned for the individual nanocrystals, a nanocrystalline diamond film can, for example, find application in Micro-

and Nano- Electro-Mechanical systems (MEMS and NEMS respectively), making use of the high Young's Modulus (values ranging between 840-1100 GPa) associated with such diamonds.[11]

1.2: Synthesis of Diamond

The two main methods for growing high-quality single crystal or polycrystalline diamond are HPHT - a thermodynamic conversion of graphitic carbon into diamond using a molten metallic catalyst described in Section 1.2.1, and Chemical Vapour Deposition (CVD) – the processing of carbon-containing gases as described in Section 1.2.2. Further detail on the known processes occurring within microwave-activated (MW-activated) methane/hydrogen CVD plasmas is provided in Section 1.4.

1.2.1: High Pressure High Temperature Method

The HPHT method was developed in 1954 by Bundy *et al*. working at General Electric. The method uses a press and recreates the naturally occurring conditions in which natural diamonds form within the Earth's crust and upper mantle. Under such extreme conditions (~6 GPa and 1300 – 1700 ˚C), diamond is the most stable allotrope on the carbon phase diagram. Under these conditions, the HPHT method exploits a thermodynamically-favoured and kinetically-allowed conversion of graphitic material into diamond.[4,12,13]

Carbon demonstrates increasing solubility with increasing temperatures within metallic melts. By saturating a metallic melt (typically made up of combinations of Fe, Ni, Co, and Mn-C) with carbon (graphite or diamond grit), the melt sets up a convection current and deposits carbon as diamond on a diamond seed crystal in a cooler region of the chamber. By increasing the temperature of growth the diamond quality increases and encourages (111)-oriented growth over (100). By introducing additional elements, such as Ti, Al, B, Cu or Ge into the melt nitrogen content can be removed, increasing the diamond purity.[12,13] Due to the nature of the growth method, HPHT grown diamonds are prone to incorporating metallic inclusions.

Single crystal diamond can cleave along the (111) plane.[14] As such, polycrystalline diamond is advantageous within mechanical applications and is generally cheaper to manufacture. Polycrystalline diamond is grown and then sintered within a cobalt-alloy matrix for polycrystalline diamond drill bit cutters used in oil and gas exploration.[12,13]

1.2.2: Chemical Vapour Deposition

Under less extreme conditions diamond can be grown through CVD. CVD employs methane/hydrogen (CH_4/H_2) gases activated through an energy source (for example hot filaments, direct current plasmas, and microwave-activated plasmas) enabling kinetic (rather than thermodynamic) control of diamond deposition on a suitably positioned substrate.[2,4,5,15,16,17] The use of a single crystal diamond substrate enables the growth of single crystal diamond films, whilst the use of polycrystalline diamond and silicon

substrates, for instance, will result in polycrystalline diamond films. The rate of diamond film growth is entirely dependent on operating conditions and substrate temperature, but is typically reported to be between 2-10 microns per hour – higher rates have been reported ranging from 40 [16] up to 100 microns per hour.[17] Lower growth rates are desirable for the highest quality growth, whilst higher growth rates are desired to reduce running costs. CVD diamond can be grown to a range of sizes from the nanometre scale to centimetre scale.[2,4,15,17] CVD diamond films typically find technological applications in coating materials, as well as thermal management of electronic and lasing devices.[2,4]

CVD diamond readily incorporates dopants and defects into its structure ranging from atomic-level vacancy sites to microcrystalline stacking faults and graphitic grain boundaries.[18] Structural imperfections can have visible effects, including colour change (typically blue with light boron doping, and yellow with nitrogen doping), and crystal twinning along the (111)-orientation.[19] The incorporation of defects during the growth process can compromise some useful bulk properties, for example a reduction of crystallographic isotropy can reduce the thermal conductivity.[20]

There are advantageous reasons for introducing dopants into the gas phase and therefore into the diamond lattice. For instance, introducing trace nitrogen into the CVD feed gas (between 20-100 parts per million) can enhance CVD diamond growth rate significantly (between 2- and 5-fold).[15,21] Diamond can demonstrate p-type semi-conductive (acceptor level 0.38 eV above valence band maximum), metallic and even low-temperature superconductive behaviour upon increasing boron dopant concentration.[15,22,23] This can be achieved by introducing diborane into the feed gas during CVD growth. This makes diamond applicable in some semi-conductor electronic devices, for instance Ohmic Shottky barrier diodes and field effect transistors.[24] Despite a lack of shallow n-type donor level dopants, phosphorus demonstrates a deep donor level (0.6 eV below the conduction band minimum), and as such diamond p-n and p-i-n junctions do not typically contribute to room temperature semiconductor devices, but have been used to create deep UV Light Emitting Diodes.[25,26]

Diamond has a high breakdown voltage, which makes it appealing for high power electronics. At present, diamond technology only permits a high current or voltage.[27] In spite of this, it is possible to engineer low power devices. Alternatively, it is also possible to introduce 3-D graphitic (electrically conductive) wires into a diamond through laser ablation, which can be used as particle detectors.[28]

CVD was first developed in 1958 by William Eversole at Union Carbide Corporation via pyrolysis. This was achieved utilising an electrical furnace to heat a silica tube and dissociate carbon-containing gases. The original patent states some knowledge that methyl-containing gases were required to incorporate carbon onto a diamond seed crystal.[29] CVD utilises kinetic control of diamond synthesis; the relatively low temperatures and pressures (*cf.* HPHT conditions) are conditions under which diamond is metastable. Despite success in sp^3 carbon formation, black graphitic carbon was a commonly reported by-product.[29]

In 1965 Gulbransen *et al.* demonstrated that graphitic material could be efficiently etched into the gas phase with hydrogen atoms.[30] Spitsyn's PhD thesis, published in 1966, advanced this into a CVD growth method, achieving 1 micron an hour growth rate on (111)-oriented diamond seed crystals.[31] The method requires graphite to be heated to 2000 ˚C in the proximity of hydrogen atoms. Gas phase H atoms etch graphitic carbon into the gas phase generating $CH_x (0 \leq x \leq 3)$ radicals, some of which then deposit on a diamond seed crystal held at 1000 ˚C. The chemistry is comparable to that described in Section 1.4.

Angus *et al.* found that hydrogen etches graphite more efficiently than diamond, and therefore a higher concentration of atomic hydrogen increases diamond quality.[32] In 1981 Spitsyn *et al.* attempted diamond growth on non-diamond substrates, with limited success.[33] In the two consecutive years (1982 and 1983) additional methods of gas phase activation were developed – hot filaments and microwave-activated plasmas respectively – facilitating a method for diamond growth on non-diamond material.[34,35] Additional growth techniques, such as DC plasma jets and combustion were later developed.[31]

There are currently four main methods for gas phase activation enabling the CVD of diamond. These include thermal activation, e.g. hot filament activation, electric field activation (also referred to as plasma – enhanced or PE), e.g. DC discharge, DC arc-jet, radio frequency, microwave and electron cyclotron resonance activation. The other two methods are chemical activation, e.g. acetylene-oxygen torches, and photochemical activation, which stretch beyond the focus of this thesis.[31]

Whilst hot filament growth is a cheaper means to produce diamond, electrodeless CVD has the advantage of an improved diamond quality. Hot filament and electrode-activated CVD methods, like the HPHT growth method, are prone to incorporating metallic defects within the diamond.[15,31] Microwave-activated (MW) CVD, an electrodeless CVD method, avoids this issue. Compared to most other electric field activated plasmas, MW-activated plasmas achieve a higher degree of ionization and dissociation of hydrogen, which enhances the processing of carbon.[36] DC arc-jet reactors also demonstrate these advantages, but utilises significantly higher power input (20-30 kW versus 1-10 kW for MW CVD), thereby increasing operating costs.[37] MW CVD diamonds are regularly reported to incorporate etched silicon (from quartz windows and Si substrates present within the chamber) forming silicon-vacancy defects.[38] Such defects can be used to distinguish natural and lab-grown CVD diamond.[38]

For thermal management of devices, it is desirable to grow diamond on other materials.[2,4,39] The development of nucleation techniques allows diamond to be grown on non-diamond materials in MW-activated CVD. In 1987, Mitsuda *et al.* demonstrated a nucleation density of 10^7–10^8 cm^{-2} through roughening non-diamond surfaces with diamond grit. This enabled nucleation and film growth on non-diamond substrates due to increased available surface sites from the presence of small diamond grit seed crystals.[5,40]

Polycrystalline MW CVD diamond is grown through such nucleation methods and a typical film demonstrates increased grain size further from the growth substrate, as illustrated in Figure 1.2 (a). This can arise due to slower growing plane orientations overgrowing the faster growing planes. The effect of such inhomogeneous structures is spatial and orientation-dependent thermal conductivities.[41]

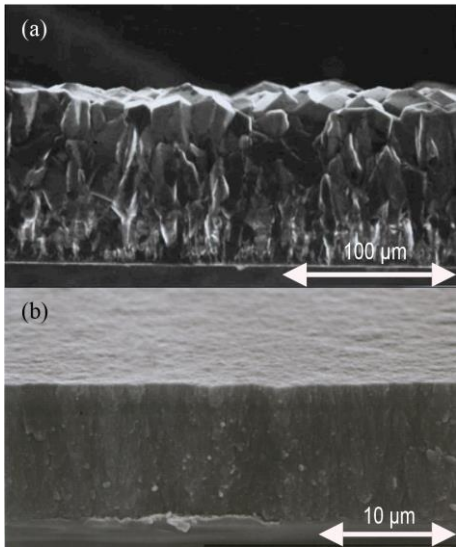

Figure 1.2: SEM side view images of (a) micro-crystalline and (b) nano-crystalline diamond film. Figure features in Reference 14.

In 1991, Yugo *et al.* demonstrated that negative bias enhancement could achieve higher nucleation densities (10^9–10^{10} cm^{-2}) on Si substrates.[5,42] Stoner *et al.* expanded this for SiC substrates.[43] The success of negative bias enhancement is attributed to cations accelerating to the substrate and forming nucleation sites. Shreck *et al*. demonstrated that this technique can be used to facilitate ion bombardment induced buried lateral growth of single crystal diamond on Ir(100) and Ir(111) – an alternative growth mechanism to the accepted standard model of CVD diamond growth discussed in Section 1.4.[44] Jiang *et al.*, in 1993, gave an early indication that positive bias enhancement might also have a similar effect.[45] This was conclusively demonstrated in 2001 – Chiang *et al*. achieved nucleation densities of 10^{10} cm^{-2} in the presence of high methane fractions. The result was attributed to electron bombardment of the substrate by the authors.[46] Additional nucleation methods, such as ion implantation enhanced nucleation have since been developed.[5]

Since the development of plasma-enhanced chemical vapour deposition of diamond, some research groups have struggled to grow thicker diamonds with smooth surfaces, instead producing convex and/or concave diamond, dependent on methane fraction, operating conditions and the consequential plasma appearance.[47,48] Whilst References 47 and 48 refer to observations reported for diamond grown via DC-activated plasmas, the optimisation of substrate holder designs carried out by Mokuno *et al.* infers that this is also an issue that impacts MW-grown CVD diamond.[49] Yamada *et al*. proposed that the inhomogeneous growth could arise due to an inhomogeneous absorbed power density, which therefore results in a gas (and substrate) temperature gradient across the growth surface.[50] Chapter 3 focuses on

MW-activated H and H/Ar plasmas,which are regularly used in the context of hydrogen termination and etching of diamond. Such plasmas are a simpler system than that of a MW-activated C/H plasma, which can be used to further enhance an understanding of the inter-link between plasma parameters, gas phase processes, and any extrapolatable impacts that the findings may have on diamond growth and spectroscopic studies carried out on MW-activated C/H plasmas.

Chapters 4 and 5 focuses on furthering the understanding behind the physical and chemical processes occurring within MW-activated CH_4/H_2 CVD plasmas (both in the plasma and at the plasma–substrate interface), whilst Chapter 6 focusses on understanding the processes occurring within MW-activated $SiH_4/CH_4/H_2$ plasmas (and SiH_4/H_2 plasmas as a prerequisite). Such an understanding is necessary for diamond quality optimisation, i.e. minimising Si-containing defect incorporation during hydrogen termination and diamond growth. For a comprehensive understanding of the physical and chemical processes occurring in such a system, 2-D physical chemical plasma modelling is required.

1.3: The Moscow-Bristol 2-D Plasma Modelling

The Moscow-Bristol 2D modelling of MW CVD processes is described thoroughly in Reference 51. The model enables an enhanced understanding behind the more prominent physical and thermochemical gas phase processes under the conditions relevant to diamond growth and those explored in this thesis. The modelling is self-consistent and simplified through an assumed cylindrical geometry of the plasma and reactor, which has a radius, *r*, and height, *z*, both extending 60 mm from the centre of the substrate surface (modelled centrally in the chamber) with 1 mm resolution. The modelling has three major components:

1. Power absorption, gas heating and mass transfer (predominantly achieved through rovibrational excitation of H_2 by electron impact and thermodiffusion).
2. Physical and chemical kinetics of the gas phase, for example diffusion, thermal dissociation and the chemical reactions discussed in Section 1.4.
3. Gas-surface processes, such as deposition and the loss (/generation) of radicals, ions and electrons.

Integration times > 1 s are used to capture the steady-state. The gas replacement time is far larger than the time required for physical changes, hence diffusion processes (e.g. thermal diffusion) are the dominant processes in the transfer of mass and chemical species. After such an integration time, the physical processes included within the model are assumed to be in a local steady-state dictated by the local plasma parameters, for example, electron impact excitation and electron impact ionization (and consequentially the local number densities of excited state and ionized species) depend on local electron number densities, local electron temperatures, the cross-sections presented by an electron to different

atoms / molecules (also sensitive to the electron temperature), and consequentially rate coefficients of such interactions.

Such processes (and modelling calculations) are therefore sensitive to the Electron Energy Distribution Function (EEDF). The EEDF is a characteristic plasma parameter, which describes the number of electrons that carry a defined energy interval, as a function of electron energy, at a plasma position. The electron temperature, T_e, (centred around ~1.28 eV) is described by a thermal Maxwell-Boltzmann distribution, whilst an additional hyper-thermal component is used to describe electrons with energies ≥ 10.2 eV. The full integral of the EEDF with respect to energy gives the number density of electrons at a position in the reactor under the modelled condition, whilst a partial integral between two energies describes the number density of electrons holding energies within the integrated energy range. The EEDF is a function of the oscillating (sinusoidal) electric field component of the input microwave radiation and is in the form $E = E_0 \sin(\omega t)/(\omega^2+\nu^2)^{0.5}$, whereby $\omega = 2\pi f$, the input microwave frequency, f = 2.45 GHz, whilst ν describes the effective collision frequency of an electron. Under previously studied conditions, $\nu \gg \omega$, whereby ν is proportional to N, the total particle density. The microwave wavelength, λ, is ~12 cm, whilst the chamber is ~ 6 cm in height and radius. Consequently, on a local scale (i.e. on the order of mm) the electrons experience the microwave as a stationary electric field and the local EEDF is a function of the reduced electric field; EEDF(*E/N).*

There are two assumptions that underpin the model:

1. The height, H_{pl}, and radius, R_{pl}, of the plasma ball are indicated by experimental optical emission and absorption studies. This allows alteration of the MW power and activation volume to be included within the model and thus, also, an estimation of *E/N*, T_e ,and the EEDF as outputs for any input power.

2. Only a narrow range of *E/N* values are physically realised within the plasma for a given power density.

Such calculations require initial conditions, such as the feed gas mixing ratio and flow rate, boundary conditions (for the MW standing waves) and experimental-specific parameters, such as the reactor wall temperature, substrate size, the plasma volume and the physical and chemical kinetics. Over 240 physical and chemical interactions are calculated for a MW-activated CH_4/H_2 plasma, which varies spatially and as a function of the absorbed power density, the gas temperature, both of which depend on the reduced electric field strength, the local mole fraction of hydrogen atoms, all of which spatially vary and rely on consideration of local formation / loss mechanisms (e.g. chemical production / losses, physical diffusion processes etc). Through consideration of a full description of physical and chemical kinetics, the 2D model calculates the steady-state production and loss rates for all species at each position within the plasma, (includes local diffusion effects from regions of production), and can

therefore also calculate number densities, e.g. hydrogen number density [H], as a $f(r, z)$. Number densities, kinetic rates and plasma parameters are all calculated with a 1 mm resolution in each dimension (radial and axial) and can provide an understanding of the prominent chemistry / physical processes (described in Section 1.4), rationalise experimental observations, and the interdependence of plasma parameters as a function of position, as demonstrated throughout this Thesis.

Prior modelling has used an assumed electron density, which was developed by physical intuition to generate an agreement between experimental observations (inferred by prior OES studies) and the 2-D model. The modelling has since been developed by Yuri Mankelevich (presented in Chapter 3) to generate the first self-consistent model of MW-activated H plasmas operating under moderate pressure conditions for describing plasmas that might be used for the hydrogen termination and etching of diamond.

The modelling provides insight into the prominent processes occurring within MW-activated CH_4/H_2 plasmas (and can be used to probe the impact that dopant addition has on the physical processes / gas phase chemistry) and contributes significantly to the understanding described in Section 1.4. Such modelling has limitations. For instance, the neglect of a significant physical / chemical process could impact plasma parameters, formation / loss mechanisms of species, number densities, and the gas phase kinetics overall. The modelling therefore requires a careful consideration of all major contributing processes.

1.4: Overview of Gas Phase Processes in MW-activated C/H(/Ar) Plasmas

2.45 GHz microwaves are tuned and coupled by an antenna into a cavity chamber containing hydrogen gas held at a pressure of ~20 Torr. The microwaves pass through a vacuum sealed quartz window and activate a hydrogen plasma - purple in colour, as can be seen in Figure 1.3. The plasma is activated initially through electrons induced by cosmic rays. These electrons accelerate in the microwave electric field, and collide with H_2. This facilitates vibrational excitation and electron impact dissociation.[15,51] Once the plasma has activated, pressure and power are adjusted appropriately for the experiment, the microwave radiation is tuned appropriately to the cavity, and the plasma reaches a steady-state after some time. Gicquel *et al*. demonstrated that for the conditions relevant to this thesis, i.e. $T_g > 2500$ K and $p > 15$ Torr, thermal dissociation of H_2 dominates over electron impact dissociation in the formation of H atoms, as described by process 1, whereby v is the vibrational quantum number, and the † symbol represents high vibrational quantum states ($v > 13$).[15,51,52]

$$\mathrm{H_2}\left(X^1\Sigma_g^+, v = 0-3\right) + \mathrm{M} \rightarrow \mathrm{H_2}\left(X^1\Sigma_g^+\right)^\dagger + \mathrm{M} \rightarrow 2\mathrm{H}(n=1) + \mathrm{M} \qquad (1.1)$$

At moderate conditions (e.g. an input MW power of 1.5 kW and a base pressure of 150 Torr), the addition of methane visually transforms the plasma into a distinct off-white colour - a consequence of a significant change in gas phase chemistry. The initial purple colour in MW-activated H plasmas arises

from the dominant H and H_2 emissions, whereas the off-white colour arises from additional well-studied C_2 Swan band and CH band emissions, which dominate the visible optical emissions of the MW-activated CH_4/H_2 plasma.[15,53,54,55,56]

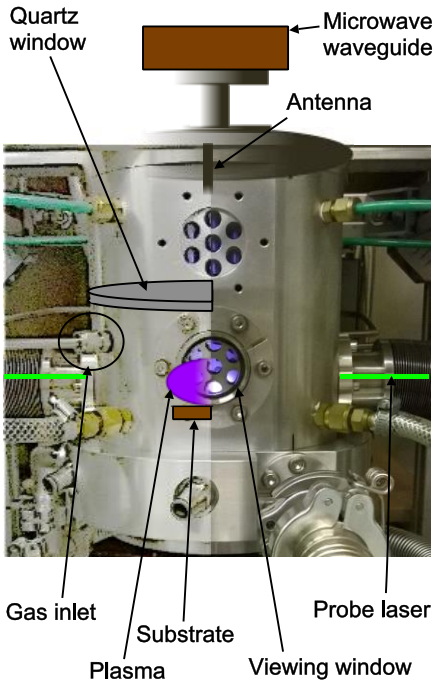

Figure 1.3: A depiction of a typical MW-activated H_2 plasma with a green laser indicated for illustrating plasma diagnostic through laser absorption. Figure appears in Reference 15.

The chemistry occurring within the MW-activated CH_4/H_2 plasma can be approximated to a steady-state of fast and reversible H-shifting reactions acting on CH_x ($0 \leq x \leq 4$) and C_2H_y ($0 \leq y \leq 6$) species, CH_x-CH_x addition reactions and the slower, reverse decomposition of C_2H_y upon collision with a spectator body.[15,51] These reactions are depicted simplistically in Figure 1.4. Such reactions create an [H]/[H_2] and local T_g dependant spatial distribution of [CH_x] and [C_2H_y] species. Under higher [C]/[H] ratios, it is possible to generate additional C_3H_z ($0 \leq z \leq 8$) species, however these are considered negligible minority species under the mixtures and conditions studied within this thesis.

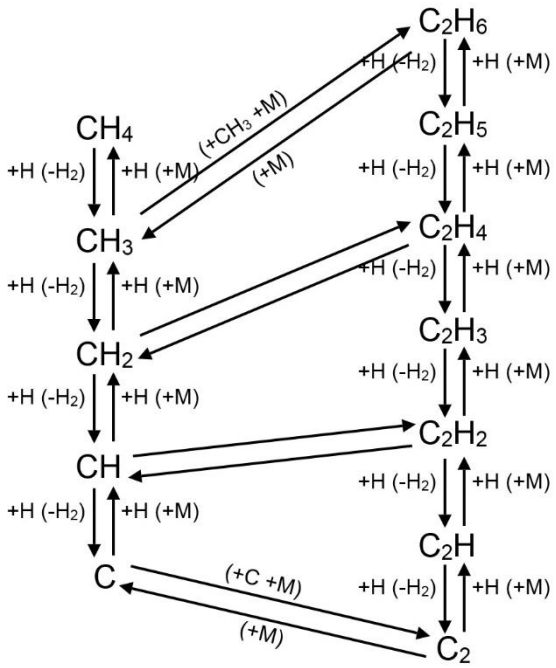

Figure 1.4: Simplistic depiction of the H-shifting reactions of methyl and ethyl groups with examples of methyl-methyl addition/dissociation reactions occurring within MW-activated C/H plasmas.

plasmas.

Figure 1.4 depicts a simplistic summary of the prominent carbon gas phase chemistry occurring within MW-activated C/H plasmas; it neglects the minor contribution from larger C_3H_z ($0 \leq z \leq 8$) molecules. The plasma is weakly ionised with ~ 1 in 10^6 species charged – electrons are predominantly formed through Electron Impact Ionization (EII) of the dominant species C_2H_2 and C_2H_3 (which has the lowest ionization energy from the C_2H_y group), forming $C_2H_2^+$ and $C_2H_3^+$ respectively.[57] EII of C_2H_2 is described by Process 1.2. Despite its lower ionization energy, ionization of C_2H_3 is 3 orders of magnitude lower than C_2H_2 and is instead formed via a charge transfer reaction between H_3^+ and C_2H_2, as described by Process 1.3. $C_2H_y^+$ species, like C_2H_y species, also react through steady-state H-shifting reactions. Electrons are lost through recombination reactions with $C_2H_y^+$ as described by Process 1.4:

$$C_2H_2 + e \rightarrow C_2H_2^+ + 2e \quad (1.2)$$

$$C_2H_2 + H_3^+ \rightarrow C_2H_3^+ + H_2 \quad (1.3)$$

$$C_2H_y^+ + e + M \rightarrow C_2H_y + M \quad (1.4)$$

Figure 1.5 demonstrates spatially-resolved false colour plots for various parameters generated by the 2-D Moscow-Bristol model described in Section 1.3. The conditions demonstrated are defined by Jie Ma *et al*. as an input power of 1.5 kW, total gas pressure of 150 Torr, with a 4.4% methane, 7.1% Ar, 88.5% hydrogen flow mixture.[51,59] Figure 1.5 (a) shows the modelled electron density distribution, n_e, which has considered formation, loss and ambipolar diffusion of electrons. Overall the plasma maintains a local and net charge neutrality. Figure 1.5 (b) illustrates T_g ranging from ~300-500 K at the water-cooled

reactor walls to 3000 K at the centre of the plasma. H(n = 1) is generated in the hottest region of the plasma through thermal dissociation of H_2. In this region, the number density of H, relative to H_2 is approximately 8%, i.e. [H]/[H_2] ~ 8%. H atoms thermally diffuse from the hot region into the surrounding cooler regions.[59] Due to their low mass, this is an efficient process, which leads to a high [H(n = 1)] in the cooler regions in proximity to the hottest region, which can be seen by comparing Figures 1.5 (b) and 1.5 (c).

Figure 1.5 (c) illustrates that the [H(n = 1)] drops by at least a factor of 12, however the number associated with the lightest colour in Figures 1.5 (a), (c) and (d), e.g. 0.31×10^{16} cm^{-3} for Figure 1.5 (c), describes the upper limit for such a colour shade. The lower limit being much closer to 0. The excited state [H($n \geq 2$)] are prominent in regions of high n_e – the predominant formation mechanism of excited state species being electron impact excitation as described by Process 1.5.

$$\mathrm{H}(n = 1) + \mathrm{e} \rightarrow \mathrm{H}(n > 1) + \mathrm{e} \qquad (1.5)$$

Jie Ma *et al*. provides an experimental vindication for electron impact excitation being the prominent excitation method for H(n > 1) states, and more generally for most excited states of C-containing diatomic species. This was achieved through demonstrating an excellent spatial agreement between measured ground state / metastable state column densities and excited state optical emissions from common diatomic species.[15,51,58,59]

Conversely to [H] atoms, [H_2], which can be seen in Figure 1.5 (e), holds the greatest number density in the coolest regions of the plasma due to the ideal gas law ($n = pV/RT_g$). The mole fraction of CH_4 decreases as the carbon-containing gas diffuses into the plasma from the gas inlet (gas inlet is assumed to be top corner in Figure 1.5 (f), i.e. r = 6 cm, z = 6 cm) and undergoes fast H-shifting reactions as it diffuses into the plasma.

The chemistry depicted in Figure 1.4 is highly sensitive on [H]/[H_2] and T_g. The plasma can be approximated into 3 distinct regions based on the chemistry inferred by the modelling described in Section 1.3. These regions are indicated in Figure 1.5 (g).

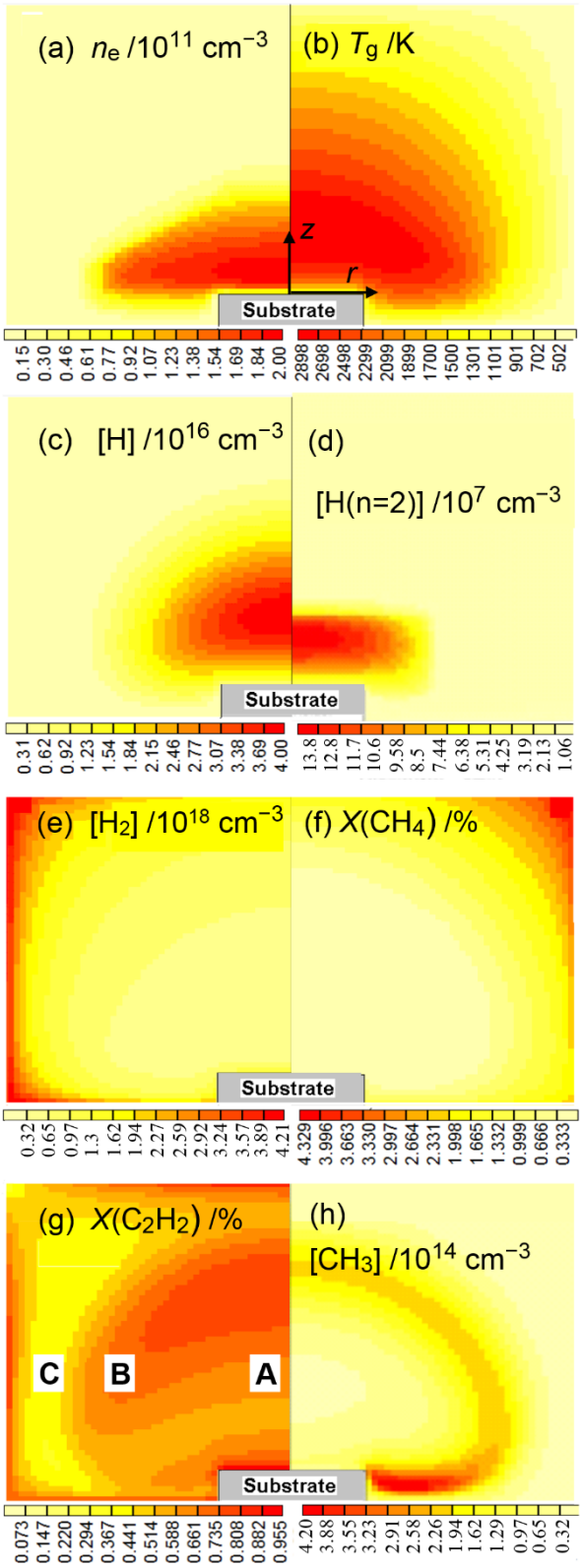

Figure 1.5: False colour plots produced from 2-D Moscow-Bristol plasma modelling demonstrating as a function of height (vertical axis) and radius (horizontal axis), (a) electron density, (b) gas temperature, (c) atomic hydrogen number density, (d) atomic H(n = 2) number density, (e) diatomic hydrogen number density, (f) mole fraction of methane, (c) mole fraction of acetylene, (h) number density of CH_3 for conditions defined by Jie Ma *et al*. This Figure has been modified from References 15 and 51.

Region C, the outer region of the reactor, has a relatively low T_g ($500 < T_g < 1400$ K) and [H]/[H_2]. The steady-state chemical equilibrium, depicted in Figure 1.4, is consequently shifted towards methane, and as such creates an annular outer layer of methyl radicals (CH_3) at the edge of the hot plasma region, which can be seen in Figure 1.5 (h).[15,51,58,59] In region B, where $1400 \text{ K} < T_g < 2000$ K, there is a generation of acetylene, however there is a net consumption of H atoms. Acetylene, C_2H_2, and methane, CH_4, are in thermal equilibrium in region A, where the temperature ranges between $2000 \text{ K} < T_g < 3000$ K. Due to the high [H] concentration, the H-shifting and H recombination reactions are particularly fast, and at such temperatures, dissociation through third body collisions is lower than the faster methyl-methyl addition reactions. Overall, this favours the production of the thermodynamically more stable species C_2H_2. Acetylene is generated predominantly in this region, and diffuses throughout the plasma – due to its stability under such conditions, [C_2H_2] contributes ~97% of total carbon content in plasma region A. It is therefore implicit that all carbon content from the original feed gas that samples the hot plasma region is processed – and hence varying the carbon source does not significantly vary the gas phase chemistry and as such these plasmas can be considered MW-activated C/H plasmas, rather than MW-activated CH_4/H_2 plasmas under conditions relevant to diamond growth.[15,51,58,59] This has been experimentally verified through studies comparing CH_4 and C_2H_4 as a source of carbon.[15,51,58,59]

From the centre of the plasma ($r = 0$, $z \sim 10$ mm), towards the substrate surface ($z = 0$ mm), the axial T_g rapidly drops when contrasted to the radial T_g gradient, as can be seen in Figure 1.5 (b) – this results in a spatially confined region of B and C with a relatively high [H] and [CH_3] radical density just above the substrate. These are the growth species that are associated with the standard model for the chemical vapour deposition of diamond.

The standard model of the CVD of diamond is most easily explained with an appropriately placed diamond substrate. H atoms from the gas phase abstract the diamond surface-terminating H atoms forming gaseous H_2 and leaves a vacant lattice site. Typically, ~10% of the surface consist of radical sites under growth conditions. This method can be used to grow diamond at a controlled orientation. Most computational methyl incorporation studies are carried out on a (100):2×1 reconstructed diamond surface, but the principle likely extends to the (110) diamond surface. CH_3 radicals can either bond onto such dimer sites, undergo further H-shifting and reconstruction reactions to incorporate, or alternatively, CH_x ($0 \leq x \leq 3$) radicals can migrate across the surface and upon reaching a step edge, a CH_x ($0 \leq x \leq 2$) radical can bond to a second carbon atom. This provides additional stabilisation and facilitates the step-edge diamond growth typically associated with CVD diamond.[15,60]

1.5: About This Thesis

There are many well-established, non-invasive diagnostic tools for investigating MW-activated C/H-containing plasmas and the prominent gas phase processes, which have contributed a wealth of background understanding required for this thesis. Such techniques include optical emission

spectroscopy and laser techniques, such as gas phase Raman spectroscopy, laser-induced fluorescence, and infra-red absorption.[21,22,53,54,55,56,59,61,62,65] This thesis focuses on two experimental techniques; optical emission spectroscopy, and cavity ring down spectroscopy, an ultra sensitive laser absorption technique, both of which are described in Chapter 2. A significant contribution toward the understanding of the experimental measurements presented within this thesis is provided by the Moscow-Bristol 2-D plasma modelling, developed appropriately from what has been described in Section 1.3.

There are still many open questions regarding diagnostic measurements (and their validity), particularly with regards to T_e sensitive measurements. It is not possible to make direct electron temperature measurements with Langmuir probes – such apparatus would not withstand the gas temperature (~3000 K) and would perturb the MW standing wave setting up the plasma. Therefore, T_e sensitive measurements for such plasma conditions typically consist of optical emission studies and 2-D plasma modelling, both of which are indicative.

The electrons are accelerated by the microwave standing wave and therefore are not in thermal equilibrium with the gas phase (T_g ~ 3000 K = 0.259 eV). The EEDF can, however, be described by two major components; a thermal component describing electron energies with a Maxwell-Boltzmann distribution characterised by an electron temperature, $T_e \approx 1.28$ eV and a hyper-thermal component, which describes electrons with $\varepsilon \geq 10.2$ eV and is experimentally evidenced by high energy electronic state emissions (e.g. H-Balmer series). There are studies within the literature, which assume that, under lower pressure conditions to those investigated in this thesis, the hyper-thermal component can be inferred through monitoring a variation in the optical emission ratios of the H-Balmer series, for instance H_β/H_α.[63,64] Prior work reported by the Bristol group make similar assumptions, for conditions more comparable to those investigated in this thesis.[58,59,65] There are two issues associated with equating the H_β/H_α emission ratio to a Boltzmann distribution. The first is that the difference in the H(n = 4) and H(n = 3) energy levels (0.65 eV) is substantially smaller than the electron energies required to excite these states ($\varepsilon \geq 12.09$ eV); prior studies note that any changes in such a ratio due to the variation in T_e are lost within the experimental error.[59] The second is that the high energy states of the H atom, which sample the hyper-thermal component of the EEDF, are being used as a comparator to estimate the thermal component of the EEDF, whereby $T_e \approx 1.28$ eV.[59,66]

There have also been relatively few spatially-resolved [59] or operating condition dependent studies [22,67] on H_2 emission intensities in MW-activated (C/)H plasmas in the context of diamond CVD growth. Most H_2 emission studies instead focus on analysis of the rotational temperature, which for other diatomic species (for example C_2 or CH emissions in MW-activated C/H plasmas) can be extrapolated to infer T_g. H_2 emission studies, however, consistently and significantly underestimate gas temperatures.[64,68,69,70,71] Studies on pure hydrogen plasmas have demonstrated a constant *E/N* (and

therefore T_e) within the plasma, except at the plasma edge, noting that T_e drops by ~10% at increasing distance, *z*, away from the substrate.[51]

Chapter 3 uses the simplest possible system – a MW-activated H plasma – to develop an understanding behind the EEDF(*E/N*, *z*, *r*) and challenge the assumptions underpinning prior T_e or EEDF-sensitive measurements made through monitoring the H_β/H_α ratio. Chapter 3 addresses whether these ideas apply to the conditions under investigation, and if not, what additional unstudied processes are contributing to the excitation and/or de-excitation of the upper state (H($n \geq 3$)) of the H-Balmer emission to invalidate these assumptions. The study investigates the possibility of more EEDF-sensitive measurements using spatially-resolved H_2 optical emissions; an idea previously proposed by Fantz *et al*. in the context of Deuterium fusion reactors.[72] With the insight developed from 2-D plasma modelling, this chapter addresses the highlighted concerns above and concludes with investigating the effects that argon addition and lesser studied parameter spaces, like substrate diameter and substrate temperature, have on H-Balmer and H_2 optical emissions, the absorbed power density, and the EEDF. The study also makes a significant and novel contribution to the observation of enhanced emissions originating close to and around the periphery of the substrate, which have otherwise only been noted. These emissions may be directly or indirectly related to the observed concave/convex diamond grown in previous growth studies.[47,48,49,50] They also highlight some of the limitations associated with 2-D plasma modelling.

Chapter 4 reviews some of the more prominent gas phase processes that occur within MW-activated C/H plasmas and attempts to provide direct evidence for the existence of cations and anions via optical emissions originating from within the plasma. CH and C_2 have an ionisation energy of +11.1 eV [73] and +12.0 eV [74] and electron affinities of +1.24 eV [75] and +3.27 eV [75], respectively, making the existence of anions within MW-activated C/H plasmas an unconsidered possibility. Whilst the existence of cations is a necessity for balancing electrons and ensuring charge neutrality, cations have also been inferred indirectly by the success of negative bias enhancement nucleation studies.[42,43,44,51] Prior to this thesis, there have not been observations of optical emissions originating from CH or C_2 diatomic species in either charge state. Instead, it has been assumed that electrons are the only negatively charged species within the plasma and as such, this chapter attempts to provide direct evidence of charged state species (and additional anion candidates), and therefore provide an insight into the successful positive bias enhanced nucleation studies carried out by Jiang *et al.* and Chiang *et al.*[45,46]

Chapter 5 attempts to probe the thermal component of the EEDF in MW-activated C/H plasmas. This is achieved through monitoring spatially-resolved intensity variations in three different CH emission bands (CH(A-X), CH(B-X), and the lesser studied CH(C-X) band emissions) with changes in process conditions. The purpose is to determine whether these bands can be utilised to make a sensitive thermal EEDF probe. It also assesses the assumption that the CH band systems make a good *in situ* probe for

monitoring methyl radicals (i.e. $CH_x (0 \leq x \leq 3)$, typically associated with the standard model of diamond CVD growth) during growth.

Chapter 6 is split into two components; investigations into MW-activated Si/H plasma systems, by contrasting the spatial dependence of Si-related emissions upon introducing silicon into the plasma by etching a silicon substrate and through flowing in dilute silane/hydrogen gas. The understanding of the processes occurring in MW-activated Si/H plasmas may be interesting from a chemist's perspective, exploring a gas temperature higher than those typically attributed to radio-frequency activated silane/hydrogen plasmas (used for amorphous silicon film growth).[76] Perhaps more relevantly for this thesis, the study acts as a precursor and benchmark model for the second half of Chapter 6, which investigates the prominent physical and chemical processes occurring within MW-activated Si/C/H plasmas. Such processes are important to understand from a diamond growth perspective. For high quality diamond growth, it is important to minimise silicon incorporation during growth, which may etch from the quartz window during hydrogen termination / diamond growth. There is also interest in understanding these processes for controllable silicon doping of a diamond in order to create the SiV^0 defect, a candidate defect which may be of interest in long distance quantum communication in the future.[38] Whilst there have been studies introducing silane [77,78,79] and deliberately etching silicon substrates [80] into MW-activated C/H plasmas for silicon doping, there have been very limited thorough studies on the gas phase kinetics of Si/H and Si/C/H reactions under the higher temperatures (2000 K < T_g < 3000 K) present.[81] The study also acts as a confirmation that some of the more significant conclusions drawn in Chapter 3 extend to MW-activated C/H(/Si) plasmas.

Chapter 7 offers an overview of the work presented in this thesis with a summary of the key conclusions drawn from the results and additional questions for further lines of investigation.

References

[1] Tabor, D. "The hardness of solids," Reviews of Physics in Technology, vol. 1, no. 3, pp.145-179, 1970.

[2] Balmer, R. S., Brandon, J. R., Clewes S. L., Dhillon, H. K., Dodson, J. M., Friel, I., Inglis, P. N., Madgwick, T. D., Markham, M. L., Mollart, T .P., Perkins, N., Scarsbrook, G. A., Twitchen, D. J., Whitehead, A. J., Wilman, J. J. and Woollard, S. M. "Chemical vapour deposition synthetic diamond: materials, technology and applications," Journal of Physics: Condensed Matter, vol. 21, no. 36, pp. 1-23, 2009.

[3] Asmussen, J. and Reinhard, D. "Diamond films handbook," New York: Marcel Dekker, 2002.

[4] May, P. W. "Diamond thin films: a 21st-century material," Philosophical Transactions of the Royal Society A: Mathematical, Physical and Engineering Sciences, vol. 358, no. 1766, pp. 473-495, 2000.

[5] Lee, S. T., Lin, Z. and Jiang, X. "CVD diamond films: nucleation and growth," Materials Science and Engineering: R: Reports, vol. 25, no. 4, pp. 123-154, 1999.

[6] Pierson, H. O. "Handbook of Carbon, Graphite, Diamonds and Fullerenes: properties, processing and applications," New Jersey: Noyes publications, pp. 25-45, 1993.

[7] bbc.co.uk BBC - GCSE Bitesize: Carbon. [online], pre-2011 Available at: http://www.bbc.co.uk/schools/gcsebitesize/science/add_gateway_pre_2011/chemical/nanochemistryrev1.shtml [Accessed 26 Jul. 2018].

[8] Guan, B., Zou, F. and Zhi, J., "Nanodiamond as the pH-Responsive Vehicle for an Anticancer Drug," Small, vol. 6 no. 14, pp. 1514-1519, 2010.

[9] Pope, I., Payne, L., Zoriniants, G., Thomas, E., Williams, O. A., Watson, P., Langbein, W. and Borri, P., "Coherent anti-Stokes Raman scattering microscopy of single nanodiamonds," Nature Nanotechnology, vol. 9, no. 11, pp. 940-946, 2014.

[10] Bose, S., Mazumdar, A., Morley, G. W., Ulbricht, H., Toros, M., Paternostro, M., Geraci, A. A., Barker, P.F., Kim, M. S. and Milburn, G., "Spin Entanglement Witness for Quantum Gravity," Physical Review Letters, vol. 119 no. 240401, pp.1-6, 2017.

[11] Williams, O. A. "Nanocrystalline diamond." Diamond and Related Materials, vol. 20, no. 5-6, pp. 621-640, 2011.

[12] Giardini, A. A. and Tydings, J. E. "Diamond Synthesis: Observations on the Mechnaism of Formation," The American Mineralogist, vol. 47, November-December, pp. 1393-1421, 1062.

[13] Abbaschian, R., Zhu, H. and Clarke, C. "High pressure–high temperature growth of diamond crystals using split sphere apparatus," Diamond and Related Materials, vol. 14, no. 11-12, pp. 1916-1919, 2005.

[14] Ramaseshan, S. "The cleavage properties of diamond," Proceedings of the Indian Academy of Sciences – Section A. pp. 114-121, 1946.

[15] Ashfold, M. N. R., Mahoney, E. J. D., Mushtaq, S., Truscott, B. S. T. and Mankelevich, Yu. A., "What [plasma used for growing] diamond can shine like flame?" Chemical Communications, vol. 53, no 76, pp. 10482-10495, 2017.

[16] Derkaoui, N., Rond, C., Hassouni, K. and Gicquel, A. "Spectroscopic analysis of H_2/CH_4 microwave plasma and fast growth rate of diamond single crystal," Journal of Applied Physics, vol. 115, no. 23, p. 233301.

[17] Liang, Q., Yan, C., Meng, Y., Lai, J., Krasnicki, S., Mao, H. and Hemley, R. "Recent advances in high-growth rate single-crystal CVD diamond," Diamond and Related Materials, vol. 18, no.5-8, pp. 698-703, 2009.

[18] Zhu, W., Kochanski, G.P., Jin, S. and Seibles, L., "Defect-enhanced electron field emission from chemical vapor deposited diamond," Journal of Applied Physics, vol. 78, no. 4, pp. 2707-2711, 1995.

[19] Wild, C., Kohl, R., Herres, N., Müller-Sebert, W. and Koidl, P. "Oriented CVD diamond films: twin formation, structure and morphology," Diamond and Related Materials, vol. 3, no. 4-6, pp. 373-381.

[20] Twitchen, D. J., Pickles, C. S. J., Coe, S. E., Sussmann, R. S. and Hall, C. E. "Thermal conductivity measurements on CVD diamond," Diamond and Related Materials, vol. 10, no. 3-7, pp. 731-735, 2001.

[21] Truscott, B. S., Kelly, M. W., Potter, K. J., Ashfold, M. N. R. and Mankelevich, Yu. A. "Microwave Plasma-Activated Chemical Vapor Deposition of Nitrogen-Doped Diamond. II: $CH_4/N_2/H_2$ Plasmas," The Journal of Physical Chemistry A, 120(43), pp.8537-8549, 2016.

[22] Ma, J., Richley, J. C., Davies, D. R. W., Ashfold, M. N. R. and Mankelevich, Yu. A. "Spectroscopic and Modeling Investigations of the Gas Phase Chemistry and Composition in Microwave Plasma Activated $B_2H_6/CH_4/Ar/H_2$ Mixtures," The Journal of Physical Chemistry A, vol. 114, no. 37, pp. 10076-10089, 2010.

[23] Yokoya, T., Nakamura, T., Matsushita, T., Muro, T., Takano, Y., Nagao, M., Takenouchi, T., Kawarada, H. and Oguchi, T. "Origin of the metallic properties of heavily boron-doped superconducting diamond," Nature, vol. 438, no. 7068, pp. 647-650, 2005.

[24] Kawarada, H., Aoki, M. and Ito, M. "Enhancement mode metal-semiconductor field effect transistors using homoepitaxial diamonds," Applied Physics Letters, vol. 65, no. 12, pp. 1563-1565, 1994.

[25] Alexenko, A. E. and Spitsyn, B. V. "Semiconducting diamonds made in the USSR," Diamond and Related Materials, vol. 1, no. 5-6, pp.705-709, 1992.

[26] Makino, T., Yoshino, K., Sakai, N., Uchida, K., Koizumi, S., Kato, H., Takeuchi, D., Ogura, M., Oyama, K., Matsumoto, T., Okushi, H. and Yamasaki, S. "Enhancement in emission efficiency of diamond deep-ultraviolet light emitting diode," Applied Physics Letters, vol. 99, no. 6, p. 061110, 2011.

[27] Wort, C. and Balmer, R. "Diamond as an electronic material." Materials Today, vol. 11, no. 1-2, pp. 22-28, 2008.

[28] Kononenko, T. V., Konov, V. I., Pimenov, S. M., Rossukanyi, N. M., Rukovishnikov, A. I. and Romano, V. "Three-dimensional laser writing in diamond bulk," Diamond and Related Materials, vol. 20, no. 2, pp. 264-268, 2011.

[29] Eversole, W. G., "Synthesis of Diamond," Union Carbide Corporation, Patent US3030188A, 1958.

[30] Gulbransen, E. A., Andrew, K. F. and Brassart, F. A. "The Reaction of Hydrogen with Graphite at 1200° to 1650°C," Journal of The Electrochemical Society, vol. 112, no. 1, p. 49, 1965.

[31] Spitsyn, B. V., Bouilov, L. L. and Alexenko, A. E., "Origin, state of the art and some prospects of the diamond CVD," Brazilian Journal of Physics, vol. 30, no. 3, pp. 471-481, 2000.

[32] Angus, J. C., Will, H. A. and Stanko, W. S. "Growth of Diamond Seed Crystals by Vapor Deposition," Journal of Applied Physics, vol. 39, no. 6, pp. 2915-2922, 1968.

[33] Spitsyn, B. V., Bouilov, L. L. and Derjaguin, B. V., "Vapor growth of diamond on diamond and other surfaces," Journal of Crystal Growth, vol. 52, pp. 219-226, 1981.

[34] Matsumoto, S., Sato, Y., Kamo, M. and Setaka, N. "Vapor Deposition of Diamond Particles from Methane," Japanese Journal of Applied Physics, vol. 21, no. 4 part 2, pp. L183-L185, 1982.

[35] Kamu, M., Sato, Y., Matsumoto, S. and Setaka, N., "Growth and Formation of Diamond on Steel," Journal of Crystal Growth, vol. 62, p. 642, 1983.

[36] Szabó, D. V. and Schlabach, S. "Microwave Plasma Synthesis of Materials—From Physics and Chemistry to Nanoparticles: A Materials Scientist's Viewpoint," Inorganics, vol. 2, no. 3, pp. 468-507, 2014.

[37] Mallik, A. "Microwave Plasma CVD Grown Single Crystal Diamonds – A Review." Journal of Coating Science and Technology, vol. 3, no. 2, pp.75-99, 2016.

[38] D'Haenens-Johansson, U. F. S., Edmonds, A. M., Green, B. L., Newton, M. E., Davies, G., Martineau, P. M., Khan, R. U. A. and Twitchen, D. J. "Optical properties of the neutral silicon split-vacancy center in diamond," Physical Review B, vol. 84, no. 24, 2011.

[39] Pomeroy, J. W., Bernardoni, M., Dumka, D. C., Fanning, D. M. and Kuball, M. "Low thermal resistance GaN-on-diamond transistors characterized by three-dimensional Raman thermography mapping," Applied Physics Letters, vol. 104, no. 8, p. 083513, 2014.

[40] Mitsuda, Y., Kojima, Y., Yoshida, T. and Akashi, K. "The growth of diamond in microwave plasma under low pressure," Journal of Materials Science, vol. 22, no. 5, pp. 1557-1562, 1987.

[41] Fiege, G. B. M., Altes, A., Heiderhoff, R. and Balk, L. J. "Quantitative thermal conductivity measurements with nanometre resolution," Journal of Physics D: Applied Physics, vol. 32, no. 5, pp. L13-L17, 1999.

[42] Yugo, S., Kanai, T., Kimura, T. and Muto, T. "Generation of diamond nuclei by electric field in plasma chemical vapor deposition," Applied Physics Letters, vol. 58, no. 10, pp. 1036-1038, 1991.

[43] Stoner, B. R., Ma, G. H., Wolter, S.D., Zhu, W., Wang, Y. C., Davis, R. F. and Glass, J. T. "Epitaxial nucleation of diamond on β-SiC via bias-enhanced microwave plasma chemical vapor deposition," Diamond and Related Materials, vol. 2, no. 2-4, pp. 142-146, 1993.

[44] Fischer, M., Brescia, R., Gsell, S., Schreck, M., Brugger, T., Greber, T., Osterwalder, J. and Stritzker, B. "Growth of twin-free heteroepitaxial diamond on Ir/YSZ/Si(111)," Journal of Applied Physics, vol. 104, no. 12, p.123531, 2008.

[45] Jiang, X., Six, R., Klages, C. P., Zachai, R., Hartweg, M. and Füßßer, H. J. "The effect of substrate bias voltage on the nucleation of diamond crystals in a microwave plasma assisted chemical vapor deposition process," Diamond and Related Materials, vol. 2, no. 2-4, pp. 407-412, 1993.

[46] Chiang, J. M. and Hon, M. H. "Positive dc bias-enhanced diamond nucleation with high CH4 concentration," Diamond and Related Materials, vol. 10, no. 8, pp. 1470-1476, 2001

[47] Hartmann, P., Haubner, R. and Lux, B. "Deposition of thick diamond films by pulsed d.c. glow discharge CVD." Diamond and Related Materials, vol. 5, no. 6-8, pp. 850-856, 1996.

[48] Baik, Y. J., Lee, J. K., Lee, W. S. and Eun, K. Y. "Large size plasma generation using multicathode direct current geometry for diamond deposition." Journal of Materials Research, vol. 13, no. 4, pp. 944-946, 1998.

[49] Mokuno, Y., Chayahara, A., Soda, Y., Horino, Y. and Fujimori, N. "Synthesizing single-crystal diamond by repetition of high rate homoepitaxial growth by microwave plasma CVD." Diamond and Related Materials vol. 14, no. 11-12, pp. 1743-1746, 2005.

[50] Yamada, H., Chayahara, A., Mokuno, Y., Horino, Y. and Shikata, S. "Numerical analyses of a microwave plasma chemical vapor deposition reactor for thick diamond syntheses." Diamond and Related Materials, vol. 15, no. 9, pp. 1389-1394, 2006.

[51] Mankelevich, Yu. A., Ashfold, M. N. R. and Ma, J. "Plasma-chemical processes in microwave plasma-enhanced chemical vapor deposition reactors operating with C/H/Ar gas mixtures," Journal of Applied Physics, vol. 104, no. 11, p.113304, 2008.

[52] Gicquel, A., Hassouni, K., Silva, F. and Achard, J. "CVD diamond films: from growth to applications," Current Applied Physics, vol. 1, no. 6, pp. 479-496, 2001.

[53] Mortet, V., Hubicka, Z., Vorlicek, V., Jurek, K., Rosa, J., Vanecek, M. "Diamond Growth by Microwave Plasma Enhanced Chemical Vapour Deposition: Optical Emission Characterisation and Effect Argon Addition," Physica status solidi A, vol. 201, pp. 2425–2431, 2004.

[54] Gries, T., Vandenbulcke, L., de Persis, S., Aubry, O., Delfau, J. L. "Diagnostics and Modelling of CH_4/CO_2 Plasmas for Nanosmooth Diamond Deposition: Comparison to Experimental Data" Journal of Vacuum Science and Technology B, vol. 27, pp. 2309–2320, 2009.

[55] Tallaire, A., Rond, C., Benedic, F., Brinza, O., Achard, J., Silva, F., Gicquel, A. "Effect of Argon Addition on the Growth of Thick Single Crystal Diamond by High-Power Plasma CVD" Physica Status Solidi A, vol. 208, no. 9, pp. 2028–2032, 2011.

[56] Vikharev, A. L., Gorbachev, A. M., Muchnikov, A. B., Radishev, D. B., Kopelovich, E. A., Troitskiy, M. M. "Investigation of the Optimized Parameters of Microwave-Plasma-Assisted Chemical Vapour Deposition Reactor Operation in a Pulsed Mode," Journal of Physics D: Applies Physics, vol. 45, no. 39, 2012.

[57] Blush, J. A. and Chen, P. "Photoelectron spectrum of the vinyl radical: downward revision of the C_2H_3-ionization potential." The Journal of Physical Chemistry, vol. 96, no. 11, pp. 4138-4140, 1992.

[58] Ma, J., Richley, J. C., Ashfold, M. N. R. and Mankelevich, Yu. A. "Probing the plasma chemistry in a microwave reactor used for diamond chemical vapor deposition by cavity ring down spectroscopy," Journal of Applied Physics, vol. 104, no. 10, p.103305, 2008.

[59] Ma, J., Ashfold, M. N. R., and Mankelevich, Yu. A. "Validating optical emission spectroscopy as a diagnostic of microwave activated $CH_4/Ar/H_2$ plasmas used for diamond chemical vapor deposition," Journal of Applied Physics, vol. 105, no. 4, p. 043302, 2009.

[60] Butler, J. E., Mankelevich, Yu. A., Cheesman, A., Ma, J. Ashfold, M. N. R., "Understanding the chemical vapor deposition of diamond: recent progress," Journal of Physics, Condensed Matter, vol. 21, no. 36, pp. 1-20, 2009.

[61] Hempel, F., Davies, P. B., Loffhagen, D., Mechold, L. and Röpcke, J. "Diagnostic studies of H_2–Ar–N_2 microwave plasmas containing methane or methanol using tunable infrared diode laser absorption spectroscopy," Plasma Sources Science and Technology, vol. 12, no. 4, pp. S98-S110, 2003.

[62] Boogaarts, M. G. H., Mazouffre, S., Brinkman, G. J., van der Heijden, H. W. P., Vankan, P., van der Mullen, J. A. M., Schram, D. C. and Döbele, H. F. "Quantitative two-photon laser-induced fluorescence measurements of atomic hydrogen densities, temperatures, and velocities in an expanding thermal plasma," Review of Scientific Instruments, vol. 73, no. 1, pp. 73-86, 2002.

[63] Behringer, K., and Fantz, U. "The influence of opacity on hydrogen excited-state population and applications to low-temperature plasmas," New Journal of Physics, vol. 2, p. 23, 2000.

[64] Rayar, M., Le Quoc, H., Lacoste, A., Latrasse, L. and Pelletier, J. "Characterization of hydrogen microwave plasmas produced by elementary sources in matrix configuration," Plasma Sources Science and Technology, vol. 18, no. 2, p. 025013, 2009.

[65] Ma, J. "Exploration of the gas phase chemistry in microwave activated plasmas used for diamond chemical vapour deposition," PhD Thesis, University of Bristol, 2008.

[66] Gicquel, A., Derkaoui, N., Rond, C., Benedic, F., Cicala, G., Moneger, D., Hassouni, K., "Quantitative analysis of diamond deposition reactor efficiency." Chemical Physics, vol. 398, pp 239-247, 2012.

[67] Ma, J., Richley, J. C., Davies, D. R. W., Cheesman, A., Ashfold, M. N. R. and Mankelevich, Yu. A. "Spectroscopic and Modeling Investigations of the Gas-Phase Chemistry and Composition in Microwave Plasma Activated $B_2H_6/Ar/H_2$ Mixtures," The Journal of Physical Chemistry A, vol. 114, no. 7, pp. 2447-2463, 2010.

[68] Gicquel, A., Hassouni, K., Breton, Y., Chenevier, M. and Cubertafon, J.C. "Gas temperature measurements by laser spectroscopic techniques and by optical emission spectroscopy," Diamond and Related Materials, vol. 5 no. 3-5, pp. 366-372, 1996.

[69] Shikama, T., Kado, S., Zushi, H. and Tanaka, S. "Molecular Zeeman spectroscopy for H_2 Fulcher-α band spectra as a local measurement of rovibrational structures," Physics of Plasmas, vol. 14, no. 7, p.072509, 2007.

[70] Tatarova, E., Dias, F. M., Ferreira, C. M. and Puač, N. "Spectroscopic determination of H, He, and H_2 temperatures in a large-scale microwave plasma source," Journal of Applied Physics, vol. 101, no. 6, p.063306, 2007.

[71] Garg, R. K., Anderson, T. N., Lucht, R. P., Fisher, T. S. and Gore, J. P. "Gas temperature measurements in a microwave plasma by optical emission spectroscopy under single-wall carbon nanotube growth conditions," Journal of Physics D: Applied Physics, vol. 41, no. 9, p. 095206, 2008.

[72] Fantz, U., Heger, B., Wünderlich, D. "Using the radiation of hydrogen molecules for electron temperature diagnostics of divertor plasmas," Plasma Physics and Controlled Fusion, vol. 43, no. 7, pp. 907-918, 2001.

[73] Douglas, A. E. and Herzberg, G. "Band Spectrum and Structure of the CH^+ Molecule; Identification of three Interstellar Lines," Canadian Journal of Research, vol. 20a, no. 6, pp. 71-82, 1942.

[74] Drowart, J., Burns, R., DeMaria, G. and Inghram, M. G. "Mass Spectrometric Study of Carbon Vapor," The Journal of Chemical Physics, vol. 31, no. 4, pp. 1131-1132, 1959.

[75] Rienstra-Kiracofe, J. C., Tschumper, G. S. and Schaefer III, H. F., Nandi S. and Ellison G. B. "Atomic and Molecular Electron Affinities: Photoelectron Experiments and Theoretical Computations," Chemical Reviews, vol. 102, no. 1, pp. 231-282, 2002.

[76] Matsuda, A. "Thin-Film Silicon –Growth Process and Solar Cell Application–," Japanese Journal of Applied Physics, vol. 43, no. 12, pp. 7909-7920, 2004.

[77] Sedov, V., Ralchenko, V., Khomich, A. A., Vlasov, I., Vul, A., Savin, S., Goryachev, A. and Konov, V. "Si-doped nano- and microcrystalline diamond films with controlled bright photoluminescence of silicon-vacancy color centers." Diamond and Related Materials, vol. 56, pp.23-28, 2015.

[78] Grudinkin, S. A., Feoktistov, N. A., Bogdanov, K. V., Baranov, M. A., Baranov, A. V., Fedorov, A. and Golubev, V. G. "Chemical vapor deposition of isolated spherical diamond particles with embedded silicon-vacancy color centers onto the surface of synthetic opal." Semiconductors, vol. 48, no. 2, pp. 268-271, 2014.

[79] Grudinkin, S. A., Feoktistov, N. A., Medvedev, A. V., Bogdanov, K. V., Baranov, A. V., Vul, A. and Golubev, V. G. "Luminescent isolated diamond particles with controllably embedded silicon-vacancy colour centres." Journal of Physics D: Applied Physics, vol. 45, no. 6, p. 062001, 2012.

[80] Sedov V. S. M, Vlasoc I. I., Ralchenko V. G., Khomich A. A., Konov V. I., Fabbri A. G., Conte G. "Gas-phase growth of silicon-doped luminescent diamond films and isolated nanocrystals," Bulletin of the Lebedev Physics Institute, vol 38, no. 10, pp. 291-296, 2011.

[81] Allendorf, M. "A Model of Silicon Carbide Chemical Vapor Deposition," Journal of the Electrochemical Society, vol 138, no. 3, p. 841, 1991.

Chapter 2: Experimental Theory and Practice

This chapter begins with a brief description of the theory behind atomic and molecular electronic structures, and how an electron transitioning between an excited occupied state to a lower unoccupied state results in atomic and molecular emission spectra. In this thesis, the latter spectra are simulated on PGOPHER, a spectral simulation software package developed by Dr. Colin Western at the University of Bristol. There is then a brief description of the experimental equipment and experimental practice used to carry out spatially-resolved optical emission spectroscopy, which allows the measurement of relative column densities of excited state species in MW-activated plasmas. The chapter follows on with a description of laser theory, the interaction of light with matter, as well as the experimental apparatus and practice used for Cavity Ring Down Spectroscopy. This technique enables absolute column density measurements of ground state species present within MW-activated plasmas.

2.1: Spatially-resolved Optical Emission Spectroscopy

2.1.1: Electronic Structure of Atoms

An atom or molecule is described by a spatial and time-dependent wavefunction, $\Psi_{tot}(\theta, \phi, r, t)$.[1,2,3] The wavefunction describes the nucleus of an atom (or nuclei of a molecule), and encapsulates information on the occupancy of atomic orbitals by bound electrons (i.e. their location), the overall electron and nuclear spin angular momentum, and in the case of molecules, the rotation and vibration of the nuclei.[1,2,3]

Through solving the Schrödinger equation, which involves a Hamiltonian operating on the wavefunction, given by Equation 2.01, the overall energy of the system can be calculated:

$$\hat{H}\Psi = \left(\hat{T} + \hat{V}\right)\Psi = E\Psi \tag{2.01}$$

The Hamiltonian operator can be expressed in terms of a kinetic energy operator, $\hat{T}$ and a potential energy operator, $\hat{V}$ for an atom.[1,2,3] The Schrödinger equation is solved as a time-independent standing wave when appropriate boundary conditions are applied:

$$\hat{H}\Psi(\theta,\phi,r) = \left(\frac{-\hbar^2}{2m}\nabla^2 + \hat{V}\right)\Psi(\theta,\phi,r) = E\Psi(\theta,\phi,r) \tag{2.02}$$

With a suitable $\hat{V}$ and appropriate boundary conditions, the Schrödinger equation can be solved exactly for a one electron system.[1,2,3] The wavefunction is the solution of such an equation and gives the exact quantised energy level occupied, described by the principal quantum number n.[1,2,3] This can hold integer values between $1 \leq n \leq \infty$. For a single electron system, all n states are bound, however exceeding the

ionization energy, defined by $n = \infty$, results in the ionization of an atom. The principal quantum number is encapsulated within $\Psi_{elec}(r)$, which governs the shape of the electron density distribution and can be used to calculate the probability of finding an electron at a particular position within a potential energy well (e.g. an electric field potential well generated by protons within the nucleus of an atom). Solving the Schrödinger equation becomes more complicated for a many-body electron system due to electron-electron interactions.[1,2,3] Instead, the Born-Oppenheimer approximation is implemented to simplify the problem.[1,3,4] The approximation acts to decouple the electronic and the various nuclear wavefunction components. In the case of diatomic molecules, the idea extends to decouple vibrational and rotational wavefunction components from the electronic wavefunction, as described by Equation 2.03:

$$\Psi_{tot} = \Psi_{elec}\Psi_{nuc}\Psi_{vib}\Psi_{rot} \tag{2.03}$$

This is an important concept, particularly for understanding homonuclear diatomic emissions, as will be discussed in the case of H_2 in Chapter 3, as well as C_2 and C_2^- in Chapter 4. $\Psi_{nuc}(r, t)$ describes the nucleus of the atom / molecules, whilst $\Psi_{vib}(r, t)$ and $\Psi_{rot}(r, t)$ describes molecular vibrational and rotational states.

In a classical picture, an atom is often thought of as electrons orbiting a nucleus, as depicted in Figure 2.01:

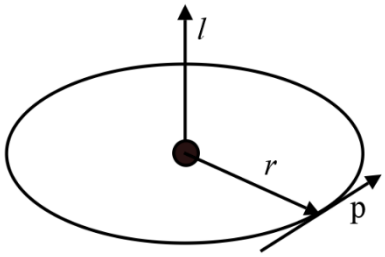

Figure 2.01: The classical depiction of an electron orbiting a nucleus.

The classical notion of an electron orbiting a nucleus is one that has been discredited; if the picture were a realistic description, it would imply continual acceleration of an electron. This would result in bremsstrahlung radiation and an unstable electron orbit and therefore prevent the stability found within the structure of an atom.[1,2,3,5] The principal quantum electron state for a single electron system is degenerate with various associated orbital angular momentum quantum states, which has its own quantum number, l, and can take integer values between $0 \leq l \leq n - 1$.[1,2,3] Term symbols are given to different values of l, for instance $l = 0$ is referred to as the *s* orbital, $l = 1$ as the *p* orbital and so on. The electron orbital angular momentum is itself degenerate with a degeneracy of $2l + 1$. This degeneracy can be lifted resulting in a quantised projection when placed within a magnetic field. Typically, the direction of the magnetic field is defined as the *z*-direction. This quantised angular momentum projection has its own quantum number referred to as the magnetic quantum number, m_l, and can hold integer values between $-l \leq m_l \leq +l$ and is depicted in Figure 2.02.[1,2,3]

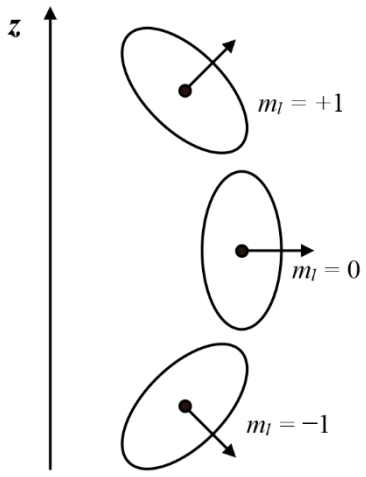

Figure 2.02: A semi-classical depiction of m_l projections for an atomic orbital l = 1 along a defined z direction. Typically, the degeneracy between these states is lifted when a magnetic field is applied along z direction.

Electrons, neutrons and protons have an intrinsic angular momentum property referred to as spin, for which there is no classical comparison. Spin, *s*, as with orbital angular momentum, is a degeneracy, which can be lifted in the presence of a magnetic field, as first demonstrated by Stern and Gerlach.[6,7] The projected spin angular momentum quantum number, m_s, can hold a value of $m_s = \pm ½$ for a single electron.[1,2,3] Half-integer spin entities are referred to as fermions, and also includes neutrons and protons.[8,9] No two fermions may occupy the same state of a system with the exact same quantum numbers. This is known as Pauli's exclusion principle, and hence only two spin paired electrons may occupy an *s* orbital, 6 spin paired electrons may occupy 3 degenerate *p* orbitals and so on.[1,2,3,10] Electrons fill the lowest energy shells and orbitals, and generally assumes the lowest possible energetic configuration.

A new total angular momentum quantum number encapsulating *l* and *s* referred to as *j* can hold half-integer or integer projected values between $|l - s| \leq j \leq |l + s|$. The purpose of *j* is to generate a convenient term symbol used by spectroscopists to describe atomic states and transitions. Such a term symbol takes the form ${}^{2s+1}l_j$.[1,3]

In the simplest case of a hydrogen atom, there is only one proton and electron present. The energy levels can be accurately calculated through solving the radial component of the Schrödinger equation:

$$E_n = -\frac{\mathrm{me}^4}{32\hbar^2\pi^2{\varepsilon_0}^2\mathrm{n}^2} = -\frac{\mathrm{R}\hbar\mathrm{c}}{\mathrm{n}^2} \tag{2.04}$$

in units of J, whereby ε_0 is the vacuum permittivity, e is the charge of an electron, c is the speed of light in a vacuum in units of cms^{-1}, and R is the Rydberg constant traditionally expressed in units of cm^{-1}.[1,2,3] An electron transitioning from an excited energy level state to a lower energy state results in a change in the electric dipole moment. This results in the emission of a photon with an energy proportional to

the difference between two energy levels. The frequency, ω in Hz, (or used to calculate the wavelength) of a photoemission is proportional to the energy difference, as expressed in Equation 2.05:

$$\omega = |\frac{Rc}{n_{upper}^2} - \frac{Rc}{n_{lower}^2}| \tag{2.05}$$

The H Lyman series involves an electron transitioning from $n > 1$ states to the $n = 1$ state, whilst the H Balmer series, studied in Chapters 3 and 6 involve electronic transitions between $n > 2$ and $n = 2$, as depicted in Figure 2.03 (a). The $n = 3$ state has a maximum $l = 2$, $m_l = 2$, and s = ½. The $n = 3$ state also holds $l = 1$ and $l = 0$ states, *p* and *s* orbitals, as described above. This leads to a total number of 18 possible orbital/spin angular momentum combinations, which a single electron occupying the $n = 3$ state can possess.[1,2,3] By consideration of the spectroscopic term symbol, *j*, the 18 possible orbital/spin combinations can be simplified to 5 degenerate spin-orbit states for $n = 3$, whilst the $n = 2$ state has 8 possible spin-orbit combinations, of which there are 3 degenerate states.[1,2,3] Photons carry away a single quantum of angular momentum, $l = \pm 1$, and therefore an electron transitioning between two states requires a change in orbital angular momentum, $\Delta l = \pm 1$. Spin, on the other hand is conserved, and as such $\Delta s = 0$.[1,2,3] There are no selection rules on *n*. Consideration of these selection rules, result in 7 possible transitions between states when considering the fine structure of the H atom, as depicted in Figure 2.03 (b):

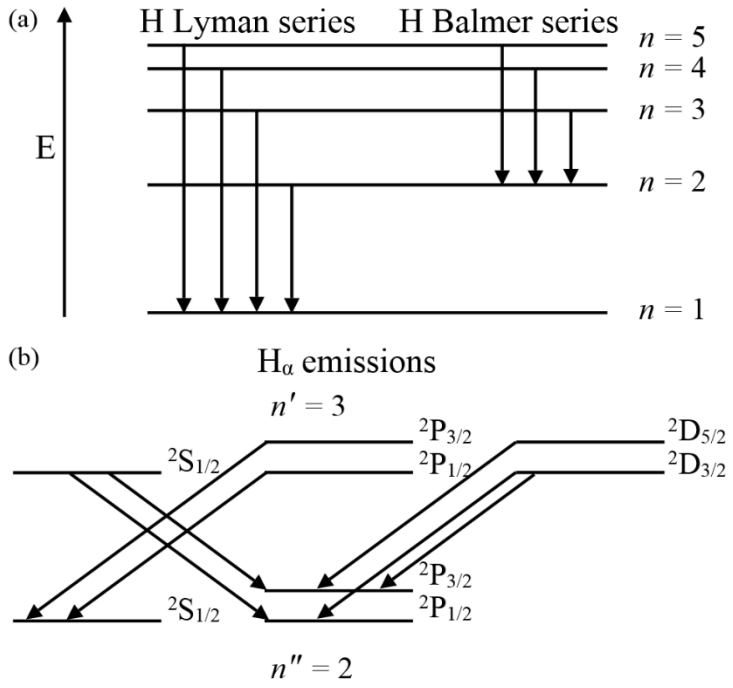

Figure 2.03: Quantisation of H atom with labelled principle quantum *n* states up to n = 5; H Lyman and H Balmer emission series labelled. (b) 7 allowed transitions between H($n = 3$) and H($n = 2$), i.e. the H_α transition.

In light atoms, which contain multiple electrons occupying partially-filled orbitals, the spin angular momenta of the electrons are coupled, as are their orbital angular momenta, such that $L = \sum_{\alpha=1}^{\alpha=i} l_\alpha$, and

$S = \sum_{\alpha=1}^{\alpha=i} s_\alpha$. Integer values of L are allowed between $|l_1 - l_2| \leq L \leq |l_1 + l_2|$ and similarly for S, where half integer values are also allowed. A redefined spectroscopic term, J, takes values integer (or half-integer) values between $|L - S| \leq J \leq |L + S|$.[1,2,3] The spectroscopic term symbol becomes ${}^{2S+1}L_J$ with selection rules of $\Delta L = 0, \pm 1$, $\Delta J = 0, \pm 1$, $\Delta S = 0$, except in the cases of $L' = 0 \rightarrow L'' = 0$ and $J' = 0 \rightarrow J'' = 0$, which are not allowed in atoms. Figure 2.03 (b) demonstrates how consideration of these selection rules facilitate 7 possible transition contributions to the H($n = 3$) → H($n = 2$) transition. Contrastingly, in heavy atoms, spin angular momenta and orbital angular momenta are negligibly coupled, but rather spin-orbit coupling occurs.[1,2,3]

2.1.2: Electronic Structure of Diatomic Molecules

The overall electronic structure of a diatomic molecules is considerably more complicated than that of atoms. As well as electronic states, molecular states also include quantised vibrational and rotational states with quantum numbers v and J respectively. Optical emissions resulting from optical transitions between electronic diatomic states include vibrational and rotational structure. The potential energy of a diatomic state is described by an anharmonic oscillator, which gives an equilibrium bond length r_e and a bond dissociation energy, D_0, defined as the energy required to seperate the atoms by an infinite distance from an equilibrium distance, r_e, depicted as a dashed line in Figure 2.04:

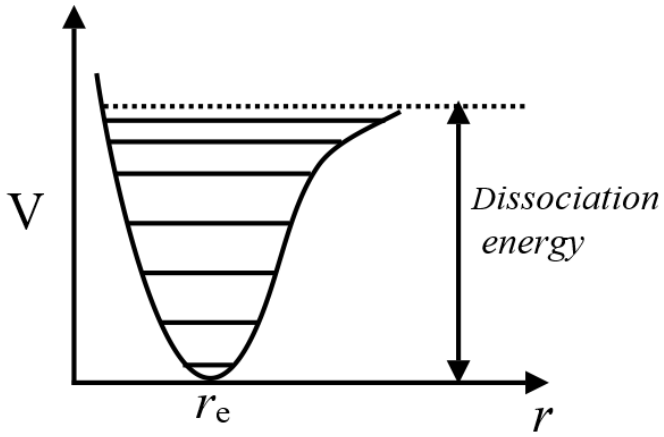

Figure 2.04: Anharmonic potential energy well curve of a diatomic molecule in an electronic state; the lines across the curve represent vibrational levels.

The couplings described for many-electron light atoms also apply to diatomic molecules; electron spin and angular momentum are coupled in diatomic species with quantum numbers Σ and Λ, replacing L and S respectively.[1]

Λ is defined as the axial orbital momentum summed over all electrons; $\Lambda = |\sum m_l|$, whilst Σ is defined by the sum of total unpaired electron spin; $\Sigma = |\sum S|$. The total orbital angular momentum and spin angular momentum along the internuclear axis is defined by $\Omega = |\Lambda + \Sigma|$. These molecular quantum numbers are depicted in Figure 2.05 (a), whilst Figure 2.05 (b) demonstrates how the atomic orbitals of two carbon atoms interact with one another producing molecular bonding and anti-bonding orbitals

through the linear combination of atomic orbital method used for constructing molecular orbitals.[1,11] The overall effect results in a reduction of the overall electronic configuration energy when the lowest energy configuration of C_2 is assumed in comparison to two individual C atoms.

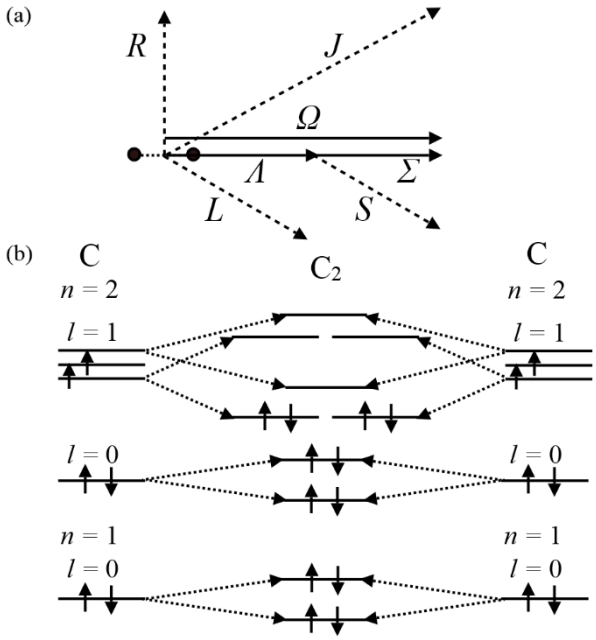

Figure 2.05: (a) Labelled quantum numbers of angular momenta contributing to a diatomic molecule with their respective direction depicted by an arrow. (b) Molecular orbital diagram of ground state C_2 formed by linear combination of the orbital states of two interacting C atoms.

A molecular term symbol describing a diatomic electronic state is given as $Z^{2\Sigma+1}\Lambda_\Omega$, whereby Z describes the electronic state; the ground state is depicted by X. The letters then incrementally increase alphabetically from A for increasingly energetic electronic states. Excited states are not necessarily required to have the same spin as the ground state; the same lettering system applies for this scenario using lower case letters increasing from lower case a. Λ has allowed values of 0, ±1, ±2 and so on corresponding to Σ, Π, Δ states respectively, hence in the C_2 ground state example given in Figure 2.05 (b), the ground state is described by $X^1\Sigma^+_g$.[1,12] The first metastable excited state of the C_2 molecule is the excitation of a single electron from the highest occupied orbital into the first vacant orbital with a single electron spin flipped; this would produce two unpaired spin-aligned electrons, i.e. an overall spin, $\Sigma = 1$. The excited electron has been removed from a π orbital and excited into the σ bonding orbital, resulting in a total angular momentum, $\Lambda = 1$, i.e. a Π state. Therefore, the lowest metastable state of C_2 is described by the term $a^3\Pi_u$. The addition of a single electron to the ground state of C_2, i.e. C_2^- ground state, would give a total spin $\Sigma = ½$, but still contribute a total orbital angular momentum of 0, hence holding a ground state of $X^2\Sigma^+_g$.

The rotation of the diatomic molecule's nuclear framework is depicted in Figure 2.05 as vector, *R*, and couples with Ω to give a total angular momentum of $J = R + \Omega$. These quantum numbers are depicted in Figure 2.05 (a).[1]

There are two additional considerations for Σ states and homonuclear diatomic molecules respectively; the Σ state is accompanied with a + or – label describing whether a reflection of the electronic wavefunction along the inter-nuclear axis plane is symmetric or anti-symmetric, whilst homonuclear diatomic molecule term symbols are accompanied with a 'g' or 'u' label dependent on whether the wavefunction describing the electronic configuration is symmetric or anti-symmetric with regards to an inversion through the centre of symmetry of the molecule.[1]

Molecular constants can be used to describe the electronic, vibrational and rotational energies of a state. The total energy of a given molecular state is given by Equation 2.06:

$$E(state) = T_{state} + G(v) + F(J) \tag{2.06}$$

$G(v)$ can be expressed as $G(v) = w_e(v + ½) + w_e x_e(v + 1/2)^2 + w_e y_e(v + 1/2)^3$ to third order, where v is the vibrational state quantum number, w_e is the oscillating frequency, and x_e and y_e are anharmonicity constants.[1]

$$F(J) = BJ(J+1) + DJ^2(J+1)^2 + HJ^3(J+1)^3 \tag{2.07}$$

B, D, H are rotational constants. *B* can be expressed as a function of the moment of inertia, *I*, between two atoms within a diatomic molecule with masses m_1 and mass m_2, separated by distance *r*. The moment of inertia is given by $I = \mu_m r^2$, where $\mu_m = m_1m_2/(m_1+m_2)$, i.e. the reduced mass of the system:

$$B = \frac{h}{8\pi^2 cI} \; in\ units\ of\ cm^{-1} \tag{2.08}$$

T, G, B, D and any additional terms, are unique to a rotational-vibrational-electronic (rovibronic) state and are required, along with additional electronic state information (e.g. spin state, total orbital angular momentum etc) to produce a spectral simulation of a rovibronic transition between two such states. Such a simulation can be generated using PGOPHER, a spectral simulation software package developed by Dr. Colin Western.[13] This software is used for analysis of data presented in Chapters 4, 5, and 6.

As is the case with atomic transitions, diatomic rovibrational electronic transitions also have associated selection rules, as described below:

$\Delta\Lambda = 0, \pm1$. $\Delta\Omega = \pm1$. $\Sigma^+ \leftrightarrow \Sigma^+$, and $\Sigma^- \leftrightarrow \Sigma^-$ only, and $\Lambda_u \leftrightarrow \Lambda_g$ only. Typically, $\Delta J = -1$ is referred to as the P branch, $\Delta J = 0$ as the Q branch, whilst $\Delta J = +1$ as the R branch.[1]

Diatomic transitions also contain vibrational quantum number changes guided by the Franck Condon principle.[1,14] Electronic transitions, and by extension emissions, are instantaneous relative to the finite response time of nuclei. As such, an emission appears as a vertical line in a transition depiction illustrated in Figure 2.06. Consequently, the probability, *P*, of a transition from one vibrational state to another is dependent on the overlap of the initial and final vibrational wavefunction states squared; this is known as the Franck Condon factor.

$$P = < \Psi_{final} | \hat{\mu} | \Psi_{initial} >^2 \tag{2.09}$$

Equation 2.09 is expressed in Bra-Ket notation, where $\hat{\mu}$ is the Hamiltonian for a change in the electronic dipole moment.[1,14] Equation 2.09 describes the overall probability of a ro-vibronic transition. Through consideration of the Born-Oppenheimer approximation, which allows separation of the vibrational and electron wavefunction, this can be expressed as Equation 2.10.[1]

$$P = < \Psi_{v,f} | \Psi_{v,i} >^2 < \Psi_{e,f} | \hat{\mu}_e | \Psi_{e,i} >^2 < \Psi_{S,f} | \Psi_{S,i} >^2 \quad (2.10)$$

The nuclear contribution of $\hat{\mu}$ operator generally equates to zero. This is because it does not operate on the initial state of the electron wavefunction. The orthogonality of the electronic initial and final state components results in this contribution equating to zero.[1] The vibrational component of Equation 2.10 describes the Franck-Condon factor (FCf), whilst the electronic component is described by orbital angular momentum selection rules, and the spin component describes spin selection rules. Figure 2.06 depicts two electronic transition cases, where (a) the Franck Condon factor, FCf, = 1, and (b) where the FCf < 1:

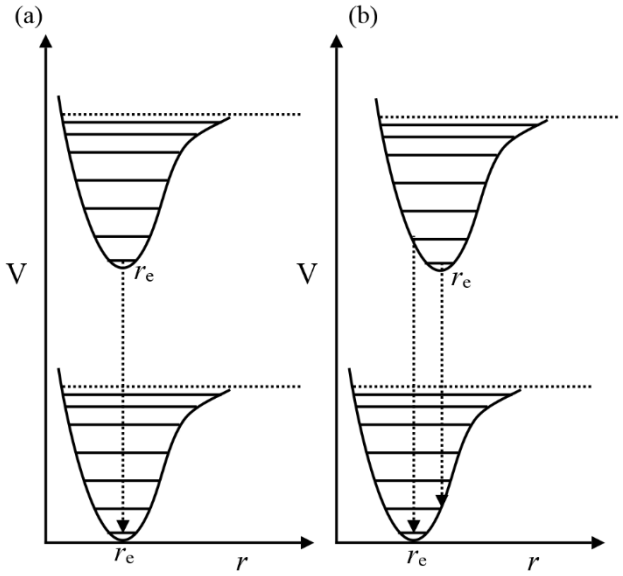

Figure 2.06: Anharmonic potential energy curves of two diatomic molecule electronic states showing transitions from a $v' = 0$ level with a Franck Condon Factor of (a) 1 and (b) < 1.

An allowed transition (i.e. an electron transitioning between two states as allowed by the selection rules) emits a photon with a transition energy equal to the difference between two rovibronic states, as described by Equation 2.11:

$$\Delta E = T' + G(v') + F(J') - T'' - G(v'') - F(J'') \quad (2.11)$$

The photon can be observed at wavelength, λ, described by Equation 2.12:

$$\lambda = \frac{hc}{\Delta E} \; in \; units \; of \; nm \quad (2.12)$$

2.1.3: Experimental Set-up and Practice

For spatially-resolved optical emission spectroscopy, it is necessary to ensure that a Czerny-Turner Spectrometer is set up to image a central slice of a plasma with a focussed lens. The focus can be ensured by imaging an object placed in the centre of the chamber. Alignment can be verified through imaging the chamber on a zeroth order grating with a wide slit width and making use of the physical features of the chamber. Further, the centre of the front and back windows must align on the same pixels as used with a narrow slit width, which is indicated by a white dashed line in Figure 2.07 (a) (and 2.07 (b)):

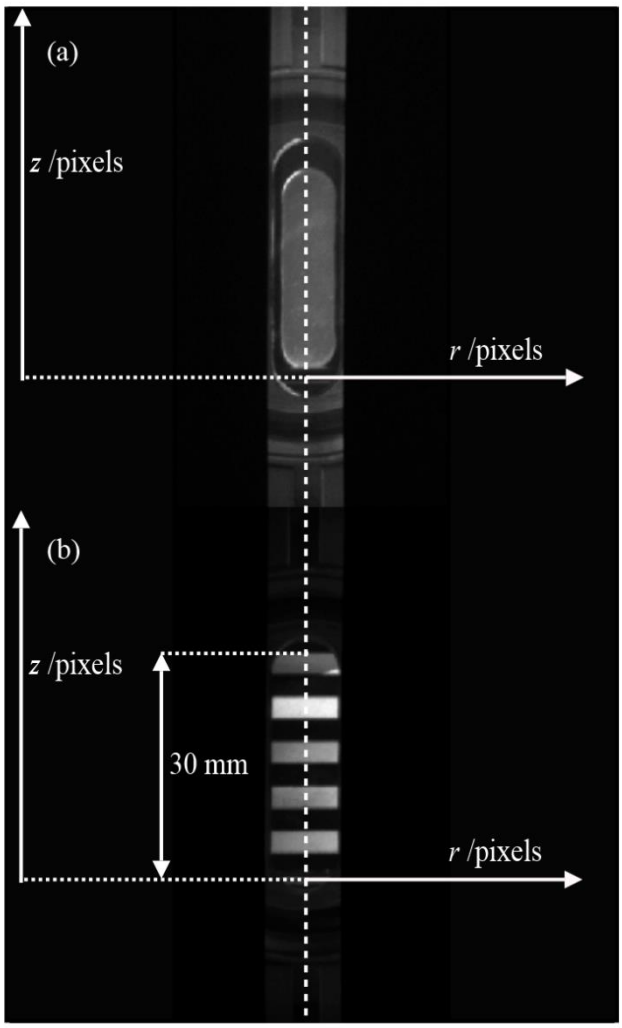

Figure 2.07: Zeroth order image with a wide slit width of (a) an aligned reactor, and (b) an illuminated card placed centrally within the aligned reactor with alternating 3mm black and white strips.

Figure 2.07 (b) demonstrates an image of an appropriately placed black and white striped image target for spatial calibration collected as a zeroth order image with a large slit width and illuminated. By illuminating the striped target with an appropriate wavelength and narrowing the slit to a small size (generally ~ 10 μm) it is possible to obtain the spatial calibration and resolution required to analyse optical emissions.

The image must be accumulated using the same grating and wavelength settings as that for which the experimental data is collected. Post-processing of experimental data relies on such a calibration image for deskewing data and obtaining spatial information. Figure 2.08 (a) demonstrates an example spatial calibration collected using the target featured in Figure 2.07 (b) collected on first order, with the grating centred on λ = 600 nm, using a narrow slit; i.e. an image collected along the dashed vertical line seen in Figure 2.07 (b). The dashed horizontal lines across Figure 2.08 (a) define $z = -3$ and +27 mm, where $z = 0$ defines the top of the substrate. Figure 2.08 (b) demonstrates how post-processing selects the relevant spatial region imaged on the CCD and deskews the image, the dashed line in Figure 2.08 (b) indicates the top of the substrate, $z = 0$ mm. The horizontal axis can be converted from pixels into wavelength through a polynomial conversion.

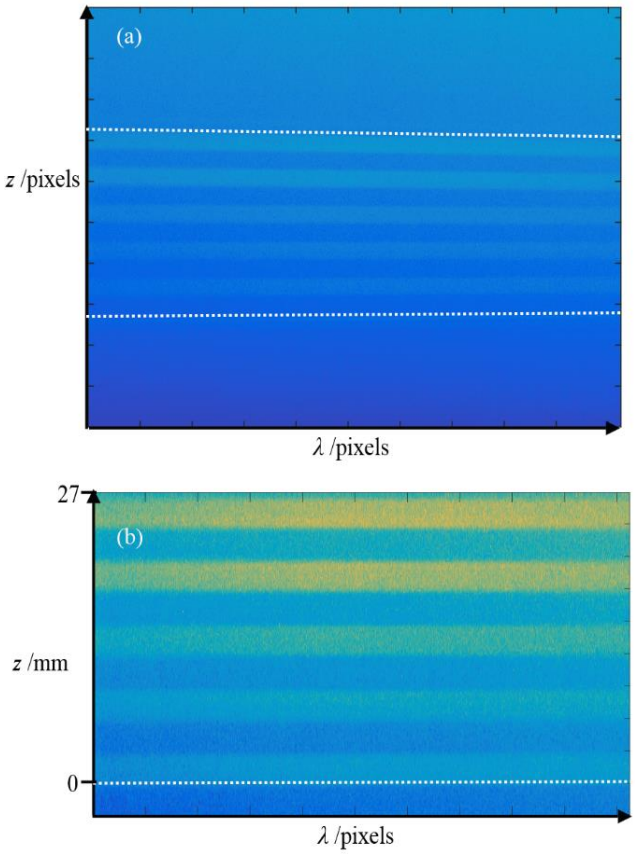

Figure 2.08: First order image of 3 mm black and white strips, centred on λ = 600 nm, using a narrow slit width of 10 µm (a) as seen on CCD and (b) after post-processing. In (a) the dashed lines indicate constant height at $z = -3$ mm and +27mm above the substrate. In (b) the dashed line indicates the top of the substrate (i.e. $z = 0$ mm).

The experimental data can be further processed by summing the intensity into more manageable sized bins (e.g. strips) if further analysis is required via PGOPHER (typically required for diatomic emission analysis). This thesis generally uses a binning of 1.5 mm in the z dimension within Chapters 3, 4, 5 and 6 for illustrating spatial distributions of diatomic emissions, and 3 mm binning for investigations into 'peak' intensities of both atomic and diatomic emissions as a function of process conditions (typically

featuring between $9 \leq z \leq 12$ mm, i.e. the 4th strip from the dashed line in Figure 2.08). For atomic spatial distributions, no binning post-deskewing is generally necessary for spatial distributions.

The imaging apparatus set up consists of 7 main components: a focussing lens, through which light enters a Czerny-Turner spectrometer, with a small entrance slit (typically 10 microns). The light is reflected by a collimating mirror onto a diffraction grating and is dispersed into its wavelength components through Bragg's law of diffraction ($m\lambda = 2d \sin\theta$), where m is the diffraction order, d is the separation of the diffracting material outcrops and θ is the angle at which the incident ray hits the grating.[15] The diffracted light is focussed onto a cooled CCD for detection. Figure 2.09 demonstrates the insides of the Andor Shamrock 500i Spectrograph, focal length of 50 cm with an attached Andor Newton 950 CCD used for imaging. This equipment features in Chapter 3, 5, 6, and some further studies in Chapter 4. Chapter 4 is predominantly carried out using a Newport MS127i with a focal length of 125 mm using an imaging objective 25 mm in focal length, f/16 and an Andor Newton 970 camera.

Data collection for optical emission spectroscopy is relatively straight forward; after simple tests optimising signal/noise and preliminary studies to avoid pixel saturation, data is accumulated by altering the plasma conditions and collecting emissions of interest across the relevant wavelength range of interest for a user-determined period of time. Typically, one parameter is investigated at a time (e.g. input MW power), whilst all remaining conditions are kept constant with the plasma operating under steady-state.

Between condition alterations, it is necessary to wait at least 3 gas residence times (i.e. the time it requires to replenish ~87.5% of the original gas content, which under base conditions p = 150 Torr, is 6 minutes) prior to data collection. This ensures that the plasma has reached a steady-state, which reflects the condition under investigation

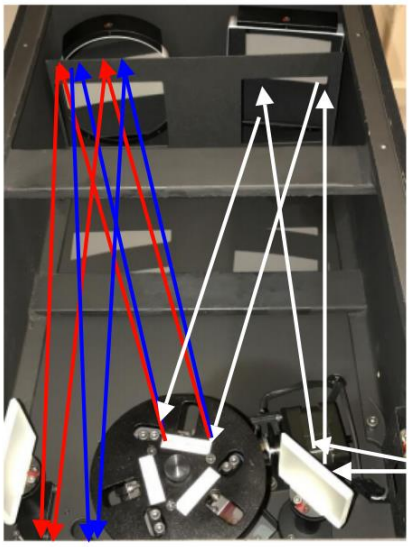

Figure 2.09: Inside of a Czerny-Turner Spectrometer with arrows demonstrating how light entering is collimated onto a diffraction grating, split into wavelength components and focussed onto a CCD for detection.

2.1.4: Leak Rate Testing and Mass Flow Control Calibration

It is important to ensure that mass flow controllers are accurately calibrated and correctly zeroed for investigations with respect to flow rate, particularly in the instance of two or more gases. Further, it is important to monitor (and minimise) air leaks. Such leaks predominantly introduce oxygen (and nitrogen) into the gas phase; oxygen has the potential to fundamentally change the prominent cations, whilst both impurities have the potential to vary the gas phase processes and diamond growth quality.

Flow rates are calibrated relative to one another through measuring the time it takes for the pressure to rise, for example by Δp = 100 Torr starting from an evacuated (non-pumping) sealed chamber. The mass flow controllers (mfcs) can be adjusted (i.e. multiplied by a scaling factor), such that Equation 2.13 is satisfied for all gas mfcs, where *F*(gas) is the operational flow reported in this thesis:

$$\frac{dp}{dt} \times \frac{1}{F(gas)} = constant \tag{2.13}$$

Similarly, to estimate the leak rate, the chamber should be evacuated for ~24 hours. The gas lines are closed, and the evacuation of the chamber is switched off. The leak rate can be estimated by measuring the rate of pressure rise to give an effective flow using Equation 2.13. This can be translated into a leak through consideration of plasma operating pressure (~ 150 Torr for base conditions relative to atmospheric pressure (~ 760 Torr)) and in relation to flow rates utilised. The vacuum leak concentration can be estimated by Equation 2.14.

$$X_0(leak) = \frac{F(leak)}{\sum F(gas)} \cdot \frac{760\ - p}{760} \cdot\ 10^6\ in\ ppm \tag{2.14 a}$$

In this thesis, the leak rate quoted is calculated for $F(H_2)$ = 300 sccm, p = 150 Torr; no attempt has been made to calculate the leak for the addition of $F(CH_4)$, F(Ar) or change in p. This, however, does not account for the supplied gas contaminants, which are generally larger (or of the same order) as vacuum leak contributions in the studies featuring in this Thesis. To include such a contribution, Equation 2.14 (a) would be expressed as Equation 2.14 (b), where $x_i \cdot F_i$ describes the air impurity associated with a particular gas multiplied by the flow rate used:

$$X_0(leak) = (\frac{F(leak)}{\sum F(gas)} \cdot \frac{760\ - p}{760} + \sum_i F_i\ (gas) \cdot x_i) \cdot\ 10^6\ in\ ppm \tag{2.14 b}$$

2.2: Cavity Ring Down Spectroscopy

2.2.1: Laser Theory

As with emission, light absorption requires the energy of the light to be equal to the difference between two energy levels, and results in a change in dipole moment. The term “laser” is an abbreviation from the term “**l***ight* **a***mplification by* **s***timulated* **e***mission of* **r***adiation*”. For the laser absorption experiments

featuring within this thesis, the investigated species is atomic Si in MW-activated Si/H and Si/C/H plasmas, and hence this thesis focuses predominantly on atomic electronic state absorption, but the ideas also apply to rotational, vibrational and electronic state occupancy and transitions (required to understand the principals facilitating dye lasers).

In thermal equilibrium, the population of the absorbing and excited state in thermal equilibrium is dictated by the Boltzmann distribution and the degeneracy of the two states:

$$\frac{N_k}{N_i} = \frac{g_k}{g_i} e^{-\frac{\Delta E}{kT}} \tag{2.15}$$

Where g_k and g_i are degeneracies for the upper and lower state respectively, and N_k and N_i are the populations of these states, where ΔE defines the energy difference between the states.[16,17,18]

The probability of a transition occurring is dictated by Einstein emission and absorption coefficients, depicted in Figure 2.10 (a).[16] Spontaneous emission is depicted by A_{ki} and dictates emission rates occurring in optical emission spectroscopy, whilst B_{ik} and B_{ki} represent induced absorption and stimulated emission respectively:

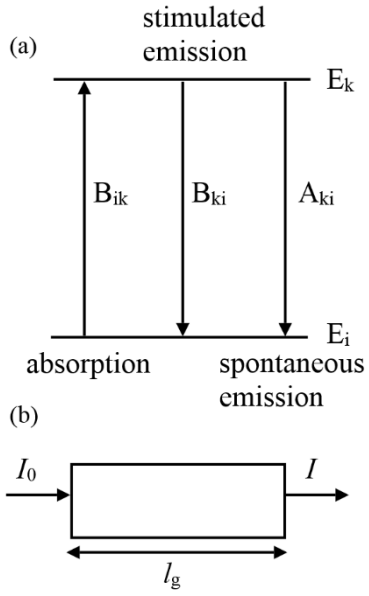

Figure 2.10: (a) Einstein absorption and emission coefficients connecting electronic states with energies E_i and E_k and (b) Light with intensity I_0 entering a gain medium length l_g, and exiting with intensity I.

Figure 2.10 (b) demonstrates the simple concept of a laser; light with an intensity I_0 enters into a laser, reflects between two highly reflective mirrors separated by distance l_g, with some light leaking out with intensity I.[16] In an absorbing material, the light would decay exponentially with the Beer-Lambert law, Equation 2.16, where the absorption coefficient, $\alpha > 0$, whereas in a lasing material $\alpha < 0$, and the output intensity I is greater than the input intensity, I_0.[16]

$$I = I_0 e^{-\alpha l_g} \tag{2.16}$$

To achieve lasing, there are two requirements; a population inversion between the upper and lower state, and a lasing material with a gain coefficient $G > 1$. G can be related to α via consideration of a Equation 2.16 and the reflectance of the two mirrors, for a single round trip, i.e. $G = R_1R_2e^{-2\alpha l_g}$. An Nd:YAG crystal consists of Nd^{3+} within a $Y_3Al_5O_{12}$ lattice and is used in this thesis to generate light at 1064 nm; the third harmonic is generated through the use of a frequency tripling crystal to produce 354.4 nm light.[19] An Nd-YAG laser is an example of a pulsed 4 level laser system, which can be seen in Figure 2.11.

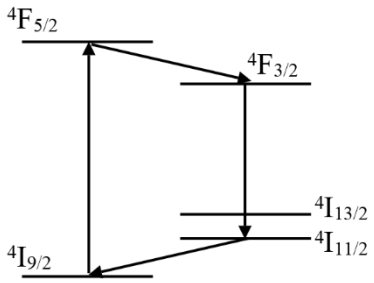

Figure 2.11: Nd^{3+} energy level diagram with arrows indicating light absorption by an electron, and electron de-excitation through non-radiative and radiative decay.

The Nd-YAG laser is pumped using a Xe flash lamp emitting with a broad band emission, typically centred at e.g. $\lambda \sim 806$ nm, populating the $^4F_{5/2}$ state, which has a fast non-radiative decay rate.[19] This relaxes to the metastable $^4F_{3/2}$ state, which has a lifetime $\tau \sim 230$ μs. This irradiates to two lower levels of $^4I_{13/2}$ and $^4I_{11/2}$ at 1332 and 1064 nm respectively. These states depopulate rapidly into the ground state, $^4F_{9/2}$, through non-radiative relaxation; this enables a population inversion between the $^4F_{3/2}$ and $^4I_{11/2}$ states, as derived in the Appendix.[19]

The 1064 nm light is released from the cavity with a frequency of 30 Hz. This is achieved through Q-switching.[16,19] Q-switching adjusts the quality of the laser, in particular, the Q factor, defined as $Q = \nu/\Delta\nu$, whereby ν is the frequency of the light and $\Delta\nu$ is the laser line width. When Q is high, there are fewer loses, whereas when Q has a low value results in high losses from the cavity. By holding a high Q, the population inversion is achieved. Reducing the Q factor to a low value for a short period of time, allows the laser to pulse light out.[16,19] The laser is run at 30 Hz, producing 30 outputs of laser light per second. The 354.4 nm light, (produced by a frequency tripling crystal), is used to excite a tuneable dye laser (Coumarin 503 dye), to produce lasing at double the desired wavelength ~505 nm. The energy level diagram for a typical dye laser can be seen in Figure 2.12.[20]

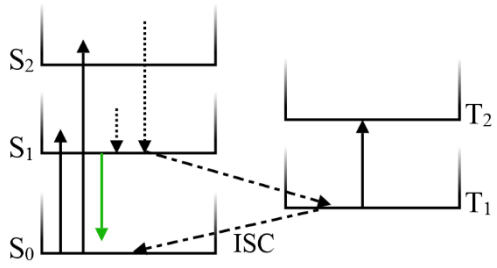

Figure 2.12: A typical energy level diagram for a dye laser with solid arrows indicating light absorption and dashed arrows indicating intersystem crossing. The green line indicates the 505.06 nm lasing emission

Coumarin 503 laser dye is dissolved in methanol and fluoresces at a range of wavelengths due to the close lying vibrational states. The dye is pumped from the Singlet ground state, S_0, to the higher energy singlet states S_1 and S_2.[20] These excited rotational-vibrational states relax non-radiatively into the $S_1(v = 0)$, which will emit to the $S_0(v > 0)$, where v is sufficiently high that it will not have a significant Boltzmann population (i.e. a free population inversion). There is the possibility of intersystem crossing (ISC) between singlet and triplet states, acting to decrease the desired population inversion and therefore reduce the dye power output.[20] Through T_1 absorbing light, i.e. populating T_2, there is also a lower intensity acting to populate S_1, acting to further decrease the overall population inversion.[20] The emitted lasing light passes through frequency doubling optics generating ~ 252.5 nm required for investigating triplet ground state Si atoms.

2.2.2: Experimental Set-up and Practice

The chamber is set up, such that a height adjustable laser, has an optimised λ of 252.53 nm to investigate Si atoms. The light passes through the centre of the chamber; two cavity arms are added to the chamber holding two carefully positioned UV reflective mirrors with an alleged reflectivity of 99.5%. These mirrors are placed 1 metre, L, apart. The lasing light reflects through the cavity making many hundreds of round trips. The signal detected by a photomultiplier tube, behind the second mirror as shown in Figure 2.13, is described by Equation 2.17. If correctly aligned, some light will be lost per round trip producing an exponential time decaying signal, with a time constant, referred to as the Cavity Ring Down time, τ_0, described by Equation 2.18.[21] Prior to detection, the signal passes through a UV filter to remove any residual green laser light from the dye laser.

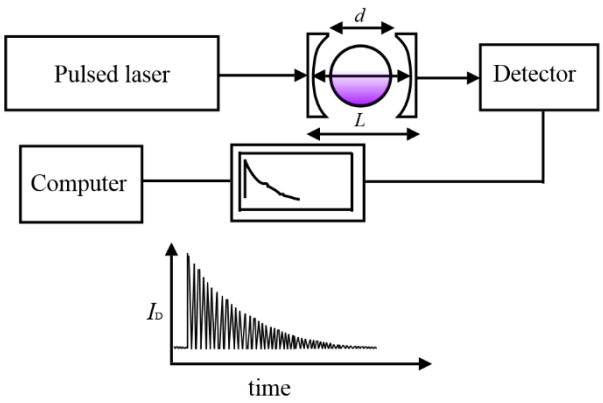

Figure 2.13: Cartoon illustrating Cavity Ring Down Spectroscopy set-up.

The detected intensity can be described by an exponentially time-decaying signal described by a time constant τ or τ_0 when no absorber is present.

$$I_D = I_0\, e^{-t/\tau} \tag{2.17}$$

τ_0 can be written in terms of the reflectivity of the mirrors, *R*, as described by Equation 2.18, where c is the speed of light in a vacuum:

$$\tau_0 = \frac{L}{c|\ln(R)|} \approx \frac{L}{c(1-R)}\ for\ R \sim 1 \tag{2.18}$$

The time constant decreases with an absorber present:

$$\tau = \frac{L}{c(1-R+\alpha d)}\ for\ R \sim 1 \tag{2.19}$$

The absorption coefficient, *α*, appearing in Equations 2.19 and 2.20 also features in Equation 2.16, and is proportional to the number density of the absorbing species Si, [Si], where σ is the absorption cross section.[21]

$$\alpha = \frac{\sigma[Si]}{c} = \frac{h\upsilon}{c^2}\, B_{ij}[\mathrm{Si}] \tag{2.20}$$

B_{ij} is the Einstein-B absorption coefficient and υ is the frequency of the transition. Given that c is in the denominator (whereby $c = \lambda\,\upsilon$), Equation 2.20 can be written in terms of $\bar{\upsilon}$ (the wavenumber of the transition) in cm^{-1}.

$$\alpha = \frac{\sigma[Si]}{c} = \frac{h\bar{\upsilon}\, B_{ij}[\mathrm{Si}]}{c} \tag{2.21}$$

The Einstein-B stimulated emission (B_{ji}) coefficient can be related to the Einstein-A emission coefficient via Equation 2.22, whilst the Einstein-B absorption coefficient (B_{ij}) can be related to the Einstein-B stimulated emission coefficient via Equation 2.23:

$$A_{ji} = 8\pi h\bar{\upsilon}^3 B_{ji} \tag{2.22}$$

$$B_{ij} = B_{ji}\,\frac{g_j}{g_i} \tag{2.23}$$

Whereby g_i and g_j describe the degeneracy of the lower and upper state respectively. Equation 2.20 can therefore be rewritten in terms of the Einstein-A emission coefficient as follows:

$$\alpha = \frac{1}{8\pi c}\,\frac{1}{\bar{\upsilon}^2}\frac{g_i}{g_j}\,A_{ij}[\mathrm{Si}] = \frac{\sigma[\mathrm{Si}]}{c} \tag{2.24}$$

The difference in decay rates between an empty chamber and an absorbing species present is given by Equation 2.21, where [Si] indicates the number density of Si ground state atoms, and can be related to the column density of Si, {Si} via {Si}=d[Si] by substituting in Equation 2.20 for α:

$$\Delta k = \frac{1}{\tau} - \frac{1}{\tau_0} = \frac{c(1 - R + \alpha d + R - 1)}{L} = \frac{c\alpha d}{L} = \frac{d[\mathrm{Si}]\sigma}{L} = \frac{\{\mathrm{Si}\}\sigma}{L} \tag{2.25}$$

Equation 2.25 demonstrates that it is possible to measure the column density of species Si, {Si}, through a Cavity Ring Down Absorption measurement. By scanning the laser wavelength across a suitable wavelength range, noting that such an atomic Si absorption line is prone to thermal (and possible saturation) broadening, it is possible to capture the entire atomic absorption line. It is necessary to integrate the reciprocal difference in ring down times, Δk described in Equation 2.25, with respect to wavenumber across the absorbing peak to calculate {Si}. This can then be rearranged to calculate {Si} described by Equation 2.26: .

$$\{Si\} = \frac{8\pi\,L\,\bar{\upsilon}^2}{\mathrm{A}_{ji}}\frac{g_i}{g_j}\int \Delta k\; d\bar{\upsilon} \tag{2.26}$$

To calibrate the wavenumber, the constructive and destructive interference patterns of an etalon were compared to a calibrated spectrum collected with the use of a wavemeter. The wavenumber range scanned is of the order of 10 cm^{-1} used, and so it is assumed that the wavenumber varies linearly across this wavelength range.

Figure 2.14 demonstrates an example absorption peak, the interference pattern of the data, the calibration pattern, and an example Gaussian fit, which peaks at 39,606.0 cm^{-1}.

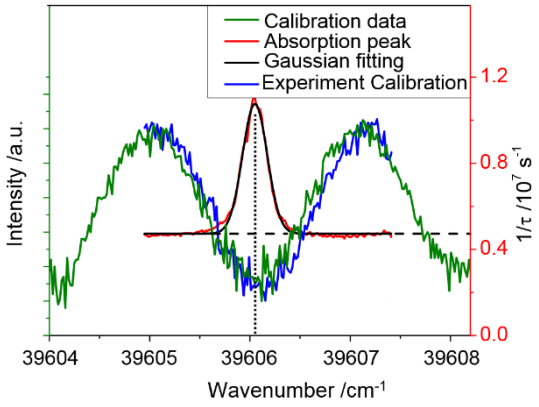

Figure 2.14: Example absorption data (red) of Si($3s^2 3p4s$, $^3P^o$, $J = 0 \leftarrow 3s^2 3p^2$, ^3P, $J = 1$), $\bar{\upsilon}$ = 39606.048 cm^{-1}, with a best fit Gaussian curve (black), the associated calibration data (blue), which have both been calibrated against the wavenumber calibration dataset (green).

By adjusting the laser height on a translatable stage, Si column densities can be measured as a function of plasma height, *z*.

References

[1] Atkins, P. and Friedman, R. "Molecular quantum mechanics." Oxford, Oxford University Press, 2011.

[2] Holzner S. "Quantum physics for dummies." Hoboken, N.J., Wiley, 2013.

[3] Cowan, R. D. "The Theory of Atomic Structure and Spectra." London: University of California Press Ltd, 1981.

[4] Born, M, Oppenheimer, R. "Zur Quantentheorie der Molekeln." Annalen der Physik, vol. 389, no. 20, pp. 457-484, 1927

[5] James, C. W., Falcke, H., Huege, T., Ludwig, M. "General description of electromagnetic radiation processes based on instantaneous charge acceleration in "endpoints"." Physical Review E., vol. 84, no. 5, 2011.

[6] Gerlach, W., Stern, O. "Der experimentelle Nachweis der Richtungsquantelung im Magnetfeld." Zeitschrift für Physik. vol. 9, no. 1, pp. 349-352, 1922.

[7] Rosen, N., Zener, C. "Double Stern-Gerlach Experiment and Related Collision Phenomena." Physical Review. vol. 40, no. 4, pp. 502-507, 1932.

[8] Sherwood, J. E., Stephenson, T. E., Bernstein, S. "Stern-Gerlach Experiment on Polarized Neutrons." Physical Review. Vol. 96, no. 6, pp. 1546-1548, 1954.

[9] Arias, J. M., Alonso, C. E., Bijker, R. "Description of the odd-even xenon and cesium isotopes in the proton-neutron interacting boson-fermion model." Nuclear Physics A, vol. 445, no. 2, pp. 333-349, 1985.

[10] Pauli, W. "Zur Quantenmechanik des magnetischen Elektrons." Zeitschrift für Physik. vol. 43, no. 9-10, pp. 601-623, 1927.

[11] Yiannopoulou, A., Jeung, G., Park, S., Lee. H. S., Lee, Y. S. "Undulations of the potential-energy curves for highly excited electronic states in diatomic molecules related to the atomic orbital undulations." Physical Review A. vol. 59, no. 2, pp. 1178-1186, 1999

[12] Ballik, E. A., Ramsay, D. A. "Ground State of the C_2 Molecule." The Journal of Chemical Physics, vol. 31, no. 4, p. 1128, 1959.

[13] Western, C. M., "PGOPHER, A Program for Simulating Rotational, Vibrational and Electronic Spectra," University of Bristol, http://pgopher.chm.bris.ac.uk.

[14] Coon, J. B., DeWames, R. E., Loyd, C. M. "The Franck-Condon principle and the structures of excited electronic states of molecules." Journal of Molecular Spectroscopy, vol. 8, no. 1-6, pp. 285-299, 1962.

[15] Hiltner, P. A., Papir, Y. S., Krieger, I. M. "Diffraction of light by nonaqueous ordered suspensions," The Journal of Physical Chemistry, vol. 75, no. 12, pp. 1881-1886, 1971.

[16] Demtroder, W. "Laser Spectroscopy 1: Basic principles" 5th edition, Berlin, Springer, 2014.

[17] Katzenstein, J. "Laser theory. Optics & Laser Technology" vol. 5, no. 6, p. 276, 1973.

[18] Ostrander, P. "Maxwell-Boltzmann distribution." The Physics Teacher, vol 17, no. 9, p. 615, 1979.

[19] Krupke, W. "Ytterbium solid-state lasers. The first decade." IEEE Journal of Selected Topics in Quantum Electronics, vol. 6, no. 6, pp. 1287-1296, 2000.

[20] Ferguson, A. "Dye Laser Principles with Applications." Journal of Modern Optics, vol. 38, no. 5, p. 1010, 1991.

[21] Demtroder, W. "Laser Spectroscopy 2: Experimental Techniques" 5th edition, Berlin, Springer, pp. 23-27, 2016.

Chapter 3: Investigating Hydrogen Emissions Originating from MW-activated H and H/Ar Plasmas

This chapter investigates spatially-resolved optical emissions from the Hydrogen Balmer series, H((n > 2)→(n = 2)), and three molecular hydrogen emission bands, the H_2(d→a) band (also known as the H_2 Fulcher-α), the H_2(G→B) and the H_2(e→a), within MW-activated H and H/Ar plasmas. By investigating how these emissions vary as a function of operating conditions (total gas pressure, input microwave power, argon flow, substrate diameter, and a combination of these), a self-consistent 2-D physical chemical kinetic models of MW-activated H and H/Ar plasmas have been developed by our Russian collaborator, Yuri Mankelevich. Under conditions comparable to those studied in this thesis, such plasmas are typically used for H-termination, etching, and for actinometry purposes. This chapter provides an advancement in the understanding of the plasma parameters, and their interdependent coupling with the physical processes occurring within the plasma. The consideration of additional processes, such as associative ionization of H(n = 2) with H_2 and the coupling between excited states of H_2* with H(n = 1), and H(n > 1) with H_2, provides an insight into prior diagnostic studies using the H Balmer series and H_2 emission bands. The addition of argon into the gas phase results in a change of plasma parameters, axial contraction and radial expansion of the plasma, advantageous for those attempting to grow over larger surface areas or with an enhanced plasma homogeneity. Further near resonant excitation transfer couplings are identified between ground and excited states of H (and H_2) with Ar* and Ar respectively. This study provides a sensitive diagnostic tool for investigating the hyper-thermal component of the Electron Energy Distribution Function and uses the developed understanding to rationalise an unstudied emission contribution originating from I(H*) and I(H_2*) situated at low z near to and around the circumference of the substrate. This contribution was found to be enhanced (and relocated) using smaller substrate diameter – a previously unexplored parameter space, and by increasing the smaller substrate temperature. The introduction of high argon fractions was found to quench I(H*) and I(H_2*) emissions across all plasma heights but enhance the relative contribution of low z emission, encouraging a bimodal distribution in I(H*). Whilst there is no definitive explanation behind these emissions, the causes are speculated upon. Chapter 3 builds an understanding upon which the rest of this thesis is built. Many of the results and discussion featured in this chapter are published in References 1 and 2.

3.1: Introduction: MW-activated H Plasmas

Stars, a form of H plasmas, have been a source of bewilderment and inspiration throughout the history of humanity. They are one of the most prominent objects in the observable universe, featuring within

mythologies (e.g. modern-day religions), philosophy, culture, science, art and films. The Lion King, 1994, features a conversation between characters Simba, Timon and Pumba, in which they speculate over whether stars are "great kings watching over us", "fireflies, that uh.. got stuck on that big bluish-black thing" or "balls of burning gas billions of miles away".[a] Fusion, the "burning" process, generates a huge source of power within stars. Scientists are attempting to replicate the extreme temperatures necessary for fusion through magnetic confinement of H plasmas with the ambition of creating an efficient sustainable energy source. One of the more obscure designs (stellarator) uses MW-activated H plasmas for this purpose.[3]

Under more moderate conditions, such as those explored in this thesis, the MW-activated H plasma finds technological applications within material processing. Such plasmas can be used to etch silicon and diamond substrates, hydrogen-terminate material surfaces, and upon the addition of methane, facilitate diamond growth through the Chemical Vapour Deposition method, as outlined in Chapter 1, Section 1.4.[4,5] MW-activated H plasmas have also been studied with the addition of dilute diborane,[6] oxygen (via carbon dioxide),[7] nitrogen and ammonia [8] to provide benchmark models for understanding the gas phase processes involved when these dopants are introduced to MW-activated C/H plasmas. Chapter 6 uses MW-activated H and H/Ar plasmas to investigate the addition of dilute silane in MW-activated Si/H (and Si/H/Ar) plasmas and develop such a model to facilitate an understanding of Si-related gas phase processes occurring within MW-activated Si/C/H plasmas.

The H_2 molecule has a high density of electronic excited states at energies approaching the ionization limit, and as such, most are perturbed by their interactions with other close lying energy states.[9,10] This results in a complicated rovibrational emission structure, which spans from the infra-red through to the visible-UV emission continuum (the dissociative $a^3\Sigma_g^+ – b^3\Sigma_u^+$ transition highlighted in Figure 3.01). Emission spectra are further complicated by overlapping ro-vibronic emission lines from other H_2 transitions, and exacerbated by high temperatures (via Doppler Broadening and high J emissions) as well as the wavelength resolution of the spectrometer; for example the $H_2(d \rightarrow a)(0\text{-}0)$ Q3 line has a FWHM ~ 0.11 nm.[9,10,11,12] This contrasts to the simplicity held by the excited states of the H atom, which can also be seen in Figure 3.01. The upper state of the H* and H_2* emissions investigated within this chapter all have emitting state energies $E \geq 12$ eV above their respective ground states and therefore the investigated emissions (indicated in Figure 3.01) are probing the hyper-thermal component of the EEDF, $\varepsilon \geq 10.2$ eV, as defined by the H(n = 2) state by the plasma modelling featuring in Section 3.3.1.

[a] Dir. Minkoff R., Allers R. "The Lion King", Walt Disney Pictures, 1994.

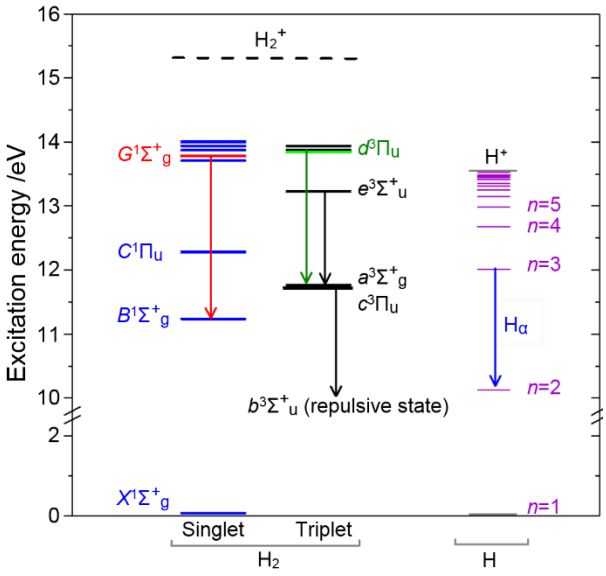

Figure 3.01: Energy states of H(n), and H_2 singlet and triplet states. Marked on the diagram are arrows demonstrating the main transitions investigated in this Chapter. Figure from Reference 1.

Despite substantial literature on moderate H plasma modelling [13,14,15,16,17,18,19,20,21,22,23,24,25,26] and electron-hydrogen cross sections, [27,28,29,30,31,32,33,34,35,36] fundamental processes within MW-activated H plasmas are a source of contradiction. For instance, the literature lacks clarity on the interplay between associative ionization of excited states of H (i.e. H($n \geq 2$) referred to as H*) with the ground state of H_2 ($H_2(X^1\Sigma^+_g)$, henceforth referred to as H_2(X)) and electron impact ionization of H(n = 1) and H_2(X). The MW-activated H plasma is the simplest plasma system obtainable with the experimental equipment described in Chapters 1 and 2, and therefore the best system to resolve such issues, to develop an enhanced understanding between the interdependency of plasma parameters (e.g. the spatially variant electric field $|E|$, the reduced electric field, and absorbed power density) with physical processes, such as electron impact ionization. It also makes a good system for investigating new (/ lesser studied) parameter spaces, such as substrate diameter (/ substrate temperature), and the impact that these variables have on the plasma parameters, gas phase processes, electron densities, and the hyper-thermal component of the EEDF. In Reference 37, Gicquel *et al.* report that under their operating conditions, (p ~ 150 Torr, P = 3 kW), there is a minor (< 15%) increase in T_e across all plasma heights with increasing substrate temperature from 630 °C to 900 °C, as indicated by an increase in measured H Balmer series ratios. The same substrate temperature increase demonstrated that electron density, n_e, remained approximately constant, as indicated by microwave interferometry. The inference is that under their explored operating conditions, an enhancement in T_{sub} resulted in an enhanced T_e, whilst n_e remained ~ constant within the plasma.

Many H_2 emission band structures have been studied within MW-activated H-containing plasmas for estimating rotational (T_{rot}) and vibrational temperatures (T_{vib}), as well as to probe the EEDF. Such studies are also used to inform MW-activated H plasma modelling and physical chemical modelling for diamond growth.[14,15,17,18,38,39] However, as outlined in Chapter 1, Section 1.5, there are unresolved

controversies surrounding the underestimation of T_{rot} and T_{vib} from optical measurements carried out using Boltzmann plot analyses of H_2 emission bands, as well as controversies in the use of H Balmer series ratios (measured under moderate pressures in MW-activated H-containing plasmas) to infer the value of T_e and changes in T_e with changes in operating conditions. Prior to this work, there has not been a fully developed self-consistent MW-activated H plasma model under conditions comparable to those required for the CVD of diamond. This work seeks to inform a self-consistent MW-activated H plasma and use the output to provide insight into the physical parameters, the processes occurring, and their coupling in order to resolve these outlined long-standing questions within the field.

3.2: Experimental Details

This chapter investigates optical emissions from the H Balmer series, H((n > 2)→(n = 2), (predominantly H_α, emission originating from H(n = 3), but also higher n terms), H_2 via the $d^3\Pi_u \rightarrow a^3\Sigma_g^+$, $G^1\Sigma_g^+ \rightarrow B^1\Sigma_u^+$, and $e^3\Sigma_u^+ \rightarrow a^3\Sigma_g^+$ transitions, henceforth referred to as H_2(d→a), H_2(G→B) and H_2(e→a) respectively or interchangeably as H_2*. Upon the addition of argon, the Ar($3s2p^5(^2P_{3/2})4p^1 \rightarrow 3s^2p^5(^2P_{3/2})4s^1$) transition in Russell-Saunders notation and more specifically ($2p_9 \rightarrow 1s_5$) transition in Paschen notation, is also monitored at 811.5 nm and referred to as Ar*. Russell-Saunders notation describes a number of different states (and transitions) for Ar, whereas Paschen notation describes all excited states of Ar. In this notation, the 4s is described by 1s, 4p is described by 2p, whilst the small subscripted number denotes the occupied state, where the largest number denotes the lowest energy state. Numbers run from 2 to 5 and 1 to 10 for the 1s and 2p states respectively.

The experimental set up and practice is described in Chapter 2 is implemented (i.e. an Andor Shamrock 500i spectrograph with a 50 mm focal length, f/16 objective lens, and a 10 μm entrance slit). The H_2* and Ar* data are dispersed on a 700 grooves mm^{-1} diffraction grating, whilst a 400 grooves mm^{-1} grating is used for monitoring the H Balmer series – these return a spectral resolution for a single pixel of ~ 0.04 nm and 0.06 nm respectively. The experiment achieves a spatial resolution of ~ 0.5 mm, and a spatial magnification of ~ 0.08 on a cooled (−60°C) Andor Newton 940 CCD camera. Each H*, H_2*, and Ar* image were accumulated for (or normalised to a collection time equivalent of) 640 s.

For this chapter, base conditions are defined as: 3 mm thick tungsten substrate with diameter, d_{sub} = 32 mm, placed on a spacer wire with thickness d_{wire} = 0.01″, a total gas pressure p = 150 Torr, a microwave input power P = 1.5 kW, and a H_2 flow rate $F(H_2)$ = 300 standard cm^3 per minute (sccm). Whilst one parameter is varied, the remaining parameters are kept constant at their base values. It is worth noting that neither P nor p are fundamental plasma properties, and that varying either impacts the plasma parameters (i.e. power density, plasma volume, gas temperature, gas number densities, electric field and reduced electric field strengths), gas phase processes (e.g. ionization and recombination rates), and gas phase species (e.g. electron density, neutral and charged species). The microwave cavity is retuned between many of the condition changes to ensure that the reflected microwave power is minimised. The

parameter ranges explored are $50 \leq p \leq 275$ Torr, $0.7 \leq P \leq 1.85$ kW, $0 \leq X_0(\text{Ar}) \leq 50$ %, and $d_{\text{sub}} = 32$ mm, 27 and 17 mm. Further studies were carried out using: $d_{\text{sub}} = 17$ mm, both placed on a thinner spacer wire thickness ($d_{\text{wire}} = 0.004''$) for $P = 0.9$, 1.5, and 1.85 kW, $p = 75$, 150 and 275 Torr; $d_{\text{sub}} = 17$ mm as a function of d_{wire}, which enables a crude T_{sub} control under otherwise base conditions; $d_{\text{sub}} = 32$ mm with a 3.4 mm × 3.4 mm × 1.0 mm Al_2O_3 substrate placed centrally on the W substrate under base conditions. The substrate temperature is measured using a 2-colour pyrometer between 700 – 2400 °C or else indicated by a calibrated one colour pyrometer. The typical air leak attributed to the majority of data (excluding the argon addition experiment, and additional smaller substrate studies) is estimated to be ~25 ppm at base conditions.

3.3: Experimental Results and Modelling

3.3.1: Probing Base Conditions and Developing an Understanding of Prominent Processes

Figure 3.02 (a), and the accompanying Appendix Figures (A3.1 and A3.2) show illustrative $I_{\text{em}}(\lambda, z)$ for the H_2(e→a), H_2(d→a) and H_2(G→B) bands respectively under base conditions. The horizontal axis of each Figure shows the monitored wavelength range in nanometres and spans an appropriate wavelength range for the respective H_2 emission band under investigation. The vertical axis corresponds to the height of the plasma between $-3 \leq z \leq 27$ mm, whereby the top of the substrate is defined as $z = 0$ mm. The relevant rotational lines that have been utilised were identified using References 9 and 10. Figures 3.02 (b), A3.1 (b) and A3.2 (b) demonstrate the respective Q and R branches used for the three different H_2* transitions. Spectroscopists use the lower J state, J'', to define P, Q and R transitions. The intensity of the H_2(e→a) emission is defined by Equation 3.01 as the sum of the H_2(e→a)(0-0) R branch lines from R(0) to R(11), noting that only R(0) to R(9) are displayed on the expanded view in Figure 3.02 (b):

$$I(H_2(e \rightarrow a)) = \sum_{J''=0}^{11} I\big(H_2(e \rightarrow a)(0-0)(R(J''))\big) \tag{3.01}$$

I(H_2(d→a)) and I(H_2(G→B)) have similar definitions and are defined by summing the asterisked lines of the Q and R branches shown in A8.01 (b) and A8.02 (b). Figure 3.02 (b) demonstrates a clear 3:1 ratio between even:odd J' (upper state) lines. This phenomenon is a consequence of Pauli's exclusion principle for two indistinguishable fermions; the requirement is that the overall wavefunction describing the H_2 molecule must be anti-symmetric as it consists of two identical I = ½ nuclei.[40,41] The overall nuclear spin wavefunction may either be $S = 0$ described by a single anti-symmetric wavefunction, or $S = 1$, consisting of 3 possible symmetric wavefunctions. The upper $e^3\Sigma_u^+$ state is ungerade, indicated by the u, which contributes an anti-symmetric contribution to the electronic (and therefore overall) wavefunction, irrespective of the nuclear spin state. This forces an anti-symmetric rotational wavefunction (J'= odd) in the case of an anti-symmetric nuclear spin wavefunction, $S = 0$, and a

symmetric rotational wavefunction (J' = even) in the case of the symmetric $S = 1$ nuclear wavefunction. Hence, there is a 3:1 ratio between symmetric and anti-symmetric nuclear wavefunctions, resulting in an approximate 3:1 population ratio between odd:even J' upper states in an ensemble of H_2(e) species. This manifests within the emissions originating from the $H_2(e^3\Sigma_u^+)$ state, as demonstrated in Figure 3.02 (b). Similar effects (i.e. 3:1 alterations, not necessarily between odd:even J' states) are observed within the H_2(d→a) and H_2(G→B) emission bands.

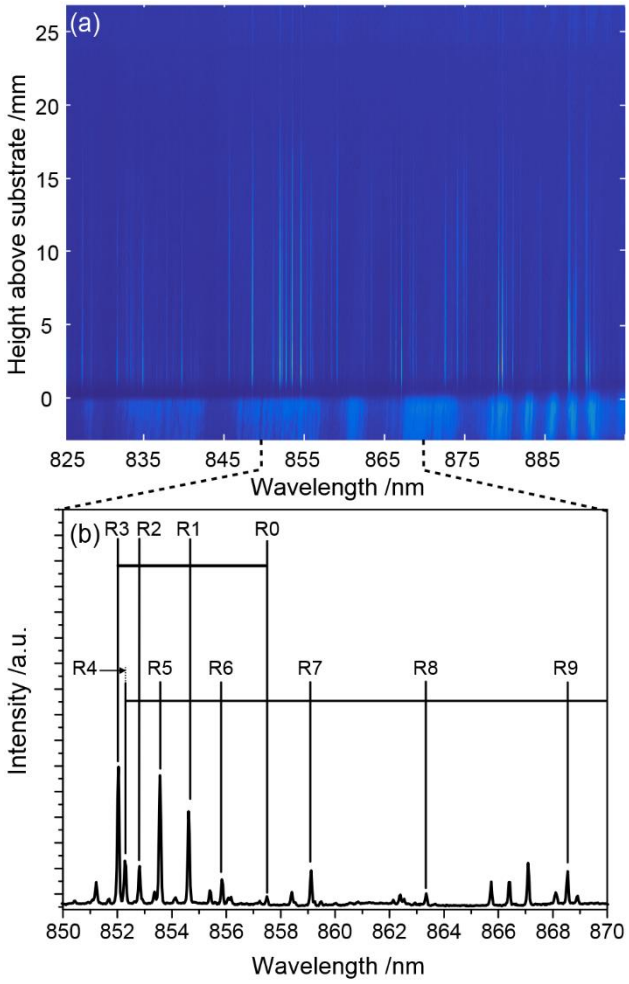

Figure 3.02: (a) $I_{em}(\lambda, z)$ image taken under base conditions in the λ range (horizontal axis) between 825 and 895 nm, and a vertical axis spanning $-3 \leq z \leq 27$ mm, whereby $z = 0$ defines the top of the substrate. (b) The H_2(e→a)(0-0) R-band lines up to R9 are identified with the intensity summed between $3 \leq z \leq 6$ mm.

Figure 3.03 demonstrates the striking similarity of $I(H_2^*)(z)$ (i.e. the spatial distribution of the emission intensity) between the 3 H_2^* emission bands under base conditions. These intensities each peak at $z \sim 2.5$ mm, which makes a stark contrast to $I(H_\alpha)(z)$, peaking at $z \sim 7.5$ mm. Figure 3.04 demonstrates the similarity in normalised $I(H^*)(z)$ (i.e. $I(H(n \geq 3) \rightarrow (n = 2))(z)$ for $n = 3$, 5, 6 and 7) under base conditions. With increasing n, i.e. increasing upper state energy, the signal/noise ratio of the emission originating from H(n) decreases – this is clearly demonstrated through a comparison of $I(H_\varepsilon)(z)$ to $I(H_\alpha)(z)$ in Figure 3.04.

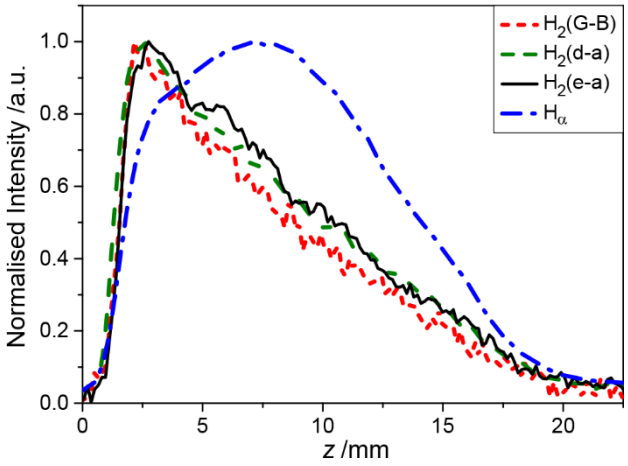

Figure 3.03: Spatially-resolved normalised intensities from the three H_2* emission bands - H_2(d→a) (green), H_2(e→a) (black), H_2(G→B) (red) and H* - H_α (blue) under base conditions.

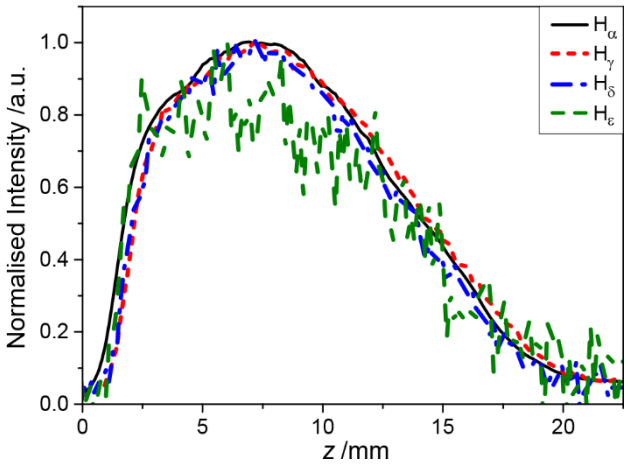

Figure 3.04: Spatially-resolved normalised intensities for H Balmer series - H_α (black), H_γ (red), H_δ (blue) and H_ε (green).

The differences between the normalised I(H*) and I(H_2*) z-profiles are (in part) attributable to the different spatial distributions of ground state number densities ([H(n = 1)] and [H_2(X)] respectively) and $n_e(\varepsilon)$. As discussed in Chapter 1, Section 1.4, H(n = 1) (and H_2) can be excited with hyper-thermal electrons through electron impact excitation. This generates H*, i.e. Process 1.5, featuring in Chapter 1 Section 1.4 (or H_2* via Process 3.02). H(n = 1) is predominantly generated in the hottest regions of the plasma through thermal dissociation of H_2 (i.e. Process 1.1 featuring in Chapter 1, Section 1.4) and due to their light weight, H atoms diffuse efficiently from maximal production height (z ~ 11 mm). Instead, [H(n = 1)] maximises at z ~ 15 mm. Contrastingly, [H_2(X)] maximises in the coolest regions of the plasma (and reactor) in accordance to the ideal gas law, as to first order $X(H_2)$ ~ constant across the plasma.

$$e + H_2(X) \rightarrow H_2^* + e \qquad (3.02)$$

As can be seen in Table 3.1, Process 3.02 is a generalised expression, as it can form many excited states of H_2. Process 3.03 demonstrates that H(n = 1) can also be generated through electron impact excitation

of H_2 into the $H_2(b)$ dissociative state (labelled on Figure 3.01), which spontaneously dissociates to form 2 H atoms. Below z < 4 mm, this mechanism contributes significantly more than thermal dissociation in the formation of H(n = 1) due to the lower gas temperature:

$$e + H_2(X) \rightarrow H_2(b) + e\,;\;\; H_2(b) \rightarrow 2H(n = 1) \tag{3.03}$$

All I(H*) and I(H_2*) emissions tail off by z ~ 20 mm. This is a significant contrast to I(C_2*)(z) and I(CH*)(z) emission band intensities originating from MW-activated C/H plasmas investigated in Chapters 4 and 5 respectively. These emissions extend to z ~ 27 mm and are excited by thermal (i.e. lower energy) electrons. This is indicative that hyper-thermal electrons do not extend beyond z > 20 mm and, in a simplistic picture, reflects a decreasing T_e with respect to height above the substrate, maximising with the reduced electric field at z ~ 2.5 mm.

This interpretation of the I(H*)(z) and I(H_2*)(z) spatial distributions has been vindicated by an appropriately advanced MW-activated H plasma model from that described in Chapter 1, Section 1.3. Improvements on the modelling include the calculation of self-consistent MW electromagnetic fields using Maxwell's Equations, solved through finite difference time domain and a careful consideration of boundary conditions.[1,2,20] The modelling has been improved further through consideration of the interdependencies between the EEDF and n_e with the reduced electric field, the absorbed power density with T_g and neutral species concentrations, as well as neutral species concentrations, n_k with n_e, and the corresponding cation concentrations when considering associative ionization / recombination inter-conversions. In Chapter 1, Section 1.3, $\upsilon \gg \omega$ (i.e. the collisional frequency of electrons was much greater than the microwave frequency) was assumed for describing a sinusoidal electric field in a MW-activated C/H plasma, whilst now ω/υ is required to vary between $0.05 \leq \omega/\upsilon \leq 0.7$.

To quantify the hyper-thermal component of the EEDF, a second electron temperature referred to as T_{tail} has been introduced. T_{tail} is defined as the high energy tail gradient of the EEDF and has the functional form $f(E_i) = c(|E| / (N \times (1 + (\omega/\upsilon)^2)^{1/2}, T_g, X(H))\, e^{-Ei/Ttail}$ for $E_i \geq 10.2$ eV.[1] Note T_e is defined loosely in Chapter 1, Section 1.4, and a more detailed definition provided in Reference 1 and Chapter 5, Section 4.3. Henceforth $1 + (\omega/\upsilon)^2$ is referred to as 'a' in Equation 3.04, and Figures 3.06 and 3.22 and the reduced electric field is referred to interchangeably as $|E|/N$ and $|E|/(N \times a)$ within the thesis text.

The spatial OES data recorded for different p and P allows an investigation into the sources and sinks of the excited H($n \geq 2$) species and of H_2* to identify the prominent production and loss mechanisms for these excited states – this analysis relies on experimentally derived rate coefficients, which hold the analytical form expressed by Equation 3.04 for electron impact excitation processes involving hyper-thermal electrons.[1]

$$k_i = k0_i \times T_{tail}^2 \times u(T_g) \times 0.0033 \times \exp\left(150 / \left(\frac{|E|}{N \times a}\right)^{0.93}\right) \times \exp\left(-\frac{E_i}{T_{tail}}\right) \tag{3.04}$$

$u(T_g) = (T_g/2900)\times(1 + 3.3 \times e^{(-5000/T_g)}$ for $H_2(X)$ + e processes, and $u(T_g) = T_g/2900$ for H(n = 1) + e processes. The pre-exponential factors $k0_i$ are calculated through rate cross-sections, and are presented in Table 3.1 for X(H) = 0.12, reduced electric field (REF) = 33.5 Td, T_g = 2900 K and T_{tail} = 0.76 eV. The EEDF and T_{tail} are highly sensitive to the reduced electric field, mole fraction of H, X(H), and T_g. This is illustrated in Figure 3.05 with examples of normalised EEDF forms for different combinations of these parameters.

Process	Excited state	Pre-exponential factor $k0_i$ /cm^3 eV^{-2} s^{-1}	State Energy /eV	Rate constant / cm^3 s^{-1}
1.4	H(n = 2)	3.52×10^{-6}	10.2	8.72×10^{-13}
1.4	H(n = 3)	7.60×10^{-7}	12.09	1.57×10^{-14}
3.07	H^+	1.10×10^{-6}	13.6	3.11×10^{-15}
3.02 (a)	$H_2(B^1\Sigma_u^+)$	7.74×10^{-7}	11.3	1.56×10^{-13}
3.02 (b)	$H_2(c^3\Pi_u)$	1.91×10^{-6}	11.75	2.13×10^{-13}
3.02 (c)	$H_2(a^3\Sigma_g^+)$	3.18×10^{-6}	11.79	3.36×10^{-13}
3.02 (d)	$H_2(C^1\Pi_u)$	5.15×10^{-7}	12.40	2.44×10^{-14}
3.02 (e)	$H_2(e^3\Sigma_u^+)$	1.95×10^{-7}	13.36	2.61×10^{-15}
3.02 (f)	$H_2(d^3\Pi_u)$	3.51×10^{-7}	13.97	2.10×10^{-15}
3.02 (g)	$H_2(G^1\Sigma_g^+)$	1.52×10^{-7}	13.99	8.89×10^{-16}
3.06	$H_2^+(X)$	1.60×10^{-6}	15.43	4.13×10^{-16}

Table 3.1: Pre-exponential factors, state energies and rate constants for electron impact excitation (and ionization) of H(n = 1) and H_2(X) into some of the excited states under conditions of X(H) = 0.12, REF = 33.5 Td, T_g = 2900 K, and T_{tail} = 0.76 eV.

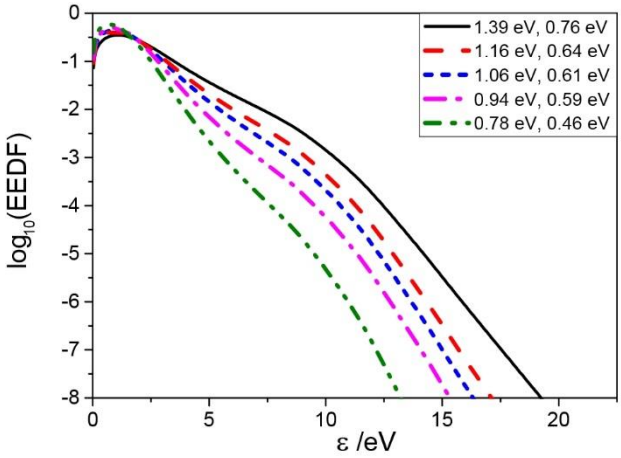

Figure 3.05: The EEDF values on the vertical axis have been normalised through $f(\varepsilon)/\int f(\varepsilon)d\varepsilon$ and presented on a logarithmic scale against electron energy, ε, on horizontal axis. The inset labels T_e and T_{tail}, expressed in eV, and match to the following values of reduced electric field (REF), T_g and X(H); (T_e = 1.39 eV, T_{tail} = 0.76 eV, REF = 33.5 Td, T_g = 2900 K, X(H) = 0.12), (T_e = 1.16 eV, T_{tail} = 0.64 eV, REF = 27 Td, T_g = 3200 K, X(H) = 0.18), (T_e = 1.06 eV, T_{tail} = 0.61 eV, REF = 26.5 Td, T_g = 2900 K, X(H) = 0.12), (T_e = 0.94 eV, T_{tail} = 0.59 eV, REF = 27.3 Td, T_g = 1653 K, X(H) = 0.04), (T_e = 0.78 eV, T_{tail} = 0.46 eV, REF = 19.6 Td, T_g = 2900 K, X(H) = 0.12).

The dominant ionization (i.e. electron production) process under most investigated conditions is the associative ionization of H(n = 2) with H_2(X), as described by Process 3.05. Contributions from H(n > 2) are 2 orders of magnitude lower.[1,39,42]

$$H(n \geq 2) + H_2(X) \rightarrow H_3^+ + e \quad (3.05)$$

Under base conditions, there are lesser contributions from electron impact ionization of H_2 and H, as described by Processes 3.06 and 3.07 respectively:

$$e + H_2(X) \rightarrow H_2^+ + 2e \quad (3.06)$$

$$H(n = 1) + e \rightarrow H^+ + 2e \quad (3.07)$$

The rate constant for associative ionization of H(n = 3) with H(n = 1) (Process 3.08) is calculated to be an order of magnitude lower than other H(n = 3) loss mechanisms, including associative ionization with H_2, i.e. Process 3.05. Associative ionization of H_2* with H(n = 1) (Process 3.09) has been neglected from the modelling due to insufficient data on the rate constant, but is not believed to impact plasma parameters or ground/excited state distributions significantly.[1,43,44,45]

$$H(n = 3) + H(n = 1) \rightarrow H_2^+ + e \quad (3.08)$$

$$H(n = 1) + H_2^* \rightarrow H_3^+ + e \quad (3.09)$$

H^+ and H_2^+ are generated through these processes and are quickly converted through fast reactions into H_3^+ via Processes 3.10 and 3.11 [8] respectively:

$$H^+ + 2H_2(X) \rightarrow H_3^+ + H_2(X) \quad (3.10)$$

$$H_2^+ + H_2(X) \rightarrow H_3^+ + H(n = 1) \quad (3.11)$$

Under base conditions, the 25 ppm air impurity contributes 5 ppm O_2. Oxygen is predominantly converted into H_2O under the high T_g and X(H) conditions present in the plasma. Water converts H_3^+, which would otherwise be the main cation, into H_3O^+ via Process 3.12.[7,42] Further modelling [1,2] implies reducing the air impurity to 5 ppm (1 ppm O_2) reduces the prominence of H_3O^+ and the electron-ion recombination rate, but has no major bearings on the MW electric fields or neutral species concentrations:

$$H_3^+ + H_2O \rightarrow H_3O^+ + H_2 \quad (3.12)$$

The prominent formation mechanisms for H(n = 3) (and more generally H($n \geq 2$)) are described by Process 1.5 (electron impact excitation of H(n = 1), given in Chapter 1, Section 1.4) and Process 3.13, [8,44,45] near-resonant excitation transfer from H_2*:

$$H(n = 1) + H_2^* \rightarrow H(n > 1) + H_2(X) \quad (3.13)$$

The H_2(B) state is assumed to represent near-resonant H_2* levels – similar rates are achieved with H_2(a), as shown in Table 3.2.[1] One of the more significant loss mechanism for the H(n = 3) state is described

by Processes 3.14, (i.e. the reverse reaction of Process 3.13).[1,8,44,45] One of the main experimental observables of this Chapter, I(H*), is produced by integrating the total intensity of photoemission, a minority loss process, which produces the observed photons, γ. The observed photoemission results from de-excitation of H(n > 2) to H(n = 2) (i.e. the H Balmer series), as described by Process 3.15.

It is worth noting at this point that ~ 1% of absorbed power density manifests itself as rovibronic state excitation, most of which is dispended in rotational and vibrational excitation of H_2. Process 3.15 also describes the H Lyman series (i.e. emissions into the H(n = 1) state). Photoemission is not a significant loss mechanism of H($n \geq 2$) due to the strong reabsorption – the Lyman-α emission at 121.6 nm has a mean-free path of ~ 2×10^{-4} cm.[1,46]

$$\mathrm{H}(n > 1) + \mathrm{H}_2(X) \rightarrow \mathrm{H}(n = 1) + \mathrm{H}_2^* \tag{3.14}$$

$$\mathrm{H}(n > 1) \rightarrow \mathrm{H}(n \geq 1) + \gamma \tag{3.15}$$

H_2* can be formed both through Process 3.14, and EIE (electron impact excitation), described by Process 3.02 and is predominantly lost through Process 3.03 (i.e. population of the dissociative H_2(b) state) in the hot plasma, whilst in the cooler plasma, H_2* is quenched through collisions with H_2(X) described by Process 3.16. There are additional loss mechanisms of H_2* already described by associative ionization with H(n = 1), Process 3.09, excitation transfer with H(n = 1) described by Process 3.13, and photoemission (photon represented by γ in Process 3.17). These are not significant loss processes, yet it is the photoemission from Process 3.17, which makes another experimental observable in this chapter:

$$\mathrm{H}_2^* + \mathrm{H}_2(X) \rightarrow products \tag{3.16}$$

$$\mathrm{H}_2^* \rightarrow \mathrm{H}_2(\text{lower E state as allowed by selection rules}) + \gamma \tag{3.17}$$

The rate coefficients of Processes 3.05 through to 3.16 are provided in Table 3.2 (excluding electron impact ionization processes, which have been provided in Tables 3.1). The rate coefficient for Process 3.16 is assumed to be constant, as variation from a set constant value leads to a decreased correlation between calculated pressure dependencies of the various {H_2*} and {H(n = 3)} and their respective measured intensities.[1]

Process	Specific Reaction (/ Electronic Transition)	Rate coefficients /cm^3 s^{-1} (unless otherwise stated)
3.03 (b)	$H_2(b) + M \rightarrow 2H(n=1) + M$	~10^{-11}
3.05	$H(n \geq 2) + H_2(X) \rightarrow H_3^+ + e$	$3.82 \times 10^{-8} / T_g^{0.95}$
3.08	$H(n=3) + H(n=1) \rightarrow H_2^+ + e$	$3.32 \times 10^{-12} \times T_g^{0.5}$
3.09	$H(n=1) + H_2^* \rightarrow H_3^+ + e$	Not available
3.10	$H^+ + 2H_2(X) \rightarrow H_3^+ + H_2(X)$	$5.98 \times 10^{-5} \times T_g^{-0..5}$ cm^6 s^{-1}
3.11	$H_2^+ + H_2(X) \rightarrow H_3^+ + H(n=1)$	1.99×10^{-9}
3.12	$H_3^+ + H_2O \rightarrow H_3O^+ + H_2$	5.9×10^{-9}
3.13 (a)	$H(n=1) + H_2(B) \rightarrow H(n=3) + H_2(X)$	10^{-9}
3.13 (b)	$H(n=1) + H_2(a) \rightarrow H(n=3) + H_2(X)$	5×10^{-11}
3.14 (a)	$H(n=3) + H_2(X) \rightarrow H(n=1) + H_2(B)$	10^{-9}
3.14 (b)	$H(n=3) + H_2(X) \rightarrow H(n=1) + H_2(a)$	10^{-9}
3.16	$H_2^* + H_2(X) \rightarrow products$	Assumed 2.2×10^{-10}
3.17 (a)	$H_2(e^3\Sigma_u^+) \rightarrow H_2(a^3\Sigma_g^+) + \gamma$	2.96×10^7 (s^{-1})
3.17 (b)	$H_2(d^3\Pi_u) \rightarrow H_2(a^3\Sigma_g^+) + \gamma$	2.57×10^7 (s^{-1})
3.17 (c)	$H_2(G^1\Sigma_g^+) \rightarrow H_2(B^1\Sigma_u^+) + \gamma$	2.63×10^7 (s^{-1})
3.17 (d)	$H_2(a^3\Sigma_g^+) \rightarrow H_2(b^3\Sigma_u^+) + \gamma$	9.04×10^7 (s^{-1})
3.17 (e)	$H_2(B^1\Sigma_u^+) \rightarrow H_2(X^1\Sigma_g^+) + \gamma$	1.65×10^9 (s^{-1})
3.15 (a)	$H(n=3) \rightarrow H(n=2) + \gamma$	4.41×10^7 (s^{-1})
3.15 (b)	$H(n=4) \rightarrow H(n=2) + \gamma$	8.42×10^6 (s^{-1})
3.15 (c)	$H(n=5) \rightarrow H(n=2) + \gamma$	9.73×10^5 (s^{-1})
3.15 (d)	$H(n=6) \rightarrow H(n=2) + \gamma$	8.42×10^5 (s^{-1})
3.15 (e)	$H(n=7) \rightarrow H(n=2) + \gamma$	4.39×10^5 (s^{-1})
3.15 (f)	$H(n=2) \rightarrow H(n=1) + \gamma$	~ 4.70×10^5 (s^{-1}) *

Table 3.2: Rate coefficients (and Einstein-A emission coefficients for H* and H_2* transitions) for prominent reactions occurring within MW-activated H plasmas under the conditions listed in Table 3.1. *Lyman-α (Process 3.15 (f)) includes escape factor value of 0.001 and a statistical weighting of the 2p and 2s states.

Figure 3.06 demonstrates (a) the axial (r = 0 mm), and (b) the radial (z = 10.5 mm) distributions of T_g, T_e, and T_{tail} (left-hand axis) and average absorbed MW power density, $|jE|$, electric $|E|$, and reduced electric fields, $|E|/(N\times(1+(\omega/\upsilon)^2)^{1/2})$ (right-hand axis) for base conditions. Figure 3.06 also shows that in spite of an increasing $|E|$ towards the substrate, the steep temperature gradient at low z causes a steeper increase in gas concentration, $N = p/(kT_g)$. The combined effect is that the reduced electric field, and hyper-thermal T_{tail}, both maximise between z ~ 2.5 and 3.5 mm and decrease sharply for z < 2.5 mm, and hence, as seen in Figure 3.03, the H_2* emissions peak in the same region.[1]

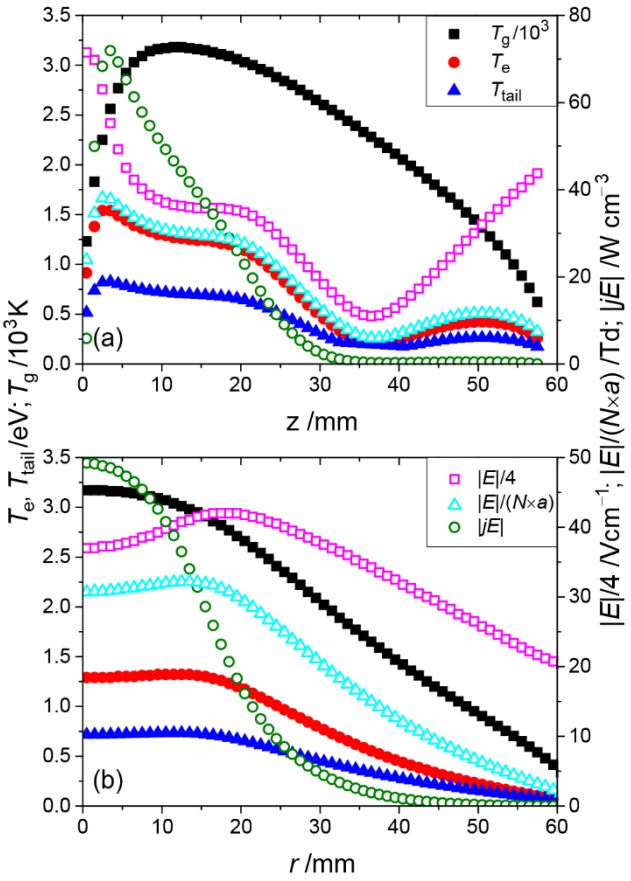

Figure 3.06: Modelled (a) axial (r = 0 mm) and (b) radial (z = 10.5 mm) variations in T_g, T_e, T_{tail} on the left hand axis and electric field $|E|$, Reduced Electric Field expressed as $|E|/N\times a$, whereby $a = (1 + (\omega/\upsilon)^2)^{1/2}$ and average absorbed MW power $|jE|$ on right hand axis for base conditions.

Electrons are predominantly formed at z ~ 3 mm through the ionization processes described (i.e. associative ionization and electron impact ionization) and efficiently diffuse, such that the electron density peaks at z ~ 8 mm. Similar arguments apply to H(n = 1) as already discussed.[1] This contrasts to other species, for example H_2, H_2* and H*, which are locally balanced by their respective formation and loss mechanisms. The strong coupling between H* and H_2*, inferred by Processes 3.13 and 3.14, do not significantly affect the upper state spatial distributions. Hence, the spatial distributions of I(H*) and I(H_2*) at base conditions can be rationalised through the now seemingly over simplistic consideration that these excited states are formed by EIE excitation and lost through radiative loss.[1] This principle extrapolates to the majority of investigated conditions when considered individually, however without consideration of such couplings, it is not possible to explain the spatially-resolved variation of I(H*) and I(H_2*) with changes in process conditions.

Figure 3.07 demonstrates the axial (z, r = 0 mm) number densities of (a) [H(n = 1, 2, and 3)] states on a logarithmic scale for steady-state under base condition, (b) the axial number densities of charged species as a function of height on a linear plot, and (c) the number density of [H_2(X)] and various [H_2*]

states on a logarithmic scale. The electron impact excitation (and ionization) rate coefficients for H* and H_2* states are provided in Table 3.1.

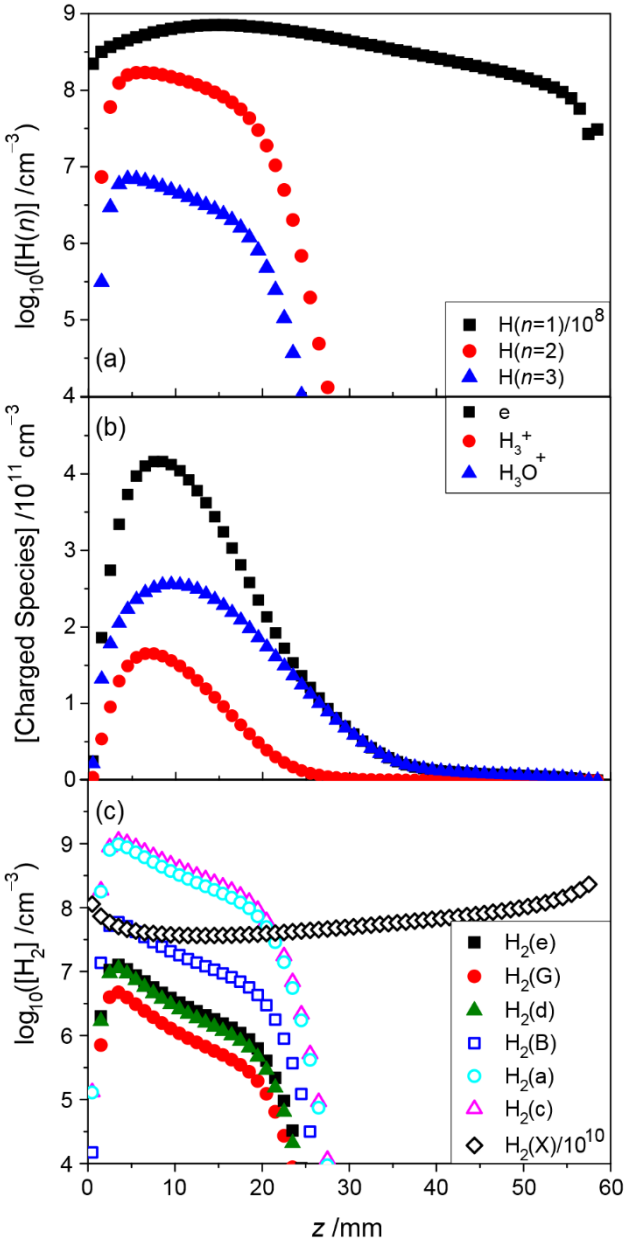

Figure 3.07: Axial (z, r = 0) number density distributions of (a) H(n) state on a logarithmic scale, (b) charged species on a linear scale, and (c) H_2 and H_2* states on a logarithmic scale.

3.3.2: Power Variation

Section 3.3.1 demonstrates spatially-resolved measurements of $I(H_\alpha)$ and $I(H_2^*)$ under base conditions and discusses the prominent mechanisms that occur under such conditions. Sections 3.3.2 and 3.3.3 investigate how these intensities vary with respect to P and p respectively. Figures 3.08, 3.09 and 3.10 demonstrate the effect that varying P has on the investigated emission intensities. Figure 3.08 (a) (and (c)) shows $I(H_2(e \rightarrow a))$ increases with near linearity upon increasing P at low z (intensities between $1.5 \leq z \leq 3$ mm summed). Analysed at a higher z range ($7.5 \leq z \leq 9$ mm), where the intensity decreases

insignificantly. Increasing P = 0.7 kW to 1.85 kW relocates the peak intensity of $I(H_2^*)$ from z ~ 6 mm to z ~ 2.5 mm, indicative that $|E|/N \times a$ maximum relocating to lower z upon increasing P. Figures 3.08 (b) and (c) show that $I(H_\alpha)$ also increases ~ linearly when summed between these height ranges.

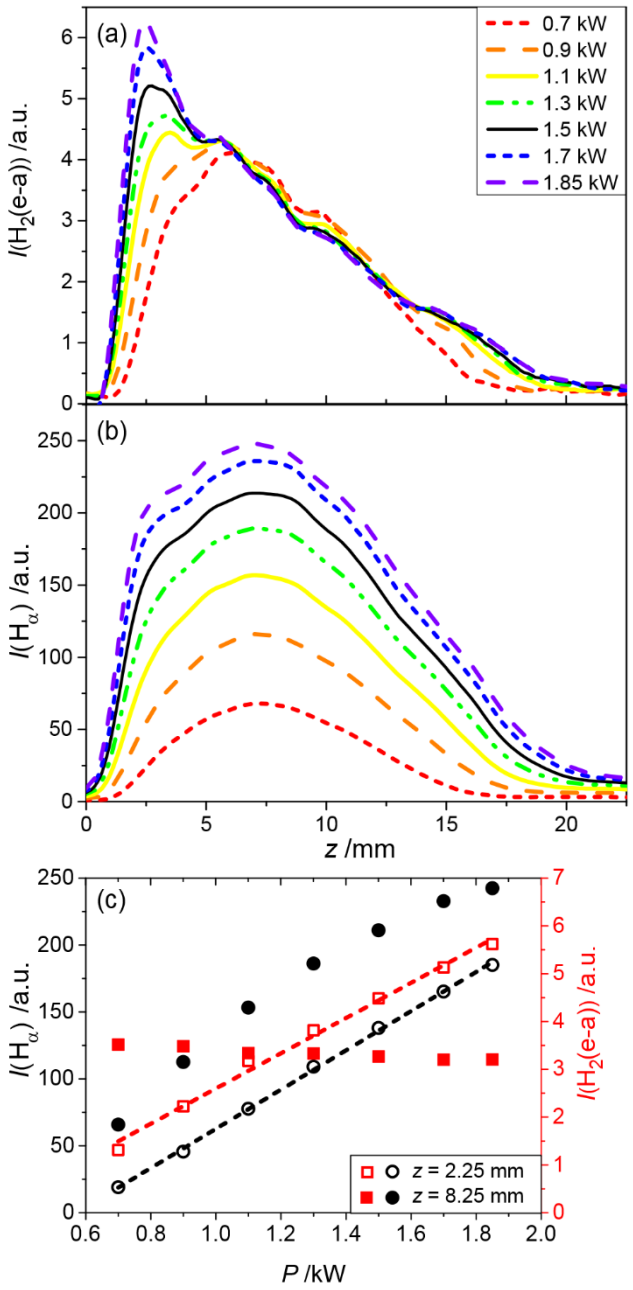

Figure 3.08: Power, *P*, variation (Powers identifiable within the inset of (a) for Figures 3.08 (a) and (b)) of (a) $I(H_2(e \rightarrow a))$, (b) $I(H_\alpha)$ emission profiles, and (c) summed intensities, between the ranges of $1.5 \leq z \leq 3$ mm (labelled as centre of range, z ~ 2.25 mm, open symbols) and $7.5 \leq z \leq 9$ mm (labelled as z ~ 8.25 mm, closed symbols), of $I(H_2(e \rightarrow a))$ (red squares) and $I(H_\alpha)$ (black circles) under otherwise base conditions.

Figure 3.09 demonstrates the similarity between $I(\mathrm{H}(n > 2 \rightarrow n = 2)$ for n = 3, 5, 6, 7 for intensities summed between z range $7.5 \leq z \leq 9$ mm (all normalised to base conditions). The $I(\mathrm{H}_\varepsilon)$ demonstrates a slightly different trend, which is likely attributable to substantially lower signal/noise as noted in Figure 3.04.

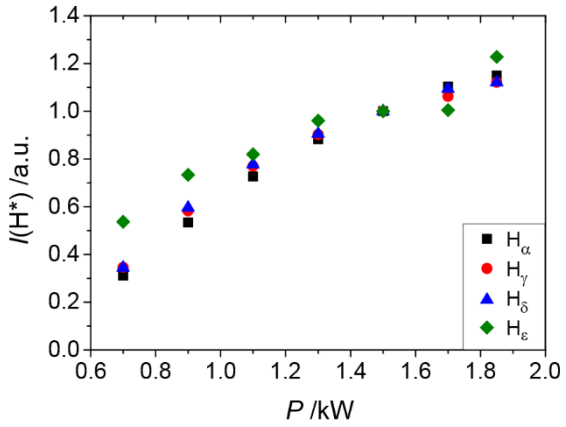

Figure 3.09: Summed Intensities (between $7.5 \leq z \leq 9$ mm) normalised to base conditions for I(H*) featuring upper state n = 3 (black), 5 (red), 6 (blue) and 7 (green), as a function of microwave input power, P, under otherwise base conditions.

Modelling produces calculated column densities for all species within the plasma. As the intensity is measured through a small aperture, it is reasonable to assume that an intensity measurement samples emission through the entire depth of the plasma, and that therefore the intensity is proportional to the column density, as has been experimentally inferred by Jie Ma *et al* for H(n = 3) and numerous other species in MW-activated C/H plasmas.[47] It is therefore meaningful to compare modelled column densities for an excited state species to their measured relative intensities as a function of height and conditions. Figure 3.10 demonstrates a comparison between (a) modelled {H_2(e, v = 0)} column densities and $I(H_2(e \rightarrow a))$ for 0.7, 1.5 and 1.85 kW, whilst (b) demonstrates modelled {H(n = 3)} and $I(H_\alpha)$ for the same operating conditions. Similar trends were also observed for $I(H_2(d \rightarrow a))$ and $I(H_2(G \rightarrow B))$.

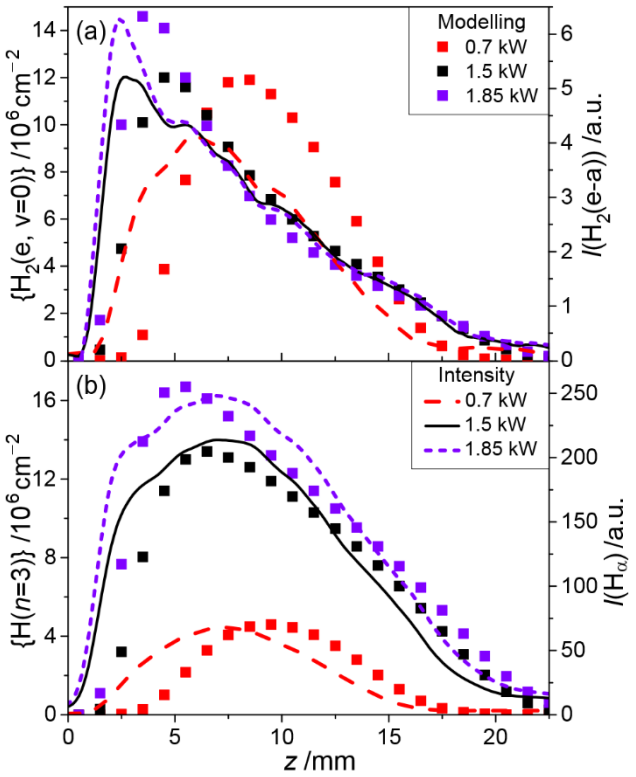

Figure 3.10: (a) Modelled {H_2(e, v = 0)} (square symbols) and measured I(H_2(e→a)) emission profiles (lines) and (b) Modelled {H_α} (square symbols) and measured I(H_α) emission profiles, for P = 0.7 (red), 1.5 (black) and 1.85 (purple) kW under otherwise base conditions. Colours co-ordinate with Figure 3.08

The modelling of {H_2(e, v = 0)} correctly reproduces the P and z dependencies seen for I(H_2(e→a)), but exaggerates {H(n = 3)} shifting toward the substrate with increasing P − something only hinted within the experimental I(H_α)(P, z) trend. Increasing P acts to expand the plasma volume, V_{pl}, and the volume of emission V_{em}, radially with an ~ P dependence. The volume of the plasma (/emission), V_{pl} (/V_{em}), is defined as the spatial extent in which ion and electron (/ emitting species) number densities are within an order of magnitude of their maximal values. Increasing P from 0.7 to 1.5 kW increases T_g by 6%, X(H) by ~ 3 fold, and n_e by ~ 40%. Above 1.5 kW, T_g and n_e saturate. T_e and T_{tail} maxima do not vary significantly in their absolute value within the explored power range, however their axial profiles appear flatter for P ~ 0.7 kW with the reduced electric field peaking at z ~ 6 mm, compared to $P \geq$ 1.5 kW, which peaks at z ~ 2.5 mm under base conditions, as shown in Figure 3.07 (a).

There is no straight forward explanation to account for the P-dependencies of I(H*) or I(H_2*) emissions, but rather the experimental intensity variations as a function of P, are a combined consequence of varying plasma volume, electron density, reduced electric field strengths (and therefore electron energies), T_g, the degree of hydrogen dissociation, and near-resonant energy transfers between high energy states of H and H_2.

3.3.3: Pressure Variation

Figure 3.11 (a) and (c) demonstrate emission trends for $I(H_2(e \rightarrow a))$, whilst Figure 3.11 (b) and (c) show similar data for $I(H_\alpha)$ with respect to increasing p. $I(H_2(e \rightarrow a))$ demonstrates ~ $1/p$ trend at both $1.5 \leq z \leq 3$ mm, and $7.5 \leq z \leq 9$ mm. Upon increasing p, the peak $I(H_2(e \rightarrow a))$ appears to remain in the same position across the pressure range of $75 \leq p \leq 250$ Torr, indicative that the reduced electric field maximum does not relocate within this pressure range. Comparatively, $I(H_\alpha)$ appears to increase linearly at low p, and plateau at higher p. Figure 3.11 (b) illustrates that by the highest pressures, $I(H_\alpha)$ no longer peaks within this spatial range due to plasma contraction, but that the relative increase in maximum $I(H_\alpha)$ is decreasing with increasing pressure, as captured in Figure 3.11 (c).

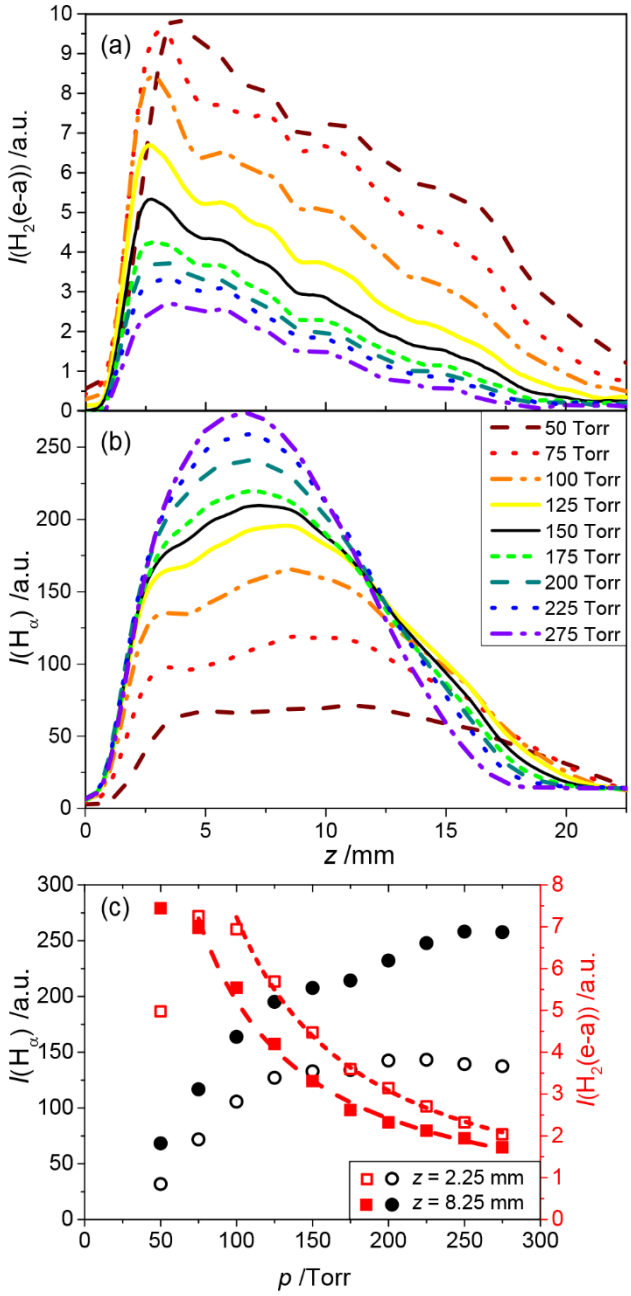

Figure 3.11: Pressure, *p*, variation (pressures labelled within the inset of (b) for Figures 3.11 (a) and (b)) of (a) $I(H_2(e\rightarrow a))$, (b) $I(H_\alpha)$ emission profiles, and (c) summed intensities, between the ranges of $1.5 \leq z \leq 3$ mm (labelled as 2.25 mm, open symbols) and $7.5 \leq z \leq 9$ mm (labelled as 8.25 mm, closed symbols), of $I(H_2(e\rightarrow a))$ (red squares) and $I(H_\alpha)$ (black circles) under otherwise base conditions.

Figure 3.12 shows that higher n valued $I(\mathrm{H}(n > 3) \rightarrow (n = 2))$ follow similar pressure trends to $I(\mathrm{H}_\alpha)$, except for a minor divergence for $p \geq 175$ Torr. Again, $I(\mathrm{H}_\varepsilon)$ demonstrates an irregular trend likely due to lower signal/noise ratio.

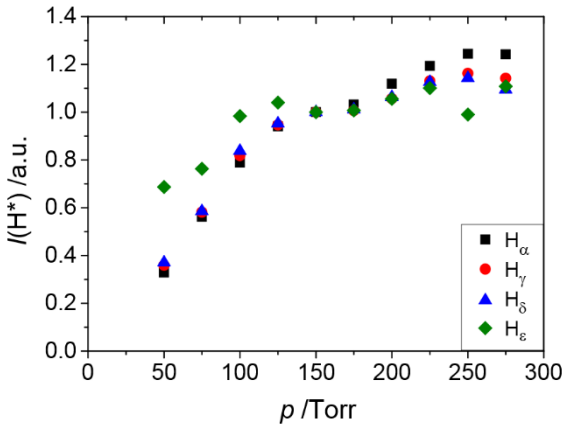

Figure 3.12: Summed intensities (between $7.5 \leq z \leq 9$ mm) normalised to base conditions for I(H*) featuring upper state n = 3 (black), 5 (red), 6 (blue) and 7 (green), as a function of total pressure, p, under otherwise base conditions.

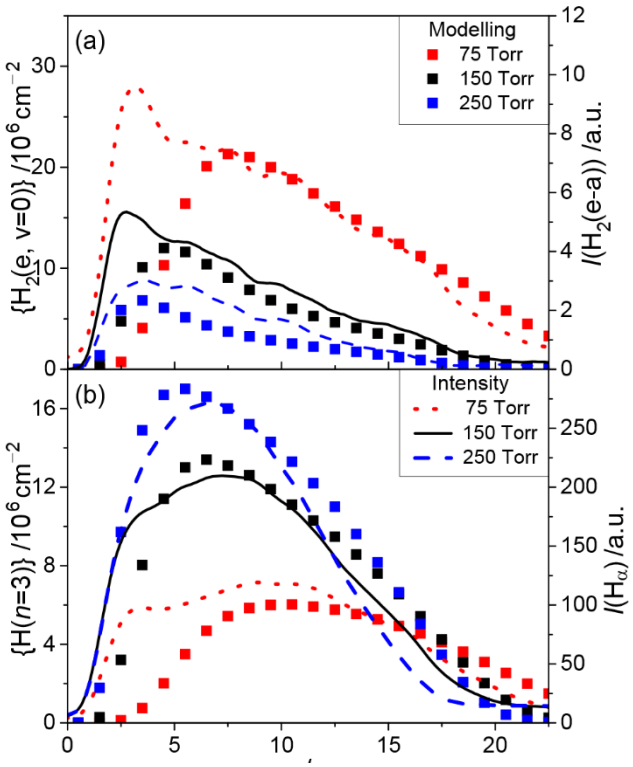

Figure 3.13: Modelled (a) {H_2(e, v = 0)} (square symbols) and measured $I(H_2(e \rightarrow a))$ emission profiles (lines) and (b) {H(n = 3)} (square symbols) and measured $I(H_\alpha)$ emission profiles, for p = 75 (red), 150 (black) and 250 (blue) Torr under otherwise base conditions.

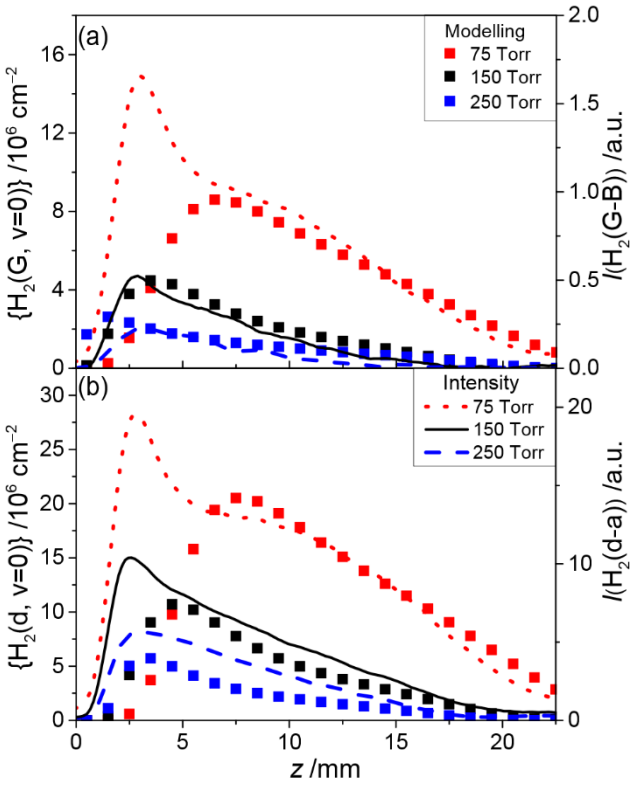

Figure 3.14: (a) Modelled {H_2(G, v = 0)} (square symbols) and measured I(H_2(G→B)) emission profile (lines) and (b) Modelled {H_2(d, v = 0)} (square symbols) and measured I(H_2(d→a)) emission profiles, for p = 75 (dotted red), 150 (line black) and 250 (dashed blue) Torr, under otherwise base conditions.

The modelled column densities of {H_2(e, v = 0)} and {H(n = 3)} can be compared to their respective intensities in Figure 3.13 (a) and (b) respectively. Figure 3.14 demonstrates a similar level of agreement between experimental and modelled trends for (a) {H_2(G, v = 0)} and (b) {H_2(d, v = 0)} with respect to p. For most heights, z > 4 mm, the modelled distributions reproduce the experimental trends seen for I(H_2*) emission bands and I(H_α)(z) at base conditions. Increasing pressure from 75 Torr to 250 Torr acts to decrease V_{pl}, the reduced electric field, and the integral of the hyper-thermal EEDF, $n(\varepsilon_{hyp})$, both of which have ~ 1/p dependencies. The reduced electric field, T_e and T_{tail} decrease by ~ 15%.[1] T_g contrastingly increases by ~ 7% in the same pressure range. The increase in p (from p = 75 to 250 Torr) results in X(H) and n_e increasing by ~ 470% (± 65% from base conditions). The latter is caused in part by an increase in T_g and associative ionization processes (i.e. associative ionization of H(n > 2) with H_2(X), Processes 3.05, and associative ionization of H(n > 2) and H_2* with H(n = 1) (i.e. Processes 3.08 and 3.09 respectively)), such that $n_e \sim p$.[1]

Other p-dependent ionization processes include electron impact ionization of H_2 (Process 3.06), which has a 2.5× larger contribution than associative ionization of H(n > 2) with H_2(X) (i.e. Process 3.05) for p = 75 Torr. The relative importance of Process 3.06 (*cf.* Process 3.05) decreases upon increasing pressure, such that for $p \geq$ 150 Torr, Process 3.05 is the prominent source of electrons. Electron impact ionization (EII) of H(n = 1) (Process 3.07), increases its relative contribution with p. For p = 75 Torr,

EII of H(n = 1) contributes ~0.25 that of electron impact ionization of H_2 (Process 3.06), and becomes comparable to Process 3.06 for $p \geq 150$ Torr; again this is significantly smaller than associative ionization of H(n > 2) with H_2(X) (Process 3.05) for $p \geq 150$ Torr.

Despite an increase in n_e, the increase in quencher concentration ([H_2(X)] ~ p) and decrease in T_{tail} (~ 1/p) have the prominent effect resulting in the observed 1/p trend demonstrated by $I(H_2^*)$. Whilst these effects also impact $I(H_\alpha)$, they are outweighed by the significant increase of H mole fraction, X(H). The increase in X(H) acts to boost H(n > 1) generated through EIE up to p = 250 Torr. With a further increase in p, the other effects, such as decreasing T_{tail}, an increase in H(n > 1) loss processes, (i.e. associative ionization with H_2(X) and H(n = 1), and near resonant excitation transfer with H_2(X) become more significant and consequently $I(H_\alpha)$ stagnates. Higher n states of I(H*) decrease for p > 250 Torr, as seen in Figure 3.12. Without the inclusion of near resonant excitation energy transfers of H_2^* with H(n = 1) and H(n > 1) with H_2(X), the $I(H_2^*)$ and I(H*) trends measured with respect to P and p could not be correctly reproduced through modelling. Further, the net loss of {H(n = 3)} through these processes is comparable to the EIE of H(n = 1) (Process 1.5) throughout the plasma under all P and p conditions investigated.

3.3.4: Description and Discussion of Results

The coupling of H_2^* and H* through near resonant energy transfer with ground state species has two significant consequences on diagnostic information extracted from both $I(H_2^*)$ and I(H*). The first is that such an interdependency would act to disrupt thermally equilibrated $H_2^*(v, J')$ populations, therefore distorting rotational and vibrational temperatures calculated through analysis of their optical emissions. This is an explanation as to why Boltzmann analysis of $I(H_2^*)$ regularly reveals perturbed J' state populations and could extend to the many T_{vib} and T_{rot} studies carried out on $I(H_2^*)$ emission bands, which resulted in low estimations of T_g.[12,13,14,19,48] This is highlighted through a Boltzmann plot analysis carried out under base conditions on $I_{em}(H_2(e \rightarrow a))$ analysed between $9 \leq z \leq 12$ mm, which can be seen in Appendix Figure A3.3. The inverse of the gradient ($(-4.7 \pm 0.7) \times 10^{19}$ J^{-1}) can be divided by the Boltzmann constant, k_B, to yield T_{rot} ~ 1500 ± 300 K, significantly below the expected $T_{rot} = T_g$ ~ 2900 K.

These mechanisms (in addition to associative ionization processes of H* (Processes 3.05 and 3.08)) also mean that H(n > 2) states cannot be treated as a simple two process system (i.e. EIE and radiative loss) when varying process conditions. This suggests that H Balmer line ratios should not be used to estimate T_e or T_{tail} as a function of a parameter without consideration of such couplings. This study does, however, vindicate that for a single condition, such a ratio may still be indicative of T_{tail} as a function of height. These findings likely extrapolate to low pressure H plasmas, where such couplings have been inferred through T_{vib} and T_{rot} studies on $I(H_2^*)$ emission bands.[48,49]

It is perhaps clearer in Figure 3.13 (a) (and Figure 3.14), than in Figure 3.10 (a), that the model is not capturing a low *z* component of $I(H_2^*)$ emission at lower pressures. With increasing pressure, however, this low *z* emission contribution diminishes, with 2-D plasma modelling reproducing experimental $I(H_2^*)$ at all heights for p = 275 Torr. This could be a result of diffusive transfer of electron energy, electron conduction, or a local maximum in the EM field not described in its entirety by the self-consistent modelling.[1]

An alternative explanation considered is the possibility of an additional electron source at low plasma heights. One conceived source was photoelectrons emitted by the W substrate when irradiated by vacuum UV radiation (e.g. the $H_2(a \rightarrow b)$ continuum). Such electrons could be ejected with initial energies up to 7 eV and accelerate across the sheath (which has a potential between ~10-30 eV). Monte Carlo simulations suggested that ~55% of the energy is expected to contribute to H_2 dissociation in proximity to the substrate with only 8% inducing additional ionization. The impact of such electrons is a negligible contribution to [H] atom, ion/electron number densities and $[H_2^*]$ as predicted by the modelling, and therefore does not explain this discrepency.[1]

Despite an incomplete understanding, additional contributions (or relative enhancements) of low *z* plasma emissions can be achieved through four methods (in addition to increasing forward MW power and decreasing total gas pressure); these are (i) decreasing the substrate diameter, (ii) increasing the wire diameter (acting to raise the substrate toward the plasma and decrease thermal contact between substrate and the cooling base plate, therefore increasing T_{sub}), (iii) introducing high fractions of argon, and (iv) placing a substrate (e.g. Al_2O_3 with dimensions of 3.4 mm × 3.4 mm × 1 mm) on the 32 mm W substrate (and / or a combination of these). It is not apparent whether the low *z* emission contributions caused by (i) a smaller substrate diameter and (ii) a larger d_{wire} (when using a smaller substrate) are directly related to those caused by (iii) argon addition and (iv) the addition of an aluminium oxide substrate. These four parameters do act to: (i) increase the gas temperature, which consequentially (ii) increases the substrate temperature (or the piece of aluminium oxide) and (iii) alter (often enhancing) the spatially-variant EM field near the substrate. The effects are visible by eye through the red-hot substrate and in some cases, the emergence of intensity emissions near the circumferential edge of the substrate. The increase in T_{sub} likely results from: (i) an enhanced transport of power density, (ii) additional H recombination events, and potentially from (iii) ion bombardment of the substrate, resulting in an enhancement of thermionic electrons, whilst circumferential edge emissions are likely reflecting changes in the spatially-variant electric fields. For the remainder of this Chapter, $I(H_2(d \rightarrow a))$ has been assumed to be representative of $I(H_2^*)$.

3.3.5: Variation of Substrate Diameter

The effect of decreasing substrate diameter under otherwise base conditions (maintaining a constant wire thickness, d_{wire} = 0.01″) can be seen in Figure 3.15 with companion modelling results shown in

Figure 3.16. Decreasing substrate diameter enhances the low z contribution of the $I(H_2(d\rightarrow a))$ with a shift in maximum $I(H_2(d\rightarrow a))$ toward $z \sim 0$ mm for the 17 mm substrate (*cf.* $I(H_2(d\rightarrow a))$, which peaks at $z \sim 2.5$ mm for $d_{sub} = 32$ mm), without significantly impacting intensities higher than $z > 3$ mm. $I(H_\alpha)$ develops a low z bimodal contribution and increases for plasma heights, $z < 13$ mm. It is worth noting that for $d_{sub} = 17$ mm, the spatially-resolved emissions featuring in Figure 3.15 extend to $z < 0$ mm, implying that some intensity originates from the periphery of the substrate, and not just from the plasma above it, which may act to introduce an eclipsing error associated with such an intensity. This behaviour is again only partially captured by the modelling presented in Figure 3.16.

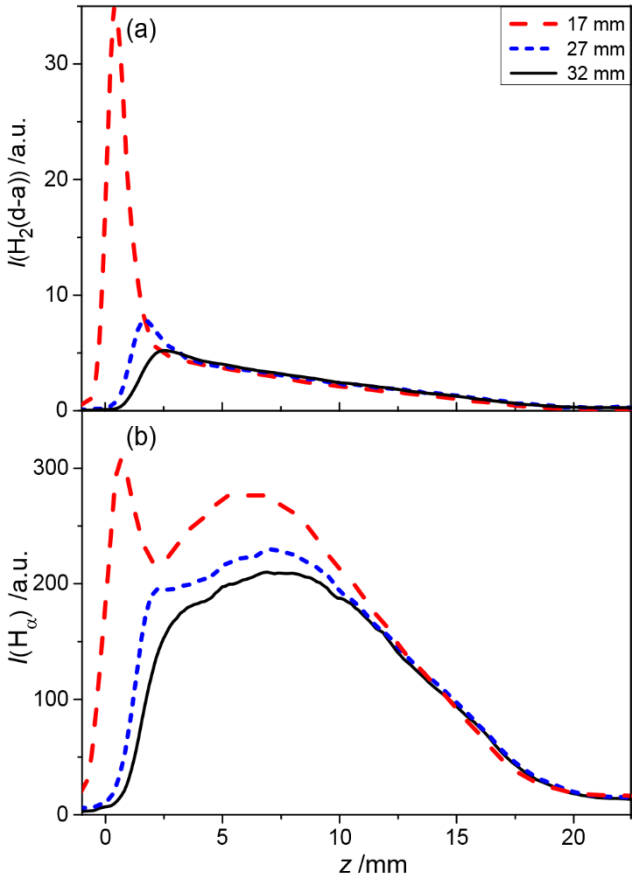

Figure 3.15: The effect of decreasing substrate diameter, d_{sub} values labelled in the Figure inset, under otherwise base conditions. (a) $I(H_2(d\rightarrow a))$ increases in contribution at low z without affecting $I(H_2(d\rightarrow a))(z > 3$ mm) and (b) $I(H_\alpha)(z < 15$ mm) increases with the development of a bimodal contribution at low z.

In order to investigate different substrate diameters, the chamber is frequently opened and evacuated. This may act to introduce a minor variability in the air leak, as well as facilitate the possibility of O_2 outgassing from the chamber walls. It may not therefore be fair to compare the relative intensities of plasma emissions originating from plasmas with different substrate diameters, however Figure 3.15 demonstrates that this has no impact on $I(H_2(d\rightarrow a))(z > 3$ mm) or $I(H_\alpha)(z > 13$ mm), which is in qualitative agreement with the modelled column densities featuring in Figure 3.16. This implies that in this case, such a change in air leak is not a significant issue.

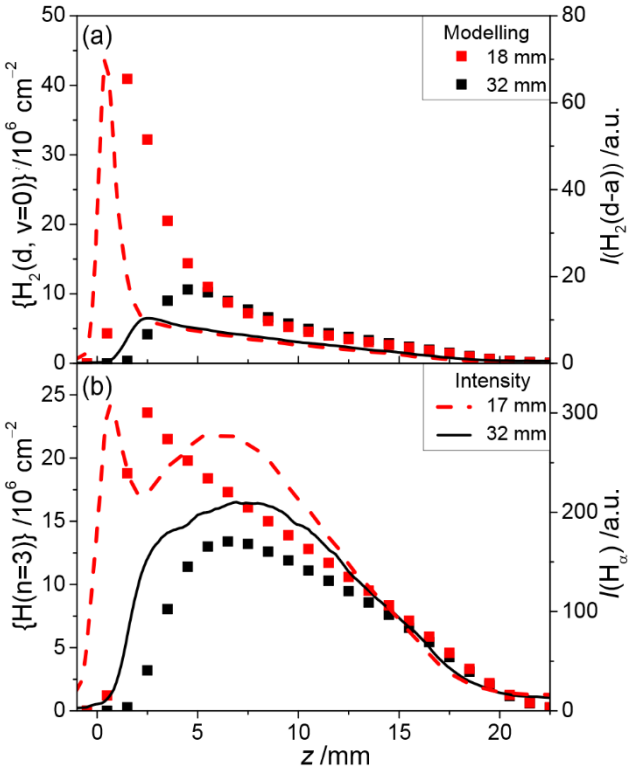

Figure 3.16: (a) Modelled {H_2(d, v = 0)} (squares) and measured I(H_2(d→a)) emission profiles (lines) and (b) modelled {H_α} (square symbols) and measured I(H_α) emission profiles (lines) for 17 mm (red) and 32 mm (black) diameter substrates under otherwise base conditions.

The modelling correctly produces a low z contribution, but at a higher height of $1.5 \leq z \leq 2.5$ mm for a modelled d_{sub} = 18 mm. The modelled low z component can be explained in terms of an increased electric field strength and the effects of an increased absorbed power density (*cf.* d_{sub} = 32 mm shown in Figure 3.06). Figure 3.17 demonstrates the (a) axial (r = 0 mm) and (b) radial (z = 0 mm) variation of T_g, T_e, T_{tail}, $|E|$, reduced electric field, and absorbed power for d_{sub} = 18 mm, under otherwise base conditions. The electric field increases by ~ 35 %, whilst the reduced electric field and the absorbed power density increase by ~ 14 % and ~ 72 % respectively at their peak values z ~ 0.5 − 1.5 mm (r = 0 mm).[1] The increases in these parameters result in a higher T_g ~ 1500 K (*cf.* ~ 1250 K for d_{sub} = 32 mm, r = 0 mm) within proximity to the substrate, a visibly hotter substrate, and ~ 100 K rise at z = 13.5 mm, r = 0 mm. The modelling implies that it is an optical illusion that V_{em} appears to contract radially and axially to the naked eye with decreasing substrate size. The increase in T_g acts to decrease gas concentration n_k by ~ 2 %. The increase in absorbed power density acts to generate an ~ 30 % increase in electron density through the associate ionization processes previously discussed, whilst [H(n = 1)] increases by ~ 1 % and ~ 2 % for z = 1.5 and 10.5 mm through thermal dissociation and population of the dissociative H_2(b) state. The changes, or lack thereof, in [H(n = 1)], n_k, and by extension H_2(X), confirms that the low z intensity contributions are not in this instance due to a variation in the number density of ground state species.

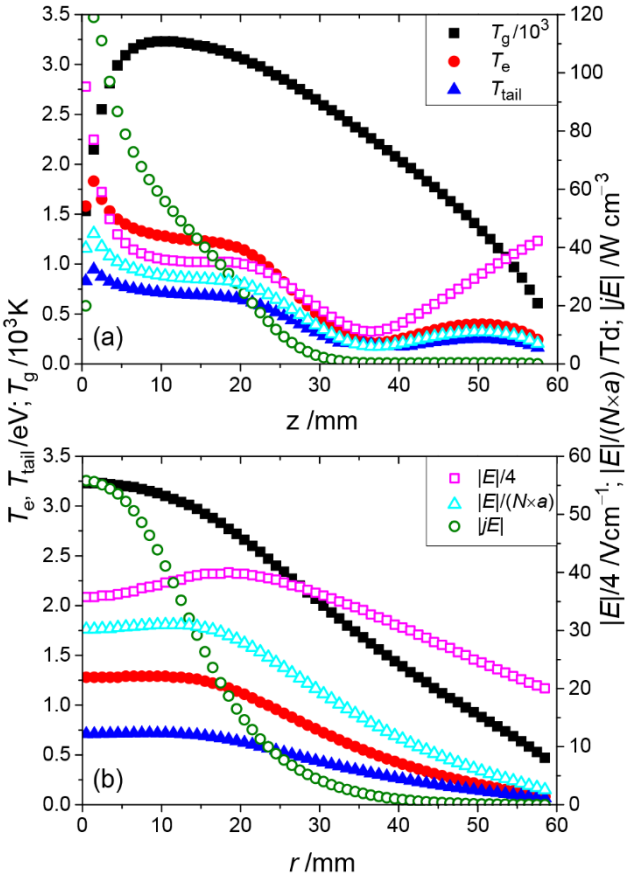

Figure 3.17: Modelled (a) axial (r = 0 mm) and (b) radial (z = 10.5 mm) variations in T_g, T_e, T_{tail} on the left hand axis and electric field $|E|$, Reduced Electric Field expressed as $|E|/N\times a$, whereby $a = (1 + (\omega/\upsilon)^2)^{1/2}$ and average absorbed MW power $|jE|$ on right hand axis for d_{sub} = 18 mm under otherwise base conditions.

The modelling for d_{sub} = 18 mm under-predicts the relative contribution of $I(H_2(d\rightarrow a))$ observed at low z (relative to $I(H_2^*)$ above z > 5 mm) by a factor of 2. Modelling of {H(n = 3)} demonstrates a similar z ~ 1.5 to 2.5 mm offset, but the low z contribution matches closer the relative increase seen for $I(H_\alpha)$. The difference between experimental and modelled z maxima may, in part, reflect the spatial resolution of the model (1 mm) not capturing the local maxima of the EM field. There is also an experimental error introduced by the possibility of intensity originating from the far edge eclipsing the substrate. It is unclear whether the modelling neglects additional processes, which could act to enhance the agreement between experimental intensities and modelled column densities or whether the modelling is capturing the electric field around the substrate edge. Whilst Process 3.09 (associative ionization of H with H_2^*) is the obvious neglected candidate, and could act to quench $I(H_2^*)$ at higher z, it is not thought to have a significant enough impact on {H_2^*} or {H(n = 3)} to account for these observations.[1]

There are two reasons as to why it might not be appropriate to compare Figure 3.18 to Figure 3.15 at face value. The results collected in Figure 3.18 were carried out a significant length of time after the results already reported in this chapter and therefore entailed a repositioned and spatially recalibrated system with a significantly improved leak rate. Whilst modelling available in Reference 1 has already confirmed that the latter should have a negligible impact on most neutral state species concentrations,

the repositioning provides an additional experimental error (spatial position being defined with an error of ~ 0.5 mm). The repositioning is also the likely explanation behind the appearance of a second low *z* feature emerging at ~ 2.5 mm in Figure 3.18, not seen in the data presented in Figure 3.15. By comparing the intensities in these Figures (d_{sub} = 17 mm, P = 1.5 kW, p = 150 Torr) at face value, there is an indication that decreasing T_{sub} through use of a thinner spacer wire (0.004″) on the 17 mm substrate has a significant impact on the plasma parameters, despite modelling implying the contrary. The use of a thinner spacer wire results in a relative decrease in low *z* intensity contribution and a possible uplift of the low *z* annular emission from *z* ~ 0 mm (compared to Figure 3.15, which uses d_{wire} = 0.01″).

The source of the low *z* emission can be identified clearly in the inset of Figure 3.18 (b), whereby for p = 75 and 150 Torr, (P = 1.5 kW) there is a bright annular ring around the periphery of the substrate. For p = 275 Torr, the ring has been displaced by a central emission. The appearance of a second low *z* intensity featuring at *z* ~ 2.5 mm is negligible relative to the larger emission contribution, and likely originates from a back-window reflection of the substrate's far radius annular emission. The annular emission is indicated by a dashed circle within an inset image featuring in Figure 3.18.

Varying P and p under these redefined base conditions (d_{sub} = 17 mm, d_{wire} = 0.004″) demonstrate comparable trends to those already discussed for the 32 mm substrate with a 0.01″ spacer wire (with the enhanced low *z* emission contribution also behaving comparably); additional P data can be found in the Appendix Figures A3.04 and A3.05.

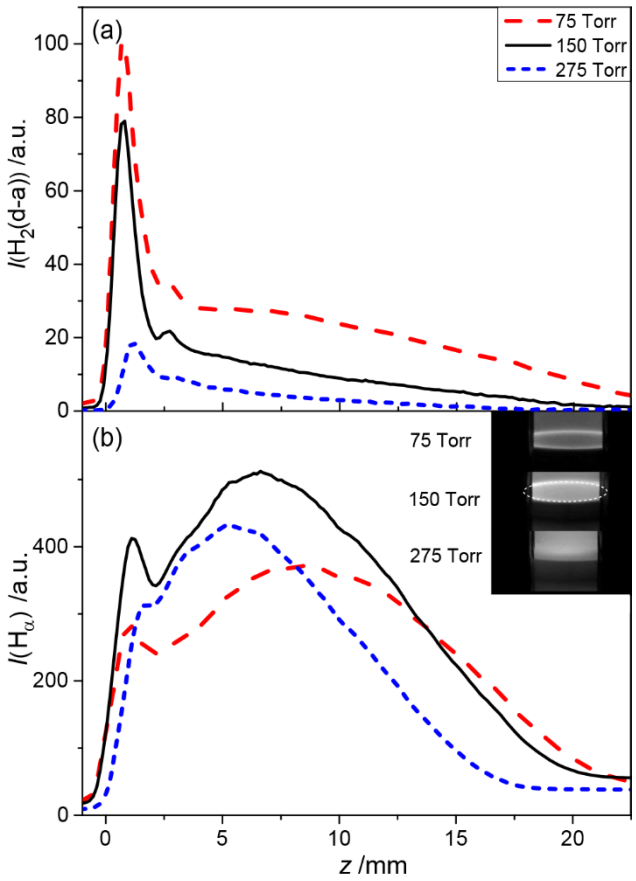

Figure 3.18: (a) $I(H_2(d \rightarrow a))$ and (b) $I(H_\alpha)$ emission profiles, for p = 75 (dashed red), 150 (continuous black) and 275 (smaller dashed blue) Torr (identified in the inset of (a)) with a 17 mm substrate and a spacer wire of 0.004″, under otherwise base conditions. Figure (b) inset illustrates a black and white photograph illustrating the annular ring present under p = 75 Torr and p = 150 Torr, d_{sub} = 17 mm under otherwise base conditions.

3.3.6: Variation of Substrate Temperature

The data presented in this Section were collected in collaboration by John Allden under my supervision, and features in his final year research project contributing towards his undergraduate Msci Chemistry degree.[50] The analysis is my own. The data were collected after yet another repositioning of the reactor and a further improvement on the vacuum leak rate (X_0(leak) ~ 1.1 ppm), i.e. the biggest source of contamination is $X_0(O_2)$ ~ 5 ppm from the hydrogen gas. The substrate temperature can be crudely controlled by varying d_{wire}. For d_{wire} = 0 (i.e. absent), it was not possible to indicate the substrate temperature. It is, however, directly in contact with an efficiently water-cooled copper baseplate, so the substrate temperature would not be higher than a few hundred °C. Figure 3.19 demonstrates the effect of varying d_{wire}, under the redefined base conditions, i.e. d_{sub} = 17 mm, P = 1.5 kW, p = 150 Torr, $F(H_2)$ = 300 sccm. To alter the wire thickness, however, as with altering the substrate diameter, the chamber must be opened. It is therefore not necessarily reasonable to compare absolute intensities of emissions, and as such Figure 3.19 (b) has been normalised to the maximum 'mid-height' intensity, i.e. z ~ 7 mm.

$I(H_2^*)$ spatial distributions and intensities are presented as collected. Note, no such normalisation was required for $I(H_2(d \rightarrow a))$ in Figure 3.19, inferring that $I(H_\alpha)$ is more sensitive to opening / closing the chamber. This might also apply to the substrate data reported in Figure 3.15.

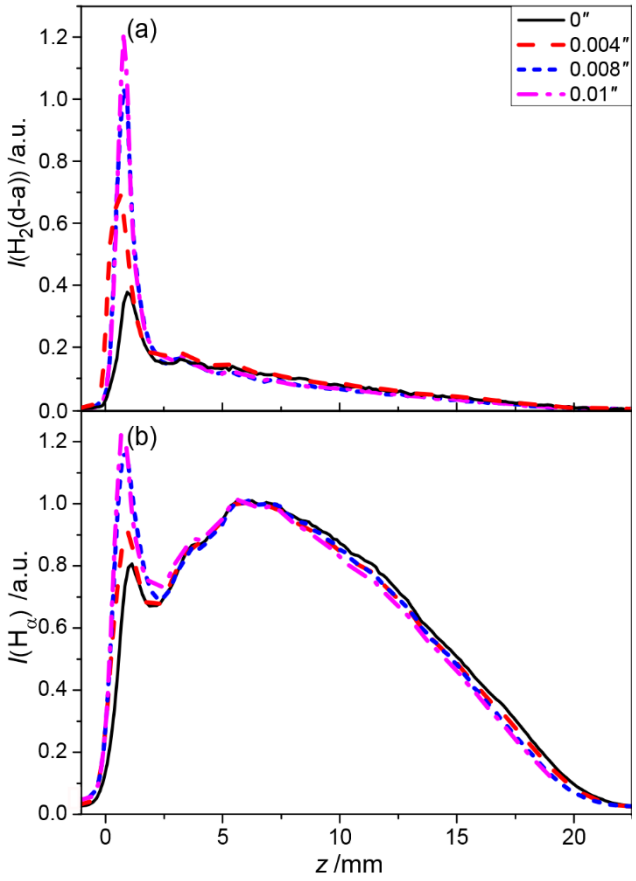

Figure 3.19: The effect of decreasing spacer wire thickness on (a) $I(H_2(d \rightarrow a))$ and (b) $I(H_\alpha)$ emission profiles, for d_{wire} = 0″, 0.004″, 0.008″ and 0.01″ (labelled in the inset) under otherwise base conditions. These d_{wire} values, listed in the inset of Figure (a), yield T_{sub} ~ a few hundred °C, ~700 °C, 1100 °C and 1200 °C respectively.

It is concluded from Figure 3.19 that the low z contribution originating from the substrate periphery is by some means related to T_{sub}, but that altering T_{sub} does not significantly shift the height of the low z emission intensity maximum (plausibly implying that plasma parameters in the hot plasma region are generally unaffected). It was observed by eye, that increasing d_{wire} above 0.004″ acted to collapse the sheath of the plasma or reduce the sheath size such that there was no apparent visible gap between the plasma and the substrate. Wire thicknesses d_{wire} = 0.01″ and 0.004″ faithfully reproduce the relative spatial variation of the intensity distributions shown for d_{sub} = 17 mm in Figures 3.15 and 3.18 respectively and acts as an experimental confirmation that the relative contribution of the low z emission is somewhat coupled to the substrate temperature. Further, the $\{H_2(d)\}$ reported in Figure 3.16 for d_{sub} = 18 mm shows a much closer resemblance to $I(H_2^*)$ with d_{wire} = 0.004″, than that of d_{wire} = 0.01″, whilst $I(H^*)$ collected with d_{wire} = 0.01″ much closer resembles modelled $\{H(n = 3)\}$.

3.3.7-E: Addition of Argon - Experiment

There is interest in MW-activated C/H/Ar containing plasmas; the addition of low argon fractions has previously been used for actinometry purposes,[47] whilst higher fractions can be used to grow nanocrystalline diamond.[51] The effect of argon addition is to decrease the thermal conductivity of the plasma, and thereby increase T_g and the [H]/[H_2] ratio, despite decreasing $X_0(H_2)$.[47,51]

The addition of argon at otherwise base conditions (i.e. 32 mm substrate, 0.01″ spacer wire, base *P* and *p*) can be achieved through method 1, maintaining a constant $F(H_2)$ = 300 sccm and appropriately adjusting the pump rate to maintain a constant pressure, or alternatively by method 2, decreasing the flow of hydrogen in a compensatory manner, such that $F(H_2) + F(Ar)$ = 300 sccm, whilst maintaining a constant pumping rate. The results reported in Figure 3.20 for $I(H_2^*)$, $I(H_\alpha)$ and $I(Ar^*)$ were collected through method 1, whilst a comparative study focussing on $I(H_\delta)$ shown in Figure 3.21 was carried out by collaborator Dr. Sohail Mushtaq using method 2. The results are reported as changes of the mole fraction of Ar in the input gas flow and defined as $X_0(Ar) = F(Ar)/(F(H_2) + F(Ar))$. The analysis of all data presented in this Section is my own.

Increasing the mole fraction of argon in the gas flow, from $X_0(Ar) = 0$ to $X_0(Ar) = 0.50$ (i.e. 0 % to 50 % of input gas flow), increases T_{sub} from ~ 700 °C to ~ 980 °C as indicated by pyrometry. The first set of results demonstrate that $I(H_2^*)$ decreases with argon addition. $I(H_2^*)$ emission reduces more efficiently for $z > 4$ mm than that of the low z ($z \sim 2.5$ mm) contribution for increasing $X_0(Ar)$. Similarly, $I(H_\alpha)$ drops with the addition of argon for $z > 4$ mm above the substrate, but develops a low z bimodal feature at $z = 2.5$ mm. Figure 3.20 (c) shows $I(Ar^*)$ increases in a non-linear manner with increasing $X_0(Ar)$ and that this increase varies as a $f(z)$. The low z intensity maximum, featuring at $z \sim 1.6$ mm, increases more rapidly (with increasing $X_0(Ar)$) than $I(Ar^*)$ for $z > 4$ mm. $I(Ar^*)$ emission peaks at a lower height than that of $I(H_2^*)$ ($z \sim 1.6$ mm versus $z \sim 2.5$ mm respectively) and declines to zero by $z \sim 20$ mm. The difference in the maximum location of $I(Ar^*)$ and $I(H_2^*)$ could be reflecting a higher mole fraction of Ar partitioning at lower heights (i.e. more effective thermodiffusion).

Method 2 studies were carried out in a carbon-contaminated reactor with an unknown leak – this is evidenced by the presence of trace CH(A→X) and CN(B→X) emissions within the experimental data set (not presented in this thesis), and hence $I(H_\delta)$ has been normalised for base conditions ($X_0(Ar) = 0$) to discourage comparison of absolute intensities between these different experiments. Despite this, Figure 3.20 demonstrates a qualitative similarity between $I(H_\delta)$ and $I(H_\alpha)$ with increasing $X_0(Ar)$, which was performed by method 1 in a carbon-free reactor. Assuming the presence of a small amount of residual carbon does not significantly impact the behaviour of $I(H_\delta)$ for large $X_0(Ar)$, these data imply that the two methods of varying Ar content are comparable. Under this assumption, the similarity between the two methods show that higher $I(H^*)$ demonstrate similar behaviour to $I(H_\alpha)$ with argon addition.

Figure 2 featuring in Reference 2 illustrates that it is possible to extract out different trends at different heights for $I(H_2^*)$, $I(H^*)$ and $I(Ar^*)$. This is reinforced in Figure 3.20 by comparing the different trends that would be demonstrated at different plasma heights (indicated by a solid lines). Both highlight a key issue with optical emission spectroscopy carried out using an optical fibre (i.e. OES without spatial resolution) and can act as a source of confusion within literature. This point is reinforced by envisioning the relative emission intensity trends at $z \sim 2$ mm, Figure 3.20:

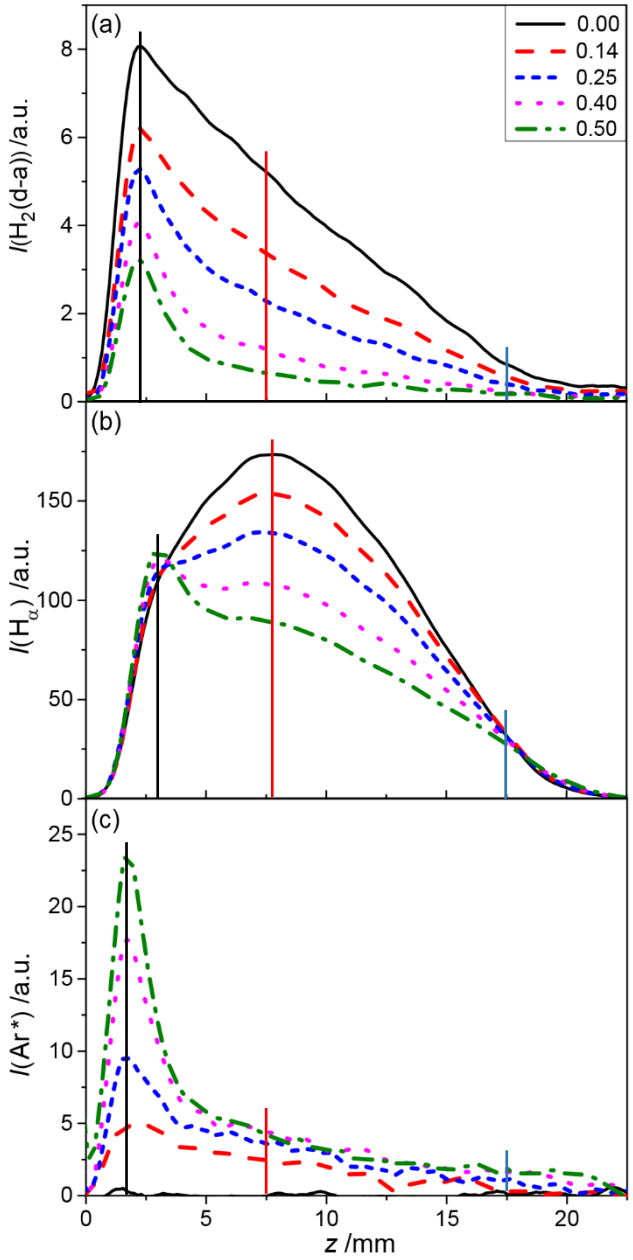

Figure 3.20: The effect of increasing Argon flow on (a) $I(H_2(d \rightarrow a))$, (b) $I(H_\alpha)$, and (c) $I(Ar^*)$ emission profiles, for $X_0(Ar)$ = 0, 0.14, 0.25, 0.4 and 0.50 (labelled in (a) Figure inset). This experiment was carried out with the 32 mm W substrate and 0.01″ spacer wire under otherwise base conditions. The black, red and blue lines represent a low, a mid-range and a higher plasma height respectively.

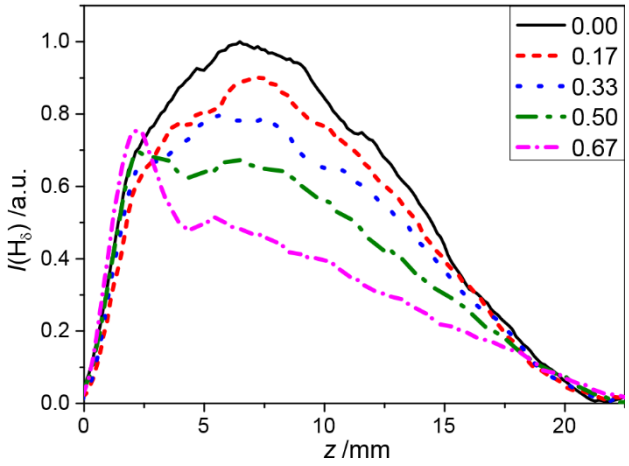

Figure 3.21: The effect of increasing Argon flow (with a compensating decrease in $F(H_2)$) on $I(H_\delta)$ emission profiles for X_0(Ar) = 0, 0.17, 0.33, 0.50, and 0.67. This experiment was carried out with the 32 mm W substrate and 0.01″ spacer wire under otherwise base conditions keeping total flow constant in a C-contaminated reactor.

3.3.7-M: Addition of Argon (continued) - Modelling

The modelling considers an F(Ar) dependent impurity contribution associated with the Ar air impurity in addition to the 4.5 ppm air leak attributed to the chamber.[2] Such a calculation returns an impurity level of 4.5, 5.7, 10.3, 11.5 ppm for X_0(Ar) = 0.00, 0.07, 0.33 and 0.40 respectively. This, however, neglects the air impurity associated with the hydrogen gas. Further modelling available in Reference 2 demonstrates that varying a leak rate within this range (as was the case in Section 3.3.1 reducing 25 ppm down to 4.5 ppm) has little effect on plasma processes and does not account for the observations made with increasing X_0(Ar).

The modelling demonstrates that for an Ar flow fraction, X_0(Ar) = 7%, the local mole fraction of Ar, X(Ar), reaches ~ 3.5% in the plasma core, whilst X_0(Ar) = 40% results in X(Ar) = 25% within the plasma core. This is attributed to the efficient thermodiffusion of Ar (and thermal dissociation of H_2 for T_g ~ 3000 K, *cf.* 2900 K in the plasma core when X_0(Ar) = 0).[52] This, in part, explains the spatially-dependent increase of I(Ar*) with increasing X_0(Ar) shown in Figure 3.19 (c). For X(Ar) = 25%, thermal conductivity and neutral species diffusion coefficients are ~ 60 and 80 % of their values when compared to an Ar-free plasma, X_0(Ar) = 0, which results in further thermal dissociation of H_2 upon introducing and increasing Ar.[2,53,54]

Electrons elastically colliding with Ar have lower rate coefficients compared to an elastic electron collision with H_2; for plasma core X(Ar) = 3.5% and 25%, the ratio of elastic electron coefficients of k_{elas}(e-Ar)/k_{elas}(e-H_2) are ~ 0.3 and ~ 0.4 respectively.[2] Consequently, an increase in core X(Ar) results in a decreasing electron collision frequency. This impacts the absorbed power density, T_g, the electric and magnetic fields, the reduced electric field, and consequently the EEDF, which as before produces two characteristic electron temperatures, T_e and T_{tail}.

For a constant X(H) = 0.12, $|E|$ and absorbed power density, T_e would be expected to increase with X(Ar), whilst T_{tail} remains ~ constant. This would be due to a reduction in electron energy loss through rovibrational collisions with H_2 (being displaced by Ar and thermal dissociation), whilst the hyper-thermal component would remain unaffected due to Ar holding similar excited state energy levels, and therefore compensating the loss of H_2 with EIE and EII interactions of Ar atoms. However, the modelling demonstrates that the addition of Ar results in absorbed power density, jE, decreasing by ~ 30% in the near axial region of the hot plasma core (z = 10.5 mm) upon increasing X_0(Ar) from 7 % to 33 %, whilst the reduced electric field drops by ~ 15 % in the plasma core, as indicated in Figure 3.22. This is compensated by an increased jE at an extended r resulting in a radial expansion of the plasma. It is noted that ~ 30-35% of MW power is absorbed outside of V_{em} for MW-activated Ar/H_2 plasmas, where T_e < 1 eV but n_e is still within the range of 10^9-10^{11} cm^{-3}. The consequence of a decreased absorbed power density in the near axial region is that T_e remains ~ constant, and T_{tail} decreases.

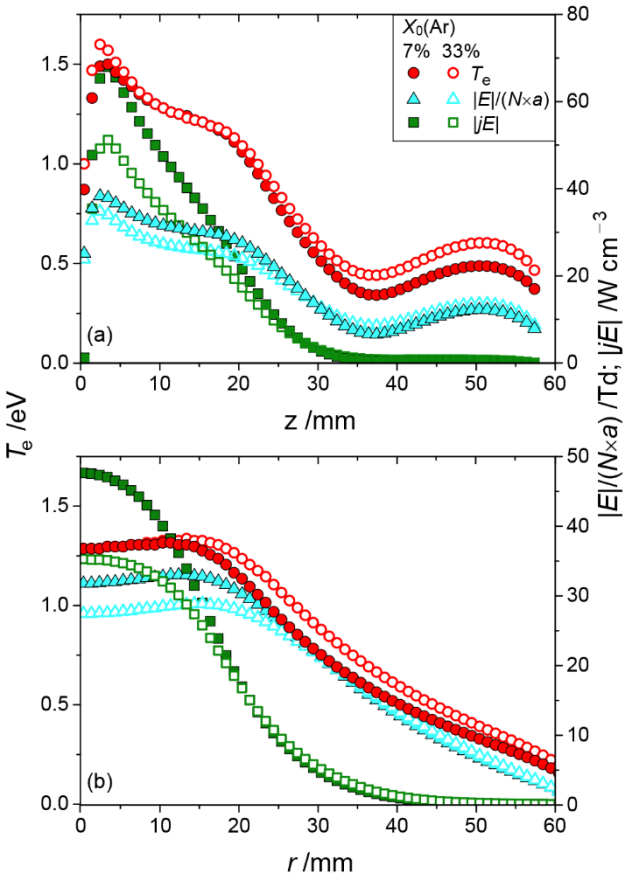

Figure 3.22: (a) Axial (r = 0 mm) and (b) radial (z = 10.5 mm) variation in T_e, REF (indicated by $|E|/N$×a), and average absorbed power density, $|jE|$ for X_0(Ar) = 7% and 33%.

3.3.7-M.1 Discussion of Charged Species

As discussed, EII of Ar, described by Process 3.18, is low relative to EII of H_2 and H (Processes 3.06, 3.07) and associative ionization of H* and H_2* with ground state species (Processes 3.05, 3.08 and 3.09). Any Ar^+ formed is converted rapidly into H_3^+ through Processes 3.19 and 3.20.[2]

$$Ar + e \rightarrow Ar^+ + 2e \quad (3.18)$$

$$Ar^+ + H_2 \rightarrow ArH^+ + H \quad (3.19)$$

$$ArH^+ + H_2 \rightarrow H_3^+ + Ar \quad (3.20)$$

Process 3.21 describes electron impact excitation to Ar* excited states. This thesis concerns itself with the Ar($2p_i$) (i = 1 – 10) states.

$$Ar + e \rightarrow Ar^* + e \quad (3.21)$$

In spite of a significantly reduced air leak to that associated with Sections 3.3.1-3.3.5, H_3O^+ is still predicted to be the prominent ion in the periphery regions beyond V_{pl}. Some of the more prominent processes occurring within MW-activated H/Ar plasmas are described by Tables 3.3 and 3.4, and additional processes are described in Reference 2. The radial variation in n_e, T_g and [H] can be seen in Figure 3.23 for X_0(Ar) = 0 %, 7 % and 33 % at (a) z = 10.5 and (b) z = 0.5 mm. The coloured bars included in Figure 3.23 (a) illustrate the radial extent of which V_{pl} increases with increasing X_0(Ar). It can be seen from Figure 3.23 (b) that [H] and T_g are more homogeneously spread across the substrate surface with increasing X_0(Ar), a beneficial advantage for homogeneous diamond growth across larger areas.

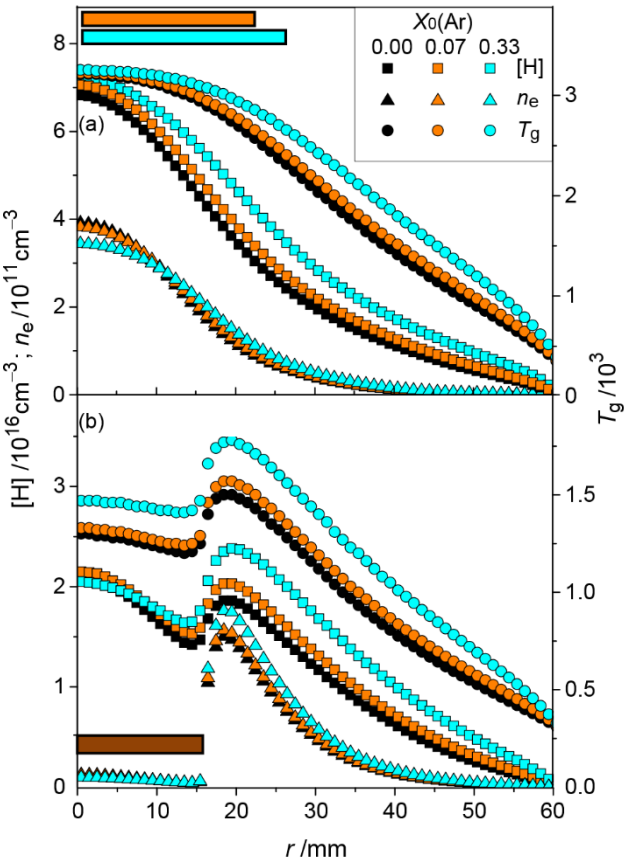

Figure 3.23: Radial variation of n_e, [H] and T_g calculated at r = 0 mm, (a) z = 10.5 mm and (b) z = 0.5 mm for X_0(Ar) = 0%, 7% and 33% under otherwise base conditions. The green and orange bars represent the radial extent in which emitting species are within an order of magnitude of their peak concentration, i.e. V_{pl}.

A secondary analysis of dissociative recombination of electrons with these cations reveals $k_{DR}(ArH^+)$ << $k_{DR}(H_3^+)$ < $k_{DR}(H_3O^+)$ and that total dissociative recombination (and therefore n_e) is sensitive on local ion distributions, X(Ar), and the achieved leak rate.

3.3.7-M.2: Discussion of Excited Species

By comparing the overall rate for electronic excitation of H*, H_2* and Ar*, the modelling reveals that ~ 72% of the input energy expended on electronic excitation is used on H_2, whilst H and Ar atom excitation share ~ 23% and ~ 5% respectively, of which ~ 90% excites the lowest excited states; H(n = 2), H_2(B), H_2(c), H_2(a) and the lowest resonance and metastable states of Ar. 66% of the total excitation is balanced through reactive quenching with H_2, e.g. Process 3.14, generating H atoms. Table 3.3 gives rate constants and rates for electron impact excitation and ionisation of Ar, H_2 and H under conditions modelled at r = 0 mm, z = 3.5 mm, where electron driven processes, e.g. electron impact excitation, are modelled to maximise for X_0(Ar) = 33%, i.e. T_g = 2713 K, X(Ar) = 0.185, and X(H) = 0.085. At this point, it is worth recalling from the plasma modelling previously discussed that electronic excitation accounts for ~ 1% of total absorbed power density. Most absorbed power density manifests in rotational and vibrational excitation of H_2(X). [2]

Process	Excited state	Rate constants, k_i for 18.5% Ar / $cm^3\,s^{-1}$	Rate for 18.5% Ar / $cm^{-3}\,s^{-1}$
1.4	H(n = 2)	4.4×10^{-12}	5.9×10^{16}
1.4	H(n = 3)	7.2×10^{-14}	9.7×10^{14}
1.4	H(n = 6)	1.5×10^{-15}	2.0×10^{13}
3.07	H^+	1.2×10^{-14}	1.6×10^{14}
3.02	$H_2(d^3\Pi_u)$	3.6×10^{-15}	4.3×10^{14}
3.06	$H_2^+(X)$	2.0×10^{-15}	2.4×10^{14}
3.18	Ar^+	1.4×10^{-15}	4.5×10^{13}
3.21	Ar(4p)	4.5×10^{-14}	1.4×10^{15}

Table 3.3: Rate constants (*cf*. Tables 3.1 and 3.2) used for H/Ar modelling; electron impact excitation (and ionization) of H(n = 1) and H_2(X), and Ar(n = 3) into various excited states, REF = 34 Td, T_g = 2713 K, T_e = 1.57 eV for X(H) = 0.085, X(Ar) = 0.185, i.e. rate constants for X_0(Ar) = 33% with a 10 ppm air impurity at r = 0, z = 3.5 mm.

The modelling reveals additional Ar* couplings with H* and H_2* states via their ground states. As in the MW-activated H plasma case, these are primarily pumped through electron impact excitation of their respective ground states. The production and loss mechanisms are in a strong local balance both axially and radially for X_0(Ar) = 0.07 and 0.33. As with H and H_2, the excitation of higher energy Ar states from low lying metastable states is negligible due to the relative concentration of excited metastable states to ground states (~ 10^{-8}).

The reversible, but direct coupling between H_2*, H* and Ar* excited states leads to a net excitation transfer of H* → H_2* (Process 3.14), H_2* → Ar* (Process 3.22), and Ar* → H* (Process 3.23) with rates given in Table 3.4 at z = 3.5 mm. These are negligible for the lower excited states, when compared to EIE of the ground state and reactive quenching / radiative loss mechanisms and as such, a variation of these excitation exchange rates do not significantly affect modelled column density profiles. Consequently, the prominent formation and loss mechanisms of H and H_2 states are the same as those described for MW-activated H plasmas. Figure 3.24 illustrates on a logarithmic scale the magnitude of rate for prominent processes acting on H, H_2 and Ar, and their excited states, where loss mechanisms of the excited states are plotted with a negative value. Table 3.4 provides the rate of loss (via reactive quenching, near-resonant energy transfer and emission) for excited state species of interest under T_g = 2713 K, X(Ar) = 0.185, X(H) = 0.085 i.e. conditions found at z = 3.5 mm for X_0(Ar) = 33%.

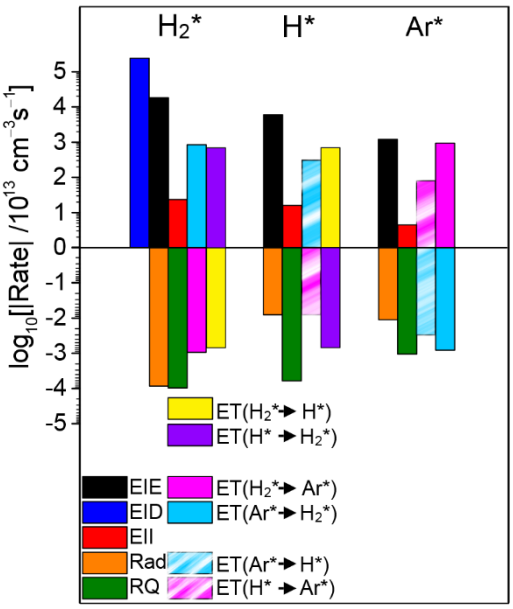

Figure 3.24: Logarithmic plot of the magnitude for the rates of electron impact excitation (EIE), electron impact dissociation (EID), electron impact ionization (EII), excitation transfer (ET) between ground and excited states of Ar, H_2 and H, radiative decay (Rad) and reactive quenching (RQ) of excited states under conditions of T_g = 2713 K, X(Ar) = 0.185, X(H) = 0.085 i.e. conditions found at z = 3.5 mm for X_0(Ar) = 33%.

Process 3.14 (c) describes excitation transfer of H(n = 6) state with $H_2(X)$ to form H_2(e) and H(n = 1), whilst Process 3.22 and Process 3.23 describe the reversible excitation transfer between H_2(e) with Ar, and Ar* with H(n = 1) respectively:

$$H_2(e) + Ar \leftrightarrow H_2(X) + Ar^* \tag{3.22}$$

$$H(n = 1) + Ar^* \leftrightarrow H(n > 1) + Ar \tag{3.23}$$

Process 3.24 describes an additional loss mechanism for H(n = 2), which was also included in the original MW-activated H plasma modelling:

$$H(n = 2) + H_2(X) \rightarrow 3\,H(n = 1) \tag{3.24}$$

Table 3.4 demonstrates rate constants and rates for various important processes occurring within MW-activated H/Ar plasmas:

Process	Specific Reaction	Rate constant / $cm^3\ s^{-1}$ unless otherwise stated	Reaction Rate / $cm^{-3}\ s^{-1}$
3.05	$H(n=2) + H_2(X) \rightarrow H_3^+ + e$	$3.82 \times 10^{-8} \times T_g^{0.95}$	1.3×10^{15}
3.10	$H_3^+ + e \rightarrow H_2 + H(n=2)\ or\ 3H$	3.5×10^{-9}	2.2×10^{14}
3.11	$H_3O^+ + e \rightarrow OH^* + 2H$ or $H_2O + H$	9.6×10^{-9}	5.9×10^{13}
3.13 (a)	$H(n=1) + H_2(a) \rightarrow H(n=3) + H_2(X)$	3.3×10^{-10}	7.0×10^{15}
3.13 (b)	$H(n=1) + H_2(e) \rightarrow H(n=6) + H_2(X)$	7.9×10^{-10}	2.6×10^{14}
3.14 (b)	$H(n=3) + H_2(X) \rightarrow H(n=1) + H_2(a)$	10^{-9}	6.7×10^{15}
3.14 (c)	$H(n=6) + H_2(X) \rightarrow H(n=1) + H_2(e)$	6.0×10^{-10}	3.5×10^{14}
3.16	$H_2^* + H_2(X) \rightarrow products$	Assumed 2.2×10^{-10}	9.7×10^{16}
3.17 (e)	$H_2(B^1\Sigma_u^+) \rightarrow H_2(X^1\Sigma_g^+) + \gamma$	$4.6 \times 10^7\ s^{-1}$	4.2×10^{16}
3.17 (d)	$H_2(a^3\Sigma_g^+) \rightarrow H_2(b^3\Sigma_u^+) + \gamma$	$9.0 \times 10^7\ s^{-1}$	4.3×10^{16}
3.22 (a)	$Ar + H_2(e) \rightarrow Ar(4p) + H_2(X)$	3.0×10^{-10}	2.2×10^{14}
3.22 (− a)	$H_2(X) + Ar(4p) \rightarrow Ar + H_2(e)$	2.0×10^{-11}	4.3×10^{14}
3.23 (a)	$H(n=1) + Ar(1s_{2,4}) \rightarrow H(n=3) + Ar$	2.4×10^{-11}	2.4×10^{14}
3.23 (b)	$H(n=1) + Ar(4p) \rightarrow H(n=6) + Ar$	3.0×10^{-11}	7.4×10^{13}
3.24	$H(n=2) + H_2(X) \rightarrow 3H(n=1)$	10^{-9}	6.1×10^{16}
3.25	$H_2(X) + Ar(1s_{2,4}) \rightarrow Ar + 2H$	7×10^{-11}	4.6×10^{15}
3.26	$Ar(4p) \rightarrow Ar(1s_{2,4}) + \gamma$	$2 \times 10^7\ s^{-1}$	1.1×10^{15}

Table 3.4: Example rate constants and rates for some of the prominent / additional reactions involving excited states of Ar*, H_2* and H* under conditions of T_g = 2700 K, X(Ar) = 0.185, X(H) = 0.085 (X_0(Ar) = 33%, z = 3.5 mm, r = 0 mm) under otherwise base conditions. Further reactions including the lower lying metastable states can be found in Reference 2.

The experimentally observed Ar* transition at 811.5 nm, $Ar(2p_9 \rightarrow 1s_5)$ in Paschen notation, has an Einstein-A emission coefficient of $3.31 \times 10^7\ s^{-1}$, whilst the modelling within Reference 2 and described by Tables 3.3 and 3.4 concerns itself with Ar(4p) states, which represent the sum of all $Ar(2p_i)$ (i = 1 – 10) states. By changing the Ar state of interest, there are no significant consequences on the discussion or experimental observations; Reference 2 demonstrates that other $2p_i$ emitting states have indistinguishable experimental behaviour (e.g. λ = 696.56 nm features $Ar(2p_2 \rightarrow 1s_5)$, which has an Einstein emission coefficient of $6.8 \times 10^6\ s^{-1}$) in the context of MW-activated H/Ar plasmas operating at p = 150 Torr.[2] The similar behaviour exists in spite of substantially different Einstein-A emission coefficients, as emission is not a dominant loss process of Ar*, as can be seen in Figure 3.24 and Table 3.4. Therefore, a change in monitored Ar state (and the associated Einstein-A coefficient) makes no significant difference to I(Ar*)(z, X_0(Ar)) or the conclusions reached by the 2-D plasma modelling of MW-activated H/Ar plasmas.

The radial (z = 10.5 mm) and axial (r = 0 mm) variation of H*, H_2*, Ar* and ion number densities can be seen in Figures 3.25 and 3.26 respectively for X_0(Ar) = (a) 0.07 and (b) 0.33. A careful comparison of Figures 3.25 (a) and (b) demonstrates a subtle increase in ArH^+ and H_3O^+ introduced through increasing X_0(Ar), and its associated air contamination, as outlined above. There are drops in H* and H_2* due to the decrease in T_{tail}, as well as increased quenching, however their radial extent increases. Ar* comparatively increases, as would be expected for increasing X_0(Ar). Comparatively, the axial height of the emitting plasma decreases upon increasing X_0(Ar); this is in part a consequence of the fractional partitioning of Ar under steady-state, which results in higher X(Ar) in cooler regions of the plasma, and acts to quench the energy of hyper-thermal electrons, i.e. reducing the number of electrons with sufficient energies ($\varepsilon \geq 10.2$ eV) available to excite the high energy states of H, H_2 and Ar. The change in axial variation of these species with increasing X_0(Ar) can be seen by comparing Figure 3.26 (a) and (b).

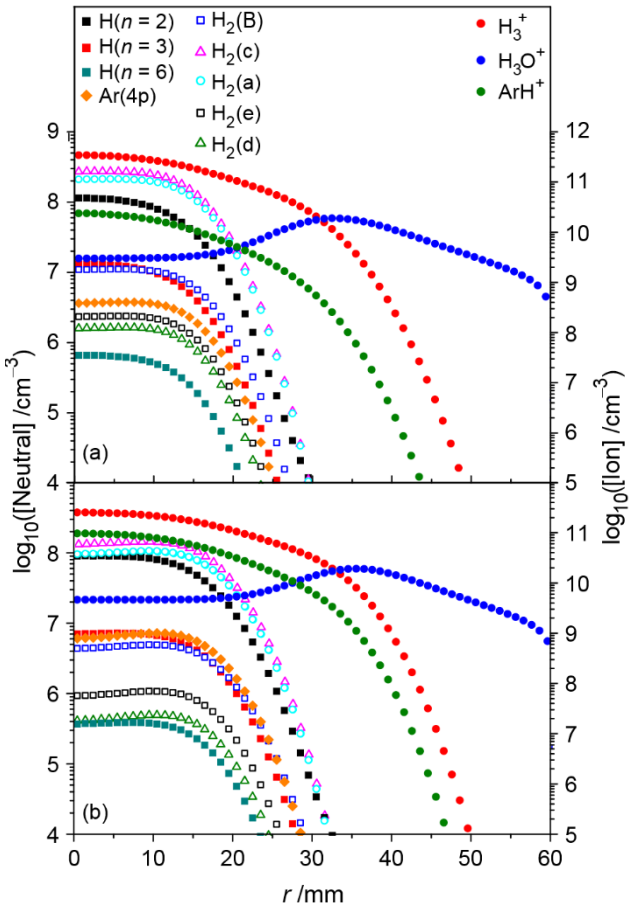

Figure 3.25: Radial variation (z = 10.5 mm) of ions, H_2*, Ar*, and H* within Ar/H_2 plasmas with X_0(Ar) = (a) 7% and (b) 33% under otherwise base conditions (i.e. P = 1.5 kW, p = 150 Torr).

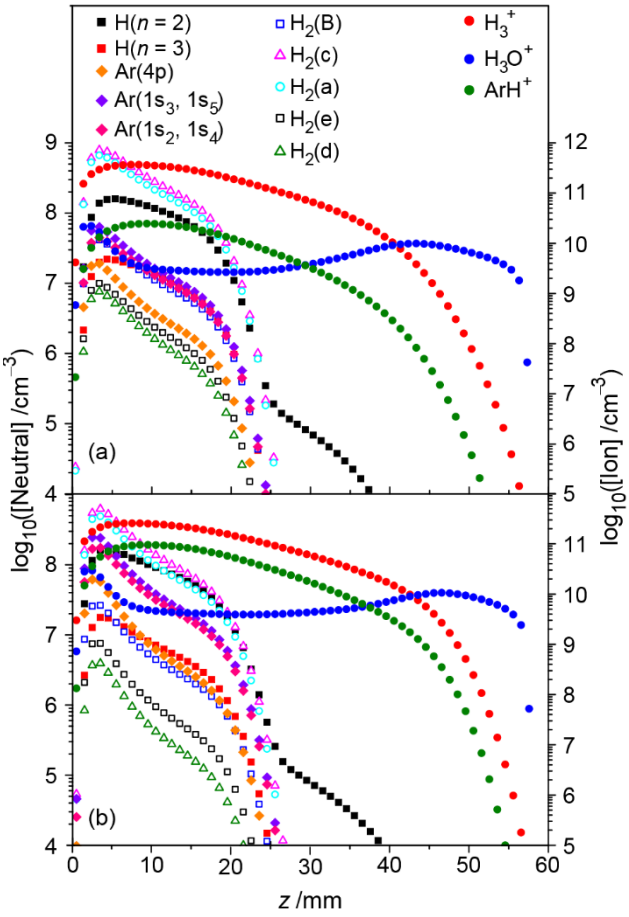

Figure 3.26: Axial variation (r = 0 mm) of ions, H_2*, Ar*, and H* within Ar/H_2 plasmas with X_0(Ar) = (a) 7% and (b) 33% under otherwise base conditions (i.e. P = 1.5 kW, p = 150 Torr).

3.3.7-EM: Addition of Argon (continued) - Comparison of Experiment and Model

The modelled column densities of the studied H*, H_2* and Ar* states are shown in Figure 3.27 and reproduce experimental trends (overlapped) with a similar level of agreement to that seen by H* and H_2* in MW-activated H plasmas. The spatial disparity again may arise from deviation of calculated and realised electromagnetic fields in the near substrate region, an incompleteness of the kinetics describing excited state species and their interdependencies, and perhaps the neglect of a process generating high temperature electrons at low z, e.g. through ionization. For further insight into this brief description of MW-activated H/Ar plasmas, please refer to Reference 2.

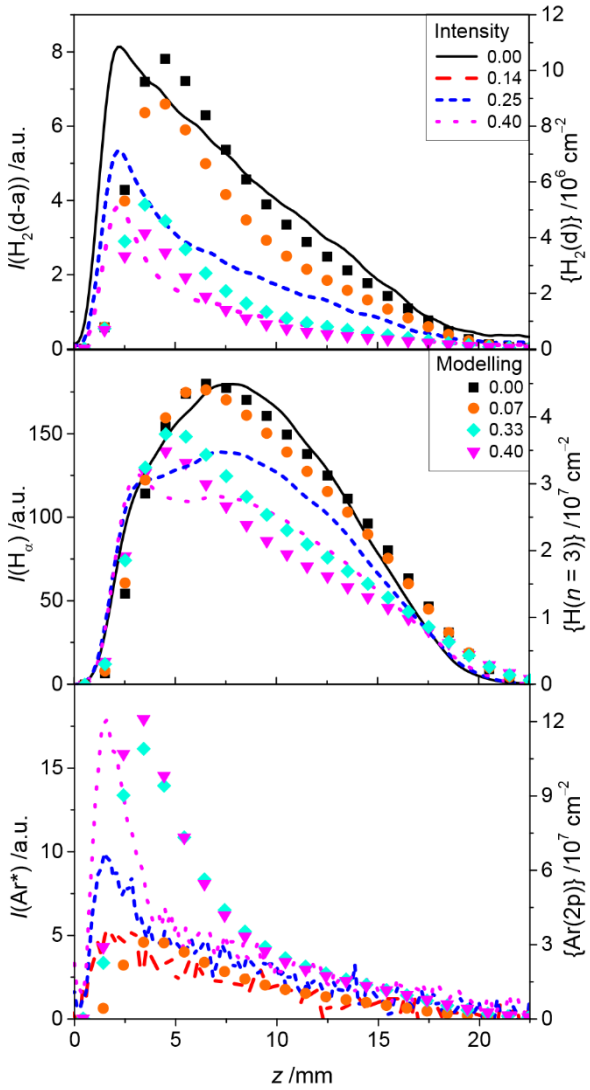

Figure 3.27: Experimental emission profile measurements (dashed lines labelled with associated X_0(Ar) labelled in the inset of (a)) and modelled column density profiles (indicated by symbols with associated modelled X_0(Ar) labelled in the inset of (b)) for (a) I(H$_2$(d→a)) and {H$_2$(d)}, (b) I(H$_\alpha$) and {H(n = 3)}, and (c) I(Ar*) and {Ar*} for the various X_0(Ar) indicated in the Figure inset. The experimental work was carried out with the 32 mm W substrate and 0.01″ spacer wire under otherwise base conditions and has previously been reported in Figure 3.20.

3.3.8: Addition of an Al_2O_3 substrate

This final study, carried out and analysed by John Allden, simply demonstrates the effect that placing a 3.4 mm × 3.4 mm × 1.0 mm Al_2O_3 substrate has on the H-Balmer emissions under otherwise base conditions (d_{sub} = 32 mm, d_{wire} = 0.01″). The ambition of this study was to investigate whether emissions originating from excited states of etched Al were sensitive enough to sample the thermal component of the EEDF. Al atoms might make a desirable plasma emitter due to the numerous and spaced excited state levels of Al, which range between energies of 3 and 5.98 eV, where 5.99 eV is the ionization energy of Al.[55] States populated by EIE would therefore allow access to the thermal component of the

EEDF. Whilst this ambition was unfruitful, the presence of such a substrate did demonstrate by eye, a substantial perturbation to the H plasma and a strong emission originating from the surface of the Al_2O_3 substrate, somewhat comparable to the annular emissions observed for d_{sub} = 17 mm. The Al_2O_3 substrate reached $T_{Al_2O_3}$ ~ 1450 K, but only produced two dominant pairs of emission intensities originating from excited states of Al in the gas phase. These spatial distributions can be found with further studies and discussion in John Allden's dissertation.[50] The *z*-dependent spatial distribution of the H Balmer emission intensity can be seen in Figure 3.28:

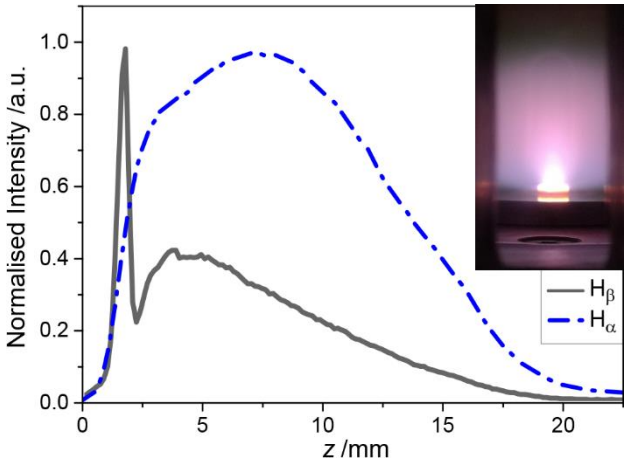

Figure 3.28: Normalised *I*(H*) for d_{sub} = 32 mm, *P* = 1.5 kW, *p* = 150 Torr, d_{wire} = 0.01″ with (grey line) and without (blue dashed line) a piece of Al_2O_3 present. The inset photograph was taken under base conditions and demonstrates the appearance of a typical plasma with Al_2O_3 present. The photograph and new data piece were taken and analysed by John Allden.

The presence of an Al_2O_3 substrate substantially alters the appearance of the plasma, as can be seen in the inset of Figure 3.28. Again, there is a low *z* enhancement to *I*(H*) upon the addition of a small piece of Al_2O_3. *I*(H*) can be seen to maximise at *z* ~ 2 mm and at a much lower height of *z* ~ 3.5 mm. It is apparent in the photograph that the substrate was red hot under most investigated conditions. The surface is also illuminated from bright optical emissions, perhaps comparable to those seen with the small substrate. The 'flame-like' appearance above the substrate could be reflecting an enhanced n_e arising from ionization of localised gas phase Al, which has an ionization energy of 5.99 eV, significantly lower than any other species in a MW-activated H plasma.[56] The effect of introducing a low ionization energy gas phase 'contaminant' into a MW-activated H plasma is demonstrated more clearly in Chapter 6, but generally such a component in the plasma acts to increase n_e and consequentially decrease T_{tail}. The additional electron source will act to fundamentally alter the absorbed power density distribution within the plasma, enhancing T_g and electron driven processes (e.g. electron impact excitation and electron impact dissociation of H_2, generating H atoms). There is likely also an enhancement of electric fields in the vicinity of the Al_2O_3 substrate, as evidenced by the bright substrate glow in the inset photograph and the bimodal distribution of *I*(H*) both featuring in Figure 3.28. Combined, these effects will alter [H], n_e, and therefore *I*(H*). Additional studies and plausible explanations are presented in John Allden's thesis.[50]

3.3.9: Speculation on Emissions Originating from Low Plasma Heights

Within the results discussed, there have been 6 parameters which demonstrate either an absolute or relative (in the case of Argon addition) enhancement to H and/or H_2 emissions at low plasma heights ($z \leq 3$ mm). These parameters were: (i) decreasing pressure, (ii) increasing MW input power, (iii) decreasing substrate diameter, (iv) increasing spacer wire thickness (when a small substrate is present), (v) addition of significant argon fractions, and (vi) the addition of an Al_2O_3 substrate.

For (i) decreasing pressure, (ii) increasing input power, and (v) increasing argon, (d_{sub} = 32 mm and d_{wire} = 0.01″ wire), these emissions enhance emission maxima at $z \sim 2.5$ mm, i.e. at the axial height where the reduced electric field maximises for a 32 mm substrate. In the case of (i) and (ii) the increases are attributed to an enhanced (reduced) electric field strength, whilst for Ar addition, these are attributed to reactive quenching and near-resonant energy transfers between excited states of Ar, H_2 and H with ground state species. The modelling successfully replicates the observed enhancement of I(H*)(z = 2.5 mm) and $I(H_2^*)(z = 2.5$ mm) behaviour for X_0(Ar) at a higher, but approximately constant plasma height, implying that the modelling is correctly describing the behaviour of Ar and the impact that Ar has on the plasma shape (e.g. radial expansion and increased homogeneity at low plasma heights), plasma parameters (e.g. the reduced electric field and the EEDF) and physical processes (for example, the coupling between excited states of H, H_2 and Ar with their ground states). The offset between modelled and experimental maxima may be the result of modelling resolution (1 mm) with a lower resolution perhaps required to describe the full spatial variation of the EM fields or an experimental spatial calibration error (estimated to be ~ ±0.5 mm). Comparatively, with pressure, the modelling accurately captures $I(H_2^*)(z)$ at high pressure (p = 250 Torr), but Figures 3.13 (a) and 3.14 demonstrate an increasing disparity between model and observed intensities (at low z) for lower pressures. The modelling infers that peak intensities of $I(H_2^*)$ should relocate towards the centre of the plasma, whilst experimentally it is observed to remain constant at z = 2.5 mm for $p \geq 75$ Torr, below which there is an indication that the $I(H_2^*)$ maxima is relocating to a slightly higher z. The modelling also infers that the I(H*) maximum should relocate as a $f(p)$, which is not presently observed for the 32 mm substrate (but is observed for d_{sub} = 17 mm). The difference between experiment and model implies that the model is likely not capturing the pressure-dependent behaviour of the reduced electric field, the electron density and/or is missing complete physical kinetics, particularly at low plasma pressures and heights.

Further modelling with H/Ar plasmas, provided in Reference 2, reveals that there is an additional contribution behind the low z emission from dissociative recombination occurring close to the substrate edge, however it is deemed unlikely to be contributing in any significant manner to the observed $I_{em}(z)$ intensity profiles.

Decreasing the substrate diameter to 17 mm (d_{wire} = 0.01″, otherwise base conditions) demonstrates an enhancement to the low z emission contribution, maximising at a lower height of $z \sim 0$ mm. The

modelling successfully captures an increase in $I(H^*)$ and $I(H_2^*)$, at a lower height than that modelled for d_{sub} = 32 mm. This additional emission is clearly identified in subset images to be originating from a luminescent ring surrounding the diameter of the 17 mm substrate, and is reflecting the substrate's sharp edges being closer to the plasma (and therefore in proximity to stronger electric fields) due to the smaller radius of the substrate. The stronger fields, combined with the additional thermionic electrons attributed to the larger T_{sub}, likely results in contributing to the additional emissions (by increasing n_e, E/N, and therefore EIE events). If correct, such effects could also be observed on larger substrate diameters at operating powers larger than those currently explored. The edge contribution for small substrates additionally prevents the pinpointing of the axial $I(H_2^*)$ and E/N maximas for r = 0 mm, which are inferred (by the modelling) to maximise at a lower plasma height than for the 32 mm substrate.

The experimental intensities originating from the substrate circumference are prone to experimental error from the intensity eclipsing the substrate, however the reported results are taken at face value. As before, the modelling demonstrates an offset, but additionally produces an incorrect relative contribution for $I(H_2^*)$ (perhaps due to not fully capturing the coupling between H* and H_2^*) and fails to capture the bimodal distribution of $I(H^*)$. The difference in height, and the failure to capture the bimodal behaviour of $I(H^*)$, are in part reflective of the modelled resolution, however the modelled profiles also suggest that the cause of the luminescent circumference emission is an effect not captured.

The modelling, does, however reveal that changes to ground state species are negligible and therefore cannot account for the observed experimental intensity changes, implicit that these are effects related to n_e, the reduced electric field, T_{tail}, and the previously discussed couplings that these parameters have to other plasma parameters (and the physical processes occurring). The minimal changes in $I(H_2^*)$ for z > 3 mm (i.e. emissions originating from the hot plasma region) perhaps infers that the plasma parameters are not varying significantly in this region.

A study of d_{wire} (d_{sub} = 17 mm) demonstrates that the relative low z contribution is enhanced with an increased spacer wire thickness under otherwise base conditions. It is thought that the sheath is observed to collapse (by eye) for $d_{wire} \geq 0.004''$. The increase in T_{sub} with increasing d_{wire} is reflecting the increase in separation distance (and the consequential decrease in thermal conductivity) between the substrate and the water-cooled base plate. This results in an enhanced power density being absorbed by the substrate (for a constant power density / surface H atom recombination / ion flux toward the substrate), some of which would be partitioned as additional thermal energy and blackbody irradiation (and might initially act to increase the rate of H atom recombination and generate additional heat until the system reaches a steady-state at a higher T_{sub}). If the findings by Gicquel *et al*. (describing the impact that T_{sub} has on n_e and T_e in the hot plasma region, as discussed in Section 3.1) apply to the electron density surrounding the circumference (assuming that these emitting states are predominantly pumped by electron impact excitation), then the most likely explanation would be that the reduced electric field

surrounding the substrate diameter is enhanced with a thicker spacer wire resulting in hotter electrons (rather than an increased electron density).[37] It is not clear, however, that the arguments put forward by Gicquel *et al*. necessarily apply to these circumferential emissions, which were not present in their study. An alternative explanation would be that there are additional electrons present from thermionic emission of electrons by the substrate (due to a significantly increased T_{sub}), or a combination of both. What is apparent, however, is that $I(H_2^*)(z \geq 2.5$ mm) was insensitive to opening / closing the chamber and changes in d_{wire} (and therefore T_{sub}) inferring minimal changes to the hyper-thermal component of the EEDF within the hot plasma regions. This finding agrees with the general conclusion from Gicquel *et al.*, who report that changes in T_{sub} had minor effects on T_e (~ 15% changes) and a negligible impact on n_e (for MW-activated C/H plasmas operating at comparable pressures and higher powers).[37]

The impact that varying these parameters (except for (i) pressure and (v) Al_2O_3 substrate), is to significantly enhance the substrate temperature. The Al_2O_3 substrate itself reaches a temperature of ~ 1450 °C. Thermionic electrons emitted from the substrate could produce electrons at low plasma heights, consequently increasing absorbed power density and pump high energy excited states of H, H_2 (and Ar when present) via electron impact excitation. This explanation may seem simplistic / unlikely based on energetics alone, as the tungsten substrate temperature, T_{sub}, does not exceed 1400 °C (~ 0.144 eV) under any investigated condition, yet the work function of W is ~ 4.47 eV for the (111) surface.[57] However, across the whole substrate surface, there must be a contribution of electron density. There might also be additional methods for generating additional electrons and/or enhancing the reduced electric field strength at low plasma heights, such as thermionic emission and ion bombardment of the substrate, as mentioned.

Figure 3.29 reproduces normalised I(H*) datasets for no wire, d_{wire} = 0.004″ and 0.01″, d_{sub} = 17 mm, under otherwise base conditions with 25 ppm ≥ X_0(leak) ≥ 4.5 ppm and ~ 1.1 ppm (neglecting the air impurity associated with the hydrogen feed gas). Despite the substantial improvement on the leak rate, which Reference 1 infers (that decreasing the leak from 25 ppm to a lower air leak of 5 ppm) might act to change the prominent cation from H_3O^+ to H_3^+ in the plasma core, (decreasing the electric field by a few percent and acts to increase n_e slightly due to the faster dissociative recombination rates of H_3O^+ versus H_3^+ with electrons and therefore slightly decreasing T_{tail}), Figure 3.29 demonstrates that there is an indistinguishability (outside of experimental error) between the low z intensities (relative to intensity at higher z) for I(H*) and $I(H_2^*)$ with the investigated leak rates. This infers that the low z contribution are either insensitive to change of prominent cation and the associated difference in their recombination rates in MW-activated H plasmas with moderate leaks or that the contamination from the hydrogen gas impurities are significantly larger than the air impurity sourced from the chamber leak rates.

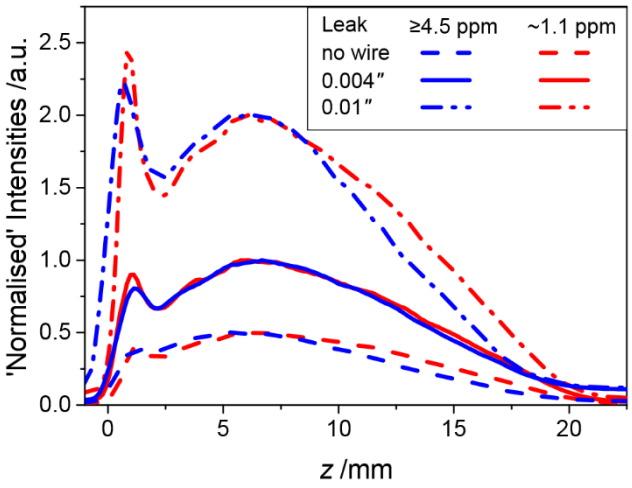

Figure 3.29: Spatial distributions of I(H*) for d_{sub} = 17 mm, P = 1.5 kW, p = 150 Torr, d_{wire} = 0″, 0.004″ and 0.01″ normalised to 0.5, 1 and 2 respectively. The figure compares relative spatial profiles of I(H*) accumulated with an associated leak contribution of 25 ≥ air leak contribution ≥ 4.5 ppm (blue and indicated by ≥ 4.5 ppm in the inset) to data collected with an air leak of ~ 1.1 ppm (red, indicated by ~1.1 ppm). Note that these values neglect any contamination associated with the hydrogen gas. The relative low z contributions are within experimental error.

Further experiment / modelling available in Reference 2, reveals an additional possibility for generating electrons at a low plasma height. Reference 2 reports the appearance of Cu emissions originating from the reactor copper baseplate upon the introduction of Ar (and Kr). The Cu emissions demonstrate a clear correlation with the calculated steady-state concentration of ArH^+ (but not other more prominent cations, i.e. H_3^+, H_3O^+) at $z \sim -3$ mm, maximising between $R_{sub} + 1.5 < r < R_{sub} + 4$ mm, i.e. at a radial distance extending that of the W substrate radius, just above the water-cooled copper base plate, noting that z = 0 mm defines the top of the 3 mm thick W substrate. This contrasts to the behaviour of n_e modelled at z = 0.5 mm and 10.5 mm (r = 0 mm), whereby n_e increases. This observation is potentially interesting in the context of the hitherto unexplained low z emissions, as it provides evidence that ions are bombarding the metallic base plate surfaces with enough energy to sputter metal atoms. If ArH^+ bombardment of the baseplate can sputter Cu, it is plausible that ions accelerating across the sheath could ionize (as well as heat) the W substrate and that increasing the spacer wire thickness (i.e. decreasing the thermal conductivity of the 17 mm substrate) might act to increase the energy partitioned as ionization and thermal heating of the substrate. Further, sputtered metal could ionize within its own right generating an additional source of electron density at lower plasma heights. Figure 3.29 provides evidence that if this hypothesis is correct, this mechanism may well be indiscriminate of prominent cation in MW-activated H plasmas so long as they hold comparable ionization energies.

In the context of MW-activated H/Ar plasmas, however, the discussion on the relative increase of plasma emission intensities at z = 2.5 mm (d_{sub} = 32 mm) is deemed most likely to be the result of changes in physical processes (e.g. introduction of near-resonant energy transfers between highly

excited states of Ar with H and H_2), the reduced electric field strength, the increase in T_g, which in its own right results in higher dissociation of H_2 and more H atom recombination reactions on the substrate surface, resulting in an enhancement of T_{sub} and additional thermionic electrons being emitted by the substrate. These are in addition to the substitution of H_2 with Ar, which preferentially diffuses due to its heavier mass, contributing to enhanced heat transfer.

Emissions at low *z* can be enhanced and relocated through use of a smaller substrate, whilst the absolute (and relative) contribution can be manipulated through varying wire thickness. These effects are in part captured by modelling. Perhaps, the differences (particularly in height) can be accounted by stronger electric fields, encouraging an enhancement in T_{tail}, n_e, (via thermionic emission and ion bombardment of the substrate), and therefore increased absorbed power density, T_g near to the substrate as a $f(r)$. The result is in an enhanced T_{sub} from H recombination events, which contributes further thermionic electrons, which are accelerated across the enhanced fields wrapped around the substrate, producing the annular emissions observed around the substrate edges. Some of these effects were not deliberately included in the modelling. This conclusion would be entirely consistent with the proposed explanation provided by Yamada *et al.* give for concave/convex grown CVD diamond in MW-activated C/H plasmas, discussed in Chapter 1.[58]

The addition of an Al_2O_3 substrate does not significantly affect the metal substrate temperature, T_{sub}, however it does demonstrate a clear plasma perturbation. The Al_2O_3 reaches $T_{Al_2O_3}$ ~ 1450 K under otherwise base conditions and demonstrates a bright glow. Without an understanding of MW-activated H/Al plasmas, it is difficult to draw any definitive conclusions about the final experiment. It is proposed that in addition to the effects aforementioned, the presence of gas phase Al might act to enhance n_e and perturb the local physical parameters / gas phase processes at low *z*, where Al is thought to be localised (given the source of the aluminium, see the silicon etching experiments in Chapter 6, Section 6.3.8). This would act to enhance emissions at low *z* (observed) and decrease their relative contribution with an enhanced T_{sub} (due to the enhanced [Al], n_e, and the associated decrease in T_{tail}). This is indicated in the additional results reported by John Allden in his dissertation regarding Al_2O_3 (which were investigated as a $f(T_{sub}(d_{wire}))$ and additional parameter spaces (e.g. pressure and power)).[50] Were his results to be taken at face value, many of these results contrast to the intensity behaviours observed in this chapter without the presence of an Al_2O_3. This leads to an interesting question of what process, or processes, lead to the introduction of substrate material into the gas phase? Thermal decomposition? Hydrogen etching? Ion bombardment? It is not possible to speculate on whether the observations are material, size, height or shape dependent without more thorough investigations. It is feasible that thermionic emission and ion bombardment (also resulting in ionization) could also apply to an Al_2O_3 substrate. Without additional studies, however, there is little point speculating. What is clear from Figure 3.28, however, is that the combined presence of a small Al_2O_3 substrate and the associated etched gas phase Al significantly perturbs the H-Balmer emission profile and enhances the low *z* component

identified in this Chapter. There is room for further investigation and the impact of Al incorporation has on the plasma processes, as well as holding a low ionization energy, the chamber walls are made from Al. Related emissions are noted at λ = 394.12 and 395.97 nm (assuming ~ −0.2 nm offset) when using extreme conditions (e.g. the small substrate) are investigated. Emissions featuring at similar wavelengths are also noted in MW-activated C/H plasmas (although it is worth noting, C atoms also emit at such wavelengths from a high energy state, highlighting an additional challenge when using OES; the ability to distinguish between different species emitting at overlapping wavelengths).

W also has a lower ionization energy of 7.86 eV [59] (*cf.* any other species present in a MW-activated H plasma, see Table 6.2 in Chapter 6). Could lower concentrations of [W] generally be present within MW-activated H plasmas? If so, what processes are involved in the introduction of W, are they the same? Could the low *z* enhancement of emission intensities be due to a more subtle increase in n_e from the presence (and changes in concentration) of gas phase [W] when altering wire thickness with a smaller W diameter substrate? What would happen to these contributions upon the addition of methane?

3.4: Conclusions

Chapter 3 has explored the complicated interdependencies between spatially variant plasma parameters and the prominent gas phase processes occurring within MW-activated H (and H/Ar) plasmas (for instance, the MW electric field and absorbed power density ↔ gas temperature, number density of gas phase species, reduced electric field strength ↔ electron energy distribution function, ionization rates, chemical kinetic rates, physical processes, such as diffusion, ↔ electron density, ion distributions, ground state species distribution ↔ MW electric field and absorbed power density) and how these vary with changes in operating conditions of MW-activated H plasmas. This has been achieved through combining spatially-resolved optical emission studies on three H_2 emission bands and the H Balmer series emissions as a function of P, p, d_{sub}, a combination of these, and argon fraction with the first self-consistent 2-D physical chemical kinetic modelling of a MW-activated H plasma (which was developed from the results reported in this chapter).

The modelling rationalises the observed distribution of various {H_2*} and {H*} states (via their emitting intensities) and identifies the significant formation and loss mechanisms associated with these gas phase species. It also adds clarity to the relative importance of considered processes, providing a rationale as to how variations in the plasma contents and parameters impact the physical characteristics of the plasma (e.g. size, ion distributions, etc) and the plasma processes, thereby providing a rationale behind the experimentally observed intensity changes under the studied parameter ranges.

In relevance to the extended title of this thesis, “Alternative Excitation Mechanisms Occurring within Microwave-activated Plasmas Operating under Conditions Relevant to the Hydrogen Termination, Etching, and Chemical Vapour Deposition of Diamond”, the modelling highlights an intimate coupling

between H* and H_2* through their ground states under all investigated conditions. Whilst this coupling does not affect the spatial distributions of the excited states (or their respective spatially-resolved emissions) for a single condition, which primarily reflects their excitation via electron impact (i.e. the pumping of these excited states) and perhaps their quenching, such couplings between excited and ground states are required to explain the complicated P and p dependencies of H* and H_2*. Such couplings between these excited state species highlight a significant flaw on using Boltzmann plot analyses of H_2* emission bands to calculate T_{vib} and T_{rot} and is likely why such analyses produces underestimations of T_g.

Further, this finding has implications on indicating the variation in T_e and T_{tail} when monitoring H Balmer intensity ratios as a function of process conditions (in addition to the issues raised in Chapter 1, Section 1.5, e.g. the differences in energy of H(n) states are small relative to electron energies being probed etc), particularly as different H(n) states couple to different H_2* states, highlighting additional issues with relying on H Balmer emission ratios for estimating T_{tail} or T_e under the investigated parameter ranges.

In spite of these significant findings, the study confirms that $I(H_2^*)$ is (generally) more reflective of the hyper-thermal component of the EEDF (e.g. under base conditions, $I(H_2^*)$ was found to maximise at z ~ 2.5 mm, where the reduced electric field $|E|/(N\times a)$, T_e, and absorbed power density all maximise). This contrasts to the H Balmer series and their spatial variations, which require additional considerations, e.g. H production, diffusion considerations etc. For a single condition, however, either method might still be indicative of the spatial variation of T_{tail} and the reduced electric field variation.

The addition of argon introduces further couplings between Ar* and H, H_2, as well as H* and H_2* with Ar via near resonant excitation transfer processes. Whilst this is not thought to significantly impact ground state spatial distributions for a single condition (at low Ar fractions) and has been demonstrated to have a significantly lower rate than other, more prominent, excitation / quenching processes, there is still the possibility that such couplings may have similar implications with regards to actinometry and the underpinning assumptions, particularly when investigating intensity ratios and their variation with changes in operating conditions at a constant height. At the very least, these findings provide an additional uncertainty to prior actinometry measurements carried out under conditions comparable to those investigated in this chapter.

By establishing the prominent processes, their interdependencies with one another, and their coupling to the physical plasma parameters, it has been possible to speculate on the effect of varying additional parameter spaces, such as substrate diameter and substrate temperature. These parameters have been found to significantly enhance the intensity of a previously unreported component of the H* and H_2* emission contribution close to the substrate, whilst Ar addition quenches these emissions at all plasma

heights but enhances the relative contribution of emissions featuring at low *z*, as shown in Figures 3.20 (a) and (b), and Figures 3.27 (a) and (b).

These effects can, in part, be explained through changes in the plasma parameters (e.g. MW EM fields, gas temperature, the reduced electric field, substrate temperature) and the prominent processes occurring at low plasma heights (and on the substrate surface, e.g. H atom recombination and electron thermionic emission from the substrate). The low *z* emission has been speculated to be insensitive to prominent plasma ions (in the case of changing between H_3^+ and H_3O^+), but highly sensitive to X_0(Ar), d_{sub} and perhaps d_{wire}. It is speculated that the cause of these emissions could be a significantly increased n_e (through electron thermionic emission from the substrate and ion impact ionization of the substrate), near-resonant energy transfers, changes in T_{tail}, or in the case of Ar, near-resonant energy transfers, as described above.

There is a spatial disparity between experiment and plasma modelling. This is particularly noticeable at low pressures, upon the addition of argon and the decrease in d_{sub}. This may be the result of underestimated electric field strengths, unknown or neglected plasma processes, or the spatial resolution (1 mm) failing to capture the full variation of the electric and magnetic fields.

Despite a significant portion of the experimental work presented in this chapter being carried out with a relatively high leak rate (25 ppm of air, which includes 5 ppm O_2), further modelling concluded that reducing the leak down to 5 ppm in the plasma core (i.e. 1 ppm O_2), does not significantly affect plasma parameters or the general conclusions drawn in the, only the prominent cation species (H_3O^+ rather than H_3^+) and the rate of ion-electron recombination. The leak rate does not fundamentally affect the conclusions drawn in this chapter.

Aside from the spectroscopic implications already inferred, there have been some interesting findings relating to diamond growth, which have been highlighted in this work. These include, but are not limited to: the effect that decreasing (/ increasing) substrate diameter and introducing argon addition may have; a smaller substrate diameter enables access to higher power density without (allegedly) compromising the plasma size (according to the 2-D plasma model, by eye, the visible plasma appeared somewhat smaller when operating with a smaller substrate, although this is not evidenced within the optical emissions). Without a compensatory decrease in wire thickness, this parameter space leads to a higher uncontrolled substrate temperature and appears to collapse the sheath. Comparatively, a larger substrate acts to enhance $|E|/N$ (and plasma) uniformity across the substrate.

Further, it is noted that argon contributes to a significant MW power absorption beyond the visible plasma resulting in a radial expansion, and an enhanced uniformity in [H] close to the substrate. This could enable homogeneous diamond growth across larger exposed surface areas – larger fractions of

argon also also act to increase gas temperature, consequently increasing [H]/[H_2] in the plasma core despite a decrease in $X_0(H_2)$.

The effect of combining both parameters might also be to alter MW field strengths closer to the substrate, which could be manipulated to facilitate further gas processing with an increase in T_g. The resulting increase in T_{sub} can be controlled through a compensatory decrease in spacer wire thickness.

Perhaps one way that these parameters could be combined to compliment one another would be to use a larger substrate with Ar addition; the use of a larger substrate will act to reduce the absorbed power density (and T_g, T_{sub}, and E/N), but provide a larger surface area to place diamond substates to grow on, whilst introducing Ar may act to enhance the plasma uniformity across the substrate diameter and T_{sub}, facilitating a more homogeneous growth over larger surface areas. Manipulation of the spacer wire could act to fine-tune the diamond substrate temperature.

Further experimental (and theoretical) work would act to strengthen this chapter. Such work would include a verification of the observed trends with a significantly lower air leak rate (and controlled gas impurities), longer accumulated studies (to improve signal/noise) for investigating higher H* emitting states within the H Balmer series, for more careful probing of subtler differences between different H* and H_2* emissions, which have been hinted at in this chapter (for instance, both H_2 triplet emissions appear to quench with the same pressure dependence, whilst H_2 singlet emissions appeared to quench more rapidly with increasing pressure).

Perhaps, more relevantly for diamond growth, these findings should be verified in the presence of methane. The impact methane has on the low plasma emissions with a small substrate present are seen in Chapters 4 and 5, whilst the H* ↔ H_2* couplings are investigated further in Chapter 6. Exploring the parameter space surrounding Ar / d_{sub} / d_{wire} in diamond growth studies would make useful complimentary further studies providing an alternative experimental verification of the results presented.

The near substrate emission contributions could be investigated further through use of a microscope to provide a higher spatial resolution. Whilst thermionic electron emission originating from the metal substrate do not necessarily seem like the most energetically feasible source of electrons, this could be experimentally confirmed / rejected by growing high quality diamond over the substrate. Such a layer might quench the production of thermionic electrons (unless graphitic content is present), whilst electrons generated by ion impact ionization of the diamond coated substrate may still be expected to occur, albeit reduced. This suggestion comes with its own set of problems; the etching of carbon might act to change the prominent cation close to the substrate, and therefore impact local n_e and relative ion distributions, amongst other plasma parameters. Further, without an improved control of T_{sub}, the

diamond coating could reconstruct to conductive graphitic carbon. Chapter 6 demonstrates that this last issue could perhaps be averted in further studies by using a silicon wafer under a suitably controlled T_{sub}. Such a study would come with its own set of demonstrated challenges (e.g. melting).

There are still open questions regarding an experimental verification of how the thermal component of the EEDF behaves. One perceived possibility is to controllably etch a substrate into the gas phase and compare emissions from lower lying excited state emissions from material etched into the plasma (relative to H* and H_2* states). This idea was pursued to some degree by John Allden with limited success using Al and Al_2O_3 substrates.[50] The presence of an Al substrate produced uncontrollable Al etching and plasma instability, whilst a 1 mm thick Al_2O_3 substrate produced two bright Al* emissions (and additional dimmer lines), but significantly perturbed the plasma, resulting in the relocation of the H Balmer series maxima to a slightly lower plasma height and a significant bimodal contribution at lower *z*. An interesting follow on study would be to determine whether this effect depends on substrate size / shape / height / material. Again, perhaps the use of a Si substrate and/or gas phase silane could be used to address these questions.

Some of these ideas are revisited within this thesis with more relevance towards the chemical vapour deposition of diamond, i.e. using MW-activated C/H plasmas. Chapter 5 attempts to investigate the thermal component of the EEDF using emissions from the 3 lowest lying singlet CH excited states in MW-activated C/H plasmas, whilst H_2* and H* are restudied in Chapter 6 for developing an understanding behind the physical and chemical processes occurring within MW-activated Si/H and Si/C/H.

References

[1] Mahoney E. J. D., Truscott B. S., Mushtaq S., Ashfold M. N. R., Mankelevich Yu. A. "Spatially Resolved Optical Emission and Modeling Studies of Microwave-Activated Hydrogen Plasmas Operating under Conditions Relevant for Diamond Chemical Vapor Deposition." The Journal of Physical Chemistry A, vol. 122, no. 42 pp. 8286-8300, 2018.

[2] Mahoney, E. J. D., Mushtaq, S., Ashfold, M. N. R., Mankelevich, Yu. A. "Combined Spatially Resolved Optical Emission Imaging and Modelling Studies of Microwave-Activated H_2/Ar and H_2/Kr Plasmas Operating under Conditions Relevant for Diamond Chemical Vapor Deposition" The Journal of Physical Chemistry A, vol. 123, no. 13, pp. 2544-2558, 2018.

[3] Shafranov, V. "Magnetohydrodynamic theory of plasma equilibrium and stability in stellarators: Survey of results." Physics of Fluids, vol. 26, no. 2, p. 357, 1983.

[4] Neu, E., Steinmetz, D., Riedrich-Möller, J., Gsell, S., Fischer, M., Schreck, M., Becher, C. "Single photon emission from silicon-vacancy colour centres in chemical vapour deposition nano-diamonds on iridium." New Journal of Physics, vol. 13, no. 2, p. 025012, 2011.

[5] Nichols, B. M., Butler, J. E., Russell, J. N., Hamers, R. J. "Photochemical Functionalization of Hydrogen-Terminated Diamond Surfaces: A Structural and Mechanistic Study." The Journal of Physical Chemistry B.vol. 109, no. 44, pp. 20938-20947, 2005.

[6] Ma, J., Richley, J. C., Davies, D. R. W., Cheesman, A., Ashfold, M.N.R., Mankelevich, Yu. A. "Spectroscopic and Modeling Investigations of the Gas-Phase Chemistry and Composition in Microwave Plasma Activated B_2H_6/Ar/H_2Mixtures." The Journal of Physical Chemistry A. vol. 114, no. 7, pp. 2447-2463, 2010.

[7] Kelly, M. W., Richley, J. C., Western, C. M., Ashfold, M. N. R., Mankelevich, Yu. A. "Exploring the Plasma Chemistry in Microwave Chemical Vapor Deposition of Diamond from C/H/O Gas Mixtures." The Journal of Physical Chemistry A. vol. 116, no. 38, pp. 9431-9446, 2012.

[8] Truscott, B. S., Kelly M. W., Potter K. J., Johnson, M., Ashfold, M. N. R., Mankelevich, Yu. A. "Microwave Plasma-Activated Chemical Vapor Deposition of Nitrogen-Doped Diamond. I. N_2/H_2 and NH_3/H_2 Plasmas." The Journal of Physical Chemistry A. vol 119, no. 52, pp. 12962-12976, 2015.

[9] Dieke, G. H. "The molecular spectrum of hydrogen and its isotopes. Journal of Molecular Spectroscopy." vol. 2, no. 1-6, pp. 494-517, 1958.

[10] Crosswhite, H. M., Dieke, G. H., "The Hydrogen Molecule Wavelength Tables", Wiley-Interscience, New York, 1986.

[11] Fantz, U., Wünderlich, D. "Franck–Condon factors, transition probabilities, and radiative lifetimes for hydrogen molecules and their isotopomeres." Atomic Data and Nuclear Data Tables, vol. 92, no. 6, pp. 853-973, 2006.

[12] Hassouni, K., Silva, F., Gicquel, A. "Modelling of diamond deposition microwave cavity generated plasmas." Journal of Physics D: Applied Physics. vol. 43, no. 15, p. 153001, 2010.

[13] Shivkumar, G., Tholeti, S. S., Alrefae, M. A., Fisher, T. S., Alexeenko, A. A. "Analysis of Hydrogen Plasma in a Microwave Plasma Chemical Vapor Deposition Reactor." Journal of Applies Physics, vol. 119, no. 22, p. 113301, 2016.

[14] Gicquel, A., Hassouni, K., Farhat, S., Breton, Y., Scott, C. D., Lefebvre, M., Pealat, M. "Spectroscopic Analysis and Chemical Kinetics Modeling of a Diamond Deposition Plasma Reactor." Diamond and Related Materials, vol. 3, no. 4-6 pp. 581-586, 1994.

[15] Hassouni, K., Gicquel, A., Capitelli, M., Loureiro, J. "Chemical Kinetics and Energy Transfer in Moderate Pressure H_2 Plasmas used in Diamond MPACVD Processes." Plasma Sources Science and Technology, vol. 8, no. 3, pp. 494-512, 1999.

[16] Hassouni, K., Lombardi, G., Duten, X., Haagelar, G., Silva, F., Gicquel, A., Grotjohn, T. A., Capitelli, M., Röpcke, J. "Overview of the Different Aspects in Modelling Moderate Pressure H_2 and H_2/CH_4 Microwave Discharges." Plasma Sources Science and Technology, vol. 15, no. 1, pp. 117-125, 2006.

[17] Hassouni, K., Grotjohn, T. A., Gicquel, A. "Self-Consistent Microwave Field and Plasma Discharge Simulations for a Moderate Pressure Hydrogen Discharge Reactor." Journal of Applied Physics, vol. 86, no. 1 pp. 134-151, 1999.

[18] Hassouni, K., Silva, F., Gicquel, A. "Modelling of Diamond Deposition Microwave Cavity Generated Plasmas." Journal of Physics D: Applied Physics, vol. 43, no. 15, p. 153001 and references therein, 2010.

[19] Dang, J., Chung, K., Hwang, Y. S. "A Simple Spectroscopic Method to Determine the Degree of Dissociation in Hydrogen Plasmas with Wide-Range Spectrometer." Review of Scientific Instrumunts, vol. 87, no. 5, p. 053503, 2016.

[20] Tan, W., Grotjohn, T. A. "Modelling the Electromagnetic Field and Plasma Discharge in a Microwave Plasma Diamond Deposition Reactor" Diamond and Related Materials, vol. 4, no. 9, 1145-1154, 1995.

[21] Gorbachev, A. M., Koldanov, V. A., Vikharev. A. L. "Numerical Modeling of Microwave Plasma CVD Reactor." Diamond and Related Materials, vol. 10, no. 3-7, pp. 342-346, 2001.

[22] Yamada, H., Chayahara, A., Mokuno, Y. "Simplified Description of Microwave Plasma Discharge for Chemical Vapor Deposition of Diamond." Journal of Applied Physics, vol. 101, no. 6, pp. 063302, 2007.

[23] Shakhatov, V. A., Lebedev, Yu. A. "Collisional-Radiative Model of Hydrogen Low-Temperature Plasma: Processes and Cross Sections of Electron-Molecule Collisions." High Temperature. vol. 49, no. 2, pp. 257–302, 2011.

[24] Shakhatov, V. A., Lebedev, Yu. A. "On the Applicability of the Optical Emission of Triplet States of Hydrogen Molecules for the Diagnostics of Non-Equilibrium Microwave Hydrogen Discharge." High Temperature, vol. 55, no. 4, pp. 496-501, 2017.

[25] Prasanna, S., Rond, C., Michau, A., Hassouni, K., Gicquel, A. "Effect of buoyancy on power deposition in microwave cavity hydrogen plasma source." Plasma Sources Science and Technology. vol. 25, no. 4, pp. 045017, 2016.

[26] Prasanna, S., Michau, A., Rond, C., Hassouni, K., Gicquel, A. "Self-consistent simulation studies on effect of methane concentration on microwave assisted H_2-CH_4 plasma at low pressure." Plasma Sources Science and Technology. vol. 26, no. 9, p. 097001, 2017.

[27] Engelhardt, A. G., Phelps, A. V. "Elastic and Inelastic Collision Cross-Sections in Hydrogen and Deuterium from Transport Coefficients." Physics Review vol. 131, no. 5, p. 2115-2128, 1963.

[28] Liu, X., Shemansky, D. E., Ahmed, S. M., James, G. K.; Ajello, J. M. "Electron-Impact Excitation and Emission Cross Sections of the H_2 Lyman and Werner Systems." Journal of Geophysical Research: Space Physics, vol. 103, no. A11, pp. 26739-26758, 1998.

[29] Wrkich, J., Mathews, D., Kanik, I., Trajmar, S., Khakoo, M. A. "Differential Cross-Sections for the Electron Impact Excitation of the $B^1\Sigma_u^+$, $c^3\Pi_u$, $a^3\Sigma_g^+$, $C^1\Pi_u$, $E,F^1\Sigma_g^+$ and $e^3\Sigma_u^+$ States of Molecular Hydrogen." Journal of Physics B: Atomic, Molecular and Optical Physics, vol. 35, pp. 4695-4709, 2002.

[30] da Costa, R. F., da Paixao, F. J., Lima, M. A. P. "Cross Sections for Electron-Impact Excitation of the H_2 Molecule Using the MOB-SCI Strategy." Journal of Physics B: Atomic, Molecular and Optical Physics, vol. 38, no. 24, pp. 4363–4378, 2005.

[31] Liu, X., Shemansky, D. E. "Non-Dissociative Electron and Photon Ionization Cross Sections of Molecular Hydrogen and Deuterium." Journal of Physics B: Atomic, Molecular and Optical Physics, vol. 45, no. 9, pp. 095203, 2012.

[32] Hargreaves, L. R., Bhari, S., Adjari, B., Liu, X., Laher, R., Zammit, M., Savage, J. S., Fursa, D. V., Bray, I., Khakoo, M. A. "Differential Cross Sections for Excitation of H_2 by Low-Energy Electron Impact." Journal of Physics B: Atomic, Molecular and Optical Physics, vol. 50, no. 22, p. 225203, 2017.

[33] Tawara, H., Itikawa, Y., Nishimura, H., Yoshino, M. "Cross Sections and Related Data for Electron Collisions with Hydrogen Molecules and Molecular Ions." Journal of Physical Chemistry Reference Data, vol. 19, no. 3, pp. 617-637, 1990.

[34] Capitelli, M., Celiberto, R., Esposito, F., Laricchiuta, A., Hassouni, K., Longo, S. "Elementary Processes and Kinetics of H_2 Plasmas for Different Technological Applications." Plasma Sources Science and Technology, vol. 11, no. 3A, pp. A7-A25, 2002.

[35] Yoon, J. S., Song, M. Y., Han, J. M., Hwang, S. H., Chang, W. S., Lee, B., Itikawa, Y. "Cross Sections for Electron Collisions with Hydrogen Molecules." Journal of Physical Chemistry Reference Data, vol. 37, no. 2, pp. 913-931, 2008.

[36] Zammit, M. C., Savage, J. S., Fursa, D. V., Bray, I. "Electron-Impact Excitation of Molecular Hydrogen." Physics Review A, vol. 95, p. 022708, 2017.

[37] Derkaoui, N., Rond, C., Gries, T., Henrion, G. and Gicquel, A. "Determining electron temperature and electron density in moderate pressure H_2/CH_4 microwave plasma." Journal of Physics D: Applied Physics, vol. 47, no. 20, p. 205201, 2014.

[38] Cortázar, O. D., Megía-Macías, A., Vizcaíno-de-Julián, A., Tarvainen, O., Komppula, J., Koivisto, H. "Ultra-Fast Intensified Frame Images from an Electron Cyclotron Resonance Hydrogen Plasma at 2.45 GHz: Some Space Distributions of Visible and Monochromatic Emissions." Review of Scientific Instrumunts, vol. 85, no. p. 02A902, 2014.

[39] Mankelevich, Yu. A., Ashfold, M. N. R., Ma, J. "Plasma-Chemical Processes in Microwave Plasma-Enhanced Chemical Vapor Deposition Reactors Operating with C/H/Ar Gas Mixtures." Journal of Applied Physics, vol. 104, pp. 113304, 2008.

[40] Feldmeier, H., Schnack, J. "Molecular dynamics for fermions." Reviews of Modern Physics. vol. 72, no. 3 pp. 655-688, 2000.

[41] Silvera I. F. "The solid molecular hydrogens in the condensed phase: Fundamentals and static properties." Reviews of Modern Physics. vol. 52, no. 2, pp. 393-452, 1980.

[42] Millar, T. J., Farquhar, P. R. A., Willacy, K., "The UMIST Database for Astrochemistry 1995". Astronomy and Astrophysics Supplier Service, vol. 121, pp. 139-185, 1997.

[43] Brouillard, F., Urbain, X. "Associative Ionisation in Low Energy Collisions." Physica Scripta, vol. T96, no. 1, pp. 86-93, 2002.

[44] Lewis, J. W. L., Williams, W. D. "Collisional Deactivation of Atomic and Molecular Hydrogen." Journal of Quantitative Spectroscopy and Radiative Transfer, vol. 16, no. 11, pp. 939-946, 1976.

[45] Catherinot, A., Dubreuil, B., Gand, M., "Quenching of Atomic States in a Low-Pressure Hydrogen Glow Discharge." Physics Review A, vol. 18, no. 3, pp. 1097-1102, 1978.

[46] Raizer, Yu. P. "Gas Discharge Physics" Springer-Verlag, Berlin, 1991.

[47] Ma, J., Ashfold, M. N. R. and Mankelevich, Yu. A. "Validating optical emission spectroscopy as a diagnostic of microwave activated $CH_4/Ar/H_2$ plasmas used for diamond chemical vapor deposition," Journal of Applied Physics, vol. 105, no. 4, p. 043302, 2009.

[48] Amorim J., Loureiro J., Baravian G., Touzeau M., "Experimental and theoretical study of dissociation in the positive column of a hydrogen glow discharge." Journal of Applied Physics. vol. 82, no. 6., pp. 2795-2804, 1997.

[49] Pealat, M., Taran, J. P. E., Taillet, J., Bacal, M., Bruneteau, A. M. "Measurement of vibrational populations in low-pressure hydrogen plasma by coherent anti-Stokes Raman scattering." Journal of Applied Physics, vol. 52, no. 4, pp. 2687-2691, 1981.

[50] Allden, J. W. R. "The use of Spectroscopic Methods to determine the state of Plasmas relevant to the Chemical Vapour Deposition of Diamond" Undergraduate final year Dissertation, University of Bristol, 2019.

[51] Richley, J. C., Fox, O. L., Ashfold, M. N. R., Mankelevich, Yu. A. "Combined experimental and modeling studies of microwave activated $CH_4/H_2/Ar$ plasmas for microcrystalline, nanocrystalline, and ultrananocrystalline diamond deposition." Journal of Applied Physics, vol. 109, no. 6, p. 063307, 2011.

[52] Dandy, D. S., Coltrin, M. E. "A Simplified Analytical Model of Diamond Growth in Direct Current Arcjet Reactors." Journal of Materials Research, vol. 10, no. 8, pp. 1993-2010, 1995.

[53] Paul, R., Srivastava, I. B. "Mutual Diffusion of the Gas Pairs H_2–Ne, H_2–Ar, and H_2–Xe at Different Temperatures." Journal of Chemical Physics, vol. 35, no. 1, pp. 1621-1624, 1961.

[54] Khouw, B., Morgan, J. E., Schiff, H. I., "Experimental Measurements of the Diffusion Coefficients of H Atoms in H_2 and in H_2–He and H_2–Ar Mixtures." Journal of Chemical Physics, vol. 50, no. 1, pp. 66-70, 1969.

[55] NIST ASD Levels Output [Internet]. Physics.nist.gov. 2019 Available from: https://physics.nist.gov/cgi-bin/ASD/energy1.pl?encodedlist=XXT2&de=0&spectrum=Al+I&submit=Retrieve+Data&units=0&format=0&output=0&page_size=15&multiplet_ordered=0&conf_out=on&term_out=on&level_out=on&unc_out=1&j_out=on&lande_out=on&perc_out=on&biblio=on&temp= [accessed 28 April 2019].

[56] Chang, E. S. "Energy Levels of Atomic Aluminum with Hyperfine Structure." Journal of Physical and Chemical Reference Data, vol. 19, no. 1, pp. 119-125, 1990.

[57] Strayer, R. W., Mackie, W. and Swanson, L. W. "Work function measurements by the field emission retarding potential method." Surface Science, vol. 34, no. 2, pp. 225-248, 1973.

[58] Yamada, H., Chayahara, A., Mokuno, Y., Horino, Y. and Shikata, S. "Numerical analyses of a microwave plasma chemical vapor deposition reactor for thick diamond syntheses." Diamond and Related Materials, vol. 15, no. 9, pp. 1389-1394, 2006.

[59] Campbell-Miller, M. D. and Simard, B. "First ionization potentials of tungsten and rhenium by mass-selected double-resonance ionization spectroscopy." Journal of the Optical Society of America B, vol. 13, no. 10, pp. 2115, 1996.

Chapter 4: Experimental Confirmation of Charged Species within MW-activated C/H and C/H/Ar Plasmas?

The C_2(d→a) Swan band is a prominent feature within the visible optical emissions originating from a MW-activated C/H(/Ar) plasma. The formation mechanism of C_2(X) and its excited states, C_2(a) and C_2(d), are already well-established under the investigated conditions. This chapter identifies the first direct evidence of anions within MW-activated C/H(/Ar) plasmas through observing optical emissions originating from the C_2^-(B→X)(0-0) Herzberg-Lagerqvist system, underlying the more prominent C_2(d→a) emission. These emissions have been investigated as a function of operating conditions (methane fraction, total gas pressure, input microwave power, argon flow, and substrate diameter). Through minor adaptations of the previously described self-consistent 2-D physical chemical kinetic modelling of a MW-activated C/H plasma, this chapter reviews the prominent formation and loss mechanisms of the C_2(X), C_2(a) and C_2(d) states and establishes the prominent processes involved in the formation and loss of the C_2^-(X) and C_2^-(B) states through comparison of experimental results to 2-D plasma modelling predictions.

Dissociative electron attachment of C_2H is found to be the prominent formation mechanism for the production of C_2^-(B). The modelling indicates that the same mechanism also applies to C_2H_2 forming a higher concentration of C_2H^- in the near-substrate region. The total anion number densities extracted from the modelling are 3-4 orders of magnitude lower than the electron concentration and counterpart cations $C_2H_2^+$ and $C_2H_3^+$.

Prior to this work, it has been assumed that electrons are the only negatively charged species present under conditions relevant for the CVD of diamond, and as such, this chapter offers insight into an alternative interpretation to enhanced nucleation densities and growth rates that have been reported for a positive bias enhancement (in bias enhanced nucleation studies), as discussed in Chapter 1. This chapter also briefly reports an unfruitful attempt to observe optical emissions from CH^+(A-X). The main results presented in this chapter have been published in Reference 1.

4.1: Introduction

As outlined in Chapter 1, diamond films can be grown through the Chemical Vapour Deposition method utilising Microwave-activated C/H plasmas.[2,3,4,5] Such films find application within a range of technologies owing to their outstanding properties.[2,3,4,5] The high thermal conductivities and low thermal expansion coefficients make diamond film an ideal material for the thermal management of electronic and lasing devices.[2,3,6] High quality single crystal diamond films are a wide band gap insulator with a negligible birefringence, making diamond films applicable as optical windows and lenses. [2,3,7]

This thesis has thus far established a means to investigate the hyper-thermal component of the EEDF for MW-activated H and H/Ar plasmas under conditions relevant to hydrogen-termination and surface etching of diamond. Through doing so, some of the more prominent gas phase processes occurring within MW-activated H and H/Ar plasmas have been reviewed and re-established.[8,9,10,11,12,13,14] Chapters 4 and 5 extend these ideas to review and establish prominent and additional gas phase processes occurring within MW-activated C/H plasmas under plasma conditions relevant to the CVD of diamond with a particular focus on the excitation mechanism(s) of observed emitting states.

The presence of electrons and their cation counter-part ($C_2H_2^+$ and $C_2H_3^+$) is well-established by theoretical modelling and indirectly inferred through experimental observation of atomic and diatomic emissions.[8,9,10,11,12,13,14,15] The production of electronically excited (i.e. emitting) states for most species generally occur through a combination of electron impact excitation (e.g. formation of H($n \geq 2$), H_2*, Ar*, CH*), (resonant and near-resonant) excitation transfer (e.g. interactions between H($n \geq 2$), H_2*, Ar* and H($n = 1$), H_2 and Ar ground states), and chemiluminescence (e.g. CH(A) state). This thesis has also established that electron impact excitation and resonant / near-resonant excitation transfer processes occurring within MW-activated H and H/Ar plasmas are intimately coupled with operating conditions, the plasma parameters, such as the reduced electric field, the electron number density, and the gas temperatures.

This chapter characterises how optical emissions from the well-studied $C_2(d^3\Pi_g \rightarrow a^3\Pi_u)$, $\Delta v = 0$ and $\Delta v = -1$ Swan band [8,16,17,18,19,20,21,22,23,24,25,26] and previously unstudied $C_2^-(B^2\Sigma_u \rightarrow X^2\Sigma_g)$, $\Delta v = 0$ transition, henceforth referred to as the C_2(d→a) and C_2^-(B→X) transitions, vary spatially and with process conditions. The study is combined with 2-D plasma chemical modelling in order to establish an understanding of the physical processes involved in the formation of C_2^- and C_2^-(B), and to confirm that the understood mechanisms in the formation of C_2(X), C_2(a) and C_2(d) within MW-activated C/H plasmas agree with experimental observation. As discussed in Chapter 1, Section 1.2.2, there are open questions regarding to explaining enhanced nucleation achieved using positive bias, which this chapter helps to address.[27,28] Chapters 4 and 5 serve as a reminder that a complete understanding of the gas phase processes occurring within MW-activated C/H plasma has yet to be achieved.

As molecules increase in size, the electronic (and rovibronic) excited states become increasingly close in energy and consequently most spectroscopic studies on molecules containing more than 2 atoms are carried out at low temperatures ($T_g < 100$ K) or through computational methods.[29,30] Larger molecules, for instance C_3, are only observable by an indicative broad ill-defined feature arising from overlapping electronic transitions at T_g of interest in this thesis ($2000 \leq T_g \leq 3000$ K). Consequently, a broad emission band from C_3 appears within emission baseline at larger methane fractions.

Any attempt to conclusively observe an emission from a cation would therefore rely on the observation of a well-defined atomic or diatomic transition resulting in photoemission. There are no physical

reasons as to why C_2^+ and CH^+ could not exist within a MW-activated plasma environment as a minority species; they could be generated through electron impact ionization (ionization energies of +11.1 and +12 eV respectively) or via reactions involving H_3^+ (e.g. $CH_2 + H_3^+ \rightarrow CH^+ + 2H_2$), with cations undergoing comparable chemistry to their neutral counterparts, CH and C_2, from dominant cations, $C_2H_2^+$ and $C_2H_3^+$, or through a new mechanism, for instance associative ionization of CH_x or C_2H_y with highly excited states of H and H_2.[1,8,9,10,11,12,13,14,31,32] A direct observation of an emission originating from either diatomic cation species would be the most direct experimental evidence to date for the existence of electrons in MW-activated C/H plasmas. Indirectly, electrons have been inferred through Stark broadening of H-Balmer lines, modelling, and emissions from high energy states (e.g. H($n \geq 3$)).

The C_2^+ has allegedly been assigned a Q-branch emission band head emitting at 249 nm (the Meinel system, $C_2^+(b^2\Sigma_g^+ \rightarrow a^2\Pi_u)$), however most spectroscopic studies on the C_2^+ have been achieved in absorption mode, e.g. $C_2^+(B^4\Sigma_u^- \leftarrow X^4\Sigma_g^-)$.[33,34] CH^+ has three reported emissions from $CH^+(A^1\Pi \rightarrow X^1\Sigma)$ with a P band head emission at ~ 422.5 nm, as well as the $CH^+(B^1\Delta \rightarrow A^1\Pi)$ and $CH^+(b^3\Sigma \rightarrow a^3\Pi)$ overlapping with one another at ~349 nm. These latter two emissions would be further complicated in the presence of trace nitrogen contamination by high J and v tail of $CN(B^2\Sigma \rightarrow X^2\Sigma)$, $\Delta v = -1, -2$, $CH(B^2\Sigma_g^- \rightarrow X^2\Pi_g)$, $\Delta v = -1$, and the $C_2(C^1\Pi_g \rightarrow A^1\Pi_u)$, $\Delta v = -1$.[35,36,37] As such, $CH^+(A \rightarrow X)$ is the more desirable transition to observe but overlaps with the high J tail of the $CH(A \rightarrow X)$, $\Delta v = 0$ transition. This chapter concludes by attempting a direct observation of the CH^+ species.

4.2: Experimental Details

This chapter investigates optical emissions originating from the C_2(d→a), and C_2^-(B→X) transitions as a function of process conditions. Observable transitions from C_2 and C_2^- are identified in Figure 4.01:

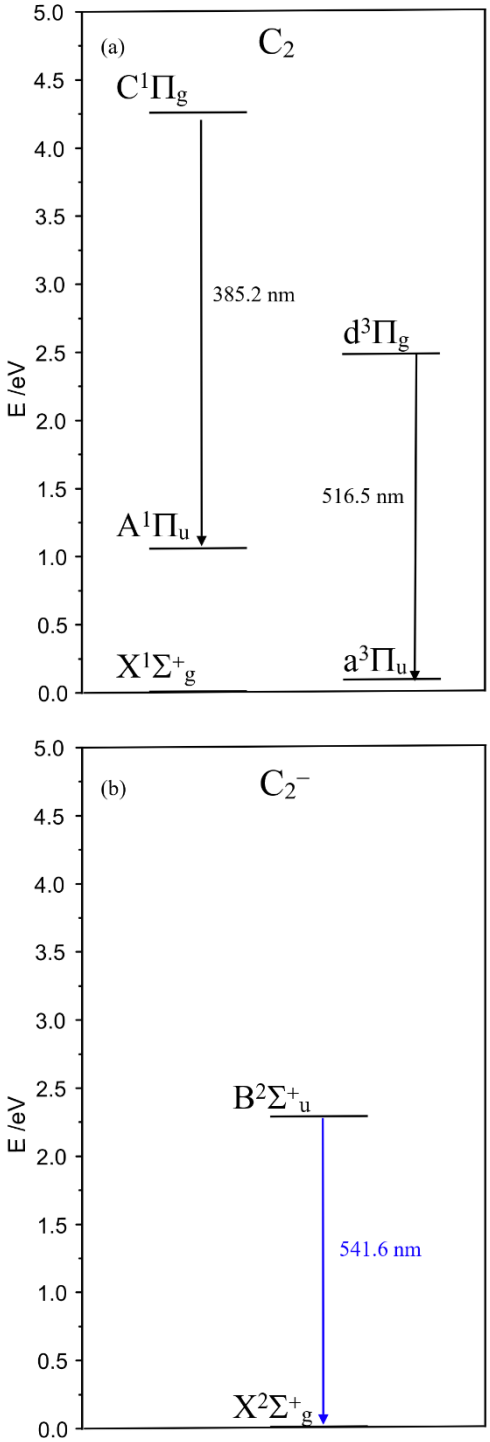

Figure 4.01: (a) Singlet and triplet states of the C_2 diatomic molecule with example transitions visible in the experimental ranges available and (b) the observed C_2^-* emission transitioning between the second bound excited doublet state of C_2^- to the C_2^- ground state. Band head wavelengths of the (0-0) transition are labelled.

In this chapter, it is the observation of the $C_2^-(B^2\Sigma_u \rightarrow X^2\Sigma_g)$, $\Delta v = 0$ transition that contributes one of the primary novelties and is therefore of particular interest. The transition falls within the high *J* tail of the $C_2(d^3\Pi_g \rightarrow a^3\Pi_u)$, $\Delta v = -1$, and hence this emission has also been studied.

Base conditions are defined as: 3 mm thick tungsten substrate with diameter, d_{sub} = 32 mm, placed on a spacer wire thickness d_{wire} = 0.01″, a total gas pressure of p = 150 Torr, a microwave input power of P = 1.5 kW, $F(H_2)$ = 300 sccm, $F(CH_4)$ = 19 sccm. One parameter is varied at a time, whilst the remaining parameters are kept constant at their base values. The microwave cavity is retuned between many of the condition changes to ensure that reflected microwave power is 0.00 kW. The parameter ranges explored are $0 \leq F(CH_4) \leq 30$ sccm, $50 \leq p \leq 275$ Torr, and $0.7 \leq P \leq 1.85$ kW. These experiments were carried out on a seperate reactor to that featuring in Chapters 3, 5 and 6; the main difference being that the reactor featuring in this Chapter has a less efficiently cooled aluminium base plate. The experimental set up described in Chapter 2, Section 2.1.3 was used (i.e. a Czerny-Turner Newport MS127i spectrograph with a 250 mm focal length, *f*/16 objective lens, 12.5 μm entrance slit, with emission detected on an Andor Newton 970 CCD and a spatial magnification of ~0.1). The emissions were dispersed using 1800 grooves mm^{-1} diffraction grating, achieving 0.11 nm FWHM; the investigated emissions were detected on a cooled Andor 970 camera. Using the same set-up and an entrance slit width of 25 μm, argon flow has also been investigated between $0 \leq X_0(Ar) \leq 20$ % with hydrogen reduced in a compensatory manner such that $F(H_2) + F(Ar) = 300$ sccm, as described in Chapter 3, Section 3.2. The pressure and power range were reinvestigated for $X_0(Ar)$ = 15% under otherwise base conditions. The intensities reflect the larger slit width (with an ~2.5 scaling for base conditions), but generally the scaling with argon present should not be directly compared to the MW-activated C/H plasma studies.

The effect of decreasing substrate diameter, d_{sub}, an unexplored parameter in the context of MW-activated C/H plasmas, has also investigated under otherwise base conditions for d_{sub} = 32 mm (d_{wire} = 0.01″), and d_{sub} = 17 mm (d_{wire} = 0.004″), such that T_{sub} ~ 700 °C for both substrate sizes. For this investigation, the upgraded reactor and Czerny-Turner spectrograph with a 50 mm focal length, featuring in Chapters 3, 4 and 6, were used with an *f*/14 objective lens and a 10 μm entrance slit. The emissions are dispersed with a 700 grooves mm^{-1} diffraction grating, achieving a FWHM ~ 0.09 nm and are detected on a cooled Andor 940 camera with a spatial magnification of ~ 0.11 and were collected alongside some of the data reported in Chapter 5.

The final experiment featuring in this chapter is an attempt to monitor the $CH^+(A \rightarrow X)$. The data has also been collected alongside the substrate diameter studies described above and those featuring in Chapter 5. The experiment has been carried out under the conditions of p = 150 Torr, P = 1.5 kW, $F(H_2)$ = 300 sccm, $F(CH_4)$ = 19 sccm, and d_{sub} = 17 mm (d_{wire} = 0.004″) at low *z*, whereby the reduced electric field maximises.

All experiments achieve a spatial resolution of ~ 0.5 mm, and unless otherwise specified, the emissions have been normalised to an accumulation time equivalent to 2048 s, or scaled, in the case of the substrate investigation, by a factor to make base conditions (d_{sub} = 32 mm) comparable between reactor set-ups. The air leak has been assumed to be negligible throughout this chapter.

4.3: Experimental Results and Modelling

4.3.1: Confirming the Presence of C_2^-

Figure 4.02 demonstrates a spatially-resolved image, much like those seen in Chapter 3, with an optical wavelength range of 489 – 566 nm under base conditions. This wavelength range is dominated by emission from the transition $C_2(d^3\Pi_g \rightarrow a^3\Pi_u)$, $\Delta v = 0$ and $\Delta v = -1$. Indicated on Figure 4.02 is the band head from these emissions and the faint band head originating from the $C_2^-(B^2\Sigma_u \rightarrow X^2\Sigma_g)$, $\Delta v = 0$ transition.

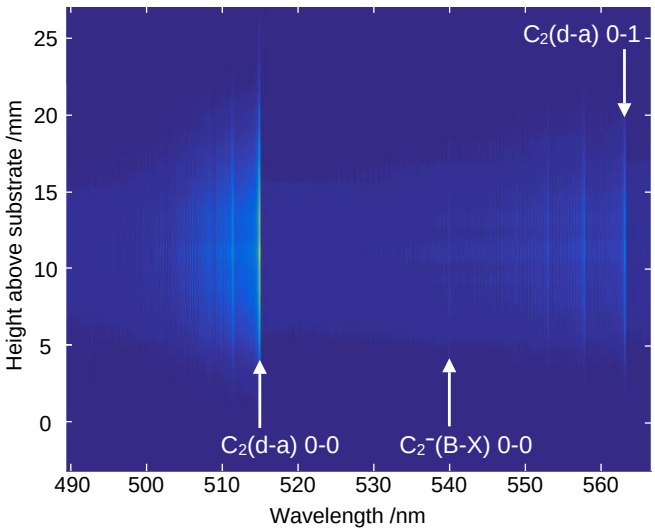

Figure 4.02: $I_{em}(\lambda, z)$ image taken under base conditions in the λ range of 489 – 566 nm on the horizontal axis with a vertical axis spanning −3 ≤ z ≤ 27 mm, whereby z = 0 defines the top of the substrate. $C_2(d^3\Pi_g \rightarrow a^3\Pi_u)$(0-0), (0-1) and $C_2^-(B^2\Sigma_u^+ \rightarrow X^2\Sigma_g^+)$ (0-0) band heads indicated.

Figure 4.03 (a) demonstrates an experimental spectrum, $I_{em}(\lambda)$, summed between 9 ≤ z ≤ 12 mm in black. The blue offset spectrum is the best fit simulation of the $C_2(d \rightarrow a)$, $\Delta v = 0$ and $\Delta v = -1$ using spectroscopic constants extracted from Reference 38 simulated using PGOPHER.[39] Figures 4.02 (b) and (c) illustrate the wavelength range indicated by the red box in Figure 4.03 (a). Figure 4.03 (b) demonstrates a clear diatomic emission residual present within the residual between the $I_{em}(\lambda)$ – best fit $C_2(d \rightarrow a)$ simulated spectra. Figure 4.03 (c) shows a simulation of the $C_2^-(B \rightarrow X)$, $\Delta v = 0$ transition fitted to the experimental diatomic structure within the residual. The simulation has been constructed using spectroscopic constants from Reference 40. The figure experimentally verifies the presence of anions within MW-activated C/H plasmas under base conditions.

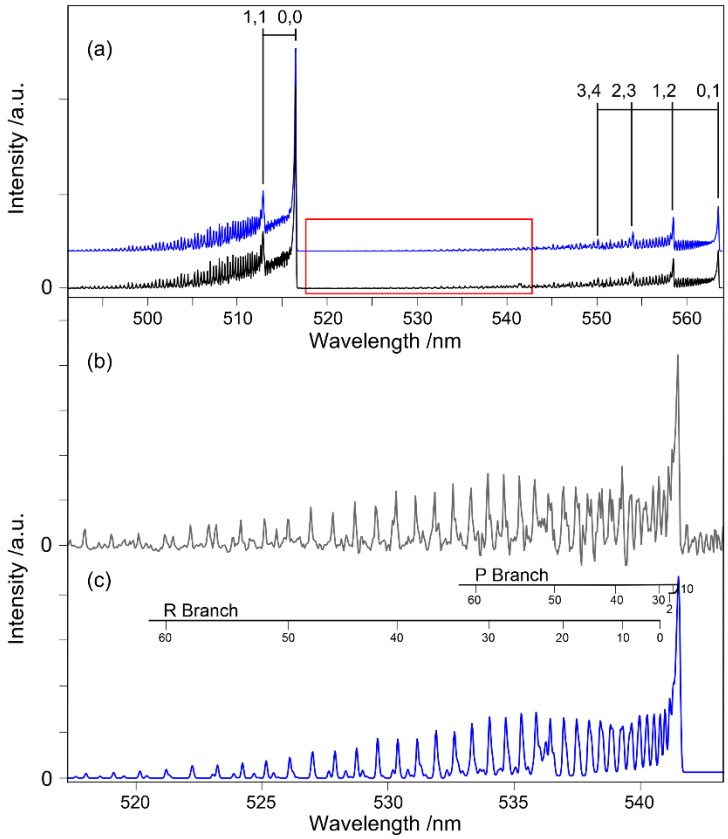

Figure 4.03: (a) In black $I_{em}(\lambda)$ summed between $9 \leq z \leq 12$ mm under base conditions across the λ range of 489 – 566 nm. Offset in blue is the best-fit $C_2(d^3\Pi g \rightarrow a^3\Pi_u)$ $\Delta v = 0$ and $\Delta v = -1$ and $C_2^-(B^2\Sigma_u \rightarrow X^2\Sigma_g)$ (0-0) band heads indicated.

Figure 4.03 (a) confirms that $C_2^-(B \rightarrow X)$, $\Delta v = 0$ emission band appears within the high *J*, high *v* tail of the $C_2(d \rightarrow a)$, $\Delta v = -1$ emission band and hence, likely due to insufficient signal/noise, it has not previously been observed or reported within literature within the context of the Chemical Vapour Deposition of diamond.[1]

Contrasting to the H_2 molecule discussed in Chapter 3, C_2 and C_2^- molecules consist of two C atoms with no net nuclear spin, i.e. $I = 0$ and are therefore both diatomic molecules are bosons, i.e. contributions from the nuclear wavefunction are symmetric with regards to an exchange of nuclei. The C_2^- has an electron spin S = ½, contributing an anti-symmetric component to the electronic wavefunction. The ground state is also a sigma state (contributing an anti-symmetric component to the electronic wavefunction) and therefore the overall electronic state is described by a small g (gerade for an overall symmetric wavefunction). As the overall wavefunction is symmetric and a sigma state, i.e. bosonic, only symmetric (even) *J* states may exist and therefore be populated. Through similar considerations, the upper state is anti-symmetric, enforcing that only odd *J* states may exist. This forces the selection rule $\Delta J = \pm 1$, as only even numbered P and R branches exist (labelled by the ground *J* state).[1,40] The $C_2(a)$ and $C_2(d)$ states are significantly more complicated due to spin-orbit coupling and the Λ-doubling associated with the $^3\Pi_{u/g}$ state, as well as the requirement for an overall symmetric

wavefunction (associated with two identical even nuclear spin atoms); briefly, the spin-orbit coupling generates three states, Ω = 0, 1, and 2 (where Ω is defined in Chapter 2, Section 2.1.2). These three states support rotational levels, which would typically hold a two-fold degeneracy attributed to the parity of the Π orbital. The requirement of an overall symmetric wavefunction means that each *J* state can only couple to one parity, such that the electronic (and therefore overall) wavefunction is symmetric. For Ω = 0, (i.e. $|\Lambda + \Sigma| = 0$), the even parity of the $^3\Pi_g^+$ orbital can only exist with even *J* states, whilst the anti-symmetric parity of the $^3\Pi_g^-$ orbital can only exist with odd *J* values. Whether an even or odd *J* state exists with even or odd parity Π orbitals depends on the exact nature of the state (i.e. whether the $^3\Pi$ state is u or g, the values of Λ and Σ etc). Proposed molecular orbital diagrams for the states are provided in the Appendix (A4.1 and A4.2) replicated from Reference 41.

This chapter now focusses on reviewing the prominent established processes involved in the formation of C_2 and speculating on possible production (and loss) processes involving C_2^-, as well as their excited states. The variation of their optical emissions with process conditions are compared to modelled predictions in order to confirm the understood formation and loss mechanisms of C_2(X), C_2(a) and C_2(d), as well as to establish these mechanisms for C_2^- and C_2^-*.

4.3.2: Modelling Considerations

The formation mechanism of C_2, and indeed C_2*, under conditions relevant for the CVD of diamond in MW-activated C/H plasmas is already well-established, and has been discussed indirectly in Chapter 1, Section 1.4; C_2(X) and C_2(a) are both products, formed through fast H-shifting reactions of C_2H_2, which makes up more than 97% of total carbon content in the hot plasma region. Processes 4.01 and 4.02 demonstrate explicitly how C_2 can be generated from C_2H_2, whereby ↔ indicates a reversible process. Despite being energetically higher, ~85% of C_2 manifests itself as the C_2(a) triplet state due to the six-fold degeneracy of the triplet state (*cf.* the C_2(X) singlet state). Both states are produced via Process 4.02. The C_2* emitting state is predominantly formed through EIE of C_2(a), as described by Process 4.03: [1,9,13]

$$H + C_2H_2 \leftrightarrow C_2H + H_2 \quad (4.01)$$

$$H + C_2H \leftrightarrow C_2 + H_2 \quad (4.02)$$

$$e + C_2(a) \rightarrow C_2(d) + e \quad (4.03)$$

Electron impact excitation of C_2(X) also occurs, however its contribution is less significant in populating the C_2(d) state due to the lower number densities (of the C_2(X) radical relative to C_2(a)), and the preference for spin conservation. The emitting C_2* state can be lost through radiative decay and reactive quenching with H_2, as described by Processes 4.04 and 4.05 respectively. Process 4.06, reactive quenching with H, has a similar rate coefficient to that of Process 4.05, but has a sufficiently low rate

(due to the lower [H] number density, relative to [H_2]) and therefore is not considered a significant loss mechanism.[1,9,42]

$$C_2(d) \rightarrow C_2(a) + \gamma \quad (4.04)$$

$$C_2(d) + H_2 \rightarrow C_2H^{\dagger} + H \quad (4.05)$$

$$C_2(d) + H \rightarrow CH + C \quad (4.06)$$

The rate coefficients for these reactions are given in Table 4.01. By assuming steady-state, i.e. that the production and loss of any species are constant and equal, it is possible to calculate the number density of the species of interest. By neglecting Process 4.03 as a significant loss mechanism of the C_2(a) state, the rate of Process 4.01 and Process 4.02 can be balanced to calculate a steady-state [C_2(a)] number density at any position within the plasma. Similarly, [C_2(d)] can be derived using [C_2(a)] and balancing the rates of loss and formation (i.e. Processes 4.03, 4.04, and 4.05). This can be used to approximate the column density of {C_2(d)}, which is assumed to be proportional to $I_{em}(C_2{}^*)$. A full derivation for Equation 4.07 can be found in the Appendix.[1]

$$I_{em}(C_2{}^*) \sim 2R_{pl}\left(\frac{n_e \times k_{5.03}}{A_{5.04} + [H_2] \times k_{5.05}}\right) \times \frac{[C_2H_2] \times k_{4.01} \times k_{4.02}}{k_{-4.01} \times k_{-4.02}} \times \frac{[H]^2}{[H_2]^2} \quad (4.07)$$

There are a range of potential mechanisms, which have been considered in the formation and loss of C_2^- and its excited state C_2^-*, as described below.[1,43,44,45,46,47,48,49]

Process 4.08 describes electron attachment of C_2 with an electron to form C_2^-*. This process requires the presence of a third body, M, to conserve momentum. C_2^-* could also be formed through electron impact excitation of the ground state C_2^-, as described by Process 4.09:

$$C_2 + e + M \rightarrow {C_2}^{-*} + M \quad (4.08)$$

$$C_2^- + e \rightarrow {C_2}^{-*} + e \quad (4.09)$$

Process 4.08 does not require a third body to conserve momentum, if C_2^-* is only considered as a transition state, emitting immediately upon formation. This photo attachment mechanism is described by Process 4.10:

$$C_2 + e \rightarrow {C_2}^{-*} \rightarrow C_2^- + \gamma \quad (4.10)$$

A loss mechanism for C_2^- is electron collision, generating C_2 and 2 electrons, as described by Process 4.11:

$$C_2^- + e \leftrightarrow C_2 + 2e \quad (4.11)$$

Dissociative electron attachment of acetylene can form both C_2^- and C_2H^-, as described by Process 4.12 and 4.13. C_2H^- and C_2^- can interchange through H-shifting reactions, as described by Process 4.14.

$$C_2H_2 + e \rightarrow C_2^- + 2H \quad (4.12)$$

$$C_2H_2 + e \leftrightarrow C_2H^- + H \quad (4.13)$$

$$C_2H^- + H \leftrightarrow {C_2}^- + H_2 \quad (4.14)$$

Formation of C_2^- would then be followed by electron impact excitation to generate C_2^-*. Alternatively, dissociative electron attachment of acetylene can also generate C_2^-*, described by Process 4.15.

$$C_2H_2 + e \leftrightarrow {C_2}^{-*} + 2H \quad (4.15)$$

As is the case with acetylene, C_2H can also undergo dissociative electron attachment, forming both C_2^- and C_2^-*, as described by Processes 4.16 and 4.17 respectively.

$$C_2H + e \leftrightarrow {C_2}^- + H \quad (4.16)$$

$$C_2H + e \leftrightarrow {C_2}^{-*} + H \quad (4.17)$$

The reversible processes above are all potential formation and loss mechanisms. Process 4.18, emission of C_2^-*, is a distinct loss mechanism from Process 4.09 (based on formation mechanism associated with Process 4.09). Either one, or both, of these processes could contribute towards the experimentally observed emissions.

$${C_2}^{-*} \rightarrow {C_2}^- + \gamma \quad (4.18)$$

The rate coefficients of these processes are also included in Table 4.01. Further discussion on the prominent mechanisms contributing to formation and loss of C_2^- and C_2^-* in MW-activated C/H plasmas based on experimental observation and 2-D physical chemical plasma modelling is provided in Section 4.3.5.

Process	Specific Reaction	Rate coefficient /cm^3 s^{-1} (unless otherwise stated)(ref)
4.01	**$H + C_2H_2 \rightarrow C_2H + H_2$**	***1.07 × 10^{21} cm^{-3}s^{-1} (ref 50)**
−4.01	**$C_2H + H_2 \rightarrow H + C_2H_2$**	***1.07 × 10^{21} cm^{-3}s^{-1} (ref 50)**
4.02	**$H + C_2H \rightarrow C_2(a) + H_2$**	***~9.49 × 10^{16} cm^{-3}s^{-1} (ref 50)**
−4.02	**$C_2(a) + H_2 \rightarrow H + C_2H$**	***~9.62 × 10^{16} cm^{-3}s^{-1} (ref 50)**
4.03	**$e + C_2(a) \rightarrow C_2(d) + e$**	**10^{-8} exp(−29065/T_e) (ref 50)**
4.04	**$C_2(d) \rightarrow C_2(a) + \gamma$**	**1.02 × 10^7 s^{-1} (ref 38)**
4.05	**$C_2(d) + H_2 \rightarrow C_2H^{\dagger} + H$**	**1.5 × 10^{-11} exp(−3012/T_g) (ref. 42)**
4.06	$C_2(d) + H \rightarrow CH + C$	< 3.7 × 10^{-12} (ref 51)
4.08	**$C_2 + e + M \rightarrow C_2^{-*} + M$**	**10^{-29} cm^6 s^{-1} (ref. 1)**
−4.08	**$C_2^{-*} + M \rightarrow C_2 + e + M$**	**7.5 × 10^{-10} exp(−11605/T_g) (ref. 52)**
4.09	$C_2^- + e \rightarrow C_2^{-*} + e$	< 10^{-9} (ref. 1)
−4.09	$C_2^{-*} + e \rightarrow C_2^- + e$	< 10^{-9} (ref. 1)
4.10	$C_2 + e \rightarrow C_2^{-*} \rightarrow C_2^- + \gamma$	< 2 × 10^{-15} (−T_e/300)$^{0.5}$ (ref. 45)
4.11	$C_2^- + e \rightarrow C_2 + 2e$	**~ 2-4 × 10^{-13} cm^{-2} for T_e ~ 7-13 eV (ref. 44)
4.12	**$C_2H_2 + e \rightarrow C_2^- + 2H$**	**2.28 × 10^{-11} exp(−93907/T_e) (ref. 46, 47)**
4.13	**$C_2H_2 + e \rightarrow C_2H^- + H$**	**4.62 × 10^{-12} exp(−34201/T_e) (ref. 46, 47)**
−4.13	**$C_2H^- + H \rightarrow C_2H_2 + e$**	**1.6 × 10^{-9}** (ref. 46,47)
4.14	$C_2H^- + H \rightarrow C_2^- + H_2$	< 10^{-13} (ref. 53)
−4.14	$C_2^- + H_2 \rightarrow C_2H^- + H$	< 10^{-13} (ref. 53)
4.15	$C_2H_2 + e \rightarrow C_2^{-*} + 2H$	*Incorrect spatial distribution.*
4.16	**$C_2H + e \rightarrow C_2^- + H$**	**3.87 × 10^{-11} exp(−20128/T_e) (ref. 1)**
−4.16	**$C_2^- + H \rightarrow C_2H + e$**	**7.7 × 10^{-10} (ref. 1)**
4.17	**$C_2H + e \rightarrow C_2^{-*} + H$**	**1.9 × 10^{-11} exp(−34777/T_e) (ref. 1)**
−5.17	**$C_2^{-*} + H \rightarrow C_2H + e$**	**~ 7.7 × 10^{-10} (ref. 1)**
4.18	**$C_2^{-*} \rightarrow C_2^- + \gamma$**	**1.3 × 10^7 s^{-1} (ref. 37, 54)**

Table 4.1: Rate coefficients (and Einstein-A emission coefficients) for considered reactions in the formation (and loss) of C_2, C_2^-, and their excited states within MW-activated C/H plasmas. T_e and T_g are in units of K; 1 eV = 11605 K. The reactions in bold were used to produce the final modelling output presented in Figures 4.05, 4.08, 4.12 and 4.13. *reaction rate at *z* = 12 mm, **rate cross-section. Reaction coefficients can be converted into a reaction rate through inserting appropriate T_e / T_g values and multiplying with reacting species number densities – this will be location dependent.

4.3.3: Addition of Methane and Argon

Figure 4.04 demonstrates $I_{em}(C_2^*)$ and $I_{em}(C_2^{-}*)$ as a function of (a) $F(CH_4)$ and (b) $F(Ar)$ under otherwise base conditions for their peak intensities summed between $9 \leq z \leq 12$ mm:

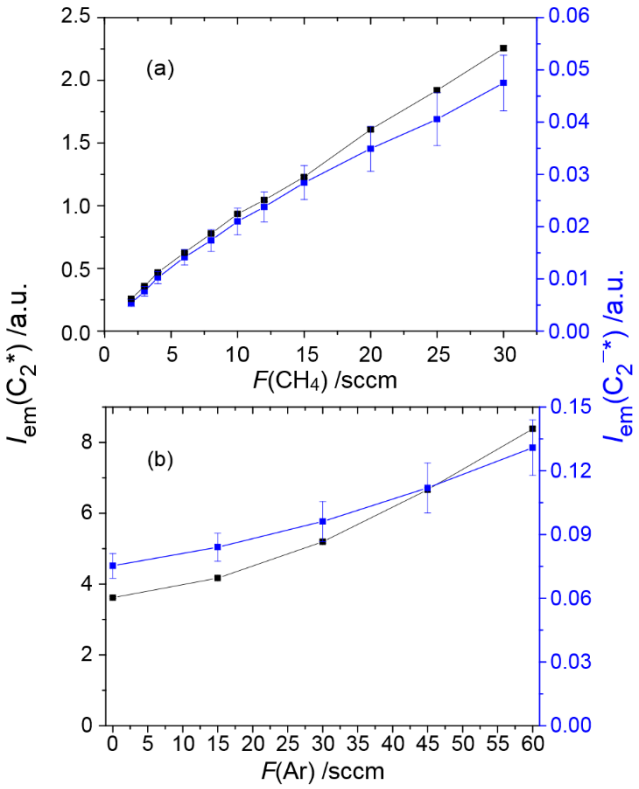

Figure 4.04: The black squares represent $I_{em}(C_2^*)$, whilst the blue squares represent $I_{em}(C_2^{-}*)$ summed between $9 \leq z \leq 12$ mm with (a) increasing methane flow rate, under otherwise base conditions and (b) increasing argon flow rate, whilst decreasing $F(H_2)$ in a compensating manner under otherwise base conditions.

Equation 4.07 demonstrates that $I_{em}(C_2^*) \sim [C_2H_2]$ is expected in the hot plasma region. $[C_2H_2]$ is known to scale linearly with $X_0(CH_4)$, which under high $F(H_2)$, is approximately linear with $F(CH_4)$. Hence, Figure 4.04 (a) demonstrates experimentally that $I_{em}(C_2^*) \sim F(CH_4)$. Figure 4.04 (a) also shows that $I_{em}(C_2^{-}*)$ also increases with a near linear dependence on $F(CH_4)$. The comparable behaviour infers that acetylene is also involved as a parent or grand-parent species in the production of $C_2^{-}*$.

Figure 4.04 (b) demonstrates that $I_{em}(C_2^*)$ and $I_{em}(C_2^{-}*)$ increase with a greater than linear trend with increasing argon flow rate, whereby $F(H_2)$ has been decreased in a compensatory manner under otherwise base conditions. Under the range investigated, $0 \leq X_0(Ar) \leq 20$ %, increasing $X_0(Ar)$ has the effect of decreasing thermal conductivity, displacing hydrogen in a non-linear manner (as discussed in Chapter 3), and increasing T_g, and therefore in this lower mole fraction range (of Ar *cf.* the range explored in Chapter 3), $[H]/[H_2]$ is expected to increase. Lesser effects may also be to enhance the rate coefficients of forward and backward reactions driven by thermal chemistry, rather than those driven

by electrons. Ar addition also acts to increase R_{pl}, whilst T_e remains ~ constant.[9,55] The overall effect would be an expected non-trivial increase in $I_{em}(C_2^*)$ and likely $I_{em}(C_2^{-*})$, as observed.

$I_{em}(C_2^{-*})/I_{em}(C_2^*)$ decreases by ~ 40% across this X_0(Ar) range, indicating that $I_{em}(C_2^{-*})$ is significantly less sensitive to the increase in T_g, and therefore is either less sensitive to the [H]/[H_2] ratio or receives a substantially smaller boost with regards to the increase in the formation and loss rate coefficients (from an increase in T_g), relative to that of C_2^*. This interpretation neglects the possibility of one excited species being preferentially quenched by argon, which will be somewhat justified in Section 4.3.4, through a comparison of experimental trends with and without the presence of some Ar. It also neglects the possibility that these states have different prominent quenchers, e.g. if the C_2^{-*} state is predominantly quenched by H atoms and the C_2^* state is not.

4.3.4: Variation of Additional Process Conditions

Figure 4.05 demonstrates the spatial distribution of $I_{em}(C_2^*)$ and $I_{em}(C_2^{-*})$ using a higher resolution of 1.5 mm for (a) 75 Torr, (b) 150 Torr (i.e. base conditions) and (c) 225 Torr. For low pressure, it can be seen that $I_{em}(C_2^*)$ and $I_{em}(C_2^{-*})$ have the same spatial distribution, whilst for higher pressures, $p \geq 150$ Torr, $I_{em}(C_2^*)$ can be seen to peak at z ~ 11.25 mm, whilst $I_{em}(C_2^{-*})$ can be seen to peak at ~ 9.75 mm, both still maximising in the spatial range between $9 \leq z \leq 12$ mm. Increasing pressure can be seen to contract the emissions with respect to height, but through a comparison of the I_{em} scaling between (a), (b) and (c), it can also be seen that $I_{em}(C_2^*)$ and $I_{em}(C_2^{-*})$ are both increasing with respect to pressure.

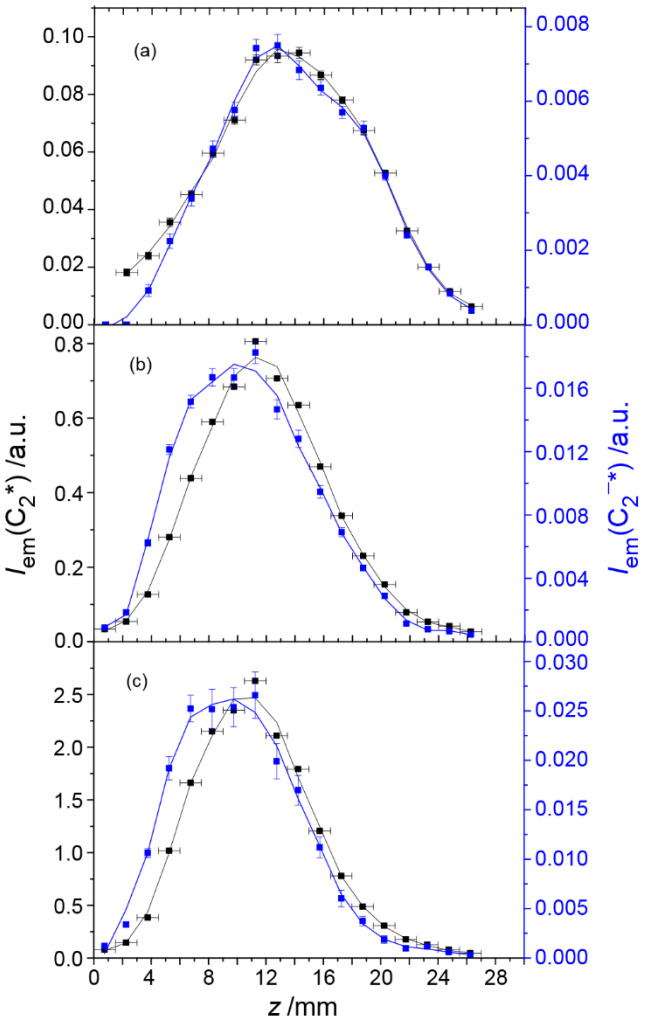

Figure 4.05: Spatially-resolved distributions of $I_{em}(C_2^{-*})$ (blue squares with an indicative blue line) and $I_{em}(C_2^*)$ (black squares with an indicative black line) for (a) p = 75 Torr, (b) p = 150 Torr and (c) p = 225 Torr under otherwise base conditions using a spatial resolution of 1.5 mm.

Figure 4.06 demonstrates more clearly that $I_{em}(C_2^*)$ increases cubically with increasing p, whilst $I_{em}(C_2^{-*})$ increases linearly for $p \leq 125$ Torr. The $I_{em}(C_2^{-*})$ trend decreases below linearity in the higher p range of $150 \leq p \leq 225$ Torr. The error (the standard deviation) associated with the $I_{em}(C_2^{-*})$ PGOPHER simulation fitting increases with respect to pressure. This is due to a significant increase in the overlapping $I_{em}(C_2^*)$ signal with respect to pressure, and is also evidenced with increasing input methane fraction (and power). The significant increase in $I_{em}(C_2^{-*})$ error for $p \geq 225$ Torr means that it is not possible to interpret whether there is a further linearity above this pressure. Figure 4.06 also demonstrates that the modelling, discussed in Section 4.3.5 using prominent mechanisms discussed in Section 4.3.2, correctly predicts the experimental trend for $\{C_2(d \rightarrow a)\}$ and $\{C_2^-(B \rightarrow X)\}$ with respect to p under the continued assumption that $I_{em}(x) \sim \{x\}$ for $x = C_2^*$ or C_2^{-*}.

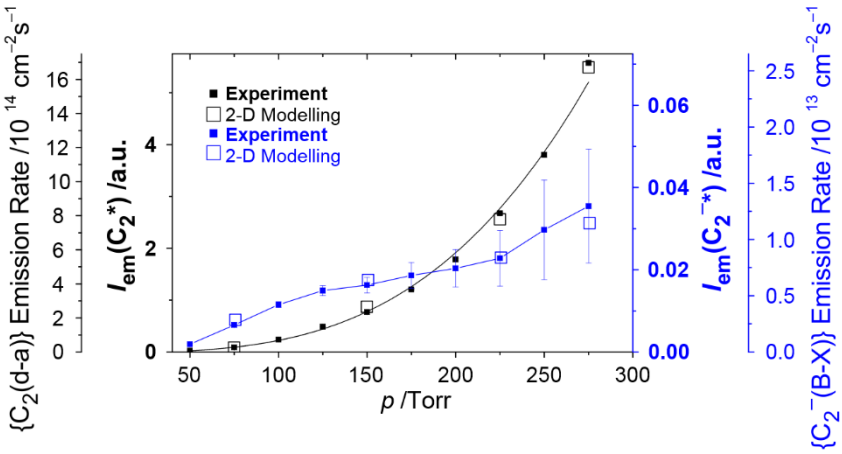

Figure 4.06: The black closed squares represent $I_{em}(C_2^*)$, and similarly the blue filled squares represent $I_{em}(C_2^{-*})$ summed between $9 \leq z \leq 12$ mm with increasing pressure under otherwise base conditions. The black curve is a cubic best fit. The square open symbols represent modelling results for the two species for p = 75, 150, 225 and 275 Torr, when considering the correct formation mechanism of C_2^{-*}, discussed in Section 4.3.5.

A near identical experimental trend can be seen with increasing pressure when X_0(Ar) = 15%, under otherwise base conditions. If Ar quenching were significant under base conditions or the range of X_0(Ar) investigated in Section 4.3.3, it is with increasing pressure that one might expect to see evidence manifest through a deviation in trends with increasing pressure. This result vindicates the prior speculation that under the low Ar fractions investigated in Section 4.3.3, Ar plays no significant role in the formation or quenching of either species under base pressure.

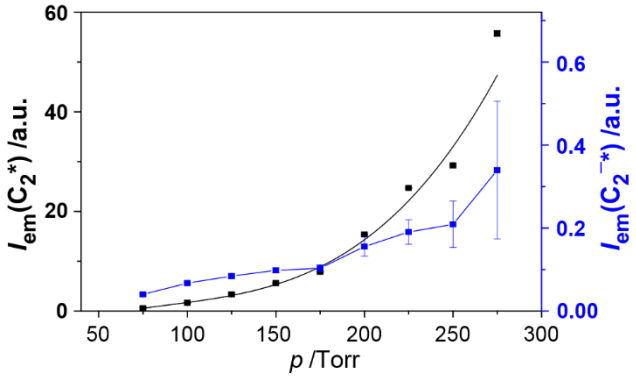

Figure 4.07: As above, the black closed squares represent $I_{em}(C_2^*)$, and the blue filled squares represent $I_{em}(C_2^{-*})$ summed between $9 \leq z \leq 12$ mm with increasing pressure in the presence of X_0(Ar) = 15 % (hydrogen decreased in a compensatory manner) under otherwise base conditions. The experimental trends are similar in likeness to those seen in Figure 4.06. It is worth noting that the measured intensities are not comparable to Figure 4.06 in part due to the use of a wider entrance slit.

Figure 4.08 demonstrates the spatial distribution of $I_{em}(C_2^*)$ and $I_{em}(C_2^{-*})$ for (a) P = 0.9 kW and (b) P = 1.85 kW under otherwise base conditions. As well as demonstrating plasma expansion, the spatial distributions becomes more distinguished with increasing P. Through comparing the vertical I_{em} scale of (a) and (b), it can also be seen that the total intensity of both species is increasing with P.

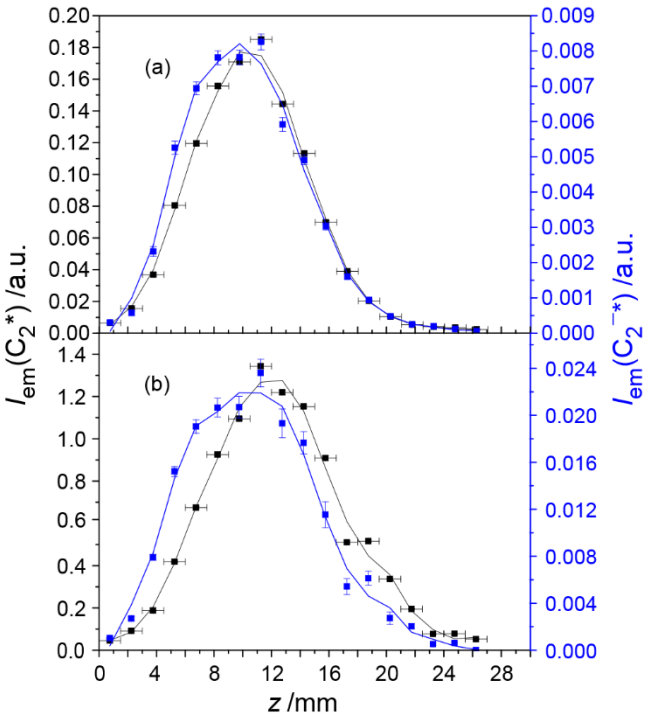

Figure 4.08: Spatially-resolved distributions of $I_{em}(C_2^{-*})$ (blue squares with an indicative blue line) and $I_{em}(C_2^*)$ (black squares with an indicative black line) for (a) P = 0.9 kW and (b) P = 1.85 kW under otherwise base conditions using a spatial resolution of 1.5 mm.

Figure 4.09 demonstrates how $I_{em}(C_2^*)$ and $I_{em}(C_2^{-*})$ vary with increasing P under otherwise base conditions. $I_{em}(C_2^*)$ can be seen to increase cubically with P, whilst $I_{em}(C_2^{-*})$ can be seen to increase linearly across this P range. The 2-D plasma modelling, discussed in Section 4.3.5, correctly predicts the experimental variation in $\{C_2(d \rightarrow a)\}$ and $\{C_2^-(B \rightarrow X)\}$ with increasing P.

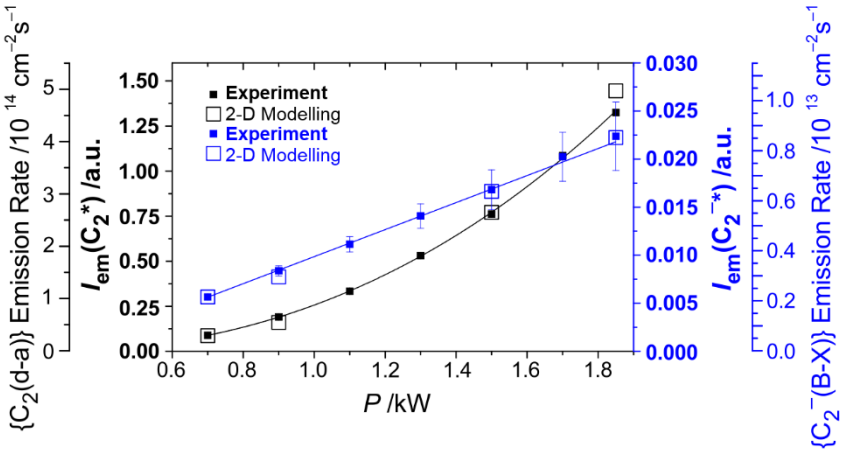

Figure 4.09: The black closed squares represent $I_{em}(C_2^*)$, and similarly the blue filled squared represent $I_{em}(C_2^{-*})$ summed between $9 \leq z \leq 12$ mm with increasing power under otherwise base conditions. The black curve is a cubic best fit. The square open symbols represent modelling results for the two species for P = 0.7, 0.9, 1.5 and 1.85 kW.

Again, the addition of X_0(Ar) = 15% has little effect on the overall trend of $I_{em}(C_2^*)$ and $I_{em}(C_2^{-*})$ with increasing P, as evidenced in Figure 4.10:

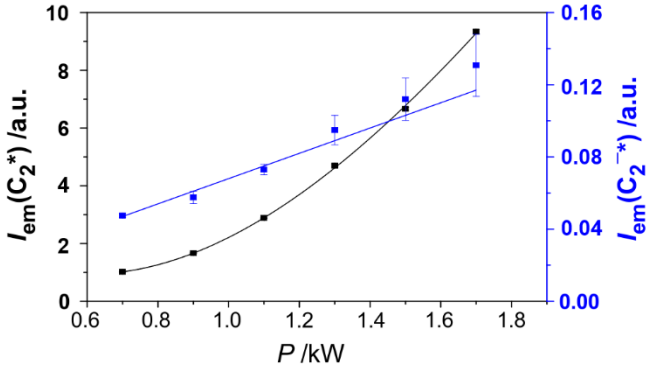

Figure 4.10: As above, the black closed squares represent $I_{em}(C_2^*)$, and the blue filled squares represent $I_{em}(C_2^{-*})$ summed between $9 \leq z \leq 12$ mm with increasing pressure in the presence of X_0(Ar) = 15 % (hydrogen decreased in a compensatory manner) under otherwise base conditions. The experimental trends are similar in likeness to those seen in Figure 4.09, but again the measured intensities are not comparable due to the use of a wider entrance slit.

The final parameter investigated is substrate size – the spatial distribution of $I_{em}(C_2^*)$ and $I_{em}(C_2^{-*})$ under base conditions (i.e. base conditions with d_{sub} = 32 mm placed on a 0.01″ spacer wire) and d_{sub} = 17 mm placed on a 0.004″ spacer wire under otherwise base conditions can be seen in Figure 4.11 (a) and (b) respectively. The spacer wire was adjusted such that T_{sub} ~ 700 °C for both substrates.

Figure 4.11 shows that decreasing d_{sub} increases $I_{em}(C_2^*)$ and $I_{em}(C_2^{-*})$ and causes both emission intensities to peak ~1.5 mm closer to the substrate, however $I_{em}(C_2^{-*})/I_{em}(C_2^*)$ ratio also decreases.

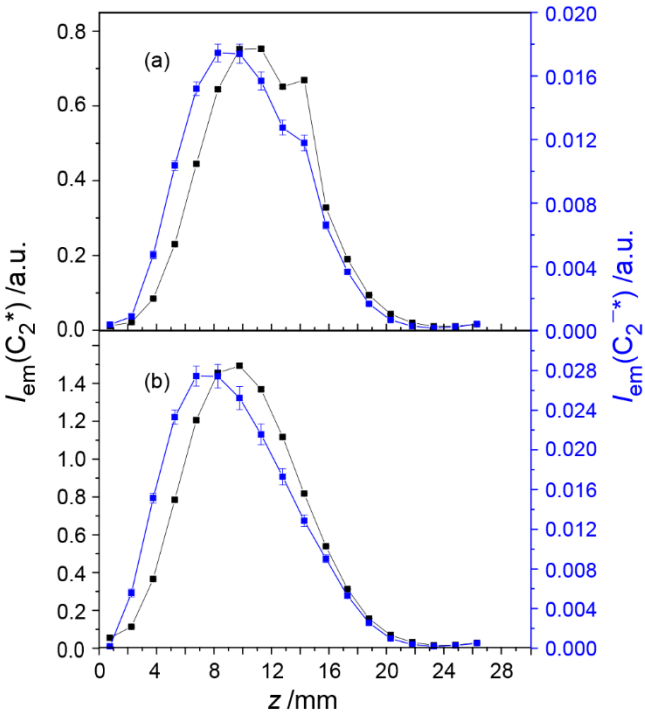

Figure 4.11: Spatially-resolved distributions of $I_{em}(C_2^{-*})$ (blue squares with an indicative blue line) and $I_{em}(C_2^*)$ (black squares with an indicative black line) for (a) d_{sub} = 32 mm on a 0.01″ wire, and (b) d_{sub} = 17 mm on a 0.004″ wire under otherwise base conditions using a spatial resolution of 1.5 mm.

4.3.5 Modelling and Discussion of Results

The p and P trends of $I_{em}(C_2^*)$ can be rationalised through Equation 4.07, which is repeated below for convenience:

$$I_{em}(C_2^*) \sim 2R_{pl}\left(\frac{n_e \times k_{4.03}}{A_{4.04} + [H_2] \times k_{4.05}}\right) \times \frac{[C_2H_2] \times k_{4.01} \times k_{4.02}}{k_{-4.01} \times k_{-4.02}} \times \frac{[H]^2}{[H_2]^2} \qquad (4.07)$$

By increasing p, the maximum T_g increases by a few percent from T_g = 2825 K for p = 75 Torr to T_g = 2970 K for p = 275 Torr at otherwise base conditions. The parameters $[C_2H_2]$, n_e and T_e are largely unaffected by this temperature change and vary more weakly with changes in P / p. Modelling demonstrates that $A_{4.04}/([H_2]\times k_{4.05}) \sim 4$ for base conditions, and as such, emission dominates as a loss mechanism. R_{pl} does decrease with p, however this is a smaller effect and compensated by a comparable increase in $k_{4.01} \times k_{4.02} / k_{-4.01} \times k_{-4.02}$. The major effect of increasing pressure is to increase $[H]/[H_2]$ and $[C_2H_2]$, which both scale ~ p. Therefore, $I_{em}(C_2^*) \sim [C_2H_2] \times ([H]/[H_2])^2 \sim p^3$, as observed experimentally.

With increasing P, the maximum T_g increases from 2765 K to 2930 K by increasing P from P = 0.7 kW to P = 1.85 kW. With increasing P, $[C_2H_2]$ ~ constant, whilst $[H]/[H_2] \sim P$, $R_{pl} \sim P^{0.5}$ and $k_{4.01} \times k_{4.02} / k_{-4.01} \times k_{-4.02}$ increases less than linearly due to the increase in maximum T_g; the overall effect is such that $I_{em}(C_2^*) \sim ([H]/[H_2])^2 \times R_{pl} \times k_{4.01} \times k_{4.02} / k_{-4.01} \times k_{-4.02} \sim P^3$, also observed experimentally.

In a more speculative manner, increasing F(Ar), and therefore X_0(Ar) and X(Ar), would act to increase [H]/[H_2], R_{pl}, T_g and $k_{4.01} \times k_{4.02} / k_{-4.01} \times k_{-4.02}$, whilst [$C_2H_2$] would remain ~ constant, as the majority of carbon is already in this form within the hot plasma region. Ar addition could also act to increase [C_2H_3] due to the larger [H] density (e.g. via $C_2H_2 + H + M \rightarrow C_2H_3 + M$). C_2H_3 has a lower ionization energy to that of C_2H_2 and may therefore lead to further ionization (and an enhanced n_e). Overall, increasing X_0(Ar) lead to $I_{em}(C_2^*) \sim \alpha + F(Ar)^{\beta}$ at otherwise base conditions, whereby it has been experimentally observed that $1 \leq \beta \leq 2$ for X_0(Ar) < 20% for constant $F(CH_4)$, p, and P conditions.

Whilst photoemission is the more dominant loss mechanism of C_2(d), displacing H_2 (the second most prominent quenching species of the C_2(d) state) with Ar will alter $X(H_2)$ (and therefore [H_2]) as a function of position, as described in Chapter 3.

The effect of decreasing substrate diameter is found to increase $I_{em}(C_2^*)$ (and $I_{em}(C_2^{-*})$) and relocate their peak intensities slightly closer to the substrate. The explanation for the latter observation could be attributed to the increase in T_g closer to the substrate. T_g, extracted from the best fit simulations of $I_{em}(C_2^*)$ (and $I_{em}(C_2^{-*})$ using PGOPHER simulation software package, can be seen in Figure 4.12:

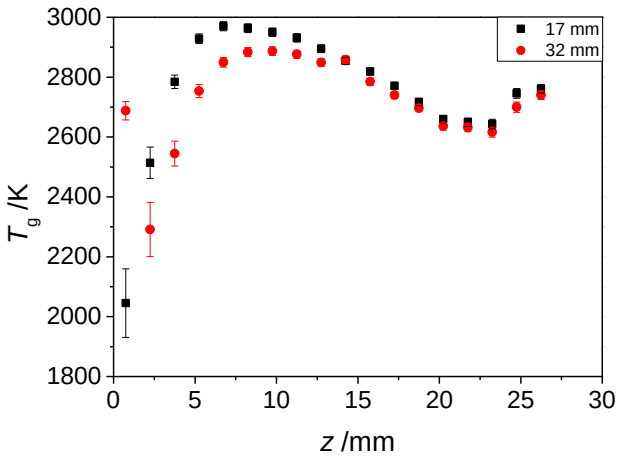

Figure 4.12: Spatially-resolved T_g for d_{sub} = 32 mm on a 0.01″ wire, red, and d_{sub} = 17 mm on a 0.004″ wire (black) under otherwise base conditions for z < 21 mm; the data this was extracted from the PGOPHER spectral simulation best fits of data shown in Figure 4.11 using a spatial resolution of 1.5 mm.

The anomalous gas temperature for the 32 mm substrate at z ~ 0.75 mm arises due to low intensities at this height. Neglecting this outlier, it can be seen (by eye) that by extrapolating the two curves featured in Figure 4.12, T_g converges at z ~ 0.75 mm for both substrate sizes. This is reflecting the similar substrate temperature (T_{sub} ~ 700 °C) controlled through careful consideration of spacer wire thickness. The increase and relocation of the maximum T_g towards the substrate, could feasibly lead to a shift in the maximum [H]/[H_2] position, and therefore production of [C_2H_2], and consequently n_e, absorbed power density, etc. This would explain the observed relocation of $I_{em}(C_2^{-*})$ and $I_{em}(C_2^*)$ toward the substrate. The increase in maximum intensity values of these species with respect to substrate diameter could arise from an increase in [H], [H]/[H_2], n_e, and / or a change in production / loss rates (/ rate

ratios). The decrease in the relative ratio of $I_{em}(C_2^-*)/I_{em}(C_2*)$ must also be reflecting a change in one or more of these plasma parameters, and highlighting a difference in their parameter dependencies, consistent with prior speculations with the addition of Ar. The sharper temperature gradient seen with the smaller substrate would result in a further axial confinement of regions B and C (discussed in Chapter 1, Section 1.4) between the plasma core and the substrate, which might act to further enhance radical densities associated to the CVD of diamond (namely H and CH_x radicals) near to a diamond growing surface.

Through a careful consideration of Process 4.08 through to Process 4.18, (i.e. the conceived formation and loss mechanisms of the C_2^- and C_2^-* states described in Section 4.3.2), it is also possible to interpret the most prominent processes contributing to the formation and loss of C_2^- and C_2^-* and rationalise the experimental observations of $I_{em}(C_2^-*)$ with varying process conditions.

Assuming a high rate coefficient $k_{4.08} > 10^{-29}$ cm^6s^{-1}, Process 4.08, electron attachment of C_2 in the presence of a third body to form C_2^-, would only contribute significantly for $p \geq 150$ Torr.[1] Process 4.08 can also be eliminated as a significant contributing mechanism through experimental observation; for this mechanism to be a major contributor in the formation of C_2^-*, $I_{em}(C_2^-*)$ would be expected to follow similar P and p trends to that of $I_{em}(C_2*)$, which is not observed experimentally. The reverse mechanism, (whose rate coefficient is available in Table 4.01), is also not a major contributor to the loss of C_2^-*. Processes 4.09, (i.e. electron impact excitation of ground state C_2^-), 4.10 (photo attachment of an electron with C_2 forming intermediate C_2^-*, resulting in C_2^- and emission) and 4.11, (electron collision with C_2^- forming C_2 and 2 electrons), are also too slow to be considered important formation or loss mechanisms under the investigated conditions.

Electron attachment of acetylene can yield products of C_2^- (+ 2 H) and C_2H^- (+ H), the prior has a threshold energy of 7.4 eV with the first resonance featuring at ~ 8.1 eV and is a major contributing process in the formation of C_2^- for $z < 5$ mm.[1] This is reflected in the 2-D plasma modelling of the ground state $\{C_2^-\}(z)$ column density shown in Figure 4.13 (b); acetylene is most prominent in the cooler regions of the plasma and as such, any products formed directly from acetylene will also be more prominent at low z. The formation of C_2H^- by dissociative electron attachment to C_2H_2 has a threshold energy of 2.7 eV and a resonance energy of 3.6 eV.[53] This is a major source of C_2H^- throughout the plasma, however H-shifting of C_2H^- (Process 4.14 followed by electron impact excitation, EIE, of C_2^- as described by Process 4.09) is too slow to be a major contributing process for the formation of C_2^-*. These mechanisms, are however, a significant contributor to the formation of ground state C_2^-.

Experimentally, these formation mechanisms can be ruled out in contributing to the production of C_2^-* through consideration of the spatial distribution of $I_{em}(C_2^-*)$ under base conditions (Figure 4.05 (b)). The number density of acetylene, $[C_2H_2]$, whose mole fraction can be seen in Figure 1.5 (g), Chapter 1, follows a similar spatial distribution to $[H_2]$, which can also be seen in Figure 1.5 (e), Chapter 1. $[C_2H_2]$

peaks in the cooler plasma regions, whilst n_e tails off at higher z, as can be seen in both Figure 1.5 (a), Chapter 1, and Figure 4.14 (b) of this Chapter. If this were a prominent formation mechanism for the excited state, one would therefore expect $I_{em}(C_2^{-*})$ to also peak in the cooler regions, such as just above the substrate, rather than the observed peak intensity at $z = 9.75 \pm 0.75$ mm under base conditions.

This argument also allows dissociative electron attachment of acetylene (Process 4.15) to be eliminated as a prominent contributor; instead C_2^{-*} must be formed from a 'hot' species more dominant in the hot regions of the plasma. 2-D plasma modelling demonstrate that C_2 and C_2H are both more dominant in the hotter plasma regions as can be seen in Figures 4.12 (b) and (c), and Figures 4.13 (c) and (d).[9] C_2H has a number density of ~ 5×10^{13} cm^{-3} in the hot plasma, which is ~ 40× that of C_2. Processes 4.16 and 4.17 consider dissociative electron attachment of C_2H to form both C_2^- and C_2^{-*}. These processes are the major contributing processes in the formation of both species in the hot plasma, whilst the reverse of Process 4.17 is the major quenching process for C_2^{-*}.

It is through assuming steady-state and balancing formation (Process 4.17) and loss (the reverse of Process 4.17 and Process 4.18 (radiative emission)) mechanisms, that a similar expression to that describing $I_{em}(C_2^*)$ in Equation 4.07 can be derived for $\{C_2^{-*}\}$ (and $I_{em}(C_2^{-*})$). Such a derivation is available in the Appendix.[1]

$$I_{em}(C_2^{-*}) \sim 2R_{pl} \times \frac{k_{4.17}\,[C_2H_2] \times n_e}{[H] \times k_{-4.17} + A_{4.18}} \times \frac{k_{4.01}}{k_{-4.01}} \times \frac{[H]}{[H_2]} \qquad (4.19)$$

This expression vindicates the near linear behaviour of $I_{em}(C_2^{-*}) \sim F(CH_4)$ seen in Figure 4.04 (a), as $F(CH_4) \sim [C_2H_2]$ under the investigated operating conditions.

Equation 4.19 demonstrates that $I_{em}(C_2^{-*})$ is less sensitive than $I_{em}(C_2^*)$ with respect to $[H]/[H_2]$ and is predominantly quenched by [H] (rather than predominantly being lost via photoemission as is the case for $I_{em}(C_2^*)$ under base conditions). Ignoring smaller order changes in the rate coefficients, an increase in T_g would therefore act to the increase $I_{em}(C_2^*)$ and $I_{em}(C_2^{-*})$, but decrease the relative $I_{em}(C_2^{-*})/I_{em}(C_2^*)$ based on their parameter-dependencies (described by Equations 4.07 and 4.19 respectively). Ar addition acts to reduce the thermal conductivity of the plasma and therefore enhances Tg (as well as [H], and [H]/[H2]). The increases in $I_{em}(C_2^{-*})$ and $I_{em}(C_2^*)$ (and decrease in $I_{em}(C_2^{-*})/I_{em}(C_2^*)$) with Ar addition can therefore be attributed to the associated enhancement of T_g. Similar arguments can also be made for the observed increase in $I_{em}(C_2^{-*})$ and $I_{em}(C_2^*)$, (and relative decrease in $I_{em}(C_2^{-*})/I_{em}(C_2^*)$) with decreasing d_{sub}.

The $I_{em}(C_2^{-*})$ dependency on p and P can also be rationalised through Equation 4.19; $[C_2H_2]/[H_2]$ is largely invariant with P, whilst the modelling indicates that $[H]/([H]\times k_{-4.17}+A_{4.18}) \sim P^{0.33}$ within the plasma core under otherwise base conditions. As before, $R_{pl} \sim P^{0.5}$, and $k_{4.01}/k_{-4.01}$ increases less strongly with P, such that overall $I_{em}(C_2^{-*}) \sim P$, as experimentally observed (and modelled for selected conditions) in Figure 4.09. As with $I_{em}(C_2^*)$, $[C_2H_2]$ and $[H]/[H_2]$ increase ~ p, whilst R_{pl} decreases.

With increasing p, $A_{4.18}/[H]\times k_{-4.17}$ is modelled to be ~ 2, 0.4 and 0.18 for p = 75 Torr, 150 Torr and 225 Torr respectively. Equation 4.19 suggests, that $I_{em}(C_2^{-}*) \sim p^{\alpha}$, such that $\alpha > 1$ for low p, $\alpha \sim 1$ for the lower pressure range investigated, and $\alpha < 1$ for higher p; Figure 4.06 demonstrates this trend between $50 \leq p \leq 225$ Torr and correctly models the observed experimental trend; the enhancement seen at high $p \geq 225$ Torr may be attributed to Process 4.08, (third body assisted electron attachment to C_2), however this is speculative due to the significant error bars.

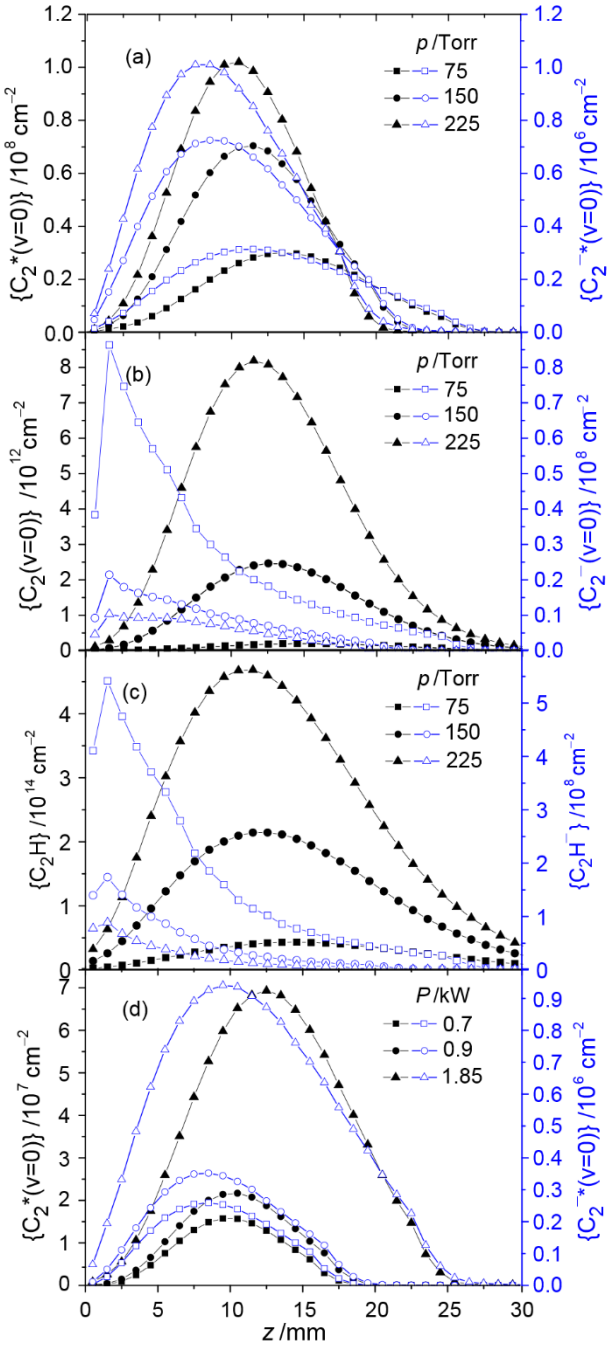

Figure 4.13: 2-D plasma kinetic modelling demonstrating spatially-resolved column densities of (a) C_2^{-}* and C_2*, (b) ground state C_2^{-}(v = 0) and C_2(a, v = 0), (c) for p = 75, 150 and 225 Torr under otherwise base conditions, and (d) C_2^{-}* and C_2* for P = 0.7, 0.9 and 1.85 kW under otherwise base conditions.

Figure 4.13 demonstrates the calculated column density spatial distributions of C_2^{-}* and C_2*, which demonstrate excellent agreement to the experimental $I_{em}(z)$ shown in Figures 4.04 and 4.07 for a range of pressure and power conditions. The agreement not only vindicates the approximation that measured intensities scale with column densities, but also demonstrates that the plasma modelling is correctly describing the experimental observations with changes in operating conditions.

Figure 4.13 also demonstrates that the column density of C_2H^{-} is almost an order of magnitude larger than that of C_2^{-} for base conditions.

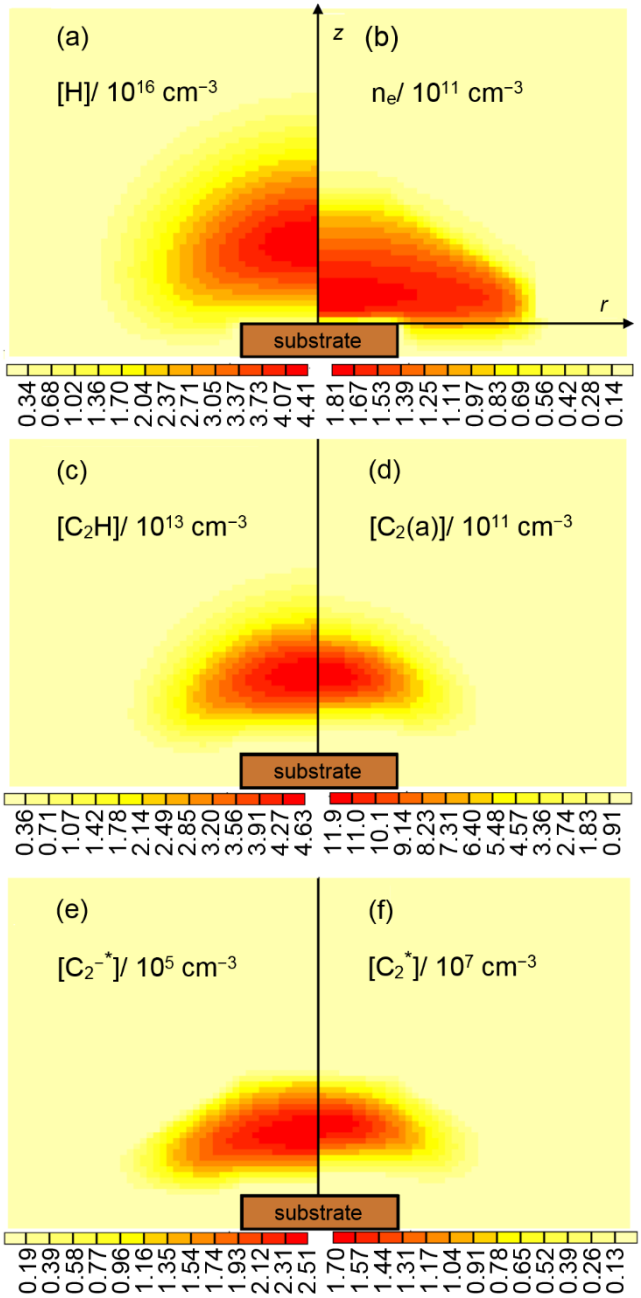

Figure 4.14: 2-D plasma kinetic modelling demonstrating spatially-resolved number densities of (a) [H], (b) n_e, (c) [C_2H], (d) C_2(a), (e)C_2^{-}* and (f) C_2* on false colour plots for base conditions.

Figure 4.14 demonstrates the steady-state number densities for [H], n_e, [C_2H], [C_2(a)], [C_2^-*] and [C_2*] produced by 2-D plasma modelling under base conditions when considering the mechanisms shown in bold in Table 4.01. The broader spatial distribution of [C_2H], the proposed parent species of C_2^-* (*cf.* [C_2(a)], the proposed parent species of C_2*) provides a rationale as to why $I_{em}(C_2^-*)$ peaks at a lower z than $I_{em}(C_2*)$ under most conditions.

4.3.6: Presence of Cations?

Figure 4.15 demonstrates a PGOPHER simulation of the $CH^+(A\rightarrow X)$ transition using rotational constants from Reference 56:

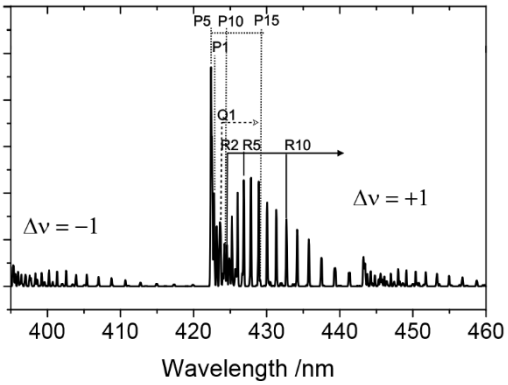

Figure 4.15: Simulation of $CH^+(A\rightarrow X)(0\text{-}0)$ transition at T_g = 1200 K with (1,0) and (0,1) also included. Frank Condon factors were assumed to be 1.

Figure 4.16 demonstrates (a) a best fit CH(A→X) simulation spectrum to experimental data shown in (b). The simulation is generated using rotational constants referenced in Chapter 5, and spanning across a wavelength range in which the $CH^+(A\rightarrow X)(0\text{-}0)$ would be expected to emit, (b) demonstrates the experimental data under the height and conditions defined in the methodology and the Figure caption, (c) demonstrates the residual, i.e. the difference between (b) − (a). Figure 4.16 (d) demonstrates an optical emission spectrum collected from a MW-activated H plasma under conditions defined in the Figure caption, whilst (e) shows the spectral simulation of the $CH^+(A\rightarrow X)$ shown in Figure 4.15.

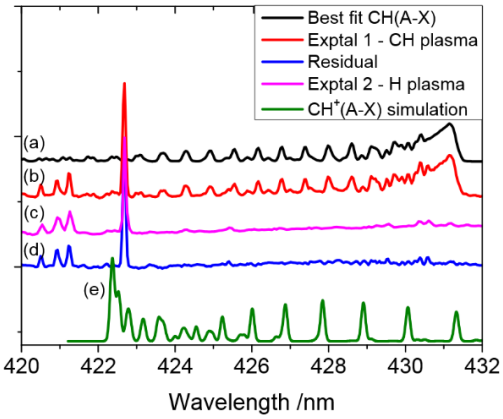

Figure 4.16: (a) Best fit simulation of the CH(A-X) for experimental data displayed in (b) between the wavelength range of 420-432 nm. (b) Experimental data collected under the conditions of $F(H_2)$ = 300 sccm, $F(CH_4)$ = 19 sccm, P = 1.5 kW, p = 150 Torr, d_{sub} = 17 mm, d_{wire} = 0.004″ analysed at z = 2.25 ± 0.75 mm above substrate. (c) residual, i.e. (b) – (a). (d) Experimental data scaled and offset from a dataset collected with data presented in Chapter 3 under conditions of $F(H_2)$ = 300 sccm, P = 1.5 kW, p = 150 Torr, d_{sub} = 17 mm, d_{wire} = 0.01″ analysed at z = 2.25 ± 0.75 mm, (e) Simulation of $CH^+(A\rightarrow X)$, also shown in Figure 4.15.

It is evident from a comparison of Figures 4.16 (c), (d) and (e) that the residual emissions present in (c) can be accounted for by emissions present in a MW-activated H plasma (shown in (d)), and that the simulated $CH^+(A\rightarrow X)(0\text{-}0)$ structure shown in (e) is not present in (c).

The data presented in Figure 4.16 were collected in the studies carried out in Chapters 3 and 5. The residual shown in Figure 4.16 (c) highlights 4 larger emissions between the wavelength region of 420-432 nm that are not accounted for by the $CH(A\rightarrow X)$ simulation in Figure 4.16 (a). These emissions are also present at a similar height and under similar conditions, in a methane-free plasma, i.e. emission originating from a MW-activated H plasma. The three emissions arising between 420-422 nm are thought to belong to H_2 emissions, whilst the emission featuring at 422.69 nm could alternatively be an emission originating from atomic W (Einstein-A emission coefficient of 3.7×10^6 s^{-1}) sourced from the W substrate.

The simulation in Figure 4.16 (e) demonstrates the $CH^+(A\rightarrow X)$ transition, which is not evident within the experimental data presented, nor the residual. Additional conditions, not presented, for instance high power, low pressure (P = 1.85 kW, p = 75 Torr) and low methane fraction were also attempted with no success. It is inferred that the steady-state column densities of $\{CH^+(A)\}$ are insufficient to detect optical emissions under the available parameter range.

4.4: Conclusions

This work conclusively demonstrates the first direct evidence for the presence of anions, or more generally charged species, within standard CVD operating conditions in MW-activated C/H(/Ar) plasmas. Additional work carried out by final year undergraduate research project student, Talia Solel, demonstrated that C_2^-* emissions also originate from DC-activated C/H plasmas under operating plasma conditions relevant to the CVD of diamond.[57] The results presented in this chapter investigate how optical emissions originating from the $C_2(d\rightarrow a)$ Swan Band and the $C_2^-(B\rightarrow X)$ Herzberg-Lagerqvist system varied with respect to process conditions. By careful consideration of potential formation and loss mechanisms, dissociative electron attachment of C_2H was confirmed by 2-D plasma modelling to be the prominent formation mechanism for C_2^-*. This yields a plausible rationale behind the observed experimental behaviour of $I_{em}(C_2^-*)$ with changes in operating conditions. C_2^-* demonstrates an example of alternative excitation mechanisms within MW-activated C/H plasmas under conditions relevant to the chemical vapour deposition of diamond. Comparatively, the prominent formation mechanism of $C_2^-(X)$ also included dissociative electron attachment of acetylene, forming C_2^- as a product directly and indirectly through the production of C_2H^- followed by an H-shifting reaction. C_2H^- has a calculated number density ~ an order of magnitude higher than that of C_2^-. Despite diatomic anions consisting of < 0.1% of total negatively charged species, i.e. electrons, the results of this chapter offer an alternative rationale behind positive bias enhanced nucleation results, which have previously been attributed to electron bombardment, as discussed in Chapter 1, Section 1.5. This chapter

confirms that the addition of some argon has little effect on the overall behaviour of $I_{em}(C_2^-*)$ and $I_{em}(C_2*)$ with respect to varying other process conditions (e.g. P and p) but infers that an increase in T_g (generated by introducing Ar) acts to increase both intensities, but decrease the relative intensity ratio, i.e. $I_{em}(C_2^-*)/I_{em}(C_2*)$. This is reflective of their different sensitivity to $[H]/[H_2]$ and their difference in their prominent loss mechanisms under base pressure (photoemission vs. reactive quenching with [H] atoms for the C_2* and C_2^-* respectively). The use of a smaller substrate increased the intensity of $I_{em}(C_2^-*)$ and $I_{em}(C_2*)$, relocates their peak ~1.5 mm closer to the substrate, and decreases their relative intensities; this effect has been speculated to be attributable to a shift and increase in the T_g toward the substrate (and therefore acting to alter $[H]/[H_2]$ as a function of height). The assumed formation and loss mechanisms of the $C_2(d)$ state (EIE of the $C_2(a)$ state, photoemission and reactive quenching with $[H_2]$) provides a rationale behind the observed changes in $I_{em}(C_2*)$ with process conditions. The assumed formation mechanism is drawn into question in Chapter 5.

This chapter then proceeds to investigate the possibility of emissions from $CH^+(A\text{-}X)$ under conditions / the height at which the cation might be expected to be relatively most prominent. No evidence of cation emissions has been found. This chapter serves to highlight that there is plenty of room for further refinement on the knowledge of the processes, which occur within MW-activated C/H and C/H/Ar plasmas, and that 2-D plasma modelling will only provide a consideration on mechanisms that are included.

References

[1] Mahoney, E. J. D., Truscott, B. S., Ashfold, M. N. R., and Mankelevich, Yu. A. "Optical Emission from C_2^- Anions in Microwave-Activated CH_4/H_2 Plasmas for Chemical Vapor Deposition of Diamond." The Journal of Physical Chemistry A, vol. 121, no. 14, pp. 2760-2772, 2017.

[2] Balmer, R. S., Brandon, J. R., Clewes, S. L., Dhillon, H. K., Dodson, J. M., Friel, I., Inglis, P. N., Madgwick, T. D., Markham, M. L., Mollart, T. P., Perkins, N., Scarsbrook, G. A., Twitchen, D. J. , Whitehead, A. J., Wilman, J. J. and Woollard, S. M. "Chemical Vapour Deposition synthetic diamond: materials, technology and applications." Journal of Physics: Condensed Matter, vol. 21, no. 36, pp. 364221-364244, 2009.

[3] Field, J. E. "The Properties of natural and synthetic diamond." Academic Press: 1992.

[4] Nazari, M., Hancock, B. L., Anderson, J., Hobart, K. D., Feygelson, T. I., Tadjer, M. J., Pate, B. B., Anderson, T. J., Piner, E. L., and Holtz, M.W. "Optical characterization and thermal properties of CVD diamond films for integration with power electronics." Solid-State Electronics, vol. 136, no. 10, pp. 12-17, 2017.

[5] Gicquel, A., Hassouni, K., Silva, F. and Achard, J. "CVD diamond films: from growth to applications." Current Applied Physics, vol. 1, no. 6, pp. 479-496, 2001.

---

[6] Via, G. D., Felbinger, J. G., Blevins, J., Chabak, K., Jessen, G., Gillespie, J., Fitch, R., Crespo, A., Sutherlin, K., Poling, B., Tetlak, S., Gilbert, R., Cooper, T., Baranyai, R., Pomeroy, J. W., Kuball, M., Maurer, J. J., and Bar-Cohen, A. "Wafer-scale GaN HEMT performance enhancement by diamond substrate integration." physica status solidi (c), vol. 11, no. 3-4 , pp. 871-874, 2014.

[7] Woerner, E., Wild, C., Mueller-Sebert, W. and Koidl, P. "CVD-diamond optical lenses." Diamond and Related Materials, vol. 10, no. 3-7, pp. 557-560, 2001.

[8] Ma, J., Ashfold, M. N. R. and Mankelevich, Yu. A. "Validating optical emission spectroscopy as a diagnostic of microwave activated $CH_4/Ar/H_2$ plasmas used for diamond chemical vapor deposition," Journal of Applied Physics, vol. 105, no. 4, p. 043302, 2009.

[9] Mankelevich, Yu. A., Ashfold, M. N. R. and Ma, J. "Plasma-chemical processes in microwave plasma-enhanced chemical vapor deposition reactors operating with C/H/Ar gas mixtures," Journal of Applied Physics, vol. 104, no. 11, p.113304, 2008.

[10] Ma, J., Cheesman, A., Ashfold, M. N. R., Hay, K., Wright, S., Langford, N., Duxbury, G. and Mankelevich, Yu. A. "Quantum cascade laser investigations of CH_4 and C_2H_2 interconversion in hydrocarbon/H_2 gas mixtures during microwave plasma enhanced chemical vapor deposition of diamond." Journal of Applied Physics, vol. 106, no. 3, p. 033305, 2009.

[11] Ma, J., Richley, J. C., Ashfold, M. N. R. and Mankelevich, Yu. A. "Probing the plasma chemistry in a microwave reactor used for diamond chemical vapor deposition by cavity ring down spectroscopy," Journal of Applied Physics, vol. 104, no. 10, p. 103305, 2008.

[12] Butler, J. E., Mankelevich, Yu. A., Cheesman, A., Ma, J. Ashfold, M. N. R., "Understanding the chemical vapor deposition of diamond: recent progress," Journal of Physics, Condensed Matter, vol. 21, no. 36, pp. 1-20, 2009.

[13] Ashfold, M. N. R., Mahoney, E. J. D., Mushtaq, S., Truscott, B. S. T. and Mankelevich, Yu. A., "What [plasma used for growing] diamond can shine like flame?" Chemical Communications, vol. 53, no. 76, pp. 10482-10495, 2017.

[14] Mahoney, E. J. D. and Ashfold, M. N. R., "Diamond growth using microwave-activated methane/hydrogen plasmas," Atlas of Science. [online] Atlasofscience.org, 2018, Available at: http://atlasofscience.org/diamond-growth-using-microwave-activated-methane-hydrogen-plasmas/ [Accessed 31 Aug. 2018].

[15] Gicquel, A., Hassouni, K., Silva, F. and Achard, J. "CVD diamond films: from growth to applications" Current Applied Physics, vol. 1, no. 6, pp. 479-496, 2001.

[16] Reeve, S. W., Weimer, W. A. "Plasma Diagnostics of a Direct-Current Arcjet Diamond Reactor. 2. Optical-Emission Spectroscopy." Journal of Vacuum Science and Technology A, vol. 13, pp. 359-367, 1995.

---

[17] Luque, J., Juchmann, W., Brinkman, E. A., Jeffries, J. B. "Excited State Density Distributions of H, C, C_2 and CH by Spatially Resolved Optical Emission in a Diamond Depositing DC-Arcjet Reactor." Journal of Vacuum Science and Technology A, vol. 16, pp. 397–408, 1998.

[18] Brinkman, E. A., Raiche, G. A., Brown, M. S., Jeffries, J. B. "Optical Diagnostics for Temperature Measurement in a DC Arcjet Reactor used for Diamond Deposition." Journal of Applied Physics B. vol. 64, pp. 689–697, 1997.

[19] Wills, J. B., Smith, J. A., Boxford, W. E., Elks, J. M. F., Ashfold, M. N. R., Orr-Ewing, A. J. "Measurements of C_2 and CH Concentrations and Temperatures in a DC Arc Jet using Cavity Ring Down Spectroscopy." ," Journal of Applied Physics vol. 92, pp. 4213–4222, 2002.

[20] Mortet, V., Hubicka, Z., Vorlicek, V., Jurek, K., Rosa, J., Vanecek, M. "Diamond Growth by Microwave Plasma Enhanced Chemical Vapour Deposition: Optical Emission Characterisation and Effect Argon Addition." Physica Status Solidi (a), vol. 201, pp. 2425–2431, 2004.

[21] Gries, T., Vandenbulcke, L., de Persis, S.; Aubry, O., Delfau, J.L. "Diagnostics and Modelling of CH_4/CO_2 Plasmas for Nanosmooth Diamond Deposition: Comparison to Experimental Data." Journal of Vacuum Science and Technology B, vol. 27, pp. 2309-2320, 2009.

[22] Griffin, J., Ray, P.C. "Role of Inert Gas in the Low-Temperature Nanodiamond Chemical Vapour Deposition Process." Nanotechnology, vol. 17, no. 5, pp. 1225-1229, 2006.

[23] Tallaire, A., Rond, C., Benedic, F., Brinza, O., Achard, J., Silva, F., Gicquel, A. "Effect of Argon Addition on the Growth of Thick Single Crystal Diamond by High-Power Plasma CVD." Physica Status Solidi, vol. 208, no. 9, pp. 2028-2032, 2011.

[24] Vikharev, A. L., Gorbachev, A. M., Muchnikov, A. B., Radishev, D. B., Kopelovich, E. A., Troitskiy, M. M. "Investigation of the Optimized Parameters of Microwave-Plasma-Assisted Chemical Vapour Deposition Reactor Operation in a Pulsed Mode." Journal of Physics D, Applied Physics, vol. 45, no. 39, p. 395202, 2012.

[25] Derkaoui, N., Rond, C., Hassouni, K., Gicquel, A. "Spectroscopic Analysis of H_2/CH_4 Microwave Plasma and Fast Growth Rate of Diamond Single Crystal." Journal of Applied Physics, vol. 115, no. 23, p. 233301, 2014.

[26] Hemawan, K. W., Hemley, R. J. "Optical Emission Diagnostics of Plasmas in Chemical Vapor Deposition of Single-Crystal Diamond." Journal of Vacuum Science and Technology A, vol. 33, no. 6, p. 061302, 2015.

[27] Jiang, X., Six, R., Klages, C. P., Zachai, R., Hartweg, M. and Füβer, H. J. "The effect of substrate bias voltage on the nucleation of diamond crystals in a microwave plasma assisted chemical vapor deposition process," Diamond and Related Materials, vol. 2, no. 2-4, pp. 407-412, 1993.

[28] Chiang, J. M. and Hon, M. H. "Positive dc bias-enhanced diamond nucleation with high CH_4 concentration," Diamond and Related Materials, vol. 10, no. 8, pp. 1470-1476, 2001.

---

[29] Krieg, J., Lutter, V., Endres, C., Keppeler, I., Jensen, P., Harding, M., Vázquez, J., Schlemmer, S., Giesen, T. and Thorwirth, S. "High-Resolution Spectroscopy of C_3 around 3 μm." The Journal of Physical Chemistry A, vol. 117, no. 16, pp. 3332-3339, 2013.

[30] Pitarch-Ruiz, J., Sánchez-Marín, J. and Maynau, D., "Vertical spectrum of the $C_2H_2^+$ system. An open shell (SC)2-CAS-SDCI study." Journal of Computational Chemistry, vol. 24, no. 5, pp. 609-617, 2003.

[31] Douglas, A. E. and Herzberg, G. "Band Spectrum and Structure of the CH^+ Molecule; Identification of three Interstellar Lines," Canadian Journal of Research, vol. 20a, no. 6, pp. 71-82, 1942.

[32] Drowart, J., Burns, R., DeMaria, G. and Inghram, M. G. "Mass Spectrometric Study of Carbon Vapor," The Journal of Chemical Physics, vol. 31, no. 4, pp. 1131-1132, 1959.

[33] O'Keefe, A., Derai, R., and Bowers, M. T. "The First Experimental Observation Of Electronic Transitions In C_2^+ And C_2D^+," Chemical Physics, vol. 91, no. 1, pp. 161-166, 1984.

[34] Forney, D., Althaus, H., and Maier, J. P. "An Electronic Absorption Spectrum of Carbon Ion (C_2^+): $B^4\Sigma_u - X^4\Sigma_g^-$." The Journal of Physical Chemistry, vol. 91, no. 26, pp. 6458-6461, 1987.

[35] Brzozowski, J., Elander, N., Erman, P., and Lyyra, M. 1974. "On The Interstellar Abundance Of The CH^+ Radical." The Astrophysical Journal, vol. 193, p. 741, 1974.

[36] Tsuji, M., Ogawa, T., Nishimura, Y., and Ishibashi, N.. "Emission Spectra of CH^+ Produced From CH_4 and C_2H_2 by Controlled Electron Impact." Chemistry Letters, vol. 4, no. 4, pp. 317-318, 1975.

[37]Brooke, J. S. A., Ram R. S., Western, C. M., Li, G., Schwenke, D. W., and Bernath, P. F., "Einstein A coefficients and oscillator strengths for the $A^2\Pi$-$X^2\Sigma$+ (RED) and $B^2\Sigma^+$-$X^2\Sigma^+$ (violet) systems and rovibrational transitions in the $X^2\Sigma^+$state of CN." The Astrophysical Journal Supplement Series, vol. 210 p. 23, 2014.

[38] Brooke, J. S. A., Bernath, P. F., Schmidt, T. W., Bacskay, G. B., "Line Strengths and Updated Molecular Constants for the C_2 Swan System." Journal of Quantitative Spectroscopy and Radiative Transfer, vol. 124, pp. 11–20, 2013.

[39] Western C. M., "PGOPHER, A Program for Simulating Rotational, Vibrational and Electronic Spectra," University of Bristol, http://pgopher.chm.bris.ac.uk.

[40] Jones, P. L. Mead, R. D., Kohler, B. E., Rosner, S. D., Lineberger, W. C. "Photodetachment Spectroscopy of C_2^- Autodetaching Resonances." Journal of Chemical Physics, vol. 73, pp. 4419–4432, 1980.

[41] Gulania, S., Jagau, T. C., Krylov, A. "EOM-CC guide to Fock-space travel: The C_2 edition." Faraday Discussions. Manuscript accepted, 2018.

[42] Pasternack, L., Pitts, W. M., McDonald, J. R. "Temperature Dependence of Reactions and Intersystem Crossing of C_2(a3Πu) with Hydrogen and Small Hydrocarbons from 300-600 K." Journal of Chemical Physics, vol. 57, pp. 19-28, 1981.

[43] Ervin, K. M., Lineberger, W. C. “Photoelectron-Spectra of C_2^- and C_2H^-.” Journal of Physical Chemistry, vol. 95, pp. 1167-1177, 1991.

[44] Andersen, L. H., Hvelplund, P., Kella, D., Moklery, P. H., Pedersen, H. B., Schmidt, H. T., Vejby-Christensen, L. “Resonance Structure in the Electron-Impact Detachment Cross Section of C_2^- Caused by the Formation of C_2^{2-}.” Journal of Physics B: Atomic, Molecular and Optical Physics, vol. 29, no. 17, 1996.

[45] Vuitton, V., Lavvas, P., Yelle, R. V., Galand, M., Wellbrock, A., Lewis, G. R., Coates, A. J., Wahlun, J. E., “Negative Ion Chemistry in Titan’s Upper Atmosphere.” Planetary and Space Science, vol. 57, no. 13, pp. 1558–1572, 2009.

[46] May, O., Fedor, J., Ibănescu, B. C., Allan, M. “Absolute Cross Sections for Dissociative Electron Attachment to Acetylene and Diacetylene.” Physical Review A, vol. 77, p. 040701, 2008.

[47] Szymańska, E., Čadež, I., Krishnakumar, E., Mason, N. J. “Electron Impact Induced Anion Production in Acetylene.” Journal of Physical Chemistry and Chemical Physics, vol. 16, pp. 3425-3432, 2014.

[48] Locht, R. “Mass Spectrometric Investigation of the Appearance of Negative Ions by Dissociative Electron Attachment in Polyatomic Molecules.” Bull. de la Classe des Sciences, Académie Royale de Belgique, pp. 788–817, 1970.

[49] Leutwyler, S., Maier, J., Misev, L. “Lifetimes of C_2 in Rotational Levels of the $B^2\Sigma^+_u$ State in the Gas Phase.” Chemical Physics Letters vol. 91, pp. 206-208, 1982.

[50] Ma, J. "Exploration Of The Gas Phase Chemistry In Microwave Activated Plasmas Used For Diamond Chemical Vapour Deposition." PhD, University of Bristol, 2008.

[51] Richley, J. C., Kelly, M. W., Ashfold, M. N. R. and Mankelevich, Yu. A. “Optical Emission from Microwave Activated C/H/O Gas Mixtures for Diamond Chemical Vapor Deposition.” The Journal of Physical Chemistry A, vol. 116, no. 38, pp. 9447-9458, 2012.

[52] Caledonia, G. E. “A Survey of the Gas-Phase Negative Ion Kinetics of Inorganic Molecules: Electron Attachment Reactions.” Chemical Reviews, vol. 75, pp. 333-351, 1975.

[53] Barckholtz, C., Snow, T. P., Bierbaum, V. M. “Reactions of C_n^- and C_nH^- with Atomic and Molecular Hydrogen.” Journal of Astrophysics, vol. 547, pp. L171-L174, 2001.

[54] Cathro, W. S., Mackie, J. C. “Oscillator Strength of the C_2^- $B^2\Sigma$–$X^2\Sigma$ Transition: A Shock-Tube Determination.” Journal of the Chemical Society, Faraday Transaction Series II, vol. 69, pp. 237-245, 1973.

[55] Richley, J. C., Fox, O. J. L., Ashfold, M. N. R., Mankelevich, Yu. A. “Combined experimental and modeling studies of microwave activated CH_4/H_2/Ar plasmas for microcrystalline, nanocrystalline, and ultrananocrystalline diamond deposition.” Journal of Applied Physics, vol. 109, no. 6, p. 063307, 2011.

---

[56] Hakalla, R., Kępa, R., Szajna, W. and Zachwieja, M. "New analysis of the Douglas-Herzberg system ($A^1\Pi$-$X^1\Sigma^+$) in the CH^+ ion radical." The European Physical Journal D, vol. 38, no. 3, pp. 481-488, 2006.

[57] Solel, T. "Analysing the Growth Characteristics of a Pulsed Direct Current Plasma Deposition Reactor (PDC PDR)" Undergraduate final year Dissertation, University of Bristol, 2017.

Chapter 5: Is it Possible to Probe the Thermal Component of the Electron Energy Distribution Function (EEDF) in MW-activated C/H Plasmas?

Chapter 3 investigated the emissions from H_2*, H* and Ar*, which are proven to be sensitive to the hyper-thermal component of the EEDF. Chapter 4 reviews some of the prominent gas phase processes that occur within MW-activated C/H plasmas and provides the first direct evidence for the presence of anions under conditions relevant to the Chemical Vapour Deposition (CVD) of diamond. This chapter attempts to extend such work, whilst probing the thermal component of the EEDF in MW-activated C/H plasmas. Spatially-resolved optical emissions originating from the 3 lowest lying doublet excited states of the CH radical (i.e. the CH($A^2\Delta$), CH($B^2\Sigma^-$), and CH($C^2\Sigma^+$)) have been monitored under a range of MW-activated C/H plasma operating conditions relevant to the chemical vapour deposition (CVD) of diamond.

The emitting states have energies of 2.876, 3.208 and 3.944 eV above the ground state respectively, making emissions originating from these states (if predominantly generated via electron impact excitation, EIE) sensitive to the thermal component of the EEDF. In literature there has been recognition of a chemiluminescent component of the lowest lying CH(A) state through C + H + M→ CH(A) + M → CH(X) + γ + M, whilst the $C_2(a^3\Pi_u)$ state, due to its six-fold degeneracy, is populated significantly more than the C_2 ground state, via H + $C_2H(X) \rightarrow C_2(a) + H_2$.

Previous literature has inferred that the investigated excited states of the CH radical are predominantly formed through EIE.[1,2] Through consideration of CH* intensity ratios, and the quenching of such states, of which there is limited literature available, it should therefore be possible to calculate experimentally derived, spatially-resolved, and process condition dependent electron temperatures which describes the thermal component of the EEDF. This chapter illustrates how such data analysis would be used to make spatially-resolved T_e calculations.

It transpires that attempting such analysis relies on introducing two empirical parameters within a Boltzmann distribution to reproduce the modelled T_e; one such parameter would typically describe the difference in energy between the excited states of the CH radical, whilst the second parameter is a multiplication factor applied to the calculated intensity ratios. The latter parameter may be reflective of detection efficiencies, differences in quenching mechanisms / rates etc. The reliance of empirical values infers that either the modelling is not describing the EEDF (particularly at low *z*) in its entirety or that there are unconsidered CH* formation / loss mechanism(s). This is reinforced by the disparity between

experimental $I_{em}(C \rightarrow X)/I_{em}(A \rightarrow X)(z)$ and modelled {CH(C)}/{CH(A)} ratios, used as a comparator, as produced through consideration of EIE, radiative decay, and the deduced quenching mechanism $H_2 + CH^* \rightarrow CH_2 + H$.

Experimentally, it is observed that $I_{em}(C \rightarrow X)/I_{em}(A \rightarrow X)(z)$ maximises at $z \sim 2.5$ mm and decreases sharply until $z \sim 10$ mm. The ratio then plateaus / decreases gradually up to $z \sim 20$ mm. Comparatively, the modelling infers comparator {CH(C)}/{CH(A)} maximises at $z \sim 5$ mm, which plateaus / gradually decreases with increasing z. The failure of the model in capturing $I_{em}(C \rightarrow X)/I_{em}(A \rightarrow X)(z \sim 2.5$ mm) (and the local low z variation) is implicit that there are intensity contributions (or plasma parameter variations) that the modelling is not capturing at present.

The first explanation is consistent with the failure of the 2-D plasma modelling to reproduce the low z emission contributions originating in MW-activated H plasmas. An increase in 'warm' electrons with a higher $T_e(z \sim 2.5$ mm) would act to increase {CH(C)}/{CH(A)} at low z and improve agreement between model and experiment.

Alternatively, through the inclusion of an additional CH* formation mechanism, (hydrogen abstraction of the $CH_2(X)$ state, which predominantly forms CH(X), but also populates the excited states of the CH* radicals, i.e. $H + CH_2(X) \rightarrow CH^* + H_2$, with a Maxwell-Boltzmann contribution), an agreement is produced between the spatial dependency of $I_{em}(C \rightarrow X)/I_{em}(A \rightarrow X)(z)$ emission ratios with modelled {CH(C)}/{CH(A)}(z). Crucially, in this latter interpretation, the rate is demonstrated to be significant and perhaps larger than that of EIE (of the CH(X) radical) in the production of the CH(A) state within the hot plasma region. Comparatively, EIE is still the prominent formation mechanism for the CH(C) state. This would imply that whilst such a ratio may still be sensitive to the thermal component of the EEDF within MW-activated C/H plasmas, as outlined, they may not be used to directly calculate $T_e(z)$ and hence acts as a justification for the introduction of empirical values in the calculation of $T_e(z)$. Such a conclusion would also infer that CH* emission intensities are more representative of $CH_x(0 \leq x \leq 3)$ radicals, i.e. species attributed with the standard model of diamond growth, than previously thought.

Further, a similar mechanism, ($H + C_2H(X) \rightarrow C_2(d) + H_2$) would be expected to produce a larger rate than the $C_2(d)$ formation mechanism assumed in Chapter 4, EIE of the $C_2(a)$ radical.

It is concluded that either of the two mechanisms could explain the disparity between model and experiment, and that the majority of experimental parameters would be incapable of distinguishing between these possibilities within the available parameter ranges. It is speculated, however, that very low fractions of methane addition might. These results are in the process of being published.

5.1: Introduction

The physical gas phase processes and plasma chemistry facilitating diamond growth in MW-activated C/H plasmas are generally thought to be well-understood. Such an understanding has been achieved

through a combination of diagnostic techniques, (such as laser absorption, optical emission spectroscopy, [1,2,3,4] and microwave interferometry studies, [4] used for measuring absolute ground state, relative excited state and absolute electron column densities respectively) and plasma modelling.[1,2,3,4]

Spatially-resolved optical emission spectroscopy (OES) is a non-intrusive technique, which enables emitting excited atomic and diatomic radicals to be investigated with spatial resolution. Such investigations can infer diagnostic information, such as T_g, [5,6] and inform plasma modelling.[6,7,8,9,10] OES is desirable as a non-invastive *in situ* diagnostic technique for monitoring the plasma content (and any time evolution) during CVD diamond growth. For instance, the CH($A^2\Delta \rightarrow X^2\Pi$) and CH($B^2\Sigma^- \rightarrow X^2\Pi$) emission bands are commonly used as an indicator for $CH_x (0 \leq x \leq 3)$ radicals, whilst the $C_2(d^3\Pi_g \rightarrow a^3\Pi_u)$ emission is indicative of the total carbon content, as demonstrated in Chapter 4.[11,12,13,14,15] A comparison of I_{em}(CH)/ $I_{em}(C_2)$ radical emissions has been used as an *in situ* proxy for assessing material and surface quality during growth, as qualified post-growth through characterisation techniques, such as Scanning Electron Microscopy and Raman Spectroscopy.[11,12,13,14,15]

Emitting excited states tend to be populated through electron impact excitation of ground states, or in the case of C_2, low lying metastable states.[1,16] There have been a few additional excitation mechanisms noted as a more comprehensive understanding of MW-activated C/H systems has been developed. Chapter 4 illustrated that the $C_2^-(B^2\Sigma_u)$ state is likely populated through dissociative electron attachment of C_2H. Excitation energy transfers have been noted for CH and C_2 emissions within MW-activated C/H/O plasmas through excitation energy transfer excitation with metastable CO($a^3\Pi$), whilst near resonant energy transfer between highly excited states of H*, H_2* and Ar* and their ground states have been reported in Chapter 3 for MW-activated H (and H/Ar) plasmas with such ideas likely extending to MW-activated C/H(/Ar) plasmas, as qualified in Chapter 6.[7,8,9]

The electron energy distribution function (EEDF) is an important plasma characteristic, which determines the number density of electrons within a defined energy range and is described by a Maxwell-Boltzmann distribution around electron temperature, T_e. Experimentally, T_e (or the EEDF) is difficult to measure directly. Traditionally in low pressure, low temperature plasmas, T_e could be measured through use of a Langmuir probe, however such a probe would not withstand the high T_g conditions present in this thesis. Supposing it could, such a device would act to perturb the MW standing wave and consequently the plasma parameters.[17,18] Thompson scattering is another method facilitating the determination of electron temperatures, however the experimental set-up is non-trivial and impractical in bright luminous plasmas.[18]

As highlighted in Chapter 3, the EEDF is highly sensitive to plasma parameters, such as absorbed power density, T_g, n_e, reduced electric field strength, etc and that these spatially-variant plasma parameters, (as well as the EEDF) are interdependently coupled with the prominent gas phase processes occurring within MW-activated H (and H/Ar) plasmas.[8,9] Monitoring the intensity of H_2 emission bands proved

to be a sensitive tool for probing the hyper-thermal component of the EEDF. However, the work also illustrated that, under the studied conditions, couplings between highly excited states of H, H_2 (and Ar when present) with their ground state species can complicate the interpretation of OES for estimating T_e through traditional OES probes, in particular the use of H-Balmer ratios and actinometry measurements through the use of trace rare gases. [8,9,19]

Alternatively, computation, and modelling, can be used to estimate the relative intensities and/or column densities of excited states expected for different T_e. The use of relative intensities should consider experimental factors, such as the detection efficiency of different emission wavelengths prior to calculation of T_e.

This work seeks to expand the available toolset for monitoring thermal electrons within MW-activated C/H plasmas by comparison of optical emission measurements carried out on the $CH(A^2\Delta \rightarrow X^2\Pi)$, $CH(B^2\Sigma^- \rightarrow X^2\Pi)$, and the lesser studied $CH(C^2\Sigma^+ \rightarrow X^2\Pi)$. These excited states have energies of 2.876, 3.208 and 3.944 eV respectively.[20]

5.2: Experimental Details

This experiment monitors the CH($A^2\Delta \rightarrow X^2\Pi$), CH($B^2\Sigma^- \rightarrow X^2\Pi$) and CH($C^2\Sigma^+ \rightarrow X^2\Pi$) emission bands originating from MW-activated C/H plasmas using the optical set-up described in Chapters 2 and 3. The states, their respective emissions to the ground state, and the emission wavelength of the 0-0 band head are depicted below in Figure 5.01:

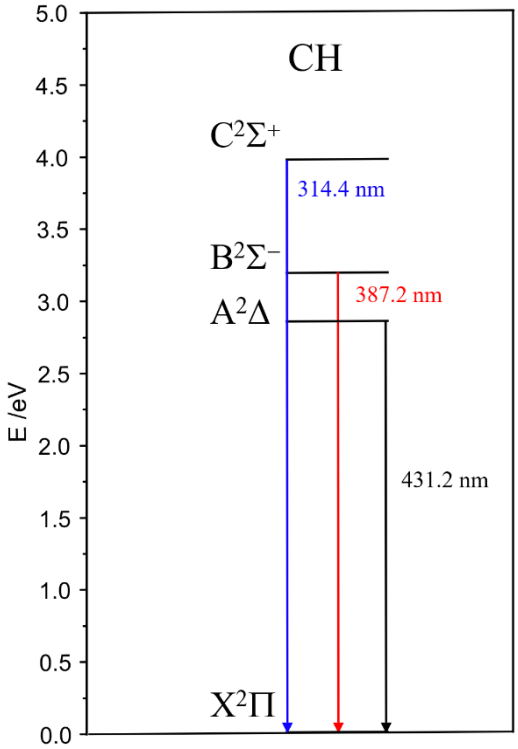

Figure 5.01: 4 lowest lying doublet states of the CH radical, transitions between the three lowest lying excited doublet states of the CH radical and the ground state are indicated by arrows with (0,0) band heads labelled.

The emission intensities of these transitions are henceforth referred to as I_{em}(A→X), I_{em}(B→X), I_{em}(C→X) or, collectively, as I_{em}(CH*). The emissions were monitored with a 50 mm focal length, *f*/14 objective lens attached to an Andor Shamrock 500i Spectrograph. The emissions enter a 10 μm entrance slit and are dispersed using a 700 grooves mm^{-1} diffraction grating. The set-up provides an experimental FWHM ~ 0.09 nm and a spatial magnification of ~ 0.11 on the cooled Andor 940 CCD used for detection. This choice of grating provides a higher wavelength resolution but meant that the CH(C→X) emission had to be recorded separately from the more closely spaced I_{em}(A→X) and I_{em}(B→X) signals. In order to ensure no time-dependent drift in signals between the accumulations of these spectra, the emissions were monitored before and after the data presented in this chapter on a lower resolution (400 groove mm^{-1}) grating, which yields a spectral FWHM resolution of ~ 0.13 nm. The lens aperture was minimised, such that the emission is from across the entire diameter of the plasma, as is assumed in Chapters 3 and 4.

Base conditions were selected as P = 1.5 kW, p = 150 Torr, $F(H_2)$ = 300 standard cm^3 per minute (sccm), $F(CH_4)$ = 19 sccm with the air leak impurity lower than 3 ppm (i.e. the main source of contamination is via the hydrogen feed gas). $F(CH_4)$, P and p were varied over the ranges of $0 \leq F(CH_4) \leq 30$ sccm, $0.7 \leq P \leq 1.85$ kW and $75 \leq p \leq 275$ Torr using a W substrate with a diameter of d_{sub} = 32 mm, placed on a thin Mo spacer wire $d_{wire} = 0.01''$ between the substrate and the water-cooled baseplate.

A further investigation was undertaken into the effect of decreasing substrate diameter. Thinner wire spacers were used for smaller d_{sub} to maintain $T_{sub} \sim 700$ °C for each substrate size under otherwise base conditions. The substrate diameters investigated are d_{sub} = 32 mm ($d_{wire} = 0.01''$), d_{sub} = 27 mm ($d_{wire} = 0.006''$), and d_{sub} = 17 mm ($d_{wire} = 0.004''$) under otherwise base conditions.

5.3: Results and Discussion

5.3.1: Optical Emission Images and Spectral Analysis

The $CH(A^2\Delta \rightarrow X^2\Pi)(0,0)$, $CH(B^2\Sigma^- \rightarrow X^2\Pi)(0,0)$ and $CH(C^2\Sigma^+ \rightarrow X^2\Pi)(0,0)$ band heads appear at λ = 431.2, 387.2 and 314.4 nm respectively. These emissions are contained within the monitored wavelength ranges of (i) 307-382 nm and (ii) 370-447 nm. Figure 5.02 (a) demonstrates a spatially-resolved false colour image monitoring a wavelength range of 307-382 nm, imaging plasma heights between $-3 \leq z \leq 27$ mm, where z = 0 mm defines the top of a 3 mm thick W substrate. Figure 5.02 (b) demonstrates an experimental spectrum of the $CH(C \rightarrow X)$, $\Delta v = 0$, a best fit simulation generated using PGOPHER, a simulation software package, and makes use of rotational constants describing the $C^2\Sigma^+$ and $X^2\Pi$ states taken from Reference 20, and the residual generated by subtracting the simulation from the experimental data.[21] Proposed molecular orbital state diagrams are available in Appendix A5.1.

5. Is it Possible to Probe the Thermal Component of the Electron Energy Distribution Function (EEDF) in MW-activated C/H Plasmas?

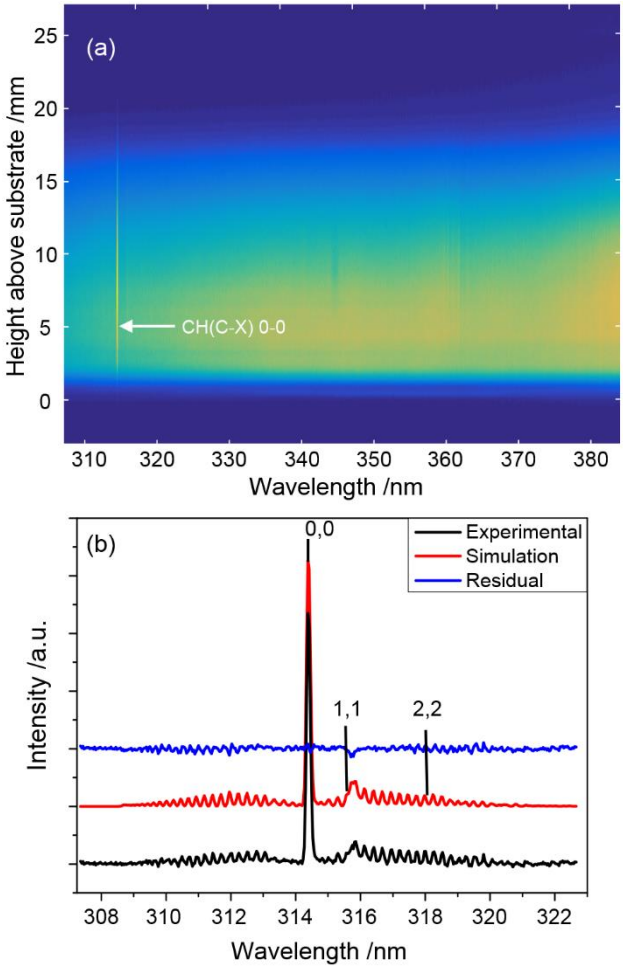

Figure 5.02: (a) $I_{em}(\lambda, z)$ image between the wavelength range of 307-382 nm taken under base conditions, i.e. P = 1.5 kW, p = 150 Torr, $F(CH_4)$ = 19 sccm, $F(H_2)$ = 300 sccm, where z = 0 defines the substrate surface. The band head associated with I_{em}(C→X)(0,0) is labelled. (b) Zoomed wavelength range between 307 and 323 nm illustrating experimental $I_{em}(\lambda)$ between 10.5 ≤ z ≤ 12 mm above the substrate, (black), the best fit CH(C→X) simulation (red) and residual (blue).

Figure 5.03 is a similar figure to that of Figure 5.02 for I_{em}(A→X), $\Delta v = 0$ and I_{em}(B→X), $\Delta v = 0$ with simulations generated using rotational constants for the $A^2\Delta$ and $B^2\Sigma^-$ states. To relate emission intensities to relative excited state column densities, the Einstein-A emission coefficient of each emission should be considered, along with the response function of the set up i.e. the diffraction grating and CCD detector efficiency as a $f(\lambda)$, $\varepsilon(\lambda)$. No attempt has been made to account for these constants in Section 5.3.2. Instead, it is noted that these factors should not impact the relative variation of intensity ratios but should be considered in an attempt to extract T_e estimates.

Section 5.3.2 simply describes the experimental measurements, whilst Section 5.3.3 illustrates how such results might be used for the calculation of spatially-resolved $T_e(z)$. Section 5.3.4 adds insight into the observed experimental trends through a brief comparison with 2-D plasma modelling.

5. Is it Possible to Probe the Thermal Component of the Electron Energy Distribution Function (EEDF) in MW-activated C/H Plasmas?

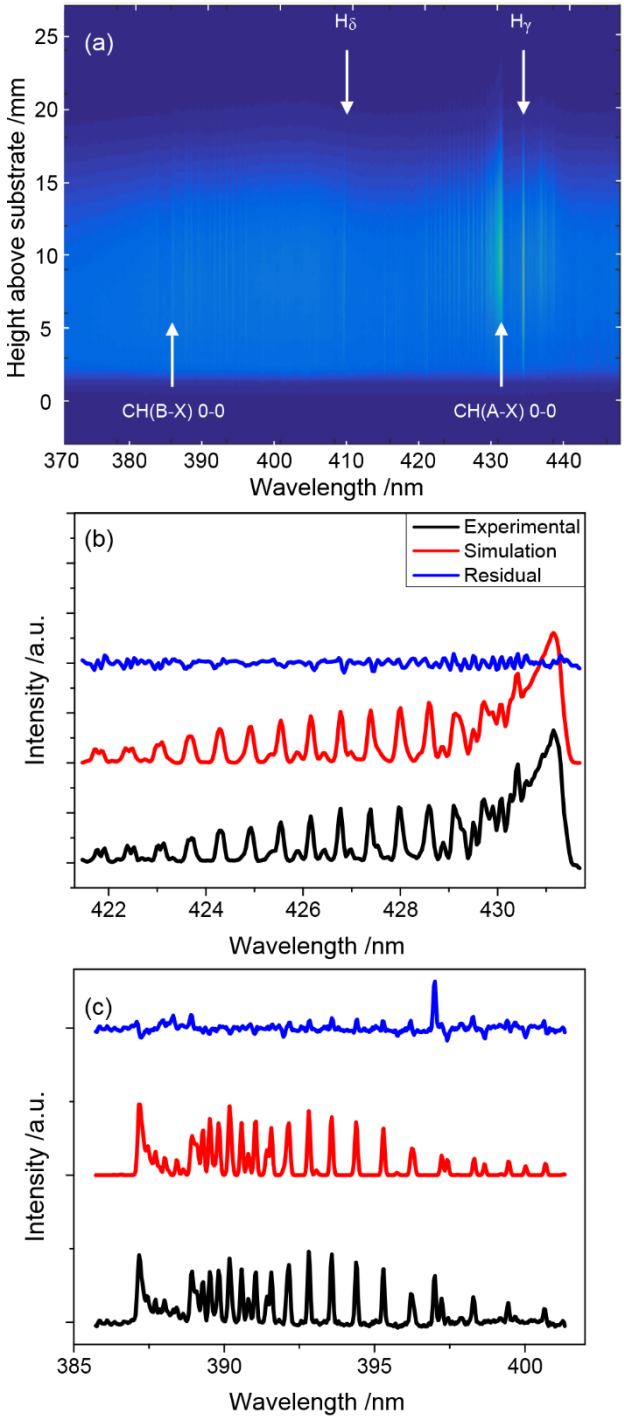

Figure 5.03: $I_{em}(\lambda, z)$ image between the wavelength range of 370-447 nm taken under base conditions, i.e. P = 1.5 kW, p = 150 Torr, $F(CH_4)$ = 19 sccm, $F(H_2)$ = 300 sccm, where z = 0 defines the substrate surface. Two I(H*) emissions and the band heads associated with I_{em}(A→X)(0,0), I_{em}(B→X)(0,0) are labelled. Zoomed wavelength range between (b) 421 - 434 nm and (c) 385 - 402 nm illustrating experimental $I_{em}(\lambda)$ between $10.5 \leq z \leq 12$ mm above the substrate, (black), best fit (b) CH(A→X) and (c) CH(B→X) simulation (red) and residual (blue) for (b) I_{em}(A→X)(0,0) and (c) I_{em}(B→X)(0,0) respectively.

5.3.2: Trends of CH* Emission Intensities with Variation in Process Conditions

I_{em}(CH*) has been analysed using a high spatial resolution of Δz = 1.5 mm for spatial distributions and a low spatial resolution of Δz = 3 mm between the heights of $9 \leq z \leq 12$ mm for variation with process conditions.

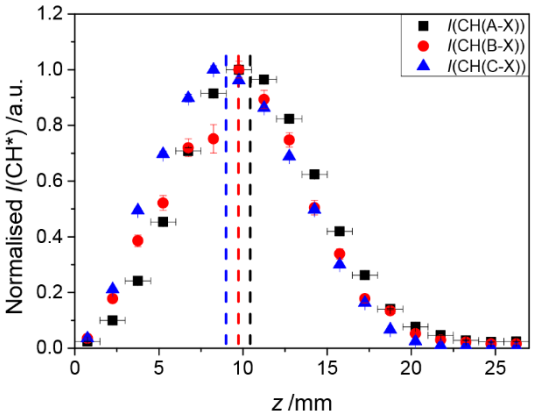

Figure 5.04: Normalised spatial distributions of 3 I_{em}(CH*) bands (identified in the inset) under base conditions. The centre point of the FWHM for each emission band is indicated by a colour co-ordinated dashed line.

Figure 5.04 illustrates normalised I_{em}(CH*)(z) under base conditions. The 3 emission bands have broadly similar spatial distributions, peaking between $8.25 \leq z \leq 11.25$ mm above the substrate with negligible values by $z \sim 27$ mm. The centre point of the full width half maximum (FWHM), indicated by the coloured dashed lines, along with the peak intensity, can be seen to decrease in z with increasing upper state energy. This result, and those that follow have been reproduced twice using two different MW reactors and spectrometers by postgraduate MSc student, Bruno Rodriguez, who worked under my supervision for his MSc research project. The final datasets that feature in his Thesis [22] demonstrate a high z emission component from the CH(C→X) emission band, which only appeared in one of the two investigated reactors. This arose due to the implementation of an incorrect methodology, whilst accumulating data; this had no major bearing on his reported for I_{em}(CH*)(z < 12 mm), or any intensity ratios reported for low plasma heights, nor the results he produced from the second reactor, all of which agree with the results reported in this Chapter. The purpose of drawing attention to these preliminary studies, is that it provides clarity and confirmation that the results reported in this Chapter are not reflecting a slight spatial/wavelength-dependent calibration error but are rather a physical and reproducible observation between different (but comparable) experimental set-ups. The collection and analysis of the data presented in this Chapter is of my own.

Figure 5.05 illustrates the spatial variation in I_{em}(CH*) for p = (a) 75, (b) 150 and (c) 275 Torr under otherwise base conditions, whilst Figure 5.05(d) illustrates I_{em}(B→X)/I_{em}(A→X) and I_{em}(C→X)/I_{em}(A→X), labelled as R(B/A) and R(C/A) respectively as a function of z. As before, the dashed lines indicate the estimated centre point of the FWHM for each of the emission intensities.

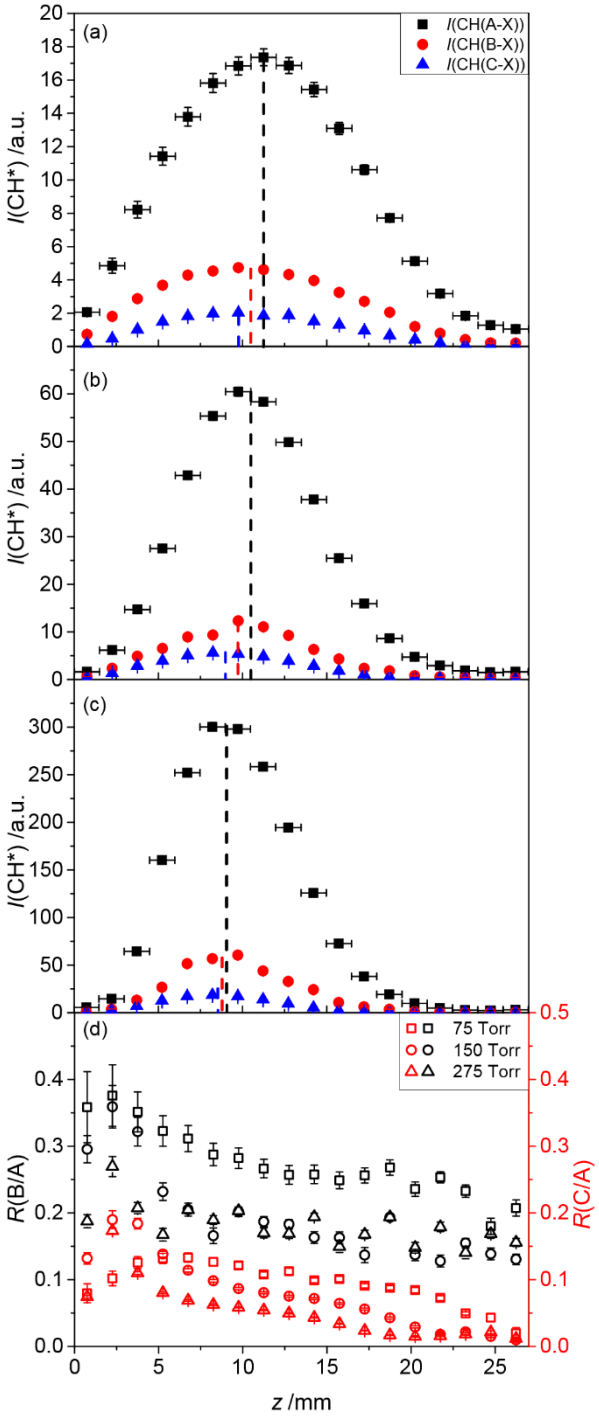

Figure 5.05: I_{em}(CH*) spatial distributions, analysed with a higher spatial resolution of Δz = 1.5 mm, for p = (a) 75 Torr, (b) 150 Torr (i.e. base conditions) and (c) 275 Torr under otherwise base conditions, i.e. P = 1.5 kW, $F(CH_4)$ = 19 sccm, $F(H_2)$ = 300 sccm. (d) Ratios of $I_{em}(B \rightarrow X)/I_{em}(A \rightarrow X)$ and $I_{em}(C \rightarrow X)/I_{em}(A \rightarrow X)$ labelled as R(B/A) and R(C/A) respectively, as a $f(z)$ for p = 75, 150 and 275 Torr under otherwise base conditions.

Comparison of Figures 5.05 (a), (b) and (c) demonstrate that with increasing pressure, (i) the emitting plasma volume contraction, which results in: (ii) the FWHM centre of each emission band intensity decreasing in z, and (iii) an overall increase in each emission band intensity. The decrease in FWHM centre points with z for an increasing upper state energy is almost lost by p = 275 Torr. Figure 5.05 (d)

shows intensity ratios as a function of height for p = 75, 150 and 275 Torr. There are two notable effects demonstrated, the first featuring effect is the spatial variation of the intensity ratios for I_{em}(B→X)/I_{em}(A→X) and I_{em}(C→X)/I_{em}(A→X). Under most pressure conditions, both ratios maximise at z ~ 2.25 mm and decrease with a further increasing z. In the case of I_{em}(B→X)/I_{em}(A→X), at z ~ 20 mm, the ratio has decreased to ~ 35% of its maximum value under base conditions, whilst for I_{em}(C→X)/I_{em}(A→X), this decreases to a negligible ratio.

Figures 5.04 and 5.05 demonstrate that emission intensities above z ~ 20 mm are small relative to the intensity maximum at z ~ 9.75 mm. Prior work has implied that at high z, there is a minor chemiluminescent contribution to the generation of the CH(A) state, and whilst perhaps this data may also be indicating a smaller chemiluminescent contribution to the CH(B) state emission, further speculation is not warranted at this point. Instead, attention is drawn to plasma heights, $z \leq 20$ mm. The second notable effect in Figure 5.05 (d) is the clear decrease in intensity ratios with increasing pressure. The pressure dependency of these emissions (and the ratio of I_{em}(CH(B→X) and I_{em}(CH(C→X) relative to I_{em}(CH(A→X)) are shown in Figure 5.06.

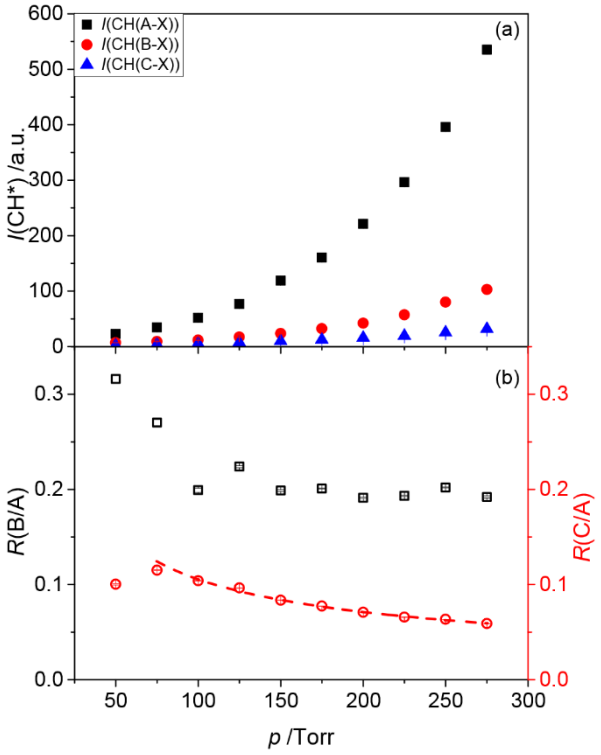

Figure 5.06: (a) I_{em}(CH*) as a $f(p)$, analysed with a lower spatial resolution of Δz = 3 mm between $9 \leq z \leq 12$ mm above the substrate under otherwise base conditions, i.e. P = 1.5 kW, $F(CH_4)$ = 19 sccm, $F(H_2)$ = 300 sccm. (b) Ratios of I_{em}(B→X)/I_{em}(A→X) and I_{em}(C→X)/I_{em}(A→X) labelled as R(B/A) and R(C/A) respectively, as a $f(p)$.

Figure 5.06 (a) illustrates I_{em}(CH*) as a $f(p)$ with more clarity for intensities analysed with a lower resolution of Δz = 3 mm between $9 \leq z \leq 12$ mm above the substrate. The exponents from the relationship I_{em}(CH*) ~ p^n return values of n = 2.2 ± 0.1, 2.0 ± 0.2, and 1.71 ± 0.09 for I_{em}(A→X), I_{em}(B→X) and

I_{em}(C→X) respectively. The attributed error bars, retrieved from the PGOPHER fit, are too small to see, indicative that they are perhaps underestimated. Figure 5.06 (b) illustrates the variation of I_{em}(B→X)/I_{em}(A→X) and I_{em}(C→X)/I_{em}(A→X) as a $f(p)$. Whilst I_{em}(B→X)/I_{em}(A→X) demonstrates a clear decrease with increasing p for $p \leq 150$ Torr, it appears relatively flat for $p \geq 150$ Torr. Hence, there is no clear exponent calculated for the relationship R(B/A) ~ p^n. Comparatively, Figure 5.06 demonstrates I_{em}(C→X)/I_{em}(A→X) ~ p^n for $p \geq 75$ Torr. The red dashed line indicates such a trend and yields an exponent value of $n = -0.57 \pm 0.02$.

The spatial distributions for P = 0.9 and 1.85 kW can be seen in Figures 5.07 (a) and (b) respectively, whilst Figure 5.07 (c) demonstrates the spatially-resolved intensity ratios for P = 0.9, 1.5 and 1.85 kW. With increasing P, there is an expansion in the emitting volume of the plasma, resulting in an increase in FWHM centre height, as well as an increase in I(CH*). The ratios of I_{em}(B→X)/I_{em}(A→X) and I_{em}(C→X)/I_{em}(A→X) decrease between P = 0.9 and 1.5 kW for $z \geq 5$ mm, whilst any difference between these ratios for a further increase in P, i.e. P = 1.5 and 1.85 kW is subtle.

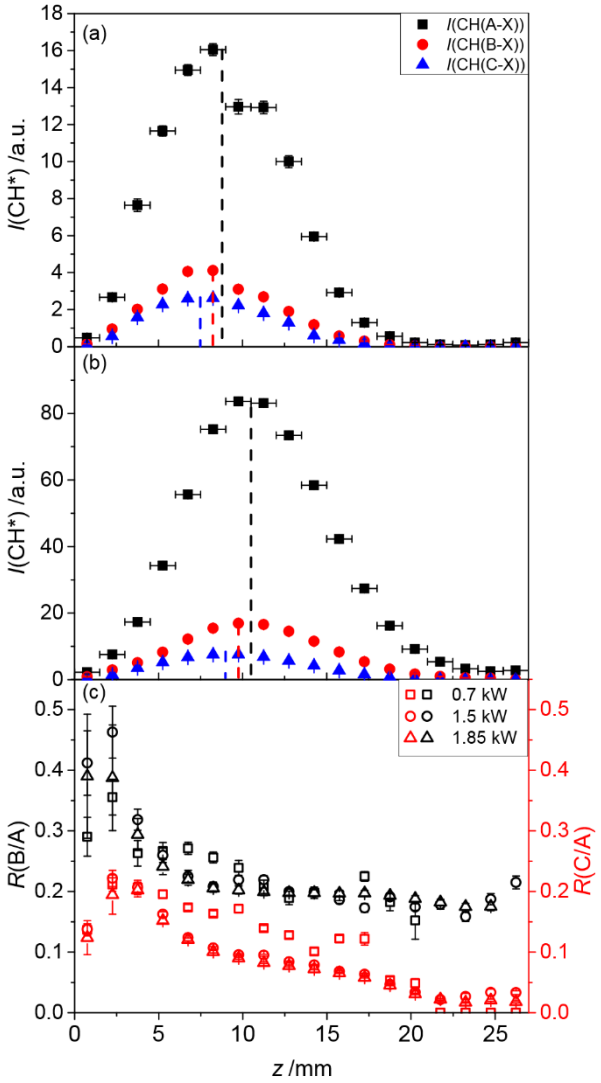

Figure 5.07: I_{em}(CH*) spatial distributions, analysed with a higher spatial resolution of Δz = 1.5 mm, for P = (a) 0.9 kW, (b) 1.85 kW under otherwise base conditions, i.e. p = 150 Torr, $F(CH_4)$ = 19 sccm, $F(H_2)$ = 300 sccm. (d) Ratios of I_{em}(B→X)/I_{em}(A→X) and I_{em}(C→X)/I_{em}(A→X) labelled as R(B/A) and R(C/A) respectively, as a $f(z)$ for P = 0.9, 1.5 (i.e. base conditions) and 1.85 kW under otherwise base conditions.

These findings are reinforced in Figures 5.08 (a) and (b), which demonstrate (a) I(CH*) ~ P^n and (b) I_{em}(B→X)/I_{em}(A→X) and I_{em}(C→X)/I_{em}(A→X) ~ P^n analysed at the lower spatial resolution. I_{em}(A→X) ~ P^n yields an exponent of n = 1.88 ± 0.03, whilst I_{em}(B→X) and I_{em}(C→X) have exponent values of n = 1.69 ± 0.03 and 1.37 ± 0.03 respectively. I_{em}(B→X)/I_{em}(A→X) ~ P^n and I_{em}(C→X)/I_{em}(A→X) ~ P^n retrieve exponents of n = − 0.20 ± 0.03 and − 0.51 ± 0.03 respectively.

5. Is it Possible to Probe the Thermal Component of the Electron Energy Distribution Function (EEDF) in MW-activated C/H Plasmas?

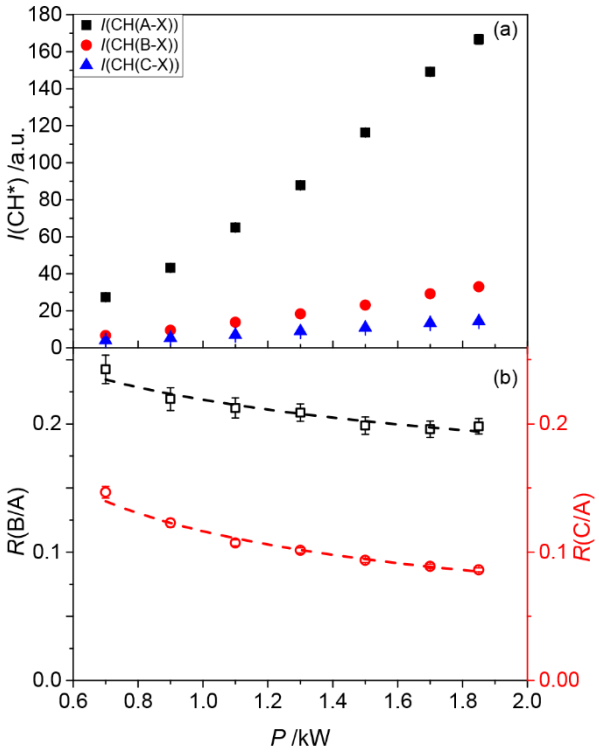

Figure 5.08: (a) I_{em}(CH*) as a $f(P)$, analysed with a lower spatial resolution of Δz = 3 mm between 9 ≤ z ≤ 12 mm above the substrate under otherwise base conditions, i.e. p = 150 Torr, $F(CH_4)$ = 19 sccm, $F(H_2)$ = 300 sccm. (b) Ratios of I_{em}(CH(B→X)/I_{em}(CH(A→X) and I_{em}(CH(C→X)/I_{em}(CH(A→X) labelled as R(B/A) and R(C/A) respectively, as a $f(P)$.

Figure 5.09 illustrates that I_{em}(CH*) bands increase with $F(CH_4)$. This particular experiment was carried out in a less than pristine chamber with regards to carbon contamination, and hence, for $F(CH_4)$ = 0 sccm, some I(CH*) signal is present. At low carbon fractions, I_{em}(CH*) is more sensitive than $I_{em}(C_2^*)$ to the presence of carbon, which was not observed for $F(CH_4)$ = 0 sccm. All 3 bands demonstrate good agreement between their respective exponents for $I_{em}(CH^*) \sim F(CH_4)^n$. I_{em}(A→X) holds an exponent with a value of n = 0.171 ± 0.007, whilst I_{em}(B→X) and I_{em}(C→X) hold exponents of 0.186 ± 0.006 and 0.188 ± 0.005 respectively, i.e. the three exponents for $I_{em}(CH^*) \sim F(CH_4)^n$ are within 2 standard deviations of one another. It is therefore unsurprising that both intensity ratios reported in Figure 5.09 (b) appear relatively flat with increasing methane fraction. The anomalous decrease in I_{em}(C→X)/I_{em}(A→X) for $F(CH_4)$ = 0 sccm under otherwise base conditions is not seen in I_{em}(B→X)/I_{em}(A→X). This observation is noted and reserved for speculation in discussion.

5. Is it Possible to Probe the Thermal Component of the Electron Energy Distribution Function (EEDF) in MW-activated C/H Plasmas?

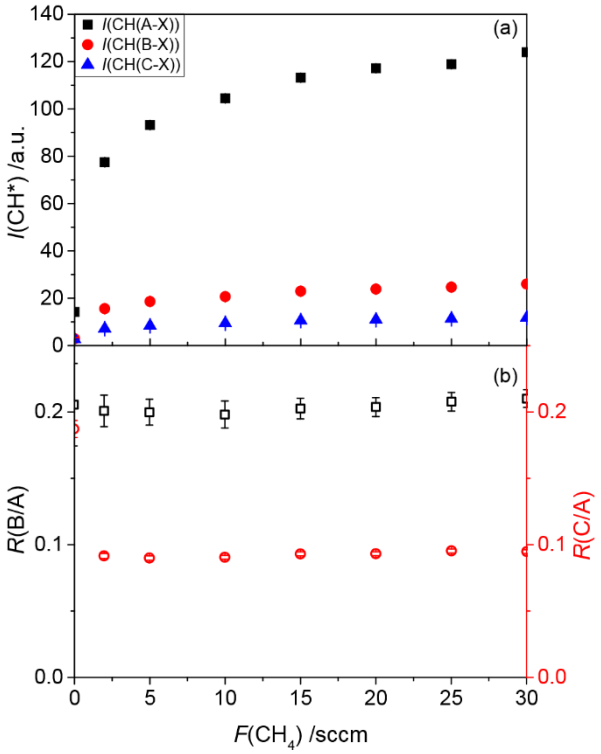

Figure 5.09: (a) I_{em}(CH*) as a $f(F(CH_4))$, analysed with a lower spatial resolution of Δz = 3 mm between 9 ≤ z ≤ 12 mm above the substrate under otherwise base conditions, i.e. p = 150 Torr, P = 1.5 kW, $F(H_2)$ = 300 sccm. (b) Ratios of I_{em}(CH(B→X)/I_{em}(CH(A→X) and I_{em}(C→X)/I_{em}(A→X) labelled as R(B/A) and R(C/A) respectively, as a $f(F(CH_4))$.

Figure 5.10 reports the variation of I_{em}(CH*) with decreasing substrate diameter, d_{sub}, varying spacer wire thickness to ensure T_{sub} ~ 700 °C. The substrate diameters reported in Figure 5.10 are (a) 32 mm, (b) 27 mm and (c) 17 mm with wire thicknesses of 0.01″, 0.006″ and 0.004″ respectively under otherwise base conditions. As before, to alter the substrate, the chamber requires opening and closing, and so a comparison of absolute intensities between substrate diameters may not be reasonable. Assuming, however, that the results may be taken at face value, the main effect of decreasing substrate diameter (and wire thickness) are (i) an increase in I(CH*) and (ii) a minor shift in the centre point of the FWHM of I(CH*) toward the substrate. Figure 5.10 (d) illustrates that the I_{em}(B→X)/I_{em}(A→X) and I_{em}(C→X)/I_{em}(A→X) decrease subtly with decreasing substrate diameter. This difference is most apparent at lower z, i.e. $z \leq 8.25$ mm with values converging for different substrate diameters (and wire thicknesses) at a higher z of ~ 18.75 mm.

5. Is it Possible to Probe the Thermal Component of the Electron Energy Distribution Function (EEDF) in MW-activated C/H Plasmas?

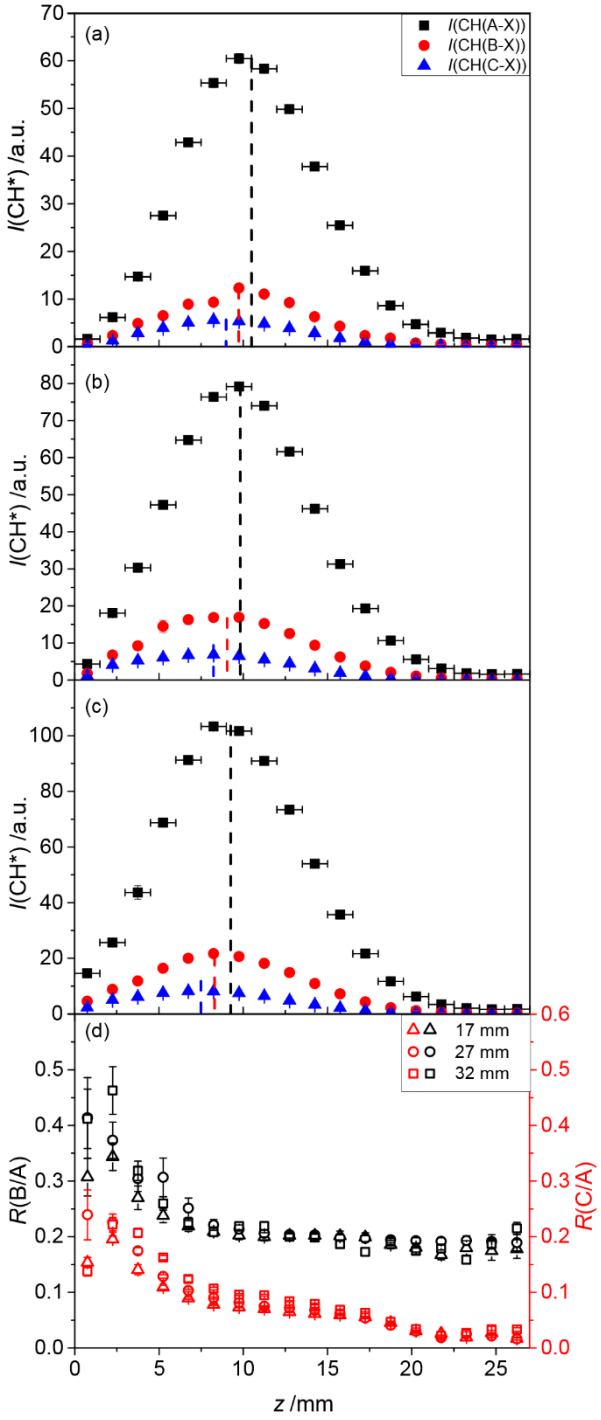

Figure 5.10: I_{em}(CH*) spatial distributions, analysed with a higher spatial resolution of Δz = 1.5 mm, for d_{sub} = (a) 32 mm (i.e. base conditions), (b) 27 mm and (c) 17 mm using 0.01″, 0.006″ and 0.004″ spacer wire thicknesses under otherwise base conditions, i.e. P = 1.5 kW, p = 150 Torr, $F(CH_4)$ = 19 sccm, $F(H_2)$ = 300 sccm. (d) Ratios of I_{em}(B→X)/I_{em}(A→X) and I_{em}(C→X)/I_{em}(A→X) labelled as R(B/A) and R(C/A) respectively, as a $f(z)$ for d_{sub} = (a) 32, (b) 27 and (c) 17 mm under otherwise base conditions.

Attention is now drawn to exploring whether it is possible to probe the thermal component of the EEDF, its spatial and condition variation, i.e. $T_e(z$, conditions) through use of the I_{em}(C→X)/I_{em}(A→X) ratio, so chosen to maximise ΔE between the two emitting states.

5.3.3: CH* ratios as a thermal electron temperature probe?

The number density of an excited state formed by electron impact excitation (EIE) is proportional to the ground state number density, i.e. [CH(X)], the electron density, n_e, the rate coefficient for electron impact excitation (EIE) of the CH(X) state populating the CH(A) state, $k_{EIE}(A \leftarrow X)$. By assuming that EIE is the main form of excitation, and that the plasma is under steady-state, Equation 5.01 can be used to describe the number density of [CH(A)] by equating prominent formation and loss rates:

$$[CH(A)] = \frac{n_e(E)[CH(X)]k_{EIE}(A \leftarrow X)}{A_A + k_{QA}[Q]} \quad (5.01)$$

Here, A_A describes the Einstein-A emission coefficient for the CH(A→X)(0,0) transition, (A_A = 1.87×10^6 s^{-1}), whilst k_{QA} describes the rate coefficient for the quenching of the CH(A) state.[23] This can be achieved, for example, through inelastic scattering. The prominent quencher, *Q*, will likely be *Q* = H_2, H or C_2H_2, i.e. the most prominent species present. Similar equations can be derived for [CH(B)] and [CH(C)]. The CH(A→X) emission intensity, abbreviated to I_A, would be described by Equation 5.02 at any given height above the substrate, *z*:

$$I_A = \varepsilon_{detA} \frac{c}{\lambda_A} A_A \frac{n_e[\mathrm{CH(X)}]k_{EIE}(A \leftarrow X)}{k_{QA}[Q] + A_A} \quad (5.02)$$

Where ε_{detA} describes the detection efficiency at detection wavelength, λ_A. Of the monitored bands, the CH(C) and CH(A) states have the largest difference in energy (E(C) – E(A) = 1.07 eV, *cf.* *E*(B) – *E*(A) = 0.35 eV and E(C) – E(B) = 0.72 eV) and therefore a comparison of these bands would provide the most sensitive probe for a change in T_e. The intensity ratio of I_C/I_A, i.e. *R*(C/A), can be approximated as Equation 5.03 through assuming a Boltzmann relationship for electron impact excitation, where ΔE defines the difference in energies between the two states, i.e. ΔE = 1.07 eV:

$$R\left(\frac{\mathrm{C}}{\mathrm{A}}\right) = R(A)R\left(\frac{1}{\lambda}\right)R(\varepsilon)\frac{(k_{QA}[Q] + A_A)}{(k_{QC}[Q] + A_C)}e^{-\frac{\Delta E}{kT_e}} \quad (5.03)$$

Additional steps between Equation 5.02 and 5.03 are available in Appendix A5.2. Similar equations can also be derived for *R*(B/A), where the Einstein-A emission coefficients are $A_B = 2.63\times10^6$ s^{-1} and $A_C = 1.1\times10^7$ s^{-1}. *R*(λ) is the ratio of the emitting wavelength band heads, *R*(A) is the ratio of the Einstein-A emission coefficients, and *R*(ε(λ)) is the ratio of the equipment response functions at the band head, estimated using indicative values from the supporting specification documents of the grating and CCD sensitivity as a function of λ are available in Appendices A5.3 and A5.4 respectively. These produce values of 1/1.18 and 1/3.88 for comparing λ ~ 380 and 315 nm (i.e. the approximate wavelength of the band heads I_{em}(CH(B→X)(0-0) and I_{em}(CH(C→X)(0-0) respectively) relative to λ ~ 430 nm, the approximate wavelength of I_{em}(CH(A→X)(0-0). The $k_Q(T_g)$ values are poorly characterised for all 3 states with limited data available for the quenching of CH(A) with H_2, H, and C_2H_4 (assumed to be indicative of C_2H_2).[24,25,26,27,28,29] Heinrich *et al.* [24] and Chen *et al.* [27] provide temperature-dependent rate

coefficients (in an Arrhenius equation) for the quenching of the CH(A) state with quenchers H_2 (300 K $\leq T_g \leq$ 950 K) and C_2H_4 (297 K $\leq T_g \leq$ 653 K) respectively, whilst Tamura *et al.* [29] provide similar quenching rate coefficients for H and H_2 calculated between (240 K $\leq T_g \leq$ 1300 K). The temperature-dependent coefficients provided by Heinrich *et al.* [24] and Chen *et al.* [27] are in good agreement with CH(A) quenching rate constants reported at T_g ~ 300 K by Cooper *et al.* [28] for $Q = C_2H_4$ and H_2 and Nokes *et al.* [25] for $Q = H_2$, C_2H_2 and C_2H_4. Under the assumption that the Arrhenius rate equations for CH(A) state quenching provided by Heinrich *et al.* and Chen *et al.* extrapolate to T_g = 3000 K, these equations yield comparable k_{QA} rate coefficients for C_2H_4 and H_2; 4.52×10^{-10} and 5.75×10^{-10} cm^3s^{-1} respectively. Whilst Tamura *et al.* provide overestimations of calculated rate coefficients for T_g = 300 K, their calculated values at T_g = 3000 K reinforces that the calculated rate coefficient for $Q = H_2$ (T_g = 3000 K) is of the correct magnitude, and demonstrate that Q = H and H_2 would be expected to have similar rate coefficients for quenching CH(A). A summary of values for measured / calculated rate coefficients are provided in Table 5.01 for T_g ~ 300 K and 3000 K:

Quenching species, Q	T_g /K	Experimental Rate coefficient / 10^{-10} $cm^3molecule^{-1}s^{-1}$	Calculated Rate coefficient / 10^{-10} $cm^3molecule^{-1}s^{-1}$
H	300	-	0.339 [ref. 29]
H	3000	-	2.653 [ref. 29]
H_2	300	0.123 ± 0.006 [ref. 28], 0.090 ± 0.08 [ref. 25]	0.104 [ref. 24], 0.247 [29]
H_2	3000	-	5.753 [ref. 24], 1.938 [ref. 29]
C_2H_x	300	1.81 ± 0.20 [ref. 28 (x=4)], 1.9 ± 0.1 [ref. 25 (x=2 and 4)]	2.200 [ref. 27, (x=4)]
C_2H_x	3000	-	4.522 [ref. 27 (x=4)]

Table 5.1 Experimental / calculated rate coefficients for the quenching of the CH(A) state, Q = H, H_2, and C_2H_x at T_g ~ 300 K and T_g = 3000 K.

The agreement between the reported rate coefficients for $Q = C_2H_4$ and C_2H_2 at T_g ~ 300 K is an encouraging validation of the assumption that C_2H_4 is indicative of C_2H_2.[25, 27] To calculate the rate for [CH(A)] state quenching with Q, the product of the calculated rate coefficient, [CH(A)], and the number density of quencher, [Q], is required. Under conditions previously modelled by Mankelevich *et al.* [30] ($F(CH_4)$ = 25 sccm, $F(H_2)$ = 500 sccm, F(Ar) = 40 sccm, P = 1.5 kW, p = 150 Torr), [C_2H_2] yields axial (r = 0 mm) number density of ~ 1.05×10^{16} cm^{-3} and 2.81×10^{15} cm^{-3} at z = 0.5 and 10.5 mm respectively. [H_2] yields number densities of two orders of magnitude larger at both heights (1.03×10^{18} cm^{-3} and 3.89×10^{17} cm^{-3} respectively), whereas [H] yields number densities of 8.19×10^{15} cm^{-3} and 3.93×10^{16} cm^{-3} respectively. The comparable rate coefficients and significantly larger [H_2] (relative to [C_2H_2] and [H]) implies that the prominent CH(A) state quencher, Q, is [H_2] under the conditions investigated in this chapter.

Less is known about the quenching temperature dependence of the CH(B) and CH(C) states, however at T_g ~ 297 K, Cooper *et al*. report that as with the CH(A) state, the CH(B) and CH(C) states are more effectively quenched by C_2H_4 than H_2 with similar rate coefficient values. It seems probable that these species follow similar temperature-dependent rate coefficients with increasing T_g, and therefore it would be reasonable to assume that the conclusion drawn for the CH(A) state (i.e. $Q = H_2$) extrapolates to these higher energy CH states by T_g ~ 3000 K. It is also worth noting that the CH(B) state is reported to be collisionally coupled to the CH(A) state by some quenchers, a further justification for focusing on R(C/A).[28]

In the hot plasma region, it is estimated that $k_Q[H_2] \sim 2.2 \times 10^8$ cm^{-3}s^{-1} for the removal of all CH* states, using $[Q = H_2] \sim 3.89 \times 10^{17}$ cm^{-3}. This provides a quenching rate, which is significantly larger than the Einstein-A emission coefficients of the 3 CH* states. If $R(k_Q)$ were to hold a z independence, (i.e. the ratio of quenching coefficients for these 3 CH* states have the same T_g dependency), Equation 5.03 could be further simplified to Equation 5.04, where m is a constant.

$$R\left(\frac{\mathrm{C}}{\mathrm{A}}\right) = m\, e^{-\Delta \mathrm{E}/kT_e} \tag{5.04}$$

This gives the electron temperature a functional form of $T_e(z) = \Delta E/\ln(mI_A/I_C)(z)$. An alternative derivation can be found in the Appendix A5.5, producing the functional form $T_e(z) = \beta/\ln(mI_A/I_C)(z))$, whereby physically one would expect $\beta \equiv \Delta E$. Assuming T_e = 1.22 eV at z = 9.75 mm, m retrieves a value of ~ 4.81, but significantly over predicts T_e at low z. Choosing an alternative T_e / z combination does not act to relieve this problem; generating an agreement at low z generates an underprediction of T_e at higher z. This problem can be addressed through relaxing the physical constraints on $T_e(z) = \Delta E/\ln(mI_A/I_C)(z)$ to $T_e(z) = \beta/\ln(mI_A/I_C)(z))$, whereby β and m are both unknown variables, such that $\beta \neq \Delta E$ (i.e. the difference in energy between the two states is being treated as an unknown variable and is being allowed to vary from its physical value). Varying these parameters can significantly impact the shape of $T_e(z)$. Here, logarithmic rules apply, such that $T_e(z) = 1/\ln(mI_A/I_C)^{\beta}(z))$.

Figure 5.11 demonstrates calculated $T_e(z)$ under base conditions using 3 different combinations of β and m under the assumptions specified above. These are compared to axial (r = 0.5 mm) $T_e(z)$ produced from 2-D modelling of MW-activated C/H plasmas under base conditions. It demonstrates that using the expected values of β (i.e. $\beta = \Delta E$) and m (assuming $R(k_Q) = 1$) underpredicts T_e at all plasma heights. The actual shape of the graph appears reasonable with modelled $T_e(z)$ variation with a negative offset. However, the derivation for Equation 5.04, does not allow for a simple offset, making it difficult to physically justify. Keeping β at the expected value and setting the value of m, such that T_e = 1.22 eV at $z = 9.75 \pm 0.75$ mm, causes a significant overestimation in $T_e(z < 8.25$ mm). Excellent agreement can be produced between calculated and modelled $T_e(z)$ through the use of empirical β and m values, however such values lack a physical justification at present. There are similar issues when attempting

to make use of R(B/A) and R(C/B) to calculate $T_e(z)$. These have not been reported as they do not provide any significant new information.

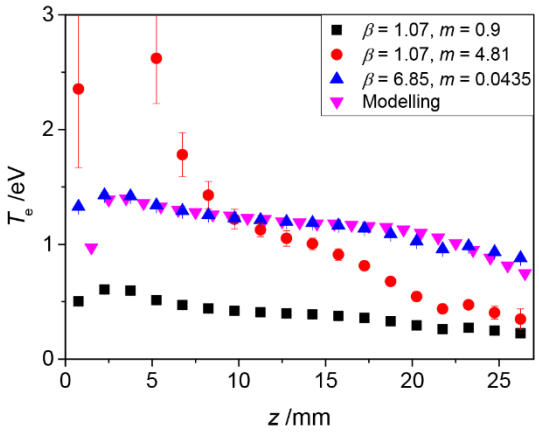

Figure 5.11: $T_e(z)$ calculated using R(C/A) and Equation 5.04 with β = 1.07, m = 0.900, β = 1.07, m = 4.81, and β = 6.85, m = 0.0435. Note that for presentation purposes, the graph has been cut off at T_e = 3 eV, which excludes the data point kT_e = 11.81 ± 2.91 eV and 8.71 ± 2.43 eV at the height of z = 2.25 and 3.75 mm respectively for β = 1.07, m = 4.81 dataset (red circles).

Whilst there are no definitive conclusions that can be drawn from Figure 5.11, there are a few speculative points which can be made. The disagreement between the more physically viable plots (i.e. $\beta = \Delta E$ = 1.07 eV) and the modelled T_e values infers that there is an inaccuracy within one or more of the underpinning assumptions behind the relaxed variant of Equation 5.04.

The most conspicuous assumptions include: (i) $R(k_Q)$ = constant across all plasma heights, i.e. over the gas temperature range $1000 \leq T_g \leq 3000$ K, (ii) the assumed excitation and/or the loss mechanisms for these emitting states are the same and correct, (iii) T_e = 1.22 eV for z = 9.75 ± 0.75 mm under base conditions. Alternatively, although less likely, it is possible that (iv) the modelled T_e values are significantly underpredicted at low plasma heights. This might provide an alternative explanation for the disparity between observed emissions and modelled column densities at low plasma heights in Chapter 3. In any of these cases, the agreement between modelled T_e and those calculated using empirical β and m values could be a red herring.

Using the empirical values deduced for β and m under base conditions and previous $T_e(z)$ for different pressures, Figure 5.12 demonstrates a comparison between modelled and calculated $T_e(z)$ for p = 75, 150 and 275 Torr.

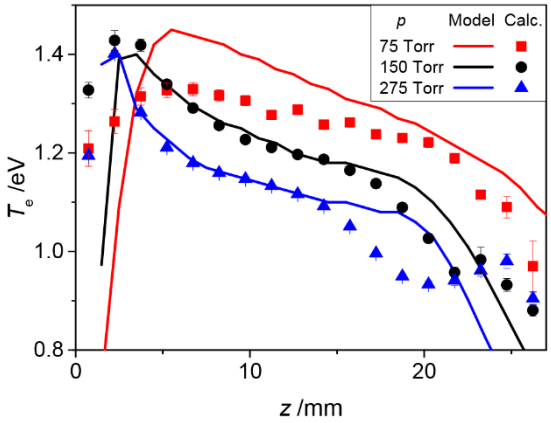

Figure 5.12: $T_e(z)$ calculated using R(C/A) and Equation 5.04 with empirical values, i.e. β = 6.85, m = 0.0435 for p = 75 (red squares), 150 (black circles) and 275 (blue triangles) Torr, under otherwise base conditions. The lines illustrate modelled axial (r = 0 mm) T_e values from 2-D physical chemical modelling for these pressure conditions.

The agreement between modelled and calculated $T_e(z, p)$ infers that the CH bands can still be used to probe the relative variation of the thermal component of the EEDF as a function of height and conditions, however this method is reliant on a well-defined $T_e(z)$ for a single condition. Figure 5.13 demonstrates $T_e(z, P)$, whilst Figure 5.14 demonstrates $T_e(z, d_{sub}$ (d_{wire}))

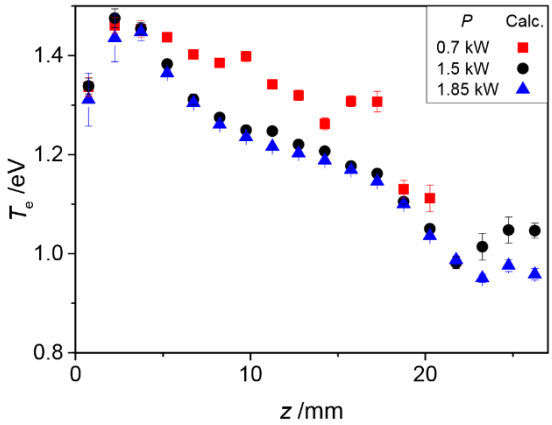

Figure 5.13: $T_e(z)$ calculated using R(C/A) and Equation 5.04 with empirical values, i.e. β = 6.85, m = 0.0435 for P = 0.7 (red squares), 1.5 (black circles) and 1.85 (blue triangles) kW, under otherwise base conditions.

With decreasing P, maximal T_e does vary significantly, but becomes increasingly flat, in agreement with modelling reported for MW-activated H plasmas in Chapter 3. With decreasing substrate diameter, T_e is also calculated to decrease for z < 17 mm. Above which, T_e values are calculated to converge.

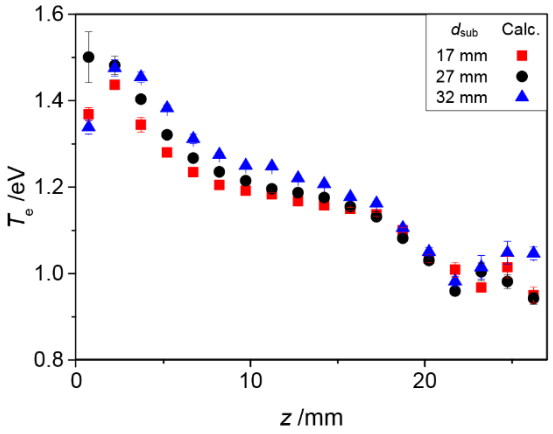

Figure 5.14: $T_e(z)$ calculated using R(C/A) and Equation 5.04 with empirical values, i.e. β = 6.85, m = 0.0435 for d_{sub} = 17 (red squares), 27 (black circles) and 32 (blue triangles) mm, under otherwise base conditions. (Note d_{wire} has been compensatingly decreased with decreasing substrate diameter, such that T_{sub} ~ 700 °C as previously noted).

5.3.4: Discussion with 2-D Physical Chemical Modelling

Excited states above the CH($C^2\Sigma^+$) e.g. CH($D^2\Sigma^+$) are short lived and pre-dissociative. Such states have only observed through absorption e.g. CH($X^2\Pi \rightarrow D^2\Sigma^+$). Such an emission would also be outside of the detectable experimental wavelength range. The CH($D^2\Sigma^+ \rightarrow B^2\Sigma^-$), which would emit close to 300 nm was not observed in preliminary studies carried out by Bruno Rodriguez. Prior literature would suggest that these excited states of the CH radical are predominantly formed through electron impact excitation within MW-activated C/H plasmas with small chemiluminescent contributions to the CH($A^2\Delta \rightarrow X^2\Pi$) emission additionally noted in MW-activated C/H(/Ar) plasmas, as described by Processes 5.05 and 5.06 respectively:

$$e + CH(X) \rightarrow CH(A^2\Delta) + e \rightarrow CH(X) + \gamma + e \quad (5.05)$$

$$C + H + M \rightarrow CH(A^2\Delta) + M \rightarrow CH(X) + \gamma + M \quad (5.06)$$

Whilst Process 5.06 has previously been identified as a proposed chemiluminescent contribution, the pressure dependency of I(CH*) (I(CH*) ~ p^2) can eliminate this mechanism from being a prominent contributor; assuming that the prominent quencher is H_2, such a mechanism might be expected to yield I(CH*) ~ p^3, as the intensity from such a contribution would scale with [H]/[H^2] ~ p, [M = H_2] ~ p and [C] ~ p (not observed). Instead, the pressure dependency infers that any chemuluminescence contribution is most likely a two-body process. The quenching mechanisms and respective rate coefficients of the 3 lowest CH doublet excited states with prominent plasma species (i.e. H, H_2, C_2H_2) under the investigated conditions (T_g ~ 2900 K) are poorly characterised, with the most relevant studies found focussing on the CH($A^2\Delta$) state, as discussed.

The most prominent quencher of CH* states, Q, has been deduced to be H_2 and is described by an example quenching reaction in Process 5.07.

5. Is it Possible to Probe the Thermal Component of the Electron Energy Distribution Function (EEDF) in MW-activated C/H Plasmas?

$$CH^* + H_2 \rightarrow CH_2 + H \qquad (5.07)$$

The 2-D physical chemical modelling, previously described [8,10,30] compares the calculated R(C/A) under base conditions with consideration of EIE (Process 5.06), reactive quenching with H_2 (Process 5.07), and photoemission, described by Process 5.08:

$$CH^* \rightarrow CH(X) + \gamma \qquad (5.08)$$

The modelled column density ratio for $CH(C^2\Sigma^+)/CH(A^2\Delta)$, i.e. $\{CH(C^2\Sigma^+)\}/\{CH(A^2\Delta)\}$ is referred to as $R\{(C/A)\}$, whereby the expectation is that $R\{(C/A)\} \equiv R(C/A)$ once detection efficiencies etc have been considered. Figure 5.15 shows modelled $R\{(C/A)\}$ under base conditions, as calculated with consideration of the prominent formation / loss processes discussed, i.e. Processes 5.05, 5.07 and 5.08. Figure 5.15 demonstrates that the modelled $R\{(C/A)\}$ is expected to peak at $z \sim 5.5$ mm above the substrate with a relatively shallow decrease across the hot plasma region, which contrasts to what is seen experimentally, where R(C/A) peaks at $z \sim 2.25$ mm and decreases sharply with increasing height, as seen in Figures 5.04, 5.06 and 5.09. R(C/A) is reproduced under base conditions in Figure 5.15 for a comparison with modelled $R\{(C/A)\}$ under comparable conditions.

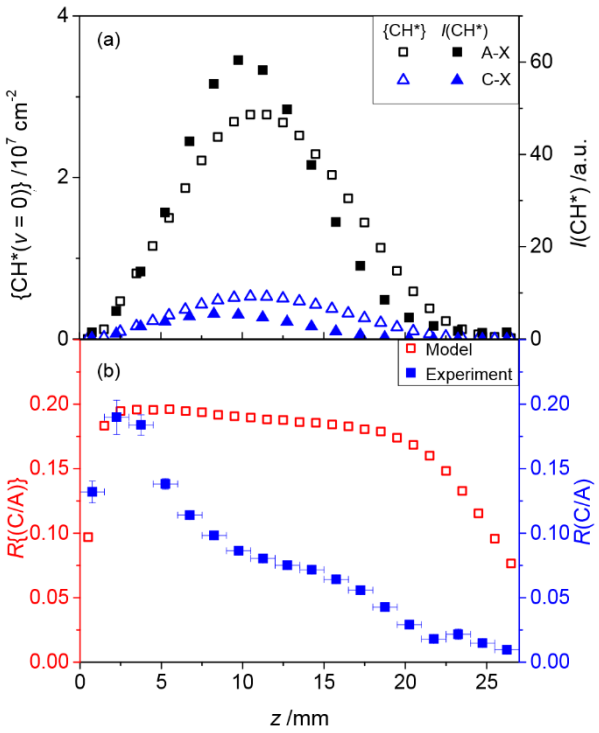

Figure 5.15: I_{em}(C→X), I_{em}(A→X), R(C/A), modelled {CH(A)}, {CH(C)} and their ratio, i.e. {CH(C)}/{CH(A)} labelled as $R\{(C/A)\}$ under base conditions with consideration of Electron Impact Excitation, reactive quenching with H_2, and photoemission.

The inclusion of Processes 5.05, 5.07 and 5.08 alone fails to adequately describe the experimentally observed R(C/A). Similarly, the removal of Process 5.07 also fails to describe the spatial variation of experimental R(C/A) but does act to half the value of $R\{(C/A)\}$; this can be seen in Appendix A5.6. It

seems unlikely, however, that the model is failing to capture the temperature dependence of Process 5.07 and there is no physical justification for its removal.

In Chapter 3, the reduced electric field, E/N, (and consequently T_e and a hyper-thermal electron temperature, T_{tail}) were demonstrated to maximise at $z \sim 2.5$ mm above the substrate in a MW-activated H plasma, for d_{sub} = 32 mm. Consequently, emission intensities, sensitive to T_{tail}, originating from multiple excited states of H_2 (and Ar when present) were demonstrated to maximise in this region. The relative (and in most cases, absolute) low z emission intensities were demonstrated to be enhanced by decreasing pressure, increasing MW forward power, increasing mole fraction of Ar and most dramatically by decreasing substrate diameter (with the largest available spacer wire thickness) from the standard 32 mm (d_{wire} = 0.01″) to 17 mm (d_{wire} = 0.01″ and 0.004″).

These parameters acted to enhance the reduced electric field and, in some cases, (e.g. decreasing substrate diameter) relocate such emissions, which could be observed by eye to originate from the periphery of the substrate, i.e. at $z \sim 0$ mm. The two concerns of such data were an unexplained low z emission intensity contribution resulting from an additional 'hot' electron source close to the substrate and the possibility that emissions originating from the substrate periphery is prone to eclipsing the substrate. The latter concern can be addressed immediately; with R(C/A) maximising at z = 2.5 mm, emission contributions immediately above / below this height are unlikely to be eclipsing the substrate.

The prior concern may be addressed by contrasting $I(H_\gamma)(z)$ to $I(H_\alpha)(z)$ collected with and without methane present respectively for d_{sub} = 17 mm (d_{wire} = 0.004″) under otherwise base conditions (i.e. a comparison of conditions under which the 'hot' electrons were evident in MW-activated H plasmas). Such a comparison can be seen in Figure 5.16 under otherwise base conditions.

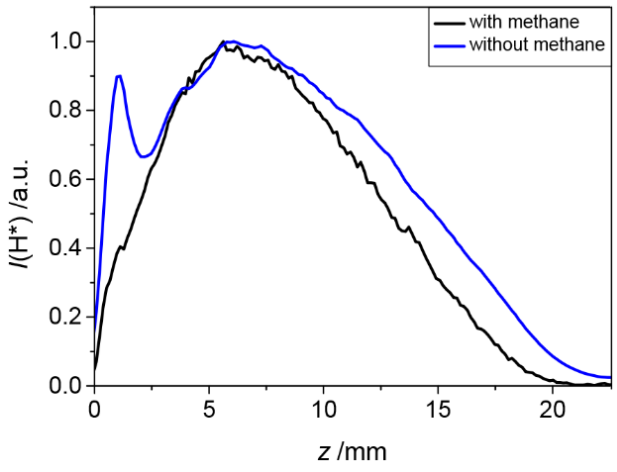

Figure 5.16: Spatial distribution of H Balmer series for d_{sub} = 17 mm, d_{wire} = 0.004″, $F(H_2)$ = 300 sccm, P = 1.5 kW, p = 150 Torr, $F(CH_4)$ = 0 (blue) and 19 sccm (black).

In the methane-free case, $I(H_\alpha)(z)$ demonstrates the familiar bimodal distribution under base p and P conditions in a MW-activated H plasma, with $I(H_\alpha)$ maximising at $z \sim 1$ mm and 6 mm above the

substrate. Comparatively, when methane is present, $I(H_\gamma)(z)$ does not demonstrate this bimodal behaviour for d_{sub} = 17 mm (d_{wire} = 0.004″), i.e. there is no peak intensity for $I(H_\gamma)$ at z = 1 mm, but still maximises at z ~ 6 mm. At this point, it is worth recalling that the model was failing to accurately capture this low z contribution. The introduction of methane acts to introduce high number densities of acetylene and change the prominent ion from H_3^+ (and H_3O^+) to $C_2H_2^+$ and $C_2H_3^+$. The change in prominent cation results in an increased n_e due to the lower ionization energy of C_2H_x ($0 \leq x \leq 6$) species, an exampler of how methane addition results in electron cooling for a constant reduced electric field. It is not unreasonable, therefore, to propose that the disappearance of the low z bimodal behaviour of the H Balmer series spatial distribution with significant methane fractions could be reflecting a decrease in the number of hyper-thermal electrons with their energies reducing to below E = 10.2 eV. The bimodal peak can be forced to appear under base conditions (methane present) for d_{sub} = 17 mm when d_{wire} = 0.01″, however the contribution is minimal relative to the intensity contribution at z = 6 mm and relative to the methane-free case. Additional mechanisms for cooling the 'hot electrons' include collisional cooling and reactive quenching with C_2H_2. These electrons may, however, still hold 'warm' energies exceeding the thermal T_e. As these electrons were not captured in the original MW-activated H plasma modelling, the expectation is that upon the addition of methane any changes to these electrons would not be captured by the present modelling. Such an increase in high energy thermal electrons would consequently be expected to result in electron temperatures exceeding the modelled T_e values, and a failure in capturing the expected increase of R(C/A) at low z. Whilst this effect may have been demonstrated using d_{sub} = 17 mm, where the effect is most prominent, the argument would extend to most explored conditions if this interpretation were correct.

It is also plausible that due to the prominence of C_2H_2 (and C_2H_3), (generated in the hot plasma regions), the electron density (and therefore absorbed power density) are relocated away from the substrate toward the hot plasma regions.

Such interpretations would be consistent with the anomalous decrease observed in R(C/A) for transitioning between $F(CH_4)$ = 0 (carried out in a dirty chamber with an unknown, but sufficiently low C content that $I(C_2(d \rightarrow a))$ cannot be observed) and 2 sccm shown in Figure 5.09. Such a change in C content would result in a significant n_e increase. For a ~ constant reduced electric field, the increase in n_e would act to decrease T_e. A similar drop would not necessarily be expected for R(B/A) if they are collisionally coupled under such p and P conditions, as already speculated.[28] It is worth noting, however, that $I_{em}(B \rightarrow X)$ and $I_{em}(C \rightarrow X)$ are sufficiently small for $F(CH_4)$ = 0 (dirty chamber), and although PGOPHER provides a good spectral fit, it would not necessarily require a significant change or time variation in either measured intensity to double / half the ratio.

Under the interpretation of additional 'warm' electrons neglected by the modelling, it would be unsurprising that R(C/A) maximises at the same height as E/N and T_e, with sufficient sensitivity to the

thermal component of the EEDF to enable the band ratio to calculate relative (and once calibrated, absolute) changes in the spatially-varying T_e across a range of pressure and power conditions.

An alternative explanation behind the discrepancy of modelled $R\{(C/A)\}$ and experimental $R(C/A)$, could be additional formation / loss mechanism(s), affecting either (or both) states. Such a mechanism would require $R(C/A)$ to still have the demonstrated sensitivity to the reduced electric field and might account for the requirement of empirical factors in the calculation of T_e. This second possibility is explored in Section 5.3.5 with adjustments to the 2-D physical chemical plasma modelling.

5.3.5: Alternative Interpretation; Modifications to the 2-D Physical Chemical Modelling

As established, Reaction 5.07, reactive quenching of CH* with H_2, has limited data available for the excited states of CH*. There is even less information on the possibility of Process 5.07 being a reversible reaction (i.e. an alternative CH* excitation mechanism, chemiluminescence via H-shifting of the CH_2 radical).

Such a reaction would be a two-body process (as established is likely required to explain the pressure dependency of I(CH*)) and would be expected to predominantly populate the ground state of the CH(X) radical. Such a reaction could, however, be envisaged to include a thermal Maxwell-Boltzmann contribution, contributing to the population of excited CH* states.

$$CH_2(a^1A_1) + H \rightarrow CH^{(*)} + H_2 \qquad (5.09)$$

Figure 5.17 demonstrates the energetics of Process 5.09 in producing CH* states, illustrating that it is plausible that a high energy tail of the reactants, described by a Maxwell-Boltzmann distribution centred on T_g = 3000 K, could facilitate such a chemiluminescent contribution. The plotted value, $f_E(E)$, describes the number of reactants on a Maxwell-Boltzmann distribution (for T_g = 3000 K, i.e. 0.259 eV) with a particular energy as a function of reactant energy. With an appropriate normalisation, the full integral of $f_E(E)\mathrm{d}E$ provides the number of reactants present at a singular position, whilst a partial integral could provide the number of reactants that could provide a chemiluminescent contribution.

It is evident from Figure 5.17 that such an excitation mechanism is endothermic and would preferentially excite the lower lying CH(A) state (*cf.* the CH(C) state) with a $f_E(E)$ value two orders of magnitude larger than that calculated for the CH(C) state at T_g = 3000 K. This excitation mechanism would be most prominent where [CH_2] and [H] maximise (i.e. in the hotter regions of the plasma) and would act to decrease $R(C/A)$ in this region. The requirement would be that such a mechanism has comparable (or larger) excitation rates to those of electron impact excitation for one or more of the CH* states in the hot plasma regions.

5. Is it Possible to Probe the Thermal Component of the Electron Energy Distribution Function (EEDF) in MW-activated C/H Plasmas?

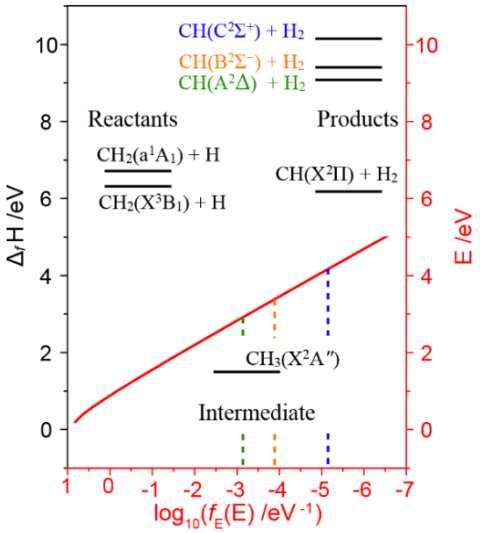

Figure 5.17: The sum of the heat of formation are shown for reactants CH_2 (for two different states) and H, ground state intermediate CH_3, and products $CH(X^2\Pi) + H_2$ in the reaction $CH_2 + H \rightarrow CH(X^2\Pi) + H_2$. It can be seen that the formation of $CH(X^2\Pi)$ via this route is exothermic by ~ 0.53 eV. The red curve demonstrates a Maxwellian-Boltzmann distribution centred on T_g = 3000 K (i.e. 0.259 eV) using a logarithmic scale. The intersecting dashed lines colour co-ordinate with excited states of CH and indicate the expected $f_E(E)$ for the excited states of CH, once degeneracies have been accounted (acting to half values for CH(B) and CH(C) relative to CH(A) and CH(X)), assuming that they could be populated by with a Boltzmann-like distribution (relative to the ground state of $CH(X^2\Pi)$) via $CH_2 + H \rightarrow CH^* + H_2$.

Through the inclusion of Process 5.09, there is no noticeable improvement in spatial agreement of I_{em}(CH*) and {CH*}, however the spatial variation of R{(C/A)}(z) reproduces measured R(C/A)(z) more closely, as demonstrated in Figure 5.18.

The modelling infers that the rate for populating the CH(A) state via H-shifting of the $CH_2(a^1A_1)$ radical compares to that of EIE at z = 10.5 mm, whilst the CH(C) state is predominantly populated by EIE relative to any such chemiluminescent contribution at z = 2.5 and 10.5 mm. Table 5.02 provides example formation / loss rates for conditions found at z = 2.5 and 10.5 mm above the substrate. The reported EIE rates are comparable to those calculated for the modelling featuring in Figure 5.15, where chemiluminescent contributions were omitted.

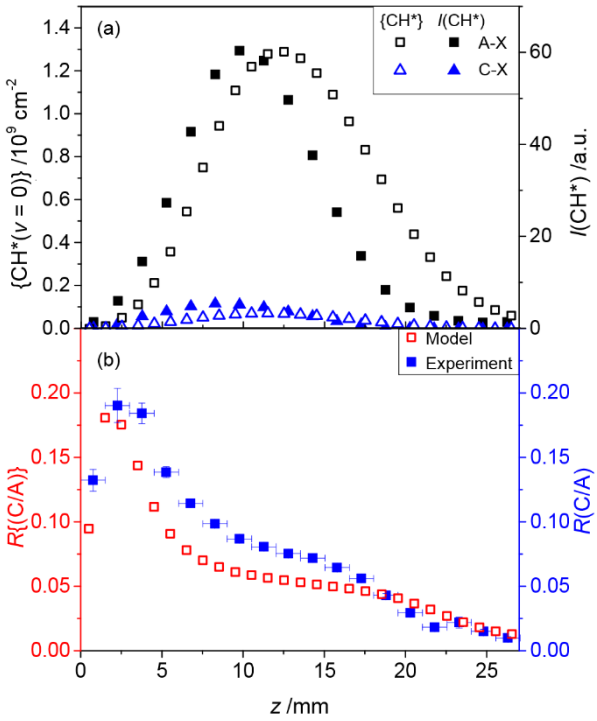

Figure 5.18: I_{em}(C→X), I_{em}(A→X), R(C/A), modelled {CH(A)}, {CH(C)} and their ratio, i.e. {CH(C)}/{CH(A)} labelled as R{(C/A)} under base conditions with consideration of Electron Impact Excitation, reactive quenching with H_2, photoemission, and an additional chemiluminescence contribution via Reaction 9.

Comparable agreement can also be achieved by including chemiluminescent contributions from Processes 5.10 and 5.11:

$$CH_2(X^3B_1) + H \rightarrow CH^{(*)} + H_2 \qquad (5.10)$$

$$C + H_2 \rightarrow CH^{(*)} + H \qquad (5.11)$$

All three mechanisms (modelled individually) provide comparable agreement with the reported experimental trends for I_{em}(CH*) and R(C/A) as a function of pressure and power; whilst these modelling results are noted, they are not reported in this Thesis. With the experimental (and modelling) resolutions available, it is not feasible to distinguish between these mechanisms. The discussion put forward using Process 5.09 regarding larger contributions in hotter plasma regions (acting to reduce R{(C/A)} therefore applies to the additional plausible chemiluminescent contributions discussed above.

It is, however, worth noting the agreement between R(C/A) and R{(C/A)} in Figure 5.15 (where chemiluminescent reactions were omitted) for $z \leq 4.5$ mm. The inference is that once experimental factors and reactive quenching have been considered, electron temperatures can be estimated for these plasma heights (and associated gas temperatures), but that for higher plasma heights, where $T_g > 2000$ K, there is a significant chemiluminescent contribution, which acts to favour the population of the CH(A) state and therefore reduces the measured R(C/A) ratio (and the inferred T_e, as noted in the discussion surrounding Figure 5.11 in Section 5.3.3).

5. Is it Possible to Probe the Thermal Component of the Electron Energy Distribution Function (EEDF) in MW-activated C/H Plasmas?

	Production / loss rate of CH(A) state /10^{13} $cm^{-3}s^{-1}$		Production / loss rate of CH(C) state /10^{13} $cm^{-3}s^{-1}$	
z /mm / Mechanism	2.5 mm	10.5 mm	2.5 mm	10.5 mm
CH + e → CH* + e	**30.2**	133	**17.4**	**69.3**
$CH_2(a^1A_1)$ + H → CH* + H_2	3.56	**471**	0.0629	27.2
CH* + H_2→$CH_2(a^1A_1)$ + H	**33.2**	**590**	**16.7**	**91.4**
CH* → $CH(X^2\Pi)$ + γ	0.607	14.4	0.670	5.11

Table 5.2: Rate constants for conditions (T_g /K, T_e, /eV, E/N×a /Td, [H] /10^{16} cm^{-3}, [H_2] /10^{17} cm^{-3} [$CH_2(a^1A_1)$] /10^{11} cm^{-3}, [CH(A)] 10^6 /cm^{-3}, [CH(C)] / 10^5 cm^{-3}) present at z = 2.5 mm (2380, 1.36, 36.3, 3.65, 4.27, 5.66, 3.28, 6.09) and 10.5 mm (3150, 1.19, 29.6, 7.21, 14.9, 3.84, 77.8, 46.4) respectively.

Table 5.2 demonstrates that the rate of CH(C) excitation (relative to CH(A)) via $CH_2(a^1A_1)$ + H → CH* + H_2 is ~ 5%, slightly higher than the 2 orders of magnitude expected from Figure 5.17. This may be reflective of the higher T_g (~ 3150 K) used to produce the values presented in Table 5.2.

The dependency on both T_g (for the population of CH(A)) and T_e for the production of CH(A) and CH(C) provides an alternative rationale behind why the R(C/A) is sensitive to E/N, and therefore T_e, whilst the ratio itself cannot be treated as a simple Boltzmann population, (i.e. a calculation of T_e from such ratios requires the use of empirical values (rather than the physical value) for describing the difference in energy between the CH(A) and CH(C) states). Further, this conclusion would extend across the full parameter range investigated, as indicated by the similarity of R(C/A)(z) within the parameter range, to that seen under base conditions. The success in calculating $T_e(z)$ using R(C/A)(z) using empirical values for changing process conditions should therefore be approached with a healthy caution.

There is yet a further implication of Processes 5.09 and 5.10 if confirmed as prominent excitation mechanisms, which could act to undermine the assumed C_2(d) excitation mechanism in Chapter 4. It is already acknowledged that the metastable $C_2(a^3\Pi)$ state, which holds significantly larger number densities than the $C_2(X^1\Sigma)$ ground state due to its low energy and six-fold degeneracy, is populated via Process 5.12. It would be unreasonable for H-shifting chemiluminescent reactions to contribute to the population of low-lying CH* states of the CH radical and the $C_2(a^3\Pi)$ state, without considering whether it could contribute to the production of the low-lying $C_2(d^3\Pi)$ state.

$$C_2H + H \rightarrow C_2^{(*)} + H_2 \qquad (5.12)$$

Further modelling reveals that the inclusion of such a chemiluminescent excitation mechanism for the low-lying C_2(d) state would also have a comparable excitation rate to that of EIE for z = 10.5 mm.

Chapter 4, Figure 4.11 demonstrated C_2(d→a) (and its anion counterpart C_2^-(B→X)) emissions for d_{sub} = 17 and 32 mm, d_{wire} = 0.004″ and 0.01″ respectively (under otherwise base conditions). This Figure, and the T_{rot} (~ T_g) values associated with the best fit ro-vibronic analysis provided by PGOPHER, were shown in Figure 4.12. These have been reproduced below for convenience.

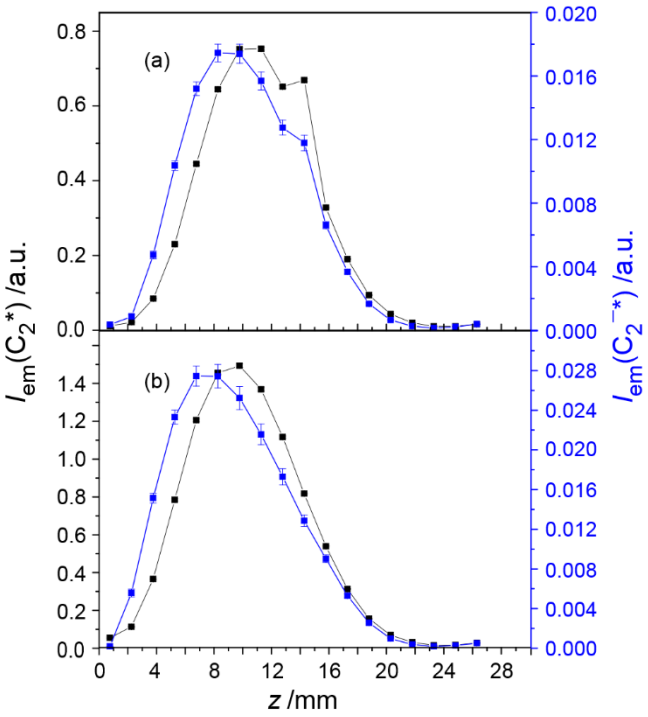

Figure 4.11 (repeated): Spatially-resolved distributions of $I_{em}(C_2^{-*})$ (blue squares with an indicative blue line) and $I_{em}(C_2^*)$ (black squares with an indicative black line) for (a) d_{sub} = 32 mm on a 0.01″ wire, and (b) d_{sub} = 17 mm on a 0.004″ wire under otherwise base conditions using a spatial resolution of 1.5 mm.

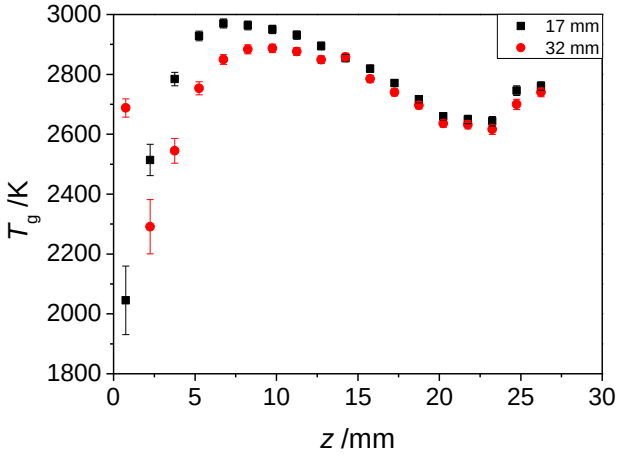

Figure 4.12 (repeated): Spatially-resolved T_g for d_{sub} = 32 mm on a 0.01″ wire, red, and d_{sub} = 17 mm on a 0.004″ wire (black) under otherwise base conditions for z < 21 mm; the data this was extracted from the PGOPHER spectral simulation best fits of data shown in Figure 4.11 using a spatial resolution of 1.5 mm.

Figure 4.11 demonstrates two notable features: the first, is the lower peak intensity of $I(C_2^-*)$ when compared to $I(C_2*)$. Whilst this is attributed to differences in proposed parent species (C_2H and $C_2(a)$) in Chapter 4, if the $C_2(d)$ state truly does hold a significant chemiluminescent contribution, the difference between these spatial profiles would be more reflective in differences in n_e (noting $I(C_2^-*)$ was found to be formed via dissociative electron attachment of C_2H), [H], (noting C_2^-* is predominantly quenched by H atoms, whilst $C_2(d)$ is predominantly lost via photoemission under base conditions), and [H]/[H2], which the $C_2(d)$ state would still be more sensitive to. The second notable feature is an increase in both intensities, but a relative decrease in $I(C_2^-*)/I(C_2*)$. These latter points are returned to.

It is clear from Figure 4.12 that T_g increases and maximises closer to the substrate using a smaller d_{sub}, but T_g can be seen to converge at $z \sim 0$ and 20 mm. The low z convergence of T_g was a deliberate consequence of d_{wire} thickness choice, whilst the convergence of T_g at high z is likely a reflection that the quartz window temperature is cooled by constantly flowing air at room temperature, therefore loosely acting as a $T_{quartz} \sim$ constant boundary condition. The increase in T_g between these heights is indicative of an increase in absorbed power density and is consistent with previous 2-D plasma modelling of MW-activated H plasmas.[9] Such an increase in absorbed power density and gas temperature may result in further thermal dissociation of H_2 and ionization of C_2H_2, increasing both $[H]/[H_2]$ and n_e (decreasing T_e). Dependent on interpretation, either (or both) of these plasma parameter changes might act to produce the observed decrease in R(C/A) (and therefore calculated decreases in $R(C/A)(z, d_{sub})$ and $T_e(z, d_{sub})$) with decreasing d_{sub}, as can be seen in Figures 5.09 and 5.13 respectively.

With an increase in $[H]/[H_2]$, one may also expect the relative chemiluminescent contribution of the CH(A) state to increase in the hotter plasma region, which would result in a decrease in R(C/A) at higher z (and perhaps therefore enhance the maximisation of R(C/A) at low plasma heights *cf.* the hotter plasma region). The relocation in maximal T_g would act to alter the height of maximal [H], ($[H]/[H_2]$ and n_e) production toward the substrate, and hence the H Balmer intensity profile was demonstrated in Figure 5.16 to maximise closer to the substrate at $z \sim 6$ mm, (*cf.* I(H*) maximising at $z \sim$ 7-7.5 mm for d_{sub} = 32 mm, d_{wire} = 0.01″ observed in Chapters 3 and 6).[9]

There is also a relocation in peak $I_{em}(C_2*)$ towards the substrate, which could be indicative of varying $n_e(z)$ and/or changes in $[H]/[H_2](z)$. As both of these parameters vary in such a way so as to have comparable impacts on the measured intensities (and intensity ratios) for a decreasing substrate diameter, it is not possible to conclude as to whether EIE (with an unconsidered 'warm' / thermalised n_e present at low z) or the H-shifting chemiluminescent excitation mechanism dominate under the investigated conditions.

Additional variation of parameter spaces within the accessible range, are not necessarily thought to resolve this inconclusive controversy. The addition of argon, for instance, will act to increase $[H]/[H_2]$, which could also act to increase n_e (and therefore to decrease T_e). Despite the decrease in absorbed

power density, shown for MW-activated H(/Ar) plasmas (which resulted in T_e remaining ~ constant), there are more H atoms present, which speculatively could increase H addition reactions to C_2H_2, generating a larger [C_2H_3] steady-state concentrations. C_2H_3 has a substantially lower ionization energy and an enhancement in its generation could hence increase n_e and decrease T_e. Therefore, if Ar addition were to increase T_g or decrease T_e, it would act to decrease R(C/A) and would therefore not help in distinguishing between chemiluminescent contributions and EIE contributions, and hence argon has not been investigated in this study.

Perhaps the most significant result for distinguishing these mechanisms is the subtle anomalous decrease observed in R(C/A) for $F(CH_4)$ = 0 and 2 sccm under otherwise base conditions. The significantly increased carbon fraction would be expected to result in a large T_e decrease and an insignificant increase in [H]/[H_2], consistent with observation. Whilst not observed in R(B/A), this might be accounted for if the CH(B) and CH(A) states were collisionally coupled at such pressure conditions (another alternative excitation mechanism). It could, however, also be reflecting a time-evolving I_{em}(CH*) as C content is being etched into the plasma for $F(CH_4)$ = 0 sccm; there has been no further evidence as of yet, that this was not the case. Further, there might be an expected continual decrease in T_e (and therefore R(C/A)) with further methane addition (not observed).

5.4: Conclusions

Three low-lying doublet excited states of the CH radical have been monitored by their optical emissions through spatially-resolved imaging. These emissions, and their spatially-resolved relative ratios, have been investigated as a function of methane flow, total gas pressure, input microwave power, and substrate diameter. Using empirical values (within a Boltzmann distribution) and a known $T_e(z)$ for base conditions, electron temperatures can be estimated as a function of process conditions, e.g. p and P. The implication is that the ratio of these emission bands is somewhat sensitive to the thermal component of the electron energy distribution function.

The reliance on empirical values in calculating $T_e(z)$ and the failure of 2-D plasma chemical modelling to capture the spatial variation of CH* radical intensity ratios infers that there is a missing component within the model and / or T_e calculations. The prominent quencher of the CH* states is deduced to be H_2 under the explored conditions. With 2-D modelling, the removal of CH* quenching with H_2 acts to half the calculated column density ratio between the CH(C) and CH(A) states. Whilst it would be unphysical to infer that such a mechanism could simply be active at some heights and not others, it does highlight that a change in prominent quenching mechanism as a $f(z, [Q], T_g)$ for one or more of these states could theoretically account for the spatial variation in the observed experimental intensity ratios. However, additional quenching mechanisms of CH* with other potential candidates, e.g. with H atoms, have also been considered (in Section 5.3.3 and within the plasma modelling) and is deemed unlikely to yield a sufficiently high quenching rates to compete with $Q = H_2$ between T_g ~ 300 K and 3000 K.

Instead, two alternative explanations are proposed; the first is the presence of 'warm' electrons at low plasma heights, which the modelling has previously failed to capture in MW-activated H plasmas. The second proposal is one or more of three alternative chemiluminescent excitation mechanisms contriubuting in the hot plasma region. This chapter focuses on preliminary modelling studies of one such mechanism (H-shifting reaction acting on $CH_2(a^1A_1)$, in addition to electron impact excitation of the CH(X) radical), which acts to prominently generate CH(X), but also the various excited states of the CH radical with a Maxwell-Boltzmann contribution, but also notes there could be additional / alternative chemiluminescent contributions from the $CH_2(X^3B_1)$ radical and from C atoms. At present, it is not possible to distinguish or infer relative contributions of these possible contributions.

The first explanation seems feasible, the addition of methane is known to reduce T_e and T_{tail}. The disappearance of a bimodal I(H*) contribution at low z (d_{sub} = 17 mm, d_{wire} = 0.004″, $F(H_2)$ = 300 sccm, P = 1.5 kW, p = 150 Torr) upon the addition of methane may be demonstrative of a cooling of 'hot' electrons present in MW-activated H plasmas to 'warm' electrons with energies ≤ 10.2 eV in MW-activated C/H plasmas. These electrons (and similar electron densities evidenced by H_2* maximisation at z = 2.5 mm in MW-activated H plasmas in Chapter 3) were not captured in the modelling of MW-activated H plasmas, and therefore would not likely be described in further modelling of MW-activated C/H plasmas. The impact of including these electrons in the 2-D modelling might be to improve agreement between the ratios of modelled column densities and measured intensities of the CH* states. A superficial enhancement of T_e at low z in additional modelling, however, does not appear to alter the ratio distribution in a meaningful manner.

In keeping with the thesis title, the latter interpretation provides an alternative excitation mechanism for the CH(A) (and possibly the CH(B)) state. The proposed endothermic chemiluminescent reactions would act to significantly favour the excitation of the CH(A) state in the hot plasma region, whereby reactant [H] (or [C]) atoms are more prominent. Hence, there is a decrease in the relative ratio of modelled {CH(C)}/{CH(A)} state ratios in the hot plasma region. Comparatively, in this scenario, the CH(C) state is still predominantly excited via EIE (*cf.* a chemiluminescent contribution). As such, a ratio between the two states would still be expected to remain somewhat sensitive to the thermal component of the EEDF. With the inclusion of chemiluminescent mechanisms, there is an agreement between the spatial variation of the modelled column density and measured intensity ratios of the CH* states, as well as a rationale behind the requirement of empirical values in the calculation of $T_e(z)$. In some chemiluminescent contribution cases, the conclusion would also extend to the C_2(d) state, with a chemiluminescent H-shifting contribution yielding comparable rates to EIE in the hot plasma region.

One means to test this would be to carry out a comparative study between the C_2(d→a) triplet band and the C_2(C→A) singlet band, the latter of which is transitioning from a significantly higher energy state and is subtly present within Figure 5.03 (a), featuring at λ = 385 nm.

Also in keeping with the thesis title, there may also be minor hints that CH(B) and CH(A) states could be collisionally coupled, (i.e. M + CH(B) → CH(A) + M (+ 0.332 eV)), as might be indicated by the subtle deviations of $I_{em}(B\rightarrow X)/I_{em}(A\rightarrow X)$ (*cf.* $I_{em}(C\rightarrow X)/I_{em}(A\rightarrow X)$), i.e.. the pressure dependency of these ratios plateaus for $p \geq 150$ Torr under otherwise base conditions.

The inconclusive nature of this chapter highlights an incomplete understanding on the increasingly more complex processes that could be occurring within MW-activated C/H plasmas. Further, it highlights the awkward difficulty in decoupling the plasma parameter effects from one another with the experimental variables / ranges available. In this instance, it has proven difficult to distinguish between the impact of increasing $[H]/H_2]$ and a reduction in T_e; increasing P and p both act to increase $[H]/[H_2]$ and decrease $n_e(E \sim 3.944 \text{ eV})/n_e(E \sim 2.876 \text{ eV})$, whilst decreasing d_{sub} acts to increase $[H]/[H_2]$ and decrease $n_e(E \sim 3.944 \text{ eV})/n_e(E \sim 2.876 \text{ eV})$.

Further studies with very low methane fractions might prove the most informative distinguishment if carried out with sufficient signal-to-noise ratio. Such a study would require careful consideration of methane mass flow controller to enable control over small $F(CH_4)$ ($\leq$ 1 sccm) or the use of dilute methane/hydrogen mixtures. Either method would likely prove somewhat problematic with the anticipated reduction in intensity signals (and consequential signal-to-noise reduction).

Whilst still sensitive to T_e, the implication of this study is that one should approach with caution in attempting to make use of these emission bands to monitor variation of T_e. For diamond growers measuring these optical emissions as an *in situ* diagnostic analysis of their plasma content, there are no negative repercussions from this work. If anything, it indicates that CH* (and C_2*) emissions could well be more representative of CH_x ($0 \leq x \leq 3$) growth species (and total carbon content) than has been previously appreciated, but that the CH(C) state is more indicative of n_e and [CH(X)] than other lower lying CH* states.

References

[1] Ma, J., Ashfold, M. N. R. and Mankelevich, Yu. A. "Validating optical emission spectroscopy as a diagnostic of microwave activated $CH_4/Ar/H_2$ plasmas used for diamond chemical vapor deposition." Journal of Applied Physics, vol. 105, no. 4, p. 043302, 2009.

[2] Ma, J., Richley, J. C., Ashfold, M. N. R. and Mankelevich, Yu. A. "Probing the plasma chemistry in a microwave reactor used for diamond chemical vapor deposition by cavity ring down spectroscopy." Journal of Applied Physics, vol. 104, no. 10, p. 103305, 2008.

[3] Gicquel, A., Silva, F. and Hassouni, K. "Diamond Growth Mechanisms in Various Environments." Journal of The Electrochemical Society, vol. 147, no. 6, p. 2218, 2000.

[4] Derkaoui, N., Rond, C., Gries, T., Henrion, G. and Gicquel, A. "Determining electron temperature and electron density in moderate pressure H_2/CH_4 microwave plasma." Journal of Physics D: Applied Physics, vol. 47, no. 20, p. 205201, 2014.

[5] Gicquel, A., Hassouni, K., Breton, Y., Chenevier, M. and Cubertafon, J. "Gas temperature measurements by laser spectroscopic techniques and by optical emission spectroscopy." Diamond and Related Materials, vol. 5, no. 3-5, pp. 366-372, 1996.

[6] Lombardi, G., Bénédic, F., Mohasseb, F., Hassouni, K. and Gicquel, A. "Determination of gas temperature and C_2 absolute density in $Ar/H_2/CH_4$ microwave discharges used for nanocrystalline diamond deposition from the C_2 Mulliken system." Plasma Sources Science and Technology, vol. 13, no. 3, pp. 375-386, 2004.

[7] Richley, J. C., Kelly, M. W., Ashfold, M. N. R. and Mankelevich, Yu. A. "Optical Emission from Microwave Activated C/H/O Gas Mixtures for Diamond Chemical Vapor Deposition." The Journal of Physical Chemistry A, vol. 116, no. 38, pp. 9447-9458, 2012.

[8] Mahoney, E. J. D., Truscott, B. S., Mushtaq, S., Ashfold, M. N. R. and Mankelevich, Yu. A. "Spatially Resolved Optical Emission and Modeling Studies of Microwave-Activated Hydrogen Plasmas Operating under Conditions Relevant for Diamond Chemical Vapor Deposition." The Journal of Physical Chemistry A, vol. 122, no. 42, pp. 8286-8300, 2018.

[9] Mahoney, E. J. D., Mushtaq, S., Ashfold, M. N. R. and Mankelevich, Yu. A. "Combined Spatially Resolved Optical Emission and Modeling Studies of Microwave-Activated H_2/Ar and H_2/Kr Plasmas Operating under Conditions relevant for Diamond Chemical Vapor Deposition." The Journal of Physical Chemistry A, vol. 123, no. 13, pp. 2544-2556, 2019.

[10] Mahoney, E. J. D., Truscott, B. S., Ashfold, M. N. R. and Mankelevich, Yu. A. "Optical Emission from C_2^- Anions in Microwave-Activated CH_4/H_2 Plasmas for Chemical Vapor Deposition of Diamond." The Journal of Physical Chemistry A, vol. 121, no. 14, pp. 2760-2772, 2017.

[11] Vandevelde, T., Nesladek, M., Quaeyhaegens, C. and Stals, L. "Optical emission spectroscopy of the plasma during CVD diamond growth with nitrogen addition." Thin Solid Films, vol. 290-291, pp. 143-147, 1996.

[12] Elliott, M. A., May, P. W., Petherbridge, J., Leeds, S. M., Ashfold, M. N. R. and Wang, W. N. "Optical emission spectroscopic studies of microwave enhanced diamond CVD using CH_4 /CO_2 plasmas." Diamond and Related Materials, vol. 9, no. 3-6, pp. 311-316, 2000.

[13] Lang, T., Stiegler, J., von Kaenel, Y. and Blank, E. "Optical emission diagnostics and film growth during microwave-plasma-assisted diamond CVD." Diamond and Related Materials, vol. 5, no. 10, pp. 1171-1184, 1996.

[14] Rabeau, J. R., John, P., Wilson, J. I. B. and Fan, Y. "The role of C_2 in nanocrystalline diamond growth." Journal of Applied Physics, vol. 96, no. 11, pp. 6724-6732, 2004.

[15] Taylor, A., Ashcheulov, P., Čada, M., Fekete, L., Hubík, P., Klimša, L., Olejníček, J., Remeš, Z., Jirka, I., Janíček, P., Bedel-Pereira, E., Kopeček, J., Mistrík, J. and Mortet, V. "Effect of plasma composition on

nanocrystalline diamond layers deposited by a microwave linear antenna plasma-enhanced chemical vapour deposition system." physica status solidi (a), vol. 212, no. 11, pp. 2418-2423, 2015.

[16] Gicquel, A., Chenevier, M., Hassouni, K., Tserepi, A. and Dubus, M. "Validation of actinometry for estimating relative hydrogen atom densities and electron energy evolution in plasma assisted diamond deposition reactors." Journal of Applied Physics, vol. 83, no. 12, pp. 7504-7521, 1998.

[17] Jones, L. A. "Comparison of Langmuir probe and Thomson scattering measurements of electron temperature and density." Journal of Applied Physics, vol. 45, no. 12, pp. 5206-5208, 1974.

[18] Rajesh, R., Kumar, B. R., Varshney, S. K., Kumar, M., Chavda, C., Thakkar, A., Patel, N., Kumar, A. and Team, A. "Electron temperature (T_e) measurements by Thomson scattering system." Pramana, vol. 55, no. 5-6, pp. 733-740, 2000.

[19] Malyshev, M. V. and Donnelly, V. M. "Trace rare gases optical emission spectroscopy: Nonintrusive method for measuring electron temperatures in low-pressure, low-temperature plasmas." Physical Review E, vol. 60, no. 5, pp. 6016-6029, 1999.

[20] Masseron, T., Plez, B., Van Eck, S., Colin, R., Daoutidis, I., Godefroid, M., Coheur, P. F., Bernath, P., Jorissen, A. and Christlieb, N. "CH in stellar atmospheres: an extensive linelist." Astronomy & Astrophysics, vol. 571, pp. A47, 2014.

[21] Western C. M., "PGOPHER, A Program for Simulating Rotational, Vibrational and Electronic Spectra," University of Bristol, http://pgopher.chm.bris.ac.uk.

[22] Rodriguez, B. J. "Optical emission spectroscopy studies on microwave activated CH_4/H_2 plasmas used for diamond chemical vapor deposition" Diamond Science and Technology Master's Thesis, University of Bristol, Diamond Science and Technology Centre for Doctoral Training, 2017.

[23] Hinze, J., Lie, G. C., Liu, B. "Valence Excited States of CH. 111. Radiative Lifetimes." The Astrophysical Journal. vol. 196, pp. 621-632, 1975.

[24] Heinrich, P. and Stuhl, F. "Temperature dependent quenching of CH($A^2\Delta$), NH($A^3\Pi$), NH($c^1\Pi$), and PH($A^3\Pi$) by H_2." Chemical Physics, vol. 199, no. 2, pp. 297-304, 1995.

[25] Nokes, C. J., and Donovan, R. J. "Time-resolved kinetic studies of electronically excited CH radicals II. Quenching efficiencies for CH(A 2Δ)." Chemical Physics, vol. 90, no. 1-2, pp. 167-174, 1984.

[26] Garland, N. L. and Crosley, D. R. "Collisional quenching of CH A $^2\Delta$, v' = 0 at 1300 K." Chemical Physics Letters, vol. 134, no. 2, pp. 189-194, 1987.

[27] Chen, C., Wang, F., Chen, Y. and Ma, X. "Temperature effect on quenching of CH($A^2\Delta$)." Chemical Physics, vol. 230, no. 2-3, pp. 317-325, 1998.

[28] Cooper, J. C. and Whitehead, J. L. "Collisional removal rates for electronically excited CH radicals $B^2\Sigma$–and $C^2\Sigma$+." Journal of the Chemical Society, Faraday Transactions, vol. 88, no. 16, pp. 2323-2327, 1992.

---

[29] Tamura, M., Berg, P. A., Harrington, J. E., Luque, J., Jeffries, J. B., Smith, G.P. and Crosley, D. R. "Collisional Quenching of CH(A), OH(A), and NO(A) in Low Pressure Hydrocarbon Flames. Combustion and Flame." vol. 114, no. 3-4, pp. 502-514, 1998.

[30] Mankelevich, Yu. A., Ashfold, M. N. R. and Ma, J. "Plasma-chemical processes in microwave plasma-enhanced chemical vapor deposition reactors operating with C/H/Ar gas mixtures." Journal of Applied Physics, vol. 104, no. 11, p. 113304, 2008.

Chapter 6: Diagnostic Studies carried out on MW-activated Si/H and Si/C/H Plasmas

This Chapter reports optical emission and absorption studies on a range of MW-activated Si/H, Si/H/Ar and Si/C/H plasma systems. The first set of experiments investigate numerous emissions from the Si atom, the SiH radical, the H atom and the H_2 molecule. The second set of experiments investigates optical absorptions of three different spin-orbit states from the Si triplet ground state. These experiments are combined with a literature review to yield an insight into some of the prominent gas phase processes that occur within MW-activated Si/H plasmas.

These experiments are repeated in the presence of methane (monitoring additional emissions from the C_2 and CH radicals) to begin developing a basic understanding of processes that could be occurring within MW-activated Si/C/H plasmas.

These studies are briefly contrasted to a comparative study carried out using a Si wafer as the Si source in MW-activated H, H/Ar, and C/H plasmas.

6.1: Introduction

Optical emission spectroscopy (OES) is an experimental technique that enables ready identification of excited species present within a plasma. The investigation of how relative emission intensities, and thereby relative excited state column densities, vary with changes in process conditions, yields insight into their sensitivity to operating conditions, as well as the excitation (by electron impact, chemiluminescence, collisional coupling of states, resonant/near-resonant excitation transfers and/or additional mechanisms) and the quenching of these states, as exemplified in Chapters 3, 4 and 5 for MW-activated H, H/Ar, C/H and C/H/Ar plasmas. OES data has previously been combined with ground state column density measurements (obtained by cavity ring down spectroscopy (CRDS)) and 2-D plasma chemical modelling to provide a good understanding of the important processes occurring within MW-activated C/H plasmas facilitating the CVD of diamond,[1] and such gas mixtures upon the addition of dopant-containing gases, e.g. diborane,[2] nitrogen [3] and oxygen.[4] Introducing dopant gases can be useful for technological applications. For instance, upon the addition of boron, diamond films demonstrate semi-conducting, metallic and even superconducting properties, whilst the addition of nitrogen can enhance growth rate, as well as generate a range of defects, of which the NV centre can be manipulated as a sensitive magnetometer.[5,6,7]

There is a desire within the semiconductor and diamond communities to understand microwave (MW) activated Si/H and Si/C/H-containing plasmas. Amorphous, micro-crystalline and poly-crystalline

silicon have perceived advantages relative to monocrystalline silicon as a semi-conducting photovoltaic material in the solar cell industry. The former materials exhibit a higher optical absorption coefficient across the visible spectrum due to the relaxation of absorption selection rules, resulting in a direct band gap. This enables thinner silicon films to be used to absorb the same amount of light as compared to single crystal silicon films.[8] Radio-frequency (rf) plasma enhanced chemical vapour deposition (PECVD) is a method used to grow such materials, typically from SiH_4/H_2 gas mixtures, at relatively low temperatures, $T_g \leq 500$ K (*cf.* MW-activated Si/H plasmas).[8,9,10] The low (typically 0.1-0.3 nm s^{-1}) deposition rate is disadvantageous, however.[8] It is understood that increasing rf frequency tends to increase deposition rate, power transfer, and therefore, plasma uniformity and amorphous silicon quality.[9] Compared to MW plasmas, rf plasmas also tend to have a higher T_e (~ 5 eV).[10] It is therefore unsurprising that literature on MW-activated Si/H plasma studies, and Si/H kinetics related to the T_g of interest (T_g ~2000-3000 K), is scarce. There is, however, a study [11] on amorphous silicon growth using direct MW-activated SiH_4/Xe plasmas at low pressures (≥ 1.3 Torr), amorphous silicon-carbide growth [12] using indirect MW-activated Si/C/H plasmas, and a few studies [13,14,15] on Si/H kinetics at more relevant gas temperatures. Despite the established advantage of higher frequencies, a study establishing MW-activated Si/H processes would either reaffirm this consensus or provide interesting and/or unexpected insight, particularly for diamond growers concerned with silicon contamination during hydrogen termination (and growth) of diamond. An understanding of MW-activated Si/H growth is also interesting from an academic perspective and a necessary prerequisite for understanding MW-activated Si/C/H plasmas.

Defects within diamond can compromise desirable properties, such as thermal conductivity. An understanding of MW-activated Si/H and Si/C/H plasmas can help minimise (unwanted) incorporation of Si-related defects in diamond as a result of etching silicon substrates and/or quartz windows during hydrogen termination and the chemical vapour deposition growth of diamond.[16]

Alternatively, a good understanding of MW-activated Si/C/H plasmas can also be used for the controllable introduction of silicon vacancy (SiV) defects in CVD diamond. The SiV^- centre can produce a sharp zero phonon line (λ = 737 nm) consisting of ~ 70% of its fluorescence at room temperatures, with a weak vibronic side band and a long spin relaxation lifetime, T_1 = 2.4 ms at 5 K, essential for producing indistinguishable photons in quantum encryption.[17,18] There is also a promise for optical access to the Si^{29} nuclear spin, which is expected to have longer coherence lifetimes than electron spins.[18] Additional advantages of understanding MW-activated Si/C/H plasmas might be to improve crystalline quality and/or the growth rate of silicon carbide under higher Si/C fractions. Deliberate attempts of doping diamond with Si during MW-activated CVD growth include incorporation via the use of silicon (and SiO_2) substrates [19,20,21,22] and through introducing silane into the gas phase.[23] Si can be incorporated post-growth through ion beam implantation.[24]

This chapter reports optical emissions originating from MW-activated Si/H and Si/C/H gas mixtures under a range of process conditions relevant to hydrogen termination and the chemical vapour deposition of diamond. These studies are combined with column density measurements of the spin-orbit levels of the Si atom ground state using Cavity Ring Down Spectroscopy (with 2-D plasma modelling in progress) to begin developing an understanding of the important physical and chemical gas phase processes occurring within MW-activated Si/H and Si/C/H plasmas, to provide a plausible rationale behind the observed emission variations with changing process conditions, and to understand the dominant Si-containing species / ions within the plasma and in the near substrate region under conditions of greatest relevance to diamond growth.

6.2: Experimental Details

This chapter describes multiple studies carried out on MW-activated Si/H and Si/C/H plasmas. These studies include investigations on the optical emissions originating from such plasmas, as well as laser absorption on the Si atom triplet ground states ($^3P^o \leftarrow ^3P$). More specifically, the first section reports optical emissions originating from the Si atom, via different lines associated with the $3s^2 3p4s \rightarrow 3s^2 3p^2$ transition; this includes two singlet transitions; $^1P_1^o \rightarrow ^1D_2$ and $^1P_1^o \rightarrow ^1S_0$ observed at λ = 288.15 nm and 390.55 nm with Einstein-A emission coefficients of 2.17×10^8 s^{-1} and 1.33×10^7 s^{-1} respectively, and six triplet transitions; $^3P^o \rightarrow ^3P$ centred around $\lambda \sim 252$ nm, but recorded in second order at 2λ = 501.37, 502.88, 503.24, 503.89, 504.83 and 505.70 nm.[25,26] These transitions have Einstein-A emission coefficients in the range of 5.47×10^7 s^{-1} to 2.22×10^8 s^{-1}. The relevant Si atom energy states, transitions, and Einstein-A emission coefficients are identified in Figure 6.01 and Table 6.1 using data taken from References 25 and 26.

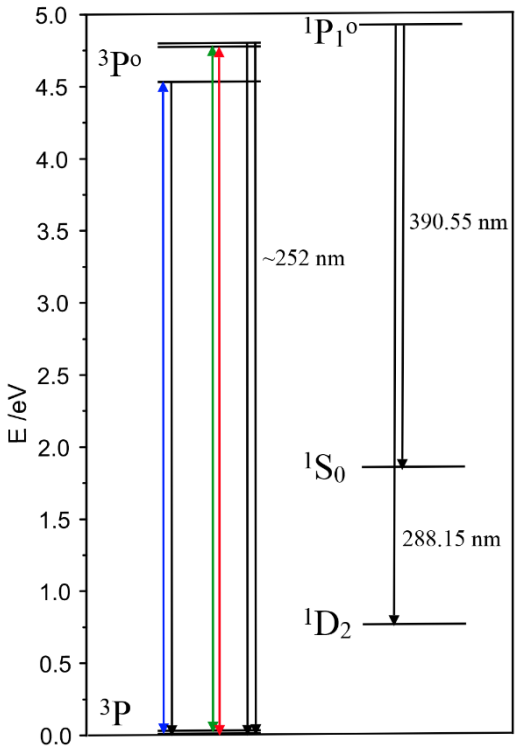

Figure 6.01: Diagram identifying the energy levels of the Si atom that have been investigated within this chapter. The triplet (left) and singlet (right) energy levels are connected by downward facing arrows, which represent the transitions and emissions that have been investigated via Optical Emission Spectroscopy. The coloured double headed arrows represent transitions that have been investigated through both emission and absorption via OES and Cavity Ring Down Spectroscopy respectively. These are the Si($3s^2 3p4s$, $^3P^o$, J = 0←$3s^2 3p^2$, ^3P, J = 1), Si($3s^2 3p4s$, $^3P^o$, J = 1←$3s^2 3p^2$, ^3P, J = 2), and Si($3s^2 3p4s$, $^3P^o$, J = 1←$3s^2 3p^2$, ^3P, J = 0) transitions identified as a green, blue and red arrows respectively.

Species	Investigated transitions	Upper State energy level /eV	Lower State energy level /eV	Emitting (/absorbing) wavelength /nm	Einstein-A emission coefficients / 10^7 s^{-1}
Si*	$3s^23p4s \rightarrow 3s^23p^2$	-	-	-	-
Si*	$^3P_2^o \rightarrow {}^3P_1$	4.95	0.01	250.69	5.47
Si*	$^3P_1^o \leftrightarrow {}^3P_0$	4.93	0	251.43	7.39
Si*	$^3P_2^o \rightarrow {}^3P_2$	4.95	0.03	251.61	16.8
Si*	$^3P_1^o \rightarrow {}^3P_1$	4.93	0.01	251.92	5.49
Si*	$^3P_0^o \leftrightarrow {}^3P_1$	4.91	0.01	252.41	22.2
Si*	$^3P_1^o \leftrightarrow {}^3P_2$	4.92	0.03	252.85	9.04
Si*	$^1P_1^o \rightarrow {}^1D_2$	5.08	0.78	288.16	21.7
CH*	$B^2\Sigma^- \rightarrow X^2\Pi$	3.208	0		0.263
Si*	$^1P_1^o \rightarrow {}^1S_0$	5.08	1.91	390.55	1.33
H*	^2S (and ^2D) $\rightarrow$ $^2P^o$ (and $^2P^o \rightarrow {}^2S$)	13.05	10.20	434.05	~0.94
SiH*	$A^2\Delta \rightarrow X^2\Pi$	3.00	0	~409-425	0.288
CH*	$A^2\Delta \rightarrow X^2\Pi$	2.876	0		0.187
H*	^2S (and ^2D) $\rightarrow$ $^2P^o$ (and ^2S)	12.75	10.20	486.13	~2.06
C_2*	$d^3\Pi_g \rightarrow a^3\Pi_u$	2.48	0.088	~460-565	0.763
H_2*	$d^3\Pi_u \rightarrow a^3\Sigma_g^+$	13.97	11.79	~600-615	2.57

Table 6.1: Table identifying and summarising all investigated transitions of the Si and H atoms, SiH, CH, C_2 and H_2 molecules monitored via Optical Emission Spectroscopy within this Chapter. The coloured Si transitions have been investigated through both emission and absorption via Cavity Ring Down Spectroscopy and colour coordinate with Figure 6.01. References for SiH transition are available within the text, references for H and H_2 transition are available in Chapter 3, references for the C_2 transition are available in Chapter 4, whilst references for the CH transitions are available in Chapter 5.

The SiH radical was also monitored via the $A^2\Delta \rightarrow X^2\Pi$ transition (analysed using PGOPHER)[27], H_2 via the $d^3\Pi_u \rightarrow a^3\Sigma_g^+$ transition and H atoms via the n=5→n=2 and n=4→n=2, i.e. the H Balmer γ and β transitions respectively. The experimental method for the detection of these emissions are near identical to those described in Chapter 5, except for the use of a molybdenum substrate (d_{sub} = 32 mm) and the accumulation time, equivalent to 50 s. Base conditions are defined as P = 1.5 kW, the total gas pressure, p = 150 Torr, and the respective gas flow rates were $F(H_2)$ = 300 sccm and $F(SiH_4/H_2)$ = 15 sccm (using a 1 part per thousand SiH_4 in H_2 mixture). The effects of changing process conditions were explored by varying one parameter at a time, holding all others at their base value. The parameter space explored includes: $0 \leq F(SiH_4/H_2) \leq 40$ sccm, $50 \leq p \leq 275$ Torr and $0.7 \leq P \leq 1.85$ kW. The impurity contributed

from the air leak associated with the OES experiments has a negligible value of ~ 0.25 ppm, and thus, for these experiments, the larger air impurity origins from the H_2 gas, which itself consists of $X_0(H_2O) \leq 3$ ppm, $X_0(O_2) \leq 2$ ppm and $X_0(N_2) \leq 5$ ppm.[28]

These optical emission studies have been repeated in the presence of methane. The study includes the optical emissions noted above and, in addition, A→X and B→X transitions of the CH radical, d→a transition of the C_2 radical, all of which have been explored in previous chapters. Base conditions are redefined as P = 1.5 kW, p = 150 Torr, with respective gas flow rates of $F(H_2)$ = 270 sccm, $F(SiH_4/H_2)$ = 30 sccm, $F(CH_4)$ = 19 sccm. The transition emissions originating from the Si atom triplet states are detected in second order, and this overlaps with the more prominent C_2(d→a), $\Delta v = 0$ transitions. Whilst the residual between the experimental data and the best PGOPHER fit can produce a reasonable assessment of the variations of these triplet emissions, this method was found to produce a high level of analysis error. Instead, the triplet and singlet emissions were repeated in a separate experiment using a narrow band pass filter to suppress light outside of the UV range of interest. All of the aforementioned emissions were investigated as a function of p, P, $F(SiH_4)$ and in addition, $F(CH_4)$. The parameter ranges explored match those investigated in MW-activated Si/H plasmas under newly defined base conditions, with the addition of $0 \leq F(CH_4) \leq 30$ sccm. One parameter is varied at a time, keeping the remaining parameters constant at base conditions, except upon increasing gas flow rates; $F(H_2)$ is reduced in a compensatory manner, such that the total gas flow remains constant, as outlined in Chapter 3, Section 3.2 and Chapter 4, Section 4.2 in the context of Ar addition to MW-activated H and C/H plasmas respectively. The majority OES data collected for MW-activated Si/C/H plasmas have been accumulated for an equivalent of 100 s, but rescaled so that the reported intensities are as if the data had been collected for 50 ns (i.e. more comparable to the MW-activated Si/H plasma studies).

These studies are contrasted to a brief study on MW-activated H, H/Ar, and C/H plasmas (operating at base pressure and power) with the full diameter of the molybdenum substrate was covered by a thin (0.7 mm thick) silicon disc. The experimental details of this are described with the reported results in Section 6.3.8.

The second major component of this chapter consists of atomic Si column density measurements using Cavity Ring Down Spectroscopy (CRDS). The Nd:YAG laser operated at 30 Hz with a third harmonic output power ranging between 1.3-1.6 W at a wavelength of 354.4 nm, as described in Section 2.2.2. This output pumps a tuneable dye laser operating with Coumarin 503 diluted in methanol (with oscillator and amplifier concentrations of, respectively, ~0.4 gL^{-1} and ~0.08 gL^{-1}, with the set up optimised to scan over two wavelength ranges; ~ 504.79 to 504.85 nm and 505.67 to 505.73 nm. The dye laser output power is ~ 60 mW, and gradually decays over time. The desired frequency ranges were achieved utilising a frequency doubling crystal to generate UV light with wavenumbers centred around 39606.1 cm^{-1} (i.e. the triplet emission featuring at 252.41 nm in OES experiments, identified as the green double headed arrow within Figure 6.01) for the Si($3s^2 3p4s$, $^3P^o$, J = 0←$3s^2 3p^2$, ^3P, J = 1)

absorption. The experiments were repeated using the Si($3s^2 3p4s$, $^3P^o$, $J = 1 \leftarrow 3s^2 3p^2$, ^3P, $J = 2$) transition centred at 39537.1 cm^{-1} (i.e. the triplet emission featuring at 252.85 nm, identified as the blue double headed arrow in Figure 6.01). These transitions have Einstein-B absorption coefficients of 6.43×10^{19} $m^3 J^{-1} s^{-2}$ and 1.46×10^{20} $m^3 J^{-1} s^{-2}$ respectively (calculated using the relationship between Einstein-A emission and Einstein-B absorption values given by Equations 2.22 and 2.23 in Chapter 2, Section 2.2.2).[25] The lack of a spatial filter in the optical set-up allowed more than one laser mode to enter the cavity. Whilst this may act to increase the error associated with the measured ring down time, generally the mean squared error was reduced as much as possible, and therefore had little bearing on the values reported. Prior to detection on a photomultiplier tube, light exiting the cavity passes through the UV wavelength transmitting filter described above to remove any scattered fundamental laser light.

To prevent silicon (and carbon upon the introduction of methane, see below) deposition on the cavity mirrors (with a specification reflectivity of $R \sim 0.995$ for 250 nm light, but a practical reflectivity of $R \sim 0.986$), hydrogen gas is flowed into the ends of the cavity arms, as well as into the main reactor chamber. These flows are distinguished as $F_{arms}(H_2)$ and $F_{reactor}(H_2)$, which provides an effective hydrogen flow rate of $F_{eff}(H_2) = F_{arms}(H_2) + F_{reactor}(H_2)$, an assumption which has been tested between the range of $50 \leq F_{arms}(H_2) \leq 250$ sccm as evidenced in Appendix A6.2 (and A6.3 carried out on {Si($J = 0$)} using the transition described below). For this experiment, base conditions are defined as $P = 1.5$ kW, $p = 150$ Torr, with gas flow rates $F_{reactor}(H_2) = F_{arms}(H_2) = 300$ sccm, (i.e. $F_{eff}(H_2) = 600$ sccm) and $F(SiH_4/H_2) = 0.5$ sccm (using a 1 part per thousand SiH_4 in H_2 mixture). The parameter ranges explored were $150 \leq F_{eff}(H_2) \leq 1800$ sccm; $50 \leq p \leq 275$ Torr; $0.7 \leq P \leq 1.85$ kW. As with previous studies, one parameter was adjusted at a time, whilst the remainder are kept at base conditions. Due to the nature of the CRDS experiments, the estimated leak (10 ppm under base conditions plus hydrogen feed gas impurities), is considerably larger than $X_0(SiH_4)$ (0.83 ppm under base conditions). To illustrate the impact of leak rate, additional experiments were carried out under base pressure and power using a third absorption Si($3s^2 3p4s$, $^3P^o$, $J = 1 \leftarrow 3s^2 3p^2$, ^3P, $J = 0$) transition centred at 39760.3 cm^{-1}, which has an Einstein-B absorption coefficient of 2.32×10^{20} $m^3 J^{-1} s^{-2}$ and is identified as a red arrow in Figure 6.01. The exact methodology and findings are reserved for the discussion in Section 6.3.5.v.

The CRDS absorption studies were repeated using Si($3s^2 3p4s$, $^3P^o$, $J = 0 \leftarrow 3s^2 3p^2$, ^3P, $J = 1$) for MW-activated Si/C/H plasmas. Due to continuous etching and deposition of silicon on the chamber walls, substrate and base plate, a light layer of carbonaceous material was deposited to facilitate reproducibility. Due to thermal mismatch (and consequential delamination) it was not possible to coat the Mo substrate for these experiments. A further issue, previously noted by Jie Ma in his thesis, is a build up of absorbing material along the laser path in MW-activated C/H plasmas.[29] Only by switching off the plasma and allowing the chamber sufficient time to evacuate (~ 12 hours) could the problem be resolved. Consequently, each experiment was undertaken in the shortest time possible to minimise the progressive deterioration of data quality. Base conditions are redefined to $P = 1.5$ kW, $p = 150$ Torr,

with gas flow rates $F_{reactor}(H_2)$ = 300 sccm, $F_{arms}(H_2)$ = 300 sccm (i.e. $F_{eff}(H_2)$ = 600 sccm), $F(SiH_4/H_2)$ = 0.5 sccm, $F(CH_4)$ = 10 sccm, and again, a similar parameter space range is explored to those previously discussed with one parameter varied at a time under otherwise base conditions, except when altering gas flow rate, in which there is a compensatory decrease of $F_{reactor}(H_2)$ as described.

Two very brief additional studies were carried out. One, at $F(SiH_4/H_2)$ = 0 sccm, $F_{eff}(H_2)$ = 600 sccm, P = 1.85 kW, p = 75 Torr, probing {Si} absorption at z = 24 mm, the second at $F(SiH_4/H_2)$ = 0 sccm, $F_{eff}(H_2)$ = 600 sccm, P = 1.5 kW, p = 150 Torr with the presence of the 0.7 mm Si substrate, probing at z ~ 1 mm (above the substrate) to assess whether there is a measurable Si column density, {Si}, originating respectively from the quartz window or a silicon substrate under these operating conditions.

Some preliminary efforts have been made in the 2-D physical chemical modelling of MW-activated Si/H plasmas, which have been loosely drawn upon where appropriate. These results are awaiting a more thorough modelling to provide a more in-depth understanding to the experimental observations reported and a better understanding of the prominent gas phase processes.

6.3: Results and Discussion

Section 6.3.1 reviews the gas phase processes that might be expected to occur within weakly ionized MW-activated Si/H plasmas. Section 6.3.2 reviews plausible excitation (and quenching) mechanisms for the production of various excited states of Si and SiH. Section 6.3.3 provides example spectral analysis and further detail of the OES experiment. Section 6.3.4 presents the results from OES studies on a MW-activated Si/H plasma with a qualitative interpretation based on an understanding developed from the literature. Section 6.3.5 presents results from CRDS studies on a MW-activated Si/H plasma with a qualitative and semi-quantitative interpretation. Section 6.3.6 moves on to describe possible processes occurring within MW-activated Si/C/H plasmas. Section 6.3.7 presents OES and CRDS measurements carried out on MW-activated Si/C/H plasmas with a qualitative, albeit speculative, interpretation of these results. Section 6.3.8 contrasts MW-activated Si/H and Si/C/H plasmas to a MW-activated H plasma with a 0.7 mm Si wafer present.

6.3.1: Likely Chemical Processes Occurring Within MW-activated Si/H plasmas

Without full 2-D plasma modelling, it is difficult to understand the exact details of the physical and chemical processes occurring within MW-activated Si/H plasmas. Nonetheless, it is possible to speculate on processes that are occurring within MW-activated Si/H plasmas by combining literature and a basic understanding of MW-activated H and C/H plasmas with the OES and CRDS results reported in Sections 6.3.2 and 6.3.3. Everything discussed and presented in this section is a working interpretation with the aim of developing a rationale behind the experimental observations with an understanding of the prominent processes that are occuring within MW-activated dilute Si/H plasmas.

Species	Ionization Potential Energy /eV	Enthalpy of Formation / eV
SiH_4	11.00	0.355
SiH_3	8.01	2.071
SiH_2	9.02	2.872
SiH	7.91	3.904
Si	8.151	4.664
H_2	15.427	0
H	13.598	2.259
H_2O(g)	12.62	−2.506
OH(g)	13.18	0.387
SiO(g)	11.6	−0.928
SiOH(g)	6.59	0.004

Table 6.2: Enthalpy of formation (calculated at T = 298 K) and ionization potentials for SiH_x ($0 \leq x \leq 4$), H, H_2, gaseous H_2O, OH, SiO, and SiOH.

Table 6.2 demonstrates the enthalpy of formation and ionization potentials of SiH_x ($0 \leq x \leq 4$) and oxygen-containing species and are compared to that of H and H_2. These values have been taken from References 30, 31, 32, 33, 34, 35, 36, and 37.

SiH_4 can undergo thermal decomposition and as a Group 4 element (one row below carbon), it seems reasonable that SiH_x ($x \leq 4$) species undergo H-shifting reactions comparable to those of CH_x species, as described by Processes 6.01 to 6.05, where M is a collision partner:

$$SiH_4 + M \rightarrow SiH_3 + H + M \quad (6.01)$$

$$SiH_4 + H \rightarrow SiH_3 + H_2 \quad (6.02)$$

$$SiH_3 + H \rightarrow SiH_2 + H_2 \quad (6.03)$$

$$SiH_2 + H \rightarrow SiH + H_2 \quad (6.04)$$

$$SiH + H \rightarrow Si + H_2 \quad (6.05)$$

These reactions are oversimplified (as were the comparable carbon-containing reactions depicted in Figure 1.4, Chapter 1), for instance, Process 6.05 can populate (a) the ground state Si triplets, or (b) the lowest lying metastable Si singlet state. As with CH_2, there are additional spin-orbit state considerations for SiH_2. These reactions are accompanied by additional reactions, e.g. H and H_2 addition/thermal decomposition reactions. As with thermal dissociation of silane to form SiH_3 + H, (given by Process 6.01), the reverse reactions of Processes 6.01 to 6.05 (i.e. recombination reactions) require a collision partner, M. Alternatively, such processes could result in a chemical reaction (without the need of a collision partner) as highlighted by Process 6.06 (b). Examples of such addition reactions are provided by Processes 6.06 to 6.12.

$$SiH_3 + H + M \rightarrow SiH_4 + M \quad (6.06\ a)$$

$$SiH_3 + H_2 \rightarrow SiH_4 + H \quad (6.06\ b)$$

$$SiH_2 + H\ (+M) \leftrightarrow SiH_3\ (+M) \quad (6.07)$$

$$SiH + H\ (+M) \leftrightarrow SiH_2\ (+M) \quad (6.08)$$

$$Si + H\ (+M) \leftrightarrow SiH(+M) \quad (6.09)$$

$$SiH_2 + H_2\ (+M) \leftrightarrow SiH_4\ (+M) \quad (6.10)$$

$$SiH + H_2\ (+M) \leftrightarrow SiH_3\ (+M) \quad (6.11)$$

$$Si + H_2\ (+M) \leftrightarrow SiH_2\ (+M) \quad (6.12)$$

Reference 15 provides values required to solve the Arrhenius equation for calculating temperature-dependent rate coefficients for these reactions. These values are regularly reported for p = 10 Torr and 760 Torr. Rughunath *et al*. demonstrate that for some processes, (e.g. Processes 6.07, 6.10, (−)6.11 and (−)6.12) rates calculated as a $f(1/T_g)$ for p = 100 Torr are approximately an average (on a logarithmic scale) of those calculated for p = 10 Torr and 760 Torr, and that for other processes, the rate coefficients are independent of pressure in the pressure range of interest. Table 6.3 provides some example rate coefficient estimates for T_g = 750 and 3000 K and p ~ 150 Torr.

Reaction	Rate coefficient (T_g = 750 K) /cm^{3}molecule^{-1}s^{-1} unless otherwise stated	Rate coefficient (T_g = 3000 K) /cm^{3}molecule^{-1}s^{-1} unless otherwise stated
6.01	3.6×10^{-12}	4.3×10^{5}
(−)6.10	1.0×10^{10}	4.9×10^{6}
(+)6.10	3.0×10^{-13} (high pressure limit)	6.7×10^{-12} (high pressure limit)
6.06 (a)	6.2×10^{-17} cm^{6}molecule^{-2}s^{-1}	5.0×10^{-20} cm^{6}molecule^{-2}s^{-1}
6.03	2.3×10^{-10}	2.0×10^{-10}
6.07	2.4×10^{-16}	1.3×10^{-18}
6.04	5.8×10^{-10}	3.9×10^{-10}
6.08	1.4×10^{-16}	6.1×10^{-18}
6.05 (a)	1.4×10^{-10}	8.9×10^{-11}
6.05 (b)	4.2×10^{-11}	4.0×10^{-11}
6.09	Not available from Reference 15	Not available from Reference 15

Table 6.3: Rate coefficients for a number of reactions connecting SiH_x ($0 \leq x \leq 4$) via addition / loss of H, and H_2 calculated at T_g = 750 and 3000 K, p = 150 Torr. Note Reactions 6.05 (a) and (b) result in

Whilst incomplete, Table 6.3 demonstrates that the rate coefficients of Processes 6.01 and (−)6.10 (i.e. dissociation of silane forming SiH_3 (+ H) and SiH_2 (+H_2) as products) are many orders of magnitude larger than recombination reactions (Processes 6.06 and (+)6.10) for T_g = 750 and 3000 K. From Table

6.3, it can be seen that the relative rate coefficient for silane dissociation favours SiH_2 (+ H_2) over SiH_3 (+ H) by an order of magnitude for a gas temperature of 3000 K (i.e. in the hot plasma region, calculated by dividing $k_{-6.10}/k_{6.01}$ i.e. ~ $4.9 \times 10^6/4.3 \times 10^5$, and neglecting the requirement of an additional body) and by ~22 orders of magnitude in the cool plasma regions (~ $1.0 \times 10^{10}/3.6 \times 10^{-12}$). Further, it can be seen from Table 6.3 that the relative rate coefficient for Process 6.06 (i.e. $SiH_3 + H \rightarrow SiH_4$) is much smaller than SiH_3 undergoing an H-shifting reaction (Process 6.03) to form SiH_2 (+ H_2). The comparison of these simple dynamics would suggest that SiH_2 should be significantly larger than SiH_3 and SiH_4. Similar arguments can be applied to SiH_y ($0 \leq y \leq 2$) radicals using the calculated rate coefficients given in Table 6.3 and the discussion provided in Reference 15 (which uses T_g = 500 K, p = 10 and 750 Torr). The expectation is that most of the silicon in the hot plasma region should be in the form of Si atoms.

Without a high [H] density in the cool regions, it is possible that silane may dominate in the cool regions for $T_g \leq 1100$ K.[14] With the relatively high [H], previously calculated in 2-D modelling, the expectation would be that the rate coefficients would favour the production of Si atoms throughout the reactor, including the cool regions. This is reinforced by the positive enthalpies of reaction for the products $SiH_{z-1} + H_2$ ($0 \leq z \leq 4$) formed via H-shifting reactions (reactants SiH_z + H), which have been calculated using values provided in Table 6.2. Preliminary efforts in 2-D plasma modelling reinforce the suggestion that Si atoms dominate as Si-containing species throughout the plasma and its periphery.

6.3.2: Potential Excitation Mechanisms within MW-activated Si/H plasmas

In order to interpret the OES data, it is important to understand the possible formation and loss mechanisms of the observed singlet Si*, triplet Si* states, and SiH*. Processes 6.13 (a)-(f) and 6.14 describe electron impact excitation of ground and lowest lying metastable Si singlet states and SiH respectively.

$$Si(^3P) + e \rightarrow Si(^3P_0) + e \quad (6.13\text{ a})$$

$$Si(^3P) + e \rightarrow Si(^1P^0) + e \quad (6.13\text{ b})$$

$$Si(^3P) + e \rightarrow Si(^1D) + e \quad (6.13\text{ c})$$

$$Si(^3P) + e \rightarrow Si(^1S) + e \quad (6.13\text{ d})$$

$$Si(^1D) + e \rightarrow Si(^1P^0) + e \quad (6.13\text{ e})$$

$$Si(^1S) + e \rightarrow Si(^1P^0) + e \quad (6.13\text{ f})$$

$$SiH + e \rightarrow SiH^* + e \quad (6.14)$$

The non-conserving spin nature of Processes 6.13 (b), (c) and (d) will act to reduce these production rates, relative to the rate of other spin-conserving EIE (electron impact excitation) processes, and other competing singlet excitation mechanisms. Therefore, prominent alternative excitation mechanisms,

which produce singlet metastable / excited states must also exist. These mechanisms likely apply to the formation of Si* triplet states and SiH* as well.[38,39] Based on the aforementioned discussion, which concluded that the majority of silicon content ought to be in the form of Si atoms, EIE of SiH (involving two minority species, SiH and electrons) seems unlikely to be yield a sufficiently large rate to be a prominent formation mechanism of SiH*.

It is reported that vacuum UV photons and electrons can dissociate silane via Processes 6.15 and 6.16 (a) and (b) producing Si* and SiH* state populations.

$$SiH_4 + \gamma(UV) \rightarrow Si^* + 2H_2 \quad (6.15\ a)$$

$$SiH_4 + \gamma(UV) \rightarrow SiH^* + 3H \quad (6.15\ b)$$

$$SiH_4 + e \rightarrow Si^* + 2H_2 + e \quad (6.16\ a)$$

$$SiH_4 + e \rightarrow SiH^* + 3H + e \quad (6.16\ b)$$

Given that the plasma is optically thick in the vacuum UV (i.e. vacuum UV has a short mean free path before being reabsorbed), and that SiH_4 and electrons are minority species within the hot plasma region, Processes 6.15 (a) and (b) are not expected to yield large excitation rates. Processes 6.15 (a) and (b) are reported to have an efficiency on the order of ~1% per vacuum UV photon.[38] In literature, this process has been noted as a mechanism in the production of the SiH(A) state, and both $Si(^3P^0)$ and $Si(^1P^0)$ states.[39]

Processes 6.17 and 6.18 (a) and (b) describe electron-ion recombination reactions:

$$Si^+ + e \rightarrow Si^* \rightarrow \gamma + Si \quad (6.17)$$

$$SiH^+ + e \rightarrow SiH^* \rightarrow \gamma + SiH \quad (6.18\ a)$$

$$SiH^+ + e \rightarrow Si^* + H \rightarrow \gamma + Si + H \quad (6.18\ b)$$

Process 6.17, Si^+-e recombination, has a typical rate coefficient of ~ 2×10^{-12} $cm^{-3}molecule^{-1}s^{-1}$, of which a small fraction will branch into the various excited singlet and triplet states of Si.[40,41]

As has now been proposed to occur within MW-activated C/H plasmas in Chapter 5, one could also envisage various plausible chemiluminescent reactions within MW-activated Si/H plasmas. A few proposed mechanisms are described by Processes 6.19 to 6.21:

$$SiH_2 + H \rightarrow SiH^* + H_2 \rightarrow \gamma + SiH + H_2 \quad (6.19)$$

$$Si(^1D) + H \rightarrow SiH^* \rightarrow \gamma + SiH \quad (6.20\ a)$$

$$Si(^1D) + H_2 \rightarrow SiH^* + H \rightarrow \gamma + SiH + H \quad (6.20\ b)$$

$$SiH + H \rightarrow Si^* + H_2 \rightarrow \gamma + Si + H_2 \quad (6.21)$$

Under steady-state, [SiH_2] is not expected to have a large number density in the hot plasma region, but the rate coefficient of Process 6.04 (H-shifting of SiH_2 to form SiH) and [H] are expected to be modest (on the order of 10^{-10} $cm^3molecule^{-1}s^{-1}$ and 10^{16} cm^{-3} for T_g = 3000 K, see Table 6.3 and Figure 3.07 (a) respectively). The SiH(A) state is comparable in energy to that of the CH(A) state investigated in Chapter 5. Such a mechanism resulted in a Maxwell-Boltzmann contribution factor on the order of 10^{-3} for the CH(A) state relative to the production of the CH(X) ground state once degeneracies were considered. With similar logic and the rate coefficients reported in Section 6.3.4.a, the effective rate coefficient for Process 6.19 could be ~ 4×10^{-13} $cm^3molecule^{-1}s^{-1}$ for T_g = 3000 K, i.e. it is unlikely to be significant.

Figure 1 from Reference 42 infers that Process 6.20 (a) is an exothermic process with an enthalpy of reaction ~ − 0.91 eV. This contrasts to Process 6.21, which involves a minority species and has an enthalpy of reaction of ~ + 3.58 eV for the monitored singlet state of Si and would therefore be unlikely to contribute significantly. Whilst Process 6.20 (b) is also endothermic (~ + 3.61 eV), it includes a majority species, H_2. Given the monitored triplet states differ in energy from the investigated Si singlet state by ~ 0.13 eV, the same argument applies to the singlet states. Process 6.21 could, however, populate the lowest lying metastable Si(^{1}D) state. Such a reaction yields an enthalpy of reaction value of ~ − 0.72 eV, i.e. exothermic.

The similarity in energy between the emitting Si singlet and triplet levels could also facilitate a spin-orbit coupling upon an inelastic collision with a H atom (or in the presence of the MW magnetic field), as described by Process 6.22.[42]

$$\mathrm{Si}(\,^1P^o) + \mathrm{H} \leftrightarrow \mathrm{Si}(\,^3P^o) + \mathrm{H} \qquad (6.22)$$

The most prominent conceivable quenching mechanisms include collisional quenching of emitting Si* and SiH* species with either H and/or H_2, as exampled by Process 6.23 for the emitting Si triplet state:

$$\mathrm{Si}(\,^3P^o) + \mathrm{H} \rightarrow \mathrm{Si}\left(\,^3P\right) + \mathrm{H}\ (\text{or } \mathrm{SiH}(X^2\Pi) + \mathrm{M}) \qquad (6.23)$$

Monitored H* and H_2* states will most likely undergo the same formation and loss mechanisms as those in a MW-activated H plasma, described in Chapter 3, i.e. these excited states are pumped via Electron Impact Excitation and undergo near-resonant energy transfers, and are most likely quenched via non-radiative collisions with H and H_2. As before, they are still anticipated to be highly sensitive to the plasma parameters, such as the reduced electric field strength and the hyper-thermal component of the EEDF. Further discussion on these states is not warrented at this point, except noting that they could additionally facilitate ionization / collisional quenching upon collision with Si species.

In light of the above, it is a poor assumption to assert that the excited states of Si and SiH radicals are generated predominantly by EIE. Particularly considering that under base conditions, I(SiH*) and I(Si*) extend to beyond z = 27 mm (noting the high energy of these states, and I(H_2*) and I(H*) are tailing off

by z ~ 20 mm), which makes a case for chemiluminescent contributions. It does, however, make a reasonable starting point for developing a better understanding and a rationale behind their variations with changes in process conditions. The intensity of these radical emissions can be described crudely by Equations 6.24 (a) and (b) respectively, noting no attempt is being made at present to distinguish between formation of emitting singlet and triplet emissions.

$$I_{em}(\mathrm{Si}^*) = \varepsilon_{det}\frac{c}{\lambda}\mathrm{A}\frac{n_e(T_e,\mathrm{E})[\mathrm{Si}]k_{EIE}}{k_Q[Q]+\mathrm{A}} \qquad (6.24\ \mathrm{a})$$

$$I_{em}(\mathrm{SiH}^*) = \varepsilon_{det}\frac{c}{\lambda}\mathrm{A}\frac{n_e(T_e,\mathrm{E})[\mathrm{SiH}]k_{EIE}}{k_Q[Q]+\mathrm{A}} \qquad (6.24\ \mathrm{b})$$

Equation 6.25 provides an alternative way to describe *I*(SiH*) using Processes 6.13 (a), 6.20 (a) (using Si triplet excited state as opposed to Si singlet state), and versions of Process 6.23 to describe formation / loss mechanisms of Si* and SiH*.

$$I_{em}(\mathrm{SiH}^*) = \varepsilon_{det}\frac{c}{\lambda}\mathrm{A}\left(\frac{n_e(T_e,\mathrm{E})[\mathrm{Si}]k_{6.13\,(a)}}{(k_{6.23}(\mathrm{Si}^*)[Q=\mathrm{H\ or\ H_2}]+\mathrm{A})}\right)\left(\frac{[\mathrm{H}]k_{6.20\,(a)}}{(k_{6.23}(\mathrm{SiH}^*)[Q=\mathrm{H\ or\ H_2}]+\mathrm{A})}\right) \qquad (6.25)$$

The additional symbols used in Equations 6.24 and 6.25 have previously been defined in Chapter 5 for Equations 5.01 and 5.02. These Equations may still be indicative were these states formed by electron-ion recombination. Attention is now drawn to the presentation and interpretation of the OES data MW-activated Si/H plasmas.

6.3.3: Optical Emission Images and Spectral Analysis

As aforementioned, the SiH($A^2\Delta \rightarrow X^2\Pi$)(0,0) band head appears at λ = 414.27 nm, whilst the atomic Si singlet emissions appear at 288.2 nm and 390.5 nm. The Si triplet emissions are detected in second order at 2λ = 501.37, 502.88, 503.24, 503.89, 504.83 and 505.70 nm.[26] It is the sum of all 6 triplet emissions (in second order) that has been reported as the intensity for these Si triplet emissions. These emissions are contained within the monitored wavelength ranges of (i) 307-382 nm, (ii) 372-447 nm and (iii) 462.95-536.7 nm, and were collected alongside H_2(d→a) and H(n = 5 → n = 3) emissions, as previously reported in Chapter 3. Figure 6.02 (a) demonstrates a spatially-resolved false colour image collected under base conditions (with no methane present) between the wavelength ranges of 372.5-447.2 nm and between the height range of $-3 \leq z \leq 27$ mm, whereby z = 0 mm defines the top of a 3 mm thick Mo substrate. SiH(A→X), Si(390.5 nm) and H_γ emissions have been highlighted. Figure 6.02 (b) demonstrates an experimental spectrum of the SiH(A→X), Δv = 0 bands, a best fit simulation generated using PGOPHER, a simulation software package, and makes use of rotational constants describing the $A^2\Delta$ and $X^2\Pi$ states taken from Reference 43. A proposed molecular orbital diagram of SiH excited and ground state can be found in Appendix A6.1.

As before, the residual has been generated by subtracting the simulation from the experimental data and a comparison dataset collected from a MW-activated H plasma, both of which are also shown. It is evident that most residual peaks can be accounted for by emissions originating from a MW-activated H plasma. There is just one peak, observed at λ = 411.6 nm, that is unaccounted for. This is attributed to the Si($3s^2 3p5s\ (^1P^o) \rightarrow 3s^2 3p^2 (^1D)$) transition emitting at λ = 205.8 nm, which has been inadvertently detected in second order. Spatially-resolved images demonstrating the other Si singlet and triplet emissions can be seen in Figure 6.03 (a) and (b) respectively, whilst similar images for the monitored hydrogen (/ carbon-containing species upon the addition of methane in Section 6.3.6) emissions have already been illustrated in Chapter(s) 3(to 5).

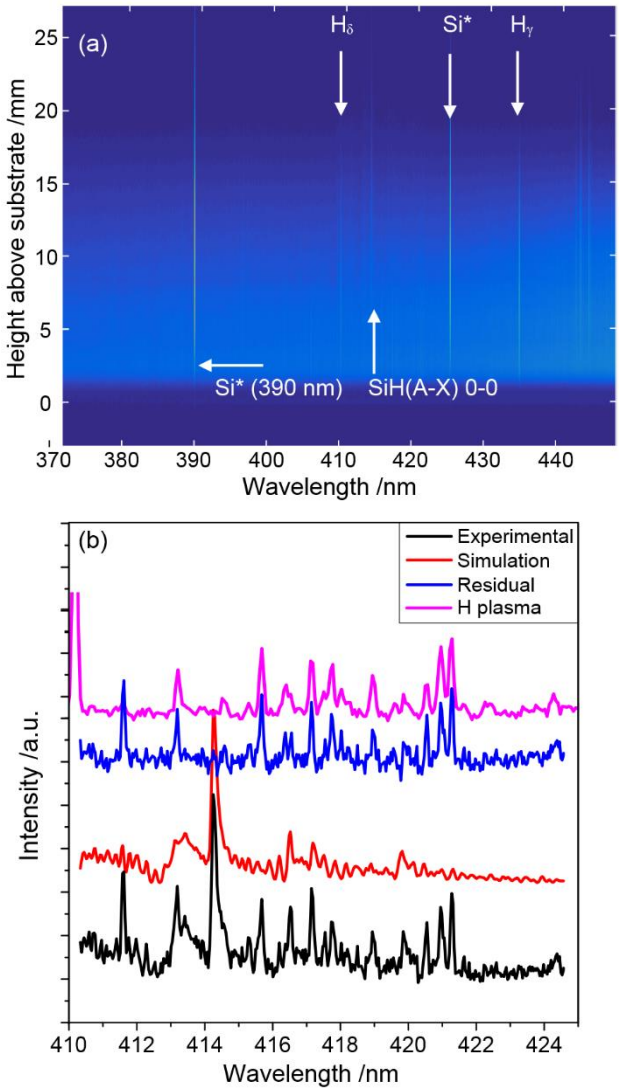

Figure 6.02: (a) $I_{em}(\lambda, z)$ image between the wavelength range of 372-447 nm taken under base conditions, i.e. P = 1.5 kW, p = 150 Torr, $F(SiH_4/H_2)$ = 15 sccm, $F(H_2)$ = 300 sccm, where z = 0 defines the substrate surface. The band head associated with I_{em}SiH(A→X)(0,0) is labelled, as are the emissions originating from Si* at 390 nm, and two of the H Balmer series. (b) Zoomed wavelength range between 410 and 425 nm illustrating experimental $I_{em}(\lambda)$ between $10.5 \leq z \leq 12$ mm above the substrate, (black), the SiH(A→X) best fit simulation (red), residual (blue), and emissions originating from a MW-activated H plasma operating under otherwise base conditions (pink).

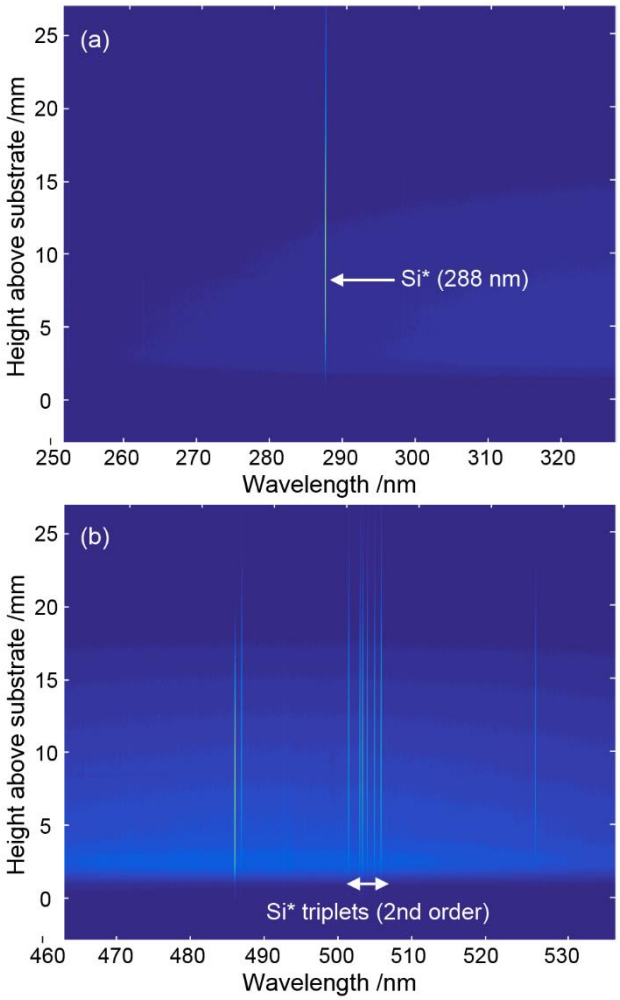

Figure 6.03: $I_{em}(\lambda, z)$ image between the wavelength ranges of (a) 252-327 nm and (b) 463-534 nm taken under base conditions, i.e. P = 1.5 kW, p = 150 Torr, $F(SiH_4/H_2)$ = 15 sccm, $F(H_2)$ = 300 sccm, where z = 0 defines the substrate surface. Emissions originating from Si* are visible as (a) a singlet emitting at 288 nm and (b) triplet emissions in the range 250-253 nm observed in second order (i.e. in the range 500-506 nm).

Figure 6.04 demonstrates the spatial distribution of various Si- and H- containing emission intensities monitored in a MW-activated Si/H plasma operating under base conditions. It is evident that each species has a very different spatial distribution and peaks at different heights; as before, H_2(d→a) and H_γ emissions peak at z ~ 2.5 mm and z ~ 7.5 mm respectively and do not extend beyond z = 20 mm. The Si atomic emissions peak at z ~ 10 mm above the substrate, while SiH(A→X) appears to peak at z ~ 12.75 mm. The SiH_x (x = 0, 1) emission intensities extend beyond z = 27 mm, implicit of excitation occurring at high z. The difference between the Si and SiH emission spatial distributions is returned to in Section 6.3.4.

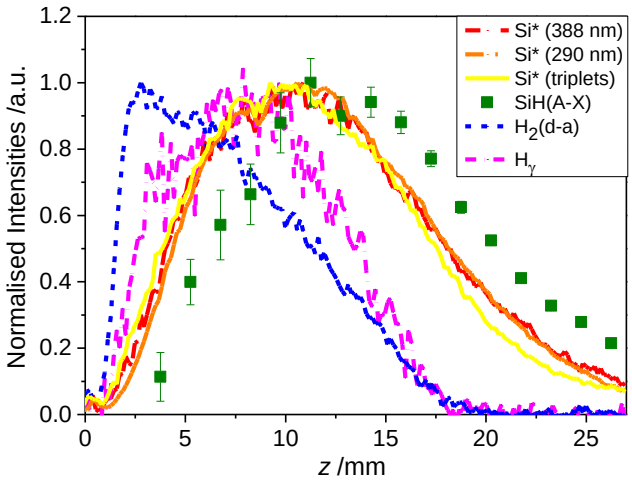

Figure 6.04: Normalised spatial distributions of various Si and H containing emitters under base conditions, i.e. P = 1.5 kW, p = 150 Torr, $F(SiH_4/H_2)$ = 15 sccm, $F(H_2)$ = 300 sccm.

6.3.4: Optical Emissions originating from MW-activated Si/H Plasmas

The collection and analysis of the optical emission data (and the results reported) for MW-activated Si/H plasmas were my own. The presented results reproduce an earlier study carried out by Alim Lalji, a final year project student working under my supervision toward his Chemistry MSci degree. Alim's results had a higher air impurity of ~10 ppm attributed with the chamber (*cf.* the ~0.25 ppm air leak impurity associated with the OES data presented in this chapter).[44] These quoted air impurities neglect feed gas impurities. Base conditions are defined as: P = 1.5 kW, p = 150 Torr, Mo substrate with d_{sub} = 32 mm, d_{wire} = 0.01″, $F(H_2)$ = 300 sccm and $F(SiH_4/H_2)$ = 15 sccm.

6.3.4.1: Varying Silane Flow

6.3.4.1.i: Neutral Species

Figure 6.05 illustrates how $I(H_2^*)$ and $I(H^*)$ vary as a function of silane input mole fraction maintaining otherwise OES-defined base conditions. Between $F(SiH_4/H_2)$ = 0 and 3 sccm, there is a slight decrease in both emissions, $I(H_2^*)$ maximises at z ~ 2 mm above the substrate (noting that there is an ~ ± 0.5 mm uncertainty, as is also the case with the results reported in Chapter 3). Upon further silane addition ($F(SiH_4/H_2)$ = 5 sccm), the emissions appear to contract spatially with the maximum of $I(H_2^*)$ shifting from z ~ 2 mm to z ~ 2.5 mm, (i.e. the equivalent of z ~ 2.5 mm shifting to z ~ 3 mm based on the intensity distributions described in Chapter 3) with both $I(H^*)$ and $I(H_2^*)$ decreasing. Further increasing silane flow, i.e. above $F(SiH_4/H_2)$ = 5 sccm, appears to have no significant impact on either emission's spatial distribution or relative intensity.

Note arrows have been added to the following Figures to highlight how peak intensities (black) vary. On occasion intensities featuring at low z and high z have substantially different behaviours to the peak intensity. When such differences are present, changes in intensities at these heights are indicated with

blue and orange arrows respectively. To avoid repetitiveness, this information is not repeated in the Figure captions.

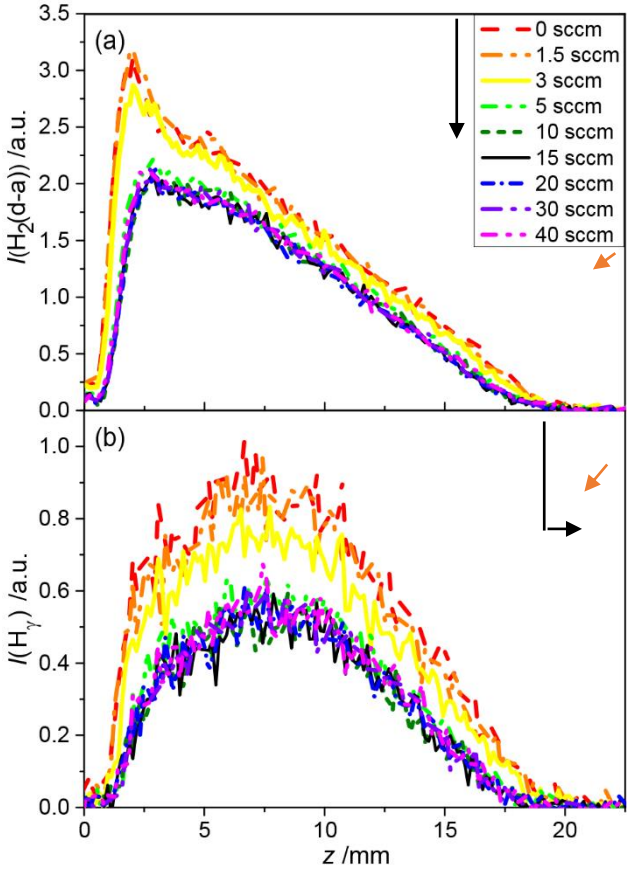

Figure 6.05: (a) $I(H_2^*)$ and (b) $I(H^*)$ as a $f(F(SiH_4/H_2)$ under otherwise base conditions.

Figure 6.06 demonstrates how the triplet and singlet Si emission intensities vary as a function of $F(SiH_4/H_2)$ under otherwise base conditions. The two singlet emissions exhibit identical spatial profiles to one another and identical changes in their relative emission intensities with increased silane flow rate. A careful comparison at higher silane flow rates suggest that the singlet emission peaks slightly higher in z than that of the summed triplet emissions, but the shift is sufficiently small that it could fall within experimental uncertainty. The triplet emissions also appear to have a subtly broader spatial profile than the singlet emission profiles and demonstrate an increase in intensity with increasing silane. Figure 6.06 illustrates a significant difference in the relative increase of singlet and triplet Si spin state emissions with increasing silane fraction. This is highlighted more clearly in Figure 6.07.

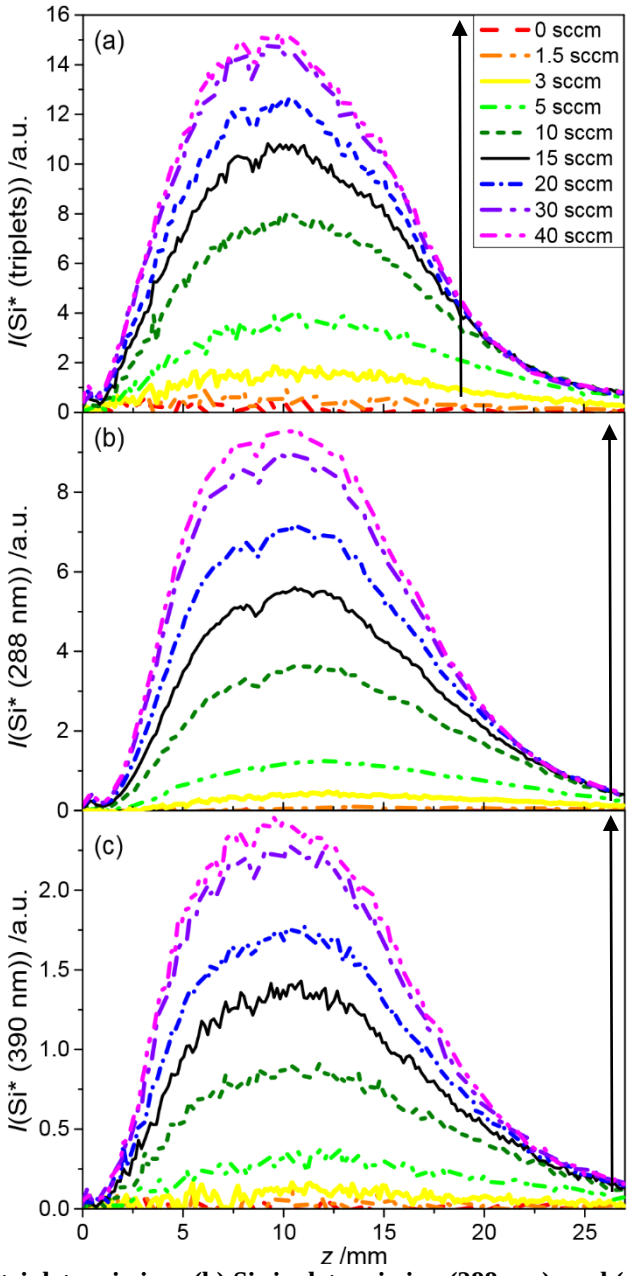

Figure 6.06: (a) summed triplet emissions (b) Si singlet emission (288 nm), and (c) Si singlet emission (390 nm) as a *f*(*F*(SiH₄/H₂), *z*).

Figure 6.07 demonstrates how $I(H_2^*)$, various $I(H^*)$, $I(Si^*)$, and $I(SiH^*)$ vary as a function of silane flow rate. $I(H_2^*)$ is analysed by summing intensities between $0 \leq z \leq 3$ mm, whilst H*, Si* and SiH* have been analysed by summing intensities between $9 \leq z \leq 12$ mm. For display purposes, all conditions have been normalised so that the intensity is unity at base conditions. The differences between $I(SiH^*)$, the singlet and the triplet $I(Si^*)$ emissions are more apparent, as are the similarities between the two $I(Si^*)$ singlet emissions. The non-linearity of these emissions at low $F(SiH_4)$ likely corresponds with changes in the prominent ions, as discussed in the following subsection. The non-linearity above $F(SiH_4) \geq 30$ sccm might be attributable to effective (non-linear) mass-dependent thermodiffusion of Si from the hot plasma region, as was seen with Ar in Chapter 3. Further, the Si triplet emissions are prone to self-absorption in the cooler regions. Such an effect would become increasingly apparent with

increasing input silane mole fraction and result in the observed divergence between *I*(Si*) singlet and triplet emissions.

The two investigated *I*(H*) emissions also demonstrate identical behaviour and their peak intensity variations are similar to peak *I*(H_2*) emissions, as explained in Section 6.3.4.ii. Henceforth, the two singlet Si (and *I*(H*)) emissions may be used interchangeably and are assumed as representative of Si singlet emissions (and H* emissions).

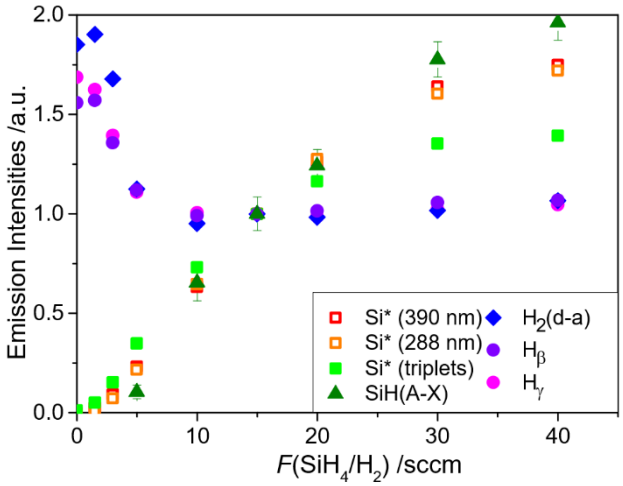

Figure 6.07: Intensities of summed triplet emissions, Si singlet emissions ((288 nm), and (390 nm)), H_2*, H* and SiH* as a *f*(*F*(SiH_4/H_2)) normalised to base conditions. The majority of species are analysed between *z* = 9 and 12 mm, whilst *I*(H_2*) has been analysed between *z* = 0 and 3 mm.

6.3.4.1.ii: Cations within MW-activated Si/H plasmas

It is evident from Table 6.1 that SiH_x ($0 \leq x \leq 4$) species have significantly lower ionization energies than H and H_2 (and H_2O when present). The addition of silane demonstrates a rapid reduction in *I*(H*) and *I*(H_2*) between *F*(SiH_4/H_2) = 1.5 and 5 sccm (i.e. between 5.0 ppm $\leq X_0(SiH_4) \leq$ 16.4 ppm) as shown in Figures 6.05 and 6.07, with changes in spatial profile also visible in Figure 6.05. The indication is that within this silane range, there is either (i) a significant increase in n_e (via ionization of SiH_x species whose attributed ionization energies are significantly lower than H and H_2) acting to decrease T_{tail} (and T_e) for a constant reduced electric field or more likely (ii) a significant decrease in the partitioning of absorbed power density toward hyperthermal electron energies, as the Si content is not yet sufficient to alter T_{tail} directly. The change in spatial profile likely reflects changes in n_e, T_e, but could also be reflecting an additional collisional quenching with silicon containing species. By *F*(SiH_4/H_2) = 5 sccm, SiH_x^+ is most likely larger than H_3^+ (and the negligible H_3O^+ attributed to the 0.25 ppm air leak). A further increase above *F*(SiH_4/H_2) > 5 sccm will act to generate additional electrons, but changes in n_e are more gradual (*cf*. the changes in n_e with a change in prominent ions). Consequently, above *F*(SiH_4/H_2) = 5 sccm, *I*(H*) and *I*(H_2*) do not vary significantly at their analysed heights. These emissions do, however, demonstrate an axial plasma contraction with increasing silane fraction. It is reasonable to deduce, therefore, that under base conditions (*F*(SiH_4/H_2) = 15 sccm, $X_0(SiH_4)$ = 47.6

ppm), SiH_x^+ ($0 \leq x \leq 4$) species are the prominent cations and will remain so under the majority of OES conditions explored. Si ions can be formed both by electron impact ionization of Si atoms, and by reactions between Si and H_3^+.

6.3.4.2: Varying Pressure

With increasing pressure, under otherwise base conditions, $I(H_2^*)$ and I(H*) demonstrate very similar behaviour to that observed in MW-activated H plasmas. This behaviour can be seen in Figure 6.08:

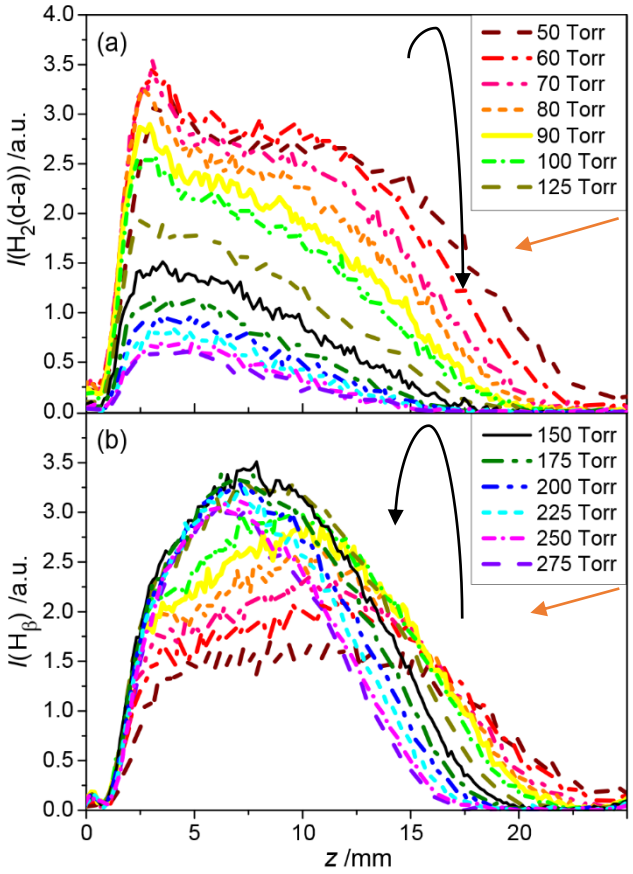

Figure 6.08: Spatial variation of (a) $I(H_2^*)$ and (b) $I(H^*)$ as a $f(p)$ under otherwise base conditions.

With increasing pressure, $I(H^*)$ and $I(H_2^*)$ demonstrate overall trends comparable to those previously seen in Chapter 3. $I(H_2^*)$ demonstrates an initial increase with pressure up to $p \sim 75$ Torr, reflecting the linear increase in $[H_2]$. Above this pressure, $I(H_2^*)$ scales with $\sim 1/p$ due to an increase in quencher, $[H_2]$, and a decrease in $T_{tail}(|E|/N \sim |E|/p)$, as previously seen for MW-activated H plasmas. $I(H^*)$ is also impacted by the pressure dependence of T_{tail} and increase in $[H_2]$, but as before, benefits from an increase in T_g (resulting in a substantial increase in [H] with increasing p, noting $[H]/[H_2] \sim p$). Therefore, $I(H^*)$ increases ~ linearly with increasing p up to $p \sim 125$ Torr. A further increase in pressure results in $I(H^*)$ decreasing less rapidly than $I(H_2^*)$, as previously observed; this can be seen more clearly in Figure 6.10. Figure 6.08 also demonstrates that both emissions are impacted by the axial plasma contraction associated with increasing p.

Figure 6.09 demonstrates the spatially-resolved profiles of (a) *I*(Si*) triplets, (b) *I*(Si*) singlets and (c) *I*(SiH*) with increasing pressure under otherwise base conditions:

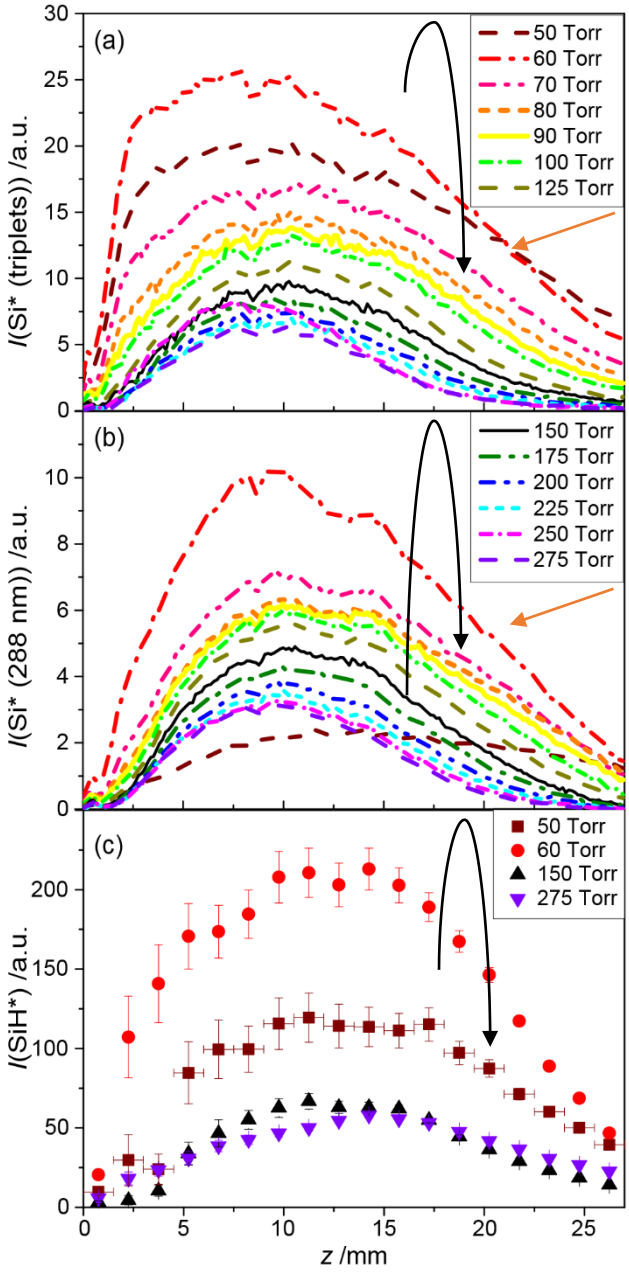

Figure 6.09: (a) summed triplet emissions (b) Si singlet emission (288 nm), and (c) SiH(A→X) emission as a *f*(*p*, *z*) under otherwise base conditions.

At face value, the OES data provide an ~ 10:1 ratio between *I*(SiH*) and *I*(Si*) singlet at 288 nm, and 5:1 between *I*(SiH*) and *I*(Si*) triplets under OES base conditions; the latter comparison is less meaningful than the first, as *I*(Si*) triplets were collected in second order (with an unknown second order reflection / detection efficiency) and all triplet intensities were summed together.

With T_e ~ 1.2 eV, a Maxwell Boltzmann distribution, f_{MB}, yields relative values of 27:7:6 for E = 3 eV (emitting SiH(A) state energy), 4.9 eV (emitting Si triplet state energy) and 5.1 eV (emitting Si singlet

state energy). Such a ratio would be taken as indicative of the relative number of electrons available to excite each state, assuming these states were excited by EIE (which has already been deemed unlikely at least for SiH). Once degeneracies have been considered, this ratio simplifies to 12:7:2. The transitions have Einstein-A emission coefficient values of ~ 2.88 × 10^6 s^{-1}, ~ 2× 10^8 s^{-1} and 2.18 × 10^8 s^{-1} respectively, [46,45] however even with these values, it is still not possible to speculate on relative [SiH]:[Si] via relative emissions without further information on other prominent formation mechanisms, prominent quenchers (likely H or H_2), quenching coefficients and electron impact cross-sections.

Figure 6.10 demonstrates how the investigated intensities vary with increasing pressure when summed between $9 \leq z \leq 12$ mm (except $I(H_2^*)$ analysed between $0 \leq z \leq 3$ mm) under otherwise base conditions. Generally, increasing the pressure results in an initial increase in the investigated H-based emission intensities followed by a decrease for p > 100 Torr. The emissions originating from Si-containing species rise more sharply between p = 50 and 60 Torr, maximise at p = 60 Torr and drop rapidly with a further increase in pressure.

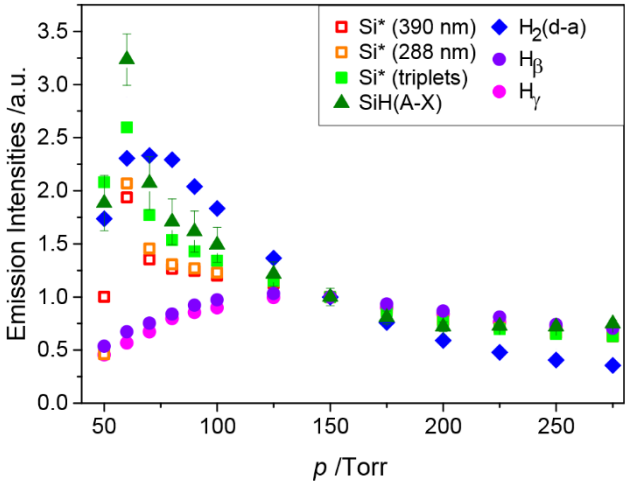

Figure 6.10: Intensities of summed triplet emissions, Si singlet emissions ((288 nm), and (390 nm)), H_2*, H* and SiH* emissions as a *f*(*p*)) normalised to base conditions. Species are analysed between *z* = 9 and 12 mm, except for *I*(H_2*) which has been analysed between *z* = 0 and 3 mm.

I(Si*) and *I*(SiH*) both increase more steeply (*cf.* *I*(H_2*) and *I*(H*)) between p = 50 and 60 Torr. Upon repeat experiments, it is seen that the relative increase between these pressures is somewhat irreproducible, which can perhaps be attributed to their sensitivity to the MW tuning and the cleanliness of the chamber walls. At p = 60 Torr, these emissions are reproducibly at their most intense and all three Si-containing emissions have distinct spatial distributions. These emissions maximise at z ~ 9 mm, 10 mm and 12.5 mm for the Si* triplet, singlet and SiH* emissions respectively. The Si triplet emissions are substantially broader than that of the Si* singlet and SiH* spatial distributions at low pressures. Perhaps the differences in these spatial distributions are inferring the reliance of [H] (most likely maximising in the hottest plasma regions) in the generation of Si* singlet and SiH*, see Processes 6.20 (a) and 6.22.

The difference in Si* spin state emission distributions may be reflecting a difference in formation mechanisms, quenchers, quenching rates of Si* triplet (relative to Si* singlet state and SiH*), or most likely, a difference in [Si(^{3}P)] ground state and [Si(^{1}D$_2$)] (e.g. if the excited Si singlet states were preferentially generated by EIE of the metastable singlet state or maintained a Boltzmann distribution population and the excitation maintains some memory of the spin-state that was excited) at low pressures. If this is the case, it would also be indicating that at lower pressure, where [H] number density is lower, there is a lack of coupling between the two Si spin excited states via Process 6.22. Alternatively, it could also be reflecting changes in the homogeneity of triplet self-absorption.

I(SiH*) comparatively maximises in a region where [H] is maximising and T_g is starting to decrease (both of which are deemed favourable in the production of SiH (and SiH* if generated by a chemiluminescent reaction between Si and H atoms), whilst the decrease in SiH* intensity with further increase in plasma height might be associated with an unfavourable decrease in T_g for chemiluminescent contributions) and crucially if the emitting state (or a parent species, e.g. Si(^{1}D) or Si(^{3}P^o)), is generated by electron impact excitation, or electron-ion recombination, n_e and T_e are also decreasing axially with further increases in z.

With a further increase in pressure, these intensities reproducibly drop more sharply than I(H$_2$*) and I(H*), with the two different I(Si*) spin state trends converging for $p \geq 125$ Torr, in spite of the two orders of magnitude difference in Einstein-A emission coefficients. This perhaps implies that above 125 Torr, the two emitting Si spin states are sufficiently coupled, or that they have the same formation / loss mechanisms, of which the quenching rates likely exceeds their emission rates. At p = 150 Torr, Si* triplet and singlet, and SiH* emissions peak at z ~ 10 mm, 11 mm and 12.75 mm respectively. The observed decrease in these intensities (with increasing pressure) is indicative of increasing quenching rates, whilst the similarity in these emission trends with pressure for $p \geq 125$ Torr implies that they maintain a constant production / quenching rate ratio to one another as a f(pressure) and are indicative that these states are likely quenched by a common species, Q, with comparable temperature-dependent quenching rates, whereby most likely, [Q] = H or H$_2$, the two most prominent plasma species. All investigated emissions highlight plasma contraction with increasing pressure.

At $p \geq 150$ Torr, I(Si*) does not extend above z = 27 mm, indicating that electron densities do not extend further than this plasma height. Comparatively, I(SiH*) extends well above z = 27 mm for all investigated pressure conditions, reinforcing the notion of a significant chemiluminescent contribution from Si atoms reacting with H or H$_2$ reactions (as exampled by Processes 6.20 (a) and (b)).

6.3.4.3: Varying Power

Increasing power under otherwise base conditions yields an improved agreement between the *P*-dependence of observed $I(H_2^*)$(z ~ 7 mm) behaviour and modelled $\{H_2\}$ for MW-activated H plasmas, as demonstrated in Chapter 3. This behaviour can be seen in Figure 6.11.

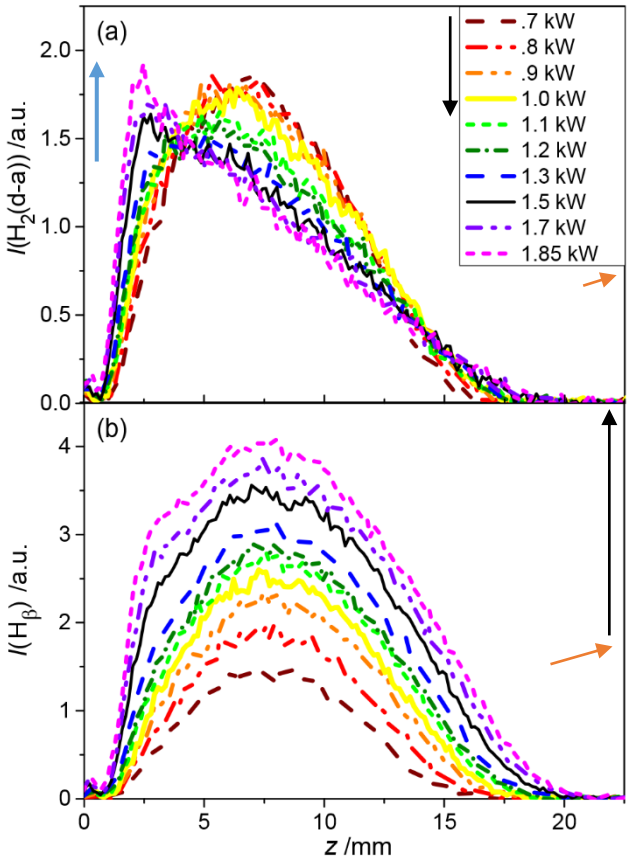

Figure 6.11: Spatially resolved $I(H_2^*)$ and (b) $I(H^*)$ as a $f(P)$ under otherwise base conditions

With increasing power, $I(H^*)$ and $I(H_2^*)$ replicate the trends observed in MW-activated H plasmas. $I(H^*)$ maximises at z ~ 7.5 mm, whilst $I(H_2^*)$ maximises at z = 6.5 mm for P = 0.7 kW. As before, $I(H^*)$ increases linearly with increasing P, whilst $I(H_2^*)$ quenches centrally and develops a low z component with increasing P (upto P = 1.3 kW). This low plasma contribution increases more significantly with further with increasing power, whilst central emissions remain somewhat more constant. Again, these emissions evidence axial plasma expansion with increasing power. At low z, the $I(H_2^*)$ is less sharp for higher powers, *cf.* a MW-activated H plasma, which might be indicative of changes in electron and ion density, T_{tail}, and / or collisional quenching with Si atoms.

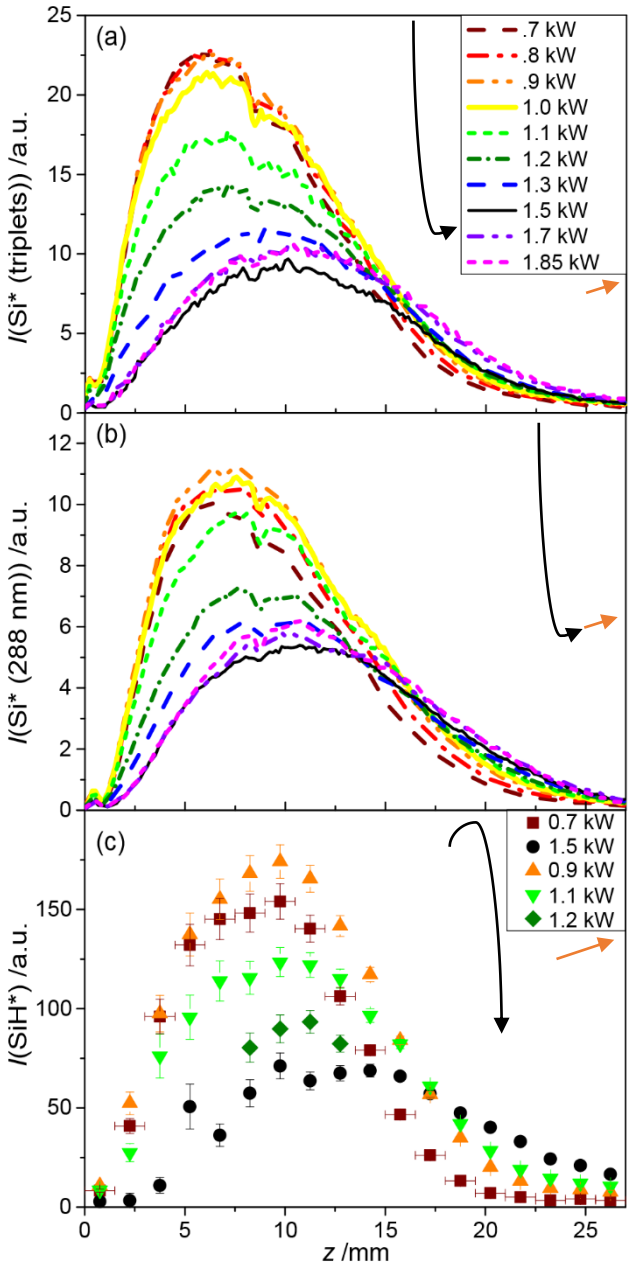

Figure 6.12: Spatially resolved intensities of (a) summed triplet emissions (b) Si singlet emission (288 nm), and (c) SiH* emission as a *f*(*P*) under otherwise base conditions.

With increasing power, *I*(Si*) singlets, triplets and *I*(SiH*) all demonstrate similar behaviour, there are only minor variations in each of their emission intensities and spatial distributions between $0.7 \leq P \leq 0.9$ kW. Above this, the behaviour is more comparable between the emitting Si species, and as can be seen with H atom emissions in Figure 6.11 (b), there is a clear axial expansion in plasma emission.

Peak *I*(Si*) triplet intensities relocate from $z \sim 6$ mm to $z \sim 10$ mm and steadily decreases in value between $0.9 \leq P \leq 1.5$ kW. Above $P = 1.5$ kW, there is a small increase in *I*(Si*) triplet emission, as seen in Figure 6.12 (a). Comparable behaviour can be seen in Figures 6.12 (b) and (c) for *I*(Si*) singlet and *I*(SiH*) with peak intensities maximising at slightly different *z*.

Figure 6.13 demonstrates how these intensities vary as a $f(P)$ at a constant height. It is clear from Figure 6.11 (a) and 6.12 that investigating the power dependence of these emission intensities at any specific height does not provide a full picture of their variations, nor does it represent variation of intensities above $z > 15$ mm, which instead demonstrates an intensity increase with power as a result of plasma expansion.

Nonetheless, Figure 6.13 demonstrates the similarity in the behaviour of all Si-containing species analysed between $9 \leq z \leq 12$ mm. These intensities increase between $P = 0.7$ kW and $P = 0.9$ kW, above which, they decrease up to $P \sim 1.5$ kW, and level off with further increase in P. I(H*) and $I(H_2^*)$, analysed between $9 \leq z \leq 12$ mm and $0 \leq z \leq 3$ mm respectively, as before, both increase linearly with increasing P.

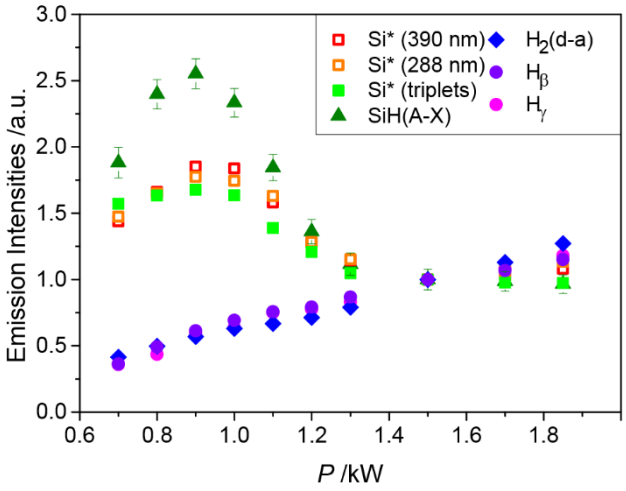

Figure 6.13: Intensities of summed triplet emissions, Si singlet emissions ((288 nm), and (390 nm)), H_2^*, H* and SiH* emissions as a $f(P)$) normalised to base conditions. The majority of species are analysed between $z = 9$ and 12 mm, whilst $I(H_2^*)$ has been analysed between $z = 0$ and 3 mm.

With increasing P, $|E|$ (and therefore $|E|/N$), T_g, n_e, jE, [H]/[H_2], plasma diameter and a rate coefficient with a functional form $T_g^{\beta}e^{-E/Tg}$ (where E represents the energy difference between reactants and activation barrier and β is a unitless exponent, which generally holds a positive value) are all parameters which increase. Upon reaching $T_g \sim 3000$ K, T_g (and $T_g^{\beta}e^{-E/Tg}$) will not increase with a further increase in P, but would instead result in further plasma expansion, an increase in [H] and perhaps n_e.

I(Si*) and I(SiH*) demonstrate comparable power trends under the investigated conditions, Si triplet and singlet emissions also demonstrate more comparable spatial distributions (*cf.* I(Si*)(z) observed at $p = 60$ Torr, which were vastly different). With increasing power, I(Si*) and I(SiH*) generally decrease and dramatically change in their spatial distributions (including their maximal intensity) and hence, analysed at a constant height, these emissions deceivingly appear to increase between $P = 0.7$ and $P = 0.9$ kW in Figure 6.13. For $P = 0.7$ kW, the triplet emissions maximise at $z = 7$ mm, whilst the singlet and SiH emissions maximise at $z = 7.5$ and 9.75 mm and extend to $22.5 \leq z \leq 25$ mm. As before, the differences in these emission intensity spatial distributions and maxima are possibly reflecting differences in the spatial distribution of ground state species (or reactive ions), $n_e(z)$ and $T_e(z)$ (or

differences in prominent formation mechanisms). Upon increasing P, these emissions expand axially beyond z = 27 mm, but decrease in relative intensity up to P = 1.5 kW. The spatial distributions at P = 1.5 kW match those described for p = 150 Torr. Increasing P above this power acts to increase emission intensity maxima subtly.

The decrease in I(Si*) and I(SiH*) between $0.9 \leq P \leq 1.5$ kW infers that the reactive quenching rate is common between the two species and increasing significantly faster than excitation rates (which may scale with n_e). The inference is that the number density of the prominent quencher, [Q], and the quenching rate coefficient are both increasing. The latter will not vary particularly significantly in the hot plasma regions, as T_g varies by only a few hundred Kelvin. The assertion therefore is that [Q] = [H] (rather than [H_2], which would decrease slightly in the hot plasma regions with increasing T_g). At P = 1.5 kW, T_g is likely approaching 3000 K, yet these emission intensities do not vary significantly with increasing power further. The likely explanation is that T_g and k_Q ~ constant. Therefore, another excitation mechanism is likely also contributing (perhaps EIE (in the case of SiH* or electron-ion recombination), and that, combined, the overall rate of production is approximately equal to the rate of loss for these excited states (as a function of further increases in P). Without 2-D plasma modelling, further reading and/or further work / analysis, it is not possible to interpret these results further.

One means to experimentally verify the inferred excitation mechanisms would be to compare the investigated I(Si*) singlet state distributions as a f(z, conditions) to the spatial distribution of I(Si($3s^2 3p5s\ (^1P^o) \rightarrow 3s^2 3p^2(^1D)$)) emission. The emission was detected in second order (2λ = 411.6 nm) and mentioned in the discussion surrounding Figure 6.01. Notably, this state has an energy level of 6.80 eV. Were these states predominantly excited by a common mechanism, e.g. EIE, the emissions might be expected to hold different spatial distributions, (as indirectly demonstrated with the different emitting CH* states investigated in Chapter 5), whereas if the prominent excitation mechanism were, for example, e-ion recombination, the spatial distributions ought to be more comparable under the assumption that the branching ratio has a weak T_e / T_g dependency. This analysis would have been included if time were permitting.

6.3.5: Atomic Si Column Density Measurements from MW-activated Si/H Plasmas

This Section establishes the analytical procedure used for converting absorption measurements into column densities and provides a developing rationale behind the measured {Si(J)} spatial variation under base conditions. {Si(J = 1 and 2)} are then explored as a function of process conditions. These values can be related via a Boltzmann distribution (assuming local thermal equilibrium) to estimate a gas temperature associated with the Si triplet ground state, T_{Si}, and a total {Si}. A theoretical calculation of total Si-containing column densities, {Si_{tot}}, is made through a consideration of the ideal gas law, using $T_g(r)$ provided from 2-D plasma modelling presented in Chapter 3. It becomes clear through such calculations that most of the silicon content has not been accounted for by such measurements.

Additional possibilities (e.g. Si_2H_x, air leaks, and the possible role of the low-lying metastable singlet state of Si) have been summarised with more detail available in the Appendices (A6.4, A6.5 and A6.6 respectively). One feasible explanation for the missing Si content is deduced to be the air impurity (through the use of impure hydrogen gas and a leaking cavity). The air leak is therefore investigated as an additional parameter space, total gas flow. With these additional considerations, it is possible to speculatively rationalise the measured {Si} variation with changes in process conditions.

6.3.5.i: Atomic Si Column Density Calculations under CRDS Base Conditions

Si column density measurements were carried out on transitions from selected spin-orbit components of the Si triplet ground state, at absorption wavenumbers centred on $\bar{\upsilon} = 1/\lambda = 39606.0$ cm^{-1} via the Si($3s^23p4s$, $^3P^o$, $J = 0 \leftarrow 3s^23p^2$, ^3P, $J = 1$) absorption and reproduced using the Si($3s^23p4s$, $^3P^o$, $J = 1 \leftarrow 3s^23p^2$, ^3P, $J = 2$) transition centred at $\bar{\upsilon} = 39537.1$ cm^{-1}. The investigated ground state $J = 1$ and 2 have energies of 77.12 and 223.16 cm^{-1} (0.00956 eV and 0.02767 eV) relative to the $J = 0$ level. The probed transitions have respective Einstein-B absorption coefficients of 7.05×10^{20} $m^3J^{-1}s^{-2}$ and 5.20×10^{20} $m^3J^{-1}s^{-2}$ calculated using Equations 2.22 and 2.23 with the Einstein-A emission coefficients reported in Table 6.1.[26,46]

Figure 2.14, reproduced below, and Figure 6.14 demonstrate an example of calibrated absorption peaks for $\bar{\upsilon} = 39606.05$ cm^{-1} and $\bar{\upsilon} = 39537.13$ cm^{-1} respectively. The calibration data are collected using an etalon, which demonstrates constructive and destructive interference patterns as a $f(\bar{\upsilon})$. The calibration data is collected over a large wavenumber range with starting / ending (and intermediate) wavenumbers recorded. The fringe maxima are separated by $\bar{\upsilon} = 2.10$ cm^{-1} and act as a means to calibrate the absorption data in frequency space. Such patterns are collected alongside the absorption data (measured as the inverse of ring down time, s^{-1}) and the mean squared error (the residual between the natural logarithm of the raw time decaying signal and its linear best fit, of which the gradient is recorded as the measured $1/\tau$, as seen in example Figures 2.20 and 6.14). The peak is baselined, indicated by the dashed horizontal lines and fitted to a Gaussian. Once aligned, a typical baseline decay time is ~ 220 to 240 ns for an empty cavity. The integrals of the fitted Gaussian areas (once baselined, as indicated in the Figure by a dashed baseline) are used in Equation 2.26 to calculate {Si, ^3P ($J = 1$)} and {Si, ^3P ($J = 2$)} respectively.

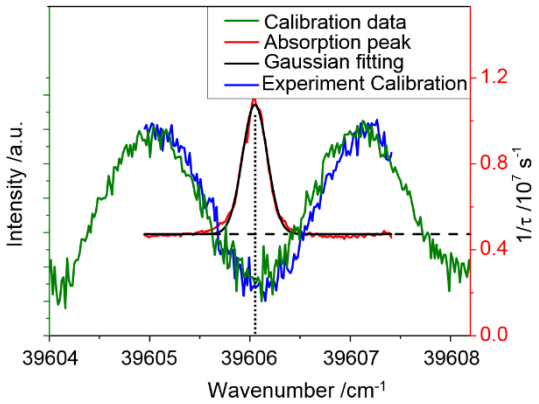

Figure 2.14 (repeated): Example absorption data (red) of Si($3s^2 3p4s$, $^3P^o$, J = 0←$3s^2 3p^2$, ^3P, J = 1), $\bar{\upsilon}$ = 39606.048 cm^{-1}, with a best fit Gaussian curve (black), the associated calibration data (blue), which have both been calibrated against the wavenumber calibration dataset (green).

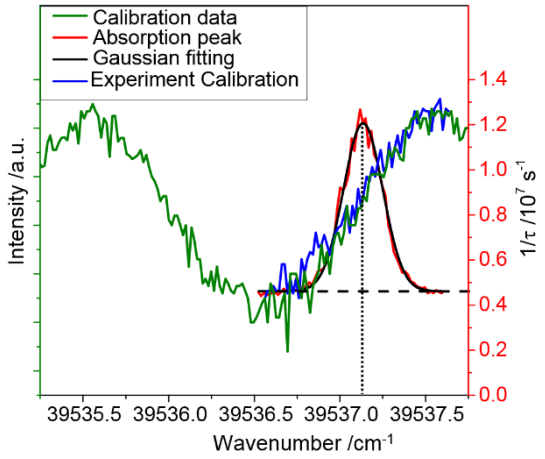

Figure 6.14: Example absorption data (red) of Si($3s^2 3p4s$, $^3P^o$, J = 1←$3s^2 3p^2$, ^3P, J = 2) transition centred at $\bar{\upsilon}$ = 39537.128 cm^{-1}, with a best fit Gaussian curve (black), the associated calibration data (blue), which have both been calibrated against the wavenumber calibration dataset (green).

Equations 6.26 and 6.27 are a reproduction of Equation 2.26 with the appropriate values (e.g. mirror separation (100 cm), upper and lower state degeneracies, g_i and g_j respectively, relating the column density to the Einstein-A emission coefficient, A, etc) included for calculating {Si, ^{3}P (J = 1)} and {Si, ^{3}P (J = 2)} respectively.

$$\{\mathrm{Si}\ {}^3P\ (J=1)\} = \frac{8\pi\ 100\ \mathrm{cm}\ (39606.05\ \mathrm{cm}^{-1})^2}{2.22\times10^8\ \mathrm{s}^{-1}} \times \frac{3}{1}\int \Delta k\ (s^{-1}) d\bar{\upsilon}\ (\mathrm{cm}^{-1}) \qquad (6.26)$$

$$\{\mathrm{Si}\ {}^3P\ (J=2)\} = \frac{8\pi\ 100\ \mathrm{cm}\ (39537.13\ \mathrm{cm}^{-1})^2}{9.04\times10^7\ \mathrm{s}^{-1}} \times \frac{5}{3}\int \Delta k\ (s^{-1}) d\bar{\upsilon}\ (\mathrm{cm}^{-1}) \qquad (6.27)$$

Base conditions are redefined as: P = 1.5 kW, p = 150 Torr, with gas flow rates $F_{\mathrm{reactor}}(H_2)$ = $F_{\mathrm{arms}}(H_2)$ = 300 sccm, (i.e. $F_{\mathrm{eff}}(H_2)$ = 600 sccm) and $F(SiH_4/H_2)$ = 0.5 sccm, equating to $X_0(SiH_4)$ = 0.83 ppm. Errors are propagated by multiplying the calculated column density to the propagated average mean error. The mean-squared error is recorded simultaneously to the etalon calibration fringes and 1/τ.

The integral can be calculated manually using Origin, a data analysis and graphing software, or can be semi-automated using MATLAB, a numerical computing software package. Figure 6.15 demonstrates excellent agreement between the two methods for calculating the spatially-resolved {Si, ^{3}P (J = 1)} column densities under the redefined base conditions, and hence, due to its efficiency, MATLAB is used for all further absorption analysis.

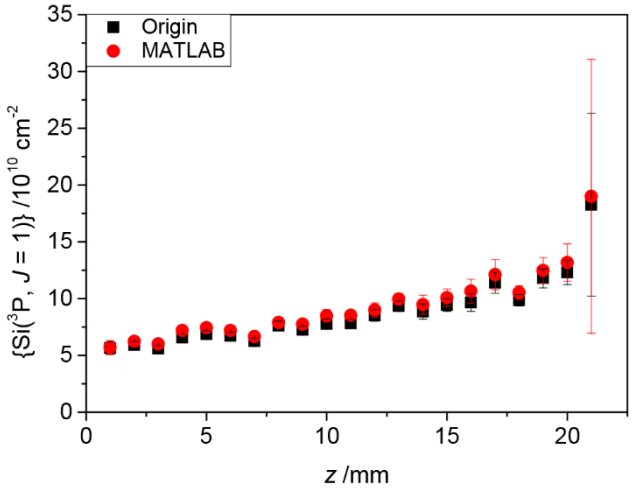

Figure 6.15: Measured {Si(^{3}P, J = 1)} analysed as a function of height above substrate manually using Origin (black squares) and through a semi-automated script using MATLAB (red circles) under redefined base conditions (P = 1.5 kW, p = 150 Torr, with gas flow rates $F_{reactor}(H_2) = F_{arms}(H_2)$ = 300 sccm, (i.e. $F_{eff}(H_2)$ = 600 sccm and $F(SiH_4/H_2)$ = 0.5 sccm). = $F_{arms}(H_2)$ = 300 sccm, (i.e. $F_{eff}(H_2)$ = 600 sccm and $F(SiH_4/H_2)$ = 0.5 sccm).

Figure 6.15 demonstrates that {Si(J = 1)} increases as a function of height above substrate, maximising at the highest measurable z. The vertical lines are propagated error bars propagated as described above and represent an estimated standard deviation. Generally, the errors are too small to see on the graph with the chosen scale. It is suspected that these have been undercalculated.

{Si} contrasts significantly to spatial distributions of previously measured {H(n = 2)}, {CH}, {C_2(a)}, (and {BH} upon the addition of diborane), which generally peak in regions of higher T_g and/or n_e (required to sustain the steady-state populations of these species).[29] This reinforces the assertion that [H] is sufficient to drive $SiH_4 \rightarrow$ Si, even in the cool regions of the plasma / chamber.

A simple test, not reported, consisted of a MW-activated H plasma operating at P = 1.85 kW, p = 75 Torr (i.e. an expansive MW-activated H plasma) and verified that without the presence of silane, there were no Si peak absorptions at high z. This indicates that under all investigated conditions, the measured {Si} is sourced by the silane with no measurable contribution etched from the quartz window. The top of the substrate, z = 0 mm, is defined as the point at which minimal laser light can be detected (as the majority is being blocked) when a 3 mm thick substrate is present. There is therefore a ± 0.5 mm offset error associated with the height at which column densities are deemed to be measured.

Figure 6.16 demonstrates that {Si(J = 2)} is more populated but holds a comparable spatial variation to {Si(J = 1)}. The ratio between these two states appears to remain at a near constant value with increase in plasma height, z. This is returned to in Section 6.3.5.iii.

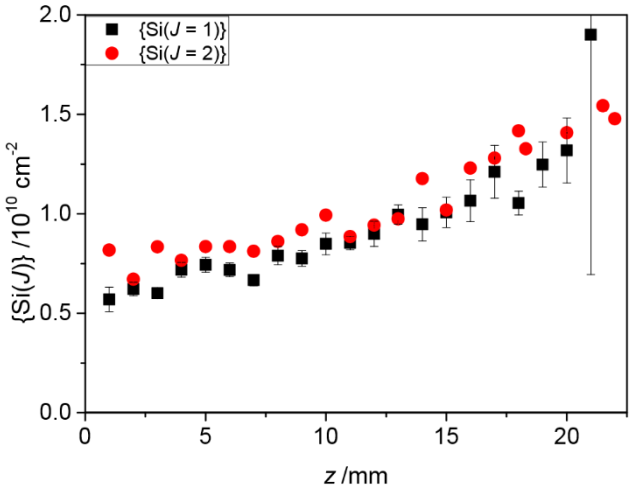

Figure 6.16: Measured {Si(^{3}P, J = 1)} (black squares) and {Si(^{3}P, J = 2)} (red circles) analysed as a function of height above substrate under redefined base conditions (P = 1.5 kW, p = 150 Torr, with gas flow rates $F_{reactor}(H_2) = F_{arms}(H_2)$ = 300 sccm, (i.e. $F_{eff}(H_2)$ = 600 sccm and $F(SiH_4/H_2)$ = 0.5 sccm).

6.3.5.ii: Atomic Si Column Density Measurements as a Function of Conditions

{Si(J = 1)} and {Si(J = 2)} are now measured and reported in Figure 6.17 as a function of (a) $X_0(SiH_4)$, (b) P and (c) p under otherwise base conditions. This data was collected collaboratively between myself and John Allden, and therefore features in his final year MSci research dissertation.[47] The analysis was my own.

Although the ring down time and laser intensity should be independent of height, there was slight variation attributed to a slightly less than perfect alignment / coupling of the laser (via an optical periscope) from the laser table onto the adjustable height stage that supports the final optics, which direct the laser beam into the cavity. Consequently, the column densities are measured at three heights of z = 5, 11 and 18.3 mm above the substrate. These heights were chosen to provide well-spaced measurements with higher laser intensities (to achieve better signal-to-noise).

The mass flow controller (mfc) used for the dilute silane (1 part per thousand in hydrogen) was adjusted to allow investigation of lower flow rates (i.e. a lower silane partial pressures). The maximum flow it facilitates in these experiments is 10 sccm. An mfc can typically control flows reliably down to ~ 5% of its maximum value (i.e. down to 0.5 sccm). Using flows much higher than $F(SiH_4/H_2)$ = 1-2 sccm lead to an obvious saturation of the ring down time or an absorption resonance, and hence, to vary silane fraction, $F_{eff}(H_2)$ was varied (with an appropriate adjustment of pumping rate to ensure constant p) with $F(SiH_4/H_2)$ kept constant at $F(SiH_4/H_2)$ = 0.5 sccm.

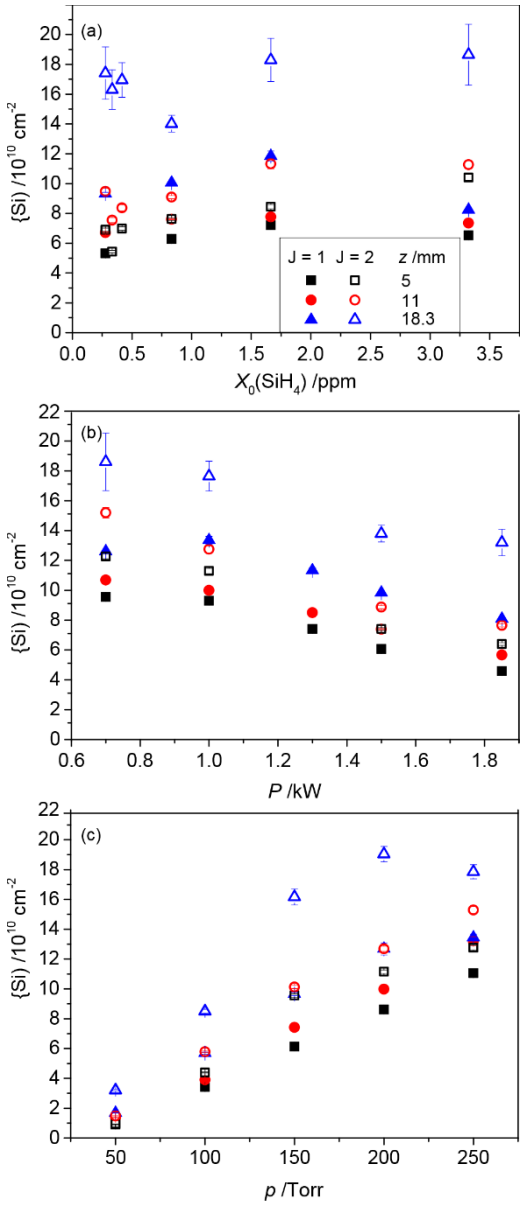

Figure 6.17: Measured {Si(^{3}P, J = 1)} (closed symbols) and {Si(^{3}P, J = 2)} (open symbols) analysed as a function of height (z = 5 mm (black squares), 11 mm (red circles) and 18.3 mm (blue triangles)) above the substrate and (a) X_0(SiH$_4$), (b) P and (c) p under otherwise base conditions (P = 1.5 kW, p = 150 Torr, with gas flow rates $F_{reactor}$(H$_2$) = F_{arms}(H$_2$) = 300 sccm, (i.e. F_{eff}(H$_2$) = 600 sccm) and F(SiH$_4$/H$_2$) = 0.5 sccm).

Figure 6.17 demonstrates that the measured {Si(J = 1)} and {Si(J = 2)} appear relatively flat with significant changes in silane fraction, decreases roughly linearly with forward MW power, and increases near linearly with total gas pressure at all investigated plasma heights. An explanation for these trends is returned to in Section 6.3.5.vi.

A careful examination shows that there is a near constant ratio between the measured {Si(J)} values at the three investigated heights, irrespective of the investigated condition. The indication is that the {Si(J = 1)} and {Si(J = 2)} spatial distributions and their variations with changes in operating conditions are similar, and that the variations with respect to height for any changes in operating conditions match the more finely resolved {Si} spatial distributions reported in Figures 6.15 and 6.16.

6.3.5.iii: Temperature Estimates using measured {Si(*J*)}

A further inspection reveals that the {Si(J = 2)} column density is greater than {Si(J = 1)} and that the ratio between measured {Si(J = 1)} and {Si(J = 2)} is approximately constant as a *f*(operating conditions, z). The ratio itself is somewhat unsurprising given their degeneracies and their state energies (0.00956 eV and 0.02767 eV, *cf.* <E> ~ 0.0259 eV at T_g = 300 K). Assuming that these two states are in local proximity to one another with populations dictated by a local thermal equilibrium (i.e. their relative ratio can be described by a Boltzmann distribution), the column density ratio between these states can be used to estimate an effective T_{Si}, which would provide some measure of the plasma region/radius at which [Si] is most prominent. Figure 6.18 (a) repeats the {Si(J)} spatial distributions reported for base conditions in Figure 6.16. Figure 6.18 (b) demonstrates that the calculated ratio between measured values of {Si(J = 1)}/{Si(J = 2)}(z) (i.e. R({Si(J = 1)/(J = 2)}), and the calculated temperature, $T_{Si}(z)$, both of which are demonstrated to be essentially independent of plasma height with values of ~ 0.87 ± 0.04 and 550 ± 100 K respectively. Under these assumptions, {Si(J = 0)} and {Si} = Σ{Si(J)} can be calculated using the average measured T_{Si} (550 ± 100 K). These are presented in Figure 6.18 (c).

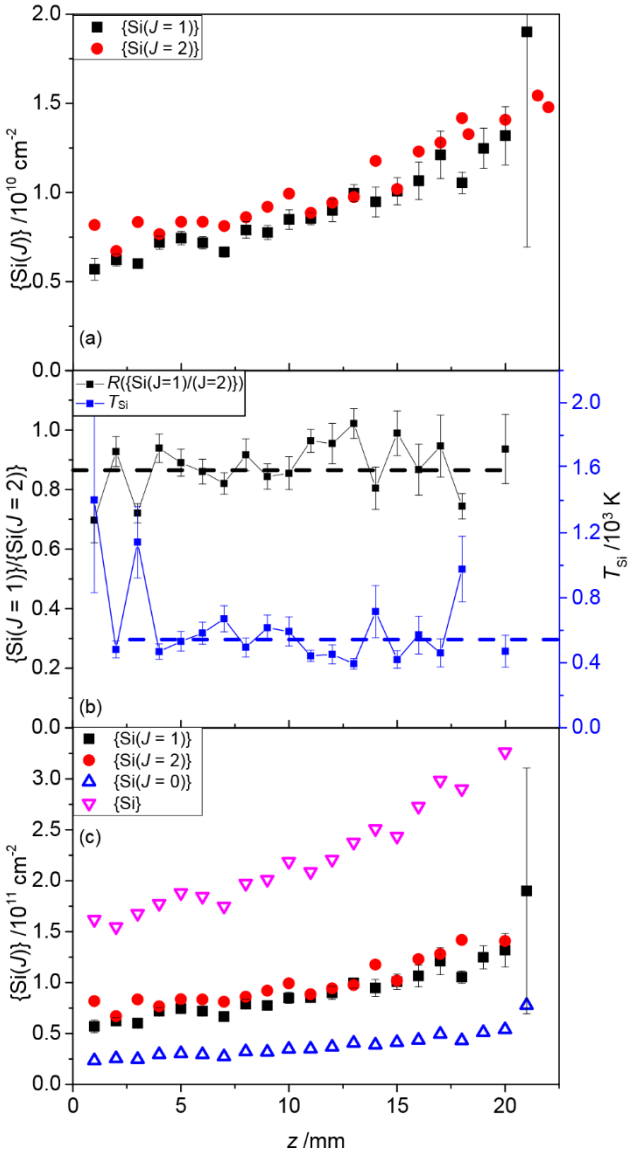

Figure 6.18: (a) Measured {Si(^{3}P, J = 1)} (black squares) and {Si(^{3}P, J = 2)} (red squares) analysed as a function of height above the substrate under base conditions. (b) R({Si(J = 1)}/{Si(J = 2)}) (black squares) and the calculated T_{Si} (blue squares) average at ~ 0.87 ± 0.04 and 550 ± 100 K respectively indicated by the dashed lines. (c) Measured (closed symbols) {Si(^{3}P, J = 1)} (black squares) and {Si(^{3}P, J = 2)} (red circles) and calculated (open symbols) {Si(J = 0)} (blue triangles) and total atomic {Si} (pink triangles) for T_{Si} = 550 K analysed as a function of height above the substrate under base conditions.

T_{Si} is now reported as a function of height and conditions in Figure 6.19.

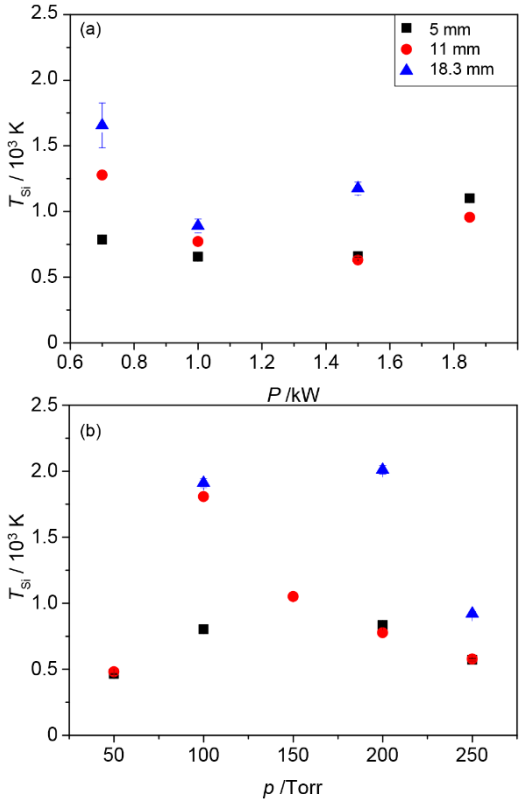

Figure 6.19: Estimated T_{Si} /10^3 K for varying (a) Power and (b) pressure under otherwise base conditions at z = 5 mm (black squares), 11 mm (red circles) and 18.3 mm (blue triangles) above the substrate.

Figure 6.19 demonstrates that the ratio of the spin-orbit state column densities (and thus the reported T_{Si}) are by and large invariant to changes in power or pressure, and largely independent of z, with a scatter concentrated in the range of $500 \leq T_{Si} \leq 1000$ K, which is in agreement with the estimated average T_{Si} calculated at base conditions ($T_{Si} \sim 550 \pm 100$ K). The observed variations and deviations are thought to reflect experimental error through imperfect alignment, signal/noise, and the possibility of minor saturation, noting that the column density measurements of the two spin-orbit states were carried out in separate plasmas. The reported errors have been propagated, as previously discussed, and are too small to see. Again, given the scatter of points in Figure 6.19, this indicates that the original errors reported in Figure 6.16 have been underestimated. The low T_{Si} values indicate that the Si atom number density, [Si], is maximal in the cooler regions of the plasma / chamber (i.e. at larger radii, $r \sim 53.5$ mm for $z \sim 10.5$ mm according to the 2-D plasma modelling provided in Chapter 3). This is also consistent with the axial variation of the column densities seen in Figure 6.18, whereby {Si} maximises axially at cat high z, i.e. in cooler plasma regions. It can be seen in Figure 6.17 that the column densities calculated at z = 18.3 mm have significantly larger errors than those measured at z = 5 and 11 mm.

6.3.5.iv: Calculating {Si_{tot}} and Measurement Concerns

Under base conditions, i.e. $X_0(SiH_4)$ = 0.83 ppm, an average of the column density measurements yields {Si(J = 1)} = 7.52 ± 0.07 × 10^{10} cm^{-2} and {Si(J = 2)} = 9.6 ± 0.2 × 10^{10} cm^{-2} at z = 11 mm with a

Boltzmann distribution reinforcing that these products maximise in the cooler region with T_{Si} ~ 750 K. From this, {Si(J = 0)} is estimated to be ~ 2.91 ± 0.03 × 10^{10} cm^{-2}, which yields a total atomic Si column density of {Si} ~ 2 × 10^{11} cm^{-2}.

Very crudely, a total SiH_x ($0 \leq x \leq 4$) species column density can be estimated by Equation 6.28, which has been derived from the ideal gas law ($n/V = p/RT$), whereby R = 8.31 $Jmol^{-1}K^{-1}$, N_A = 6.022 × 10^{23} mol^{-1}, 150 Torr at STP = 150/760 × 101,325 Nm^{-2} = 20,000 Nm^{-2}:

$$\{Si_{tot}\} = \frac{X_0(SiH_4) \times 20{,}000 \times N_A}{R} \int_0^{r=r_{max}} \frac{2}{T_{gas}(r)} \, dr \qquad (6.28)$$

The factor of 2 is required to account for the full diameter of the reactor (as opposed to considering just half of the reactor). Due to the estimated T_g ~ 750 K and net flow from the long arms, it is assumed that r_{max} = 60 mm, i.e. the Si content remains within the main chamber with negligible diffusion into the long side arms. Whilst this may seem physically unreasonable at first, there is an expected net flow of hydrogen inward from the arms into the chamber, which would act favourably for this approximation. This assumption is reinforced by a few limited studies, available in the Appendices (A6.2 and A6.3), which crudely demonstrates that {Si} ~ constant irrespective of $F_{arms}(H_2)$ ($F_{tot}(H_2)$ = constant). Equation 6.28 can be rewritten under base conditions as Equation 6.29:

$$\{Si_{tot}\} = \frac{0.83 \times 10^{-6} \times 20{,}000 \times 6.022 \times 10^{23}}{8.31 \times T(r)} \int_{0\ mm}^{r=60\ mm} \frac{2}{T_{gas}(r)} \, dr \qquad (6.29)$$

$1/T_g(r)$ for z = 10.5 mm is provided by 2-D physical plasma modelling of MW-activated H plasmas featuring in Chapter 3 and can be approximated as a 6th order polynomial. Figure 6.20 displays the polynomial and $1/T_g(r)$ as a function of radius.

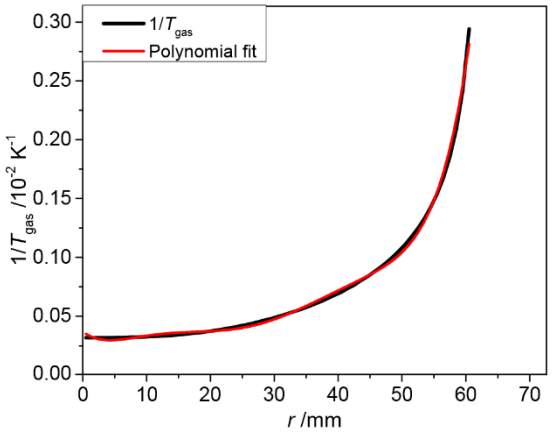

Figure 6.20: Modelled $1/T_{gas}$ /10^{-2} K^{-1} (black) as a function of radius, r (mm) at an axial height of z = 10.5 mm for a 1.5 kW, 150 Torr MW H_2 plasma. The red curve demonstrates a polynomial curve fitted to $1/T_{gas}(r)$, whereby $1/T_{gas}(r) \sim 3.64\times10^{-4} - 4.23\times10^{-5}\, r + 8.11\times10^{-6}\, r^2 - 6.07\times10^{-7}\, r^3 + 2.17\times10^{-8}\, r^4 - 3.60\times10^{-10}\, r^5 + 2.27\times10^{-12}\, r^6$.

The integral in Equation 6.13 provides $\int_0^{r=60} \frac{1}{T(r)}\ dr$ = 0.0462 mm/K. After a very careful consideration of units, Equation 6.13 produces $\{Si_{tot}\} \sim 1.12 \times 10^{13}$ cm^{-2}. It can therefore be estimated that $\{Si\}/\{Si_{tot}\} \sim 1.8$ % at $z \sim 10.5$ mm (i.e. the total estimated {Si} measured does not account for a significant percentage of total calculated $\{Si_{tot}\}$). The calculated $\{Si\}/\{Si_{tot}\}$ might be expected to reflect an average of $[Si]/[Si_{tot}]$ weighted to the cooler regions, whereby [Si] (and $[Si_{tot}]$) likely maximise.

Section 6.3.2 establishes that [Si] should be the largest Si-containing species and preliminary modelling reinforces that the column densities should be of the order 10^{13} cm^{-2}. Taking these results at face value, it is therefore somewhat surprising that the {Si} measured via CRDS experiments only accounts for ~1.8% of the total Si column density under CRDS Si/H base conditions. These measurements infer that [Si] maximises at $T_{Si} \sim 750$ K, i.e. the outer plasma regions. Decreasing the upper radial limit to r = 50 mm (i.e. the radial point at which $T_g \sim 750$ K in the 2-D plasma modelling) acts to increase $\{Si\}/\{Si_{tot}\}$ to ~ 3.1 %, i.e. a perturbation in the spatial distribution from $F_{arms}(H_2)$ does not account for the missing Si content.

As number densities vary inversely as a function of T_g, this ratio does not necessarily reflect $[Si]/[Si_{tot}]$ in the hot plasma regions. It also implies that in the coolest regions (i.e. near the water-cooled reactor walls) there could be a more prominent Si-containing species (if the spatial distribution is assumed to not experience a significantly perturbation by the net inward flow of gas from the arms).

The CRDS measurements reported, however, should be greeted with scepticism. To measure a column density on the order of 10^{13} cm^{-2} would require the measured ring down time to be ~ 2 ns, significantly smaller than the pulse width (~ 10 ns) and the PMT response time (on the order of 10 ns). With the current set up and the strong absorptive nature of the investigated peaks, a measurement of this column density magnitude is a physical impossibility. There was no evidence of saturation observed in the collection of data. The ring down trace always appeared substantially longer than the laser pulse width, except when high silane fractions were used. In these instances, the decay-component became negligible with the detected signal appearing as a laser pulse. The resulting absorption peak also demonstrated saturating features.

The FWHM of absorption peaks can be used as another means to infer saturation. From the collected data, the FWHM are inconclusive as to whether these experiments may have been saturated; Doppler broadening contributes ~ 0.14 cm^{-1} (calculated for T_g = 750 K using $\Delta\nu/\nu = (8kT\ln(2)/mc^2)^{0.5} = 7.17 \times 10^{-7} \times (T_g/28)^{0.5}$).[48] Combined with a laser broadening of ~ 0.1 cm^{-1}, the total line width of the absorption peaks should be ~ 0.17 cm^{-1}, rather than the 0.3 ± 0.03 cm^{-1} attributed to the collected data, and evidenced in the example data presented in Figures 2.14 and 6.14. This infers that the experimental broadening from the dye laser line width is ~ 0.27 cm^{-1}, significantly larger than the theoretical minimum for an optimised system. This is not necessarily physically unreasonable, previous absorption measurements on the NH molecule using the same apparatus yielded a broadening of ~ 0.3 cm^{-1}.[3]

Further, sitting on top of the absorption peak and turning off the silane flow results in an immediate exponential decay of signal, as evidenced in Appendix A6.2. This infers that these peaks are not saturated and that {Si} is sensitive to X(Si).

In spite of the CRDS measurement uncertainty and the current discrepancy between theory and preliminary modelling, the measured column densities (and their variation upon changes in operating conditions) presented above are reproducible with the measured linewidths demonstrably independent of spin-orbit J state, z, and operating process conditions. Perhaps the variation in measured column densities with process conditions and height should be regarded as indicative of a lower bound estimate of {Si}, rather than absolute {Si(J)} measurements. Of course, the obvious alternative interpretation would be that Si-containing content has not yet been fully accounted for.

6.3.5.v: Exploring the Effect of X_0(leak)

There are plausible reasons as to why the preliminary 2-D modelling and/or the measured {Si(J)} may be incorrect. These include the possibility of Si_2H_x ($0 \leq x \leq 6$) species, the possible role of gas impurities (particularly O_2 or H_2O) in gettering Si content to form H_xSiOH_m ($0 \leq x \leq 3$, $0 \leq m \leq 1$) and the possible contributions / roles that the low-lying metastable singlet Si state could play. These three possibilities are explored in further detail in the Appendices (A6.4, A6.5 and A6.6 respectively).

In summary, Si_2H_x ($0 \leq x \leq 6$) species seem physically unlikely upon consideration of the $X_0(SiH_4)$ range investigated and through a comparison of production / loss rate coefficients of Si_2H_x species. The second seems plausible, particularly in the cool plasma regions, whilst the third is deemed to account for an upper limit of ~ 2.7% of [Si] in the hot regions of the plasma (and significantly lower in cooler regions).

Given that Appendix A6.5 demonstrates a rich Si/H/O chemistry, which could facilitate a gettering of Si content, and that under the explored CRDS conditions, X_0(leak) > $X_0(SiH_4)$, X_0(leak) is an important parameter, which requires further exploration. In addition, at present, there is no obvious explanation for the non-linear behaviour in {Si(J)} as a $f(X_0(SiH_4))$, which contrasts significantly to changes in I(Si*) with silane addition, and the exponential decay noted for {Si(J)} when silane is switched off.

The OES and CRDS experiments demonstrate vastly different behaviours of I(Si*) and measured {Si} when varying $X_0(SiH_4)$ and can be seen in Figures 6.06 (and 6.07) and 6.17 (a). These differences may be accounted for by the manner in which $X_0(SiH_4)$ was varied. The mole fraction of silane investigated in OES and CRDS are $0 \leq X_0(SiH_4) \leq 11.76$ ppm and $0.28 \leq X_0(SiH_4) \leq 3.32$ ppm respectively.

In the OES experiments, $F(H_2)$ = 300 sccm, i.e. maintained at a constant flow, whilst $X_0(SiH_4)$ is increased by adjusting $F(SiH_4/H_2)$. As $F(H_2) >> F(SiH_4/H_2)$, X_0(leak) remains ~ constant in accordance with Equation 2.14. The OES experiments were also carried out in the regime where $X_0(SiH_4) >> X_0$(leak), and hence I(Si*) and I(SiH*) can be seen to increase even for low $F(SiH_4/H_2)$.

Contrastingly, the CRDS measurements on {Si(*J*)} as a function of $X_0(SiH_4)$, shown in Figure 6.17 (a) were carried out by varying $F_{eff}(H_2)$, whilst maintaining a constant $F(SiH_4/H_2)$ = 0.5 sccm. The expectation being that $X_0(SiH_4)$ and $X(Si) \sim 1/F_{eff}(H_2)$. Again, however, $F_{eff}(H_2) >> F(SiH_4/H_2)$, so any increase in $F_{eff}(H_2)$ also acts to decrease $X_0(leak) \sim 1/F_{eff}(H_2)$ in accordance with Equation 2.14 (a), (i.e. by increasing $F_{eff}(H_2)$, $X_0(SiH_4)$ and X_0(leak) both decrease whilst $X_0(SiH_4)$:X_0(leak) maintains a constant ratio of ~ 0.83:10 relative to one another).

If the Si/H/O chemistry explored in A6, or variants of such processes (e.g. $Si + O_2 \rightarrow SiO + O$), are correct, the rate at which Si content is gettered into H_xSiOH_m species would be a $f(1/F_{eff}(H_2))$. Figure 6.17 (a) demonstrates that {Si} ~ constant as a $f(F_{eff}(H_2))$. The proposed explanation for this is that any increase in [Si] achieved by reducing $F_{eff}(H_2)$ is compensated by an increased gettering of [Si] into [H_xSiOH_m] from an increased X_0(leak) contribution. Conversely, a decrease in [Si] resulting from an increased $F_{eff}(H_2)$ will be compensated by an increase in [Si] due to a decrease in X_0(leak) and therefore H_xSiOH_m.

To verify as to whether this may be the case, the final spin-orbit state, {Si(*J* = 0)}, has been investigated via the Si($3s^2 3p4s$, $^3P^o$, $J = 1 \leftarrow 3s^2 3p^2$, ^3P, $J = 0$) transition centred at 39760.29 cm^{-1} and calculated using Equation 6.30.

$$\{\mathrm{Si}\ ^3P\ (J=0)\} = \frac{8\pi\ 100\ \mathrm{cm}\ \ (39760.29\ \mathrm{cm^{-1}})^2}{7.39 \times 10^7\ \mathrm{s^{-1}}} \times \frac{1}{3} \int \Delta k\ (s^{-1}) d\bar{\upsilon}\ (cm^{-1}) \qquad (6.30)$$

This transition has a higher Einstein-B absorption coefficient of 2.09×10^{21} $m^3J^{-1}s^{-2}$, which makes it more prone to saturation. It does, however, have the added advantage of allowing an independent verification of T_{Si}. This experiment has been carried out under CRDS base conditions at a constant height of *z* = 11 mm and repeated at base pressure and power with $X_0(SiH_4)$:$X_0(H_2)$ = constant for a range of different total gas flow rates (i.e. X_0(leak) is varied for a constant $X_0(SiH_4)$). These results are shown in Figure 6.21 (a). The second investigation demonstrates changes in $X_0(SiH_4)$ by varying $F(SiH_4/H_2)$, whilst $F_{eff}(H_2)$ = 1800 sccm (i.e. X_0(leak) ~ 3.3 ppm) under otherwise base conditions and are reported in Figure 6.21 (b).

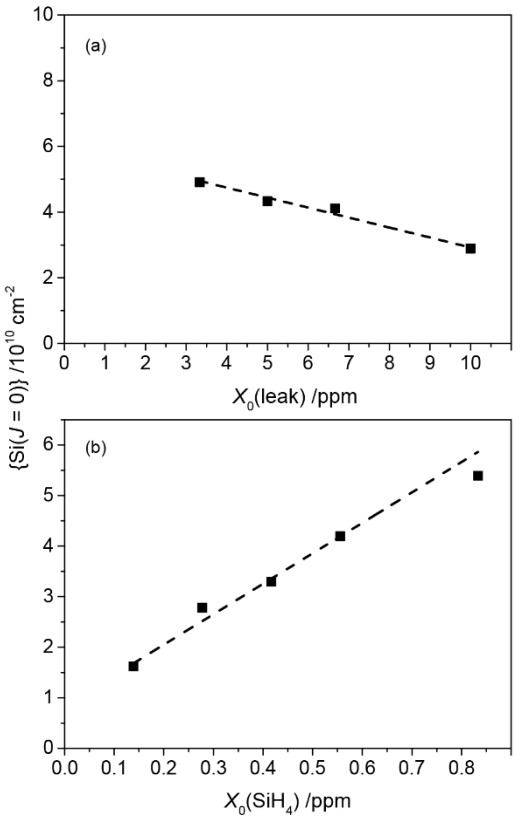

Figure 6.21: Calculated {Si(J = 0)} as a function of (a) chamber air leak, X_0(leak), by varying total gas flow, whilst maintaining a constant $X_0(SiH_4)$:$X_0(H_2)$ ratio under otherwise base conditions and (b) silane flow, maintaining a constant $F_{eff}(H_2)$ = 1800 sccm and air leak of ~ 3.3 ppm under otherwise base conditions. The dashed lines indicate that both trends are linear in the explored parameter range.

Under CRDS base conditions, {Si(J = 0)} is measured to be ~ $2.88 \pm 0.01 \times 10^{10}$ cm^{-2} at z = 11 mm. Whilst lower than the calculated value of 3.5×10^{10} cm^{-2} for T_g = 550 K (as displayed in Figure 6.18), the agreement is reasonable on the premise that the calculated error bars have been underestimated, and there is an uncertainty regarding exact air impurities. Such a value would then be consistent with previous measurements and the running idea that the ground state {Si(J)} spin-orbit states are likely in a local proximity and thermal equilibrium maximising within the cooler regions of the plasma / chamber.

Figure 6.21 (a) demonstrates that {Si} increases linearly with a reduction in X_0(leak) for a constant $X_0(SiH_4)$) within the explored parameter range. Figure 6.21 (b) demonstrates {Si} increases ~ linearly with increasing $X_0(SiH_4)$ for $F_{eff}(H_2)$ = constant (i.e. X_0(leak) ~ constant) in agreement with the preliminary 2-D plasma modelling.

The intercept of Figure 6.21 (b) is calculated to be {Si(J = 0)} = $9 \pm 2 \times 10^9$ cm^{-2}. This might be attributed to a longer residence time of Si within the chamber / ring down arms than has been allowed experimentally, a Si contribution being etched from the coated chamber, or another manifestation of the underestimated error bars. It is unfortunate that attempts to measure {Si(J = 0)}, where $X_0(SiH_4) \geq 1.6$ ppm (i.e. with an input mole fraction comparable to X_0(leak) ~ 3.3 ppm using $F_{eff}(H_2$ = 1800 sccm)

resulted in saturation. This reinforces the highlighted flaw attributed to monitoring these strongly absorptive peaks with the current apparatus (limited by the practical reflectivity of the mirrors); at present, it appears that these measurements are not physically feasible to carry out on the ground state Si triplet states without an air leak that significantly exceeds the input silane content.

Figure 6.21 (a) verifies, however, that {Si} is sensitive to the air leak, and that some of the missing Si content (unaccounted for in the prior CRDS experiments) can be attributed to the air leak and the formation of H_xSiOH_m species. Under the assumption that the intercept of the line of best fit in Figure 6.21 (a) is representative of X_0(leak) = 0 ppm, there is an expected column density of {Si(J = 0)} = 6.0 ± 0.1 × 10^{10} cm^{-2}. {Si} would therefore account for ~ 3.75% of the total Si content, (as opposed to the previous estimate of 1.8% in the presence of 10 ppm of air).

Thus far, hydrogen gas impurity has not been included. Adding the oxygen impurity present within the hydrogen gas (which would be independent of flow) yields an effective $X_0(O_2)$ = 3.5 ppm, (an equivalent additional X_0(leak) ~ 14 ppm). With this included, the new intercept of Figure 6.21 (a) is {Si(J = 0)} = 1.01 ± 0.06 × 10^{11} cm^{-2}. Assuming the same T_{Si} as base conditions (T_{Si} ~ 550 K), this now yields {Si} = 6 × 10^{11} cm^{-2}, i.e. 6.15% of total Si content. This increases to 10.6% using r_{max} = 50 mm in the integral of Equation 6.29. Unless there is a non-linearity of {Si}(X_0(leak)) when $X_0(SiH_4)$ ~ X_0(leak), then there is still substantial Si content that has yet to be accounted for. The impact of air impurity is also presently predicted by preliminary 2-D plasma modelling.

Whilst Figures 6.21 (a) and (b) facilitate a rationale behind the strange invariance of {Si(J)} with varying $X_0(SiH_4)$ (by varying $F_{eff}(H_2)$ as opposed to $F(SiH_4/H_2)$) in the original CRDS experiment featuring in Figure 6.17 (a), alone, it is an insufficient increase at present to account for the discrepancy between measured and expected {Si} values.

Additional conceived possibilities include: (i) an overprediction of [H] atoms in the cool regions; reducing [H] in this region, perhaps the net flow of H_2 (~ twice the mass of an H atom) from the arms acts to prevent effective [H] diffusion to these coolest regions; perhaps the impact might be to shift the equilibrium towards a higher $X(SiH_4)$. [H] would not necessarily vary, however, within the investigated $F_{arms}(H_2)$ range, as [H] is lower in number density in this region (*cf.* H_2). The second conceived possibility is: (ii) a settling out of the silane/hydrogen mix over the course of the two years it has taken to carry out these experiments, with the heavier silane sinking to the bottom, reducing the concentration of SiH_4 at the top of the gas cylinder (i.e. reducing the concentration of silane being fed into the chamber). To eliminate this possibility, it would be necessary to extract a sample or to carry out further experimentation after remixing the cylinder. The final conceived possibility is: (iii) an underestimation of air impurities when the plasma is operating. It is, however, now possible to speculate on {Si} with changes in power / pressure.

6.3.5.vi: Rationalising changes in {Si} with Pressure and Power

Upon increasing power, {Si} remains constant between $0.7 \geq P \geq 1.0$ kW and drops linearly at all heights for $P \geq 1.0$ kW. Perhaps with increasing P, there is enhanced gettering of Si content into H_xSiOH_m species (for a constant $X_0(SiH_4)$, X_0(leak) content and pressure), resulting from an enhanced absorbed power density, T_g and $[H]/[H_2]$. Alternatively, it is conceivable that with the associated plasma expansion, there is a reduced columnar space along the line of measurement in which the cooler region exists. This would act to reduce the sum of [Si] number densities along a column (i.e. acting to reduce the column density) under the continued assumption that the arms do not contribute significantly to measured {Si} (due to the net flow of gas toward the plasma).

Measured {Si(J)} increases linearly with pressure under constant power / silane input mole fraction. The simplest interpretation is that [Si] is increasing linearly (within the cooler regions) with total number density. This, of course, neglects the dependency that X_0(leak) has with pressure. An increase in pressure would act to decrease X_0(leak) with a $1 - p/760$ dependency, i.e. decreasing $X(H_2O)$ and $[H_2O]$:[Si] ratio, which would result in a reduced silicon gettering as H_xSiOH_m. It is worth noting that with increasing pressure, the hydrogen air impurity would maintain a constant concentration (i.e. an effective $X_0(O_2)$ of ~ 3.5 ppm), and therefore such an impurity contribution would maintain a constant $[H_2O]$:[Si] ratio. This also neglects the impact that pressure may have on the gas chemistry of H/Si/O.

6.3.5.vii: Summary of MW-activated Si/H plasmas

Section 6.3.4 began by attempting to establish prominent gas phase processes. Using thermochemical data and calculated reaction rate coefficients, it is deduced that Si should dominate under the investigated conditions. Additional species, such as Si_2H_x ($0 \leq x \leq 6$) species are ruled out as a prominent species due to slow generative reactions (relative to fast H shifting and losses with reactive H_2) and the low $X_0(SiH_4)$ under the explored conditions. A rich Si/H/O chemistry is briefly noted, along with the role that the low lying (0.78 eV) Si($^1D_2$) state may play. Unlike the Si triplet ground state, Si($^1D_2$) is reactive with H_2O, the main product of O_2 air impurity, and therefore the Si($^1D_2$) state could play a significant role in Si/H/O chemistry, making a comparison to the role that the $N_2(A^3\Sigma^+_u)$ (6.2 eV above the ground state) plays in MW-activated N_2/H plasmas. Such an involvement may act to enhance the generation of H_xSiOH_m species, which have been demonstrated to act as a getter for Si content.

Possible excitation mechanisms are reviewed with plausible contributions including electron-ion recombination of the Si^+ and SiH^+ cations to form Si* and SiH* states, electron impact excitation, and chemiluminescence.

On the basis that these states are generated through EIE (directly or in the case of Si* singlet and SiH*, indirectly), it has been possible to qualitatively (albeit speculatively) rationalise the variation in optical emission trends and measured {Si(J)} as a *f*(process conditions). Under this assumption, it can be

inferred that the prominent quencher of the emitting Si and SiH excited states are H atoms, and whilst such a conclusion would likely extrapolate in the case that other plausible excitation mechanisms dominate, at present, it is not possible to speculate any further on prominent excitation (or loss) mechanisms regarding the production / loss of excited Si and SiH radicals, except to point out that the most likely chemiluminescent reaction contributing to the population of SiH* would involve a parent Si atom, e.g. Process 6.20 (b), ($Si + H_2 \rightarrow SiH^* + H$).

The general similarities between the observed $I(H_2^*)$ and $I(H^*)$ trends within MW-activated Si/H plasmas and MW-activated H plasmas (investigated in Chapter 3) confirms that the general conclusions reached regarding MW-activated H plasma systems extend to MW-activated Si/H plasmas, particularly with regards to the general behaviour of H_2^* and H^* with changes in operating conditions and plasma parameters. Briefly, this study confirms that in MW-activated Si/H plasmas, these excited states are still coupled via non-resonant energy transfers with their ground state, sensitive to changes in absorbed power density, the reduced electric field, T_{tail}, their quenchers, and in addition, are highly sensitive to changes in prominent cations.

Through CRDS measurements it has been possible to demonstrate (indicatively) how {Si} varies with height above substrate and changes in process conditions. {Si} (and therefore by inference [Si]) is demonstrated to maximise in cooler regions of the plasma. Through measuring column densities of several spin-orbit absorption lines and assuming a local thermal equilibrium, [Si] is estimated to have a gas temperature between $500 \leq T_{Si} \leq 1000$ K. By assuming a gas temperature is appropriate, it is therefore possible to estimate total {Si}. A theoretical calculation using $X_0(SiH_4)$ and modelled radial T_g variation at $z \sim 11$ mm demonstrates that the expected $\{Si_{tot}\}$ is significantly larger than measured $\{Si(J)\}$ values and $\Sigma\{Si(J)\}$ infer. Further, such a calculation demonstrates that if $\{Si_{tot}\} = \{Si\}$, any measured $\{Si(J)\}$ ought to saturate, something not experimentally observed in most explored conditions.

Whilst the pressure and power dependencies can be explained in terms of changes in plasma volume and/or number densities, $\{Si(J)\}$ measurements demonstrate two distinct behaviours with varying $X_0(SiH_4)$. $\{Si(J)\}$ increases linearly with increasing $F(SiH_4)$, whilst maintaining a constant $F(H_2)$, whilst {Si} remains relatively flat with increasing / decreasing $F(H_2)$, whilst maintaining a constant $F(SiH_4)$.

Further CRDS measurements confirm that the air leak impacts measured $\{Si(J)\}$, providing a rationale behind the distinct behaviours when varying $X_0(SiH_4)$. but only partially accounts for the discrepancy between measured and expected {Si}, although this was not confirmed in a regime whereby $X_0(Si) > X_0(leak)$.

Attention is now turned to MW-activated Si/C/H plasmas chemistry and diagnostic studies.

6.3.6: MW-activated Si/C/H Plasmas

The prominent processes occurring within MW-activated C/H plasmas have been reviewed throughout this thesis, whilst Sections 6.3.4 and 6.3.5 have provided a developing rationale behind diagnostic studies carried out on MW-activated Si/H plasmas. In order to develop a working interpretation on similar diagnostic studies carried out on MW-activated Si/C/H plasmas, it is important to understand how Si atoms (and its excited states) react with methyl radicals and acetylene, as a function of gas temperature. It is also important to understand what becomes of the 10 ppm air leak associated with the CRDS experiments. These questions are explored in this Section. Section 6.3.7 presents the diagnostic studies and a working interpretation of MW-activated Si/C/H plasma systems relevant to the CVD of diamond.

6.3.6.i: Possible Si/C/H Chemistry

Studies on Silicon-carbide growth provide the most relevant information on Si/C/H kinetics. Such studies tend to focus on lower gas temperatures and higher silane fractions than those of interest in this thesis and therefore include Si_2H_y ($0 \leq y \leq 6$) kinetics. Under the studied silane fractions, this has been deemed an unlikely species in Appendix A6.4. Nonetheless, assuming the reported Si/C/H kinetics can extrapolate to the higher gas temperatures of interest, it is possible to speculate on the prominent gas phase processes involving Si that might be occurring within the investigated systems. Section 6.3.1 informs that without the presence of air, the prominent Si-containing species in a MW-activated Si/H system should be Si atoms. Under the assumption that the leak content (both oxygen and nitrogen) will be gettered by the significantly larger carbon content (validated in Section 6.3.6.ii), it is reasonable to approximate the neutral-charged Si/C/H chemistry to just Si atoms (and its excited states) reacting with the carbon content for a working interpretation.

A prior knowledge of MW-activated C/H chemistry developed throughout this thesis informs that in the hot regions of the plasma, C_2H_2 is the prominent species, whilst in the cooler regions, C_2H_2, CH_4 and CH_3 dominate. Therefore, it is important to understand Si atom chemistry with these three species as a function of gas temperature. It can then be assumed that these reactions are somewhat representative of SiH_x ($0 \leq x \leq 4$) species with CH_x and C_2H_y species ($0 \leq y \leq 6$). The gas phase chemistry between C_2H_y and Si is further complicated, as products can come in the form of chains and cyclic molecules.

Despite being a study on Si-C growth, Reference 13 does not provide kinetics between Si- and C-containing species. Reference 14 only provides rate coefficients for SiH_2 (the prominent Si-containing species within their model of a Si/H plasma) with CH_4. The reaction is described by Process 6.31:

$$SiH_2 + CH_4 \rightarrow SiH_3CH_3 \qquad (6.31)$$

Prior to further speculation, it is worth considering enthalpies of formation for various Si-C and C-containing species. A non-exhaustive list of potential species is presented in Table 6.4 using References

49, 50, 51, 52, 53, 54, 55, 56, and 57. These formation of enthalpy values have been used to estimate enthalpy of reaction values for proposed mechanisms.

Additional Species	Enthalpy of Formation /eV
$H_2C=CH_2$	0.544
C_2H_2	2.357
C_2H	5.887
C_2(a)	8.645
CH_4	−0.772
CH_3	1.517
CH_2 (singlet)	4.447
CH	6.178
Si=C	7.745
Si=C-H	5.403
Si=C-H_2	3.255
Si-C-H_3	3.183
H_3Si-C-H_3	−0.302
H_2Si-(C-H_3)$_2$	−0.981
HSi-(C-H_3)$_3$	−1.694
Si-(C-H_3)$_4$	−2.417
H_2Si=C-H_2	1.865
H-Si-CH_3	1.511-2.462
H-Si-CH_2	3.659-4.610
* H_2-Si(C-H)$_2$	2.97
* Si(C-H)$_2$	3.125-3.871
* Si(C_2H)	5.083
* Si-C-C	6.466
Si-C≡C-H	5.563
H-Si-C≡C-H	4.842
H_2-Si-C≡C-H	4.120
H_3-Si-C≡C-H	2.229-3.535
H_3-Si-CH=C-H_2	0.876
H-Si-CH=C-H_2	3.308-3.489
$H_2C=Si=CH_2$	4.099

Table 6.4: Enthalpy of formation (calculated at *T* = 298 K) for various carbon and carbon-silicon containing species. Those shown in red have been crudely estimated using differences in values between different species reported in the table, whilst the values in orange are provided by Reference 52. *indicates a cyclic molecule. Ranges are reported for most estimates or if two references report different values.

Process 6.31 yields an enthalpy of reaction estimated to be ~−2.755 eV, i.e. exothermic. One could envisage similar reactions for the dominant Si-containing species, Si atoms with CH_4 and CH_3.

$$Si + CH_4 + M \rightarrow HSi{-}CH_3 + M \quad (6.32)$$

$$Si + CH_3 + M \rightarrow HSiCH_2 + M \quad (6.33)$$

Processes 6.32 and 6.33 have enthalpy of reaction values of approximately ~ − 1.430 to − 2.381 eV and ~ − 1.571 to – 2.522 eV respectively for the formation of Si-C bonding. Whilst the enthalpy of formation for the product species have been estimated in Table 6.4, both reactions are expected to be exothermic, noting the latter would be more exothermic for an Si=C bond. This, however, neglects changes in entropy, which would act to decrease the exothermicity (and therefore favourability) of such a reaction and may even render such reactions unfavourable. Alternative products to Processes 6.32 and 6.33 (proposed by Reference 58) include $SiCH_2$ and SiCH (+ H_2). Such alternatives have estimated enthalpies of reaction values of ~ – 0.637 eV and ~ – 0.778 eV (i.e. exothermic assuming Si=C bonding) and are not expected to be significantly hindered by changes in entropy (i.e. the number of reactants = number of products). One could also envisage further methyl radical addition reactions to generate a family of $SiH_x(CH_y)_z$ species, where $0 \leq x \leq 4$, $0 \leq y \leq 3$ and $0 \leq z \leq 4 - x$. Table 6.4 infers that for a fully H-terminated system, such reactions may be exothermic.

Such species may be prone to H atom attacks, as exampled by Processes 6.34 (a) and (b) using $HSiCH_2$:

$$HSiCH_2 + H \rightarrow Si + CH_3 + H \quad (6.34\ a)$$

$$HSiCH_2 + H \rightarrow SiH + CH_3 \quad (6.34\ b)$$

The first reaction, Process 6.34 (a) is rendered endothermic with an enthalpy of reaction ranging between + 1.571 eV and + 2.512 eV. This value does not, however, consider the substantial change in entropy that would encourage such a reaction and could render the overall process favourable. Further, alternative pathways, such as Process 6.34 (b) are calculated to be exothermic with enthalpy of reaction values estimated to be between ~ − 1.571 and – 2.522 eV.

Consequently, in a H-rich environment, Si-C products may be shortlived. The reason for this is that the CH, C-C, C=C, C≡C and SiH bond are all stronger than (or equal to) the Si-C single bond (4.26, 3.59, 6.24, 8.65 and 3.30 ≥ 3.30 eV respectively)[59] and comparable to the Si=C double bond (reported to be ~ 5.14 eV in $H_2Si{=}CH_2$).[60]

SiH_2 is reported to react with acetylene and can result in a range of different products.[57,61] The two lowest energy products are thought to be silirene, a cyclic molecule (described by a * in Table 6.4), two CH double bonded to one another and both single bonded to SiH_2 (exothermic) in Table 6.4, and $HC{\equiv}CSiH_3$, reported to be the more exothermic product, highlighted in green within Table 6.4.[57] There are a range of additional exothermic and endothermic products, including Si triplet ground state + C_2H_4

via an intersystem crossing (reported to be endothermic, but within thermal energies available, noting that this excludes the 'metastable' Si singlet states).[61] These are described by Processes 6.35 to 6.37 and, using Tables 6.01 and 6.04, have enthalpies of reaction values of ~ − 2.259 eV, − 1.694 to – 3 eV and – 0.021 eV respectively:

$$SiH_2 + C_2H_2 + M \rightarrow (CH)_2SiH_2 + M \quad (6.35)$$

$$SiH_2 + C_2H_2 + M \rightarrow HC \equiv CSiH_3 + M \quad (6.36)$$

$$SiH_2 + C_2H_2 \rightarrow Si(\,^3P) + C_2H_4 \quad (6.37)$$

The larger disparity between the calculated enthalpy of reaction (predicting a slight exothermicity) and the endothermicity reported in Reference 57 is likely a consequence of identity confusion between C_2H_4 describing a biradical molecule with a single C-C bond and a fully H-terminated molecule with a C=C bond. In this thesis, the interest would be in the latter.

Cyclic $(CH)_2SiH_2$ is noted in Reference 57 to convert between isomers $H_3Si\text{-}C{\equiv}CH$ and $HSiCH{=}CH_2$ via Process 6.38 and 6.39. As before, these products, particularly $H_3Si\text{-}C{\equiv}CH$, are prone to H attacks, likely resulting in methyl / syliyl based radicals, noting as before * is indicative of a cyclic molecule.

$$(CH)_2SiH_2^* \leftrightarrow HSiCH = CH_2 \quad (6.38)$$

$$(CH)_2SiH_2^* \rightarrow HC \equiv CSiH_3 \quad (6.39)$$

Similar chemistry can be envisaged for the more prominent Si atom, as described by Processes 6.40 and 6.41.

$$Si + C_2H_2 \rightarrow (CH)_2Si \quad (6.40)$$

$$Si + C_2H_2 \rightarrow HC \equiv CSiH \quad (6.41)$$

Processes 6.40 and 6.41 are crudely estimated to have enthalpies of reaction values of ~ − 2.179 eV and between ~ – 3.15 eV and – 3.896 eV respectively.

As before, these products are likely prone to H atom attacks. It is possible, however, that the cyclic molecule $(CH)_2Si$ undergoes H-shifting reactions to form cyclic Si-C=C, a structure that is sufficiently stable in structure (compare number of bonds / energies required to break relative to CH bond), that it could withstand H atom attacks and getter Si content even under H-rich conditions. Cyclic Si=C-C comparatively might be more prone to H atom attacks based on the strength of the CH bond relative to a single C-C bond.

There are additional pathways for forming cyclic Si-C=C that can be fathomed for forming such a product, as exampled by Process 6.42 and Process 6.43 followed by Process 6.44:

$$C_2 + Si \rightarrow C_2Si^* \quad (6.42)$$

$$C_2H + Si \rightarrow HC_2Si^* \quad (6.43)$$

$$HC_2Si + H \rightarrow H_2 + C_2Si \quad (6.44)$$

The enthalpy of reaction for Processes 6.42 and 6.43 are highly exothermic (~ – 6.843 eV and – 5.468 eV respectively), but changes in entropy would be working against such a mechanism. Process 6.44 is also weakly exothermic, with an enthalpy of reaction estimated to be ~ – 0.876 eV.

One could also envisage such processes occurring via multi-step reactions, as exampled by Processes 6.45 (a) and (b):

$$CH_4 + Si \rightarrow SiCH_2^* + H_2 \quad (6.45\ a)$$

$$SiCH_2 + CH_4 \rightarrow H_3C_2SiH^* + H_2 \quad (6.45\ b)$$

Given the complexity of the chemistry occurring, it would be wiser to await for 2-D plasma modelling than speculate on ground state Si-C chemistry further. Section 6.3.6.ii justifies the assertion that any air leak attributed to CRDS measurements should be an irrelevancy in the Si/C chemistry occurring under the studied conditions.

6.3.6.ii: Air Leak Contributions

An air leak consists of ~ 80% N_2, and 20% O_2. Previous plasma studies available in Reference 4 and Mark Kelly's thesis [62] have demonstrated that introducing Oxygen into the plasma (via CO_2) in excess H_2 and CH_4 results in the gettering of Oxygen as C≡O via H_2O, OH and O atoms (i.e. the source of oxygen is unimportant). The C≡O has a bond strength of 11.11 eV significantly larger than that of Si-O (4.69 eV).[59]

Whilst Si/N_2 chemistry was not considered in the Appendix, A6.4, (under the assumption that it would be less significant due to the lower reactivity of N_2), it can be eliminated as being important within MW-activated Si/C/H plasmas for similar reasons to Oxygen; as noted in the Appendix (and Section 6.3.5.v), N_2 typically dissociates via its metastable state (pumped via EIE) forming NH_x radicals in MW-activated H plasmas. These radicals react with the gas phase carbon to predominantly form HC≡N with a bond strength of 9.20 eV (versus Si-N, which has a bond strength of 3.68 eV).[3,59,62,63] Hence, in the presence of excess methane, air leaks are not expected to be a concern for understanding the gas phase processes occurring between Si and C content.

Attention is finally drawn to the diagnostic studies carried out on MW-activated Si/C/H plasmas. A working interpretation is presented alongside these results.

6.3.7: Diagnostic Studies on MW-activated Si/C/H Plasmas

When methane is present, CH(A→X), CH(B→X) and C_2(d→a) emissions were also collected alongside H_2(d→a), H($n = 5 \rightarrow n = 3$), SiH($A^2\Delta \rightarrow X^2\Pi$), Si singlet emissions at 288.2 nm and 390.5 nm, and the triplets detected in second order at 2λ = 501.37, 502.88, 503.24, 503.89, 504.83 and 505.70 nm, see Table 6.1. The 2nd order triplet emissions overlap with C_2(d→a), $\Delta v = 0$. Consequently, the triplet

emissions were reinvestigated in a repeat study with Si singlet emissions using a UV filter as described in Section 6.2. An alternative analysis, investigating the emissions from residual of the experimental data and the PGOPHER best fit of the C_2(d→a), Δv = 0 qualitatively confirm the trends that are presented; as this latter analysis was prone to error, these results have not been reported, instead the triplet emissions are reported from the repeat study with a UV filter present. These emissions are contained within the same wavelength ranges as before ((i) 307-382 nm and (ii) 372-447 nm and (iii) 462.95-536.7 nm) and have all been previously investigated within this thesis. For this reason, false colour images have not been repeated.

A working interpretation is provided alongside the presentation of these results, as are column density {Si(J = 2)} measurements carried out using the Si($3s^2 3p4s$, $^3P^o$, J = 1←$3s^2 3p^2$, ^3P, J = 2) transition centred at $\bar{\upsilon}$ = 39537.1 cm^{-1}, which has been assumed representative of all {Si(J)}.

Base conditions for the following OES experiments are defined as: P = 1.5 kW, p = 150 Torr, with respective gas flow rates of $F(H_2)$ = 270 sccm, $F(SiH_4/H_2)$ = 30 sccm, $F(CH_4)$ = 19 sccm, whilst base conditions for the following CRDS experiments are defined as: P = 1.5 kW, p = 150 Torr, with gas flow rates $F_{reactor}(H_2)$ = 300 sccm, $F_{arms}(H_2)$ = 300 sccm (i.e. $F_{eff}(H_2)$ = 600 sccm), $F(SiH_4/H_2)$ = 0.5 sccm and $F(CH_4)$ = 10 sccm. The OES and CRDS have an associated X_0(leak) of ~ 0.25 ppm and 10 ppm respectively. This does not include the impurities within the methane (namely hydrogen and other hydrocarbons), and hydrogen (previously described).

6.3.7.i: Methane Addition to MW-activated Si/H plasmas

Figure 6.22 demonstrates that upon the addition of methane (i.e. increasing from $F(CH_4)$ = 0 and 2 sccm under otherwise OES-defined base conditions), $I(H_2^*)$ and $I(H^*)$ both show an initial increase. Following a further increase in methane flow rate, from $F(CH_4)$ = 2 to 5 sccm, these intensities remain ~ constant. Above $F(CH_4)$ = 5 sccm, $I(H_2^*)$ and $I(H^*)$ decrease. The spatial profile of $I(H_2^*)$ is a lot broader for $F(CH_4)$ = 1 sccm, than $F(CH_4)$ = 0 sccm, reflecting a change in prominent cations and therefore a vastly different $n_e(z, r)$ and / or significant changes in absorbed power density. A further increase in methane demonstrates minor plasma contraction (due to the heavier mass of carbon-containing species). The observed intensity changes are consistent with a change in prominent cations (from SiH_x^+ ($0 \leq x \leq 4$) ions to CH_x^+ and $C_2H_y^+$ (y = 2 and 3) ions), which have vastly different number densities and spatial distributions. Significantly, [Si], which is the dominant silicon species throughout the plasma (in a MW-activated Si/H plasma) has a low ionization energy. Comparatively, $[CH_x](0 \leq x \leq 4)$ (and $X(CH_x)(0 \leq x \leq 4)$) have an x-dependent spatial distribution with radicals of lower x ($x \leq 2$) maximising in the hotter plasma regions, whilst [CH_4] maximises in the cooler regions, as discussed in Chapters 1 and 5. The ionization energy of methane is ~ 12.63 eV, whilst CH radicals, for example, have a slightly lower ionization energy of ~ 10.64 eV.[64,65] C_2H_2 (and C_2H_3, which is more prominent in the hotter plasma core than in cooler regions) hold ionization energies of ~ 11.4 eV and ~ 8.25 eV

respectively and are generally the most prominent carbon-containing cations in MW-activated C/H plasmas.[66,67] Despite these substantially higher ionization energies (*cf.* silicon-containing species), the input mole fraction of methane at $F(CH_4)$ = 1 sccm is 3 orders of magnitude larger than that of silane under OES-defined base input mole fraction of SiH_4, and therefore increasing the input mole fraction of carbon content, results in carbon-containing ions, which dominate. The broader $I(H_2^*)$ reflects the change in spatial distribution of n_e (based on the different spatial distributions of $[CH_x]$ and $[C_2H_y]$ species and their respective ionization energies), changes to the absorbed power density, and perhaps the introduction of additional potential quenchers; $[CH_x]$ and $[C_2H_y]$.

Upon further addition of methane, i.e. $1 \leq F(CH_4) \leq 5$ sccm, the effect of decreasing T_{tail} (perhaps as a result of a decreased partitioning of absorbed power density towards the generation of electrons with hyper-thermal energies) is counterbalanced by an increase in n_e, such that $I(H_2^*)$ and $I(H^*)$ remain ~ constant. For $F(CH_4) \geq 5$ sccm, n_e continues to increase, acting to decrease the amount of absorbed power density partitioned to hyperthermal electrons, thus decreasing T_{tail}. This becomes the dominant effect on relative $I(H_2^*)$ and $I(H^*)$ emission intensities, which consequently decrease. Upon further methane increase, n_e continues to increase, resulting in a further decrease in T_{tail}, and hence $I(H_2^*)$ and $I(H^*)$ continue to decrease.

As before arrows have been included in the reported Figures highlighting how peak intensities (black) vary. On occasion intensities featuring at high *z* have substantially different behaviours to the peak intensity. When such differences occur, these are demonstrated by representative orange arrows. This information has not been repeated in the Figure captions.

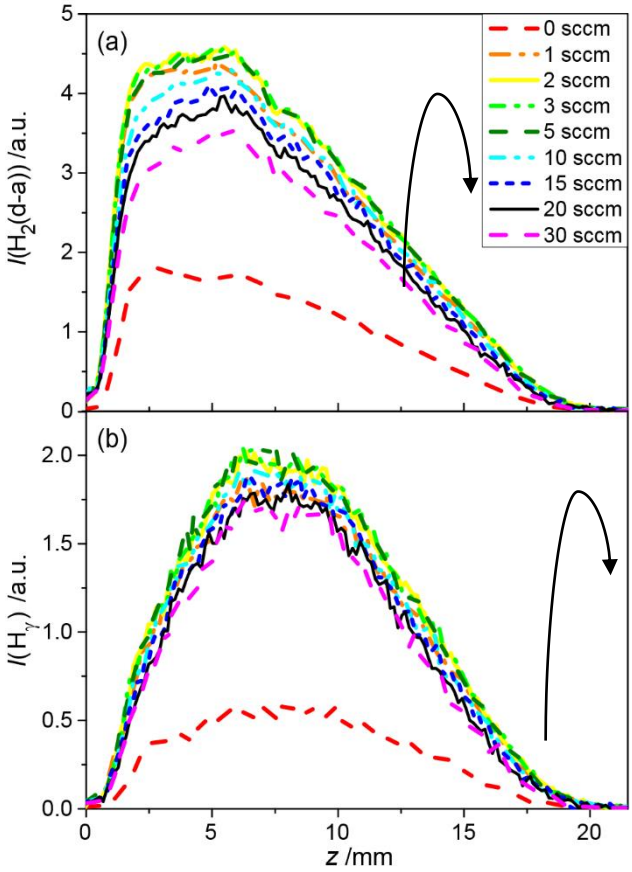

Figure 6.22: (a) $I(H_2^*)$ and (b) $I(H^*)$ as a function of $X_0(CH_4)$, altered by varying methane gas flow, whilst maintaining a constant $X_0(SiH_4)$. $X_0(H_2)$ was decreased in a compensatory manner under otherwise OES-defined base conditions.

Figure 6.23 demonstrates how the two spin states of $I(Si^*)$ varies with increasing methane content with increased methane fraction under otherwise OES-defined base conditions.

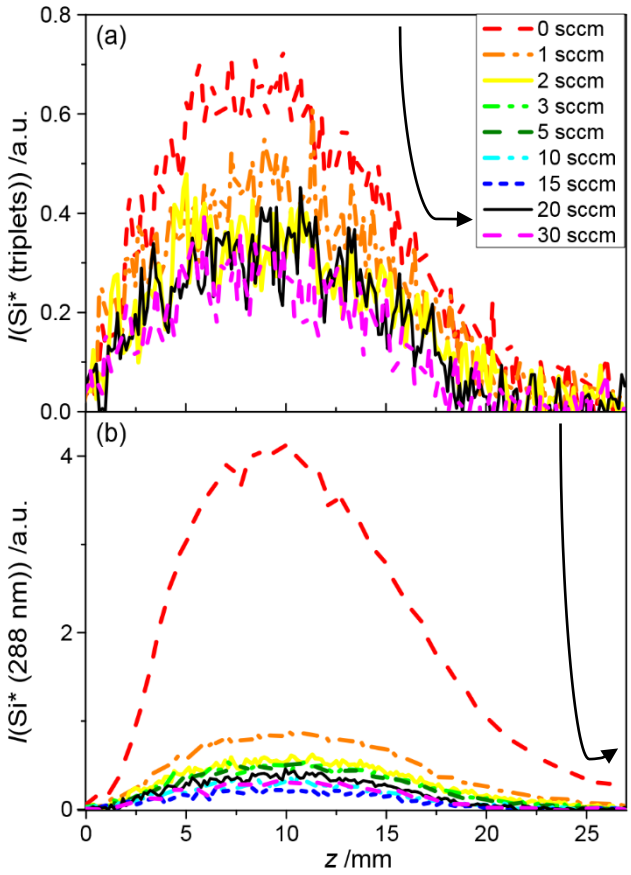

Figure 6.23: *I*(Si*) (a) summed triplet emissions monitored through a UV-selective optic and (b) singlet emissions investigated as a function of height above the substrate with increasing $X_0(CH_4)$ under otherwise OES- defined base conditions. $F(H_2)$ was decreased in a compensatory manner to maintain a constant total gas input flow rate and a constant $X_0(SiH_4)$.

It can be seen in Figure 6.23 that both triplet and singlet states are quenched upon the introduction of methane. There is a clear difference in the behaviour of the two states, namely the relative decrease in these intensities transitioning between a methane-free plasma to $F(CH_4)$ = 1 sccm. This can be seen more clearly in Figure 6.24.

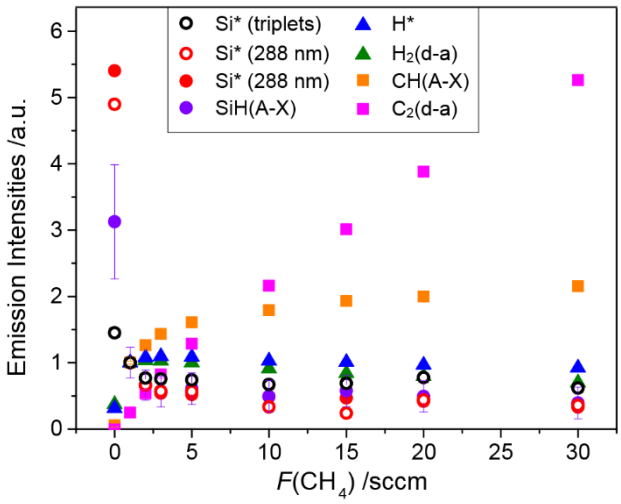

Figure 6.24: *I*(Si*), *I*(SiH*), *I*(CH*), *I*(C_2*), *I*(H*), *I*(H_2*) investigated with intensities summed between 9 ≤ *z* ≤ 12 mm (6 ≤ *z* ≤ 9 mm and 0 ≤ *z* ≤ 3 mm in the case of *I*(H*) and *I*(H_2*) respectively) as a function of *F*(CH_4) (and a compensatory decrease in *F*(H_2)) under otherwise OES-defined base conditions. Closed symbols were collected in the same plasma, whilst open symbols were collected separately. The triplet states were collected through UV-selective optics. Intensities have been normalised to *F*(CH_4) = 1 sccm (except *I*(C_2*), which has been divided by a factor of 4) for display purposes.

The emissions are generally investigated at heights corresponding to the hot plasma regions and / or where intensities maximise, n_e, T_g and perhaps *j*E maximise. Consequently, changes in intensities are reflecting relative changes in the number density of excited state species located in the hot plasma core.

It can be seen clearly, as observed in Chapters 4 and 5 respectively, $I(C_2^*) \sim F(CH_4)$ ($\sim X_0(CH_4)$), whilst $I(CH^*) \sim F(CH_4)^{\alpha < 1}$. Chapters 4 and 5 crudely infer that $I(C_2^*) \sim [C_2H_2]$, whilst $I(CH^*) \sim [CH_x]$. $I(Si^*)$ singlet and triplet drop significantly between $0 \leq F(CH_4) \leq 2.5$ sccm ($X_0(CH_4) \sim 8$ parts per thousand, referred to as "ppt" henceforth). This corresponds with the flow range under which $I(CH^*)$ increases most rapidly (and perhaps faster than $I(C_2^*)$), as well as the methane flow range in which $I(H_2^*)$ and $I(H^*)$ maximise (due to an enhancement of n_e from the presence of C_2H_y ($y = 2$ and 3), which hold lower ionization energies, and in flow ranges prior to the manifested effects of a decreasing T_{tail}. The decrease in $I(Si^*)$ singlet and triplet emissions is likely attributable to a decrease in the steady-state concentration of ground (and perhaps the lower lying metastable singlet state of) Si atoms, rather than due to changes in electron temperatures. The inference is that the additional carbon content is acting as a getter for Si. Upon further addition of methane, the Si-containing emissions remain ~ constant.

In a simplistic interpretation, i.e. by taking the results at face value, the inference is that SiH* and Si* (singlet and triplet) excited states are being quenched more effectively by CH_x species than by C_2H_y species. The difference in their relative drop in intensity between $F(CH_4) = 0$ and 1 sccm can either be explained: (i) if there are differences in quenching efficiencies for different Si spin states, (e.g. if the emitting Si singlet state was generated by EIE of the metastable Si singlet states and there is some associated memory of this, the more effective quenching of the singlet state could be reflecting the

removal of the lower lying Si singlet states), or (ii) if the emitting Si* triplet states are significantly more populated than the emitting singlet state, and as such, both states experience a comparable overall reduction in excited state number densities. This would manifest itself as a smaller percentage drop of the Si* triplet emitting state number density and therefore intensity, as observed.

The first suggested conclusion (that emitting excited states of Si are more effectively quenched by CH_x species *cf.* C_2H_y species) is consistent with {Si} measurements shown in Figure 6.25, despite the differences in the defined base conditions and plasma regions sampled by the two techniques, although it is worth noting that the {Si} decrease could also be reflecting an increase in gas temperature (in the plasma core) associated with methane addition, thereby decreasing the radial length of the cooler region in which the Si content maximises, decreasing a line-of-sight measurement of {Si}.

Whilst data for a high resolution spatial distribution of {Si(J = 2)} has been collected under CRDS-defined base conditions (for a MW-activated Si/C/H plasma), it has yet to be thoroughly analysed, and therefore does not feature in this Thesis. Under CRDS-defined base conditions, {Si(J = 2)} was observed by eye to have a comparable spatial distribution to that reported for base conditions in a MW-activated Si/H plasma.

The inference is that, as before, {Si} (and therefore [Si]) maximises in the cooler regions of the plasma. As before, CRDS measurements are also reported for 3 different heights (i.e. a lower spatial resolution), and these are reflective of increasing {Si}(z). Figure 6.25 demonstrates that measured {Si(J = 2)} has an initial plateau between $X_0(CH_4)$ = 0 and 2.5 ppt, and decreases with a further increase in methane fraction. Taken at face value, the decrease appears linear between ~ 2.5 ≤ $X_0(CH_4)$ ≤ 15 ppt (the equivalent of ~ 0.75 ≤ $F(CH_4)$ ≤ 5 sccm under OES-defined conditions). A speculative interpretation is that [CH_x] (proposed to be the prominent Si gettering species) may be increasing more rapidly than [C_2H_2] in the cooler regions of the plasma for this input methane flow range. Above $X_0(CH_4)$ ~ 15 ppt, {Si(J = 2)} decreases less rapidly. Speculatively, this could coincide with the fraction at which [C_2H_2] becomes the more prominent carbon-containing species throughout the plasma (and therefore, further increases in methane would result in a further enhancement of [C_2H_2], and substantially lesser changes in [CH_4] within the cool plasma regions, resulting in a near constant {Si}, as observed).

It has been noted in MW-activated B/C/H/O plasmas, that a small input of methane acts to significantly increase measured {B} and {BH} by an ~ order of magnitude, prior to its decrease.[2,29] The peak was notably sharper for {B} than {BH}, perhaps attributable to the 3× larger $X_0(B_2H_6)$ content used for measuring {BH}. These observations were attributed to the gettering of oxygen content as CO, as described in Section 6.3.6.ii. The increase in both cases were sharper than that seen in Figure 6.25, indicating that there is perhaps an unresolved peak between between $X_0(CH_4)$ = 0 and 2.5 sccm. As before, there is a question as to whether the experiment at present would be able to resolve such a peak.

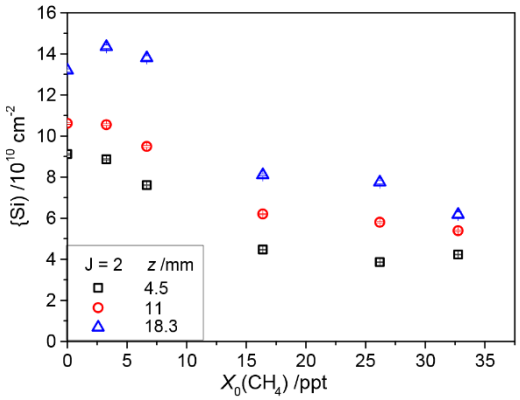

Figure 6.25: Si(J = 2)} investigated at three heights (z = 4.5, 11 and 18.3 mm) as a function of X_0(CH$_4$) with a compensatory decrease in F(H$_2$) by maintaining a constant total gas input flow rate and a constant X_0(SiH$_4$) under otherwise CRDS-defined base conditions.

In MW-activated B/C/H/O plasmas, the enhancement from the removal of the boron getter (BO) was eliminated by X_0(CH$_4$) ~ 5 ppt (preferentially forming H$_m$CO and H$_n$C$_2$O).[2,29] The effective CH$_4$/total gas ratio (25/545) used for base conditions in Ma *et al*.'s work is ~ 3× larger than the effective base condition gas input CH$_4$/total gas ratio (10/610) implemented in these experiments.[2] With a similar total gas flow and experimental set-up (F_{tot} = 565 sccm) versus that implemented presently (F_{tot} = 610 sccm), X_0(leak) between the two data sets may be comparable. It might, therefore, be expected that X_0(CH$_4$) ~ 15 ppt is required in order to eliminate the impact of the air leak.

If, however, Ma *et al*. had a larger leak rate, or if the value of {Si(J)} returning to the as-measured value for X_0(CH$_4$) = 0 ppt is taken as indicative for the leak being entirely gettered by methane, data collected for X_0(CH$_4$) ≥ 2.5 ppt would be a valid representation of MW-activated Si/C/H plasmas. An enhancement of methane acts to getter leak contributions, which as previously demonstrated would act to enhance {Si} (likely there is an unresolved peak between $0 \leq X_0(CH_4) \leq 2.5$ ppt). A further increase in methane would not therefore act to impact {Si} significantly, unless, of course, [Si], and therefore {Si}, decrease due to Si content being gettered through reactions with the carbon content.

The purpose of highlighting this is that it provides an additional warning for interpreting this data at face value. It also yields an additional question as to whether {Si} would maximise in the coolest parts of the reactor (now that oxygen content has been gettered by carbon content) or whether the net consumption of [H] in the production of acetylene for temperatures ranging between 1400 K < T_g < 2000 K (as noted in Chapter 1, Section 1.4), favours other SiH$_x$ species in the coolest regions. This is a question that can be addressed indirectly with the data presented in Figure 6.25; measured {Si(J = 2)} maintains a constant ratio as a $f(z)$ for different methane fractions, inferring that {Si} still maximises in the cooler regions. Further investigations into additional {Si(J)} states would facilitate an estimate on T_{Si} and might help resolve this query.

The linear decrease in {Si} between $2.5 \geq X_0(CH_4) \geq 15$ ppt is most likely explainable by an increase in Si-C-containing species via example Processes 6.32 and 6.33. The non-linearity / more plateaued nature of the measured {Si} for $15 \geq X_0(CH_4) \geq 32.5$ ppt is harder to explain, but likely reflects changes in $[C_2H_2]$ and $[CH_4]$ (and their reactivity with Si) in the cooler regions; with further increases in input methane acting to generate larger amounts of $[C_2H_2]$ in the cooler regions (and significantly less change in $[CH_4]$). If the prior hypothesis is correct (that ground and/or excited states) are preferentially gettered by CH_x radicals in the hot plasma region, these observations are evidence that such conclusions also extend to the cooler plasma regions.

These conclusions are drawn from both CRDS (sampling [Si] in the cooler plasma regions) and OES (sampling excited states of Si in the hot plasma regions) and draw into question the proposed Si/C/H chemistry laid out in Section 6.3.6.i. In particular, as to whether the less exothermic reactions of Si with methane and methyl radicals (Processes 6.32 and 6.33), dominate over H attacks on the products of such reactions (e.g. Process 6.34 (b)) and Si addition to C_2H_2 and C_2H (Processes 6.40, 6.41, 6.42 and 6.43), all of which have been inferred to be exothermic, or whether such reactions (and reactants) act as intermediates in generating cyclic SiC=C-based species, as exampled by Processes 6.45 (a) and (b).

6.3.7.ii: Silane Addition to MW-activated C/H plasmas

In the addition of silane (maintaining a constant methane fraction, with a compensatory decrease in $F(H_2)$) under otherwise OES-defined base conditions, there is no variation in $I(H^*)$ or $I(H_2^*)$ inferring no significant changes in n_e, prominent cations, T_e, T_{tail}, absorbed power density, etc. The conclusion is that under the OES-defined conditions, $C_2H_2^+$ and $C_2H_3^+$ ions are most prominent (i.e. the investigated silane fraction is just too small to make a notable difference).

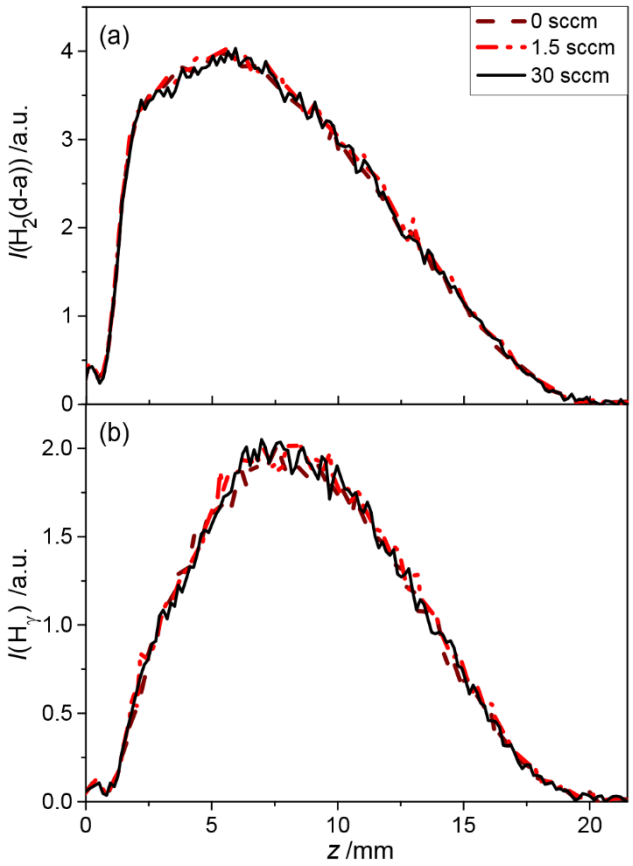

Figure 6.26: (a) $I(H_2^*)$ and (b) $I(H^*)$ as a function of X_0(silane), altered by varying silane gas flow, whilst maintaining a constant $X_0(CH_4)$. $F(H_2)$ was decreased in a compensatory manner under otherwise OES-defined base conditions.

Figure 6.27 demonstrates that both I(Si*) spin emissions increase with increasing silane fractional flow. These points are reinforced more clearly in Figure 6.28, which demonstrates that the intensities belonging to silicon-containing species (i.e. I(Si*) singlet and triplet states, and I(SiH*)) are summed and analysed between $9 \leq z \leq 12$ mm and increase ~ linearly with increasing silane fraction. The remaining intensities, $I(CH^*)$, $I(C_2^*)$, $I(H^*)$ and $I(H_2^*)$) are analysed within the same height ranges (except for $I(H^*)$ and $I(H_2^*)$, which are analysed between $6 \leq z \leq 9$ mm and $0 \leq z \leq 3$ mm respectively) are demonstrably invariant to silane fraction. This is a somewhat unsurprising conclusion given the significantly lower silicon fractions (*cf.* C/H content). Conclusively, therefore, within the investigated Si/C(/H) fractions, Si does not impact the C/H gas phase chemistry in any meaningful manner and hence there is no meaningful variation within intensity values or spatial distributions, as evidenced by $I(H^*)$ and $I(H_2^*)$ in Figure 6.26 and C-containing emissions in Figure 6.28.

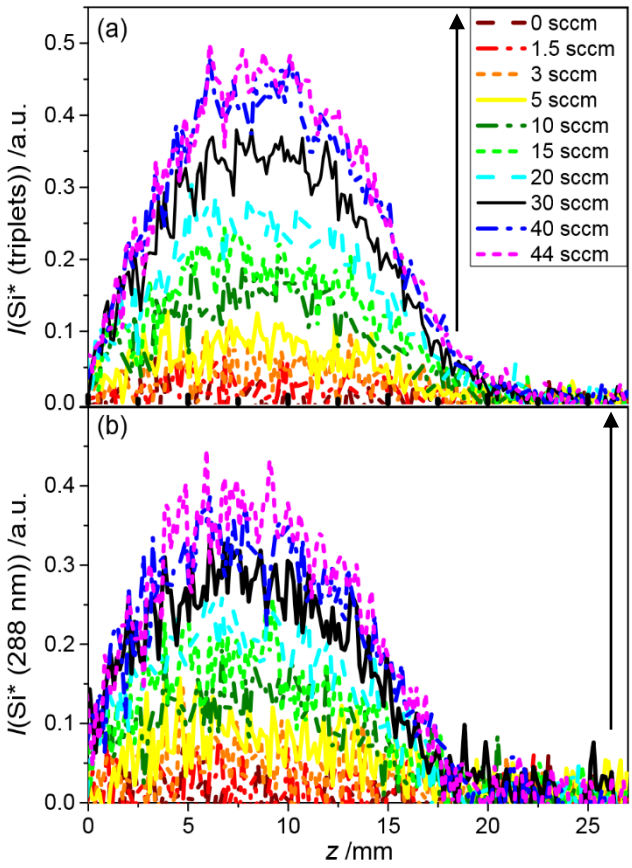

Figure 6.27: *I*(Si*) (a) summed triplet emissions monitored through a UV-selective optic and (b) singlet emissions investigated as a function of height above the substrate with increasing $X_0(SiH_4)$ under otherwise OES- defined base conditions. $F(H_2)$ was decreased in a compensatory manner to maintain a constant total gas input flow rate and a constant $X_0(CH_4)$.

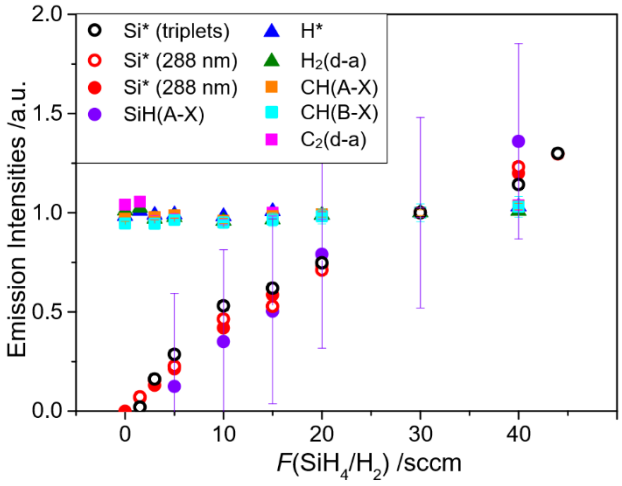

Figure 6.28: *I*(Si*), *I*(SiH*), *I*(CH*), *I*(C_2*), *I*(H*), *I*(H_2*) investigated with intensities summed between 9 ≤ *z* ≤ 12 mm (6 ≤ *z* ≤ 9 mm and 0 ≤ *z* ≤ 3 mm in the case of *I*(H*) and *I*(H_2*) respectively) as a function of *F*(SiH_4) (and a compensatory decrease in *F*(H_2)) under otherwise OES-defined base conditions. Closed symbols were collected in the same plasma, whilst open symbols were collected separately. The triplet states were collected through UV-selective optics. Intensities have been normalised to base conditions (*F*(SiH_4/H_2) = 30 sccm) for display purposes.

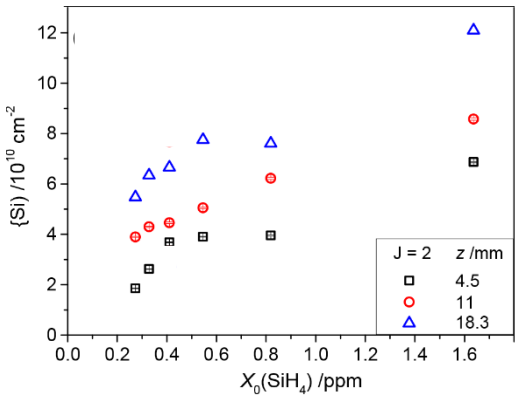

Figure 6.29: Si(*J* = 2)} investigated at three heights (*z* = 4.5, 11 and 18.3 mm) as a function of X_0(CH_4) with a compensatory decrease in *F*(H_2) by maintaining a constant total gas input flow rate and a constant X_0(SiH_4) under otherwise CRDS-defined base conditions.

Figure 6.29 demonstrates {Si} values measured at 3 heights, *z* = 4.5, 11 and 18.5 mm as a function of silane flow. At face value, increasing silane flow demonstrates a linearity at low silane fractions at all analysed *z* and a less than linear increase at higher fractions. Were it imposed that {Si} must converge to 0 cm^{-2} for *F*(SiH_4) = 0 sccm, the notion of non-linearity is reinforced for *z* = 11 and 18.5 mm. Alternatively, with an underestimation of errors, it is just as plausible that {Si} increases linearly with silane flow, with the reported values scattered around a linear line of best fit. Whilst such lines may not cross the intercept of {Si} = 0 cm^{-2} for *F*(SiH_4) = 0 sccm, this could be reflective of error or an etching contribution generating Si content in the plasma. The additional assumption being made that {Si(*J* = 2)} is indicative of all {Si(*J*)} values.

Either interpretation of this data could be consistent with the near linearity observed in I(Si) observed with increasing silane fractions under OES-defined base conditions, noting both experiments sample different regions of the plasma. Unfortunately, neither interpretation, at present, helps to endorse or exclude contributing reactions between Si and C content.

6.3.7.iii: Pressure

With increasing pressure, it can be seen in Figure 6.30 that $I(H_2^*)$ and I(H*) demonstrate comparable pressure behaviours to those previously observed in MW-activated H and Si/H chapters in Chapter 3, and Section 6.3.2 respectively. $I(H_2^*)$ demonstrates plasma contraction and $1/p$ behaviour with no major change in maximal intensity location. I(H*) increases near linearly up to $p \sim 150$ Torr. I(H*) maximises at $p = 225$ Torr and decreases upon further increase in pressure. As well as demonstrating plasma contraction at high z, the peak intensity of I(H*) decreases axially with increasing pressure from $z \sim 10$ mm at $p = 50$ Torr to $z \sim 7$ mm for $p = 275$ Torr. Whilst broader, it is interesting to note that at highest pressures, $I(H_2^*)$ maximise at ~ the same height as I(H*). The spatial distributions reflect a substantially broader n_e with more evenly spread hyper-thermal energies across the plasma when methane is present, *cf*. MW-activated H and Si/H plasmas. The changes in I(H*) spatial variation also demonstrates substantial changes in T_g, [H], $[H_2]$, [H*], n_e, E/N, and T_{tail}.

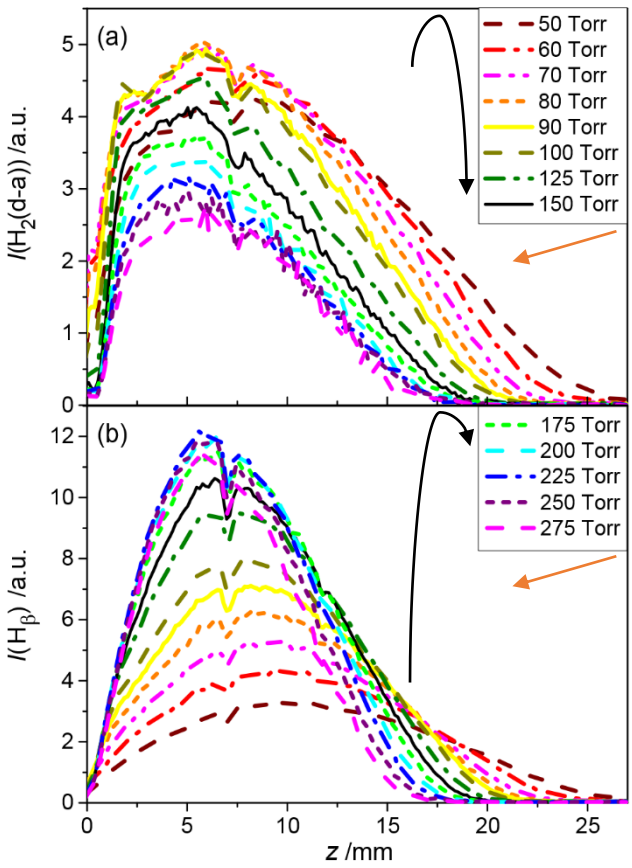

Figure 6.30: (a) $I(H_2^*)$ and (b) $I(H^*)$ as a function of X_0(silane), altered by varying silane gas flow, whilst maintaining a constant $X_0(CH_4)$. $F(H_2)$ was decreased in a compensatory manner under otherwise OES-defined base conditions.

Figure 6.31 demonstrates how both I(Si*) spin states and I(SiH*) emissions vary with increasing pressure. Selected conditions have been presented, highlighting overall changes in spatial variations and overall intensity (or lack of changes between some pressure ranges). Both states of I(Si*) demonstrate comparable spatial distributions and intensity variations. These contrast to the spatial and intensity variation of I(SiH*). I(Si*) increases between p = 50 and 70 Torr. A further increase in pressure demonstrates plasma contraction, with the peak intensity shifting from z ~ 10 mm at p = 70 Torr to z ~ 7 mm by p = 200 Torr. The magnitude of the peak intensity does not vary significantly in the range of $70 \leq p \leq 150$ Torr for the singlet state emissions (and $70 \leq p \leq 200$ Torr for the Si* triplet emissions). Above these pressures, overall intensities increase, maximising at z ~ 6 mm above the substrate.

Comparatively, I(SiH*) can be seen to maximise at a higher height of z ~ 15 mm. The spatial variation of I(SiH*) across this pressure range is minimal. There is a minor relocation toward the substrate (by ~ 2.5 mm) to z ~ 12.5 mm by p = 275 Torr. I(SiH*) appears to increase with increasing pressure up to p ~ 80 Torr, then decrease between p = 80 and p = 150 Torr, before increasing again up to p = 275 Torr.

Both emissions demonstrate plasma contraction, however I(Si*) does not extend above z ~ 20 mm for p = 150 Torr, whilst I(SiH*) extends well above z = 27 mm under all investigated pressure conditions,

inferring that either (i) Si* and SiH* have different CH_x quenchers or (ii) there is an alternative excitation mechanism facilitating the production of SiH*, particularly at higher *z*.

These trends are reinforced in Figure 6.32, which demonstrates how intensities of various emitters alter as a function of pressure analysed between the height ranges previously stated. SiH(A→X) is somewhat buried within the tail of the CH(A→X)($\Delta v = 0$) emission band, which maximises as before at around *z* ~ 10 mm and hence error bars associated with *I*(SiH*) maximise at this height. With increasing *I*(CH*) (e.g. with methane, power and in this case with pressure, as demonstrated in Chapter 5 for MW-activated C/H plasmas and in Figure 6.32 for the current MW-activated Si/C/H plasmas under study), the signal-to-noise of *I*(SiH*) decreases, and consequently, the error associated to *I*(SiH*) increases. A similar phenomenon was noted for *I*(C_2^-*), which was buried within the tail of *I*(C_2*)($\Delta v = +1$) in Chapter 4. The size of the error is larger than *I*(SiH*) variation, particularly at higher pressures, where *I*(SiH*) could be plateauing. The trend does, however, match that observed for *I*(SiH*)(*p*) at higher *z* (*z* ≥ 20 mm), where the error attributed to *I*(SiH*) is lower (due to the substantially lower *I*(CH*)), as can be seen in the spatial distributions featured in Figure 6.31 (c).

The similarity between the two *I*(Si*) emitting spin state spatial distributions suggests that either (i) these states are coupled under all investigated pressures (contrasting to the low pressure distributions in MW-activated Si/H plasmas), perhaps via inelastic collisions with H and / or CH_3, or (ii) reflect that *I*(Si*) triplet emissions are no longer prone to self-absorption. The peak intensity of *I*(Si*) is consistently lower in height than that of *I*(SiH*), which likely reflects the differences in the ground state species (dependent on $T_g(z)$, as was the case with MW-activated Si/H plasmas), the EEDF (n_e(E)), additional excitation mechanisms (e.g. chemiluminescent production of the SiH* state) and reactive quenching mechanisms.

Given that *I*(SiH*) extends beyond *z* = 27 mm under all investigated pressure conditions (i.e. beyond plasma regions containing electron density), SiH* likely has a significant contribution provided via chemiluminescence, e.g. most likely Processes 6.20 (a) or (b), but potentially additional mechanisms involving Si-C species. This is reinforced by the fact that the majority of Si content (that has not been gettered by carbon content) is in the form of Si atoms, increasing the likelihood that Si is a parent species in the formation of SiH*. The change in overall intensities could be reflecting changes in quencher number densities (most likely [H] and [CH_x]), changes in production / loss rates and perhaps a competition between different quenching / production mechanisms, etc.

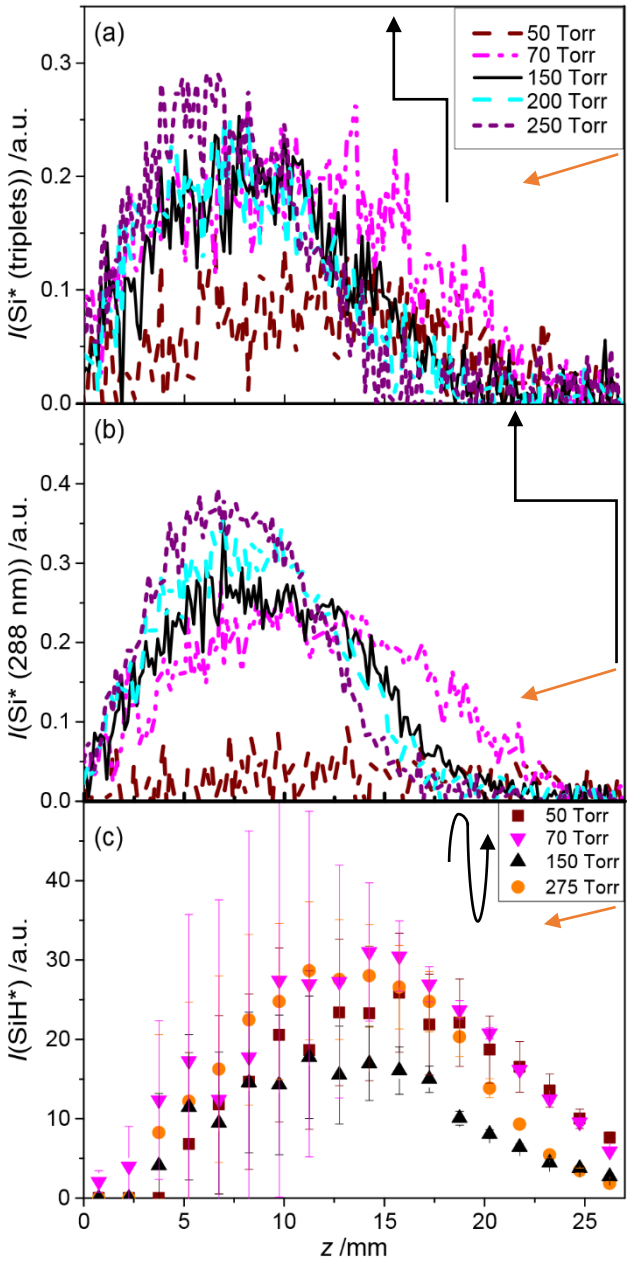

Figure 6.31: (a) *I*(Si*) triplet, (b) *I*(Si*) singlet and (c) *I*(SiH*) as a function of pressure under otherwise OES-defined base conditions.

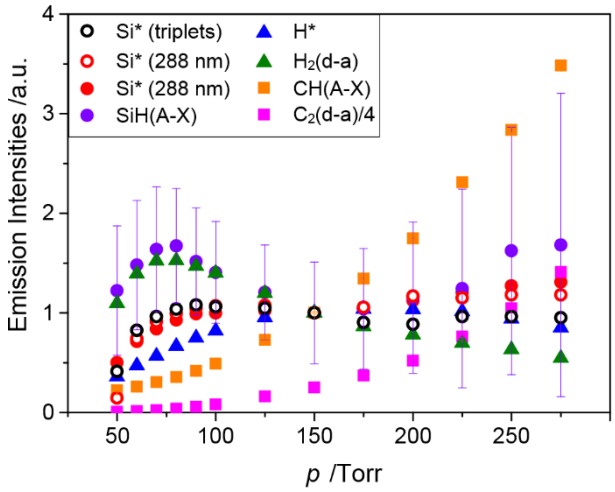

Figure 6.32: Intensities summed between $9 \leq z \leq 12$ mm (and $0 \leq z \leq 3$ mm in the case of $I(H_2^*)$) for $I(Si^*)$, $I(SiH^*)$, $I(CH^*)$, $I(C_2^*)$, $I(H^*)$, $I(H_2^*)$ as a function of pressure under otherwise OES-defined base conditions. Closed symbols were collected in the same plasma, whilst open symbols were collected separately. The triplet states were collected through UV-selective optics. Intensities have been normalised to base conditions (except $I(C_2^*)$, which has been divided by a factor of 4) for display purposes.

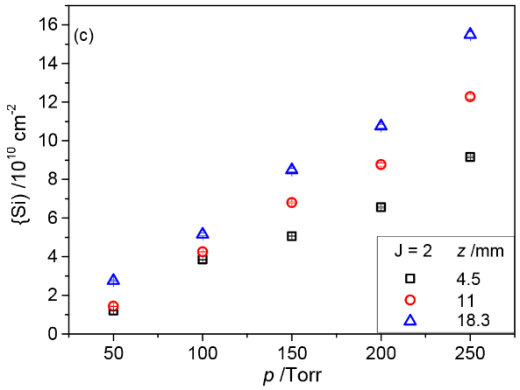

Figure 6.33: Si(J = 2)} investigated at three heights (z = 4.5, 11 and 18.3 mm) as a function of p under otherwise CRDS-defined base conditions.

Figure 6.32 demonstrates that the hydrogen- and carbon-based species behave as previously reported (in Chapters 3, 4 and 5), whilst I(Si*) and I(SiH*) display different pressure dependencies to the behaviours reported for MW-activated Si/H plasmas and to one another. Figure 6.33 demonstrates that {Si(J = 2)} increases linearly with increasing pressure in the cooler regions of the plasma. If this also reflects [Si] variation in the hot plasma region, the changes in intensity emissions and spatial extent are likely demonstrating changes in excitation and quenching mechanisms and/or parameters that such mechanisms depend upon, e.g. [H]. With increasing pressure, I(Si*) and I(SiH*) increase linearly at low pressures (p < 75 Torr), which may be explained simply by an increase in [Si].

Assuming the excited states are still affected by the same processes as MW-activated Si/H plasmas, the inference might be that there is an additional production mechanism for these excited states comes into significance for $p \geq 150$ Torr, which preferentially excites the SiH* (e.g. e-ion recombination, noting

n_e may be higher than before due to more prominent carbon-containing cations). Alternatively, the behaviour for $p \geq 150$ Torr might be reflecting a decrease in the quencher species, e.g. [CH_x], as [C_2H_2] and T_g increase. 2-D plasma modelling would provide more insight.

6.3.7.iv: Power

With increasing power, I(H*) and I(H_2*) increase at all z. At low z, I(H_2*) power dependence is somewhat comparable to MW-activated Si/H plasmas, albeit with a broader spatial distribution. For plasma heights larger than z ~ 5 mm, the behaviour substantially differs from MW-activated Si/H plasmas with I(H_2*) increasing (instead of decreasing) with increasing input power. Perhaps these differences are reflecting a broader $n_e(z, r)$ or a more spatially homogeneous $|E|/N$ with increasing P. I(H*) demonstrates comparable behaviour to MW-activated H and Si//H plasmas with peak intensities featuring at z ~ 7.5 mm as before. Both emission intensities demonstrate clear axial plasma expansion.

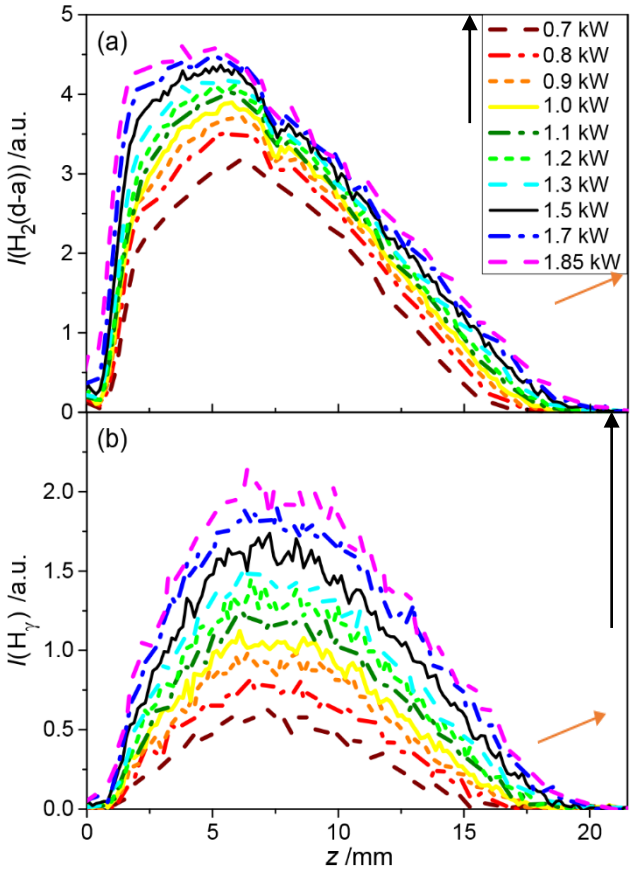

Figure 6.34: (a) I(H_2*) and (b) I(H*) as a function of P under otherwise OES-defined base conditions.

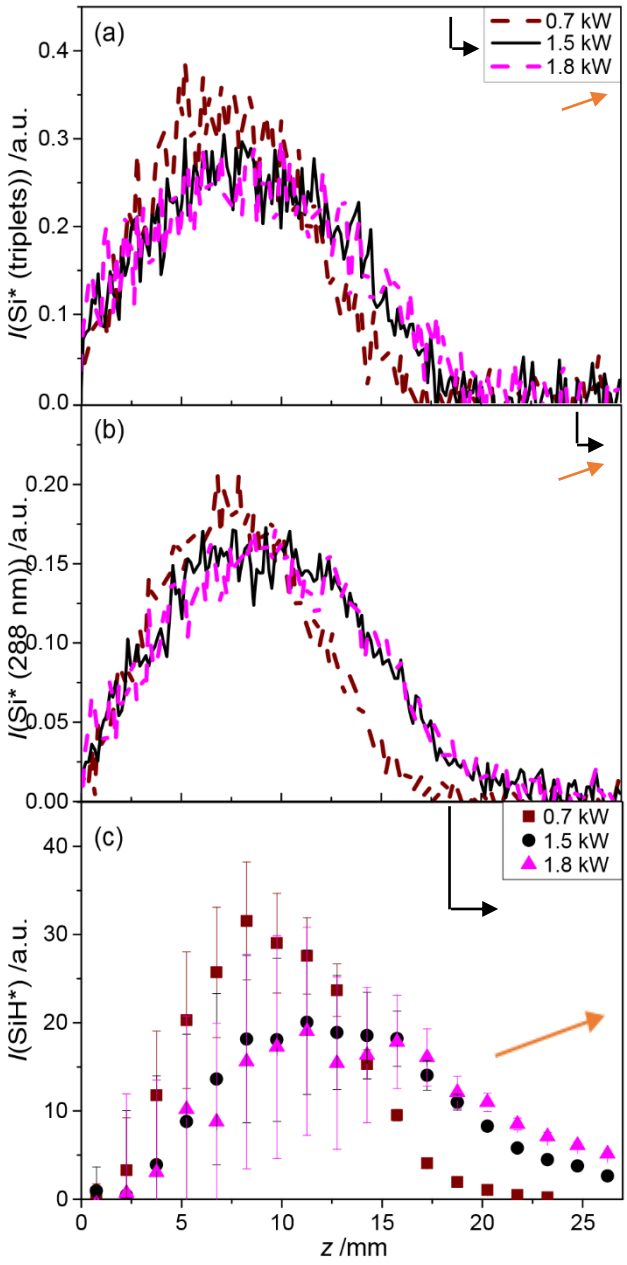

Figure 6.35: (a) *I*(Si*) triplet, (b) *I*(Si*) singlet and (c) *I*(SiH*) as a function of power under otherwise OES-defined base conditions.

Figure 6.35 demonstrates that both *I*(Si*) have comparable spatial distributions and power dependencies with neither emission extending above $z \sim 22.5$ mm. *I*(SiH*) demonstrates a sharper decrease with power (between $P = 0.7$ kW and 1.5 kW) and, as before, extends beyond $z = 27$ mm for $P \geq 1.5$ kW. The inference is a reconfirmation of the points noted with pressure variation, that there is either a different quenching mechanism for Si* and SiH* species, or that SiH* has an additional formation mechanism, most likely a chemiluminescent contribution.

The notion of different quenchers might be being reinforced in Figure 6.36, which demonstrates significantly different power dependencies between *I*(Si*), which crudely remains relatively flat when

compared to *I*(SiH*); *I*(SiH*) shows a significant decrease in intensity between *P* = 0.7 kW and *P* = 1.3 kW prior to plateauing.

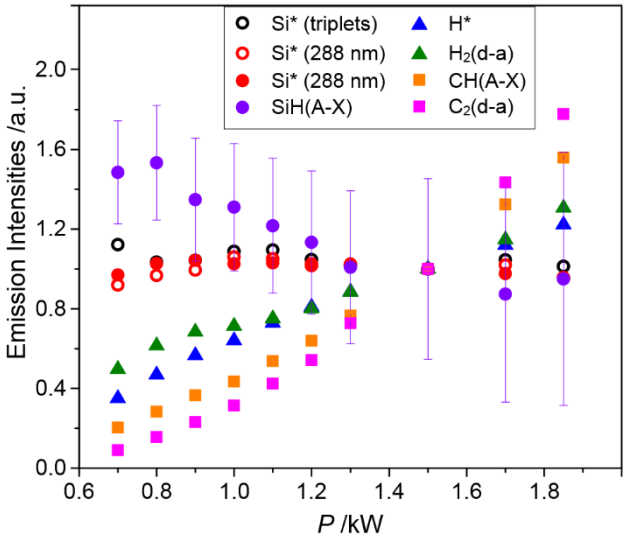

Figure 6.36: *I*(Si*), *I*(SiH*), *I*(CH*), *I*(C_2*), *I*(H*), *I*(H_2*) investigated with intensities summed between 9 ≤ *z* ≤ 12 mm (6 ≤ *z* ≤ 9 mm and 0 ≤ *z* ≤ 3 mm in the case of *I*(H*) and *I*(H_2*) respectively) as a function of power under otherwise OES-defined base conditions. Closed symbols were collected in the same plasma, whilst open symbols were collected separately. The triplet states were collected through UV-selective optics. Intensities have been normalised to base conditions for display purposes.

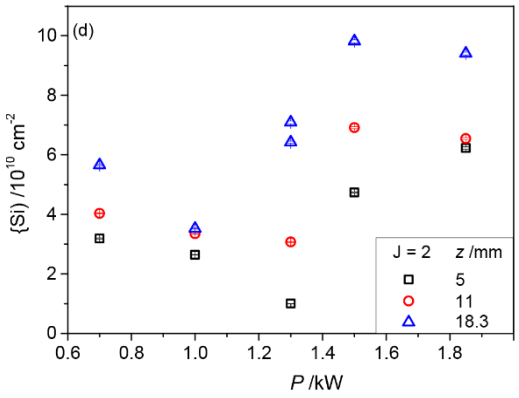

Figure 6.37: Si(*J* = 2)} investigated at three heights (*z* = 4.5, 11 and 18.3 mm) as a function of *P* under otherwise CRDS-defined base conditions.

With increasing power, {Si} appears to decrease between *P* = 0.7 and 1.3 kW and increases more significantly between *P* = 1.3 and 1.85 kW at all investigated heights. Perhaps this is indicative of a decrease in Si gettering species, [CH_4], for example, might be expected to decrease with increasing power (due to plasma expansion and an increase in [H] and [C_2H_2] throughout the reactor, as inferred within previous chapters). A deeper interpretation of Si-related gas phase processes occurring within MW-activated Si/C/H plasmas is hard to achieve at present and requires plasma modelling.

6.3.7.v: Overview of MW-activated Si/C/H Plasmas

Section 6.3.6.i proposes a number of possible gas phase chemistry between Si atoms and a range of different C-containing species. The main conclusion that can be deduced is that cyclic SiC_2-containing species would be one of the most stable conceivable Si and C containing molecules in an [H] rich environment. Section 6.3.6.ii confirmed that the air leak attributed to the CRDS experiments, and the hydrogen gas impurities, should not significantly perturb the Si-based chemistry in the presence of the hydrocarbon concentrations used in the CRDS studies (noting the chamber air leak is already minimised for the OES studies).

Section 6.3.7 demonstrates how various emission intensities and {Si} absorption column densities vary as a function of process conditions. From this data, it can be conclusively demonstrated that the presence of low concentrations of silane does not perturb the prominent C/H chemistry in the hot plasma regions. It can also be deduced that under OES-defined base conditions carbon-containing species are the most prominent ions (most likely $C_2H_2^+$ and $C_2H_3^+$). Taking the reported results at face value, Si and SiH are demonstrated to react more significantly with CH_x species (*cf.* C_2H_y) and this appears to be true irrespective of plasma region (i.e. through comparing OES and CRDS results, which sample the hot plasma regions and the outer chamber respectively). Based on the significantly different spatial extents of *I*(Si*) and *I*(SiH*), it seems probable that Si* is generated via EIE, whilst SiH* has a significant chemiluminescent contribution, plausibly Si and H_2 (or H and a third body), both of which extend beyond the plasma region, which contains a sufficient electron density / electron energies to excite these emitting states in vast quantities. The equivalent reaction involving C and H_2 was inferred to be a plausible excitation mechanism for the low lying states of CH* in Chapter 5.

Further 2-D plasma modelling would be required to develop a deeper understanding.

6.3.8: Further Studies Etching a Silicon Substrate

A silicon wafer, 32 mm in diameter and 0.7 mm in thickness, was placed on a Mo substrate (d_{sub} = 32 mm) with a spacer wire, d_{wire} = 0.002″. Under conditions of P = 1.5 kW, p = 150 Torr, $F(H_2)$ = 300 sccm, there were no emission intensities originating from *I*(Si*) or *I*(SiH*) that could be observed. Upon introducing Ar into the plasma at F(Ar) = 300 sccm (i.e. X_0(Ar) = 50%), the uncalibrated reflected power rapidly increased to P_{ref} = 0.08 kW. Notably T_{sub} did not visibly increase, as may have been expected from the work carried out in Chapter 3. After 6 minutes there were still no visible Si-containing emissions. Under comparable CRDS conditions, there was no evidence of detectable {Si} absorption at low plasma heights.

I(Si*), *I*(SiH*), and *I*(H*) were monitored as a function of time, whereby t = 0 s is defined as the moment at which the microwave waveguide was retuned, such that P_{ref} = 0.00 kW (X_0(Ar) = 50%). At this point, the substrate became visibly red hot. Figure 6.38 demonstrates (a) *I*(H*)(t) and (b) *I*(Si*)(t)

from t = 0 s. Figure 6.38 (c) contrasts I(Si*) in a MW-activated H plasma with the Si substrate present after F(Ar) had been turned off and the MW waveguide retuned to P_{ref} = 0.00 kW. This is compared to I(Si*) collected under conditions of $F(SiH_4/H_2)$ = 15 sccm, $F(H_2)$ = 300 sccm, P = 1.5 kW, p = 150 Torr (i.e. contrasting I(Si*) between silicon being introduced via silane as an input gas and being introduced via the etching / thermal decomposition of a silicon wafer). By accounting for the 0.7 mm offset associated with the Si substrate, and multiplying the latter by a $f(z)$, the two emissions become comparable for z > 5 mm, where $f(z) = \exp(-z/z_0)$, where $z_0 \sim 7.5$ mm. The reason for this will become apparent within the following discussion of these results.

Upon the introduction of methane ($F(CH_4)$ = 1 sccm, not reported), I(Si*) decayed away into the baseline within seconds when the Si is sourced from the Si substrate. This contrasts significantly to the behaviour observed in a MW-activated SiH_4/C/H plasmas, i.e. when the silicon content is sourced as gas phase silane. This finding was reinforced by a distinct lack of measurable {Si(J = 2)} under similar conditions.

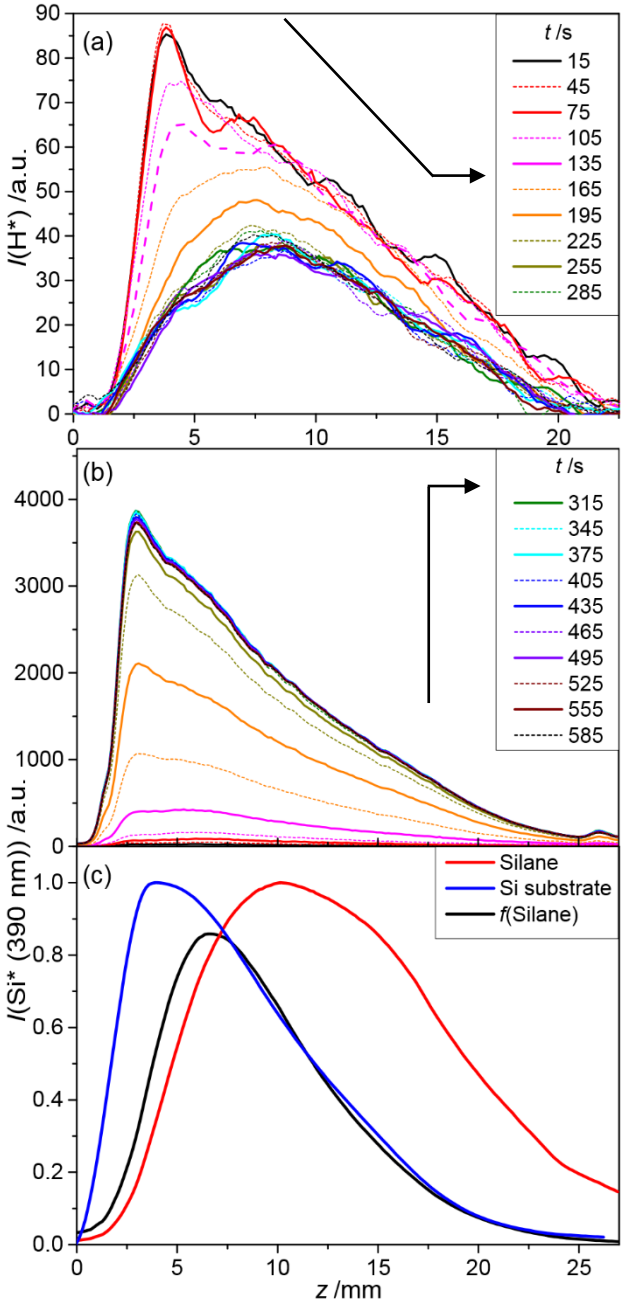

Figure 6.38: Time-resolved measurements of (a) *I*(H*) and (b) *I*(Si*) for *P* = 1.5 kW, *p* = 150 Torr, *F*(H_2) = 300 sccm, *F*(Ar) = 300 sccm with the presence of a 32 mm diameter Si wafer placed on a Mo substrate (d_{sub} = 32 mm, d_{wire} = 0.002″) and (c) a comparison of normalised *I*(Si*) collected for: (i) *P* = 1.5 kW, *p* = 150 Torr, *F*(H_2) = 300 sccm with the presence of a 32 mm diameter Si wafer placed on a Mo substrate (d_{sub} = 32 mm, d_{wire} = 0.002″) (blue), (ii) *P* = 1.5 kW, *p* = 150 Torr, *F*(H_2) = 300 sccm, *F*(SiH_4/H_2) = 15 sccm, (and a 32 mm Mo substrate sat on d_{wire} = 0.01″)(red), (iii) red curve (ii) multiplied by an exponentially-decaying *f*(*z*) (black). Note that for the blue curve, *z* = 0 mm has been defined as the top of the 0.7 mm Si wafer.

It can be seen clearly that over the course of the first 6 minutes, the intensity of *I*(H*) drops from an intensity distribution that resembles something comparable to that observed in Chapter 3 (with Ar present) to something that more closely resembling what has previously been observed for a MW-activated Si/H plasma. Similarly, over the first 6 minutes from the initial tuning of the MW waveguide,

I(Si*) increases significantly as the plasma approaches steady-state. After which, I(Si*) and I(H*) remain roughly constant.

This result has been reproduced with a roughened Si wafer and a second smooth wafer. It is only upon retuning the MW waveguide to P_{ref} = 0.00 kW that etching / thermal decomposition of the silicon wafer begins.

The interpretation of these results is relatively simplistic. A silicon wafer, irrespective of surface condition, is oxygen terminated. The Si-O bond energy is ~ 4.69 eV, significantly larger than the thermal energies available. Upon the introduction of Ar, a lot of the gas phase processes mentioned in Chapter 3 are the same, however, the reflected power is relatively high (*cf*. a tuned and equilibrated plasma, noting that there is a question as to how accurate is the reported P_{ref} = 0.08 kW). The consequence of a higher reflective power is a reduced absorbed power density, reduced ionization (and number of ions) and perhaps a weaker $|E|/N$.

Upon tuning the MW-waveguide, the silicon substrate began to visibly glow red, perhaps a result of an increased gas temperature (and associated hydrogen dissociation) occurring due to: (i) an increased flux of H atoms, which release ~ 4.518 eV of thermal energy to the Si substrate per recombination event, (ii) an increased flux of H and H_2 conducting thermal energies from the hotter plasma core, both of which would (iii) enhance T_{sub} and thermionic emissions from the substrate and / or (iv) potentially an enhancement of ion bombardment. Most likely, therefore, the reduction in reflected power acts to increase the reduced electric field strengths and absorbed power density at low plasma heights (resulting in thermal heating of the substrate). The increase in T_{sub} is substantially lower than the energy required to break the SiO surface termination, it seems reasonable to assert, therefore, that the removal of the surface oxygen requires energy released either (i) directly from H recombination events or (ii) from ions bombarding the substrate will have sufficiently high energies (noting an estimated voltage difference of ~ 10-20 V between the plasma (positive) and the substrate (neutral)).

Once the surface termination has been removed, Si is uncontrollably etched and thermally decomposes with material diffusing into the plasma, altering the prominent cation to $Si_xH_y^+$. Whilst the expectation might be that the new cations would peak at low z, the high [Si] number density at low z, reflected in I(Si*), suggests that the hyper-thermal electrons pumping the excited states of H* (and H_2*), or H* itself, are being quenched by the Si content at these plasma heights. For further results involving the Si substrate, refer to Alim Lalji's thesis.[44]

Once Ar is turned off, (i.e. F(Ar) = 0 sccm), the MW-waveguide is appropriately tuned, and the plasma is allowed to reach steady-state as a MW-activated (Si/)H plasma. I(Si*) is now apparent with the substrate is still visibly decomposing into the plasma (i.e. small silicon flakes can be seen to desorb from the surface), reinforcing the interpretation that it is the surface termination which prevented the initial introduction of Si into the plasma.

Figure 6.38 (c) demonstrates that I(Si*) peaks at z ~ 3 mm (defining z = 0 mm as the top of the 0.7 mm substrate) when an Si substrate is present (blue curve) and does not extend to beyond z ~ 27 mm. This contrasts to I(Si*) collected with silane (and no Si substrate, red curve), which peaks at z ~ 10 mm and extends beyond z = 27 mm.

Multiplying the red curve (I(Si*) collected under base pressure/power with silane present) by an axially decaying exponential ($\exp(-z/z_0)$) produces the black curve, whereby z_0 ~ 7.5 mm. The agreement between the two curves above z ~ 7.5 mm infers that the difference between the two I(Si*) curves (collected in a MW-activated SiH_4/H_2 plasma and a MW-activated H plasma with a surface-activated Si wafer) can be accounted for by the diffusion law (i.e. a well-mixed dilute silane/hydrogen plasma multiplied by an axial exponential decay reproduces the observed spatial distribution of I(Si*) when Si is sourced from a Si substrate). The implication is that the latter plasma is demonstrating the physical / chemical characteristics of a MW-activated Si/H plasma, except with an axial / differential gradient of [Si] from the silicon source. The higher I(Si*) noted at low z is inferring more low energy electrons (due to the higher [Si] content) or an unmixed / less well-mixed / unreacted Si contribution from the substrate.

Upon the introduction of methane ($F(CH_4)$ = 1 sccm), I(Si*) decays immediately into the baseline (within seconds) at all plasma heights, evidencing that the deposition of a carbon monolayer on the Si substrate prevents etching of Si. Turning the methane flow off, and awaiting a period of time, allowed the reappearance of I(Si*) once these layers had etched away.

One of the biggest challenges in the accumulation of data presented in Chapter 6.3.4 was that there were two distinct spatial distributions that I(Si*) adopted under base conditions, and as a function of conditions, those presented in this thesis, and an alternative, which appears upon striking a plasma after a significant period (on the order of days to weeks) for silane-based experimental work. These two spatial distributions are demonstrated in Appendix Figures A6.7 (a) and (b) under OES-defined base conditions for a MW-activated Si/H plasma. Upon cleaning the chamber / the substrate and baseplate, the spatial distributions return to those reported in this Chapter. From Figure 6.38 (c), it seems plausible that the second spatial distribution was a perturbation to gas phase [Si], perhaps a manifestation of Si content being continually etched / deposited onto a silicon-coated baseplate and/or substrate. As this contribution was uncontrollable, (and interestingly varied with parameters, as can be seen for $F(SiH_4)$ in Appendix Figures A6.7 (a) and (c)), except by using a clean reactor and thereby removing it, this Thesis only presented the most controllable version of these two possible spatial variations; those achieved with a clean chamber. This, however, should have little bearing on those intending to use silane in the presence of methane for silicon doping. As would be the case with the surface-activated silicon substrate, the addition of methane would act to coat any such monolayers with carbon, preventing such Si-based contributions entering the gas phase, and hence, this was not an issue exploring MW-activated Si/C/H plasmas.

An additional, more speculative conclusion that might be drawn from the additional experiments presented in this section, is that deliberate Si-doping of the diamond using a Si substrate is likely to occur through silicon migration into the lattice, rather than via the gas phase.

Another big challenge with regards to collecting the trends reported (particularly with variations in pressure in Section 6.3.4) were the irreproducibility of relative intensities (particularly at low pressures). The reason for this is likely that the silicon content (and therefore the related emission intensities) has an additional contribution from etching silicon from the chamber walls. The irreproducibility is attributed to the different levels of cleanliness that the chamber walls adopt, which is dependent upon the previous condition(s) explored, i.e. the recent history of the chamber.

6.4: Conclusions

This chapter presents a range of experimental results covering MW-activated Si/H and Si/C/H plasmas. Whilst the interpretation is still developing, there are a few conclusions that can be drawn.

From a review of literature, it is deduced that Si atoms are expected to be the dominant Si-containing species throughout the entire plasma / chamber when operating MW-activated Si/H plasmas under the investigated parameter ranges. For this reason, [Si] maximises (in accordance to the ideal gas law) in the coolest regions of the plasma / chamber. This manifests itself in {Si} measurements (carried out via CRDS experiments) as {Si} maximising at higher plasma heights (i.e. in the cooler regions of the plasma / chamber), noting that silicon contributions from etching the Quartz window (and/or a Si subtrate when present) in a MW-activated H plasma were eliminated as possible contributing sources to {Si} measurements.

It is potentially inferred through changes in $I(H_2^*)$ and $I(H^*)$ that under most explored conditions, silicon-containing species are the dominant ions in MW-activated Si/H plasmas. The formation mechanism(s) of the investigated Si* and SiH* excited states is not yet certain, but electron impact excitation seems like a feasible rationale for many of the investigated conditions. Additional mechanisms such as electron-ion recombination and chemiluminescent contributions are also proposed with the latter thought to be a prominent alternative excitation mechanism contributing towards the intensity of SiH*. These excited states are most likely quenched by H atoms.

Absorption measurements carried out on the triplet ground state of Si are inadequate for (i) confirming that Si atoms dominate the silicon-containing species and (ii) exploring a system, whereby $X_0(SiH_4) < X_0(\text{leak})$ and $X_0(\text{impurity})$. Therefore, the presented {Si} measurements are at best indicative.

Further {Si} measurements (and literature reviews) demonstrate that MW-activated Si/H has a complex chemistry with Oxygen, which acts to getter some (if not the majority?) of Si content in the cool plasma regions. This must be considered in order to provide a rationale behind some of the indicative trends achieved via CRDS measurements, e.g. variation of {Si} with changes in input silane fraction.

Upon the addition of methane, Si does not perturb the dominant C/H chemistry. The emission and absorption measurements, taken at face value, infer that [Si] is gettered by CH_x ($0 \leq x \leq 4$) species. The disparity in spatial distributions (and emission trends) of Si* and SiH* excited states infers that SiH* has a prominent chemiluminescent contribution, evident at high plasma heights.

An alternative explanation for the disparity in spatial distributions might be if the most prominent quenching species of Si* is CH_3 and CH_4 species (which are more prominent in the periphery and cooler regions of the plasma), whilst for [SiH*], the most prominent quenchers might be CH_2, CH and C species, (i.e. single carbon CH_x species that are more prominent in the hotter plasma regions).

Unless there is additional chemistry between C-containing species and Si that favours the production of SiH, the expectation is that the most dominant carbon-free Si-containing species will be Si atoms. Upon approaching the substrate, T_g decreases rapidly, increasing [CH_4] and [CH_3] radical number densities. This will have a negative impact on [Si] close to the substrate (presumed to be the incorporated species during Si-doping). Developing a better understanding behind this will be key for enhancing / minimising Si incorporated via the gas phase.

These results are compared to those achieved with a silicon wafer (0.7 mm thick, 32 mm in diameter). Silicon was found to only desorb into the MW-activated H plasma once the oxygen-terminating surface layer had been removed (achieved through the introduction of Ar). Further, there were no detectable {Si} absorptions above the substrate, prior to Ar addition. The inference might be that silicon generally incorporates into a diamond lattice through diffusion (when grown on a Si wafer), rather than via the gas phase through etching the substrate / quartz windows (of course, this would be dependent on both operating conditions and reactor design). Further, silicon content was completely gettered from the plasma by the introduction of small methane fractions when Si is sourced via substrate etching (/ decomposition), indicating that deposition occurs on a much faster time scale then etching, reinforcing the notion that Si must be entering the diamond via thermal migration from the substrate, rather than from etching of quartz windows etc.

There is still a lot of work/analysis that should be done in order to complete the understanding that this chapter has begun to develop. This includes:

CRDS measurements on the {Si($^1D_2$)} or {Si($^1S_0$)} states; the perceived advantage of probing such states is the possibility of accessing higher ring down times (from more highly reflecting mirrors in the visible range), lower number densities, allowing the use of higher silane flows (*cf.* X_0(leak)) without fear of saturation.

Analysis of intensities collected from Si($3s^2 3p5s$ ($^1P_1^o$)$\rightarrow 3s^2 3p^2$($^1D_2$)) in second order will help provide a confirmation of excitation mechanism(s) as a function of conditions. Differences / similarities in spatial profiles to other singlet states might be indicative of excitation mechanisms (most likely EIE).

Further 2-D modelling of MW-activated Si/H and Si/C/H plasmas will be crucial to provide verification of the current conclusions and develop a more indepth rationale of prominent processes, and of course, complementary growth (and material analysis) studies.

References

[1] Ma, J., Ashfold, M. N. R. and Mankelevich, Yu. A. "Validating optical emission spectroscopy as a diagnostic of microwave activated $CH_4/Ar/H_2$ plasmas used for diamond chemical vapor deposition." Journal of Applied Physics, vol. 105, no. 4, p. 043302, 2009.

[2] Ma, J., Richley, J. C., Davies, D. R. W., Cheesman, A., Ashfold, M. N. R. and Mankelevich, Yu. A. "Spectroscopic and modeling investigations of the gas-phase chemistry and composition in microwave plasma activated $B_2H_6/Ar/H_2$ mixtures." The Journal of Physical Chemistry A, vol. 114, no. 7, pp. 2447-2463, 2010.

[3] Truscott, B. S., Kelly, M. W., Potter, K. J., Ashfold, M. N. R. and Mankelevich, Yu. A. "Microwave plasma-activated chemical vapor deposition of nitrogen-doped diamond. II: $CH_4/N_2/H_2$ Plasmas." The Journal of Physical Chemistry A, vol. 120, no. 43, pp. 8537-8549, 2016.

[4] Richley, J. C., Kelly, M. W., Ashfold, M. N. R. and Mankelevich, Yu. A. "Optical emission from microwave activated C/H/O gas mixtures for diamond chemical vapor deposition." The Journal of Physical Chemistry A, vol. 116, no. 38, pp. 9447-9458, 2012.

[5] Yang N., Yu S., Macpherson J. V., Einsaga Y., Zhao H., Zhao G., Swain G., Jiang X. "Conductive diamond: synthesis, properties, and electrochemical applications." Chemistry Society Review, Advance Article, 2019.

[6] Ekimov, E. A., Ralchenko, V. and Popovich, A. "Synthesis of superconducting boron-doped diamond compacts with high elastic moduli and thermal stability." Diamond and Related Materials, vol. 50, pp. 15-19, 2014.

[7] Hong, S., Grinolds, M. S., Pham, L. M., Le Sage, D., Luan, L., Walsworth, R. L., and Yacoby, A. "Nanoscale magnetometry with NV centers in diamond." MRS Bulletin, vol. 38, no. 2, pp. 155-161, 2013.

[8] Kessels, W. M. M. "Remote plasma deposition of hydrogenated amorphous silicon." Thesis, Eindhoven University of Technology, pp. 3-6, 2000.

[9] Howling, A. A., Dorier, J. L., Hollenstein, C., Kroll, U. and Finger, F. "Frequency effects in silane plasmas for plasma enhanced chemical vapor deposition." Journal of Vacuum Science & Technology A: Vacuum, Surfaces, and Films, vol.10, no. 4, pp. 1080-1085, 1992.

[10] Kortshagen, U. "Nonthermal plasma synthesis of semiconductor nanocrystals." Journal of Physics D: Applied Physics, vol. 42, no. 11, p. 113001, 2009.

[11] Shindo, W., Sakai, S., Tanaka, H., Zhong, C. J. and Ohmi, T., "Low-temperature large-grain poly-Si direct deposition by microwave plasma enhanced chemical vapor deposition using SiH_4/Xe". Journal of Vacuum Science & Technology A: Vacuum, Surfaces, and Films, vol. 17, no. 5, pp. 3134-3138, 1999.

[12] Wrobel, A. M., Walkiewicz-Pietrzykowska, A., Ahola, M., Vayrynen, I. J., Ferrer-Fernandez, F. J. and Gonzalez-Elipe, A. "Growth mechanism and chemical structure of amorphous hydrogenated silicon carbide (a-SiC:H) films formed by remote hydrogen microwave plasma CVD from a triethylsilane precursor: Part 1." Chemical Vapor Deposition, vol. 15, no. 1-3, 39-46, 2009.

[13] Allendorf, M. "A Model of Silicon Carbide Chemical Vapor Deposition," Journal of the Electrochemical Society, vol 138, no. 3, p. 841, 1991.

[14] Stinespring, C. D. and Wormhoudt, J. C. "Gas phase kinetics analysis and implications for silicon carbide chemical vapor deposition." Journal of Crystal Growth, vol. 87, no. 4, pp. 481-493, 1988.

[15] Raghunath, P., Lee, Y., Wu, S., Wu, J. and Lin, M. "Ab initiochemical kinetics for reactions of H atoms with SiH_x(x = 1-3) radicals and related unimolecular decomposition processes." International Journal of Quantum Chemistry vol. 113, no. 12, pp. 1735-1746, 2013.

[16] Iakoubovskii, K. and Stesmans, A. "Characterization of hydrogen and silicon-related defects in CVD diamond by electron spin resonance." Physical Review B, vol. 66, no. 19, pp. 195207, 2002.

[17] Uğur, A. "Silicon Vacancy Defects in Diamond as Single Photon Source" Master of Science Thesis, Technical University of Müchen, 2006.

[18] Rogers, L. J, Jahnke, K. D., Metsch, M. H., Sipahigil, A., Binder, J. M., Teraji, T., Sumiya, H., Isoya, J., Lukin, M. D., Hemmer, P. and Jelezko, F. "All-Optical Initialization, Readout, and Coherent Preparation of Single Silicon-Vacancy Spins in Diamond." Physical Review Letters, vol. 113, no. 26, 2014.

[19] Turukhin, A. W., Liu, C. H., Gorokhovsky, A. A., Alfano, R. R. and Phillips, W. "Picosecond photoluminescence decay of Si-doped chemical-vapor-deposited diamond films." Physical Review B, vol. 54, no. 23, pp. 16448-16451, 1996.

[20] Felgen, N., Naydenov, B., Turner, S., Jelezko, F., Reithmaier, J. P. and Popov, C. "Incorporation and study of SiV centers in diamond nanopillars." Diamond and Related Materials, vol. 64, pp. 64-69, 2016.

[21] Ranjan Mohapatra, D., Rai, P., Misra, A., Tyagi, P. K., Misra, D., "Photoluminescence study of polycrystalline and single crystal diamond," International Workshop on Physics of Semiconductor Devices, pp. 891–893, 2007.

[22] Singh, S., Thomas, V., Martyshkin, D., Kozlovskaya, V., Kharlampieva, E., Catledge, S. A., "Spatially controlled fabrication of a bright fluorescent nanodiamond-array with enhanced far-red Si–V luminescence," Nanotechnology, vol. 25, p. 45302, 2014.

[23] Sedov, V., Ralchenko, V., Khomich, A. A., Vlasov, I., Vul, A., Savin, S., Goryachev, A., Konov, V., "Si-doped nano- and microcrystalline diamond films with controlled bright photoluminescence of silicon-vacancy color centers," Diamond and Related Materials, vol. 56, pp. 23-28, 2015.

[24] Sakaguchi, I., Nishitani-Gamo, M., Loh, K. P., Haneda, H., Hishita, S. and Ando, T., "Silicon incorporation into chemical vapor deposition diamond: A role of oxygen." Applied Physics Letters vol. 71, no. 5, pp. 629-631, 1997.

[25] Coutinho, L. H., and Trigueiros, A. G. "Weighted oscillator strengths and lifetimes for the Si I spectrum." Journal of Quantitative Spectroscopy and Radiative Transfer, vol. 75, no. 3, pp. 357-387, 2002.

[26] Radziemski, L. J., and Andrew, K. l. "Arc Spectrum of Silicon" Journal of the Optical Society of America, vol. 55, no. 5, p. 474, 1965.

[27] Western, C. M., "PGOPHER, A Program for Simulating Rotational, Vibrational and Electronic Spectra," University of Bristol, http://pgopher.chm.bris.ac.uk

[28] Hydrogen (H_2): Alternative Specification - Pure Gases - Speciality Gases - IUPC - Air Liquide UK. http://www.airliquide-iupcgases.co.uk/preview/speciality-gases/hydrogen-alternative-spec.php (accessed Apr. 5, 2019).

[29] Ma, J. "Exploration of the gas phase chemistry in microwave activated plasmas used for diamond chemical vapour deposition" PhD thesis, University of Bristol, 2008.

[30] Perrin, J., Leroy, O. and Bordage, M. Cross-Sections, "Rate Constants and Transport Coefficients in Silane Plasma Chemistry." Contributions to Plasma Physics, vol. 36, no. 1, pp. 3-49, 1996.

[31] Glassman, I., Yetter, R. A., Glumac, N. G., "Combustion" Elsevier Academic Press, 5th Edition: London, 2017.

[32] Robin, M. B., and Kuebler, N. A. "Excited electronic states of the simple alcohols." Journal of Electron Spectroscopy and Related Phenomena, vol. 1, no. 1, pp. 13-28, 1972.

[33] Brewer, L., and Edwards, R. K. "The Stability of SiO Solid and Gas." The Journal of Physical Chemistry, vol. 58, no. 4, pp. 351-358, 1954.

[34] Herbon, J. T., Hanson, R. K., Golden, D. M., and Bowman, C. T. "A shock tube study of the enthalpy of formation of OH." Proceedings of the Combustion Institute, vol. 29, no. 1, pp. 1201-1208, 2002.

[35] Foner, S. N., and Hudson, R. L. "Ionization Potential of the OH Free Radical by Mass Spectrometry." The Journal of Chemical Physics, vol. 25, no. 3, pp. 602-603, 1956.

[36] Hildenbrand, D. L., and Murad, E. Dissociation Energy and Ionization Potential of Silicon Monoxide. *The* Journal of Chemical Physics, vol. 51, no. 2, pp. 807-811, 1969.

[37] Lucas, D. J, Curtiss, L. A., and Pople, J. A. "Theoretical study of the silicon–oxygen hydrides SiOHn (n=0–4) and SiOH+n (n=0–5): Dissociation energies, ionization energies, enthalpies of formation, and proton affinities." The Journal of Chemical Physics, vol. 99, no. 9, pp. 6697-6703, 1993.

[38] Suto, M., and Lee, L. C. "Quantitative photoexcitation study of SiH_4 in vacuum ultraviolet." The Journal of Chemical Physics, vol. 84, no. 3, pp. 1160-1164, 1986.

[39] Glenewinkel-Meyer, T., Bartz, J. A., Thorson, G. M., and Crim, F. F. The vacuum ultraviolet photodissociation of silane at 125.1 nm. The Journal of Chemical Physics, vol. 99, no. 8, pp. 5944-5950, 1993.

[40] Nahar, S. N., and Pradhan, A. K. "Unified Electron-Ion Recombination Rate Coefficients of Silicon and Sulfur Ions." The Astrophysical Journal, vol. 447, p. 966, 1995.

[41] Nahar, S. N. "Electron-Ion Recombination Rate Coefficients for Si i, Si ii, S ii, S iii, C ii, and C-like Ions C i, N ii, O iii, F iv, Ne v, Na vi, Mg vii, Al viii, Si ix, and S xi: Erratum." The Astrophysical Journal Supplement Series, vol. 106, p. 213, 1996.

[42] Kalemos, A., Mavridis, A., and Metropoulos, A. "An accurate description of the ground and excited states of SiH." The Journal of Chemical Physics, vol. 116, no. 15 pp. 6529-6540, 2002

[43] Ram, R. S., Engleman, R., and Bernath, P. F. "Fourier Transform Emission Spectroscopy of the A2Δ–X2Π Transition of SiH and SiD." Journal of Molecular Spectroscopy, vol. 190, no. 2, pp. 341-352, 1998.

[44] Lalji, A. "The use of Optical Emission Spectroscopy to probe microwave-activated silicon-containing hydrogen plasmas" Undergraduate final year Dissertation, University of Bristol, 2018.

[45] Zhang, Y., Dou, G., Qi, J., and Cui, J. "Ab inito study on the electronic structure and laser cooling of SiH." Computational and Theoretical Chemistry, vol. 1134, pp. 8-14, 2018.

[46] O'Brian, T. R., and Lawler, J. E. "Radiative lifetimes in Si i from laser-induced fluorescence in the visible, ultraviolet, and vacuum ultraviolet." Physical Review A, vol. 44, no. 11, pp. 7134-7143, 1991.

[47] Allden, J. W. R. "The use of Spectroscopic Methods to determine the state of Plasmas relevant to the Chemical Vapour Deposition of Diamond" Undergraduate final year Dissertation, University of Bristol, 2019.

[48] Leahy, C., Hastings, J. T., and Wilt, P. M. "Temperature dependence of Doppler-broadening in rubidium: An undergraduate experiment." American Journal of Physics, vol. 65, no. 5, pp. 367-371, 1997.

[49] Kervirtis, A. E., Bohme, D. K., Hopkinson, A. C., "Theoretical Enthalpies of Formation of Compounds $SiCH_n$ (n = 0-4), SiC_2H_n (n = 0-4, 6), $SiCH_n^+$ (n = 0-5), and $SiC_2H_n^+$ (n = 0-5, 7)." Journal of Physical Chemistry, vol. 99, no. 43, pp.16121-16127, 1995.

[50] Hildenbrand, D. L., and editors Gurvich, L. V., Veyts, I. V., Alcock, C. B., "Thermodynamic Properties of Individual Substances, Volume 3, Parts 1 and 2." CRC Press: Boca Raton, FL. The Journal of Chemical Thermodynamics, vol. 27, no. 3, pp. 335-336, 1994.

[51] Dobis, O., and Benson, S. W. "Analysis of flow dynamics in a new, very low pressure reactor. Application to the reaction: $Cl + CH_4 \rightarrow HCl + CH_3$." International Journal of Chemical Kinetics, vol. 19, no. 8, pp. 691-708, 1987.

[52] Doncaster, A. M., and Walsh, R. "Thermochemistry of silicon-containing compounds. Part 2.—The enthalpies of formation of the methylsilanes, an experimental study and review." J. Chem. Soc., Faraday Trans. 2, vol. 82, no. 4, pp. 707-717, 1986.

[53] Ervin, K. M., and Lineberger, W. C. "Photoelectron spectra of dicarbon(1-) and ethynyl(1-)." The Journal of Physical Chemistry, vol. 95, no. 3, pp. 1167-1177, 1991.

[54] Ruscic, B., Pinzon, R. E., Laszewski, G., Kodeboyina, D., Burcat, A., Leahy, D., Montoy, D., and Wagner, A. F. "Active Thermochemical Tables: thermochemistry for the 21st century." Journal of Physics: Conference Series, vol. 16, pp. 561-570, 2005.

[55] Sana, M., and Nguyen, M. T. "Comment on the accurate theoretical determination of heats of formation," Chemical Physics Letters, vol. 196, no. 3-4, pp. 390-396, 1992.

[56] Ruscic, B. "Active Thermochemical Tables: Sequential Bond Dissociation Enthalpies of Methane, Ethane, and Methanol and the Related Thermochemistry." The Journal of Physical Chemistry A. vol. 119, no. 28, pp. 7810-7837, 2015.

[57] Becerra, R., Cannady, J. P., Dormer, G., and Walsh, R. "The Addition Reaction between Silylene and Ethyne: Further Isotope Studies, Pressure Dependence Studies, and Quantum Chemical Calculations." The Journal of Physical Chemistry A, vol. 112, no. 37, pp. 8665-8677, 2008.

[58] Kunz, A., Roth, P. "High-temperature kinetics of some Si- and Cl-containing ceramic precursors." International Journal of Chemical Kinetics, vol. 33, no. 11, pp. 741-754, 2001.

[59] Common Bond Energies. http://www.wiredchemist.com/chemistry/data/bond_energies_lengths.html (accessed 29 March, 2019 aka Happy no Brexit day).

[60] Schleyer, P. V. R., and Kost, D. "A comparison of the energies of double bonds of second-row elements with carbon and silicon." Journal of the American Chemical Society, vol. 110, no. 7 pp. 2105-2109, 1988.

[61] Tho Nguyen, M., Sengupta, D., and Vanquickenborne, L. "A theoretical study of the reaction of SiH_2 with C_2H_2 and C_2D_2." Chemical Physics Letters, vol. 240, no. 5-6, pp. 513-520, 1995.

[62] Kelly, M. W., "Laser Diagnosis and computer modelling of C/H/O and C/H/N plasmas used in diamond chemical vapour deposition", School of Chemistry, University of Bristol, 2014.

[63] Truscott, B. S., Kelly, M. W., Potter, K. J., Johnson, M., Ashfold, M. N. R., and Mankelevich, Yu. A. "Microwave Plasma-Activated Chemical Vapor Deposition of Nitrogen-Doped Diamond. I. N_2/H_2 and NH_3/H_2 Plasmas." The Journal of Physical Chemistry A, vol 119, no. 52, pp. 12962-12976, 2015

[64] Plessis, P., Marmet, P., and Dutil, R. "Ionisation and appearance potentials of CH_4 by electron impact. Journal of Physics B: Atomic and Molecular Physics, vol. 16, no. 7, pp. 1283-1294, 1983.

[65] Kerr, J., Huber, K. P., and Herzberg, G., "Molecular spectra and molecular structure: IV constants of diatomic molecules." Analytica Chimica Acta, vol. 144, pp. 1-298, 1982.

[66] Plessis, P., and Marmet, P. Electroionization study of acetylene and fragment ions. International Journal of Mass Spectrometry and Ion Processes, vol. 70, no. 1, pp. 23-44, 1986.

[67] Blush, J. A., and Chen, P. "Photoelectron spectrum of the vinyl radical: downward revision of the C_2H_3-ionization potential." The Journal of Physical Chemistry, vol. 96, no. 11, pp. 4138-4140, 1992.

Chapter 7: Concluding Remarks

This chapter summarizes the underlying themes and questions explored within this thesis. Whilst a large volume of work has been covered over a range of different MW-activated H-containing plasmas, the overwhelming commonality that binds this thesis together (beyond the context of diamond CVD growth, etching, termination and more generally the optical diagnostic methods carried out on MW-activated plasmas in these contexts) is the step away from the generally assumed excitation mechanism, Electron Impact Excitation, in the production of fluorescing / excited state species in these plasmas. In addition to EIE, this thesis demonstrates that there are prominent contributions from alternative excitation mechanisms. These include but are not limited to: near-resonant energy transfers, dissociative electron attachment reactions, a number of chemiluminescent reactions, and speculates on additional contributions from, for example, electron-ion recombination reactions. This chapter concludes with interesting follow-on suggestions and practical applications of this work.

7.1: Thesis Overview

This thesis begins by reviewing the state-of-the-art background understanding of the physical and chemical processes occurring within MW-activated C/H plasmas operating at conditions that underpin the Chemical Vapour Deposition of diamond. Numerous open questions are noted regarding the field of plasma-enhanced diamond growth and, more specifically to this thesis, plasma diagnostics carried out on MW-activated plasmas. Such questions include:

(i) The validity of using the H-Balmer emission ratios in measuring the EEDF (or even the hyper-thermal EEDF) in MW-activated H plasmas.

(ii) Anomalous results regarding T_g estimates using H_2 emission (and absorption) spectra.

(iii) The possibility of more sensitive and reliable probing of the thermal and hyper-thermal component of the EEDF using OES.

(iv) The effect that lesser explored parameter spaces, e.g. substrate diameter (and T_{sub}) have on the physical and chemical properties of the plasma and the effects that these parameters may have on hydrogen termination / diamond growth.

(v) Experimental evidence for the proposed explanation (inhomogeneous power absorption) for concave / convex diamond growth.

(vi) As many of these questions were addressed using MW-activated H plasmas, which (if any) of these conclusions extend to MW-activated C/H plasmas?

(vii) Whether emissions originating from the CH and C_2 radicals make good *in situ* indicators of $CH_x (0 \leq x \leq 3)$ radicals and C_2H_2 respectively during growth.

(viii) Direct experimental evidence for charged species within MW-activated C/H plasmas.

(ix) The gas phase processes involving Si (and its excited states) in (i) MW-activated Si/H and (ii) Si/C/H plasmas.

(x) Any differences in the behaviour of Si when sourced via (i) silane and (ii) a silicon wafer in either of the above systems.

This thesis addresses many of the questions above directly or indirectly using spatially-resolved optical emission spectroscopy (and cavity ring down spectroscopy). In the process, this Thesis raises (and on occasion infers answers to) additional questions:

(xi) Are there experimental parameters in the context of Questions (iv) and (v) that can enhance the homogeneity of hydrogen termination / diamond growth over larger areas?

(xii) What are the prominent formation and loss mechanisms of different excited state species?

(xiii) What parameters impact the plasma parameter(s) causing an enhancement / reduction of emission intensities observed at low plasma heights?

(xiv) Why?

(xv) How do these depend on the metal substrate's (or any additional material's) shape / size / electrically conductive properties?

(xvi) What species / mechanism(s) are involved in the incorporation of Si during diamond growth when using (i) silane and (ii) a silicon substrate as the source of silicon?

This thesis highlights that there are many plausible excitation mechanisms beyond electron impact excitation, which is commonly accepted within literature to underpin most electronic excitations.

The strengths (and weaknesses) of the non-invasive technique, spatially-resolved Optical Emission Spectroscopy, are reiterated throughout this thesis (*cf*. traditional single height OES measurements). It seems remarkable that despite probing a minority of excited state species, which consumes ~ 1% of the total power denstiy, that so much qualitative and quantitative diagnostic information can be deduced about the physical state and chemical composition of the plasma (e.g. spatially-resolved relative column densities of excited state species, gas temperatures, variations in the absorbed power density, reduced electric field and electron energy distribution function, etc) just by analysing their flourescence.

This thesis demonstrates how spatially-resolved OES can continue to advance the understanding of prominent physical and chemical processes occurring within a range of MW-activated plasmas. Through combining such studies with 2-D physical chemical plasma kinetic modelling (and in the case of MW-activated Si-containing plasmas, studies using the ultra-sensitive absorption technique, Cavity Ring Down Spectroscopy), it has been possible to address the questions above, with insight into additional queries, for instance, the interplay of physical processes and their coupling to plasma parameters within MW-activated H and H/Ar plasmas, the prominent formation mechanism of anions in MW-activated C/H plasmas, etc. This thesis serves as a good reminder that despite a huge volume of

literature and research on MW-activated C/H plasmas and the chemical vapour deposition of diamond, a complete understanding remains elusive.

Chapter 3 investigates H and H_2 optical emissions originating from MW-activated H and H/Ar plasmas. Through monitoring these emissions as a function of process conditions, it has been possible to rationalise their spatial variations and their variation with changes in operating conditions through the development of the first self-consistent MW-activated H (and H/Ar) plasma models under conditions relevant to etching of diamond. These combined studies offer insight into the first 5 questions of the first list and the first 5 questions of the second list (i.e. Questions i to v and Questions xi to xv), with many conclusions extrapolating to MW-activated C/H plasmas studies featuring in Chapters 4, 5 and 6. The modelling serves to highlight the interdependences between the physical plasma parameters, the gas phase processes, the number densities and column densities of different species. The coupling between the absorbed power density and MW electric field strengths, for example, impacts the gas temperature, thermal dissociation of H_2, and the reduced electric field strength, of which ionization and chemical kinetic rates, current densities (and therefore the absorbed power density, T_g, etc) all depend on. This thesis serves to clarify how the variation of these plasma parameters may impact the gas phase processes and therefore alter the number densities of ground states, excited states, ionized species, electrons etc, which are directly coupled to the absorbed power density and MW electric field strength, e.g. through inelastic collisions of electrons with H_2 generating ro-vibrational excitation.

The development of 2-D modelling enables the rationalisation of the observed variations in $I(H_2^*)$ and $I(H^*)$ as a function of process conditions, and further enabled additional parameters, such as substrate diameter and T_{sub}, to be explored and rationalised. In order to explain the observed experimental trends, couplings between excited H($n > 1$) atoms with ground state $H_2(X)$ molecules, and excited H_2 with ground state H($n = 1$) were required. Such couplings are demonstrated to extend to MW-activated Si/H and Si/C/H plasmas in Chapter 6, addressing Question vi, which features in the first list of questions.

Under the pressure conditions investigated in this thesis, it should not be assumed that observed variations in the H-Balmer ratio with changes in operating conditions reflect a change in the hyper-thermal component of the EEDF. Further, the couplings between H($n \geq 2$) and H_2^* via their ground states could act to distort $H_2(v, J)$ populations, resulting in perturbed T_g estimatations from T_{rot} and T_{vib} analysis of $I(H_2^*)$. The investigations carried out in Chapter 3 instead conclude that whilst near-resonant energy transfers are necessary to explain variations in $I(H^*)$ and $I(H_2^*)$ with changes in operating conditions, $I(H_2^*)$ is generally more sensitive to the axial (and process condition dependent) variation of the EEDF(z) with hyper-thermal energies. This chapter highlights that whilst hyper-thermal electrons are required to pump the high energy states of H, H_2, and Ar (when present), near-resonant excitation transfers are also required to rationalise changes in these emissions; further, it highlights that different excited states couple with one another, and hence the H-Balmer ratio is a poor means to estimate variations in the hyper-thermal component of the EEDF.

Chapter 3 uses the developed modelling and rationale to further probe the effect of decreasing substrate diameter and the impact that introducing argon into the gas flow has on the plasma parameters and gas phase processes. Both were found experimentally to increase T_{sub} and relative emissions of H and H_2 near to the substrate. For decreasing the substrate diameter, this was a reflection of enhanced and local changes (both in magnitude and radial inhomogeneity) to the electric field strengths and changes to the hyper-thermal component of the EEDF (and perhaps electron density generated near the substrate edge), whilst for Ar addition, this was due to an additional couplings between the excited states of Ar with the excited states of H* and H_2* (and Ar* with H and H_2). The use of a 17 mm diameter substrate was also speculatively observed to collapse the sheath, whilst Ar did not. Further modelling did, however, illustrate that the addition of some Ar significantly expands the plasma. The effect of this is to increase the uniformity of [H] across the substrate diameter, an effect beneficial for homogeneous hydrogen termination, etching, and when methane is present, diamond growth, across larger areas in MW-activated (C/)H(/Ar) plasmas compared to the same conditions but without the presence of Ar, i.e. in MW-activated (C/)H plasmas.

The first evidence for the presence of anions is experimentally demonstrated in Chapter 4. This was achieved through the observation of emissions originating from the transition $C_2^-(B\rightarrow X)(0\text{-}0)$. Such an emission is embedded within the well-studied $C_2(d\rightarrow a)$, $\Delta v = -1$ emission, and hence has, until recently, remained elusive. Through comparisons with 2D modelling, it has been possible to deduce the prominent formation (and loss) mechanisms of the various states of C_2, and C_2^- through developing a rationale on how their monitored emissions vary spatially and with respect to process conditions. It transpires the emitting state of C_2^-* is generated via dissociative electron attachment of C_2H (rather than electron impact excitation). Further modelling demonstrated that C_2H^- and CN^- are both also theoretical possibilities, formed through dissociative electron attachment of C_2H_2 and HCN respectively. The latter will be present whenever there is air contamination present within the plasma. This chapter addresses the second half of Question vii and Question viii on the first list of questions and contributes to Question xii in the context of anion chemistry.

Chapter 5 investigates emissions from the 3 lowest doublet excited states of the CH radical in MW-activated C/H plasmas with the intention of exploring the possibility of a sensitive thermal electron probe, and investigating the impact that varying substrate diameter would have on gas phase processes occurring within MW-activated C/H plasmas when T_{sub} is suitably controlled, i.e. expanding on Questions iii to vii on the first list of questions. It transpires that the lowest lying CH doublet excited states, the CH(A) and CH(B) states likely have a substantial reactive contribution in its formation, (i.e. a chemiluminescent contribution), that surpasses EIE (electron impact excitation) of the CH(X) state as the prominent source of these emitting states in the hot plasma regions. Dependent on which of the three (at present, indistinguished) proposed excitation mechanisms dominate, the conclusion may also extrapolate to the C_2(d) state studied in Chapter 4. Nonetheless, for $T_g \leq 2000$ K, it transpires that these

bands can still be used to probe the thermal component of the EEDF once reactive quenching has been considered. Therefore, to infer changes in n_e and / or the [CH(X)] radical, one would be better off monitoring the CH(C) state.

Chapter 6 combines OES and CRDS with 2-D plasma modelling to address Questions ix and x on the first list of questions and Question xvi in the additional list of questions, i.e. through combining a literature review of possible Si/H processes and an understanding of MW-activated H and C/H plasmas with diagnostic studies carried out on MW-activated Si/H, it is possible to speculate on prominent processes and speculatively rationalise the behaviour of Si-related species in MW-activated Si/H plasmas. Again, chemiluminescent contributions are evidenced for the production of SiH*.

By contrasting the method of introducing Si into the gas phase (by using dilute silane and through etching / thermal desorption of a surface activated silicon substrate) and the behaviour of the relevant emission intensities (and measured column densities) upon the addition of some methane, it seems probable that Si atoms are predominantly incorporated into the diamond lattice via thermal migration during the chemical vapour deposition process when grown heteroepitxially onto a silicon substrate, whilst incorporation via the gas phase is expected to be more prominent when silane is introduced as the source of silicon.

7.2: Further Work

This thesis demonstrates promising results, whilst addressing a range of questions in relation to plasma diagnostics applicable to MW-activated H, H/Ar, C/H, C/H/Ar, Si/H, Si/H/Ar and Si/C/H plasmas, and diamond growth more broadly. The findings highlight the interdependencies of various plasma parameters and the impact these have on the excitation (and quenching) of emitting species. The studies provide a critique of diagnostic techniques associated with optical emission spectroscopy, develops a better understanding behind the available toolkit and expands on both (the understanding and the available toolkit) for future MW-activated H-based plasma diagnostic investigations. Many of the conclusions reached in this thesis rely on the analysis of optical emissions being interpreted through an appropriately developed 2-D physical chemical plasma model. The requirement for such modelling highlights the difficulties associated with interpreting OES data at face value.

One of the interesting conclusions with Ar addition from a diamond growth perspective is that it can act to enhance radial uniformity of radicals across a substrate, i.e. facilitating growth uniformity, which combined with the radial expansion associated with Ar addition, could contribute an enhancement in spatial efficiency, a point of environmental interest (more diamonds can be grown across a larger surface area, reducing waste carbon contributions into the atmosphere and energy consumption per diamond grown). A natural expansion to this work would be to carry out comparative diamond growth experiments, (and diamond etching in MW-activated H plasmas) to demonstrate enhanced growth (/

etching) uniformity when Ar is present. Such experiments could be carried out as a function of radial distance with and without the presence of Ar, as a function of substrate diameter, and a combination of these. A larger substrate diameter with Ar present might be expected to provide a larger and more uniform plasma above the substrate (and therefore enhance growth uniformity) unlocking an alternative means to deposit across larger surface areas using MW-activated C/H plasmas (without compromising diamond quality or altering the input MW frequency; a parameter space worth investigating to unlock higher power densities). These studies would act to confirm, reinforce, and expand on the findings and general conclusions reached within this thesis, and further enhance the understanding behind the impact these plasma parameters have on diamond growth / etching.

For such studies to have maximal impact, it must be understood what impact the presence of a diamond substrate has on plasma parameters. This warrants further OES investigations on substrate material, size, shape, thickness, chemical activity etc, as is begun in Chapter 3 with varying substrate diameter, the introduction of Al_2O_3 substrates, and in Chapter 6 with the addition of a silicon wafer disc. This thesis contributes to the available toolkit required for such studies and illustrates how such studies could be carried out.

Chapter 6 also provides a preliminary insight into MW-activated Si/H plasmas and a proposed benchmark model for understanding MW-activated Si/C/H plasmas. Further OES analysis, CRDS collection, complementary 2-D plasma modelling of MW-activated Si/C/H plasmas and growth experiments (providing a comparison between the use of silane and silicon substrates) are required for a more complete understanding.

As demonstrated in Chapter 6, time-resolved OES studies can be useful for demonstrating how the contents of a plasma (and the impacted parameters) vary as a f(time), as exampled with silicon content (inferred by the evolution of $I(\mathrm{Si}^*)(t)$) and the hyper-thermal component of the EEDF (inferred by the time evolution of $I(\mathrm{H}^*)(t)$). With my guidance, Talia Solel demonstrated in her thesis that the concept extends to $I(\mathrm{C_2}^*)(t)$, which can be taken as a useful indicator for the time evolution of total carbon content within the hot plasma region of a custom designed DC-activated C/H plasma with a particularly large volume.[1]

There are additional time-evolutionary systems that my colleagues and I have since envisaged and experimented with in a collaborative effort to enhance the overall carbon efficiency during diamond CVD growth. These results are currently awaiting a patent application, but provide further demonstration that $I(\mathrm{C_2}^*)(t)$ and $I(\mathrm{CH}^*)(t)$ can be taken as indicative of time-evolving total carbon content and CH_x group radicals respectively.

An alternative means to grow diamond more efficiently (with regards to gas usage, in addition to those aforementioned) might be to dramatically reduce the total gas flow, whilst maintaining a constant pressure and input C/H ratio. The advantage of lower gas flows would be to conserve expensive gases,

reducing expense and environmental impact. Such a system could take a substantial time period to reach steady-state, and therefore might be expected to demonstrate some level of time-evolution within the gas phase chemistry, and hence time-resolved OES would make a suitable method to probe such systems. Theoretically, reducing gas flow should not significantly disrupt number densities of different radical species for a plasma operating under steady-state at a fixed pressure, and therefore growth rate should hypothetically be invariant within a perfectly vacuum-tight system.

In a more realistic system, however, there is a trade off between the advantages of reduced total gas flow and the advantages associated with the use of higher gas flows; in accordance to Equation 2.20 (a) in Chapter 2, the use of a higher total gas flow acts to reduce vacuum leak contributions. Therefore, care must be taken to minimise such contributions; one approach to avoid this might be to minimise air leak contributions (*cf*. air impurities of the sourced gases), another might be to minimise both air leaks and air impurities of the sourced gases.

An interesting follow on study that I will be working on as part of my Bristol postdoctoral research contract is to facilitate a bridging between these two cases, i.e. investigating the gas phase processes and diamond growth as a function of total gas flow (and time when appropriate). A careful exploration of these parameter spaces should facilitate a compromise between the conceived advantages of a large gas flow (i.e. a dilution and more rapid removal of air impurity from any vacuum air leak) and the advantages of total gas flow reduction (i.e. enhancing growth efficiency, minimising use of expensive gases, waste of gases, and a minimisation of environmental impact).

Reference

[1] Solel T. “Analysing the Growth Characteristics of a Pulsed Direct Current Plasma Deposition Reactor (PDC PDR)” Undergraduate final year Dissertation, University of Bristol, 2017.

Appendices

A2: Appendix for Chapter 2

A2.1: A brief derivation demonstrating population inversion for an Nd:Yag laser.

i.e. $N(^4F_{5/2}) \approx N(^4I_{11/2}) \approx N(^4I_{13/2}) \approx 0$, $N_{tot} \approx N(^4F_{9/2}) + N(^4F_{3/2})$

Neglecting degeneracy of states for simplicity;

$$\frac{dN(^4I_{\frac{3}{2}})}{dt} = W_p N(^4I_{\frac{9}{2}}) - A_{\left(\frac{3}{2}\rightarrow\frac{11}{2}\right)} N(^4FI_{\frac{3}{2}}) - W_{\left(\frac{3}{2}\rightarrow\frac{11}{2}\right)} N(^4F_{\frac{3}{2}}) + W_{\left(\frac{11}{2}\rightarrow\frac{3}{2}\right)} N(^4I_{\frac{11}{2}})$$

$$= W_p N(^4I_{\frac{9}{2}}) - A_{\left(\frac{3}{2}\rightarrow\frac{11}{2}\right)} N(^4F_{\frac{3}{2}}) - \rho c B_{\left(\frac{3}{2}\rightarrow\frac{11}{2}\right)} (N(^4F_{\frac{3}{2}}) - N(^4I_{\frac{11}{2}}))$$

By assuming $d\,N(^4F_{3/2})/dt = 0$, and that $N(^4F_{\frac{3}{2}}) - N(^4I_{\frac{11}{2}}) = \Delta N$;

$$0 \approx W_p N_{tot} - (W_p + A_{\left(\frac{3}{2}\rightarrow\frac{11}{2}\right)} + \rho c B_{\left(\frac{3}{2}\rightarrow\frac{11}{2}\right)})\Delta N$$

i.e. $\Delta N \approx \frac{W_p N_{tot}}{W_p + A_{\left(\frac{3}{2}\rightarrow\frac{11}{2}\right)} + \rho c B_{\left(\frac{3}{2}\rightarrow\frac{11}{2}\right)}} > 0$

where $N(X)$ = the population of state X, Wp is the effective pumping rate, A = Einstein A emission coefficient of a transition, B = Einstein-B absorption coefficient of a transition, ρ = the radiation density, and c = the speed of light.

A3: Appendix for Chapter 3

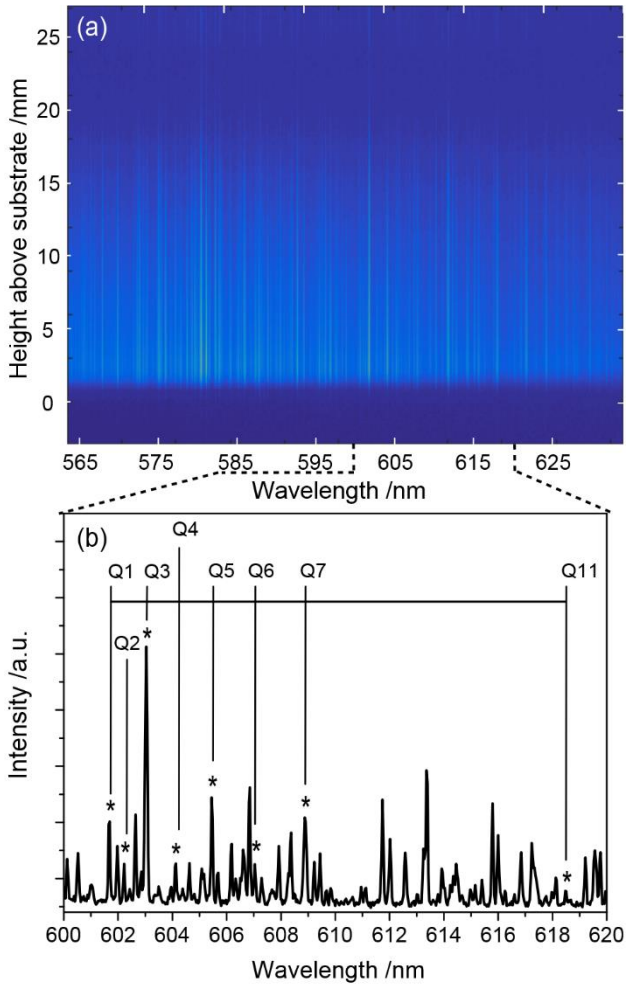

A3.1: (a) $I_{em}(\lambda, z)$ image taken under base conditions in the λ range (horizontal axis) between 564 and 635 nm, and a vertical axis spanning $-3 \leq z \leq 27$ mm, whereby $z = 0$ defines the top of the substrate. (b) The H_2(d→a)(0-0) Q-branch lines up to Q11 are identified with the intensity summed between $3 \leq z \leq 6$ mm.

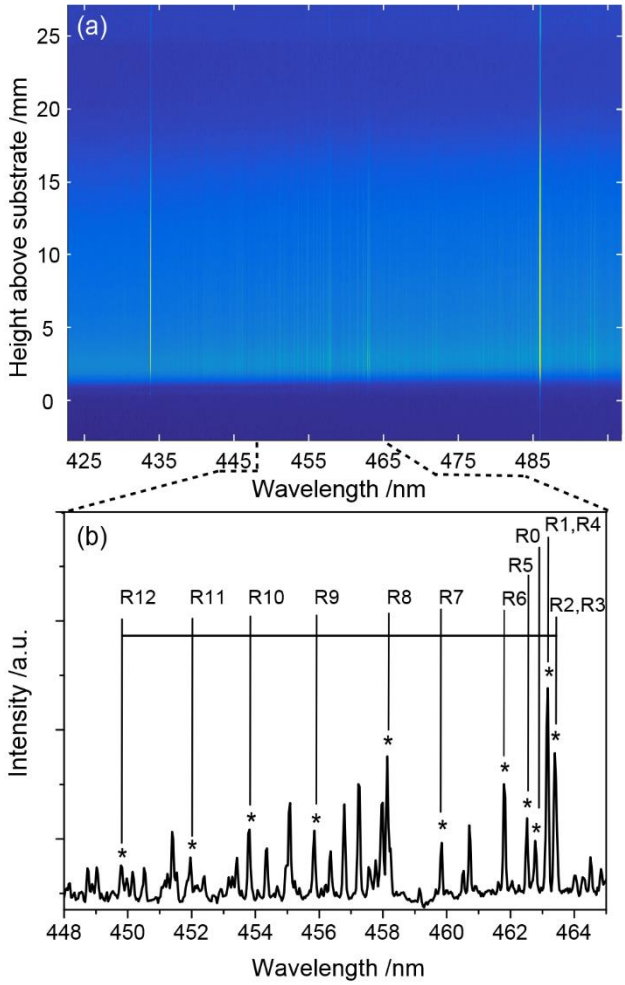

A3.2: (a) $I_{em}(\lambda, z)$ image taken under base conditions in the λ range (horizontal axis) between 422 and 497 nm, and a vertical axis spanning $-3 \leq z \leq 27$ mm, whereby $z = 0$ defines the top of the substrate. (b) The H_2(d→a)(0-0) Q-branch lines up to Q11 are identified with the intensity summed between $3 \leq z \leq 6$ mm.

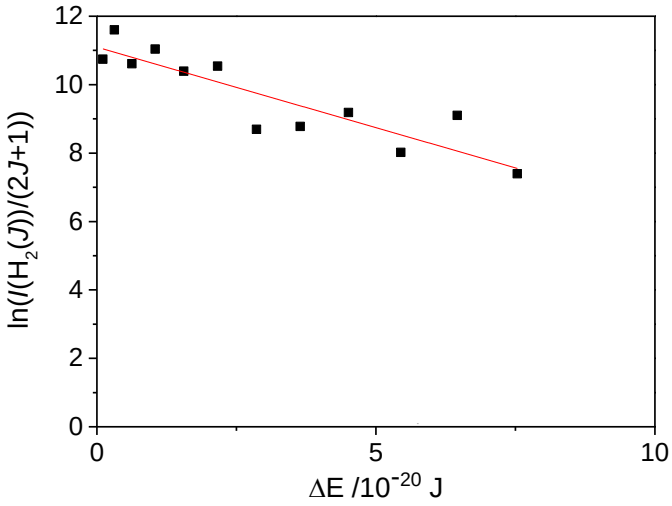

A3.3: A Boltzmann plot carried out on $I_{em}(H_2(e \rightarrow a))$ analysed between $9 \leq z \leq 12$ mm under base conditions, as defined for Chapter 3. Line of best fit gradient = $-(4.7 \pm 0.7) \times 10^{19}$ J^{-1}.

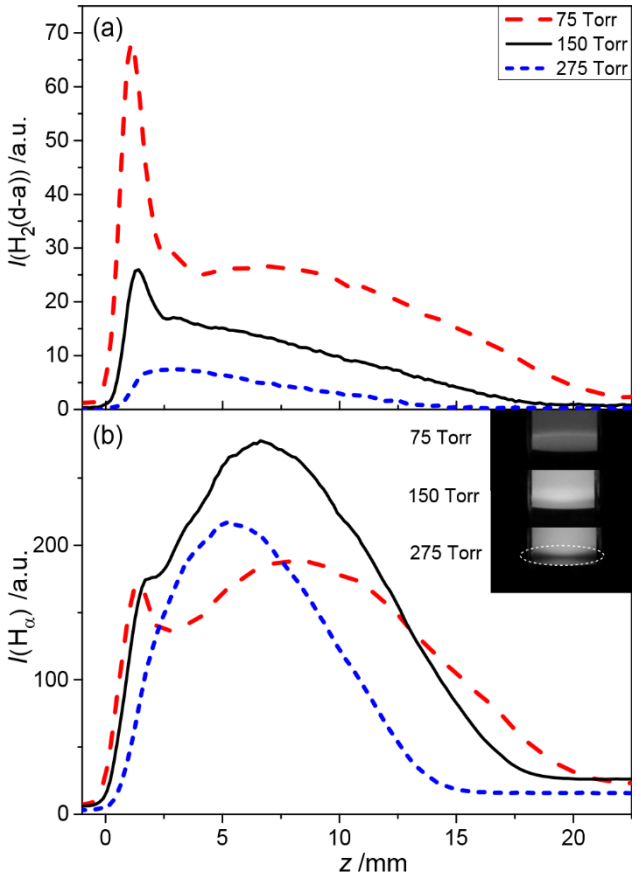

A3.4: (a) $I(H_2(d\rightarrow a))$ and (b) $I(H_\alpha)$ emission profiles, for p = 75 (dashed red), 150 (continuous black) and 275 (smaller dashed blue) Torr (identified in the inset of (a)) with a 17 mm substrate and a spacer wire of 0.004″, for P = 0.9 kW under otherwise base conditions. Figure (b) inset illustrates a black and white photograph illustrating the annular ring present under p = 75 Torr and p = 150 Torr, d_{sub} = 17 mm under otherwise base conditions.

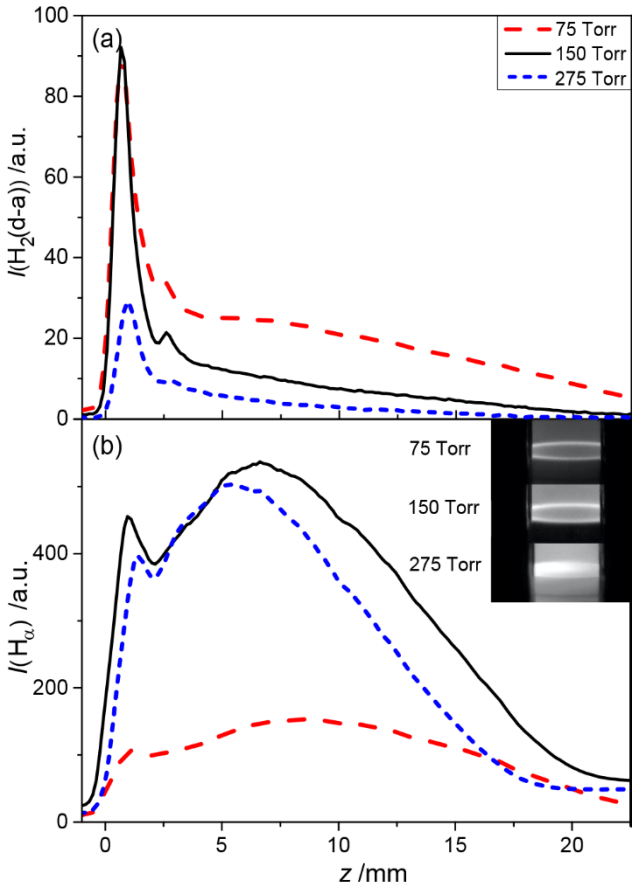

A3.5: (a) $I(H_2(d \rightarrow a))$ and (b) $I(H_\alpha)$ emission profiles, for p = 75 (dashed red), 150 (continuous black) and 275 (smaller dashed blue) Torr (identified in the inset of (a)) with a 17 mm substrate and a spacer wire of 0.004″, for P = 1.85 kW under otherwise base conditions. Figure (b) inset illustrates a black and white photograph illustrating the annular ring present under p = 75 Torr and p = 150 Torr, d_{sub} = 17 mm under otherwise base conditions.

A4: Appendix for Chapter 4

Appendix diagrams for Chapter 4:

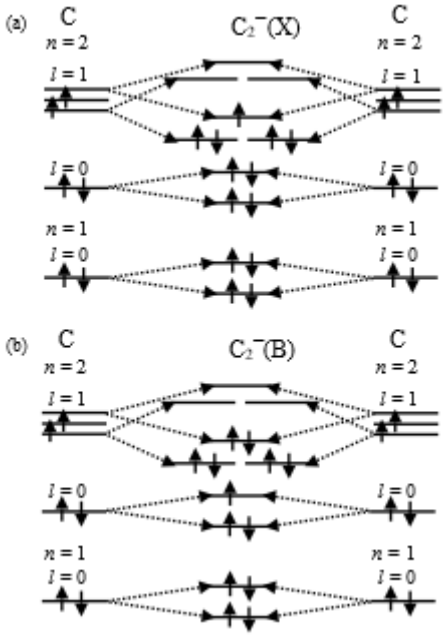

A4.1: A proposed molecular orbital diagram of C_2^- (a) ground state and (b) investigated excited state formed by linear combination of the orbital states of two interacting C atoms.

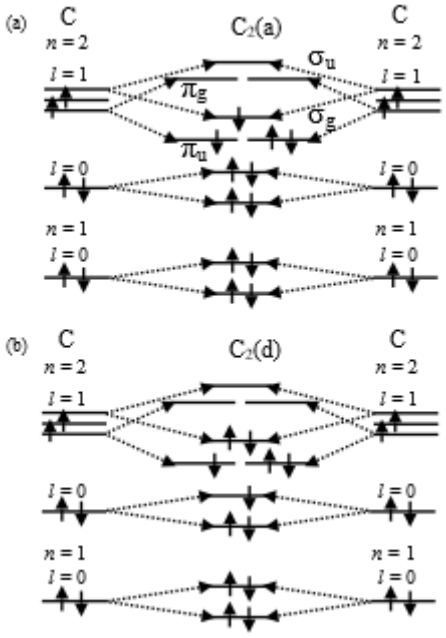

A4.2: A proposed molecular orbital diagram of C_2 (a) lowest lying metastable triplet state and (b) investigated excited state formed by linear combination of the orbital states of two interacting C atoms.

A4.3: A derivation for equating emission intensities to plasma parameters, featuring in Equation 4.07.

$$[C_2(a)] = \frac{Rate\ of\ Forward\ Reaction\ 4.01}{Rate\ of\ Backward\ Reaction\ 4.01} \times \frac{Rate\ of\ Forward\ Reaction\ 4.02}{Rate\ of\ Backward\ Reaction\ 4.02}$$

$$[C_2(a)] = \frac{[C_2H_2][H]k_{4.01}}{[C_2H][H_2]k_{-4.01}} \times \frac{[C_2H][H]k_{4.02}}{[H_2]k_{-4.02}}$$

The $[C_2H]$ cancel on the numerator and denominator to give:

$$[C_2(a)] = \frac{[C_2H_2] \times k_{4.01} \times k_{4.02}}{k_{-4.01} \times k_{-4.02}} \times \frac{[H]^2}{[H_2]^2}$$

$[C_2(d)]$ can be calculated by balancing Process 4.03 with Processes 4.04 and 4.05:

$$[C_2(d)] = [C_2(a)] \frac{n_e \times k_{4.03}}{A_{4.04} + [H_2] \times k_{4.05}}$$

Crudely, the column density of $C_2(d)$ can be approximated as:

$$\{C_2(d)\} \sim 2R_{pl}[C_2(d)]$$

By assuming that the emission observed is proportional to the column density of C_2*, one can derive Equation 4.07: [1]

$$I_{em}(C_2^*) \sim 2R_{pl}\left(\frac{n_e \times k_{5.03}}{A_{5.04} + [H_2] \times k_{5.05}}\right) \times \frac{[C_2H_2] \times k_{4.01} \times k_{4.02}}{k_{-4.01} \times k_{-4.02}} \times \frac{[H]^2}{[H_2]^2} \quad (4.07)$$

Terms have been defined in the relevant sections of Chapter 4.

A4.4: A derivation for equating emission intensities to plasma parameters, featuring in Equation 4.19.

$$Rate\ of\ {C_2}^{-*}Formation = Rate\ of\ {C_2}^{-*}\ Loss$$

$$k_{5.17}\,[C_2H] \times n_e = ([H]k_{-5.17} + A_{5.18}) \times [{C_2}^{-*}]$$

$$[{C_2}^{-*}] = \frac{k_{5.17}\,[C_2H] \times n_e}{[H]k_{-5.17} + A_{5.18}} = \frac{k_{5.17}\,[C_2H_2] \times n_e}{[H]k_{-5.17} + A_{5.18}} \times \frac{k_{5.01}}{k_{-5.01}} \times \frac{[H]}{[H_2]}$$

Following a similar conversion of $[C_2^{-}*]$ to $\{C_2^{-}*\}$ as used for $\{C_2(d)\}$, $I_{em}(C_2^{-}*)$ can be approximated, as given by Equation 4.19.

$$I_{em}({C_2}^{-*}) \sim 2R_{pl} \times \frac{k_{5.17}\,[C_2H_2] \times n_e}{[H] \times k_{-5.17} + A_{5.18}} \times \frac{k_{5.01}}{k_{-5.01}} \times \frac{[H]}{[H_2]} \quad (4.19)$$

Terms have been defined in the relevant sections of Chapter 4.

A5: Appendix for Chapter 5

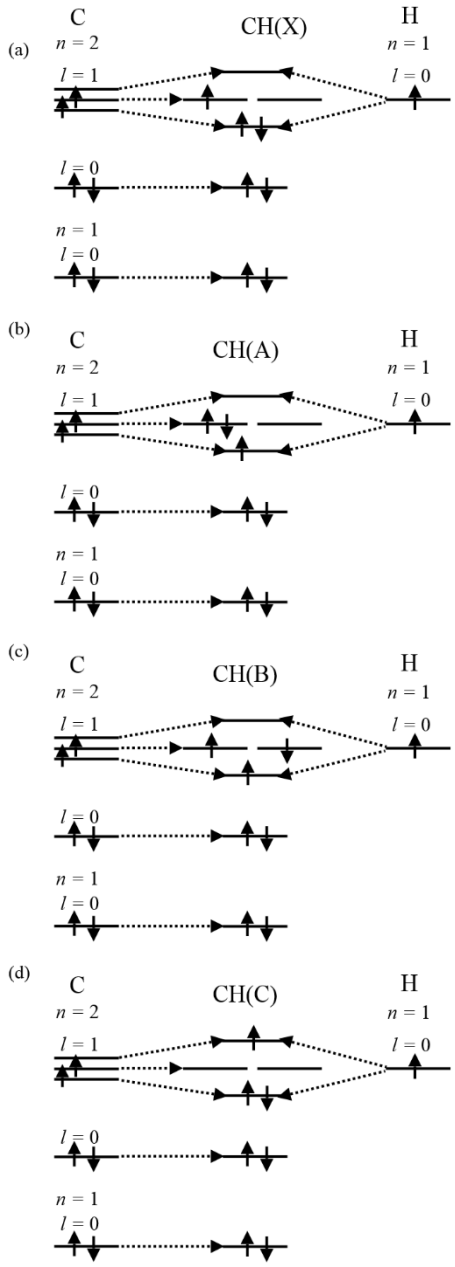

A5.1: A proposed molecular orbital diagram of CH doublet (a) ground state (b) lowest lying excited state, (c) second lowest lying excited state and (d) third lowest lying excited state formed by linear combination of the orbital states of an H atom interacting with a C atom.

A5.2: A brief derivation for Equation 5.03

$$R\left(\frac{C}{A}\right) = \frac{A_c\lambda_A\varepsilon_{detC}k_{EIE}(C \leftarrow X)(k_{QA}[Q] + A_A)}{A_A\lambda_C\varepsilon_{detA}k_{EIE}(A \leftarrow X)(k_{QC}[Q] + A_C)} = R(A)R(\lambda)R(\varepsilon)\frac{k_{EIE}(C \leftarrow X)(k_{QA}[Q] + A_A)}{k_{EIE}(A \leftarrow X)\left(k_{QC}[Q] + A_C\right)}$$

$$\frac{k_{EIE}(C \leftarrow X)}{k_{EIE}(A \leftarrow X)} = e^{-\Delta E/kT_e}$$

$$R\left(\frac{C}{A}\right) = R(A)R(\lambda)R(\varepsilon)\frac{(k_{QA}[Q] + A_A)}{\left(k_{QC}[Q] + A_C\right)}e^{-\Delta E/kT_e}$$

DIFFRACTION GRATING SPECIFICATION SHEET

Catalog no.	**53-*-455R**			2/6/2015
Grating Description	700 g/mm plane ruled reflection grating with 10.5° nominal blaze angle			
Master no.	1665			
	Maximum Ruled Area:	groove length		104 mm
		ruled width:		102 mm

Efficiency Curve	spectral order:	m = 1	polarization(s):	S, P & Average
	Coating:	aluminum		
Remarks:	Measured under near Littrow conditions on the AEC.			

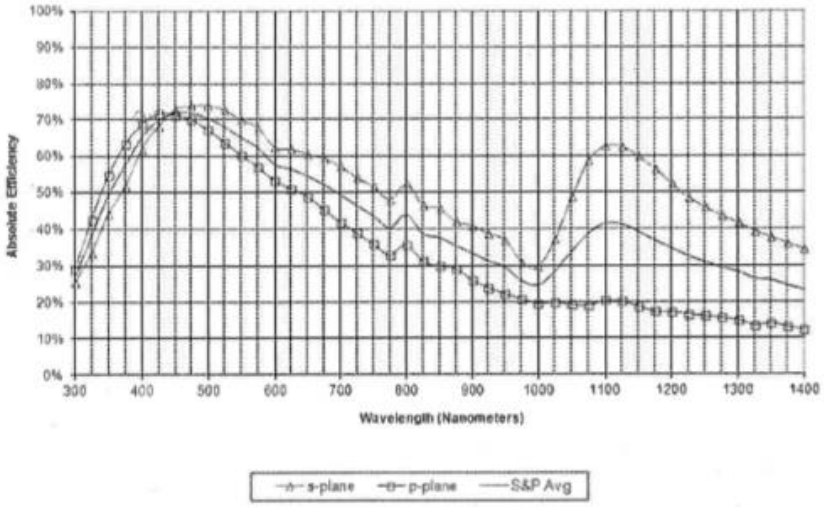

Note: The efficiency curve above is absolute and was measured in an in-plane near Littrow configuration (unless otherwise indicated). Efficiency curves are only representative: actual efficiency may vary significantly depending on use geometry and measurement technique. This efficiency curve is for master 1665; two masters with the same catalog number may have different efficiency curves. The uncertainty band on the data in the above efficiency curve(s) is +/- three percentage points.

A5.3: Reflection efficiency of the most implemented grating utilised in this Thesis, 700 groves mm^{-1} as a *f*(λ).

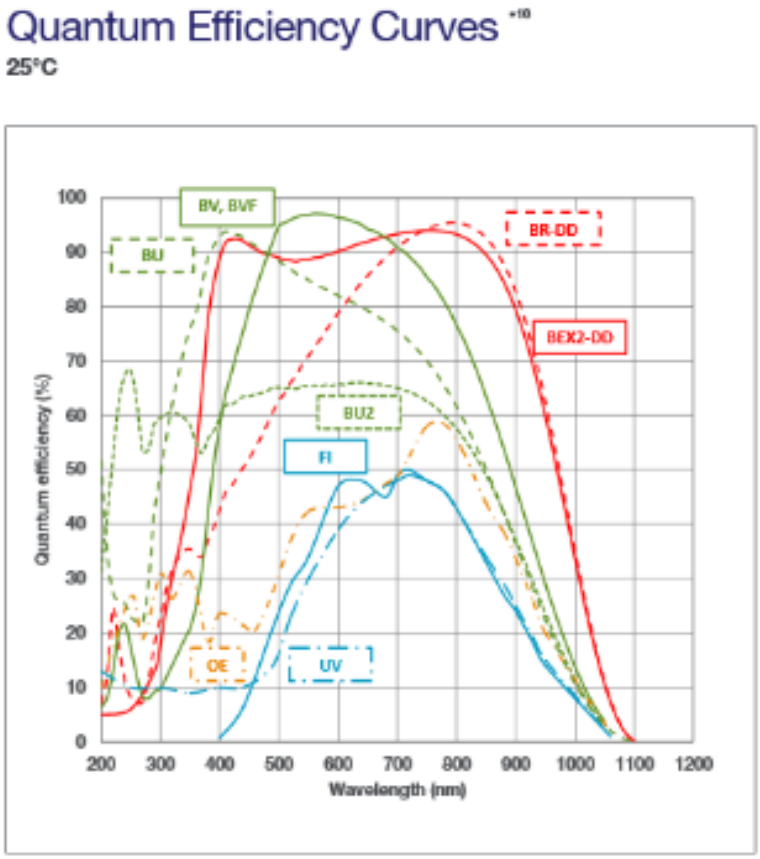

A5.4: BU curve demonstrates detection efficiency of the Newton 940 CCD as a *f*(λ).

A5.5: A Relaxation of Equation 5.04

$$R\left(\frac{C}{A}\right) = m\, e^{-\Delta E/kT_e}$$

Equation 5.04 can be differentiated with respect to kT_e:

$$\frac{dR\left(\frac{C}{A}\right)}{dkT_e} = \frac{\Delta E}{(kT_e)^2} \times m\, e^{-\frac{\Delta E}{kT_e}} = \frac{\Delta E}{(kT_e)^2} \times R\left(\frac{C}{A}\right)$$

Under the assumption that dR(C/A)/dT_e = dR(C/A)/dz × dz/ dT_e, this can be rearranged to give:

$$\frac{dkT_e}{dz} = \frac{dR\left(\frac{C}{A}\right)}{dz} \times \frac{(kT_e(z))^2}{\Delta E} \times \frac{1}{R\left(\frac{C}{A}\right)}$$

dT_e/dz can then be integrated:

$$kT_e(z) = \frac{-\Delta E}{\ln\left[R\left(\frac{C}{A}\right)(z)\right]}$$

$kT_e(z + dz)$ can be approximated as:

$$kT_e(z + dz) = kT_e(z) + \Delta z \frac{dkT_e}{dz} + \Delta z^2 \frac{d^2kT_e}{dz^2} \ldots$$

Where d^2T_e/dz^2 is given by:

$$\frac{d^2kT_e}{d^2z} = \frac{d^2R\left(\frac{C}{A}\right)}{d^2z} \times \frac{(kT_e(z))^2}{\Delta E} \times \frac{1}{R\left(\frac{C}{A}\right)} + \left(\frac{dR\left(\frac{C}{A}\right)}{dz}\right)^2 \times \frac{(kT_e(z))^2}{\Delta E} \times \frac{1}{R\left(\frac{C}{A}\right)^2} \times \left(\frac{2kT_e}{\Delta E} - 1\right)$$

Assuming that $\Delta z^2 \times d^2T_e/dz^2 << \Delta z \times dT_e/dz$:

$$kT_e(z + dz) = kT_e(z) + \Delta z \times \frac{dR\left(\frac{C}{A}\right)}{dz} \times \frac{(kT_e(z))^2}{\Delta E} \times \frac{1}{R\left(\frac{C}{A}\right)}$$

Where d(R(C/A))/dz can be derived from the previously reported R(C/A)(z) under the assumption that Δz = dz = 1.5 mm. $T_e(z + 2dz)$ and $T_e(z - dz)$ can be calculated iteratively from the above by redefining $T_e(z + dz)$ as $T_e(z)$. Produces incorrect $T_e(z)$ and even negative values at low z; requires a more careful consideration of boundary conditions. Fits the form of $T_e(z) = 1/\ln(mI_A/I_C)^{\beta}(z))$.

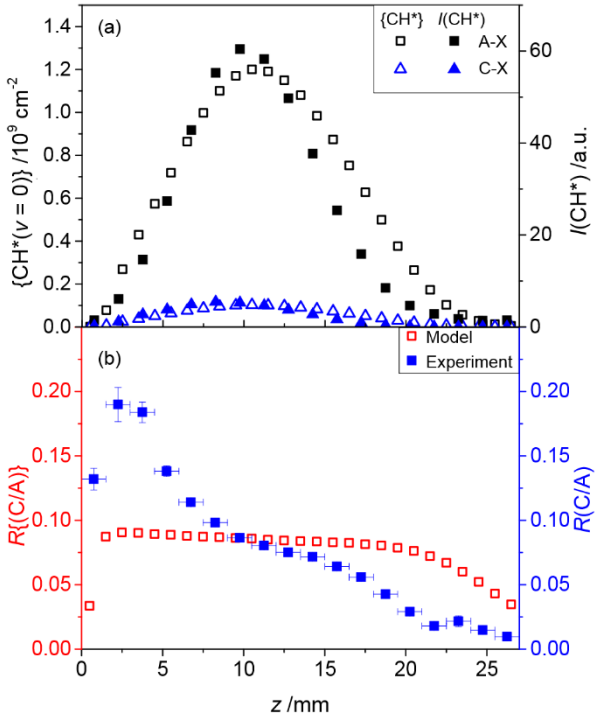

A5.6: I_{em}(C→X), I_{em}(A→X), R(C/A), modelled {CH(A)}, {CH(C)} and their ratio, i.e. {CH(C)}/{CH(A)} labelled as R{(C/A)} under base conditions with consideration of Electron Impact Excitation and photoemission.

A6: Appendix for Chapter 6

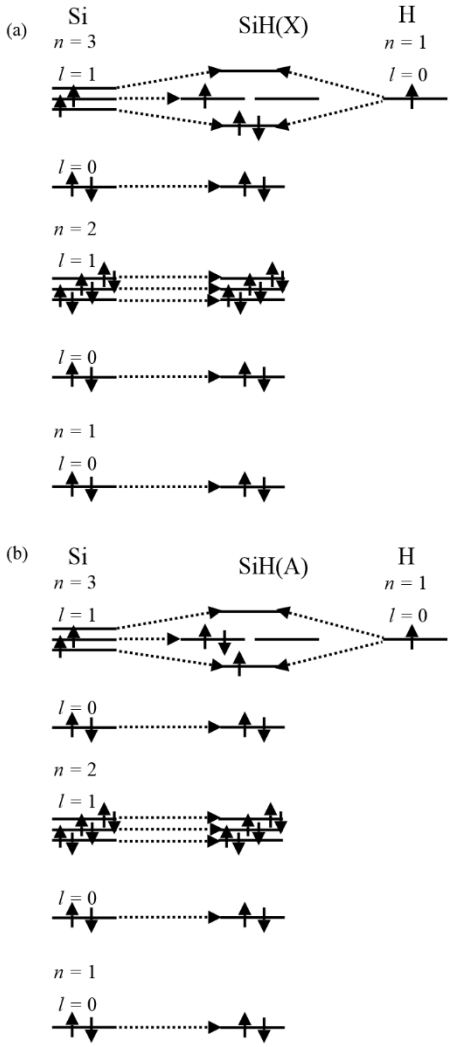

A6.1: A proposed molecular orbital diagram of SiH doublet (a) ground state (b) lowest lying excited state, formed by a linear combination of the orbital states of an H atom interacting with a Si atom.

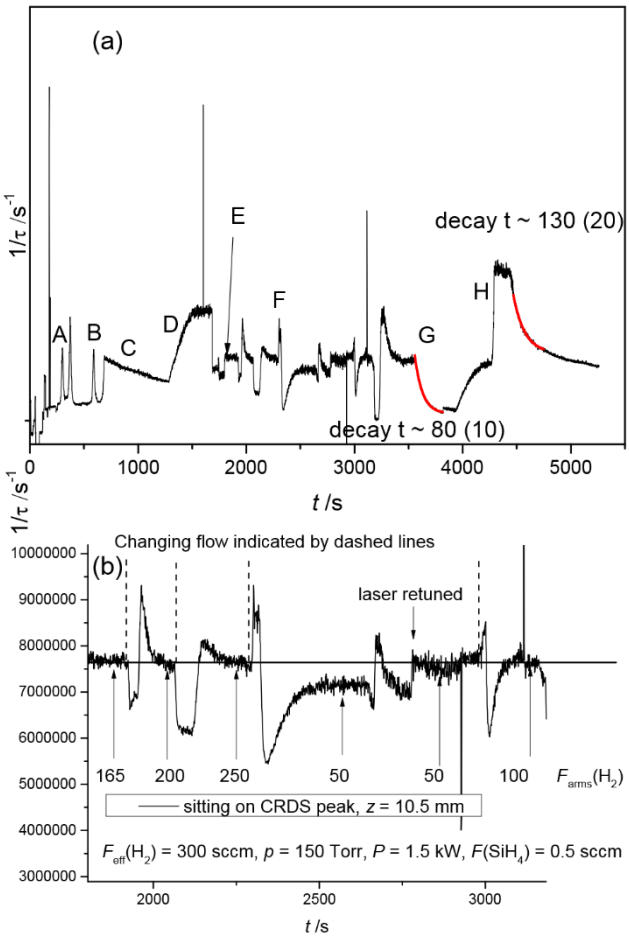

A6.2: (a) An illustrative diagram demonstrating the Si($3s^2 3p4s$, $^3P^o$, $J = 0 \leftarrow 3s^2 3p^2$, ^3P, $J = 1$). Notably, A and B demonstrate the peak as a function of wavenumber, and G demonstrates an exponential decay upon sitting on the peak absorption and turning off the silane flow. (b) a zoomed in region of (a) sitting on the peak Si absorption and varying $F_{arms}(H_2)$ (labelled on diagram), whilst maintaining a constant $F_{eff}(H_2)$. The diagram is illustrative that peak absorption did not vary substantially upon the variation of $F_{arms}(H_2)$.

Graph A6.2 illustrates Si absorption, as a function of height, gas flows, and are plotted as a function of time. No attempt has been made to spectrally calibrate this data, it is reported as collected as a function of time. In Figure A6.2 (a), A and B are wavelength scans at z = 10.5 and 25.7 mm across the Si absorption peak, C is a near absorption peak decay occurring due to a switch off at silane (z = 25.7 mm). Silane is turned on to $F(SiH_4)$ = 0.5 sccm at D, E is locating the exact Si peak absorption at z = 10.5 mm, of which region F and onward is collected. F is covered in Figure A6.2 (b), G is an exponential decay of Si after switching off silane, H features a decay from the same flow rate at z = 25.7 mm, same silane flow. Figure A6.1 (b) illustrates, that provided the laser power doesn't drop significantly and that there is no signal saturation, after a flow adjustment period, the absorption of laser light by Si atoms remains the same for $F_{eff}(H_2)$ = 300 sccm, $F(SiH_4)$ = 0.5 sccm, p = 150 Torr, P = 1.5 kW, z = 10.5 mm, between the range of $50 \leq F_{arms}(H_2) \leq 250$ sccm, i.e. gas flown through the arms is well-mixed with the plasma (and well calibrated), an assumption made in Chapter 6.

A6.3: Table of % change in {Si(J = 0)} with $F_{arms}(H_2)$ via Indicative Areas

	$F_{arms}(H_2)$ = 100 sccm	$F_{arms}(H_2)$ = 300 sccm	$F_{arms}(H_2)$ = 500 sccm
Uncalibrated Area	9.464×10^{17}	1.056×10^{18}	9.985×10^{17}
% change in {Si(J = 0)}	−10.3%	0%	−6.72%

A6.3: Table calculating an uncalibrated Guassian fitted peak area for $F_{arms}(H_2)$ = 100, 300 and 500 sccm (F_{tot}(H2) = 600 sccm) under otherwise CRDS defined base conditions (for a MW-activated Si/H plasma), as defined in Chapter 6. Second row demonstrates percentage change in peak area (and therefore {Si(J = 0)}) as a $f(F_{arms}(H_2))$ relative to $F_{arms}(H_2)$ = 300 sccm for $F(SiH_4/H_2)$ = 0.5 sccm.

A6.4: Si_2H_x species

With higher fractions of methane, C_2H_a ($0 \leq a \leq 6$) species dominate, generated by CH_z ($0 \leq z \leq 3$) radical-radical addition reactions. An explanation, which may account for the missing Si content could be the presence of $[Si_2H_{x+z-y}]$ radicals generated by SiH_x and SiH_z addition reactions, whereby $0 \leq x \leq 4$, $0 \leq z \leq 3$ and $0 \leq y \leq 2$ as described by Process A6.1:

$$SiH_x + SiH_z \leftrightarrow Si_2H_{x+z-y} + H_y \qquad \text{(A6.1)}$$

Process 6.14 is a generic reaction representing Si-Si radical addition. The forward reaction relies on two minority species, whilst the reverse reaction relies on a majority species. For Process A6.1 to be significant, the forward reaction would require large rate coefficients. References 1 and 2 both provide incomplete temperature-dependent rate coefficients for some of the proposed reactions. Reference 1 provides more recent values optimised to provide agreement with multiple other author's contributions across a temperature range of ~ $600 \leq T_g \leq 1750$ K but omits slow reactions. Reference 2 provides the temperature-dependence required to calculate rate coefficients for an incomplete list of some faster and slower rates. These values were extrapolated by the authors to T_g = 1800 K for their modelling.

Using Reference 2, it is possible to crudely calculate rate coefficients, rates for T_g = 750 K and 3000 K. The forward reaction of Process A6.1 provides the largest rate coefficient ($k_{+A6.1}$) for x = 2, z = 1, $m = x + z - y$ = 3 (y = 0, i.e. no H atoms) with values of ~ 5.5×10^{-12} and 1.50×10^{-11} $cm^3molecule^{-1}s^{-1}$ for T_g = 750 K and 3000 K. The largest reverse rate coefficient for Process A6.1, ($k_{-A6.1}$), are provided by radicals with x = 4, z = 2, m = 4 and y = 2 yielding rate coefficients of ~ 2.7×10^{-8} and 7.4×10^{-8} $cm^3molecule^{-1}s^{-1}$ for T_g = 750 and 3000 K respectively.

The forward reaction rate coefficient is sufficiently low for two reacting minority species (relative to the faster H-shifting reactions of SiH_z and Si_2H_m species and the calculated $k_{-A6.1}$, which involves collisional dissociation of Si_2H_4 with the majority species, H_2) that the $[Si_2H_m]$ content should be negligible under the investigated conditions.

A6.5: H_xSiOH_m species

There is an unavoidable leak contribution attributed to using the reflective mirrors in the CRDS experiments, (X_0(leak) ~ 10 ppm, which is much larger than the input silane fraction, $X_0(SiH_4)$ = 0.83 ppm under base conditions). This problem is unavoidable with the current setup; using higher silane fractions (under base conditions) results in saturation. Conversely, in the OES experiments reported, the silane fraction used under OES-defined base conditions ($X_0(SiH_4)$ = 47.6 ppm) was significantly larger than the attributed leak rate (0.25 ppm). Alim Lalji's preliminary OES studies [3] carried out under OES-defined base conditions ($X_0(SiH_4)$ = 47.6 ppm) demonstrated that a more comparable leak (X_0(leak) ~ 10 ppm) had little bearing on the reported trends.

As noted in Chapter 3, O_2 impurity within MW-activated H plasmas acts to generate H_2O and OH radicals. There is a rich and complex chemistry between Si- and O- containing species, which have been studied in the context of SiO_2 deposition and atmospheric plasmas. Some of the more important reactants include but are not limited to SiH_4 and SiH_3 reacting with both OH and O_2 and SiH_2 and SiH with O_2. Processes A6.2 and A6.3 (a) and (b), A6.4, A6.5 (a) and (b) and A6.6 are just a few examples.[4]

$$SiH_3 + OH \rightarrow H_2SiO + H_2 \quad \text{(A6.2)}$$

$$SiH + O_2 \rightarrow SiOH + O \quad \text{(A6.3 a)}$$

$$SiH + O_2 \rightarrow SiO_2 + H \quad \text{(A6.3 b)}$$

$$Si(\,^1S) + H_2O \rightarrow SiO + H_2 \quad \text{(A6.4)}$$

$$Si(\,^3P) + OH \rightarrow SiO + H \quad \text{(A6.5 a)}$$

$$Si(\,^3P) + OH \rightarrow SiOH \quad \text{(A6.5 b)}$$

$$SiOH + H \rightarrow Si + H_2O \quad \text{(A6.6)}$$

Processes A6.2 and A6.3 (a) and (b) are crudely reported in Reference 4 to be temperature-independent with rate coefficients of 8.31×10^{-12}, 8.5×10^{-11} and 8.5×10^{-11} $cm^{-3}molecule^{-1}s^{-1}$ respectively.[4] Process A6.5 (a) has also previously been assumed to have a temperature-independence, with an approximated value of ~ 10^{-10} $cm^{-3}molecule^{-1}s^{-1}$. The temperature-dependence has since been produced for Process A6.5 (b) with a rate coefficient of ~ 1.83×10^{-11} and 8.1×10^{-12} $cm^{-3}molecule^{-1}s^{-1}$ for T_g = 750 and 3000 K.[5] Whilst these rate coefficients may be comparable to those estimated for the production of Si_2H_m radicals in the hot plasma regions, reverse reactions are not quoted in Reference 6 indicating that, at least in the cooler regions, rates of $SiOH_x$ removal via thermal decomposition are insignificant. Gómez Martín *et al.* [7] reinforce this notion, noting that once formed, SiO has has no exothermic processes to recycle back to Si in their low temperature studies ($190 \leq T_g \leq 500$ K). Further, the dissociation energy of SiO is estimated to be 7.34 eV, much larger than the thermal energies

available. The authors also note a distinct lack of reactivity between Si(^3P_J) and H_2O, which is spin-forbidden.

Once formed, SiO would require high energy electrons or H atoms to recycle SiO (and by extension $SiOH_x$) radicals back into oxygen-free Si. Through the use of the heat of formation values provided in Table 6.1, the enthalpy of reaction for Processes A6.4, A6.5 (a) and (b), and A6.6 are calculated to be ~ − 3.09 eVmol^{-1}, ~ − 3.72 eVmol^{-1}, ~ − 5.05 eVmol^{-1} and ~ − 0.11 eVmol^{-1} starting with (/ ending in) ground state Si, (i.e. an overestimate for those involving the Si(^{1}S) state), i.e. all are exothermic. Using comparable reactions (i.e. H + $H_2SiOH \rightarrow SiH_2 + H_2O$) from Reference 8, Process A6.6 has been approximated to have rate coefficients of ~ 3.03 × 10^{-12} and 1.01× 10^{-11} cm^{-3}molecule^{-1}s^{-1} for T_g = 750 and 3000 K.

Neglecting additional routes, additional $SiOH_x$ species, and assuming [H_2O] ~ 0.2 [*leak*] ~ 0.2 X_0(*leak*)[H_2], Processes A6.5 (b) and A6.6 can very crudely be approximated to be in a steady-state within the chamber. In doing so, Equation A6.7 can be derived:

$$\frac{[\mathrm{Si}]}{[\mathrm{SiOH}]} = \frac{[\mathrm{H}]k_{A6.6}}{[\mathrm{H_2O}]k_{A6.5\,(b)}} \sim \frac{[\mathrm{H}]k_{A6.6}}{0.2X_0(leak)[\mathrm{H_2}]k_{A6.5\,(b)}} \qquad \text{(A6.7)}$$

Using [H] ~ 4.08 × 10^{15} and 6.67 × 10^{16} cm^{-3} for T_g = 750 K (r = 53.5 mm, z = 10 mm) and ~ 3000 K (r ~ 0 mm, z = 10 mm) and [H_2] ~ 1.92 × 10^{18} and ~ 3.91 × 10^{17} cm^{-3} for these temperatures, Equation A6.7 yields values of ~ 200 and ~ 110,000 for T_g = 750 K and ~3000 K for the CRDS experiments (leak rate of 10 ppm) and of ~ 7000 and ~ 43,00,000 for OES leak rate of 0.25 ppm. Whilst an oversimplified problem, there is an important point that can be taken away from this simple calculation; [$SiOH_x$] radicals are significantly higher in the cool plasma regions (*cf.* the hotter regions). Close to the reactor wall, modelling calculates T_g = 340 to 413 K with [H] ranging between 2.78 × 10^{13} to 1.04 × 10^{15} cm^{-3} and [H_2] = 4.26 to 3.51 × 10^{18} cm^{-3}. Rate coefficients are calculated to be $k_{A6.5\,(b)}$ = 2.9 to 2.6 × 10^{-11} cm^{-3}molecule^{-1}s^{-1} and $k_{A6.6}$ = 1.02 × 10^{-11} cm^{-3}molecule^{-1}s^{-1} with Equation A6.7 yielding values ranging from 1 to 50, i.e. in this particularly crude model, at best, SiOH:Si is ~ 1:1. Whilst this oversimplified model predicts that the majority of Si species should be Si atoms, the reality is many H_xSiOH_y species will be stable and can be formed by many routes, which have not been described, whilst there are fewer possible H_xSiOH_y species loss mechanisms. Further, a 1:1 ratio would act to reduce [Si] content by ~ 50% in the coolest regions (which contributes the highest weighting in {Si} measurements). Process A6.6 is just an exampler provides the largest rate coefficient for such losses. It is therefore believable that oxygen-containing species could dominate in the coolest regions providing a rationale behind the calculated T_{Si} ~ 750 K, rather than the expected T_{Si} ~ 400 K, were the CRDS measurements to be taken at face value; [Si] would otherwise be expected to maximise in the coolest regions of the plasma (assuming a negligible leak, as well as a well-mixed and processed silicon content), the addition of oxygen would act to reduce [Si] in the cooler regions (instead replacing it with

H_xSiOH_y species), and therefore reduce {Si} significantly (which is most sensitive to the coolest regions due to the larger associated number densities, in accordance to the ideal gas law).

Processes A6.2 to A6.6 do not begin to capture the full complexity of Si/H/O dynamics, and to illustrate this, Section A6.6 speculates on the role metastable Si singlet states could play in such chemistry. The reactions and discussion presented above serve to highlight two key points; oxygen may act to perturb MW-activated Si/H chemistry significantly and generate SiO-containing radicals and act as a gutter for SiH_x content in the cool plasma regions.

A6.6: Possible Roles of Metastable Si Singlet States

There is also the possible interplay of the low lying metastable states of Si; the two lowest lying $Si(3s^23p^2)$ singlet states ($^1D_2$ and $^1S_0$) have energies of 0.78 and 1.91 eV respectively (*cf.* <E> ~ 0.259 eV at T_g = 3000 K).[9] If these states maintained a thermal Boltzmann population with the ground state, the relative $Si(^1D_2)$ concentration would be small (~ 2.7% once the 5- and 9-fold degeneracies of the Si singlet ($^1D_2$) and the ground triplet states have been considered). If these states were in a thermal equilibrium dictated by T_e (assumed to be ~1.2 eV), the $Si(^1D_2)$ may account for slightly more {Si} content. Both states can be generated by alternative excitation mechanisms (explored in Section 6.3.2), e.g. by Process 6.13, 6.15 (a), 6.16 (a), 6.17, 6.18 (b), and 6.21, and are metastable at face value, which might act to increase their populations. However, as noted, $Si(^1D_2)$ has a large rate coefficient with H_2O, even at T_g = 300 K ($2.3 \pm 0.3 \times 10^{10}$ cm^3 $molecule^{-1}s^{-1}$)[7], which could facilitate a further enhancement in the gettering of Si content in the form of SiOH radicals.

The formation of such states would require a non-spin conserving EIE from the ground state and may suffer from reactive collisions with H and H_2.[10] This would act to reduce the metastability of the Si singlet states.

At this point, it seems reasonable to make a speculative comparison between Si/H plasmas and N_2/H plasmas. In MW-activated N_2/H_2 plasmas, the metastable $N_2(A^3\Sigma^+_u)$ state holds an energy of 6.2 eV above the ground state (significantly larger than the $Si(^1D_2)$ state) and plays a crucial role in the gas phase chemistry. $N_2(A^3\Sigma^+_u)$ is populated via electron impact excitation of the N_2 ground state and reacts via dissociative H-addition to form NH and N. These radicals can undergo further H-shifting reactions and form a resulting NH_x number density.[11] This draws two stark similarities / comparisons, a potential role of a metastable state, and a loss mechanism (resulting in NH radicals (comparable to SiO) in the analogy). There are two key differences in this comparison; the first is that the energies of the two states (0.78 eV versus 6.2 eV, assuming T_e ~ 1.2 eV) act in favour of producing a larger $Si(^1D_2)$ population; the second is that there are loss mechanism for the resulting NH_x radicals (e.g. two N atoms recombining to form N_2), which would not present in the Si/H case (whereby generation of SiO has been deemed semi-irreversible). In spite of this, the resulting steady-state [$N_2(A^3\Sigma^+_u)$] and [NH_x] number densities account for ~ 2% of total nitrogen content within N_2/H plasmas. Given additional production

mechanisms for the formation mechanism of Si($3s^2 3p^2$, $^1D_2$) state, the significantly lower energy (*cf.* the $N_2(A^3\Sigma^+_u)$ state) and the semi-irreversible production of SiO (when air impurity is present), it could be anticipated that [Si($^1D_2$)] + [$SiOH_z$] make up a significantly larger percentage of the total Si content than [N_2(A)] + [NH_x] do in N_2/H plasmas.[11,12] Inconclusively, this comparison makes it seem reasonable to suggest that the metastable Si singlet states may contribute to an enhancement in the gettering of Si as SiOH radicals, but alone would not account for a significant amount of the missing Si content, whether air is present or not, unless the population was dictated by alternative excitation mechanisms (e.g. quenching of excited states, electron-ion recombination and other mechanisms explored in Section 6.3.2), rather than a Boltzmann distribution centred around T_g = 3000 K (in the hot plasma regions).

The preliminary 2-D modelling is only beginning to account for the metastability of the Si spin-states and their differences in reactivity with air impurity H_2O and therefore, at present, does not comment on these effects.

A6.7: Alternative *I*(Si*) spatial distribution

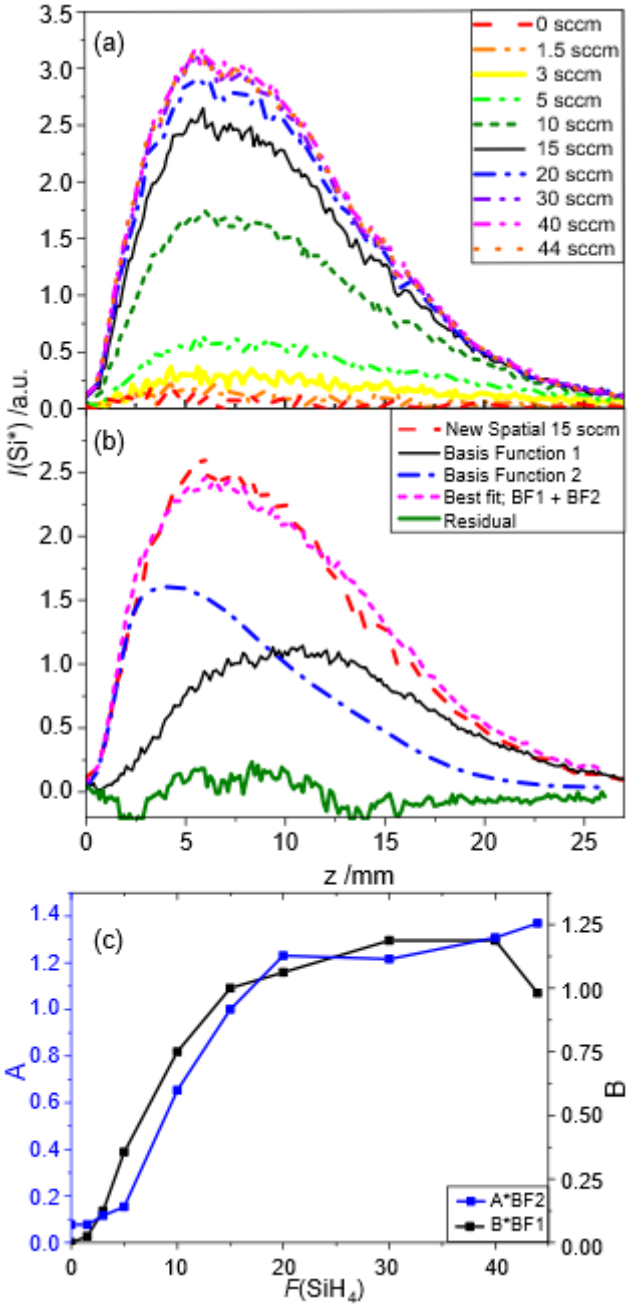

A6.7: (a) Second spatial distribution of *I*(Si*) singlet, which is speculated to arise in a 'dirty' chamber. *I*(Si*) variation with an additional low *z* component as a *f*(*F*(SiH₄)) (5 ppm air impurity) under otherwise MW-activated Si/H OES defined base conditions, as defined in Chapter 6. (b) Under base conditions, *I*(Si*) from Figure A6.7(a), shown in red, can be described by a linear combination of *I*(Si*) (Basis Function 1, the black curve, collected with 5 ppm air impurity by Alim Lalji), under base conditions in a 'clean' chamber (as reported in Chapter 6), and an etching component, Basis Function 2 (collected in a MW-activated H plasma etching a Si substrate under otherwise base conditions, as described / reported in Chapter 6, Section 6.3.8, blue curve). BF1+ BF2 produce the pink 'Best Fit' curve. The reduced residual squared was minimised to fit the 'Best Fit' curve to the red curve. The green curve demonstrates the residual between the two. (c) The multiplication factor A (*BF2 curve) and B (*BF1 curve) used to describe *I*(Si*) reported in A6.7(a), as a function of *F*(SiH₄).

References

[1] Allendorf, M. “A Model of Silicon Carbide Chemical Vapor Deposition,” Journal of the Electrochemical Society, vol 138, no. 3, p. 841, 1991.

[2] Stinespring, C. D., and Wormhoudt, J. C. “Gas phase kinetics analysis and implications for silicon carbide chemical vapor deposition.” Journal of Crystal Growth, vol. 87, no. 4, pp. 481-493, 1988.

[3] Lalji, A. “The use of Optical Emission Spectroscopy to probe microwave-activated silicon-containing hydrogen plasmas” Undergraduate final year Dissertation, University of Bristol, 2018

[4] Kushner, M. J. “Plasma chemistry of $He/O_2/SiH_4$ and $He/N_2O/SiH_4$ mixtures for remote plasma-activated chemical-vapor deposition of silicon dioxide.” Journal of Applied Physics, vol. 74, no. 11, pp. 6538-6553, 1993.

[5] Rivero Santamaría, A., Dayou, F., Rubayo-Soneira, J. and Monnerville, M. “Time-Dependent Quantum Wave Packet Study of the Si + OH → SiO + H Reaction: Cross Sections and Rate Constants.” The Journal of Physical Chemistry A, vol. 121, no. 8, pp. 1675-1685, 2017.

[6] Lucas, D. J, Curtiss, L. A., and Pople, J. A. “Theoretical study of the silicon–oxygen hydrides $SiOH_n$ (n=0–4) and $SiOH_n^+$ (n = 0–5): Dissociation energies, ionization energies, enthalpies of formation, and proton affinities.” The Journal of Chemical Physics, vol. 99, no. 9, pp. 6697-6703, 1993.

[7] Gómez Martín C. J., Blitz, M. A., and Plane, J. A. “Kinetic studies of atmospherically relevant silicon chemistry: Part I: Silicon atom reactions.” Physical Chemistry Chemical Physics, vol. 11, no. 4, pp. 671-678, 2009.

[8] Zachariah, M. R., and Tsang, W. “Theoretical Calculation of Thermochemistry, Energetics, and Kinetics of High-Temperature $Si_xH_yO_z$ Reactions.” The Journal of Physical Chemistry vol. 99, no. 15, pp. 5308-5318, 1995.

[9] Coutinho, L. H., and Trigueiros, A. G. “Weighted oscillator strengths and lifetimes for the Si I spectrum.” Journal of Quantitative Spectroscopy and Radiative Transfer, vol. 75, no. 3, pp. 357-387, 2002.

Radziemski, L. J., and Andrew, K. l. “Arc Spectrum of Silicon” Journal of the Optical Society of America, vol. 55, no. 5, p. 474, 1965.

[10] Kalemos, A., Mavridis, A., and Metropoulos, A. “An accurate description of the ground and excited states of SiH.” The Journal of Chemical Physics, vol. 116, no. 15 pp. 6529-6540, 2002.

[11] Truscott, B. S., Kelly, M. W., Potter, K. J., Johnson, M., Ashfold, M. N. R., and Mankelevich, Yu. A. “Microwave Plasma-Activated Chemical Vapor Deposition of Nitrogen-Doped Diamond. I. N_2/H_2 and NH_3/H_2 Plasmas.” The Journal of Physical Chemistry A, vol 119, no. 52, pp. 12962-12976, 2015.

[12] Raghunath, P., Lee, Y., Wu, S., Wu, J., and Lin, M. “Ab initiochemical kinetics for reactions of H atoms with SiH_x(x = 1-3) radicals and related unimolecular decomposition processes.” International Journal of Quantum Chemistry, vol. 113, no. 12, pp. 1735-1746, 2013.

Publications

1. **Mahoney, E. J. D.,** Truscott, B. S., Ashfold, M. N. R. and Mankelevich, Yu. A. "Optical Emission from C_2^- Anions in Microwave-Activated CH_4/H_2 Plasmas for Chemical Vapor Deposition of Diamond." The Journal of Physical Chemistry A, vol. 121, no. 14, pp. 2760-2772, 2017.

2. Ashfold, M.N.R., **Mahoney, E. J. D.,** Mushtaq, S., Truscott, B. S. T. and Mankelevich, Yu. A., "What [plasma used for growing] diamond can shine like flame?" Chemical Communications, vol. 53, no 76, pp. 10482-10495, 2017.

3. **Mahoney, E. J. D.,** and Ashfold, M. N. R., "Diamond growth using microwave-activated methane/hydrogen plasmas," Atlas of Science. [online] Atlasofscience.org, 2018, Available at: http://atlasofscience.org/diamond-growth-using-microwave-activated-methane-hydrogen-plasmas/

4. **Mahoney, E. J. D.,** Truscott B. S., Mushtaq, S., Ashfold, M. N. R., Mankelevich, Yu. A. "Spatially Resolved Optical Emission and Modeling Studies of Microwave-Activated Hydrogen Plasmas Operating under Conditions Relevant for Diamond Chemical Vapor Deposition." The Journal of Physical Chemistry A. vol. 122, no. 42, pp. 8286-8300, 2018.

5. **Mahoney, E. J. D.,** Mushtaq, S., Ashfold, M. N. R., Mankelevich, Yu. A. "Combined Spatially Resolved Optical Emission Imaging and Modelling Studies of Microwave-Activated H_2/Ar and H_2/Kr Plasmas Operating under Conditions Relevant for Diamond Chemical Vapor Deposition" The Journal of Physical Chemistry A, vol. 13, no. 13, pp. 2544-2558, 2018.

6. Croot, A. E., **Mahoney, E. J. D.,** Dominguez-Andrade, H., Ashfold, M. N. R. and Fox, N. A. "Diamond chemical vapor deposition using a zero-total gas flow environment" Awaiting a patent prior to submission, 2019.

Speculative future publications relevant to this PhD thesis:

7. Chapter 5 – "Imaging and Modelling the Optical Emission from CH Radicals in Microwave-Activated C/H plasmas," **Mahoney, E. J. D.,** Rodriguez, B. J., Truscott, B. S., Ashfold, M. N. R, and Mankelevich, Yu. A.

8. Chapter 6, Part I: "Diagnostic and Modelling studies on MW-activated Si/H plasmas," **Mahoney, E. J. D.,** Lalji, A., Allden, J. W., Truscott, B. S., Smith, J. A., Ashfold, M. N. R., and Mankelevich, Yu. A.

9. Chapter 6, Part II: "Diagnostic and Modelling studies on MW-activated Si/C/H plasmas," **Mahoney E. J. D.,** Allden, J., Truscott, B. S., Smith, J. A., Ashfold, M. N. R., and Mankelevich, Yu. A.